

AD-A263 215



2

PL-TR-93-2027(I)

**PROCEEDINGS OF THE SPACECRAFT CHARGING
TECHNOLOGY CONFERENCE, 1989
VOLUME I**

Editor:

R. C. Olsen

DTIC
ELECTE
APR 2 1993
S C D

**Naval Postgraduate School
Physics Department
MC 61-05
Monterey, CA 93943**

November 1989

APPROVED FOR PUBLIC RELEASE; DISTRIBUTION UNLIMITED

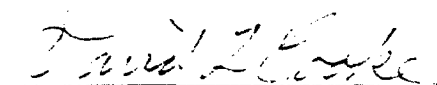


**PHILLIPS LABORATORY
AIR FORCE MATERIEL COMMAND
HANSCOM AIR FORCE BASE, MA 01731-3010**

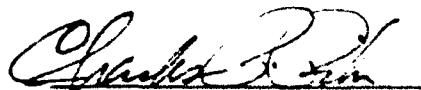
98 4 01 071

422 722
93-06809

" This technical report has been reviewed and is approved for publication "



DAVID L. COOKE
Contract Manager



CHARLES P. PIKE
Branch Chief

This report has been reviewed by the ESC Public Affairs Office (PA) and is releasable to the National Technical Information Service (NTIS).

Qualified requestors may obtain additional copies from the Defense Technical Information Center. All others should apply to the National Technical Information Service.

If your address has changed, or if you wish to be removed from the mailing list, or if the addressee is no longer employed by your organization, please notify PL/TSI, Hanscom AFB, MA 01731-5000. This will assist us in maintaining a current mailing list.

Do not return copies of this report unless contractual obligations or notices on a specific document requires that it be returned.

REPORT DOCUMENTATION PAGE			Form Approved OMB No. 0704-0188	
<small>Public reporting burden for this collection of information is estimated to average 1 hour per response, including the time for reviewing instructions, searching existing data sources, gathering and maintaining the data needed, and completing and reviewing the collection of information. Send comments regarding this burden estimate or any other aspect of this collection of information, including suggestions for reducing this burden, to Washington Headquarters Services, Directorate for Information Operations and Reports, 1215 Jefferson Davis Highway, Suite 1204, Arlington, VA 22202-4302, and to the Office of Management and Budget, Paperwork Project (0704-0188), Washington, DC 20503.</small>				
1. AGENCY USE ONLY (Leave blank)	2. REPORT DATE Nov 1989	3. REPORT TYPE AND DATES COVERED Scientific Final 1 Oct 88-3 Nov 89		
4. TITLE AND SUBTITLE Proceedings of the Spacecraft Charging Technology Conference 1989, Vol 1		5. FUNDING NUMBERS PE 62101F PR 7601 TA 760130 WU 760130CK MIPR #FY71219000005		
6. AUTHOR(S) Editor: R.C. Olsen				
7. PERFORMING ORGANIZATION NAME(S) AND ADDRESS(ES) Naval Postgraduate School Physics Dept, MC 61-05 Monterey, CA 93943		8. PERFORMING ORGANIZATION REPORT NUMBER		
9. SPONSORING / MONITORING AGENCY NAME(S) AND ADDRESS(ES) Phillips Laboratory 29 Randolph Road Hanscom AFB, MA 01731-3010 Contract Monitor: David L. Cooke/PL/WSSI		10. SPONSORING / MONITORING AGENCY REPORT NUMBER PL-TR-93-2027 (1)		
11. SUPPLEMENTARY NOTES				
12a. DISTRIBUTION / AVAILABILITY STATEMENT Approved for public release; Distribution unlimited			12b. DISTRIBUTION CODE	
13. ABSTRACT (Maximum 200 words) The Spacecraft Charging Technology Conference was held at the Naval Postgraduate School, Monterey, California, from 31 October to 3 November 1989. This was the fifth in a series of meetings jointly sponsored by the Air Force and NASA to deal with spacecraft environment interactions. The meeting was attended by 108 people with 60 talks presented. The majority of the speakers have chosen to present their work in these two volumes. Volume 1 contains pages 1 through 333, Volume 2 contains pages 334 through 624.				
14. SUBJECT TERMS spacecraft, spacecraft charging, space environment space plasma, interactions			15. NUMBER OF PAGES 342	
			16. PRICE CODE	
17. SECURITY CLASSIFICATION OF REPORT Unclassified	18. SECURITY CLASSIFICATION OF THIS PAGE Unclassified	19. SECURITY CLASSIFICATION OF ABSTRACT Unclassified	20. LIMITATION OF ABSTRACT SAR	

Table of Contents

Trends in spacecraft anomalies, D. C. Wilkinson	1
Solar and geomagnetic activity during March 1989 and later months and their consequences at Earth and in near-earth space, J. H. Allen.....	18
Review of March 1989 solar activity and resultant geomagnetic storm C. Balch.....	46
A survey of medium energy electrons at high altitude based on ISEE-1 data. E. J. Daly, and C. Tranquille.....	61
Charging of geosynchronous spacecraft by variable intensity substorm environments. N. J. Stevens.....	81
Surface charging on Engineering Test Satellite V of Japan H. Nishimoto, H. Fuji, and T. Abe.....	98
Identification and solution of a charging problem in a high-altitude detector G. J. Berzins, J. E. Valencia, H. E. Felthausen, J. E. Nanewicz, and J. S. Thayer,.....	111
Quest for the source of Meteosat anomalies A. J. Coates, A. D. Johnstone, D. J. Rodgers, and G. L. Wrenn.....	120
Sensitivity analysis with a simple charging code. A. J. Sims and G. L. Wrenn.....	147
Laboratory studies of spacecraft charging mitigation techniques. K. Giori, R. Adamo, J. Nanevich, and J. Kositsky.....	159
Electrical conductivity of ZOT after a long term exposure to thermal vacuum environment. P. Leung.....	166
Active spacecraft potential control by emission of weak ion beams K. Torkar, W. Riedler, R. Schmidt, H. Arends, and F. Rudenauer.....	174

For	
RA&I	<input checked="" type="checkbox"/>
AB	<input checked="" type="checkbox"/>
iced	<input checked="" type="checkbox"/>
on	

DTIC QUALITY INSPECTED 4

By	
Distribution /	
Availability Codes	
Dist	Avail and / or Special
A-1	

Plasma sources for active charge control. V. A. Davis, and I. Katz.....	184
Polar code simulation of DMSP satellite auroral charging D. L. Cooke, M. S. Gussenhoven, D. A. Hardy, M. Tautz, I. Katz, G. Jongeward, and J. R. Lilley.....	194
Numerical simulation of the wake of non-equipotential spacecraft in the ionosphere. A. Soubeyran and L. Levy.....	204
High-voltage auroral zone charging of large dielectric spacecraft: A wake-induced barrier-effect mechanism. J. G. Laframboise and J. Luo.....	218
Some European activities on spacecraft/plasma interactions in low Earth orbit A. R. Martin, P. M. Latham and R. A. Bond.....	219
A New 2.5-D PIC charging code for low Earth orbit D. G. Rodgers, R. L. Kessel, A. Etemadi and S. T. Brandon....	240
Charge accumulation and ion focusing for dielectrics exposed to electron and ion beams. G. McKeil and K. G. Balmain.....	255
A threshold voltage for arcing on negatively biased solar arrays D. Hastings, G. Weyl, and D. Kauffman.....	275
The nature of negative potential arcing: Current and planned research at LeRC G. B. Hillard	293
Comparison of currents predicted by NASCAP.LEO model simulations and elementary Langmuir-type bare wire models for an insulated cable containing a single pinhole J. T. Galofaro.....	300
Space Station Freedom solar array panels plasma interaction test facility. D. F. Martin and K. D. Mellott.....	334
SAMPIE - A shuttle based solar array arcing experiment. D. Ferguson.....	346
Optical Signatures of the beam-plasma interaction during the ECHO 7 sounding rocket experiment. R. C. Franz and J. R. Winckler.....	362

Neutral gas effects on the charging of Echo 7. P. R. Malcolm, W. J. Burke and G. P. Murphy.....	376
Immediate and delayed high-energy electrons due to ECHO 7 accelerator operation R. Nemzek and J. R. Winckler.....	404
Altitude effects on high time resolution measurements of vehicle charging due to electron emission at LEO altitudes N. B. Myers and W. J. Raitt.....	428
A review of the MAIMIK rocket experiment W. F. Denig, B. N. Maehlum and K. Svenes.....	443
Current saturation of electron beam emission from the SCATHA satellite. S. T. Lai.....	455
Dynamics of spacecraft charging by electron beams. M. J. Mandell and I. Katz.....	464
Spacecraft charging during electron beam injection and turnoff. R. M. Winglee.....	486
Three-dimensional computer models of the currents collected by active spacecraft in low Earth orbit. I. Katz, M. J. Mandell, G. A. Jongeward, J. R. Lilley, V. A. Davis, and D. L. Cooke.....	511
Environet: A space environment data resource M. Lauriente and H. B. Garrett.....	524
Modification of spacecraft charging and the near-plasma environment caused by the interaction of an artificial electron beam with the Earth's upper atmosphere T. Neubert, P. M. Banks, B. E. Gilchrist, A. C. Fraser-Smith P. R. Williamson, W. J. Raitt, N. B. Myers, and S. Sasaki....	541
Neutral environment with plasma interactions monitoring system on space station (NEWPIMS) E. C. Whipple and J. N. Barfield.....	556
BEAR electrostatic analyzer: Description and laboratory results D. W. Potter, H. R. Anderson and J. R. Olson.....	567
BEAR electrostatic analyzer: Flight results H. R. Anderson, D. W. Potter, D. L. Morse, J. R. Olson, J. L. Johnson, and M. Pongratz.....	575

Sheath waves on conductors in plasma and their
 implications for low-earth-orbit systems
 K. G. Balmain, C. C. Bantin, H. G. James, G. Morin, and
 A. G. McNamara.....582

Current collection in a spacecraft wake:
 Laboratory and computer simulations
 C. Chan, J. Browning, S. Meassick, M. A. Morgan,
 D. L. Cooke, C. L. Enloe, and M. F. Tautz.....601

A Preliminary spacecraft charging map for
 the near Earth environment
 R. Evans, H. Garrett, S. Gabriel, and A. Whittlesey.....615

PREFACE

The Spacecraft Charging Technology conference was held at the Naval Postgraduate School, Monterey, California, from 31 October to 3 November, 1989. This was the fifth in a series of meetings jointly sponsored by NASA and the Air Force to deal with spacecraft environment interactions. The meeting was attended by 108 people, with 60 talks presented. The majority of the speakers have chosen to present their work in this volume.

We wish to thank NASA and the Air Force for providing financial support for the meeting. This allowed funding for travel by 6 students, and the convenor's time. The Naval Postgraduate School provided the facilities, and the local chapter of IEEE provided invaluable administrative aid. My special thanks to Dr. S. Gnanalingam, Dr. Jeff Burl, and Lt. M. E. Young for their help prior to and during the meeting.

Richard Christopher Olsen
Naval Postgraduate School
14 January 1991

TRENDS IN SPACECRAFT ANOMALIES

Daniel C. Wilkinson

National Oceanic and Atmospheric Administration
National Geophysical Data Center
Solar-Terrestrial Physics Division
Boulder, Colorado 80303

SPACECRAFT CHARGING TECHNOLOGY CONFERENCE

Naval Postgraduate School
Monterey, California

October 31, 1989 - November 3, 1989

ABSTRACT

NOAA's National Geophysical Data Center maintains a data base of anomalous spacecraft behavior attributed to environmental interactions. One of the uses of these data base has been to identify trends in anomaly occurrence. Trends alone do not provide quantitative testimony to a spacecraft's reliability, but they do indicate areas that command closer study. An in-depth analysis of a specific anomaly can be difficult without on-board environmental monitors. Statistically verified anomaly trends can provide a good reference point to begin analysis of a spacecraft's susceptibility to environmental conditions. The data base currently contains over 3000 anomaly reports from 7 countries.

THE SPACECRAFT ANOMALY DATA BASE

The National Oceanic & Atmospheric Administration (NOAA) is the main U.S. civilian agency responsible for the operation of monitoring spacecraft. Those responsibilities include the GOES (Geosynchronous Operational Environmental Satellite) series of weather and space environment monitoring satellites and the lower altitude, polar orbiting NOAA satellites. Long and productive spacecraft lifetimes are of major importance to NOAA.

NOAA also operates a system of data centers. The National Geophysical Data Center (NGDC) in Boulder, Colorado has responsibility for collecting, archiving, analyzing, and disseminating solar-terrestrial data and information. NGDC,

under the auspices of World Data Center A for Solar Terrestrial Physics, services a worldwide interest in data and information about the origin of solar activity, the transfer of energy from the Sun to Earth, and its effects in interplanetary and near-Earth space. In line with these services, NGDC has made a deliberate effort to apply these data resources to the problem of spacecraft interaction with the near space environment.

Data on spacecraft anomalies is maintained at the Solar-Terrestrial Physics Division of NGDC. Date, time, location, and other pertinent information about the anomaly are included. These events range from minor operational problems to permanent spacecraft failures. The data base currently contains over 3000 anomalies spanning 1971 to the present with contributions from seven countries: Australia, Canada, Germany, India, Japan, United Kingdom, and the United States. Data suppliers are asked to provide the anomaly type and diagnosis.

The data base is maintained on an IBM compatible personal computer. To facilitate access to the information, software has been written to perform a full range of functions for managing and displaying the contents. Satellite users can use the Spacecraft Anomaly Manager (SAM) software to create a data base containing their anomalies and forward the result to NGDC on floppy disk for inclusion in the archive. In order to preserve confidentiality, when necessary, spacecraft may be identified by aliases.

SAM also includes two important functions to test anomaly collections for environmental relationships. Histograms of local time, and seasonal frequency show distinct patterns for spacecraft susceptible to static charge build-up and subsequent discharge. The current version of the software does not perform statistical validation but the user may convert the data to a standard ASCII file that can be uploaded to any computer and processed by user supplied software.

STATISTICAL METHODS

Grajek and McPherson (1977) point out the value of using statistical methods for analyzing apparent trends in anomaly occurrence. The Chi-square test for randomness can determine the probability that a given distribution, or one with similar deviations from the mean, could occur randomly.

The Pearson Product-moment Correlation Coefficient can determine both the strength of a correlation and the probability of error in establishing a correlation where none exists. A coefficient of 1 indicates perfect correlation, 0 indicates no correlation, and -1 indicates perfect anticorrelation.

These methods are used to analyze the following trends with the help of public domain software (Gustafson, 1983).

BACKGROUND

When an earthquake devastates a major highway during rush hour it attracts a great deal of attention. Those who are tasked with maintaining highways are concerned with the safety of existing structures. Highway engineers become concerned with upgrading specifications on future projects. The end result is that attention is focused on techniques to improve the reliability of structures subjected to the trauma of earthquakes.

San Francisco

Oct 17, 1989

Epicenter

Monterey

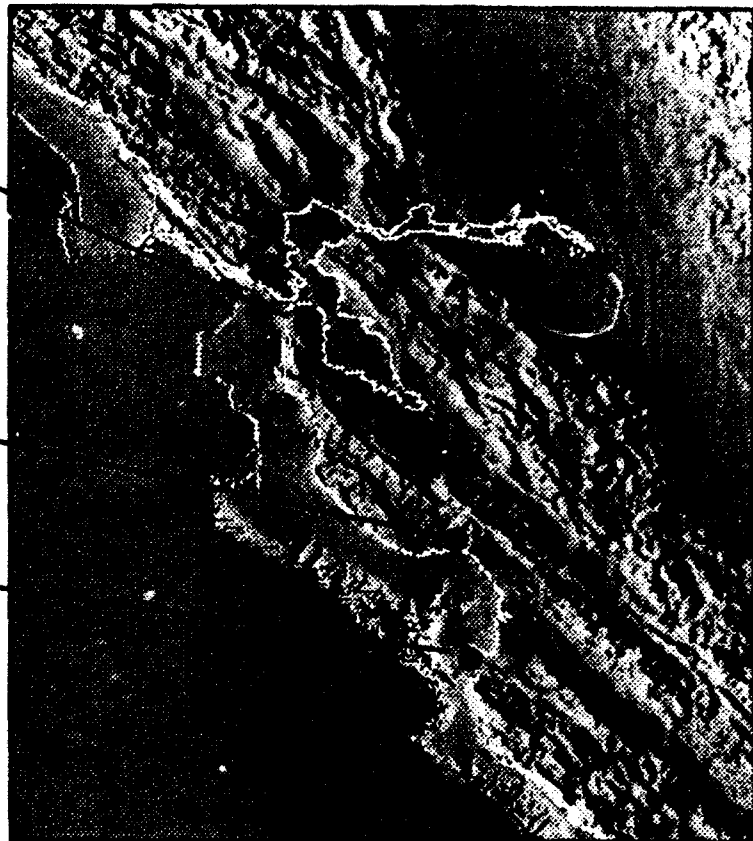


Figure 1

The historical record of earthquakes is an important part of the analysis (Figure 2). The first questions asked after an event like this are: What is the history of this type of event? Has this happened before? Can we expect it to happen again? Where? How soon? How often? What is the track record of similar structures in similar events? None of these questions could be adequately answered if someone had not undertaken the responsibility of long term record keeping. It is through such record keeping that trends appear, trends such as the clustering of earthquakes along the San Andreas fault or the susceptibility of certain civil engineering techniques.

LOMA PRIETA EARTHQUAKE $M = 7.1$ OCTOBER 17, 1989

The Loma Prieta, California earthquake was located at 37.053N 121.851W by the USGS in Golden, CO. This location is shown by the star on this map. The epicenter of the event was near the northern end of the Southern Santa Cruz Mountains segment of the San Andreas Fault (SSCMS). Preliminary aftershock locations clearly indicate that the event ruptured that segment of the fault. This segment may have had similar events during 1838, 1865, and 1890. The probability of an event of this size on this segment between 1988 and 2018 was estimated as 30% in a recent report by the USGS. This probability was not well constrained, but it was the highest probability determined for major faults in the bay area. The San Francisco Peninsula segment of the fault adjoins the SSCMS to the north. This segment has the second highest probability of experiencing a large event in the next 30 years.

MAGNITUDES
 <4.0
 5.0
 6.0
 7.0

BERKELEY EVENTS $M \geq 5$ 1911-1984

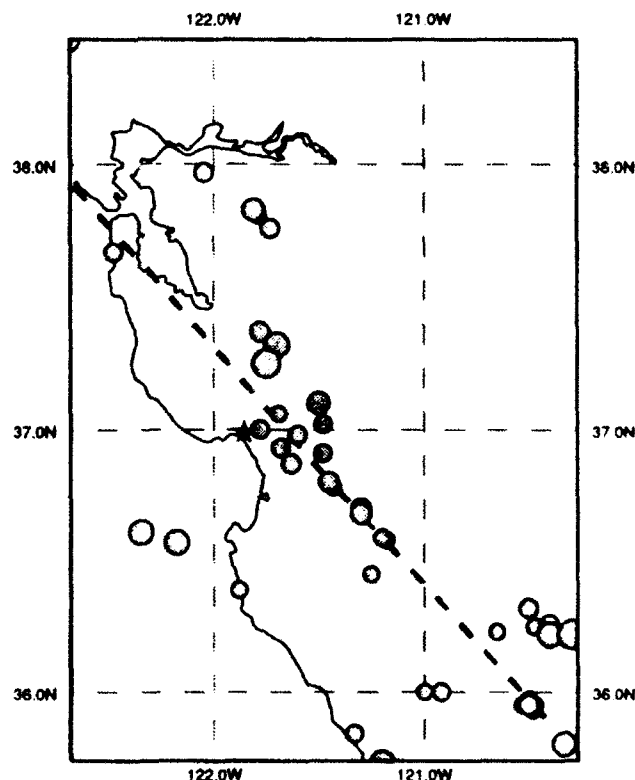


Figure 2

Interest in the environmental effects on spacecraft, like earthquakes, follows the large events. Most people who have an interest in such effects can point to a single event or series of events that piqued that interest. The event could have been the catastrophic failure of a major mission component or the sudden increase in the rate of occurrence of otherwise benign anomalies.

The failure of the Visual and Infrared Spin-Scan Radiometer (VISSR) on GOES-4 coincided with the arrival of very energetic protons associated with a large solar flare (Figure 3). What was it about this particular proton event that could cause such a failure? Are proton events of this magnitude common? Have GOES satellites survived similar proton events? Could the 12 hours of enhanced > 2 MeV electron flux cause a charge build-up on internal dielectric materials that discharged when the energetic protons arrived? Or, was it only a coincidence that GOES failed during the proton event? Some of these questions can only be answered if historical information is available about the space environment and the interaction of GOES and similar spacecraft with that environment. Others will never be answered. The failure of GOES-4 prompted the creation of the Spacecraft Anomaly Data Base in the hope that such a historical record would help answer questions about future failures.

SOLAR-TERRESTRIAL ENVIRONMENT

November 1982

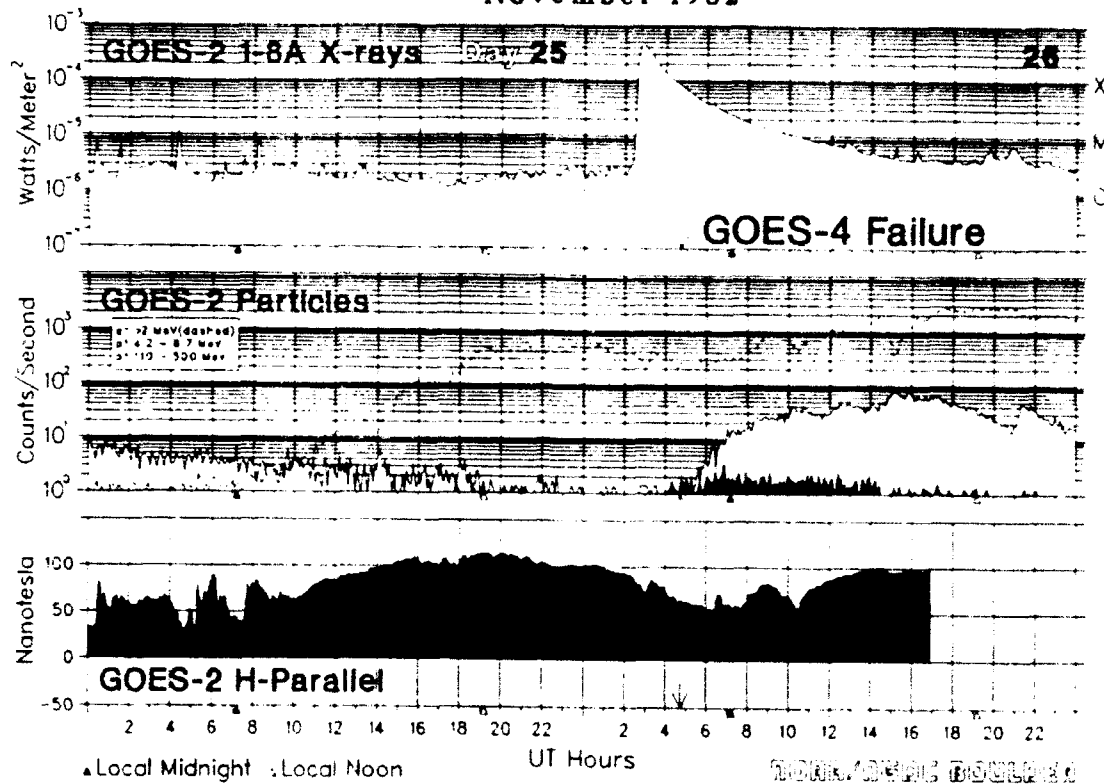


Figure 3

Events like the one displayed in Figure 4 are creating a whole new generation of believers in the potential of the space environment to threaten space operations. This X9 class flare produced protons of such energy that they caused the largest ground level event in 30 years. The proton fluxes caused sensitive electronics to malfunction and solar array output to drop dramatically on many spacecraft. What does the historical record say about the effects of this type of event? Nothing, the last time an event of this magnitude occurred there were no spacecraft.

SOLAR-TERRESTRIAL ENVIRONMENT

September 1989

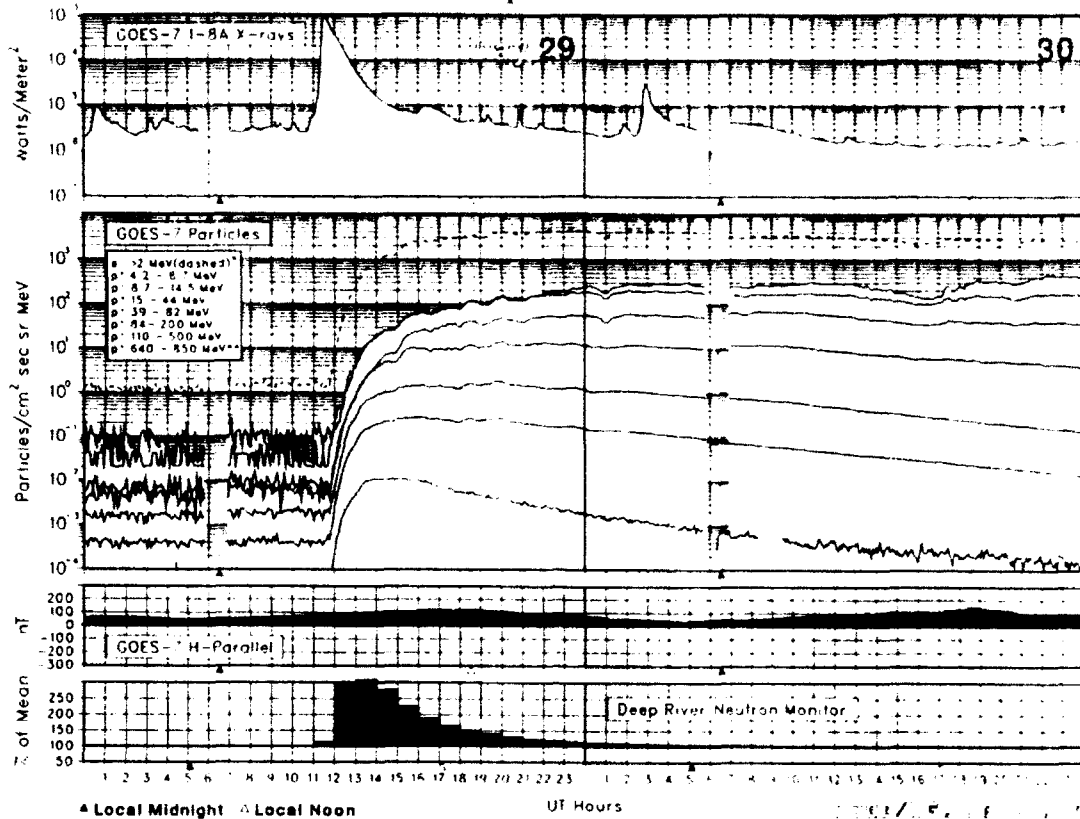


Figure 4

The solar butterfly diagram in Figure 5 is the result of 110 years of continuous, daily observations. The elegant trends of solar activity would not be apparent if observations were made intermittently or only during times of interesting activity. The butterfly diagram was named after the pattern made by the distribution in latitude of sunspot regions over a solar cycle.

Solar Butterfly Diagram

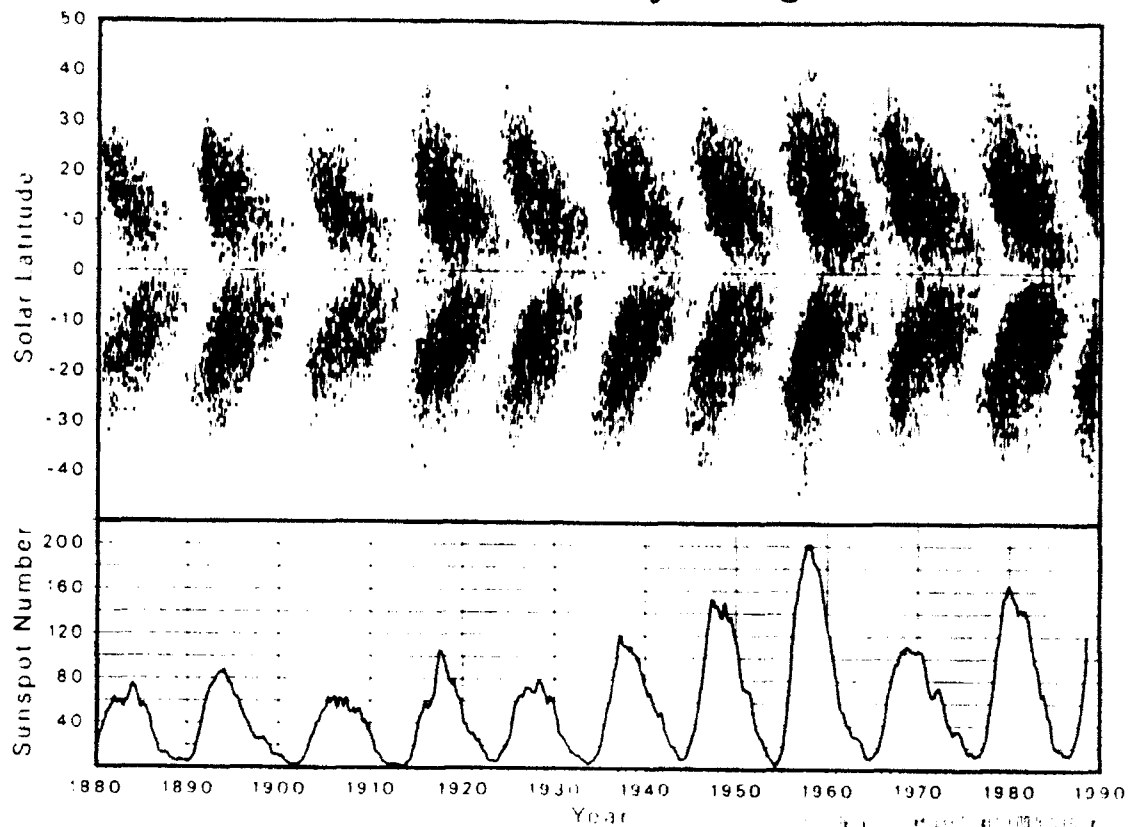


Figure 5

TRENDS IN SPACECRAFT ANOMALIES

The seasonal distribution of the entire anomaly database (Figure 6) shows an increase in the occurrence of anomalies around the spring and fall equinox. To demonstrate what this means in terms of Sun-Earth geometry, the apparent solar declination is plotted in degrees. These data, plotted as the thin line, show the Northern hemisphere tilting towards the Sun twenty-three degrees during summer and away twenty-three degrees during the winter. The thick line is the same data, but the positive declinations are plotted as negative. The symmetry of this relationship allows this modification to be made for the sake of visualization.

At equinox, geostationary satellites experience periods of solar eclipse. During these periods the boiling off of photo-electrons ceases while ambient electrons in the orbital path to continue to accumulate, resulting in abnormal surface charging.

Also, at equinox, geostationary satellites are more in line with the center of the magnetotail and the associated plasma sheet. This results in spacecraft encountering more plasma region boundaries.

This anomaly distribution has a very low probability of being random (.0000018) and a moderately high anticorrelation to the histogram of declinations (-.86) with a very small probability that the correlation is wrong (.00011)

Seasonal Distribution of Entire Database

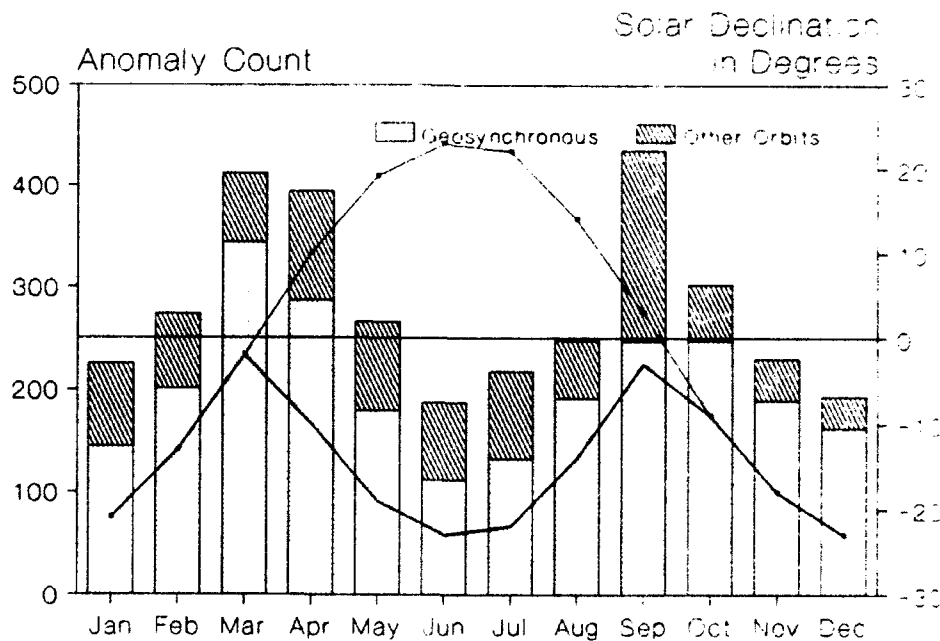


Figure 6

Figure 7 shows the local time distribution of all of anomalies in the data base whose reports have sufficient information for a local time calculation. Local time is used to represent position. Local noon being on the sun side of the Earth and local midnight being on shadow side. The largest trend shows enhanced counts in the midnight to dawn sector. The eclipse intervals occur at local midnight. When charging occurs at midnight the eventual discharge, if any, would occur between midnight and dawn. Local midnight is also where satellites would encounter the plasma enhancements associated with the magnetotail. This is particularly true during magnetic substorms when an injection of energetic electrons would enter geostationary orbit near local midnight and travel towards the dawn sector. This anomaly distribution has a small probability of being random (.00035).

Local Time Distribution - All

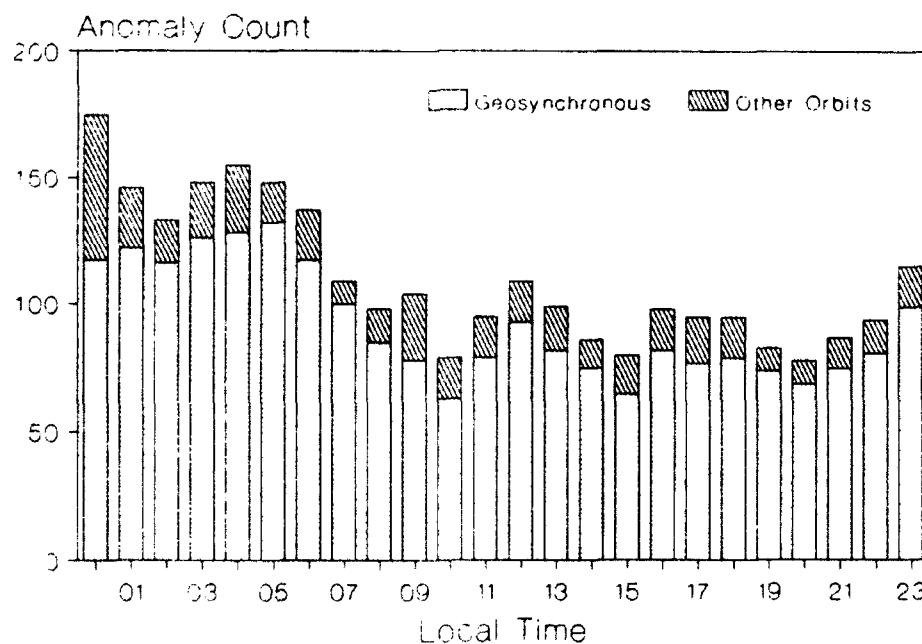


Figure 7

It is obvious from Figures 6 and 7 that the trends are riding on a background of anomaly reports that do not follow the trends. The SAM software's filtering capabilities are used to focus in on specific systems to see which are following the seasonal and local time trends and which are not.

The GOES phantom command anomalies shown in Figure 8a are a prime example of seasonal dependence. The phantom commands have been diagnosed as a surface charging problem which is consistent with the seasonal phenomenon. These charging events have a moderately high anticorrelation to solar declinations ($-.72$) with a very small probability that the correlation is wrong (.0073)

The distribution of major magnetic storms shown in Figure 8a has a very low probability of being random (.00042) and a moderately high anticorrelation to the histogram of declinations ($-.89$) with a very small probability that the correlation is wrong (.00011)

The GOES-4, -5, and -6 "other anomalies" shown in Figure 8a are predominantly telemetry errors that have been diagnosed as Single Event Upsets (SEUs). This anomaly distribution has a good probability of being random (.26) and a weak anticorrelation to solar declination ($-.23$) with a large probability that the correlation could be wrong (.47). Since galactic cosmic ray fluxes are random in the seasonal context, the statistics validate the SEU diagnosis.

In Figure 8b the GOES surface charging anomalies show a classic midnight to dawn grouping with a small probability of being random (.0000022). The other GOES anomalies show no such grouping and have a very high probability of being random (.94), consistent with SEUs.

Seasonal Distribution of GOES Anomalies

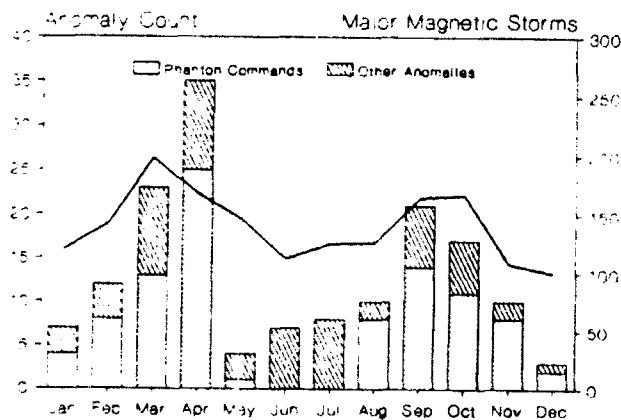
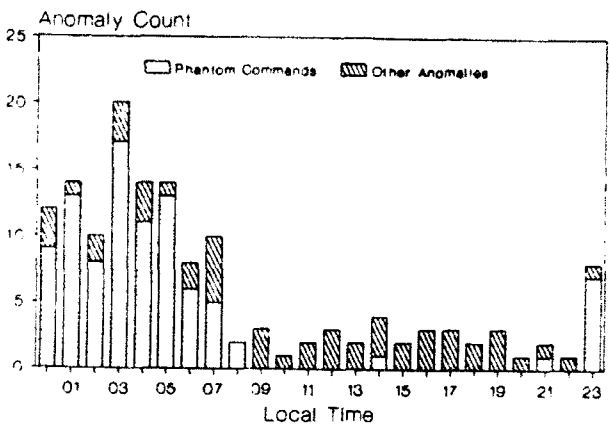


Figure 8a

Local Time Distribution - GOES Anomalies



8b

The TDRS-1 anomalies in Figure 9a show no distinct seasonal variation in anomaly occurrence. This anomaly distribution has a very good probability of being random (.44) and a moderately weak anticorrelation to solar declination (-.55) with a small probability that the correlation is wrong (.062).

The local time distribution of TDRS-1 anomalies shows no increase of anomaly occurrence during the midnight to dawn local time interval (Figure 9b) and has a very high probability of being random (.97), consistent with SEUs.

Seasonal Distribution of TDRSS Anomalies

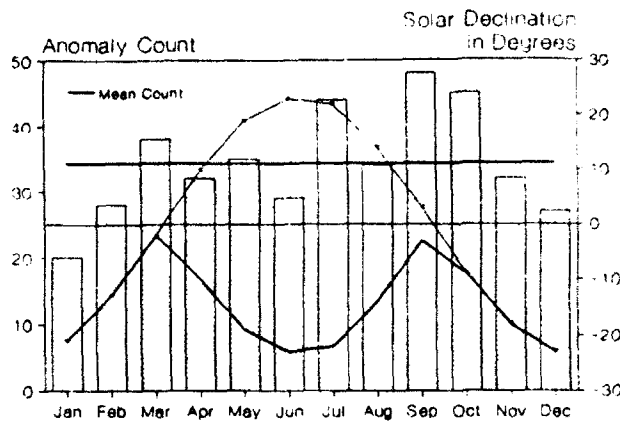
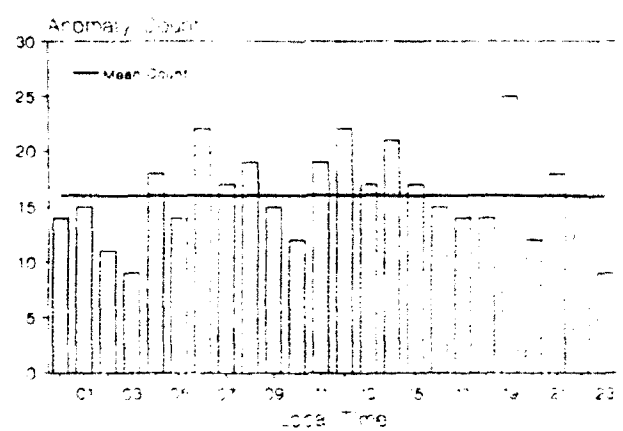


Figure 9a

Local Time Distribution - TDRSS



9b

Not all trends are as straight forward as those concerning GOES and TDRS. The Global Positioning Satellite (GPS) anomalies displayed in Figure 10a and 10b show distinct patterns that do not fit the trends expected for either surface charging or SEU anomalies. The most notable trend is the strong bimodal pattern in the local time chart (Figure 10b). The GPS orbit is inclined 60 deg at 1/2 geosynchronous altitude.

Seasonal Distribution of GPS Anomalies

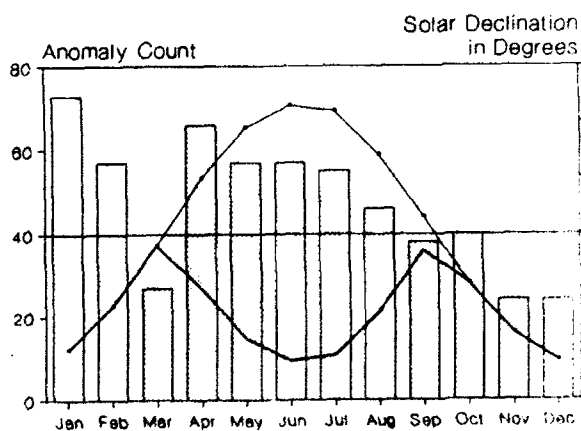
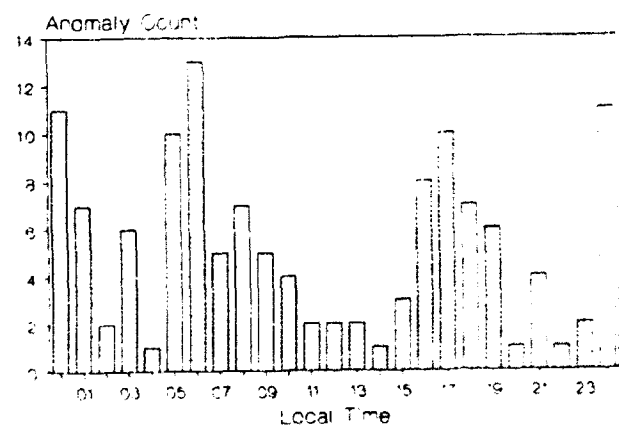


Figure 10a

Local Time Distribution - GPS Anomalies



10b

There are times when a trend in the data can be caused by artificial sources. The SCATHA reports in the data base represent discharge events that were monitored by on-board instrumentation rather than the typical anomaly report. The patterns in Figure 11a and 11b are caused by the incomplete processing of the SCATHA data. After the first year of operation data were processed only for intervals of specific interest. It is noteworthy, however, that local midnight and fall equinox garnered the most interest.

Seasonal Distribution - Scatha Anomalies

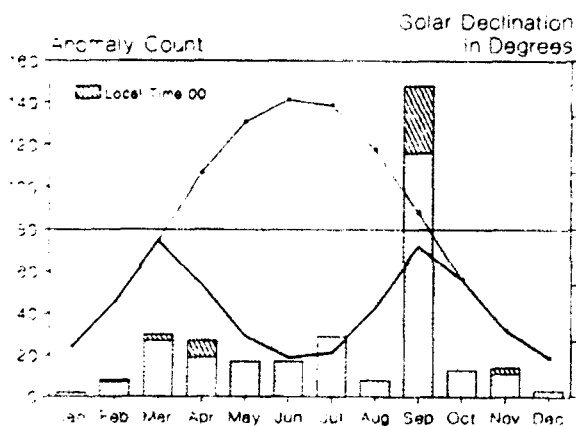
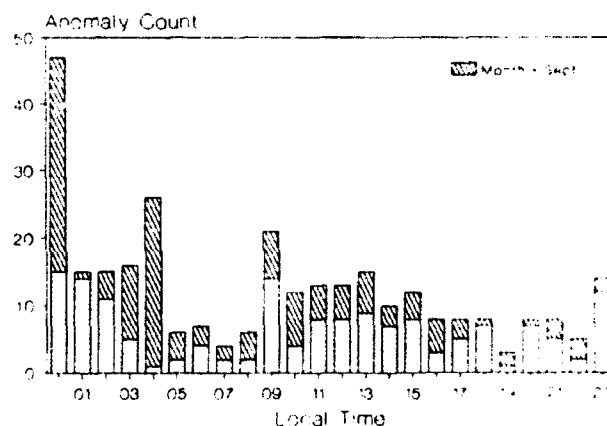


Figure 11a

Local Time Distribution - Scatha



11b

CONCLUSION

The routine reporting and archiving of spacecraft anomalies, like all routine data collection, is not a glamorous task. However, the maintaining of a complete and systematic anomaly history can be a critical part of mission success. Like the solar observations made over the centuries, anomaly archives becomes more valuable as the time base grows.

REFERENCES

1. Grajek, Michael A.; McPherson, Donald A.: Geosynchronous Satellite Operating Anomalies Caused by Interaction with the Local Spacecraft Environment, 1977. NASA NAS3-21048.
2. Gustafson, Tracy L.: EPISTAT Statistical Package for the IBM Personal Computer, version 2.1. 1983.

**SOLAR AND GEOMAGNETIC ACTIVITY DURING MARCH 1989 AND LATER MONTHS
AND THEIR CONSEQUENCES AT EARTH AND IN NEAR-EARTH SPACE**

J. H. Allen (NOAA/NESDIS/NGDC)
Spacecraft Charging Technology Conference
Naval Postgraduate School, Monterey, California
October 31-November 3, 1989

ABSTRACT

From 6-20 March 1989 the large, complex sunspot group Region 5395 rotated across the visible disc of the Sun producing many large flares that bombarded Earth with a variety of intense radiation although the energetic particle spectra were unusually "soft". Aurorae were observed worldwide at low latitudes. On 13/14 March a "Great" magnetic storm occurred for which $A_p^* = 279$ and $AA^* = 450$. By both measures, this event rates among the largest historical magnetic storms. Geostationary satellites became interplanetary monitors when the magnetopause moved earthward of 6.5 Re. Ionospheric conditions were extremely disturbed, affecting hf through X-band communications and the operation of satellites used for surveys and navigation. At lower altitudes there were problems with satellite drag and due to the large magnetic field changes associated with field-aligned current sheets. We are seeking reports of satellite anomalies at all altitudes. Reports also have been received about effects of these Solar-Terrestrial disturbances on other technology at Earth and in near-Earth space. This presentation draws heavily on material in a shorter, summary paper "in press" for "EOS" (Allen, et. al., 1989). Recent major solar activity since the abstract was submitted happened in mid-August, late September, and mid-October 1989. These events and their consequences at Earth and in Space are covered briefly.

SOLAR AND GEOMAGNETIC ACTIVITY DURING MARCH 1989 AND LATER MONTHS AND THEIR CONSEQUENCES AT EARTH AND IN NEAR-EARTH SPACE

On Monday, 6 March 1989, a very large and complex sunspot group, Region 5395, rotated into view around the east limb of the Sun and quickly gained attention when it produced an X15/3B flare (N35, E69). This event began a period of high solar activity that lasted two weeks and had many important consequences at Earth and in near-Earth space. From 6-19 March, Region 5395 produced 11 X-class and 48 M-class X-ray flares. Prolonged proton events occurred lasting several days and with an unusually high proportion of lower-energy particles. This solar activity produced an historically "great" magnetic storm, long-lasting Polar Cap Absorption events and a major Forbush decrease. The ionosphere was greatly disturbed. Many problems were reported with operational satellites; increased drag caused extensive orbit perturbations, telecommunications and navigation systems failed because of the disturbed conditions; aurorae were seen at unusually low latitudes (above the Tropic of Capricorn in Australia and from Mexico and Grand Cayman Island in North America); and there was a major electrical power outage in Quebec Province, Canada that affected some six million customers for nine or more hours.

Full analysis of this series of exciting events is just beginning, with the data bases now being assembled. Interested scientists have been in contact via e-mail and written correspondence even while the events were in progress. In addition, the spectacular imagery (some of which is shown here) has received a good deal of attention in the popular press as well. Scientists who are interested in participating in this study should contact Joe Allen (SPAN address 9555::jallen). Figure 1 summarizes the activity and its effects. Figure 1(a) shows GOES-7 solar X-rays, proton fluxes (one energy range), and magnetic field (Hp component) variations. Panels of ground-based data show the H-component of the geomagnetic field measured at Boulder Magnetic Observatory (USGS) and the flux from the Deep River Neutron Monitor (Canada), for March 5-6, 1989. Corresponding data for March 13-14 are shown in Figure 1b. A full set of the stack plots for March is given in the April and May 1989 issues of "SOLAR-GEOPHYSICAL DATA: Part 1, prompt reports".

SOLAR FLARES:

Following the long-lived X15/3B flare of 5 March, Region 5395 produced one or more flares daily near or surpassing the X1.0 level until the 18th of March. The X4.0 flare of Thursday, 9 March, peaked at 1532 UT and optically was rated a 4-Bright (4B), the highest categories of both area and intensity. Figure 2 is an H-alpha image of this flaring region taken by the USAF Solar Optical Observing Network (SOON) telescope at Holoman, NM, about five minutes before maximum.

On Friday, 10 March, another long-lasting flare reached the X4.5/3B level. At this time, Region # 5395 was still 22° east of Central Meridian and at relatively high latitude, considering that the sunspot cycle is almost at maximum. The flare on the 10th and its electromagnetic characteristics were the basis for an SESC forecast of high magnetic activity at Earth on the 12/13th. The last of the large flares from Region 5395 was an X6.5 at 1736 UT (N33,W62) on the 17th.

INJECTION OF ENERGETIC PARTICLES TO GEOSTATIONARY ORBIT:

On Tuesday, 7 March, the flux of 4.2-8.7 MeV protons began to rise gradually above the background level so that early on the 8th it was an order of magnitude higher. Just before 1800 UT the flux increased sharply by about two orders of magnitude (see April SGD, Part 1, p. 168) and continued at high levels through the 14th. Maximum was reached at about 0700 UT on the 13th (see Figure 1b). The SESC announced that at 1735 UT on the 8th the flux of >10 MeV protons exceeded 10 particles/cm²/sec/steradian so that a "Proton Event" was officially in progress. The proton flux continued at event levels until the 14th. The onset of high flux was probably caused by the flare of March 6 and was sustained by new injections from subsequent flares.

EXTREME MAGNETOSPHERIC COMPRESSION:

The March 1989 solar and geophysical activity was accompanied by a series of magnetopause crossings with extreme characteristics. Figure 1(b), third panel, shows the GOES-7 one-minute-averaged observations of the Hp component (approximately parallel to Earth's rotation axis) of the magnetic field at geostationary altitude during March 13 and 14, 1989. The reversals of the Hp component of the geostationary field to negative values indicates that the magnetopause, typically located at 10 Re distance, moved inside the geostationary orbit (6.6Re). Such rare events are called "Geostationary Magnetopause Crossings" (GMC), and are caused by extreme conditions of solar wind pressure, often coupled with strong southward IMF components. Given a reasonable model for the magnetopause shape, the minimum distance to the subsolar point was 4.7 Re, or over a factor of two compression in linear size. The first of several crossings was observed by GOES-7 on the 13th at 14:16 UT (07:02 local time), and by GOES-6 some 36 minutes later at 05:52 local time. For this episode, the magnetopause was within 6.6 Re at the dawn magnetosphere for approximately 3.2 hours. Together with the crossings later that day, these episodes comprise the longest-duration compressions observed by the GOES satellites during a study period extending from 1979 to the present.

One may estimate the energy (work) required to compress the magnetosphere from a quiescent subsolar boundary distance of 10 Re to our estimated minimum distance of 4.7 Re. The product of the projected cross-sectional dawn-dusk area of the magnetosphere and the pressure ($B^2/80$) of the dayside magnetic field, B , given by the simple model of Roederer (1970), yields the force exerted at the magnetopause. Integrating from the initial to the final subsolar distance using the magnetopause boundary shape of Holzer and Slavin (1978), we find that the work done is 4×10^{15} joules, about 1/6th the average daily US electrical energy consumption in 1987.

COSMIC RAY PENETRATION:

The geomagnetic field provides partial shielding against penetration to Earth of energetic particles of solar or galactic origin (cosmic rays). The minimum energy required to reach Earth's atmosphere or surface is a decreasing function of geomagnetic latitude; particles of the order of 100 keV or higher have essentially free access to latitudes poleward of the auroral zones. For an axially symmetric field such as that of a dipole, the fraction of the primary flux at a given energy reaching Earth as a function of decreasing latitude would suffer an abrupt transition from full transmission to none at a specific latitude, the "cutoff latitude" for that energy. For the real, asym-

metric magnetosphere, however, the transition from full transmission to no transmission occurs over a latitude range of several degrees; i.e. the cutoff is not "sharp".

Figure 3 shows 2.5-16 MeV cutoff-latitude observations by SEL instruments aboard the low-altitude, polar orbiting, NOAA-10 satellite for all 13 passes of March 13, 1989. The cutoff range is denoted by radial line segments, with the higher latitude end-bar indicating the 2.5 MeV cutoff and the lower latitude end-bar indicating the 16 MeV cutoff. These cutoffs have been defined as the latitude of a measurable decrease below full transmission for the respective energy. A region of partial transmission extends several degrees southward of the indicated boundaries. Observations of all traversed cutoff latitudes are plotted as a function of geographic longitude in the upper panel (a), and as a function of magnetic local time in the lower panel (b). Northern- and southern-hemisphere observations have been combined, since no systematic differences have been found between them for this day.

Cutoffs were observed from a minimum of about 44° to a maximum of about 72° geomagnetic latitude. It will be noted the latitude range of the observed cutoffs for that day was quite broad: about 25° wide at 60 - 120° east geographic longitude, while significantly less (about 10°) some 180° away. Panel 5(b) indicates that the cutoffs were generally lower in the evening hours, with the most equatorward being 44° latitude occurring about 1830 UT at about 82° east longitude, placing it over the central USSR.

A solar proton event was in progress on March 13, the launch date of Discovery. However the spectrum of the particle event was quite "soft;" that is, there were relatively few higher-energy (>30 MeV) protons and alpha particles present. Even with the southward excursion of cutoff latitudes on March 13, Discovery's maximum excursion to about 28° latitude, and the softness of the particle spectrum, prevented the solar proton event from posing a radiation hazard to that activity. In contrast, the Soviet vehicle MIR, with a maximum orbital latitude of about 51° , would be expected to have suffered a significantly increased exposure to energetic proton and alpha particle radiation, but fortunately was not exposed to a major hard event such as those of August 16 or September 29, 1989.

RADIATION BELT PRECIPITATION:

The energetic particle sensors aboard the NOAA-10 low-altitude, polar-orbiting satellite measure electrons and protons in the energy ranges of > 30 keV to > 300 keV, and > 300 keV to > 80 MeV, respectively. Figure 4 shows a gray-shade plot of the 10-day averages of the proton fluxes observed by NOAA-10 in the energy range 30-80 keV. The fluxes are averaged in 5° bins of geographic latitude and longitude.

The pre-activity averages (bottom panel) illustrate typical values with obvious high fluxes in the auroral regions and in the region of the South Atlantic anomaly, approximately centered at 20° S, 340° E. At mid- to lower-latitudes the average fluxes are several orders of magnitude smaller. For the average of the active (March 10 to 20) period (top panel), overall flux intensities have strongly increased. The auroral and anomaly regions are stronger and broader, as expected, and so are the equatorial fluxes. Thirteen high intensity 'striations' across the otherwise depleted mid-latitude regions imply that the most intense increases, significantly above background averages

at mid-latitudes, lasted for a total period of about a day (13 orbits). Similar behavior is observed at proton energies up to about 2 MeV and in the electron data at energies of > 30 and > 100 keV.

GEOMAGNETIC STORMS/SUBSTORMS:

Magnetic substorms were occurring in the auroral zone before the particles from the March 6th flare arrived at Earth. For example, College and Anchorage recorded about 2,000 nT amplitude negative bays in H around 1100-1200 UT on the 5th. However, at mid-latitudes across the US, magnetic conditions were rather quiet until a storm sudden commencement (ssc) at 1735 UT on the 8th. The main-phase H minimum followed at around 0100 UT on the 9th with slightly disturbed conditions lasting through the 10th.

The "great magnetic storm" of 13/14 March 1989, began with a sudden storm commencement at 0128 UT on the 13th (afternoon/evening of the 12th over N. America). Another ssc occurred around 0747 UT and a large negative-H bay was recorded at Boulder Magnetic Observatory around 1100 UT. Near 2100 UT the Boulder H-component began a rapid positive excursion that carried the flux-gate sensor off-scale at +2,000 nT. Large positive-H values continued for about 5 hours after which the trace returned to conditions of negative-H recovery from a main-phase depression. Comparison of H variations from USGS observatories and the NORDA site show large positive H deviations across the mid-latitude US for about six hours at the end of the 13th and early on the 14th (UT) [Figure 5, Herzog and Wilson personal communication]. All observatory magnetometers were off scale at +2,000 nT for part of this time.

It appears likely that for extended periods on 13/14 March the eastward Auroral Electrojet was located over the central United States for several hours. This is consistent with the DE-1 auroral imagery recorded in the southern hemisphere when it is projected onto the northern hemisphere and the wide, intense belt of discrete aurora remaining when DMSP F9 passed over N. America around 0400 UT on the 14th (cover illustration, EOS, Nov 14, 1989).

In the auroral zone, substorm conditions persisted before, during, and after the most active interval of 6-20 March. A sketch of preliminary, graphical Auroral Electrojet indices shows the character of auroral zone substorm activity on March 13/14th (Figure 6, Kamei). Plots of AU and AL variations were produced graphically in Kyoto from records of some 11 observatories that were promptly available in digital format. Preliminary AE is the range between AU and AL at each instant. It ranges from low values near zero to as large as 3000 nT. However, any AE-type index should be used with caution during this time of peak activity because, as noted above, the highly-expanded auroral zone was far south of "auroral" magnetic observatories. Toyo Kamei (Kyoto) has suggested that he may try deriving special mid-latitude AE indices using records from North American sites such as Boulder, Fredericksburg, and Newport which were closer to the electrojet.

Global magnetic activity indices were made available promptly from Goettingen (Kp) and Paris (aa). At NGDC we calculated 8-point running means of the 3-hourly ap and aa indices and selected the most-disturbed 24-hour values of each as Ap* and AA*, respectively, for comparison with the historical record. For the 13th, beginning at 0300 UT, Ap* = 279 (2 nT units). Likewise, AA* = 450 (1 nT units) starting at 0600 UT. According to these measures, this magnetic storm had one of the most disturbed 24 hour periods of any recorded since the mid-19th century. As shown in Table 1, the March Ap* value ranks as the third largest magnetic storm since 1932 based on indices of disturbance derived from records of a global network of 12 or 13 observatories. According to the March AA* this was the largest magnetic storm since 1868 as recorded by the 2-station network of almost antipodal sites in the UK and Australia.

EXTREMELY LARGE AURORAL ZONE:

Both spacecraft and ground-based sightings indicated the extreme coverage of the aurora. The satellite DE-1 was passing over the Antarctic during this key time and obtained striking auroral images at ultraviolet wavelengths (1360 Å to 1650 Å), mainly due to emissions from the Lyman-Birge-Hopfield bands of molecular nitrogen. Figure 7 is DE-1 imagery from two separate passes over the Antarctic six years apart (color images have here been reproduced as Xerographic copies in black and white). The quiet auroral oval on the left was recorded at 1623 UT on 22 March 1983 and the enormously expanded auroral oval on the right was recorded at 1826 UT on 13 March 1989 from a similar viewpoint and season, and at about the same Universal Time as the earlier image. This was during a time of widely reported auroral sightings across Australia and Tasmania. The 13 March 1989 oval was one of the largest recorded by DE-1 until that recorded on the 14th.

The second DE-1 image over Antarctica (to appear on an EOS cover) was recorded at 0151 UT on 14 March 1989, and coastlines are superposed here. The image was mapped onto the Northern Hemisphere at 200 km altitude using a MAGSAT geomagnetic field model. In this projection two broad bands of auroral emissions are seen. The northerly band is centered along the US-Canadian border and the equatorward band is at unusually low latitudes. Patches of the projected aurora appear over Alabama, Georgia, and northern Florida and over Texas, Oklahoma and New Mexico. These images agree well with visual aurora sightings reported from across the southern United States during local nighttime hours of the 13th and early 14th. This DE-1 image was obtained about one-half hour after the end of the period of extended positive-H recorded at Boulder Magnetic Observatory when the eastward Auroral Electrojet appeared to lie across the US from Washington state to Virginia.

The USAF meteorological satellite DMSP recorded the image of visible aurora around 0355 UT on 14 March 1989 (Figure 9). It shows a wide band of discrete aurora extending from just below Hudson's Bay to above Chicago at its narrowest extent. Lights of cities and other heat sources (e.g. oil field gas flares) from the east coast of the US to the central states and along the Gulf, and in Mexico and Cuba help a viewer to position the aurora. In the high contrast original imagery it is possible to see wisps of diffuse aurora in a band across New Mexico, Texas, Oklahoma, Arkansas, and spreading over most of the S.E. US.

RADIO AURORAE:

Radio aurora conditions were reported by at least 50 operators at 144 MHz across the southern US and extending down to Cancun, Mexico and the Caribbean islands. Other reported logs documented radio aurora activity on 50, 220 and 432 MHz.

Ionospheric conditions for the period 6-20 March are shown in Figure 10 which plots the recorded hourly critical frequency of the F2-layer, foF2, scaled from vertical incidence soundings at the Boulder observatory. Local noon is at 1900 UT and the rapid rise in foF2 at 1300 UT is caused by sunlight beginning to illuminate the ionosphere above Boulder. These days have their local evening foF2 values near the monthly median except for the 15th. On 13 March at 0600 UT the Boulder foF2 value drops well below the median and stays low (or missing) until 0600 UT on the 14th. Daylight values on the 14th recover to near the median until around local noon and are then depressed through the 15th and into the 16th. Daytime values on the 16th are again depressed and then near-median conditions persisted until the 19th.

CONSEQUENCES OF THE MARCH ACTIVITY AT AND NEAR EARTH:

Reported consequences of the March solar activity as sensed at or near Earth include documented effects on satellites in space (geostationary and lower altitude), ionospheric perturbations that affected telecommunications and navigation systems (satellite and ground-based), the great magnetic storm described above, aurorae reported at unusually low latitudes (mistaken for fire reflecting off clouds or other unusual phenomena), and documented effects on technological systems -- some amusing and some serious. We do not include any material from classified sources. Failures in commercial and defense systems are sensitive topics and are not referenced here. There probably are other failures of which we are unaware. In the listing below, if an item is given without specifics, it is because our sources asked us not to reveal details.

EFFECT ON SPACE SYSTEMS:

- o There was concern about the launch of the shuttle Discovery during Ground Level and PCA Events; however, as discussed above the low inclination and low-altitude orbit combined with the soft spectra of the particle event to minimize radiation exposure to the astronauts. There was concern about the injection of TDRS-D into its operating geostationary orbit during the progress of a major magnetic storm, and in fact some anomalous behavior of the TDRS-D satellite in orbit has been reported. It is being investigated whether the launch conditions or the continuing geomagnetic activity was responsible.
- o A previously stable low-altitude satellite in near circular orbit at roughly 60° inclination began episodes of uncontrolled tumbling on March 6, 8/9, and 14th, which interfered with operations.
- o GOES-7 had a communications circuit anomaly on the 12th, lost imagery and had a communications outage on the 13th.
- o Three low-altitude NOAA polar orbiting weather satellites and the USAF DMSP counterpart to the NOAA series had trouble unloading torque due to the uncommonly large ambient magnetic field changes.

- o Japanese geostationary communications satellite CS-3B had a severe problem at 1050 UT on 17 March that involved failure and permanent loss of half of the dual redundant command circuitry on-board.
- o Barnes limb sensors used to lock low-altitude polar orbiters onto CO2 brightening at the Earth's limb have sensor degradation well-correlated with rising solar activity. This was encountered in 1978-79 "but the problem went away" without engineering fixes.
- o Operational satellites of the European Space Agency were reported not to have experienced outages but MARECS-1 (177°) had many switching events on 3, 17 and 29 March.
- o A series of seven commercial geostationary communications satellites had considerable problems maintaining operational attitude orientation within specified ranges. They required some 177 manual operator interventions to make thruster adjustments in order to maintain the required attitude during the disturbed conditions on the 13/14th. These were more than are normally required during a year of regular operations.
- o The Japanese geostationary meteorological satellite GMS-3 "suffered severe scintillations during 1200-1430 UT on March 23." Data transmissions were lost for about 1 hour around 1300 UT.
- o Geostationary communications satellites reported operational anomalies on 18 and 20 March but not on earlier disturbed days.
- o The aging NASA satellite SMM was said to have made good recordings of conditions during the disturbances but "it dropped in altitude as if it hit a brick wall" during the time of highest magnetic activity. It is reported to have dropped 1/2-km at the start of the "big storm" and to have dropped "3 miles" during the entire disturbed period.
- o More than 80,000 items in orbit are tracked daily from Earth and most are identified and orbits calculated. When a new object is detected it is commonly called an "Uncorrelated Target" (UCT) and efforts are made to identify it as either a new object in space or a previously known object whose orbit has changed. Most UCTs are debris from satellite launches or breakups but some are "lost" satellites whose orbits are changed by increased drag due to heating of the upper atmosphere by solar and geomagnetic activity. Around 1000 UCTs are normally encountered daily but on 13 March there were about 2000 reported. The number rose daily by about 500 to 800 events (the largest increase was on the 17th March) to reach a maximum on 18 March of almost 6000 UCTs. After that, the number declined to around 2300 UCTs by 23 March.

COMMUNICATIONS AND NAVIGATION DIFFICULTIES:

- o On March 6 a commercial radio network warned affiliates of potential for signal relay problems during the two weeks ahead.
- o The US Coast Guard reported numerous LORAN navigation problems, particularly on 6 and 13 March. These were accompanied by problems with using hf-radio communications to alert users to the problems.

- o The US Navy MARS (marine hf-radio network) circuits on 10-20 MHz were out worldwide while 144-148 MHz transceivers used for shorter-range communications were receiving powerful signals from remote locations.
- o A new hf-Direction Finding system to be demonstrated in Texas on 13 March failed to work due to "removal of the ionosphere."
- o A ham operator in Minnesota reported "auroral radio propagation features observed down to Ecuador and Columbia." Below 50 MHz "the ionosphere disappeared" while at higher frequencies range and intensity were enhanced, e.g. California Highway Patrol messages were overpowering local transmissions in Minnesota.
- o VLBI observer in the Florida keys reported exceptional communications at frequencies > 140 MHz.
- o In Australia there were many reports of poor hf-radio conditions on 13/14 March. Polar to mid-latitude circuits were "useless" and equatorial circuits were "very weak and noisy." During daytime foF2 on the 14th was "mostly < 5 MHz". Large, rapid swings of foF2 occurred at night on the 14/15th.
- o In the US, the Boulder Ionosonde recorded foF2 at night as low as 2 MHz and there were periods when it could not be measured because of D-layer absorption. During the daytime foF2 was 4 to 5 MHz.
- o Geodetic surveys in the US and, possibly, ship navigation near Australia using signals from navigation satellites were impaired.
- o Automatic garage doors in a California coastal suburb began to raise and close without apparent reason. The phenomenon was eventually traced to a Navy ship that was employing a special shore-based system in an attempt to maintain remote radio communications while hf-radio was out of operation.

POWER FAILURES AND OTHER EFFECTS OF INTENSE AURORAL CURRENTS:

- o The Hydro-Quebec Power Company experienced a massive failure that darkened most of Quebec Province for up to nine hours. It was caused by large ambient magnetic field changes at 0244 local time on Monday morning, 13 March. The magnetic storm induced a very low frequency current in power lines of the James Bay generating station. When transformers became saturated by line harmonics, the overcurrent protection on three static "volt-ampere reactive" (var) compensators that control line voltages tripped circuit breakers shutting down about 44% of the power then being distributed. When four other vars shut down due to unbalance protection on the third harmonic filter, the system crashed. Power to Montreal and Quebec City failed and this was quickly followed by collapse of other generating capacity as the networked power grid "protected itself" from the excessive load demands caused by the first massive failure. Hydro-Quebec customers lost use of some 19,400 MW of power in Canada; there was a further loss of 1,326 MW of power exported to the US; and other available power could not be accessed because of the distribution system failure. Some 6 million customers were without

power early in the morning of a new work week. The major restoration effort took more than 9 hours and many customers were without power for longer times.

- o In central and southern Sweden there was a simultaneous power loss (within one second) on six different 130 KV power distribution lines at about the same time as the Hydro-Quebec system failure.
- o Local power systems in Pennsylvania, New Jersey, Maryland, New York, New Mexico, Arizona, and California noted effects of the magnetic storm: capacitor banks tripped, voltages were depressed and transformers were noisy but there were only short outages and no general blackout.
- o Aeromagnetic and other field survey conditions were reported as "impossible" from South Africa, Australia, Canada, and the US.
- o Declination changes of greater than 3° measured at US magnetic observatories exceeded design specifications for a new aircraft magnetic navigation system being tested in the central US.
- o Record -2000 nT H-deviations occurred at Moscow and -620 nT at Kakioka. Magnetometers in Australia were "offscale for 6 hours on the 14th centered on 0000 UT". Magnetometers at mid-latitude US observatories repeatedly off scale on the 13/14th at + 2000 nT.
- o The value $A_p^* = 279$ (derived from a_p indices) was the third largest 24-hour disturbance recorded since these global indices began in 1932. The value $AA^* = 450$ (from a 2-station global index) was the largest 24-hour disturbance recorded since 1868.

AURORAE VIEWING REPORTS FROM GROUND OBSERVERS:

- o Brilliant aurora was seen across the US on the night of Sunday/Monday (12/13 March) and Monday/Tuesday (13/14). Reports were received from upstate New York, New Jersey, Colorado (Boulder), Texas (Brownsville and San Antonio), New Mexico (Los Alamos), Arizona (Ft. Huachuca), and California (Los Angeles and San Francisco). Bright green, blue and white forms were reported over the eastern US with mainly red aurora reported from farther south. Backpackers in the mountains of western North Carolina reported interesting observations from a very isolated location. They saw mostly static bright red aurora for about four-to-six hours but with white beams converging toward the southern horizon. Red aurora were reported from Florida Keys, Grand Cayman Island and Cancun, Mexico.
- o Aurora was reported on the night of 13/14th seen from near London and extending to the southern horizon. It was "brighter than anything I have ever seen ... in terms of 630 nm F-region emissions" according to David Rees (U. College London).
- o Southern Australia was largely under cloud cover that prevented viewing aurorae; however reports were received from large regions of north Australia, including Exmouth (above the Tropic of Capricorn) on the night of 13/14 March.

SURFACE TECHNOLOGY AFFECTED:

- o Geophysical exploration surveyor reports --
S. Africa: "Conditions unlike any seen before! Nothing worked."
W. Australia: "Never seen conditions quite like it."
Bass Strait, Australia: concern over increased pipeline corrosion.
- o Microchip production facilities in N.E. US out of operation two or more times due to magnetic activity.
- o Undersea cables in Atlantic and Pacific had large voltage swings.
- o High levels of UV-B measured around time of naked eye spotting of sunspot region 5395 near Seguin, Texas.
- o Power distribution facility black outs in Canada and Scandinavia.
- o Out of worldwide hf-radio contact from southern US transmitter.

CONCLUDING THOUGHTS:

As the geophysical record is accumulated and evaluated, it is certain that other types of data and other examples of the consequences of the major solar activity of 6-20 March 1989, will become known. We know that there are instances of effects worldwide that have not been publicly reported because of commercial or national security concerns. National, regional and World Data Centers are actively seeking to gather comprehensive data sets from this time for future analysis and are also interested in receiving documented reports of effects.

From comparisons of the annual number of days of high magnetic activity with the annual sunspot number and the annual number of solar flares, it is known that the peak(s) of magnetic storminess do not occur during the years of the maximum solar activity measures. Comparison of the reported number of in-orbit operational satellite anomalies for spacecraft not mainly affected by cosmic rays shows that the frequency of anomalies follows mainly the occurrence of major magnetic storms. Although the current solar cycle is rising rapidly toward maximum (probably to occur in early 1990), the overall level of magnetic activity has not shown a similar increase (E. Hildner, personal communication). The short list of major magnetic storms in Table 1 shows that in 1940-41 and 1959-60 two or more events occurred within 18 month periods. There have been few storms, if any, as great as that of 13/14 March; however, the possibility that another may occur in 1990 or soon after must be considered.

As society continues to move to wider uses of high-technology devices, often controlled by faster and more compact micro-chip electronics, in space, in aircraft, and on the ground and as communications and power distribution grids become more important and more tightly networked, our susceptibility to major impacts on the population and systems increases.

RECENT SOLAR ACTIVITY:

After submission of the abstract for this talk and preparation of the summary review paper on the March activity, more episodes of large solar flares occurred often accompanied by major proton events; also, there were periods of increased fluctuations in the > 2 MeV electron level at geostationary altitude -- sometimes with major magnetic storms sometimes without. Flare locations ranged from central meridian to the west limb and beyond. It is not clear that spacecraft charging was a common occurrence during these episodes but some significant and many less important effects are known.

AUGUST 1989 EVENTS:

On 1 and 2 August there were large, long-lasting diurnal changes in the level of > 2 MeV electrons recorded by GOES-7 (Figure 11). These events, almost surely arising from passage of the satellite through a trapped population of energetic electrons, are not seen every day. On days when there are also energetic proton events, the electron sensor mainly records the changes of proton counts. From 2 August onwards there are one or several upper level C-type or M-type flares daily until on the 12th there was an X2/28 level (X-ray/optical) flare beginning shortly before 1400 UT and peaking around 1430 UT. The differential proton energy traces began rising out of the background about 1520 UT and the integral flux of > 10 MeV protons reached a maximum of 9,200 pfu on the 13th at 0710 UT. J. Feynman has plotted the comparable proton fluxes from the August 1972 and 1989 events (Figure 12, personal communication). Further X-level flares occurred daily on the 14th-17th with one early on the 16th from region # 5629 near the west limb that reached an off-scale estimated maximum of X20.0/28 at 0118 UT. This flare on the 16th produced a step-like increase in the highest energy proton counts around 0140 UT (Figure 13) and cosmic ray neutron monitors worldwide recorded a 7% to 10% increase, a "Ground Level Event" (GLE). Apart from a possible small GLE in July 1989, this was the first such widely recorded event in 11 years, i.e. the first of cycle # 22.

Geomagnetic storm sudden commencements (ssc's) occurred on 14, 21, 23, and 27 August and there was an intense magnetic storm on 28/29 Aug. Auroral zone magnetic conditions from Greenland across N. America to Alaska were extremely disturbed during this storm. The flux of lower energy electrons at geostationary altitude in the 290 KeV - 2 MeV range was about 10^6 and in the 30 - 300 KeV range was about 5×10^7 at 0330 UT on the 29th. These disturbed magnetic conditions and high electron fluxes corresponded exactly in time with the permanent failure of half of the GOES-6 telecommunications circuitry. This failure was progressive. It began with the start of the magnetic storm and ended at the peak with total system outage until a separate, redundant circuit was activated. This is only the second such GOES central telecommunications unit failure. The "New Scientist" magazine of 9 September 1989 carried an article "Solar storms halt stock market as computers crash" describing the failure of the Toronto Stock Exchange computer system during this magnetic activity when its three "fault-tolerant" disc drives failed in succession.

Without specifying particular satellites or orbit locations, we have heard that the hard spectrum particle events characterizing solar activity during mid-August affected star sensors and caused a greatly increased number of SEUs compared to the softer spectrum events of March and that during this period multiple flares occurred in quick succession from a sunspot group near

to central meridian until it moved onto the west limb. These events combined increased fluxes of both high-energy protons and lower energy electrons and produced major magnetic storms.

LATE-SEPTEMBER/EARLY-OCTOBER 1989 EVENTS:

On Friday, 29 September, region # 5698 (S26°,W105°) produced an X9.8 flare beginning around 1047 UT from around the far side of the sun's west limb. No optical flare was seen from Earth; however, the MAGELLAN satellite enroute to Venus was at 0.7 Re and about 45° west of Earth and well positioned to receive a direct exposure to the flare particles. From Earth, a large loop prominence truncated at the bottom was observed rising above the sun's west limb. This region was the source of X-ray emissions seen by GOES-6 and -7. Energetic protons recorded by GOES began to rise above background levels around 1150 UT and reached a maximum at 0210 UT on the 30th. The event had a very hard spectrum and lasted through 4 October.

The Thule Neutron Monitor reached a 378% increase above background level (Figure 14, SESC), making this the largest amplitude GLE since February 1956, some 33 years earlier. Margaret Smith (Canada) reported that the GLEs recorded at Deep River and Ottawa were both > 300% and at Inuvik > 475%. The event showed an unusual double-humped trace. Louise Gentile (AFGL) is compiling cosmic ray event amplitudes and related information with Peggy Shea (AFGL). She reports that two monitors near Rome, Italy recorded GLEs of 98.2% and 124.4%. John Humble (U. Tasmania) reported that the GLE at Hobart exceeded 400%.

One family of 13 geostationary communications satellites recorded 46 "hits" from 0912 UT on 29 September through 0048 UT on 5 October. On the 30th these satellites experienced about one hit per hour. Most were relatively minor "pitch glitches"; however, some were SEUs and some were phantom commands that could have fired thrusters except for software safeguards. From 09/29-10/01, TDRS-A (now a reserve satellite) recorded 53 RAM hits in the memory chips now known to be susceptible to cosmic ray energy. The normal number is about 1 hit every other day. However, the two newer satellites TDRS-C and -D did not have RAM hits due to the changeover to hardened chips. NOAA's GOES-5 and -6 experienced SEUs on 30 September. GOES-5, -6, and -7 experienced "severe drops in current" output by solar power panel arrays on the 29-30th (about 0.1 amp). The polar orbiter NOAA/TIROS-10, in 100% sunlight, experienced an uncommanded telemetry change on 1 October at N73.8°,E166.6° at 0619 UT.

Many star sensor hits are known to have caused orientation problems in some satellites and a greater incidence of SEUs was logged during these six days than during the record days in August 1989. Suddenly, it was an interesting topic to compare total fluence during the maximum 24-hours at the end of September with the maximum period in August 1972 which has long served as the anomalously large proton event.

MID-OCTOBER 1989 EVENTS:

On Thursday, 19 October 1989, at about 1230 UT a large solar flare began near the Sun's central meridian. It peaked at 1258 UT at an estimated X13 level (above X12 is off scale on GOES). Optically the flare was rated 4B (as was the large flare on 9 March 1989).

Relativistic protons began to arrive at GOES-7 just after 1300 UT and another GLE was recorded worldwide. Prompt contacts from satellite teams and operations groups revealed concerns about: communications satellites having unusually frequent pitch glitches, GALILEO enroute to circle the Sun being exposed to high energy particles that could impede important communications during these early stages of deployment, MAGELLAN had a serious star sensor hit that finally made it necessary to try and find a software contingency means to orient the satellite when it arrives at Venus.

Reports from 19 Oct and following days included:

- o GOES-6 had 2 SEUs and GOES-5 had 1.
- o GALILEO project team turned on the > 10 MeV/nucleon sensor to monitor heavy ions during the flare emissions. Since Friday at 8:00 pm PDT, Tom Garrard (Cal Tech) confirms that they recorded clear flare signatures in the particle composition and that oxygen ions are an important part of the plasma.
- o A polar orbiter lost a microwave transmitter unit. It was reset from ground control and went out again after about 2 minutes. They were advised to leave it off until the activity ends.
- o TDRS operations reported: TDRS-A had 50 RAM hits on 19/20th. TDRS-C had 2 and TDRS-D had 4 SEUs.
- o MAGELLAN star sensor not recovered as of 26 Oct and major loss of power output from solar panels.
- o Joan Feynman (JPL) estimated solar wind velocity > 2000 Km/sec.
- o ESTEC preparing SEU list for low-altitude ESA satellite UOSAT-2 in polar orbit.
- o GOES-5, -6 and -7 power panel output losses about factor of six greater than during September 29, 1989 period.
- o Strong geomagnetic storm on 21 Oct recorded in Japan. Bright red aurora seen in N. Japan at N35° geomagnetic latitude during two separate intervals on 21st. Report of large voltage fluctuations of electrical power for optical communications cable between Japan and USA.
- o Low-latitude aurora sightings reported from Australia (-S35°) at 1330 UT on 20 Oct and 1430 UT on 21 Oct. From Deltona, Florida (-N28.5°) at 0030 on 21 October. Many other sighting reports.
- o Magnetic storms recorded by US observatories on 20 and 21 October.
- o Magnetopause Crossing (MPC) by GOES-6 and -7 on Friday, 20 Oct, from 1700-1900 UT as both GOES moved outside magnetopause.
- o GLEs recorded on 19 October at Jungfrauoch (5%), Kerguelen (25%), Ottawa (41%), and Oulu (38%). Another GLE occurred on 22 October and measured 17% at Oulu.

- o Solar power panel array systems on commercial geostationary communications satellites degraded about 0.3 amp each on two oldest spacecraft and about 0.7 amp each on 11 others. These 13 satellites had the following pitch glitches and SEU counts: 19th - 7; 20th - 68; 21st - 13; 22nd - 5; 23rd - 28; 24th - 9; and 25th - 7.
- o On 24 Oct another large, long-lasting X5.7/38 flare occurred from near the west limb. It added another positive upward kick to the high levels of energetic protons persisting since the 19 Oct.

Another "Dear Colleague" memo was assembled dealing with the solar activity affecting Earth and satellites in orbit (similar to that circulated for the March events). It included selected prompt plots from SELDADS-II and was sent to a contact list maintained by Joe Allen of persons and institutions interested mainly in satellite anomalies from environmental causes.

Prompt reports of solar-geophysical activity for the days from 19 October are available in the weekly "*Preliminary Report & Forecast of Solar Geophysical Data*" from the Space Environment Services Center (SESC) of NOAA's Space Environment Laboratory. At the end of November the National Geophysical Data Center (NGDC) will publish worldwide early data in *Part 1: Prompt Report of "Solar-Geophysical Data"* (SGD) reports.

Six months later *Part 2: Comprehensive Report* of SGD will contain more extensive data listings and figures. If community support warrants the effort, NGDC's STP Division -- including WDC-A for STP -- will attempt to assemble a comprehensive multi-volume "UAG Report" on the October activity or possibly on the entire "Solar-Terrestrial Highlights of 1989", that is, unless the Sun provides even more impressive events to distract us during the months and years just after sunspot maximum (see the history of cycle 19).

ACKNOWLEDGEMENTS:

Reports of data and information collected by many different people worldwide are integrated into this paper. Sometimes they are from research projects but more often they are from monitoring systems. Often there is no known person to acknowledge or at best only an institutional or national reference is possible. So much of this paper is taken more or less directly from the joint work referenced at the beginning but not yet published (at time of submission) that I wish particularly to acknowledge the major contributions of Herb Sauer, Pat Reiff, and Lou Frank. Without access to the on-line computer system SELDADS-II (NOAA/ERL Space Environment Laboratory Data Acquisition and Display System-II) and the staff that maintain it and the many data bases there, such timely compilations and opportunity for analysis would be impossible. Access to SELDADS is a tremendous asset in trying to follow solar activity and related phenomena. Dan Wilkinson (also a Conference participant) is responsible for developing the multifacet stacked plots of satellite and ground-based data used in this report, in SGD, and in several other presentations.

MAJOR MAGNETIC STORMS

• AA* Most Disturbed 24-hours Index (2-stations from 1868)

Rank	AA*	Start Date	Start Time
1	450	1989/03/13	0600 UT
2	429	1941/09/18	0600 UT
3	377	1940/03/24	1500 UT
4	372	1882/11/17	0900 UT
5	372	1960/11/12	1800 UT
6	357	1959/07/15	0600 UT
7	356	1921/05/14	1200 UT

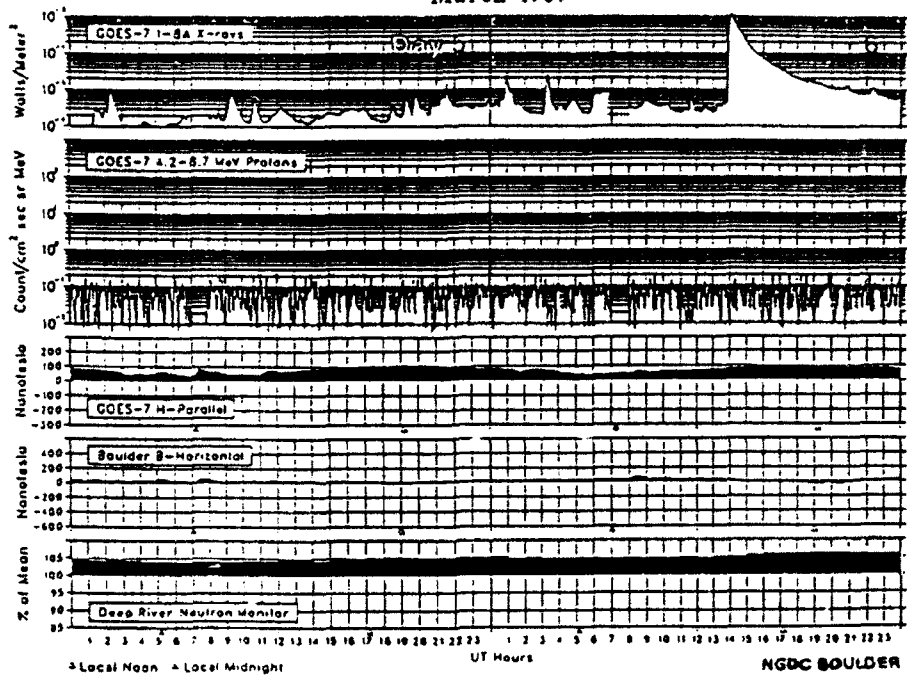
• Ap* Most Disturbed 24-hours Index (13 stations since 1932)

Rank	Ap*	Start Date	Start Time
1	312	1941/09/18	0900 UT
2	293	1960/11/12	2100 UT
3	279	1989/03/13	0300 UT
4	277	1940/03/24	1200 UT
5	258	1960/10/06	0900 UT
6	252	1959/07/15	0600 UT
7	251	1960/03/31	2100 UT

NOAA/NESDIS/NGDC May 1989

Table 1

SOLAR-TERRESTRIAL ENVIRONMENT March 1989



SOLAR-TERRESTRIAL ENVIRONMENT March 1989

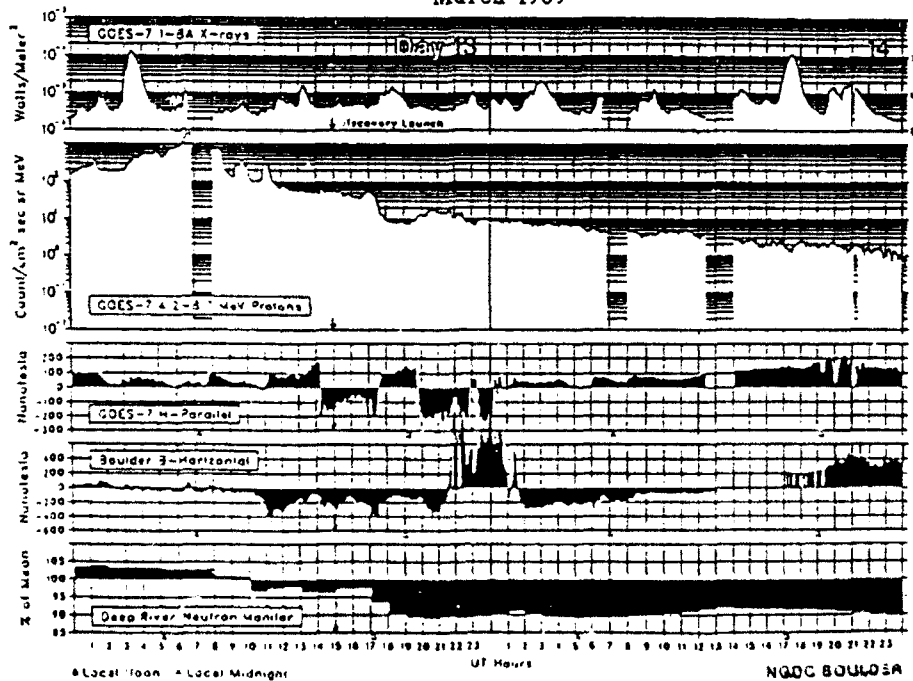


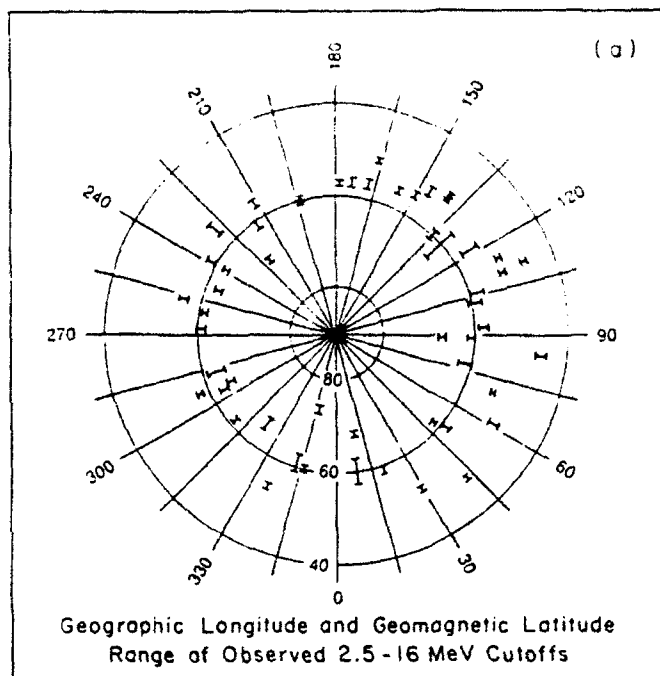
FIGURE 1



HMN 89/ 3/ 9 15:27

FIGURE 2

NOAA-10 March 13, 1989



NOAA-10 March 13, 1989

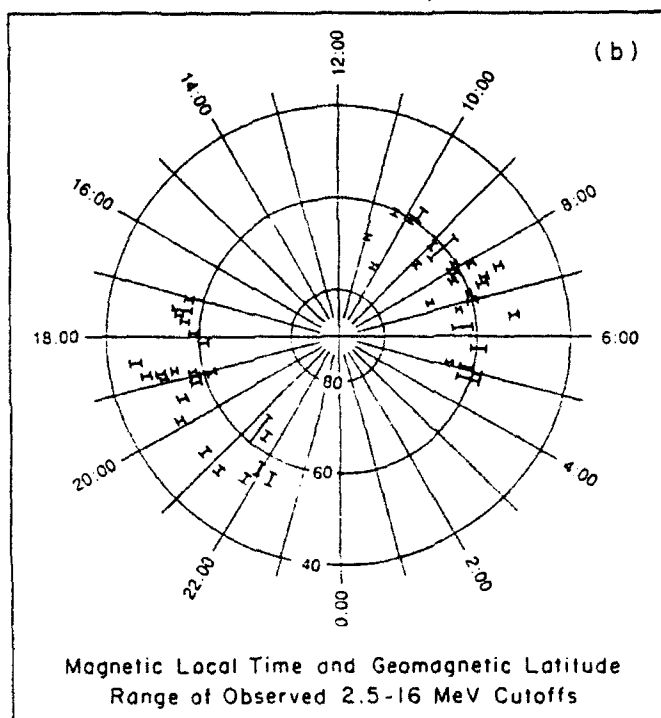
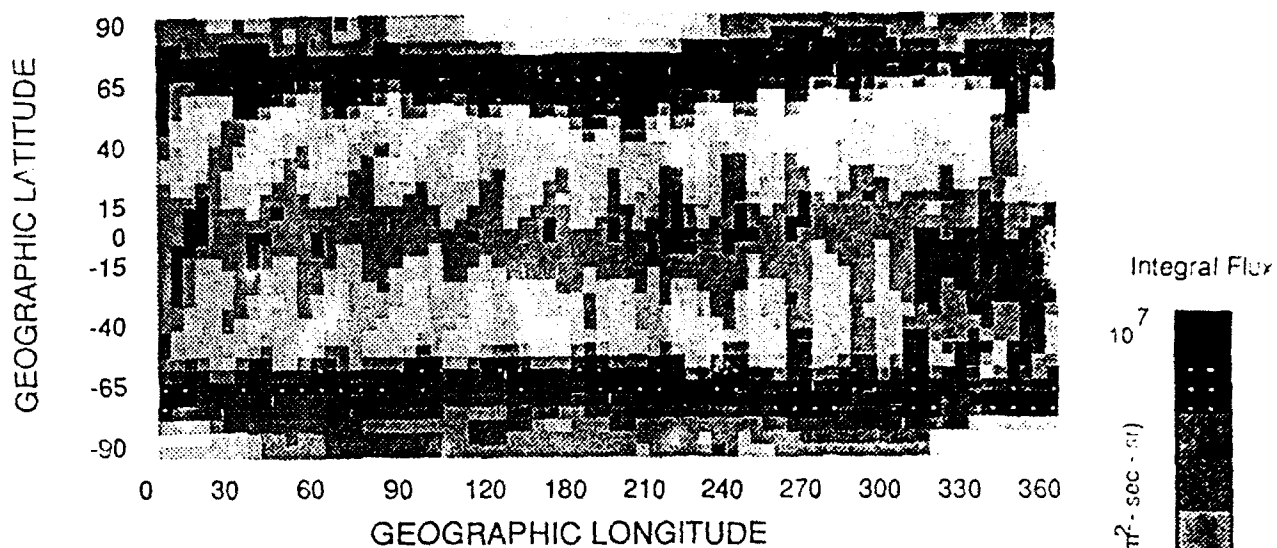


FIGURE 3

NOAA-10 30 - 80 keV PROTON FLUXES

Active: March 11 - March 20, 1989



Typical: March 1 - March 7, 1989

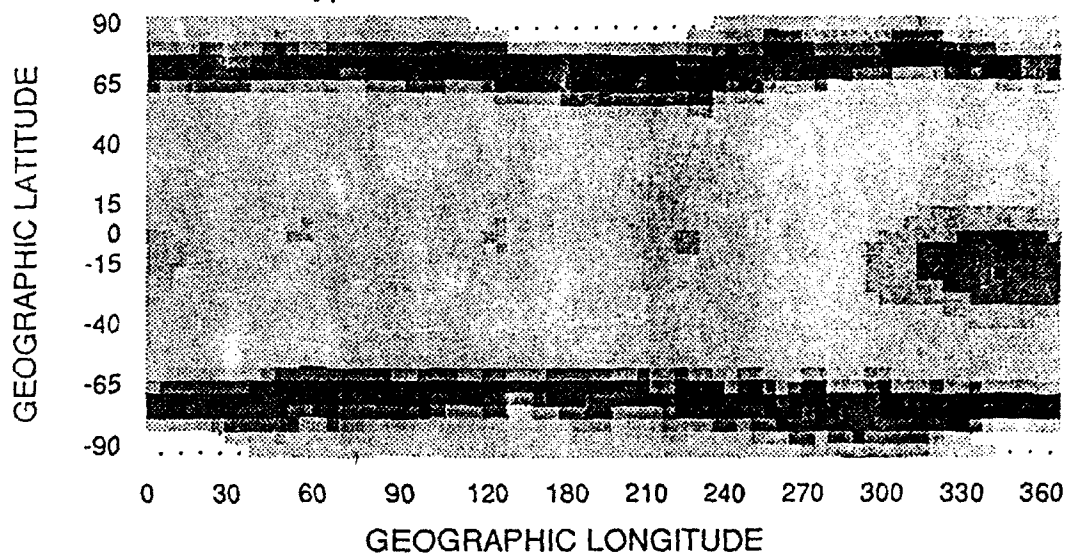


Figure 4

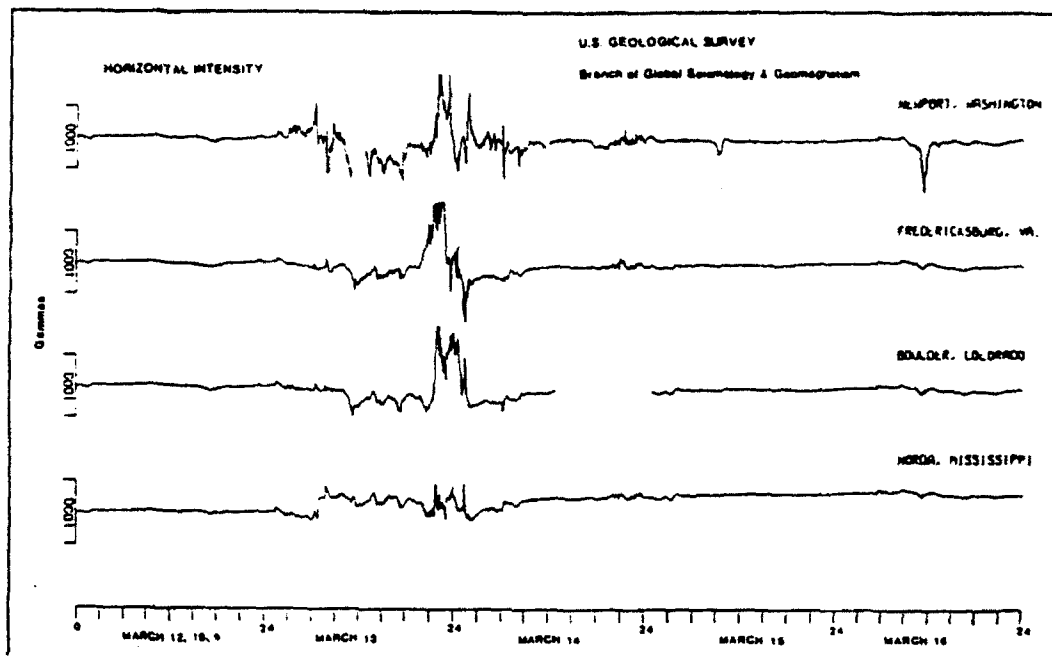


Figure 5

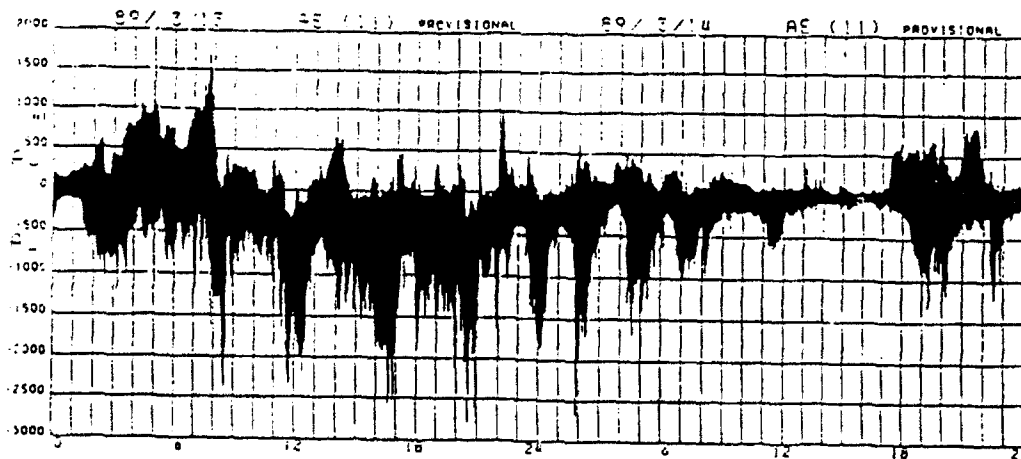
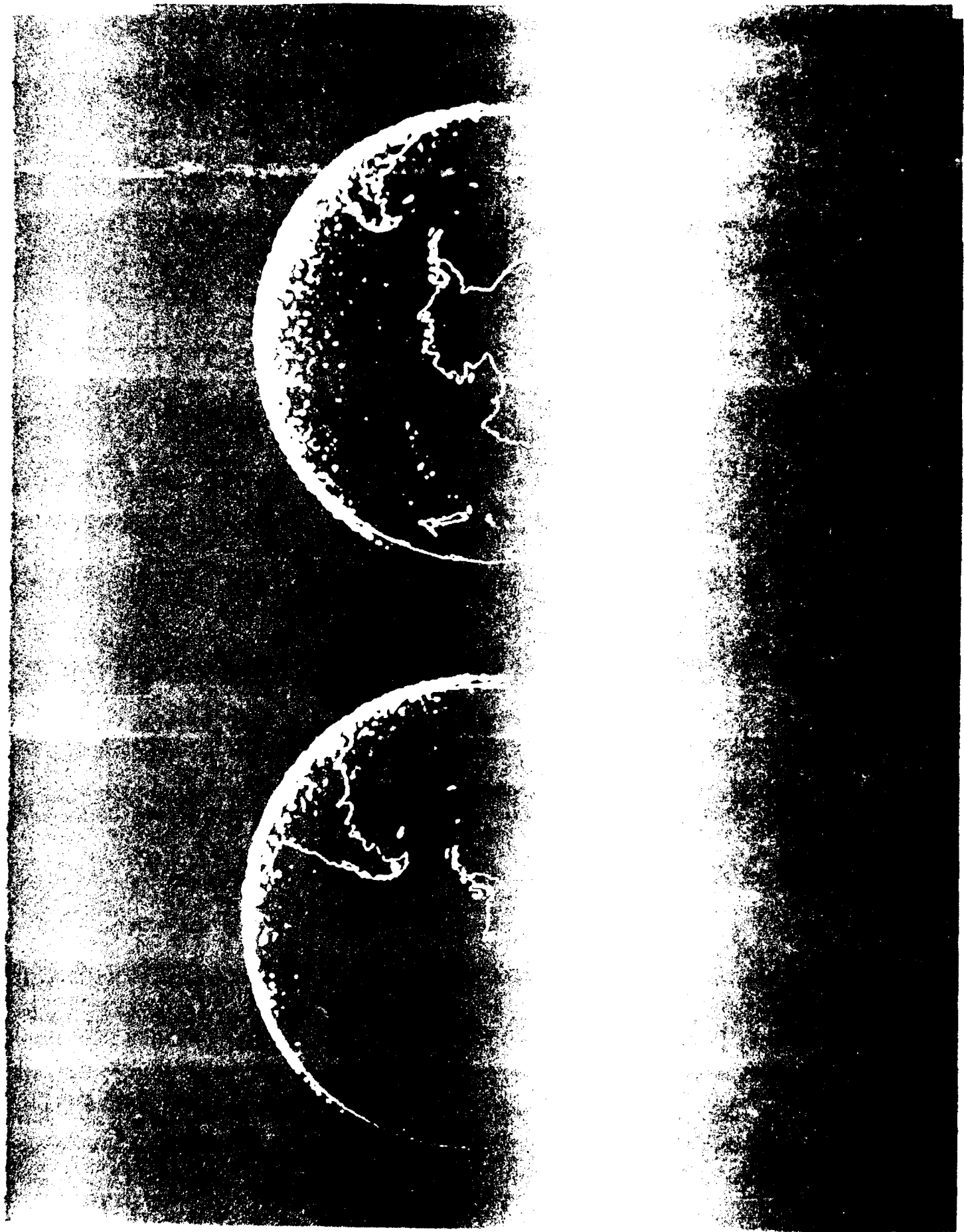


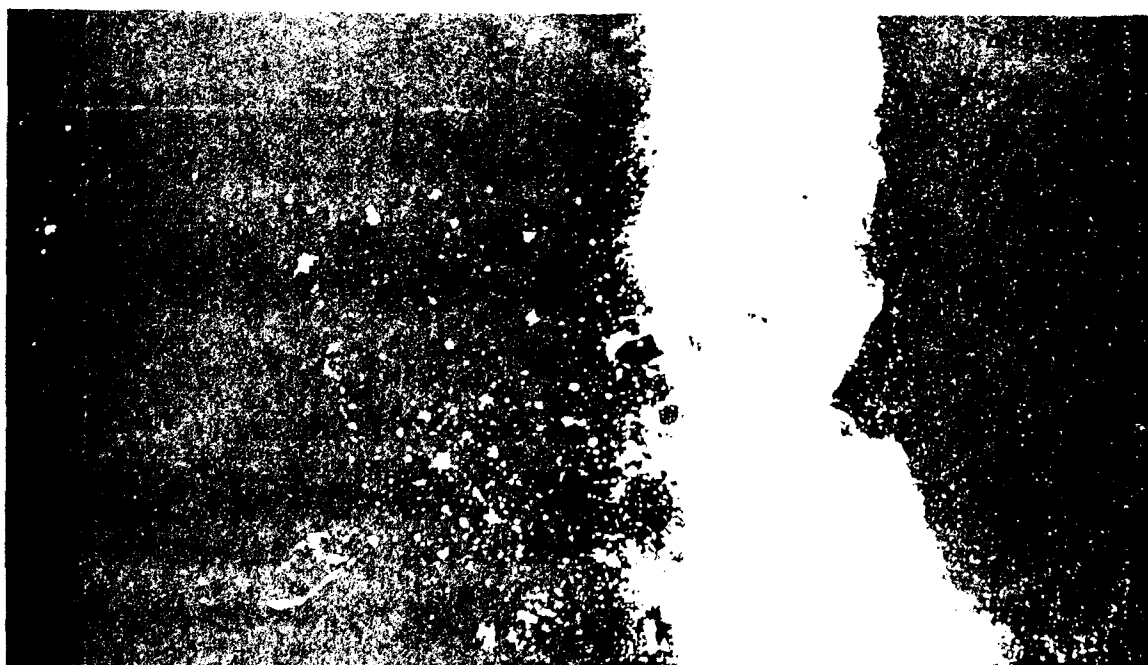
Figure 6



1. **Introduction**
 2. **Background**
 3. **Methodology**
 4. **Results**
 5. **Conclusion**
 6. **References**



Figure 1 is a schematic diagram of the experimental setup. It shows a subject seated at a table, looking at a video screen. A camera is positioned above the screen, capturing the subject's hand and the target. The target is a small object on the screen. The subject's hand is positioned near the target. The diagram illustrates the spatial relationship between the subject, the screen, the camera, and the target.



Boulder f_oF₂
Mar 1989

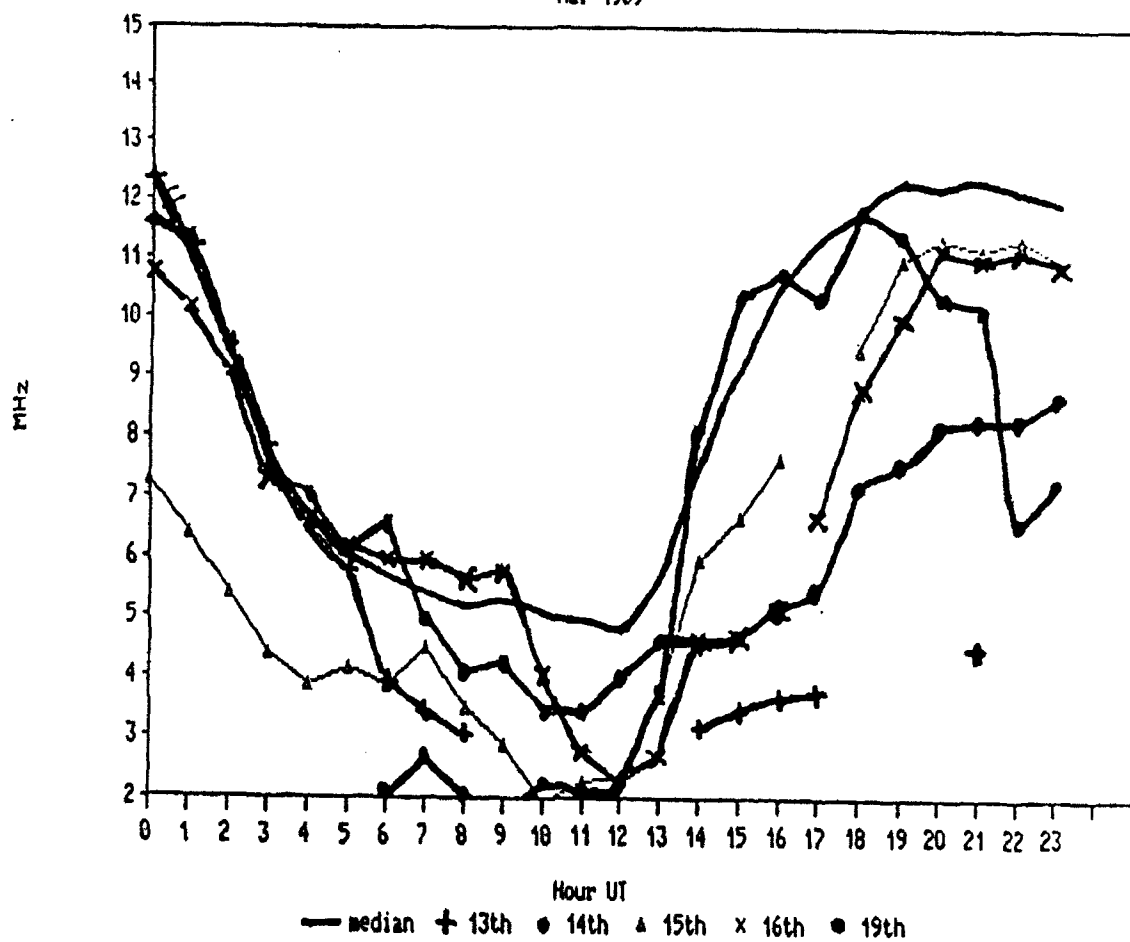
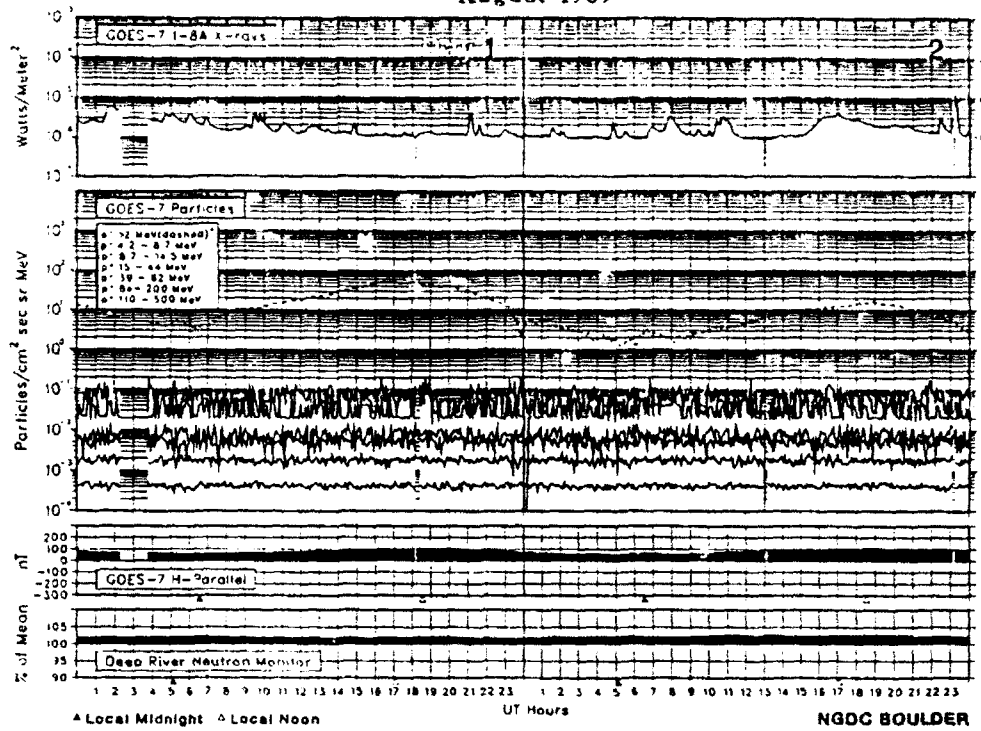


Figure 10

SOLAR-TERRESTRIAL ENVIRONMENT

August 1989



SOLAR-TERRESTRIAL ENVIRONMENT

August 1989

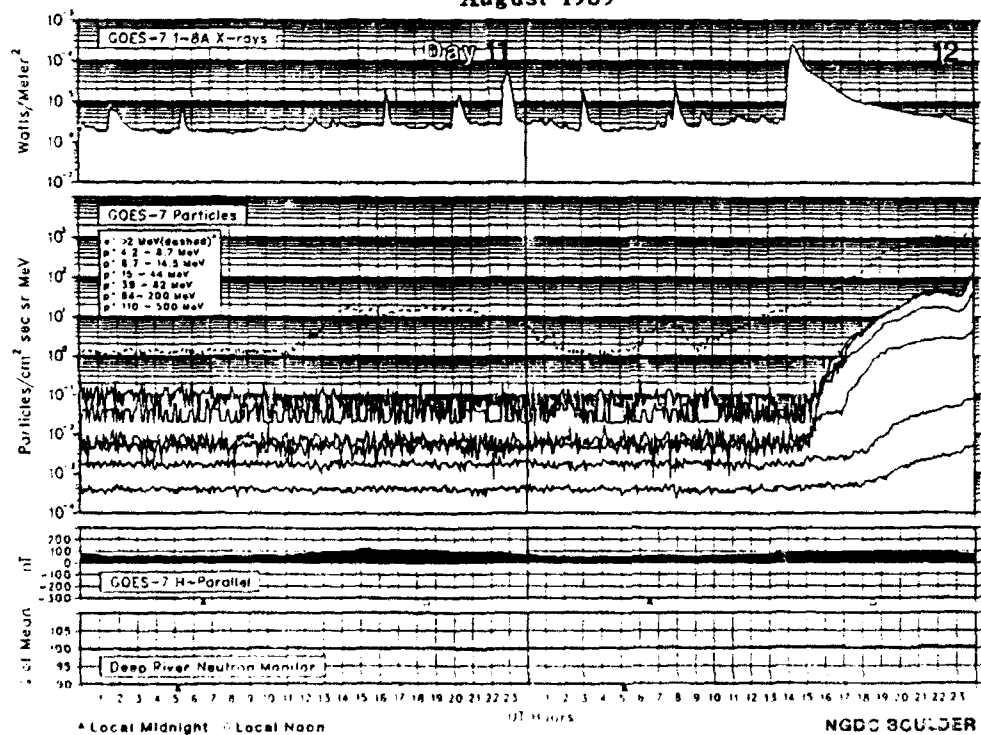
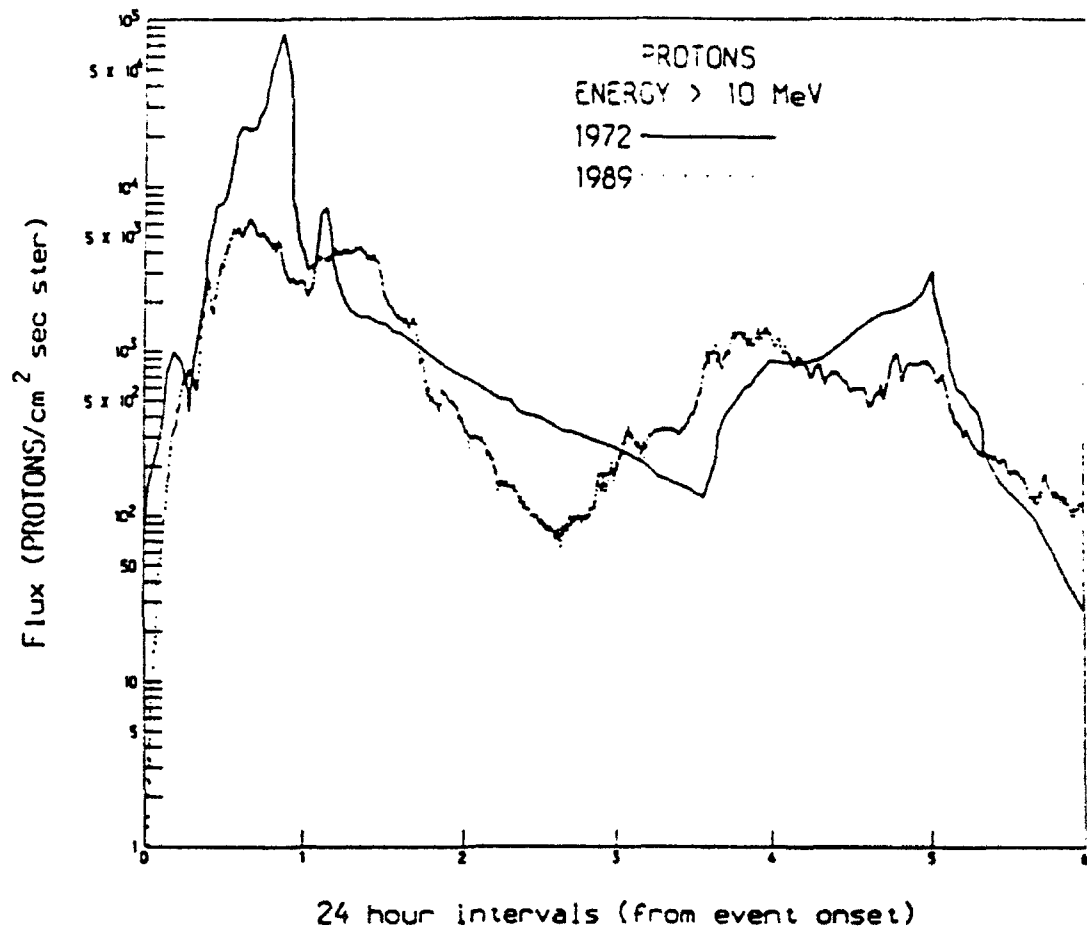


Figure 11

August 1972 and August 1989 Proton Events



From Joan Feynman (JPL)

Figure 12

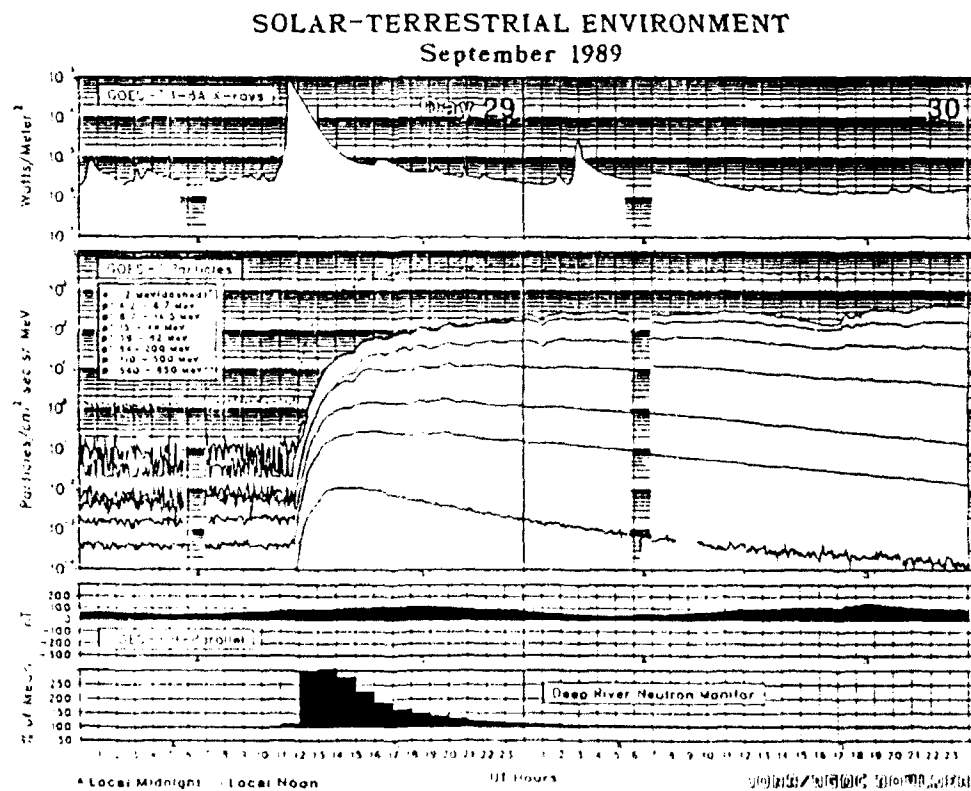
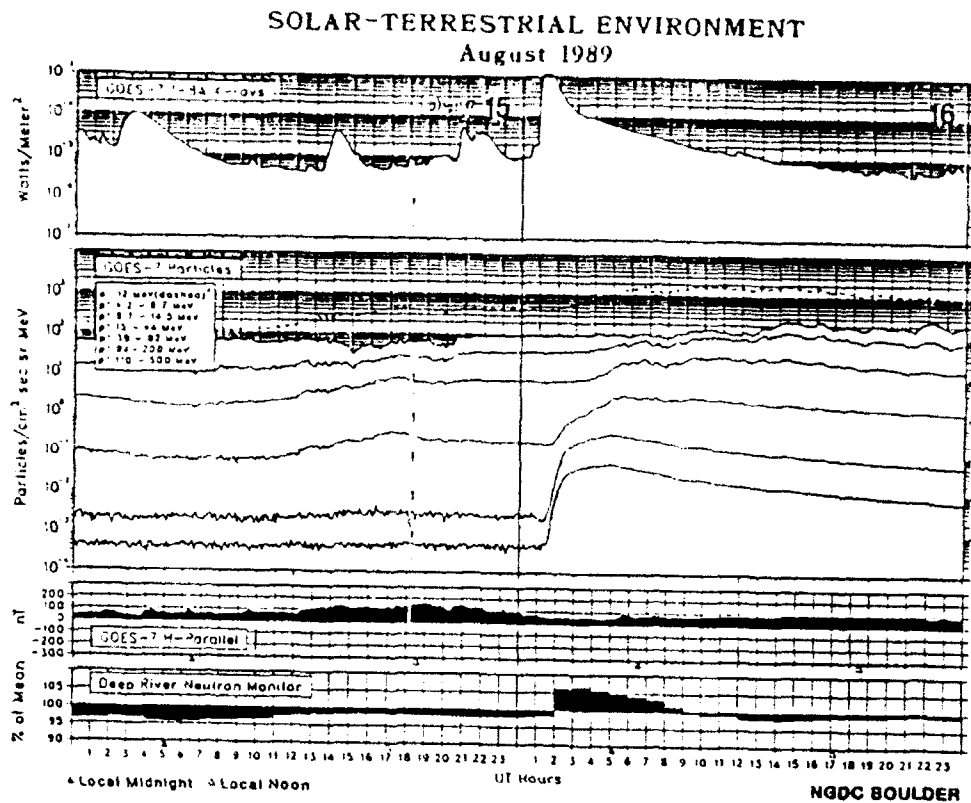
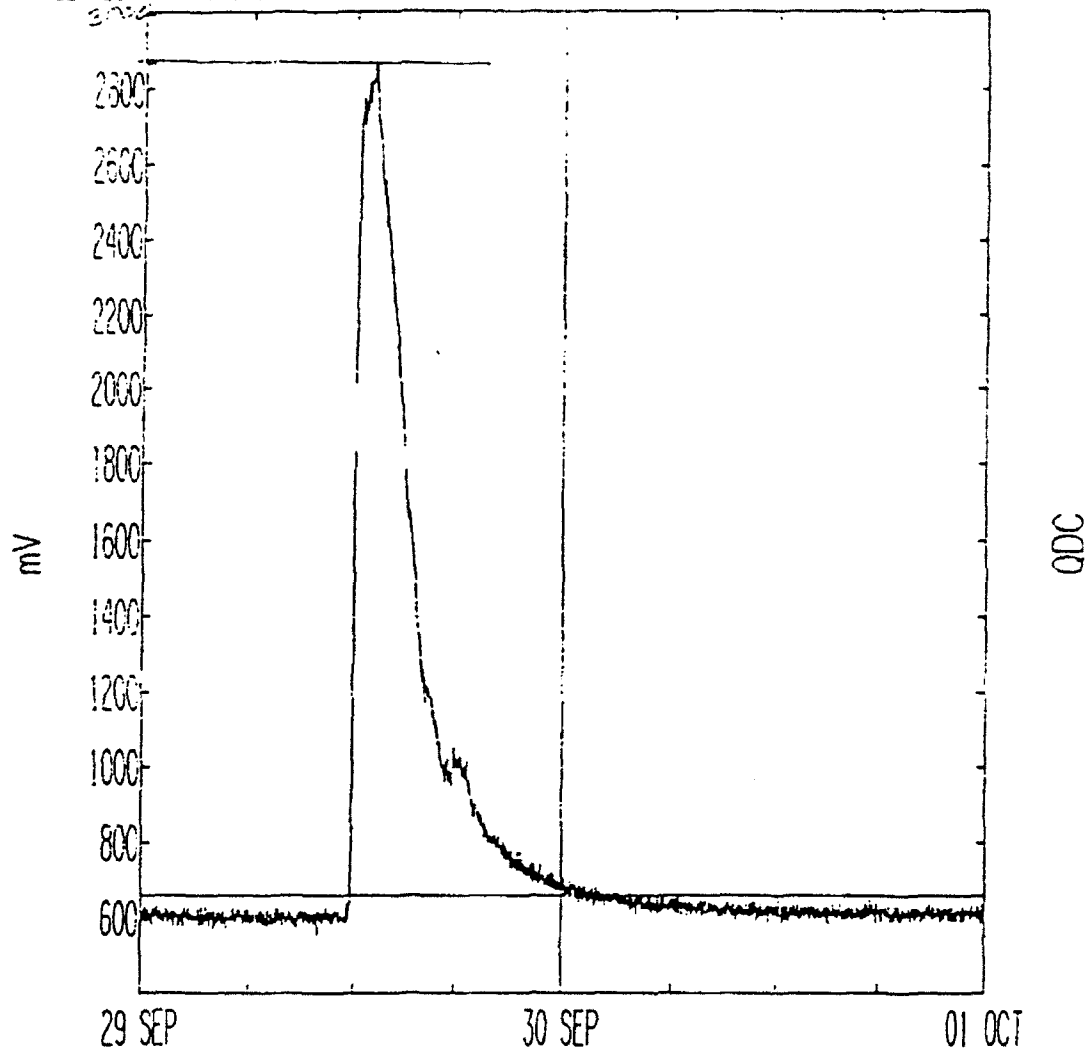


Figure 13

THULE NEUTRON MONITOR 1-WIN DATA

BEGIN: 29 SEP 89



RUN: 1723 UT
5 OCT 89

From Herb Sauer (NOAA/SEL)

Figure 14

REVIEW OF MARCH 1989 SOLAR ACTIVITY AND RESULTANT GEOMAGNETIC STORM

Christopher C. Balch
Space Environment Laboratory
325 Broadway r/e/se
Boulder, CO 80303

Abstract

A large, complicated sunspot region rotated onto the visible disk of the sun on March 6, 1989, and raised solar activity to very high levels for 06-19 March. The region's output was intense, setting new records for the current solar cycle. In particular, the largest geomagnetic storm since 1960 occurred on March 13 and produced auroral sightings as far south as Florida and Texas. Numerous technical systems were affected by the activity including spacecraft operations, the space surveillance network, HF communications, VLF (such as LORAN) communication, and electrical power systems. More recent solar-geophysical activity in August-October 1989 has also been impressive, suggesting that a remarkable solar cycle is currently in progress. Real-time information and forecasting of the space environment is available from the Space Environment Services Center (SESC), a joint National Oceanic and Atmospheric Administration (NOAA) and U.S. Air Force operation.

The Space Environment Services Center (SESC)

SESC is jointly operated by the National Oceanic and Atmospheric Administration (NOAA) and the U.S. Air Force and provides continuous real-time monitoring and predicting of solar-geophysical activity. The center also functions as the world warning agency for an international network of similar organizations. SESC issues a number of products including forecasts, warnings, and alerts of disturbances to a wide variety of users who are affected by the state of the space environment.

SESC collects solar-geophysical data from a worldwide network of ground based and spacecraft observatories. Observatories in Australia, Italy, Puerto Rico, Canada, New Mexico, Arizona, California, and Hawaii report solar optical and radio data to SESC. Measurements of geomagnetic field variations are made locally in Boulder and are received from many locations on various communication networks including an international communications network, and the Remote Geophysical Observing Network which covers much of Canada and parts of the U.S. Total solar x-ray output, the energetic particle environment, and the geomagnetic field at geostationary orbit are monitored by the NOAA Geostationary Operational Environmental Satellites (GOES). Additional particle data are received from the polar orbiting NOAA satellites.

The Solar Cycle

The discovery that sunspots follow a 10 to 11 year cycle was made in the 19th century by Schwabe (1844). Figure 1 is a plot of monthly sunspot numbers. Note that the cycles do show some variation in size and duration.

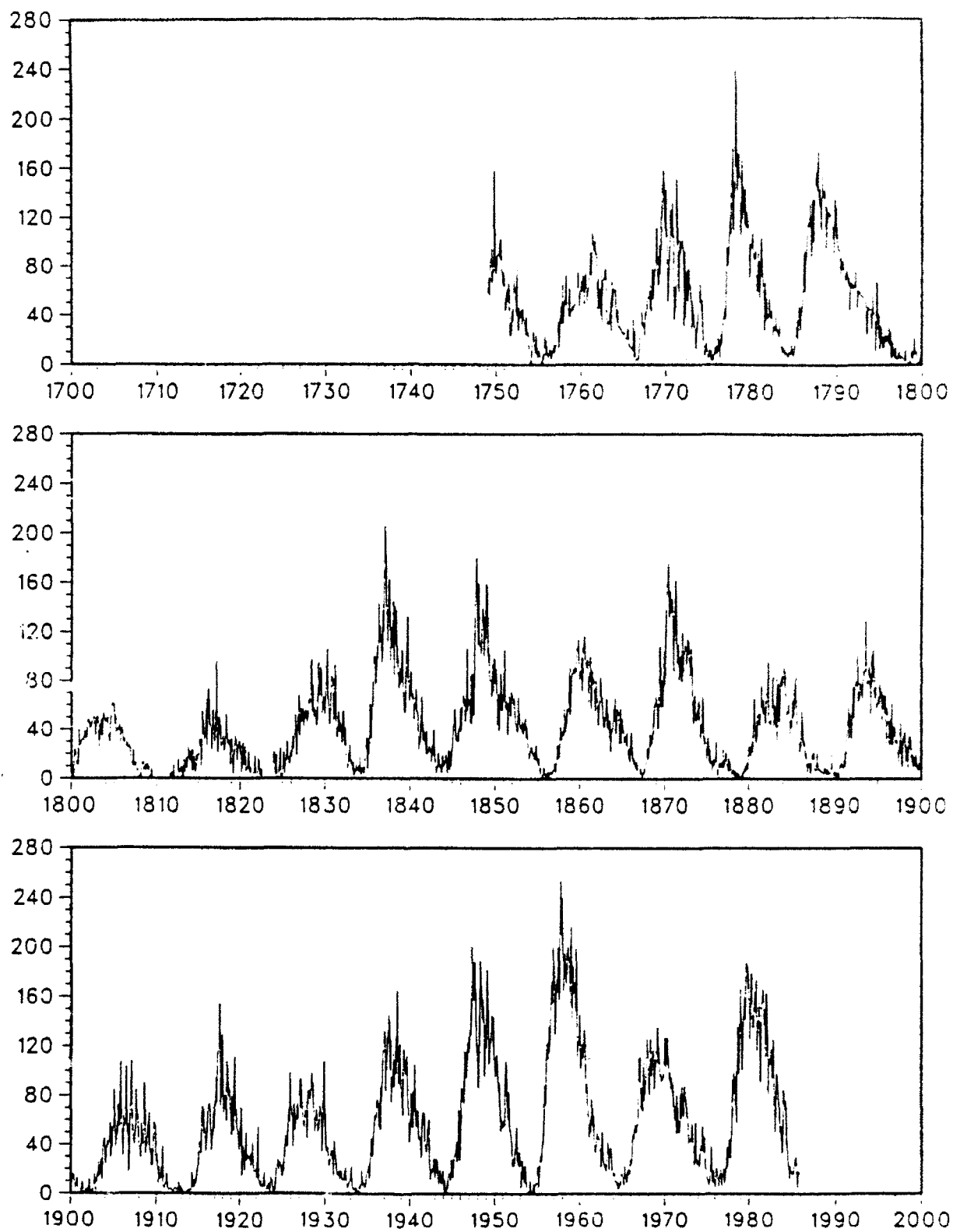


Figure 1. The sunspot cycle.

Associated with the sunspot cycle is the solar activity cycle which generally follows the sunspot cycle. One illustration of the solar activity cycle is the monthly totals for optical flares for solar cycles 20-22 as shown in Figure 2 . Optical flares are brightenings at visible wavelengths in sunspot regions as observed by special filters. Other indicators of solar activity

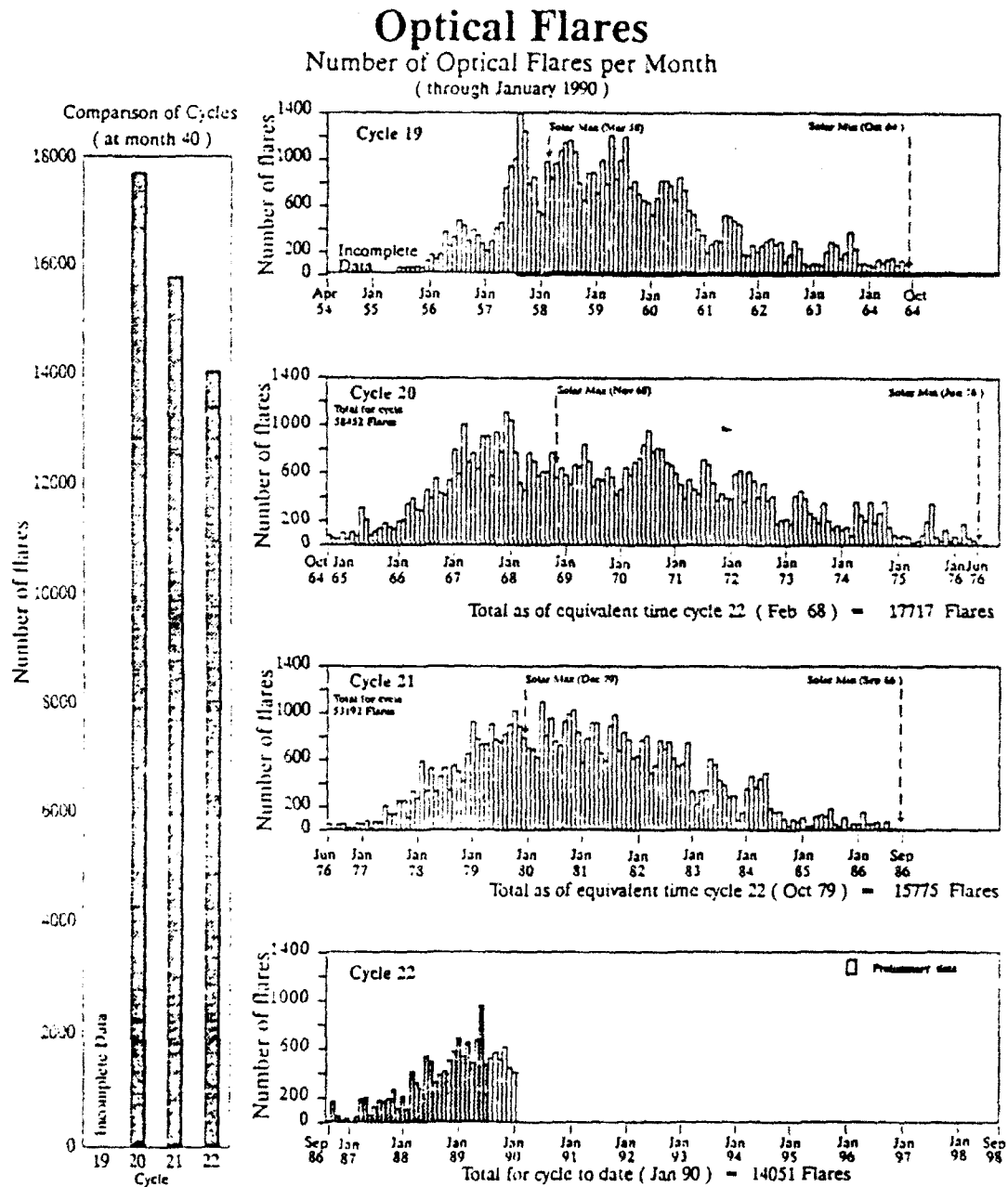


Figure 2.

Source: Preliminary Report and Forecast of Solar-Geophysical Activity, published weekly by SESC

include x-ray flares, energetic particle events, and ground level events. X-ray flares are measurements of x-ray emission during a flare, and are classified according to the peak flux measurement of the event as shown in the table below.

Peak flux range (W/m^2)(ϕ = peak flux)	X-ray flare Classification	Example
$\phi \geq 10^{-4}$	X	$\phi = 3.2 \times 10^{-4}$ is X3.2
$10^{-4} > \phi \geq 10^{-5}$	M	$\phi = 7.2 \times 10^{-5}$ is M7.2
$10^{-5} > \phi \geq 10^{-6}$	C	$\phi = 5.9 \times 10^{-6}$ is C5.9

Energetic particle events are enhancements above background of the flux of measured particles. SESC defines an event as when the flux of energetic protons reaches or exceeds 10 protons/cm²/s/steradian at greater than or equal to 10 MeV. Ground level events occur when very energetic particles from solar flares reach the earth in sufficient quantity that secondary emissions (neutrons) are measured with ground based instruments. An SESC defined ground level event is when the neutron counts exceed 5% of the background level.

Although long term predictions of the solar cycle are difficult to make, one can conclude from Figure 2 that the current solar cycle 22 is still young, and that we should be expecting high levels of activity to continue over the next 3-4 years.

Solar-Geophysical Activity for 6 - 19 March, 1989

The time period from 6 to 19 March was remarkable for solar-geophysical activity. In particular, the geomagnetic disturbance of 13-14 March was historically one of the largest on record. The usual method of measuring the level of disturbance of the earth's magnetic fields is by means of geomagnetic indices.

In this paper, reference will be made to the K-index and the A-index. The K-index is a 'quasi-logarithmic' index which is calculated every three hours by determining the difference between the actual magnetic field variation (in nanotesla) and what would be expected under quiet conditions. This difference is then converted to a K-index using a look-up table specific to each observatory. The A-index is a 24 hour index of the magnetic field disturbance and is derived from the K-indices. The method is as follows: for each K-index, there is an equivalent a_k (lowercase 'a') three hourly index known as the equivalent amplitude. The A-index is then calculated as the average of eight, three-hourly a_k indices and is a number ranging between 0 and 400. The distribution of the A-index as measured by an observatory in Fredericksburg Virginia is shown in Figure 3. This allows us to put the March 13-14 disturbance in proper perspective. The Fredericksburg A-index was determined to be 248, the largest observed since 1960.

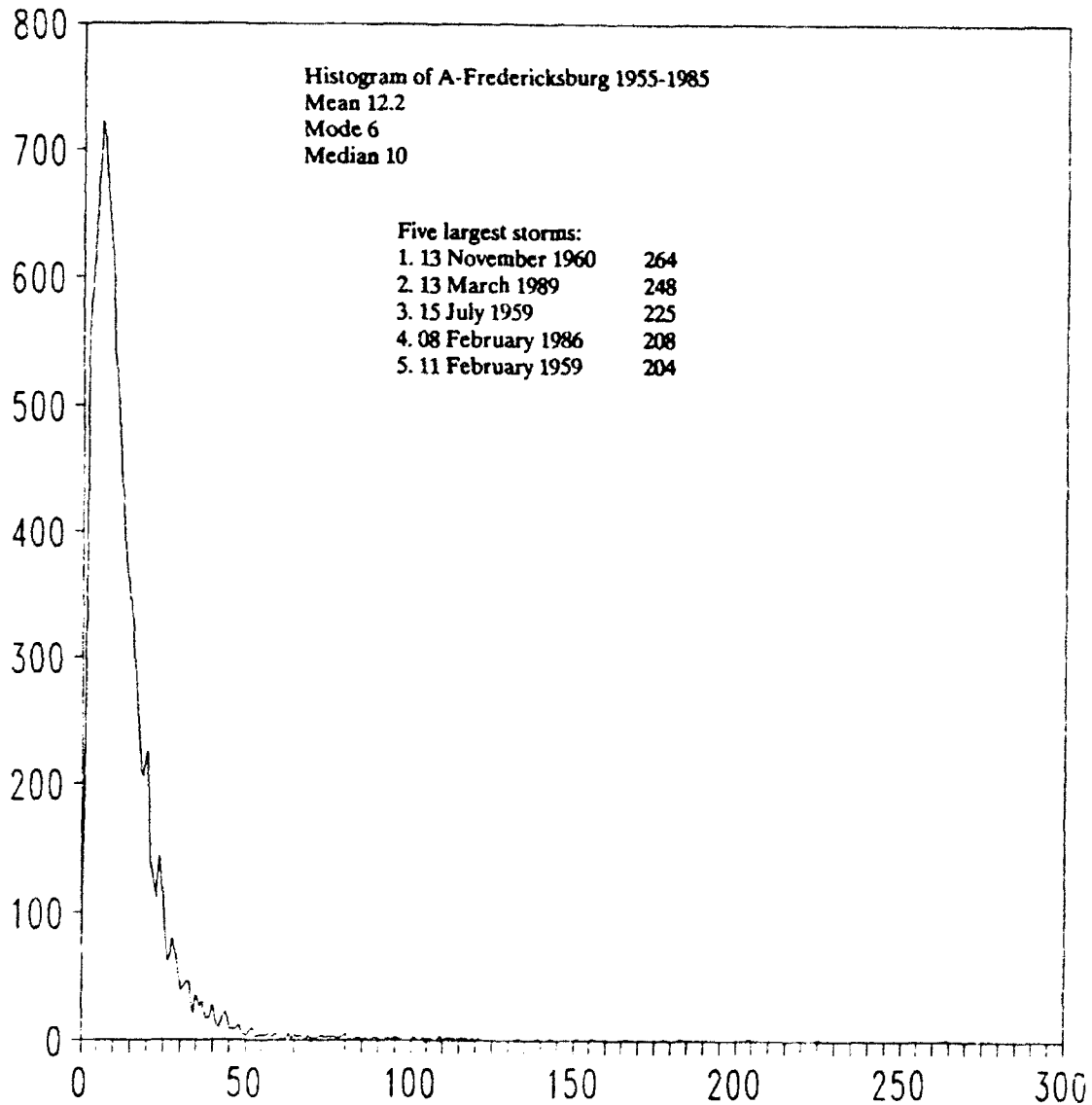
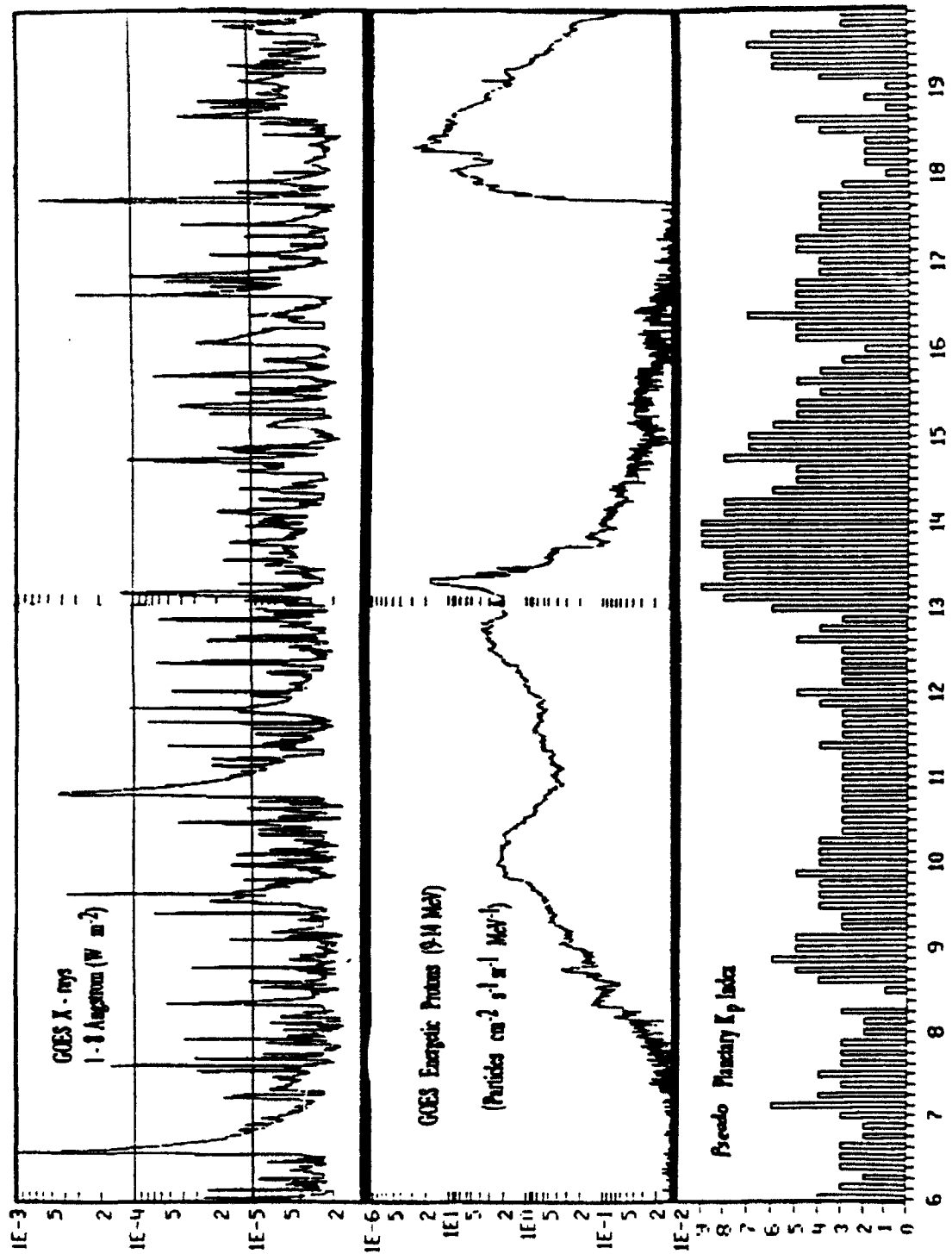


Figure 3. Histogram of the Fredericksburg A-index

Figure 4 is a composite panel of solar x-ray output, measurements of the 9-14 MeV proton fluxes, and the pseudo-Kp index (a real-time estimate of the planetary K-index) during the period. The region's x-ray flare emission consisted of 11 X-class events and 48 M-class events. Of these, three were particularly interesting: the estimated X15 (15×10^{-4} watts/m²) on the 6th, which saturated the GOES x-ray sensors, the X4/4B flare on the 9th which attained the maximum of possible optical classifications (4B), and the X4/3B of 10 March, which was of long duration and was most likely the source of the great 13 March storm.

The particle panel shows the measured proton flux during the period. These proton events did not have large fluxes of extremely energetic protons.



March 1989

Figure 4.

X-ray, Particle, and pseudo K_p from 06-19 March 1989.

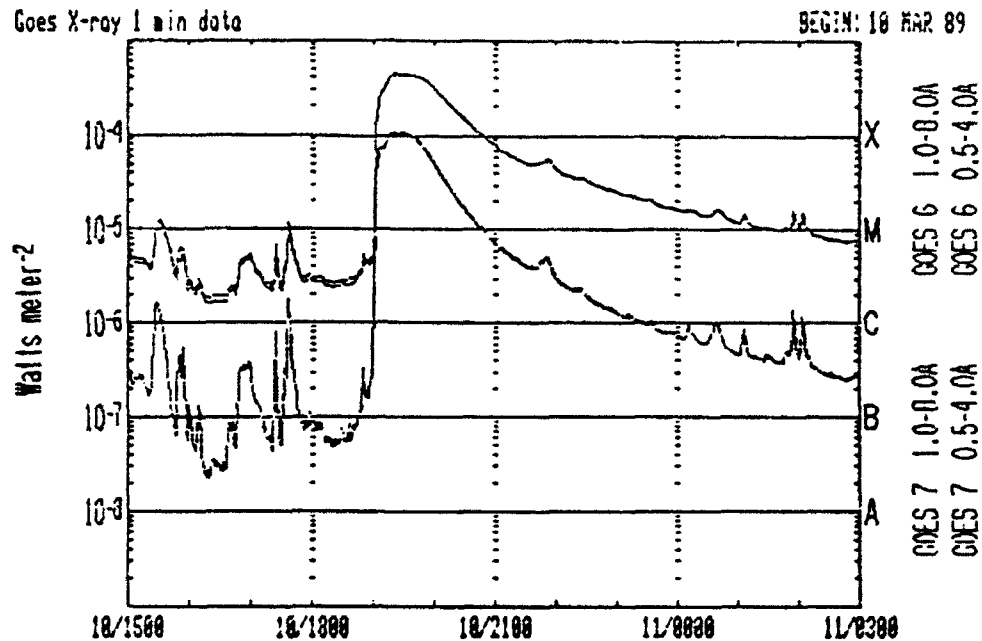


Figure 5. X-ray flux profile for X3/4B flare of 10 Mar 89

The main geomagnetic response to the solar activity was on 13-14 March. Figure 5 shows the X-ray emission from the X3/4B of 10 March. The event was very long in duration, indicative of a coronal mass ejection, an acceleration of plasma away from the sun and into interplanetary space. If the trajectory of this plasma cloud is earthward, and the magnetic fields in the cloud interact favorably with the earth's magnetosphere, a geomagnetic storm results. And such was the case of March 13. A sudden storm commencement was observed at 0128UT on 13 March, signaling the initial impact of the plasma cloud on the earth's environment. Extreme magnetic field variations were observed worldwide, but it was between 13/2100UT-14/0300UT that the disturbance was most severe in the U.S.

Numerous system effects which were observed at the time of the storm have been documented elsewhere (Allen, 1989), so these are now discussed here only in general terms. Geomagnetic storm conditions are associated with frequent injections of energetic electrons (10's to 100's of KeV), which have been known in the past to cause surface charging difficulties for some satellite systems. In addition earth surface potentials can develop in areas of non-conducting geology, and this can lead to induced currents in long line systems. Such induced currents can lead to operational difficulties; in particular electrical power systems and longline communications links can be affected. Solar x-ray activity and the geomagnetic activity affect the earth's ionosphere in differing ways yet with the same consequence: numerous radio communications which use or transit the ionosphere are affected and unusual operational behavior is observed.

Solar Activity update: major events since March 1989

Since March, 1989, the sun has continued to produce remarkable activity. In particular, high solar activity and intense particle events were observed during 12-17 August, 29 September to 05 October, and from 19-31 October. These events are briefly discussed in the following sections. It should be noted that the data for particle fluxes in figures 6 - 9, and the values referenced in the text were those available at SESC at the time of the events of interest. Recently, corrections have been made in the particle algorithm to subtract excess counts introduced by high energy particle contamination. The corrected data plots can be found in Zwickl and Kunches (1989).

12-17 August

Active region 5629 produced two weeks of remarkable solar-geophysical activity. In particular, the region produced the largest solar x-ray event on record. The event saturated the GOES sensors at X12 for about 25 minutes and the peak flux was estimated by SESC to be X20 (2×10^{-3} watts/m²). Flares from the region resulted in the largest proton event that had been seen since August 1972, although it would soon be surpassed by events which followed in later months. Figure 6 is a plot of the x-ray flux and proton flux profiles during the period.

Late on 11 August flare activity picked up noticeably: the region produced 3 M-class events within 9 hours, and one of these was the region's first major flare, an M5/1B at 2302UT. The subsequent days were marked by a series of five X-class x-ray events, a complicated proton event, and a period of increased geomagnetic activity.

The first X-class flare occurred at 12/1427UT: an X2/2B. A proton event started shortly thereafter at 1600UT. The proton event attained maximum of 9200^{*} protons/cm²/s/steradian at 13/0710UT. This peak flux was the largest since August 1972: A comparison of peak fluxes shows that the August 1972 event was about 6 times the size of this event. A major geomagnetic storm, presumed to be produced as a result of this flare, began at 14/0614UT and lasted through the 15th.

The largest X-class event from the region was the record-breaking X20/2N (S18W84) which attained maximum at 16/0118UT. The event was of long duration and had all the signatures typical of a big flare. High energy particle enhancements began at 0140UT and the high-energy fluxes rose quickly to 58^{*} protons/cm²/s/steradian at greater than 100 MeV by 16/0500UT. Increases on the already enhanced greater than 10 MeV channels were less dramatic but resulted in a secondary maximum of 2300^{*} protons/cm²/s/steradian at 16/1430UT. Neutron monitor data indicated that a ground level event also occurred as a result of this flare.

^{*}Uncorrected

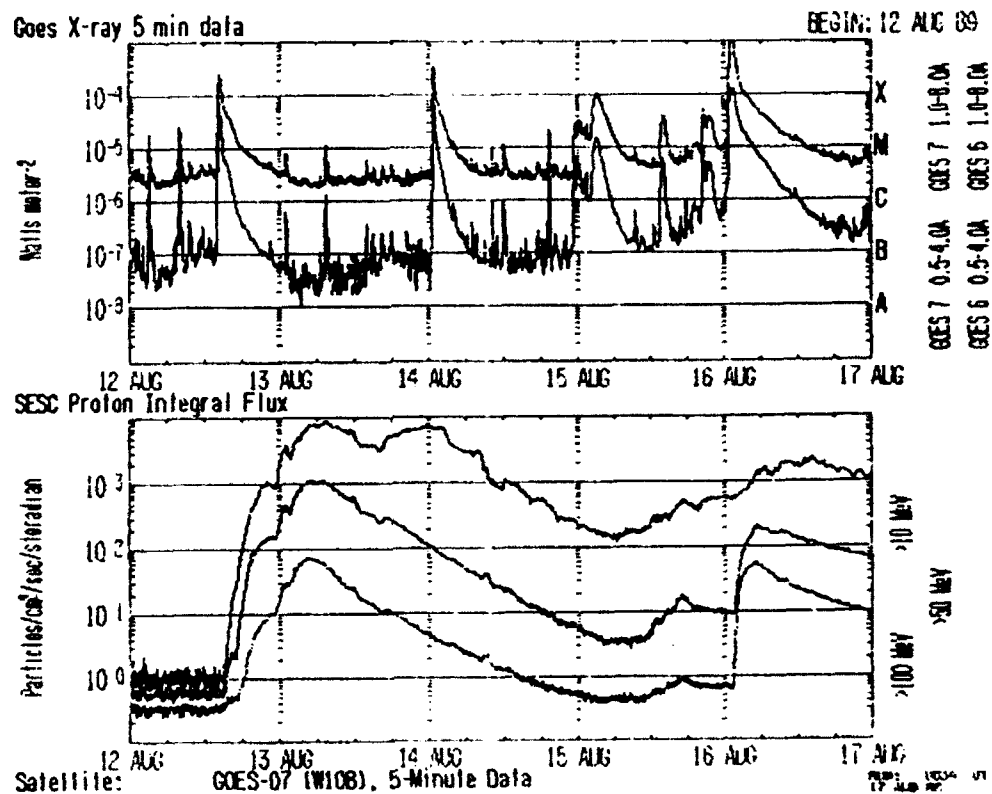


Figure 6. X-ray (top) and proton (bottom) flux profiles during the period. In the top panel, the upper trace is the x-ray emission at 1.0-8.0 Angstrom, and the lower trace is 0.5-4.0 Angstrom. X-ray classifications are based on the 1.0-8.0 Å band. In the bottom panel the different traces show the uncorrected proton fluxes which exceed different energy levels as follows: the upper trace is for energies ≥ 10 MeV, the middle trace is for energies ≥ 50 MeV, and the bottom trace is for energies ≥ 100 MeV.

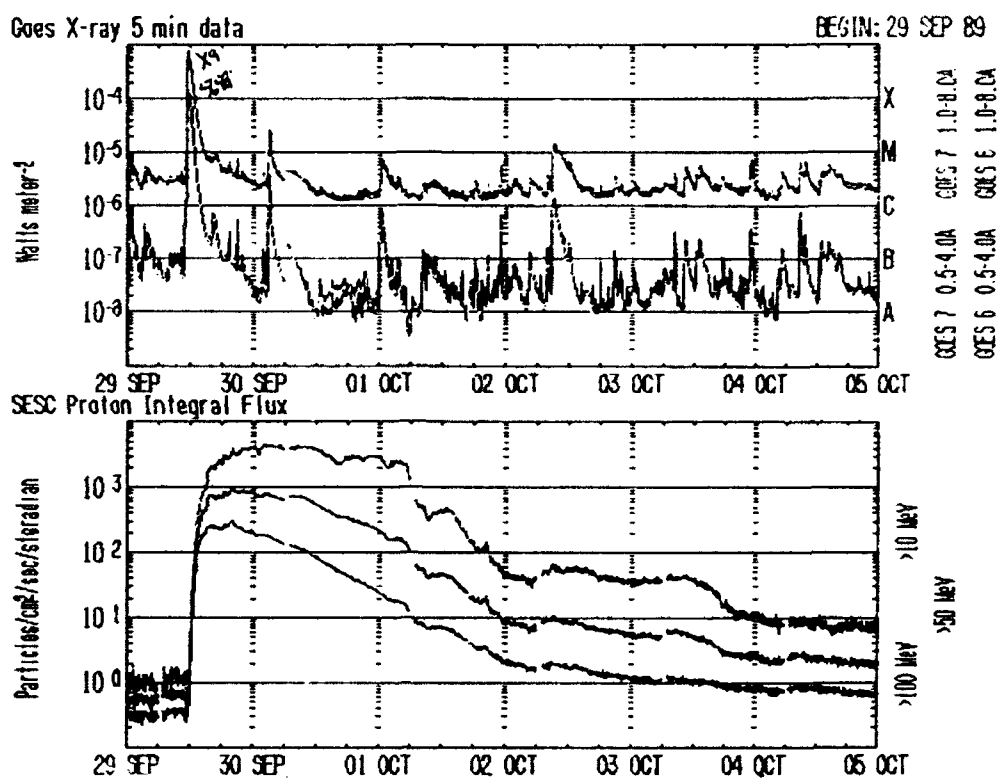


Figure 7. X-ray and particle fluxes, 29 Sep - 05 Oct 1989

29 September - 05 October

The x-ray flux and particle flux profiles for this time period are illustrated in Figure 7. High levels of solar activity occurred on 29 September as SESC region number 5698 produced an X9 x-ray flare at 1133UT as it was going around the sun's west limb. As an immediate consequence of the flare a very energetic particle event started at 29/1205UT, and a ground level event also began. The greater than 10 MeV proton fluxes attained a peak of 4800 protons/cm²/s/steradian, and the greater than 100 MeV proton fluxes attained a peak of 310 protons/cm²/s/steradian. The ground level event attained a peak of 500 percent above background and was noted as the largest GLE observed since 1959 at the time.

19-31 October

This phenomenal period of solar-geophysical activity began with the return of old region 5698 which was assigned as SESC region 5747. A plot of the x-ray and particle emission is displayed in Figure 8. During the region's transit it produced 5 X-class flares and 22 M-class flares. Three of these X-class events led to three separate ground level events and high energy particle flux enhancements in the earth's space environment. These are described as follows: on 19 October at 1958UT an X13/4B flare occurred which produced a proton event which attained a peak flux of greater than 10 MeV particles of 73000 protons/cm²/s/steradian at 20/1600UT, a peak flux of greater than 100 MeV particles of 680 p/cm²/s/steradian at 20/1530UT, and a ground level event of 45% above background. The next injection of particles occurred in response to an X2/2B flare at 22/1805UT and resulted in 8300 protons/cm²/s/steradian at greater than 10 MeV at 23/0710UT, 230 protons/cm²/s/steradian

Uncorrected

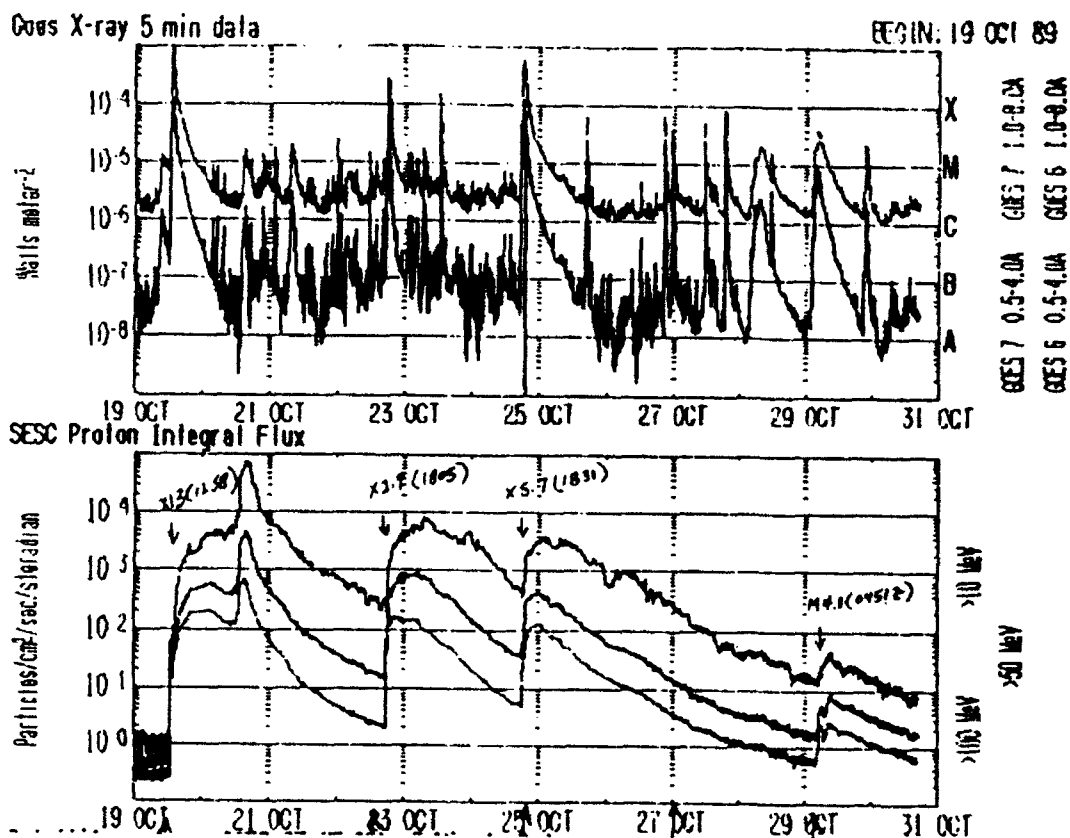


Figure 8. X-ray and particle fluxes, 19-31 October 1989

at greater than 100 MeV at 22/1855UT, and 25% ground level event. The third injection resulted from an X5/3B flare at 24/1831UT, with a peak of greater than 10 MeV protons of 4100 protons/cm²/s/steradian at 25/0210UT, 130 protons/cm²/s/steradian at greater than 100 MeV at 25/0015UT, and a 90 percent ground level event. A comparison plot of proton flux profiles for August 1972, August 1989, and October 1989 is shown in Figure 9. The geomagnetic response to these events peaked from 20-22 October which witnessed major to severe storm conditions. The Fredericksburg A-indices from 20-22 October were 64, 86, and 29.

*Uncorrected

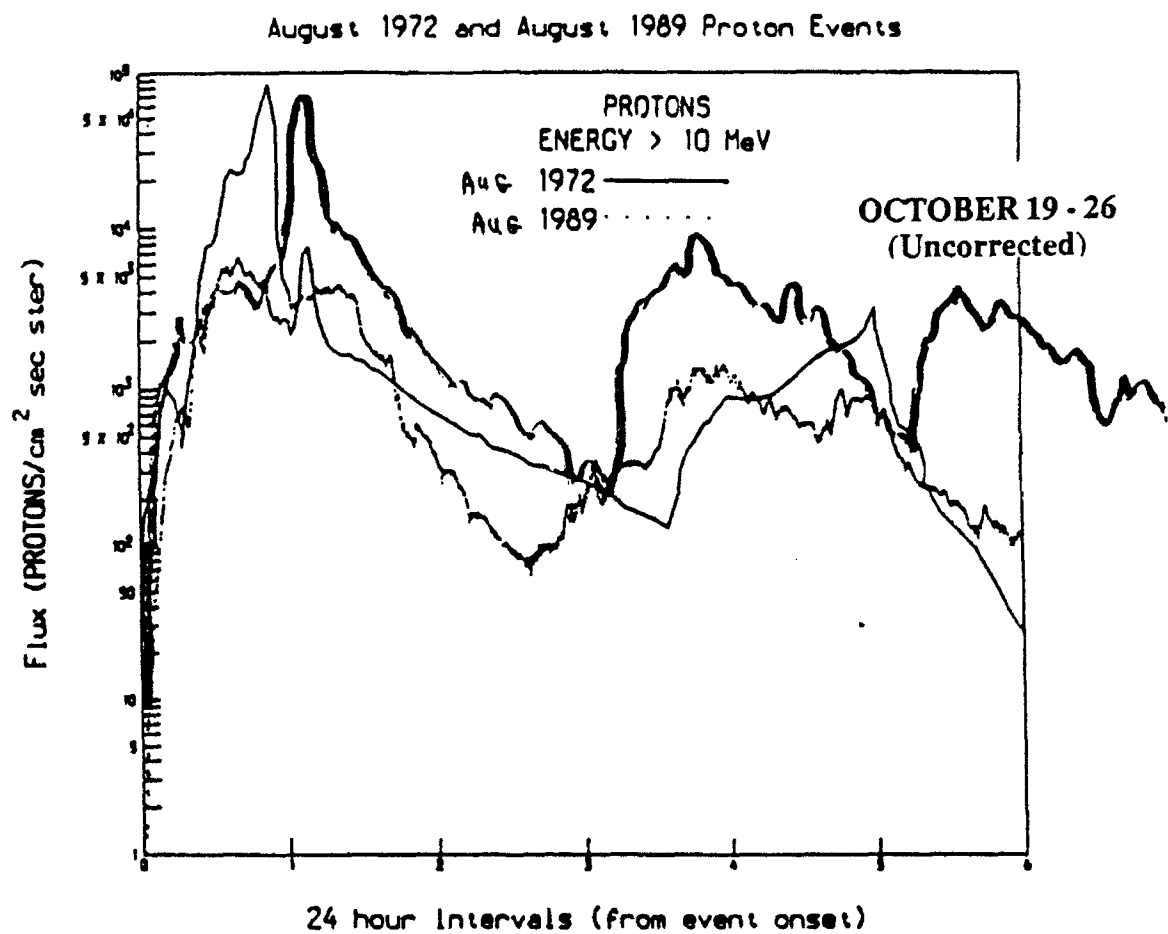


Figure 9.

Flux profiles of August 1972, August 1989, and October 1989 proton events.

YEARLY FLUENCES (>30 MeV)

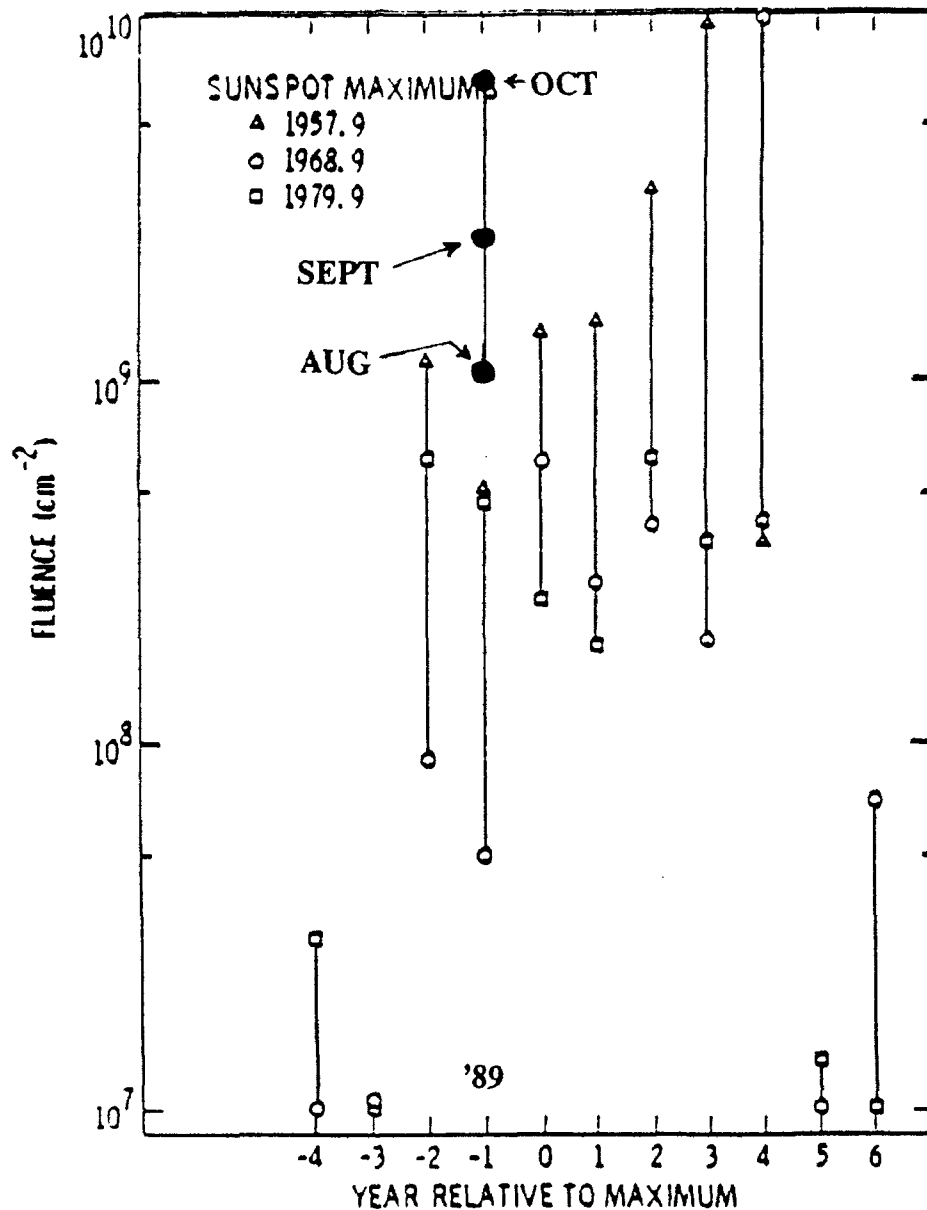


Figure 10. Yearly proton fluence comparisons

A comparison of proton fluences (a summation of proton fluxes over time) can be made to put these events in proper perspective. Figure 10 shows a plot of particle yearly fluence calculations as determined by Feynman et al (1988), but with the fluences (corrected data) from the August, September, and October 1989 events added as calculated by Zwickl (private communication, 1989). The point labeled September is cumulative (i.e. August plus September fluence), as is the October point. This graph demonstrates that recent activity has been remarkable and has exceeded total yearly output for several solar cycles.

The following table (Zickl and Kunches, 1989) is a solar cycle fluence comparison with recent events, again emphasizing the dramatic size of recent activity. It should be of concern to total dose planners that recent activity has outstripped what was known about solar cycle 21 (1975-1986) which has often been used as a reference for environmental specification.

TOTAL SOLAR CYCLE FLUENCE		
CYCLE NUMBER	FLUENCE	
	E > 10 MeV	E > 30 MeV
19	6.6×10^{10}	1.8×10^{10}
20	2.2×10^{10}	0.7×10^{10}
21	1.8×10^{10}	0.3×10^{10}
22 (August - October 89)*	3.1×10^{10}	0.5×10^{10}
October Events Corrected	1.9×10^{10}	0.3×10^{10}

The services provided by SESC

SESC provides services to meet the needs of users affected by the space environment. Daily predictions are made for a three day and seven day forecast period. Warnings are issued when geomagnetic disturbances are expected, $A \geq 20$ (active), $A \geq 30$ (minor storm), $A \geq 50$ (major storm), and alerts are issued when significant activity is observed: A-indices $\geq 20, 30$, or 50 and K-indices of $4, 5$, or ≥ 6 . Alerts are also issued for sudden impulses, solar flares, and particle events.

SESC's satellite broadcast system is an easy, quick way to get SESC's solar-geophysical data, indices, forecasts and warnings in real-time. The update is within one second of receipt and free software is available that can run on PC based systems to store data and generate real time magnetometer plots. The cost for the necessary receiving equipment is about \$3000.

A public bulletin board system containing numerous SESC data sets is available at (303) 497-5000. SESC also provides user accounts on the Space Environment Laboratory Data Acquisition and Display System (SELDADS) to users who want explore the data base in greater depth.

SESC publishes a weekly summary of solar and geophysical activity in the 'Preliminary Report and Forecast of Solar Geophysical Data'. The publication includes a 27 day outlook for activity. Users are charged a nominal yearly subscription rate.

REFERENCES

- Allen, J.H. (1989). Solar & Geomagnetic Activity during March 1989 and their consequences at earth and in near-earth space. This proceedings.
- Schwabe, H. (1844). Sonnen-Baeobachtungen in Jahre 1843. Astronomische Nachrichten, 21, 233-236.

Feynman, J., et al (1988). A New Proton Fluence Model for $E > 10$ MeV. Proceedings of a Conference on the Interplanetary Particle Environment, 15 April 1988, NASA/JPL, Pasadena, California, Feynman, J., and Gabriel, G. eds.

Zwickl, R. and J. Kunches (1989). Energetic Particle Events Observed by NOAA/GOES during Solar Cycle 22. Presented at AGU Fall Meeting, San Francisco, CA, 6 December 1989.

A SURVEY OF MEDIUM ENERGY ELECTRONS AT HIGH ALTITUDE BASED ON ISEE-1 DATA

E.J. Daly and C. Tranquille
*European Space Agency,
ESTEC
2200AG Noordwijk
The Netherlands*

ABSTRACT

The ISEE-1 and ISEE-2 spacecraft explored the outer magnetospheric environment to about 24 earth radii. The MEPI instrument provided data on electron fluxes in the energy range 22-1200 keV. We present results of a survey of a complete data set of isotropic electron fluxes measured by the ISEE-1 spacecraft between November 1977 and September 1979. This analysis provides an overview of the morphology of electrons at these energies, describing the dependence of the electron fluxes on geomagnetic coordinates and local time and showing the probabilities of given particle flux levels being exceeded.

Apart from its general interest, this information is useful in performing engineering evaluations of spacecraft-environmental interactions. ESA is planning or assessing a number of missions which will use highly eccentric earth orbits. Potential problems caused by the particle environments in these orbits include spacecraft charging, deep dielectric charging and electron- and bremsstrahlung-induced background in detectors.

We compare measured particle fluxes with the low-energy part of the electron radiation belt model AE8 and find significant differences. Electron flux enhancements are seen throughout the magnetosphere during solar events.

INTRODUCTION

Several future ESA programs will make use of highly-eccentric synchronous orbits for space-based astronomy. Typical of this type of orbit are the 24-hour orbit with apogee around 71000 km and the 48-hour orbit with apogee around 120000km. Inclinations in the range 7° - 60° are possible. For astronomy, these orbits provide extended observing time, reduced interference from the near-earth environment and good ground-station coverage. Similar orbits are under consideration for high-latitude communications satellites and navigation satellites. US and Soviet programs also make use of such orbits. Clearly these orbits will pass through the trapped radiation belts, through parts of the magnetosphere well known for electrostatic charging problems, and will also be exposed to solar particle fluxes.

The work outlined in this paper was prompted by the need to evaluate environmental interactions at the high altitudes (and therefore high geomagnetic L -values) reached by such orbits and by the lack of data from these regions in a useable form. Most data relating to charging and energetic particle interactions in Earth orbit concentrate on lower altitudes. The geostationary orbit is particularly well covered. The AE8 model for the energetic electron environment only gives data out to $L = 11R_e$.

Environmental-interaction concerns include electrostatic charging of surfaces [Frezet et al., 1989], deep-dielectric charging, and interference with the detectors of the payload. Detectors flown on astronomy satellites are very sensitive and are susceptible to background noise caused by the ambient particle environment. Primary or secondary particles can cause this background. X-ray detector systems using grazing-incidence mirror systems are also potentially exposed to particles scattering through the mirrors.

Recently, much attention has been given to the correlation between relativistic electrons (of several MeV in energy) at $6.6 R_e$ [Baker et al., 1989] and their effect on the operation of geostationary spacecraft [Baker et al., 1987]. The AE8 model is poorly suited to evaluate these effects for higher altitude eccentric orbits. For such an evaluation, extremes of fluxes are needed rather than average values.

The AE8 model provides average omnidirectional electron fluxes ranging in energy from 40 keV to 7 MeV. Fluxes at the high energy limit are mainly extrapolated from lower energy data. AE8 extends out to $11 R_e$. Extrapolation from lower altitude data is often used to provide values at this outer radial limit. The AE8 model is a static model and takes no account of the many dynamic processes which are known to occur in the magnetosphere over short time scales. There is also no dependence on geomagnetic activity or on the interplanetary magnetic field and solar wind conditions.

A local time model was built into the AE4 electron flux model and has been adapted by us for use with AE8. The local time variation of the logarithm of the flux is modelled as sinusoidal, characterised by an amplitude and a phase term, both varying as functions of energy and L .

Confidence levels for exceeding specified fluxes can also be defined by parameterising the Gaussian distribution of the logarithm of the fluxes used to define the AE4 model.

To date, no quantitative synoptic analysis has been made for charged particles outside of the Van Allen belts, and only transitions through isolated magnetospheric structures have been investigated. The standard models of the trapping region also require a new analysis, given that they are constructed from measurements made in the sixties and early seventies, and have not yet been updated to include more contemporary data sets.

The data on electron fluxes from by the Medium Energy Particle Instrument (MEPI) flown on the ISEE-1 satellite were selected for study. We compare the MEPI measurements made in the Van Allen belts with those derived from the AE8 model [Vette, 1989]. We also obtain confidence levels that given flux values will not be exceeded, as a function of L -value and electron energy.

THE ISEE-1 ORBIT AND INSTRUMENTATION

ISEE-1 was launched on October 22, 1977, as one of three satellites designed to investigate the inter-relationship between solar and geomagnetic phenomena [Ogilvie et al., 1978]. The initial orbit of ISEE-1 had an apogee of 22.6 R_e , a perigee of 270 km, a period of 57.2 hours and an equatorial inclination of 28.3°. Throughout the year, the orientation of the apogee of this orbit with respect to the sun-earth line rotates so that all local times are sampled. As a consequence, most magnetospheric features were visited. At launch, the orbit apogee was almost at noon local time. The daughter spacecraft, ISEE-2, had almost identical orbital parameters. The separation of the two satellites could be accurately controlled to make dual spacecraft measurements, with high spatial resolution. All ISEE spacecraft were equipped with a variety of instruments to measure particle, magnetic field, electric field and solar wind properties. The ISEE-1 satellite also provided data for the multi-spacecraft International Magnetospheric Study (IMS) [Ogilvie, 1984].

The Medium Energy Particles Instrument [Williams et al., 1978] was designed to measure electrons and ions with high temporal, angular and energy resolution. The hardware development was made by the Space Environment Laboratory at NOAA (USA), the Max-Planck Institute for Aeronomy (FRG) and the University of Kiel (FRG).

The energy range of the detector is 22.5 to 1200 KeV for electrons. This range is divided into eight logarithmically equidistant channels, as detailed in Table 1. Data were also acquired at high bit-rate but these are converted to low bit-rate for inclusion into the data set we use. In addition, the directional data provided by scanning and spinning are used to produce omni-directional fluxes with a time resolution of approximately 5 minutes.

Channel Number	Energy Range (keV)
E1	22.5 - 39
E2	39 - 75
E3	75 - 120
E4	120 - 189
E5	189 - 302
E6	302 - 477
E7	477 - 756
E8	756 - 1200

Table 1: MEPI Electron Energy Channels

MEPI measurements were made by ISEE-1 from launch to September 11, 1979, after which a failure in the power supply of the experiment resulted in the loss of the instrument. A total of 281 orbits were completed during the 670 days of the instrument's operation, starting 1.5 years after solar minimum and therefore covering the 'run-up' to solar maximum.

The data were provided to us by D.J. Williams and D.G. Mitchell of the Applied Physics Laboratory, Johns Hopkins University.

A similar electron experiment was flown by the ISEE-2 satellite, although with inferior energy and angular resolution. This experiment continued to make measurements right up until contact with the daughter satellite was lost, some ten years after launch (September 26, 1987).

ORBIT COVERAGE

The suitability of the ISEE-1 orbit for investigating the radiation environment for highly eccentric orbits is shown in Figure 1.

Each electron flux measurement made by MEPI is recorded with ancillary information, including UT and position in GSE coordinates. Mapping to geomagnetic B - L coordinates requires a series of transformations, together with the use of a magnetic field model. In our analysis reported here we have used an internal model of the field. This is known to provide poor information at high altitudes where external current systems strongly affect the field. However, it is used solely as an organisational aid for comparison with models and other satellite data, which also use an internal model. In future work, we hope to employ an external model such as that described by Tsyganenko [1989]. The model we use is the International Geomagnetic Reference Field (IGRF) for 1980 [Peddie, 1982]. In geomagnetic B , L coordinates there is no information about local time, therefore this is also computed.

All valid MEPI measurements were mapped into geomagnetic B - L space and the total number of data points available in each cell found. This is shown in Figure 1. The geomagnetic equator is drawn as a continuous line in the figure.

Data coverage is best above 12 R_L and close to the equator. At lower altitudes, the coverage becomes very sparse, due to the relatively quick transition through perigee, when compared to the longer periods spent close to apogee. Nevertheless, down to about 4 R_L , the coverage is acceptable when the spacecraft is not far from the magnetic equator. Above 12 R_L , the coverage is excellent, albeit limited in terms of B . If the equatorial pitch angle distribution of the electrons is known, it is possible to derive fluxes at higher B values (higher latitudes) [Garcia and Spjeldvik, 1985].

The baseline orbits of the forthcoming XMM (X-ray), ISO (infra-red) and FIRST (far infra-red) missions are projected into the geomagnetic coordinate system to illustrate the suitability of the ISEE-1 orbit for the present study. The XMM orbit is a 24 hour orbit of 60° inclination, and apogee height of ~ 71000 km. ISO has a similar orbit, but with a low inclination of 5°. The period of the FIRST orbit is 48 hours, with apogee at ~ 120000 km and again a 5° inclination. Both the ISO and FIRST orbits are totally enclosed by the ISEE-1 orbit, as is the high inclination XMM orbit below about 20 R_L .

ELECTRON FLUX PROFILES

Figures 2-4 show examples of thirty-day plots of electron fluxes in 4 of the eight MEPI energy channels. Flux increases seen in the electron count rates are clearly identifiable with the radiation belts, with energetic populations in the tail and with solar flare events. When the apogee is in the upstream region, the electron flux profiles are very clean, with the belt transitions easily distinguishable. However, when the apogee is situated in the magnetotail, the belt transitions are somewhat difficult to isolate due to the many flux enhancements seen on short timescales outside the trapping region. This is especially true at the lower energies, where high fluxes are maintained almost constantly between Van Allen belt passes.

Superimposed on the electron flux profiles, are examples of solar electron events which are easily recognisable by significant (two orders of magnitude, in the lowest energy channel) flux enhancements seen simultaneously across the complete energy range of the instrument. Associated with these events are solar flare protons and alpha particles. A table of solar proton events has been compiled by Goswami et al. [1988]. Using this table, solar flare events have been independently identified (the arrow at the bottom of the first panel) to confirm the association of the long term electron flux enhancements with flare activity on the sun in the majority of cases. Some electron events have no solar proton counterpart. Inspection of plots of IMP-7 and -8 data [Solar-Geophysical Data Comprehensive Reports] reveals a similarity between the energetic proton time behaviour and the time behaviour of the ISEE-1 MEPI electron fluxes, although this is not always the case.

Solar flares and shock fronts can also be detected from solar wind and magnetic field measurements in the interplanetary medium. A distinct signature is the sudden increase in the interplanetary solar wind velocity, V_{sw} , to well above the nominal value of 400 km/s. The third panel of the figures shows this particular solar wind behaviour very clearly for the relevant events. The solar wind velocity data were obtained from the on-line database (OMNI) supported by NSSDC. They are compiled from measurements provided by IMP-6, -7 and -8.

PROCESSING RESULTS

The MEPI data were used to define electron fluxes in each of the 8 energy channels for the parts of B - L space covered by ISEE-1. Average fluxes were computed for B , L bins and these are shown in Figure 5 (channel 2) and Figure 6 (channel 5).

When compared to predictions from the AE8 electron model, we find that fluxes are somewhat lower than predicted. Also clear from Figures 5 and 6 is the severe truncation of AE8 fluxes at around 11 R_e .

Within a number of L -bands, a distribution of electron fluxes within each channel was created. These are shown in Figure 7 for $6 < L < 7$, $9 < L < 10$ and $12 < L < 13$ in the form of plots of the percentage of data having fluxes below the value on the x-axis. These indicate the great variability of possible fluxes at given L -values. This kind of processing has been performed in the past for Geostationary orbit [Baker et al., 1981] and for the SCATHA satellite [Mullen and Gussenhoven, 1983]. Our results compare favourably with similar plots given by Mullen and Gussenhoven [1983] in the SCATHA Environmental Atlas. These plots show how the fluxes in the high energy channels remain close to the background level for most of the time at high L -values (7(c)) while displaying a considerable spread at low L (7(a)).

Fluxes were scatter-plotted against local time for various 1 R_e -wide L bins. These are shown in Figures 8-10 for the energy channels 22.5-39 keV, 120-189 keV and 302-477 keV respectively. Distributions of particle fluxes were produced within 3-hour wide local-time bins, from which the mean (50% probability) and worst-case (95%) values of the logarithm of the flux can be derived as a functions of L and local time. These are superimposed in Figures 8-10 as solid histograms. The limits of the data-set, in terms of the number of data points, becomes somewhat apparent when this is done since the number of data points making up the >95% class are small. Clearly, the 10-year ISEE-2 data set would be very useful for performing this kind of analysis. It should be noted that the plots include fluxes from solar events and so are not clean pictures of magnetospheric electrons. Nevertheless, the changing shape of the distribution of fluxes in local time reflects the electron morphology of the magnetosphere.

Figure 8 shows that, for low energies at low L , the spread of fluxes is relatively small around noon local time, with a peaking in fluxes towards the dawn quadrant. Fluxes are high at all local times although the occasional low-flux data points occur preferentially on the night side. As L increases, this pattern changes so that fluxes are low around noon, beyond the magnetopause, and are higher in the anti-sunward plasma sheet region. A bias in high flux locations towards the dawn quadrant remains. At high L there is a considerable scatter in flux levels, reflecting the dynamicism of the plasma sheet population. The 50% and 95% levels follow this changing behaviour.

The 120-189 keV electron fluxes shown in figure 9 exhibit basically the same characteristics. High fluxes at high L values are encountered principally in the dawn quadrant although fluxes are generally low. Figure 10 (302-477 keV) shows low fluxes at $L > 12$ but a similar behaviour to the lower energy channels at lower L .

The MEPI measurements were made in the period leading up to maximum activity of solar cycle 21, which in terms of average solar flare proton flux, was less severe than the preceding two cycles [Goswami et al., 1988]. Indeed, the current maximum in solar activity has already produced several flares of greater intensity than seen at any time during cycle 21.

Solar electron event flux measurements made by ISEE-1 outside of the Van Allen belts do not seem to have any spatial variation, and their profiles are essentially determined by the temporal evolution of the particles as they pass the earth. The severity and duration of the flares are variable, but some have flux increases two or three orders of magnitude above the normal background level. Such enhancements, although only lasting for a few days, can have a very detrimental effect on sensitive detectors and electronics.

CONCLUSIONS AND FUTURE WORK

Electron flux data from the complete energy range of the ISEE-1 MEPI instrument, covering the lifetime of the instrument have been analysed to provide a preliminary basis for evaluation of the energetic electron environment of highly eccentric orbits. The data have been analysed and the general morphology of energetic electrons with respect to geomagnetic coordinates and local time has been established. "Worst-case" data on the electron environment have been produced which should prove valuable for evaluating background and other effects for future missions in these regions. Related to this are the flux-probability plots produced. The local time scatter-plots reveal the morphology of electrons in the magnetosphere and their variability in the various regions. A report containing a more complete set of plots than given here is in preparation [Tranquille et al., 1990].

It is found that in regions of space where there was overlap with existing environment models, these models appear to be pessimistic for this period. In regions beyond the model limits, where modelling normally assumes zero fluxes, there were still non-negligible electron fluxes.

Partial overlap between the data on the particle-induced background of the Cos-B X-ray instrument and the ISEE particle data allowed us to look at their correlation. It is found that "flaring" of the Cos-B background coincides with solar or magnetospheric events observed by ISEE-1 in the majority of cases [Tranquille et al., 1990]. However, this correlation is less than perfect, probably because of the different locations of the two spacecraft in the magnetosphere which, as has been pointed out, is highly dynamic.

There are many possible ways in which this work could be usefully extended. As pointed out above, the ISEE-1 energetic electron data only covers a period of approximately 2 years preceding solar maximum. The equivalent instrument flown by ISEE-2, although measuring electrons of slightly lower maximum energy and at lower energy and angular resolution, collected data over a period from launch to well over ten years later, covering almost a complete solar cycle. Analysis of these data would firstly increase the statistical value of the present study, as well as providing an insight into the solar cycle dependence of the terrestrial electron environment.

A more detailed correlation between flux measurements and solar wind and geomagnetic parameters could also be performed, and, as pointed out above, the Tsyganenko external field model could be employed, incorporating activity and diurnal effects. Equatorial pitch angle distributions could also be used to derive fluxes at higher B values (and therefore higher magnetic latitudes), giving flux information which would be directly applicable to more inclined eccentric orbits.

Data from other spacecraft also exist, for which a similar analysis can be performed. Geostationary data sets from the Los Alamos National Laboratory and from NOAA could be used. These sets overlap ISEE-1 and -2 data in time.

The advantage of using data from other spacecraft is twofold: firstly, it allows flux measurements to be inter-compared, hence enhancing the confidence of the analysis; secondly, it complements the overall data coverage (such as the relatively poor sampling of ISEE-1 at lower altitudes).

Finally, an alternative model to the AE8 model could be constructed using data from the ISEE satellites, and any other suitable sources, with the functionality required for the evaluation of interactions at high altitude. Work to this effect has already been initiated. Following the impending launch of the Combined Release Radiation Effects Satellite (CRRES) [Gussenhoven et al., 1985], an extensive modelling activity will be undertaken.

ACKNOWLEDGEMENTS

We are grateful to D.J. Williams and D.G. Mitchell of the Applied Physics Laboratory, Johns Hopkins University, for providing the MEPI data and for their continued help during processing. We also thank NSSDC for data on solar wind speed and geomagnetic indices from their on-line OMNI database.

REFERENCES

Baker, D.N., R.D. Belian, P.R. Higbie, R.W. Klebesadel and J.B. Blake. Hostile Energetic Particle Radiation Environments in the Earth's Outer Magnetosphere, in *The Aerospace Environment at High Altitudes and its Implications for Spacecraft Charging and Communications*, AGARD Conference Proceedings No. 406, 1987.

Baker, D.N., J.B. Blake, L.B. Callis, R.D. Belian and T.E. Cayton. Relativistic electrons near geostationary orbit: evidence for internal magnetospheric acceleration, *Geophys. Res. Lett.*, 16, 559, 1989.

Baker, D.N., P.R. Higbie, R.D. Belian, W.P. Aiello, E.W. Hones, Jr., E.R. Tech, M.F. Halbig, J.B. Payne, R. Robinson, S. Kedge, The Los Alamos Geostationary Orbit Synoptic Data Set, A Compilation of Energetic Particle Data, LA-8843, 1981.

Frezet, M., E.J. Daly, J.P. Granger and J. Hamelin, Assessment of Electrostatic Charging of Satellites in the Geostationary Environment, *ESA Journal*, 13, 89, 1989.

Garcia, H.A. and W.N. Spjeldvik, Anisotropy characteristics of geomagnetically trapped ions, *J. Geophys. Res.*, 90, 347, 1985.

Goswami, J.N., R.E. McGuire, R.C. Reedy, D. Lal and R. Jha, Solar flare protons and alpha particles during the last three solar cycles, *J. Geophys. Res.*, 93, 7195, 1988.

Gussenhoven, M.S., E.G. Mullen, R.C. Filz, D.H. Brautigam and F.A. Hanser, New low altitude dose measurements, *IEEE Trans. Nucl. Sci.*, NS-34, 676, 1987.

Gussenhoven, M.S., R.C. Filz, K.A. Lynch, E.G. Mullen and F.A. Hanser, Space radiation dosimeter SSJ- for the block 5D/flight 7 DMSP satellite: calibration and data presentation, AFGL-TR-86-0065, Air Force Geophysics Laboratory, Hanscom AFB, Ma., 1986. ADA172178

Gussenhoven, M.S., Mullen, E.G. and Sagalyn, R.C., CRRES/SPACERAD Experiment descriptions, AFGL-TR-85-0017, Air Force Geophysics Laboratory, Hanscom AFB, Ma., January 1985. ADA160504

Lyons, R.L. and Williams, D.J., *Quantitative Aspects of Magnetospheric Physics*, D. Reidel Publ. Co., Dordrecht and Boston, 1984.

McIlwain, C.E., Coordinates for mapping the distribution of geomagnetically trapped particles, *J. Geophys. Res.*, 66, 3681, 1961.

Mullen, E.G. and M.S. Gussenhoven, SCATHA Environment Atlas, AFGL-TR-83-0002, 1983. ADA131456

Ogilvie, K.W., Some contributions to knowledge of the magnetospheric plasma by ISEE-1 investigators, in Achievements of the international magnetospheric study (IMS), ESA SP-217, 25, 1978.

Ogilvie, K.W., A. Durney and T. von Rosenvinge, Description of experimental investigations and instruments for the ISEE spacecraft, IEEE Trans. Geosci. Electron., GE-16, 151, 1978.

Peddie, N.W., International geomagnetic reference field: the third generation, J. Geomag. Geoelectr., 34, 309, 1982.

Schulz, M., Earth's radiation belts, Rev. Geophys. Space Phys., 93, 77, 1982.

Share, G.H., J.D. Kurfess, K.W. Marlow and D.C. Messina, Geomagnetic origin for transient particle events from nuclear reactor-powered satellites, Science, 244, 444, 1989.

Singley, G.W. and J.I. Vette, The AE-4 model of the outer radiation zone electron environment, NSSDC/WDC-A-R&S 72-06, National Space Science Data Center, 1972.

Solar Geophysical Data Comprehensive Reports, published monthly by NOAA, U.S. Dept. of Commerce.

Teague, M.J. and J.I. Vette, The inner zone electron model AE-5, NSSDC/WDC-A-R&S 72-10, National Space Science Data Center, 1972.

Teague, M.J. and J.I. Vette, AE 6: a model environment of trapped electrons for solar maximum, NSSDC/WDC-A-R&S 76-04, National Space Science Data Center, 1976.

Tranquille, C. and E.J. Daly, The radiation environment for earth-orbiting astronomical satellites, submitted to J. British Inter. Soc., 1989.

Tranquille, C., E.J. Daly, D.G. Mitchell and D.J. Williams, A Synoptic Survey of Magnetospheric Energetic Electron Fluxes as Measured by the ISEE-1 Spacecraft. ESTEC Internal Report in preparation, 1990.

Tsyganenko, N.A., A magnetospheric magnetic field model with a warped tail current sheet. Planet. Space Sci., 37, 5, 1989.

Vette, J.I., Trapped radiation models, in Development of Improved Models of the Earth's Radiation Environment, Technical Note 1 (Chapter 4), ESA Contract 8011/88, IASB, 1989.

Williams, D.J., E. Keppler, T.A. Fritz, B. Wilken and G. Wibberenz, The ISEE 1 and 2 medium energy particles experiment, IEEE Trans. Geosci. Electron., GE-16, 270, 1978.

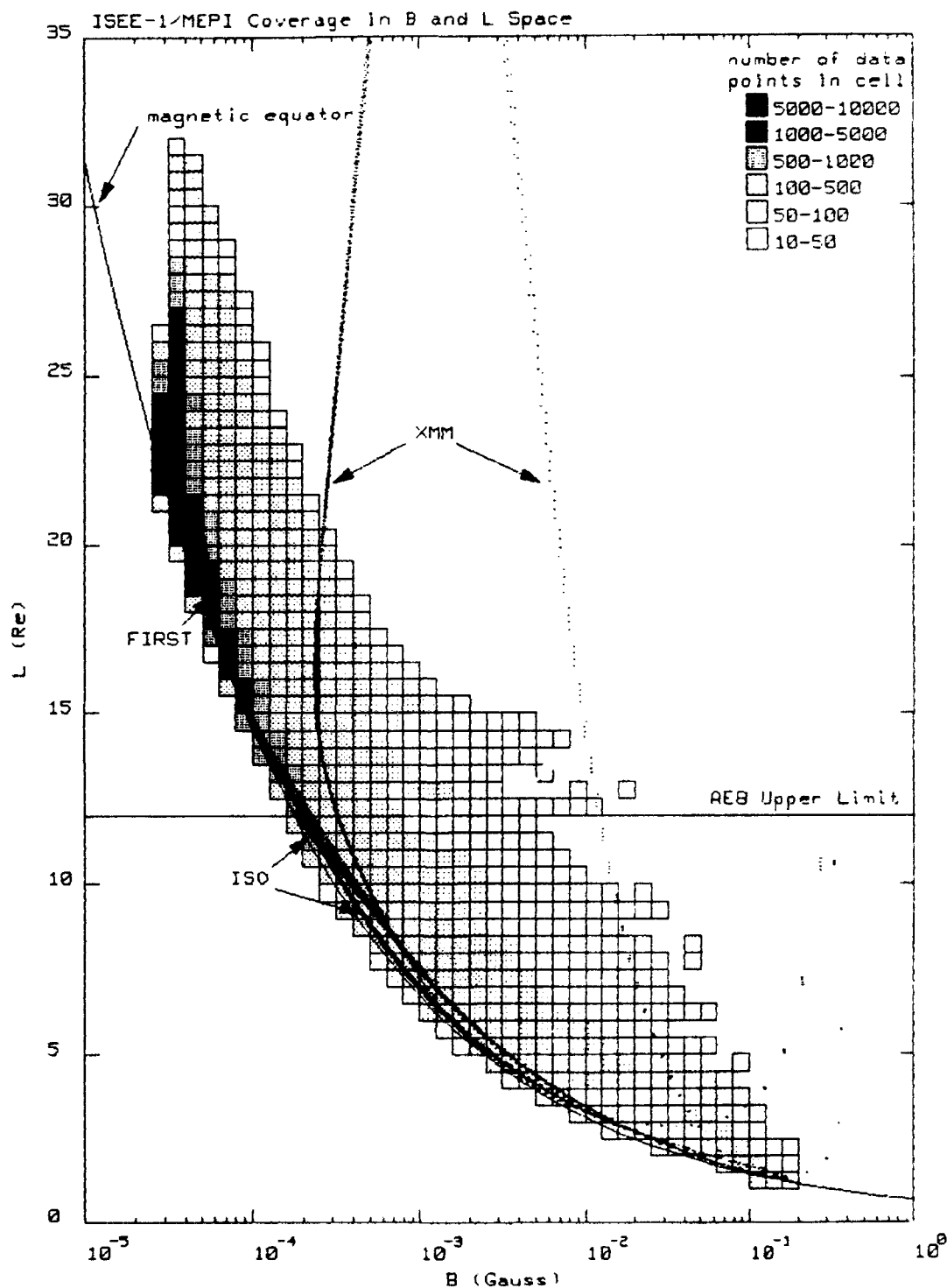


Figure 1: Orbit coverage of the ISEE-1 satellite in terms of geomagnetic coordinates. Gray-scale coded cells in B, L space indicate the number of data points available. The geomagnetic equator is shown for reference, as are the $B - L$ traces of the orbits of the future XMM, FIRST and ISO missions.

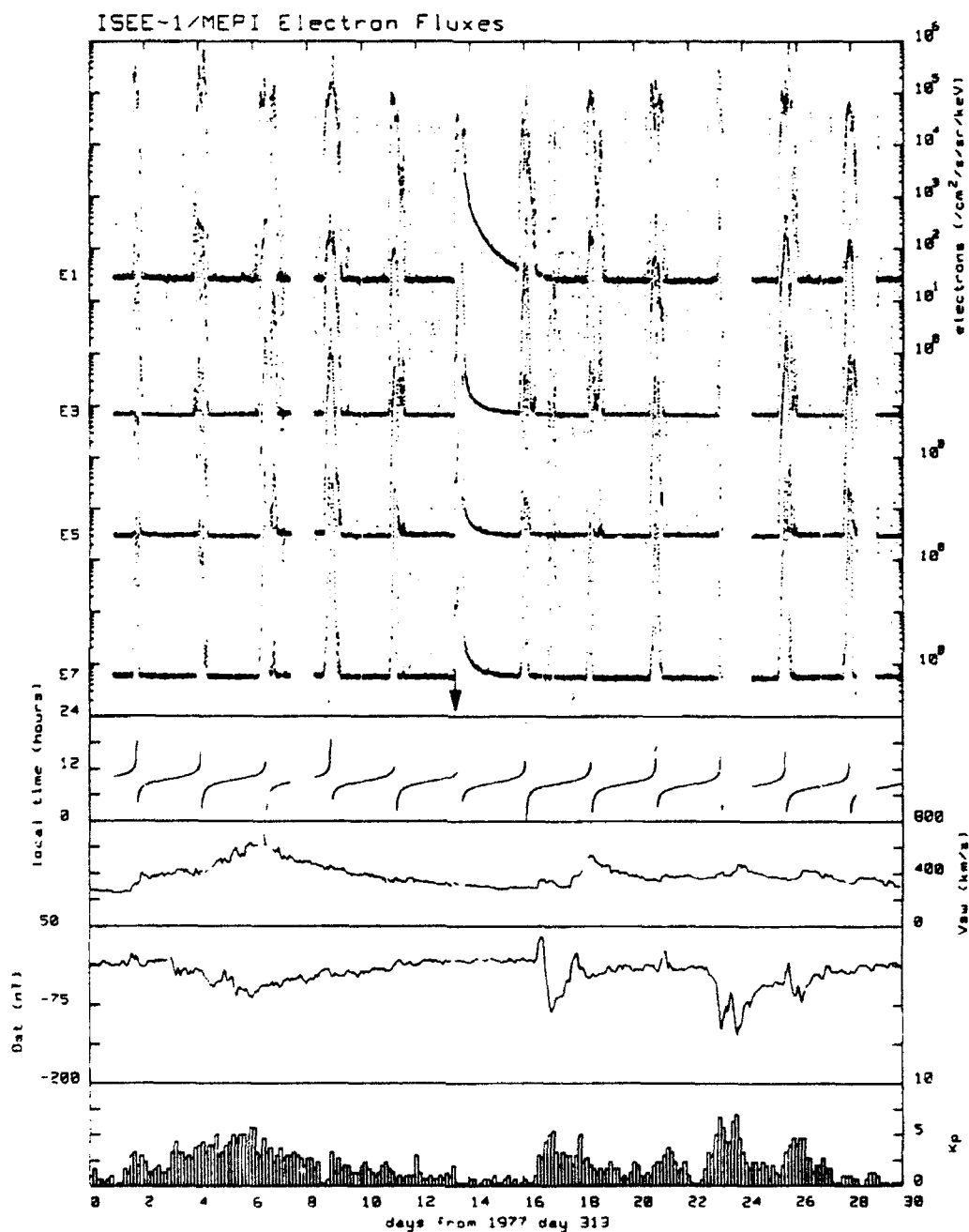


Figure 2: Thirty-day plot of MEPI data from 4 channels, showing quiet conditions (upper panel). The other panels show, from the top, satellite local time, solar wind speed, the D_{st} index and the K_p index. Arrows indicate the start of a solar proton event observed by IMP.

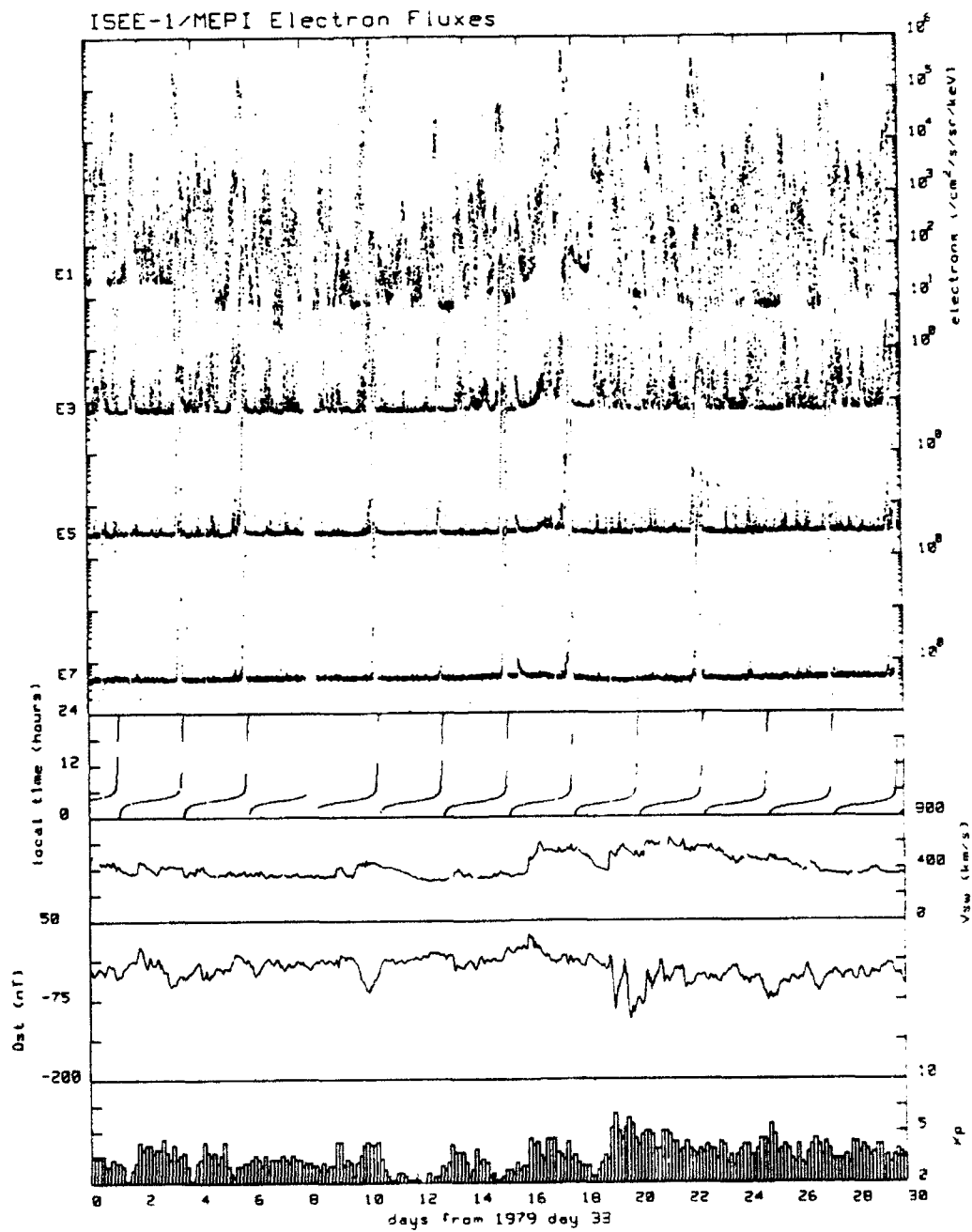


Figure 3: As figure 2 but showing disturbed conditions.

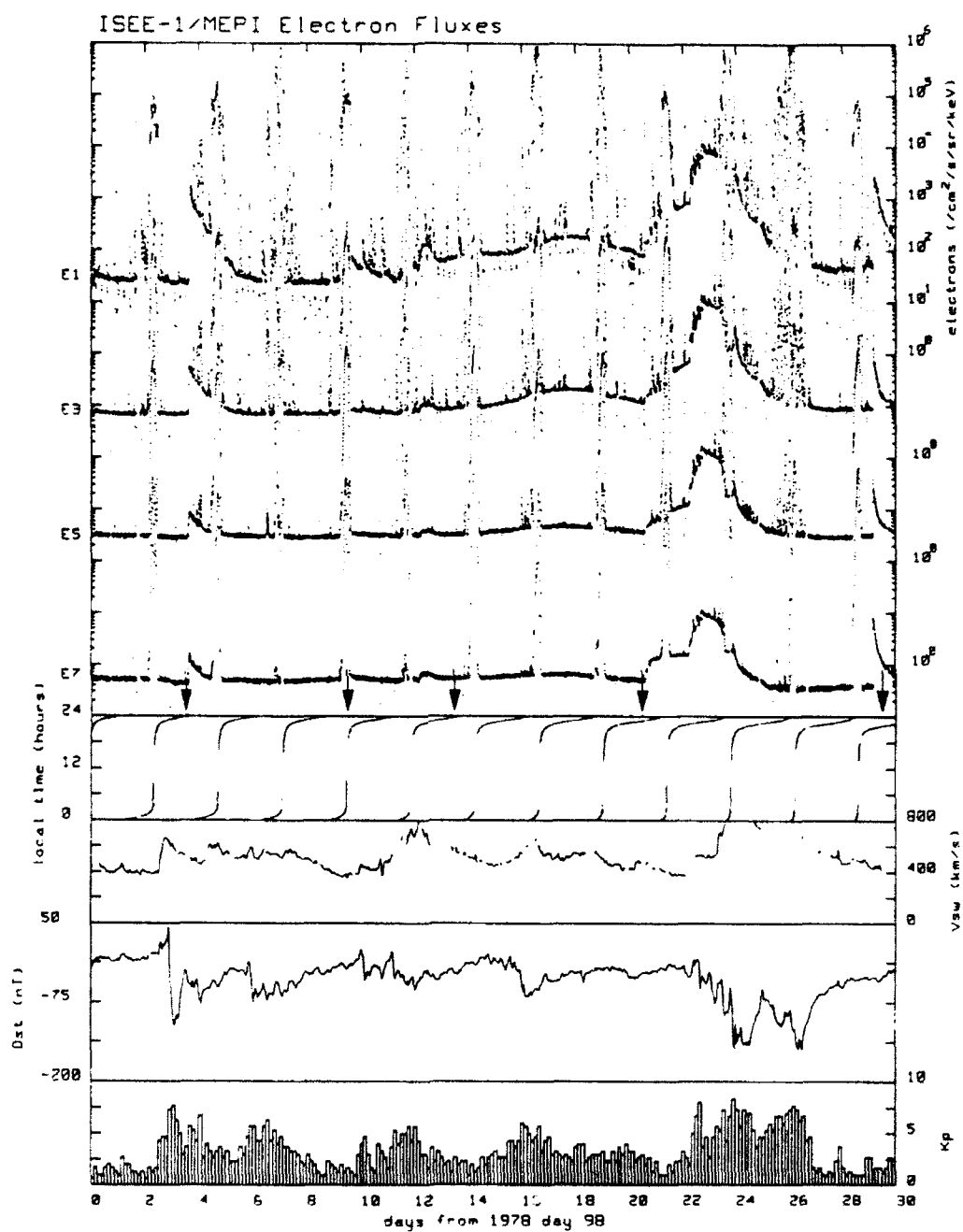


Figure 4: As the previous two figures but showing a solar event.

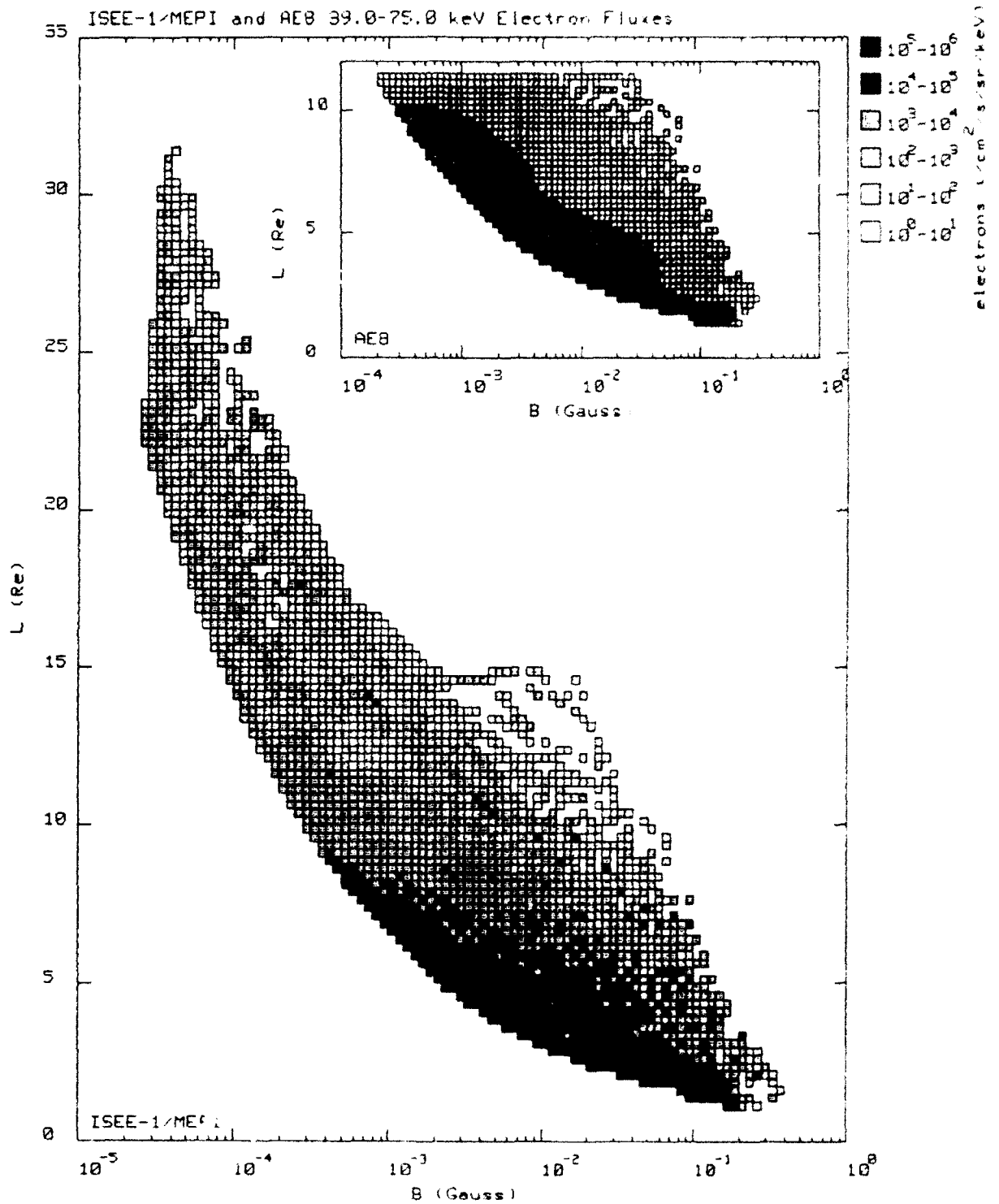


Figure 5: Differential electron fluxes for MEPI channel 2 (39 - 75 keV) are presented as a function of geomagnetic coordinates, B and L , sampled by the ISEE-1 orbit. The inset shows the predictions of the AE8 model for the same energy range.

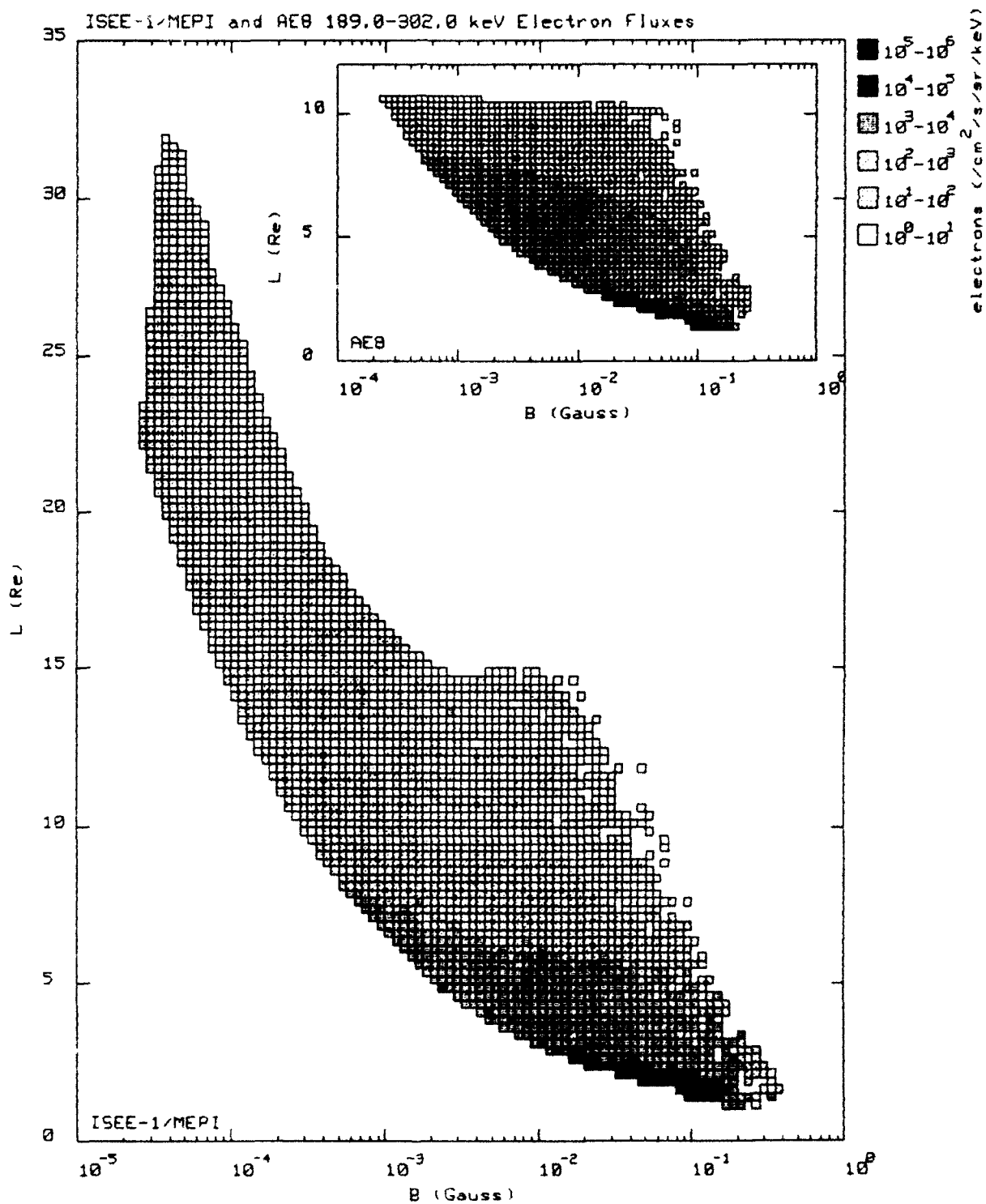
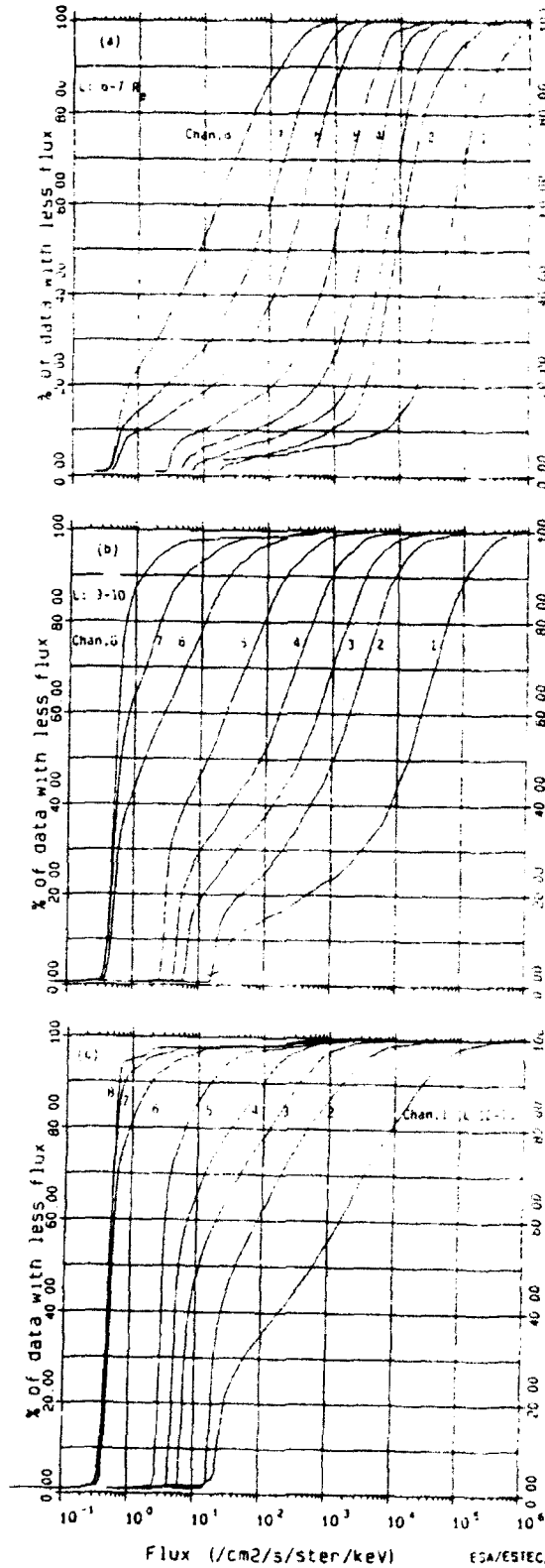


Figure 6: As figure 5 but showing data from channel 5 (189 - 302 keV).



(a)
 $6 < L < 7$

(b)
 $9 < L < 10$

(c)
 $12 < L < 13$

Figure 7: Flux probabilities: plots of the probability of fluxes being below given values, for all 8 MEPI channel energy ranges, for 3 ranges of L : (a) $6 < L < 7$; (b) $9 < L < 10$; (c) $12 < L < 13$.

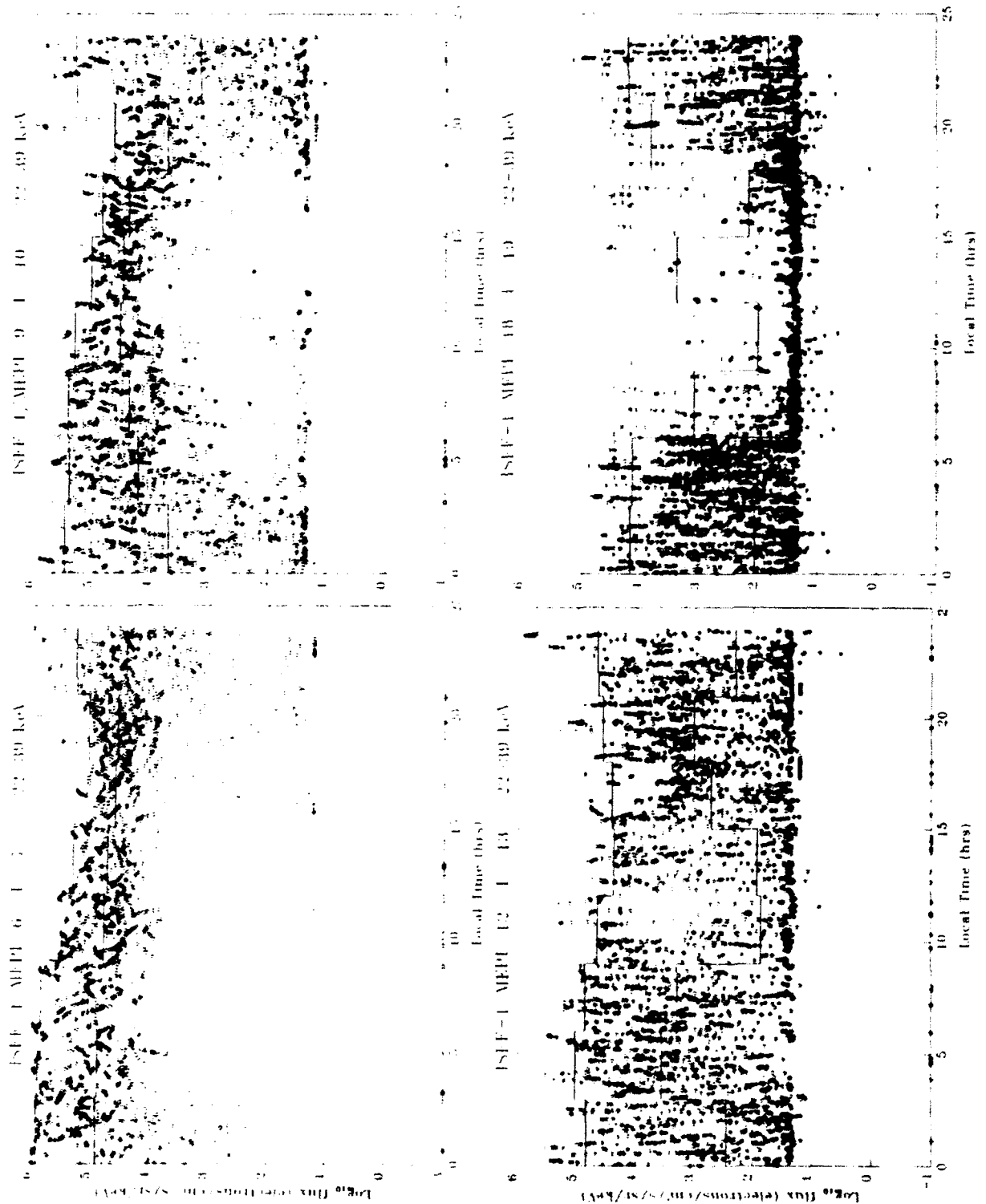


Figure 8: Scatter plots of Log_{10} 22.5-39 keV electron fluxes as functions of local time. Also shown are the mean (50 percentile) and worst-case (95 percentile) log-fluxes. Each plot shows a different L range. The transition from radiation-belt to plasma sheet morphology is clear.

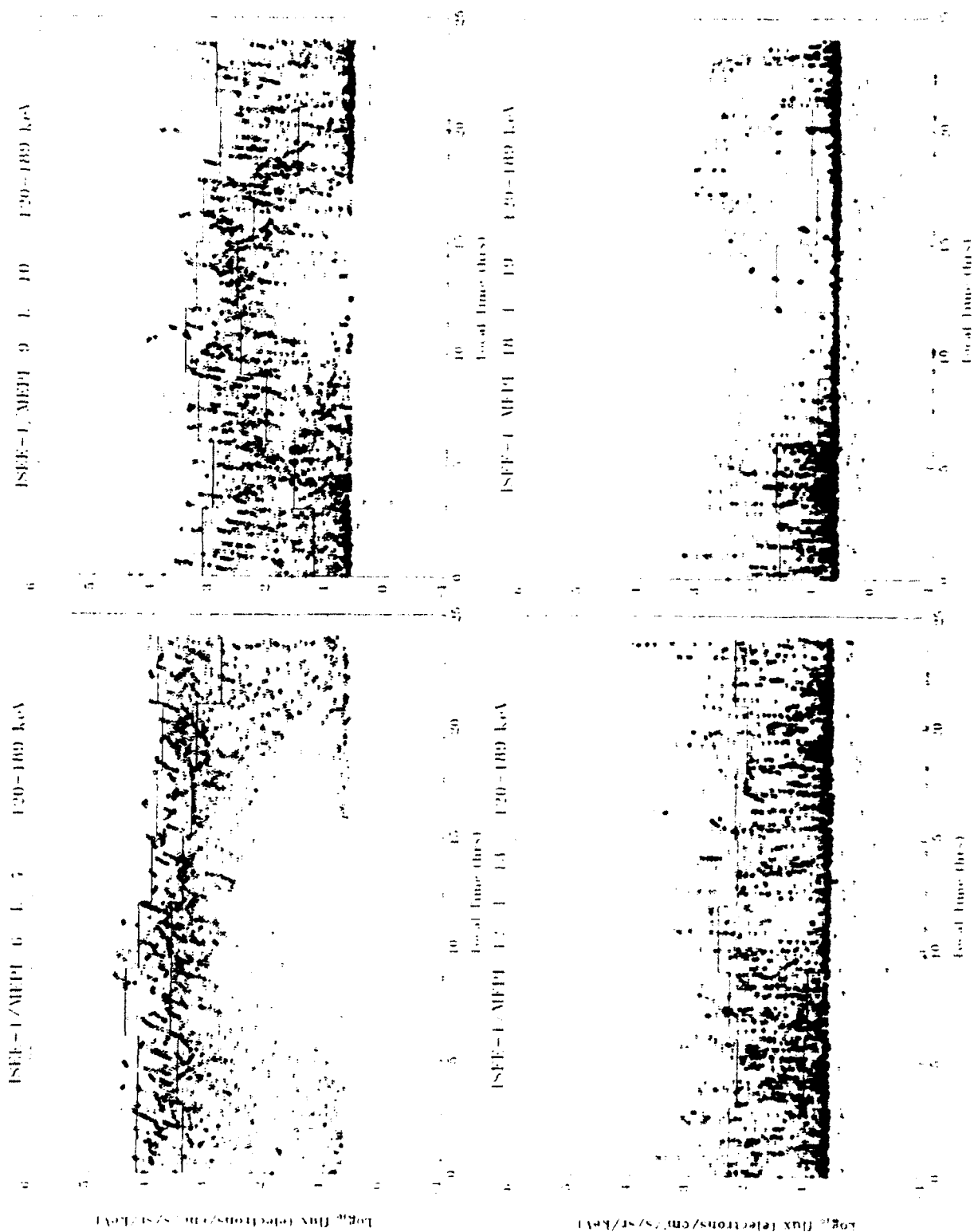


Figure 9: As figure 8 but for MEPI channel 4 (120-189 keV).

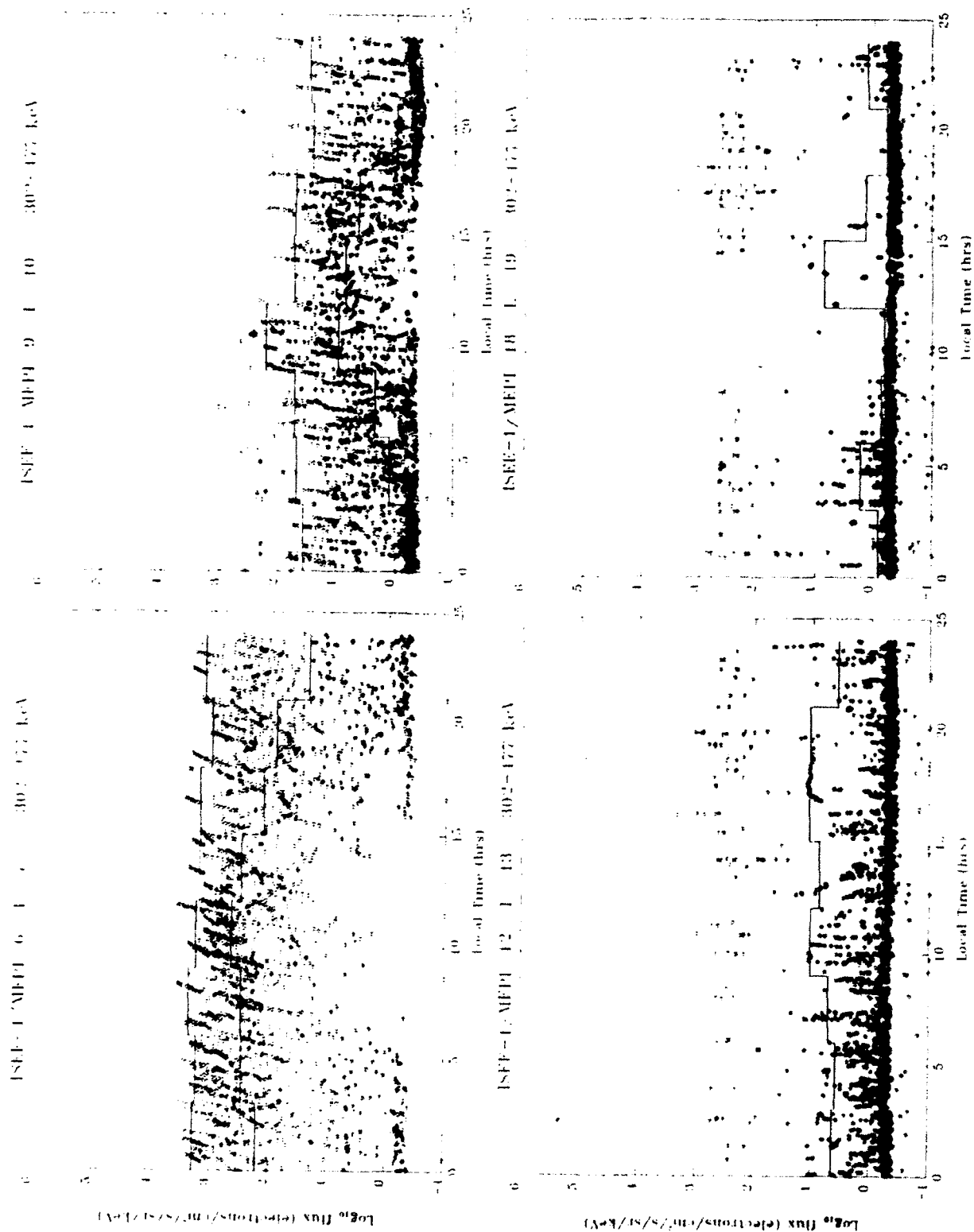


Figure 10: As figure 9 but for MEPI channel 6 (302-477 keV).

CHARGING OF GEOSYNCHRONOUS SPACECRAFT BY VARIABLE INTENSITY SUBSTORM ENVIRONMENTS

BY

N. John Stevens
TRW Space and Technology Group
One Space Park
Redondo Beach, CA 90278

ABSTRACT

An analytical study has been undertaken using engineering level computer codes to determine the charging characteristics of a spin-stabilized spacecraft subjected to variable intensity substorms. Both surface charging and buried charge effects are considered. The primary objective of this study is to determine the length of time that spacecraft surfaces would remain charged under variable environmental conditions. The study shows that, once started, surface charging can continue if the substorm level remains above 5KeV and the surfaces are not in sunlight. Buried charge effects follow the substorm intensity variations. In both cases, the most likely source for discharges are the sun/shade interfaces.

INTRODUCTION

Surfaces on geosynchronous spacecraft are charged by encounters with geomagnetic substorm environments¹. This charging has resulted in discharge generated transients that have disrupted spacecraft electronic systems and have caused mission failures². The Spacecraft Charging at the High Altitudes (SCATHA) satellite was launched in 1979 to evaluate these interactions between spacecraft surfaces and the substorm environments³. The results of the experiments on SCATHA has indicated that surface charging occurs only between 20:00 and 10:00 hours satellite local time⁴ where 12:00 hours local time occurs when the satellite is between the earth and the sun. However, system upsets seem to occur at any time in orbit- even those on SCATHA^{5,6}. With the modern tendencies of designing larger, more autonomous spacecraft, functional upsets can not be tolerated. Hence, it is important to understand the charging behavior of spacecraft surfaces in this environment in order to be able to design systems to be immune to these upsets with the minimum cost impact.

The standard analytical tool to predict surface charging of spacecraft is called NASCAP (NASA Charging Analyzer Program)⁷, an outgrowth of the AF/NASA Spacecraft Charging Investigation⁸. The recommended approach to evaluate the surface charging characteristics is to model the spacecraft using the NASCAP code and then subject it to either a constant or a series of different constant substorm environments⁹. The idea is to impose an environmental condition that will generate the worst-case electrical stress in the surface dielectrics. The use of these constant environment results in voltage predictions that are more severe than those experienced in the actual space environment¹⁰. There are no standard codes to be used to

evaluate buried charge effects although this effect is, at least, as important as surface charging. For the purposes of this paper, surface charging is defined as that condition that arises when charge is deposited on or just under the surface. This is the limitation imposed by NASCAP and hence, limits the substorm electron energies to less than 20 KeV. Buried charge or bulk charging occurs when a charge distribution is imposed within the dielectric by energetic particles (electron energies up to the MeV range).

The NASCAP code can use a variable intensity substorm environment. There have been at least two cases studied using the SCATHA data ^{11,12}. The first study considered the charging profile for an eclipse charging case. Here it was found that, for the measured environmental inputs, the code would predict the measured spacecraft potential. The difficulty was that the code had to compute at least three steps for each substorm environment change and soon reached the storage limitation of the code. When larger time steps were imposed, the code predictions started deviating from the measured values. The second study used a broader time stepping approach and found that, while it didn't predict all of the variations in structure potential, it did generate a reasonable match. However, this approach also required considerable computer time.

The computer time is just one aspect of the cost necessary to conduct analyses; they are time-consuming to set up as well as complete the evaluation. Based on this cost impact, hardware project personnel, generally, do not feel that spacecraft charging analyses produce results commensurate with the expenses involved in conducting them. If the only change that can come from the study is to change the surface coatings, then this would impact the thermal design. The thermal designers can demonstrate that mission failures will occur if an exterior change results in excessive interior component temperatures while the charging analyst can only say that the change could reduce the probability of a discharge that may affect a system. The change will not be made. The tendency, therefore is to develop engineering level codes that can provide reasonable predictive capability while minimizing the cost impact. By conducting these simpler analyses, trends can be found that allows the development of guidelines that can aid future spacecraft designs.

In this paper, an investigation of a spin-stabilized spacecraft is conducted, using engineering level analytical tools, to evaluate its behavior in a variable intensity substorm. Spin-stabilized spacecraft experience a series of system upsets that occur centered around local dawn and dusk rather than concentrated in the more traditional midnight to dawn quadrant ³. The speculation is that charging of the earth facing, despun antenna or deposition into an ungrounded substrate was the cause of the discharges that caused the anomalies. A variable intensity substorm is used to limit the structure voltages more to the values observed in space than those that would result for the standard analytical approach.

ANALYTICAL MODELS

For the surface charging analysis, the criteria under which all engineering models must be judged is the NASCAP code. For this study, the data from a NASCAP evaluation of a spin-stabilized spacecraft¹³ was used. The spacecraft considered was a cylindrical spacecraft with a despun, earth-facing antenna and a extended solar array. The NASCAP model employed a few hundred cells to describe the spacecraft exteriors shown in figure 1. The engineering code used a modified version of the TRW Spacecraft Charging Technique (TSCAT)¹⁴ and allowed the spacecraft to be described with 33 plates. The modification to TSCAT changed the code from a steady-state predictor of charging levels of several dielectrics connected to the same substrate to a transient charging predictor of up to 100 surfaces incorporating the three dimensional "barrier" effect. The reduction in detail is permissible since the NASCAP results for surfaces of the same material in the same environment have the same values. The antenna back surface is modelled as four triangular plates so that sunlight angle effects could be evaluated. This is done to simulate the fact that the antenna is a bowl shaped surface and, at shallow angles of incidence, the surfaces can be self-shaded.

The TSCAT model did not include the interior cavity of the extended solar array, but otherwise treated the spacecraft similar to NASCAP. Unfortunately, not all of the material properties for the surfaces used in the NASCAP analysis were available - the standard properties found in the NASCAP code were not always used.

The buried charge studies were conducted using the Deep-Dielectric Charging Analytical Technique (DCAT)¹⁵. This code has been checked against ground test results and other published analytical predictions.

The surface charging environmental models were derived from the NASA Guidelines Document⁹. The comparison to the NASCAP results used a "severe" environment while the variable environment study used a combination of three different environments. The buried charge study used the maximum flux of energetic particles reported¹⁶.

Surface Charging Comparisons

The comparisons to NASCAP were made under both local midnight (sunlight on the earth-facing side of the antenna) and local dawn (sunlight on the edge of the antenna). In both models, spinning was simulated by inputting 1/3 solar intensity onto to the cylindrical solar arrays. The substorm was encountered at time zero and the the intensity was held constant for the duration of the runs.

The comparison of the structure voltages are shown in figure 2. As can be seen, the comparison is generally within 10% for both cases over the substorm encounter time of about 900 seconds. The local midnight comparison starts out in excellent agreement but deviates after 600 seconds when the NASCAP predictions start to stabilize. The TSCAT predictions also tend to stabilize but not at the same rate. The local dawn predictions show an initial deviation that comes back

together at about 600 seconds. This difference between the runs is due to the lack of modeling of the cavity (additional grounded area missing) and uncertainty of the properties of the antenna screen material.

The comparison of the surface differential voltages (the difference between the surface voltage and the structure voltage) is shown in figure 3 for local midnight. Similar results were found for the local dawn runs. The agreement for the Optical Solar Reflectors (OSR) and Kapton are excellent. The comparison between the the Teflon data indicates that the resistivity value used in the TSCAT run should have been increased slightly to improve the agreement. At the end of the run, the difference is on the order of 10%. The largest discrepancy was found in the initial charging of the paint. Here, differences of up to 25% were found. At the conclusion to the run, the agreement did become much better.

The engineering code does seem to incorporate all of the capability to be useful to conduct system behavior studies. The NASCAP runs took hours on a mainframe computer to complete while the TSCAT runs took about 10 minutes on a PC. This is a reasonable trade between code precision and time.

SURFACE CHARGING IN VARIABLE ENVIRONMENTS

In this section of the report, the surface charging behavior of a spin-stabilized spacecraft in a two hour period from 05:30 to 07:30 hours, spacecraft local time charges in response to a variable intensity substorm (see figure 4). The substorm encounter starts at 05:30 hours with an intensity level of 0.60 corresponding to a substorm that could occur about 40% of the time in orbit according to the NASA Guidelines ⁹. After a short interval the substorm intensity increased to 0.9 (corresponding to a frequency of occurrence of 10%), then drops back down to the 0.6 level for a considerable period. The substorm level increases to the 0.6 level and reduces again just before 06:30 hours. The substorm intensity increases to duplicate the initial characteristics at about 6000 seconds into the simulation. This substorm characteristic is an arbitrary selection and is not meant to duplicate a specific substorm. The 0.6 and 0.9 intensity levels correspond to the "moderate" and "severe" levels in the NASA Guidelines document.

There is a constant sunlight input to the spinning solar array on the cylindrical sides of the spacecraft at 0.33 solar intensity (to provide the average sunlight to the spinning array). This assumes that the spacecraft spin rate is faster than the tens of minutes required to charge the dielectrics. Sunlight incident to the earth facing antenna is stepped every 30 minutes (corresponding to a 7.5 degree angle change). This provides an adequate simulation of the sunlight effect.

The spacecraft structure profile is shown in figure 5 along with the substorm characteristics. The structure charging reaches only to -850 volts which is more in keeping with the actual space data on charging of spin-stabilized spacecraft.

Structure charging becomes more negative as the substorm intensity increases. In the mild substorm corresponding to the 0.2 intensity (electron temperature of 2.2 KeV), discharging of the structure depends upon the sunlight incident upon the antenna back surface. This can be seen by comparing the initial behavior in the 0.2 substorm (about 1000 to 3000 seconds in the storm) to that from about 3500 to 5000 seconds. Initially, there is a period in which the structure charging did not change and then at about 06:00 hours, when one panel of the antenna back received the first shallow incident sunlight, the structure started to discharge. In the second cycle, the sunlight on the panel became stronger and the structure discharged faster. This is also apparent in the 0.6 intensity substorms: the sunlight incident upon the antenna changes the charging rates.

The antenna surface differential voltages (relative to the structure potential) are shown in figure 6. The sunshade surfaces (those that face earth) are all the same potential. The back of the antenna (Kapton surfaces) are divided into two groups: one is that surface exposed to sunlight at 05:30 and the other group is the three remaining panels that have sunlight incident upon them at 07:30. The sunshade material has a quasi-conductive surface to provide surface leakage since grounding would prevent the antenna operations. The back is modelled as a Kapton thermal blanket in which the metal sides are grounded.

For the first 600 seconds, the difference between the charging levels are too small to show on the curve. Then a small difference, due to the different grounding appears. The 7.5 degree sunlight incident upon the sunshade material does not affect the surface charging of this material. After 06:00 hour, the sunlight on the Kapton back does affect the surface voltage of the one panel in sunlight and allows a progressively stronger differential to exist between that panel and the surrounding Kapton blankets as well as the sunshade material. When the rest of the Kapton blankets are exposed to sunlight at 07:30 hours in the "moderate" substorm environment, the difference on the back side disappears while the difference between the back and sunshade material persists. This voltage difference between the front and back surfaces reaches 4 KV and can occur some time after a peak intensity of the substorm. Such differential voltages could result in discharges. This has been shown in a simulated discharge test of an antenna thermal blanket (see figure 7). Note that the discharges originate at the edges and imperfections in the blanket. The same could occur in space.

The charging of spacecraft surfaces is strongly dependent on sun/shadow effects and prior charging history. Since the dielectrics are good insulators, the discharging time without sunlight can be long resulting in unexpected differential voltages. These differential voltages can trigger discharges between sunlit and dark areas of the antenna blanket as well as between the blanket and the sunscreen or the structure. Such discharges are not considered in the NASA Design Guidelines at the present time. This study indicates that the guidelines should be expanded.

For those interested in the economics of charging analysis, the previous study required about 60 data points. The time required for the run, once the technique was established, is on the order of 30 minutes using an IBM AT personnel computer.

BULK CHARGING IN VARIABLE ENVIRONMENTS

Bulk charging effects in the antenna thermal blanket were evaluated using the Deep-Dielectric Analytical Technique (DCAT) code. This code is essentially a one dimensional computer program and hence, in common with other similar codes, assumes an infinite dielectric surface rather than specific spacecraft geometries. The charging response to a changing substorm environment for Kapton in the dark is shown in figure 8. Here, a very severe environment corresponds to the maximum high energy environment published in the literature¹⁶. The severe and moderate are then scaled versions of this high level. As can be seen, Kapton approaches equilibrium values in the very severe environment after about 150 seconds. In the severe environment, the Kapton surface becomes more negative but still approaches equilibrium after about 300 seconds longer. In the moderate environment, the surface discharges. The charge density and internal electric fields for these conditions are shown in figure 9. In the very severe environment, the charge is distributed throughout the dielectric - the particles penetrate through the material - producing the relatively low surface potential. In the severe environment, a charge centroid develops about 0.001 cm within the surface producing the more negative surface voltage. The moderate environment also causes a charge centroid but at a lower level. The electric fields within the dielectric are not large enough to cause concern for discharges.

If the Kapton surface is charged while in the shadow and then is exposed to sunlight, there is a change in the boundary conditions which can trigger discharges. In sunlight, it is assumed that the dielectric surface would be held close to the structure potential by photoemission. This changes the charge distribution and internal electric fields as shown in figure 10. If the value of the electric field exceeds a breakdown threshold, then a discharge will occur resulting in the dissipation of the difference in the charge density distributions shown.

Finally, there is a question of possible penetration of the thermal blanket and deposition of charge within the substrate material. Here, there are two consequences: one, the substrate is conductive and tied to the structure and two, the substrate is a dielectric. If the substrate is conductive and grounded, then the result will be as shown previously. If the substrate is floating, then another charging process occurs. Now, the dielectric is essentially isolated from ground and is weakly capacitively coupled to the structure. It will charge fast as shown in figure 11. Here, the code predicts that the surface potential for a 5 mil Kapton layer on a 10 mil fiberglass substrate will charge to about -10 KV at equilibrium. The internal voltage distribution through this combination is shown in figure 12. The code requires that the bottom of the substrate be grounded, so the computation would be more appropriate to a case where

the substrate were thin. This result indicates that the substrate could be charged to about 9 KV. If the substrate is attached to the structure at an edge, then this differential voltage could exist across the joint and give rise to discharges. One explanation for the spin-stabilized spacecraft anomalies is that energetic charged particles penetrated the thermal blankets charging the poorly grounded graphite epoxy substrate underneath. This resulted in discharges which caused the anomalies. While this could occur, based on the analysis conducted here, it is hard to correlate the occurrences in the local dawn and dusk periods. This penetration effect could occur anytime that there are sufficient energetic particles.

The modelling of the Kapton thermal blankets presented here is not precise. In reality, the individual layers of the metallized layers are grounded and not floating as is assumed here. The computational techniques exist to improve the simulation but they are more complicated. The results of the more precise studies agree with the trends shown here and so, the simplistic approach is used to illustrate trends.

CONCLUDING REMARKS

A study of the charging of a spin-stabilized spacecraft in variable intensity environments using engineering level computer codes to evaluate possible charging and discharging mechanisms. Both surface and bulk dielectric charging processes are evaluated.

Surface charging effects are dominated by incident sunlight. The charging characteristics can change due to shallow incidence of sunlight and to discover the possible sites for discharges, detailed studies with variable environmental conditions are required. This study has shown that it is possible to have discharges after the peak of the substorm intensities due to the long decharging time constants of spacecraft surface dielectrics. This negates the recommended design approach of using a constant intensity substorm environment to obtain the maximum electrical stress in dielectrics. Such an approach results in overpredicting spacecraft potentials (and probably overcompensating for charging effects) as well as possibly missing potential discharge sites. Furthermore, the use of a variable intensity substorm has shown that, once started, dark dielectrics remain charged for long periods of time and that discharges can be triggered in the low intensity substorm periods when charged surfaces are exposed to shallow angle incident sunlight. The discharges that can occur here vary from charge loss to space, to breakdown between dielectrics or to the structure. There can be more processes than originally given in the NASA Guidelines.

Buried charge effects have not received the consideration that they deserve since they probable cause more discharges than the surface phenomena. In this study, an engineering code has been used to evaluate the charging of the antenna coatings. It has been found that sun/shade effects here are probable source of discharges. This occurs when a surface is charged in the dark and then moves into sunlight. The rapid change in conditions forces a redistribution in the internal charge distribution and could trigger discharges. There is a

possibility that energetic electrons could penetrate to substrates. These materials could be charged if they are not adequately grounded and possibly discharge across joints.

The results of this study indicate that the prevalent view that discharges are primarily charge losses to space should be reexamined. The cases illustrated here indicate that there is a strong possibility that discharges between surfaces as well as in internal structures exists. These concepts should be factored into design criteria. The NASA Design Guidelines, developed about 10 years ago, should be reviewed and upgraded.

REFERENCES

1. DeForest, S.E.; "Spacecraft Charging at Synchronous Orbit", Journal of Geophysical Research, Vol 77, Feb 1, 1972, pp.651 - 659.
2. Allen, J.; "On-Orbit Anomalies", AIAA Paper 88-0628, Jan 1988.
3. McPherson, D.A. and Schober, W.R.; "Spacecraft Charging at the High Altitudes: The SCATHA Program", Spacecraft Charging by Magnetospheric Plasmas, A. Rosen, ed., Progress in Astronautics and Aeronautics, Vol 47, AIAA, 1976, pp.45 - 60.
4. Mullen, E.G. and Gussenhoven, M.S.; "SCATHA Environmental Atlas", AFGL-TR-83-002, A.F. Geophysics Laboratory, 1983.
5. Stevens, N.J., Rosen, A. and Inouye, G.T.; "Communication Satellite Experience in the Seventies", AIAA Paper 87-0473, Jan 1987.
6. Koons, H.; "Severe Charging Event on SCATHA in September, 1982", AIAA paper 87-0475, Jan 1987.
7. Katz, I., et al.; "The Capabilities of the NASA Charging Analyzer Program", Spacecraft Charging Technology-1978, NASA CP-2071/AFGL-TR-0082, 1979, pp.101-122.
8. Lovell, R.R., et al.; "Spacecraft Charging Investigation: A Joint Research and Technology Program", Spacecraft Charging by Magnetospheric Plasmas, op.cit., pp.3-14.
9. Purvis, C.K., Garrett, H.B., Whittlesey, A. and Stevens, N.J.; "Design Guidelines for Assessing and Controlling Spacecraft Charging Effects", NASA Technical Paper 2361, Sept 1984.
10. Stevens, N.J.; "Use of Charging Control Guidelines for Geosynchronous Satellite Design Studies", Spacecraft Charging Technology-1980, NASA CP-2182/AFGL-TR-81-0270, 1981, pp.789-801. ADA114426
11. Purvis, C.K. and Staskus, J.V.; "SSPM Charging Response: Comparison of Ground Test and Flight Data to NASCAP Predictions for Eclipse Conditions", ibid., pp.592-607.
12. Stannard, P.R., et al.; "Validation of NASCAP Model Using Spaceflight Data", AIAA paper 82-0269, Jan 1982.
13. Stevens, N.J., Barbay, G.J., Jones, M.R. and Viswanathan, R.; "Model of Environmentally Induced Transients within Satellites", Journal of Spacecraft and Rockets, Vol 24, #3, May-June 1987, pp.257-263.
14. Chakey, R.C. and Inouye, G.T.; "Characteristics of EMI Generated by Negative Metal/Positive Dielectric Voltage Stresses Due to Spacecraft Charging", Spacecraft Environmental Interactions Technology-1983, NASA CP-2359/AFGL-TR-85-0018, 1985, pp.437-452. ADA202020
15. Hansen, D.P.; "DCAT: Engineering Analysis Tool for Computing Buried Charge Effects", AIAA paper 88-0630, Jan 1988.
16. Vampola, A.; "Buried Charge Effects", AIAA paper 88-0629, Jan 1988.

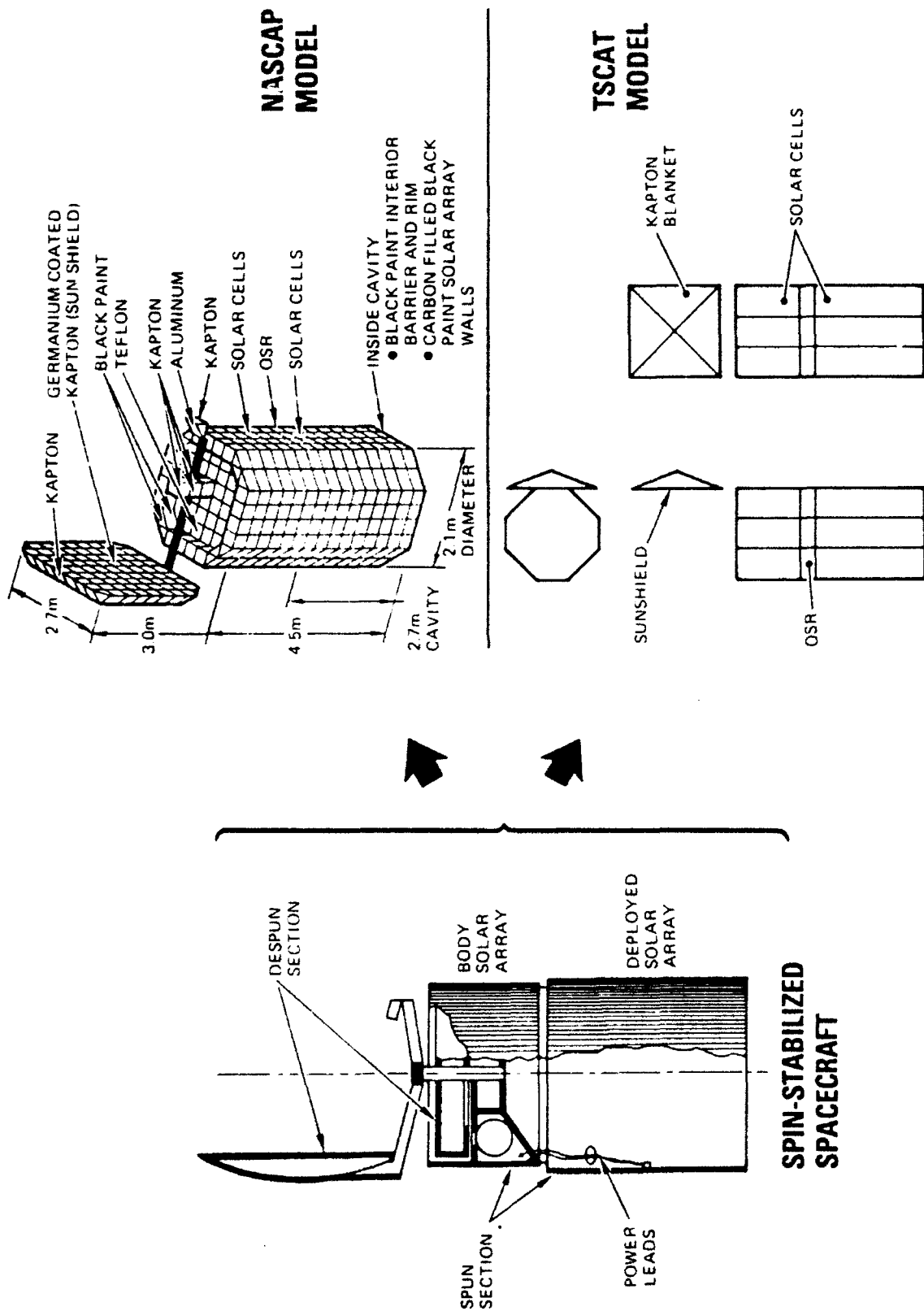
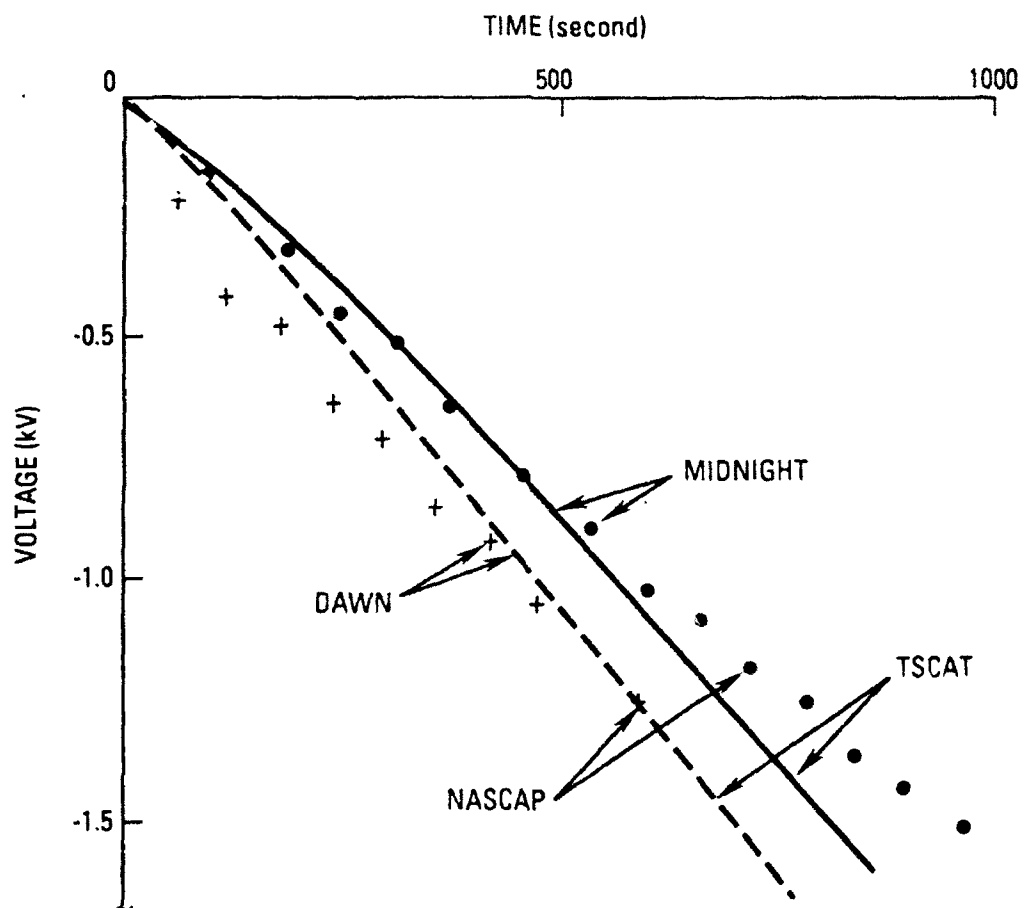


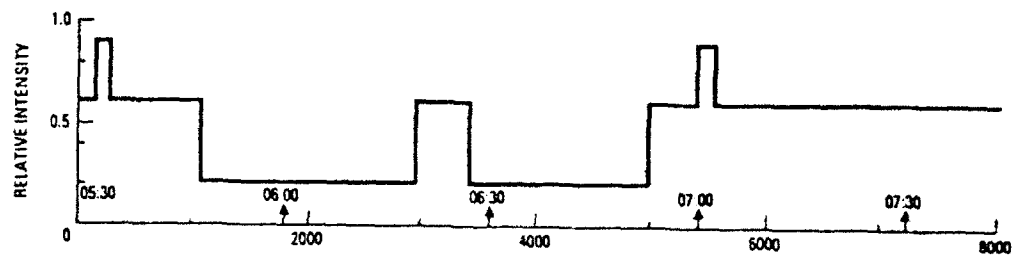
Figure 1. Spin Stabilized Spacecraft Models



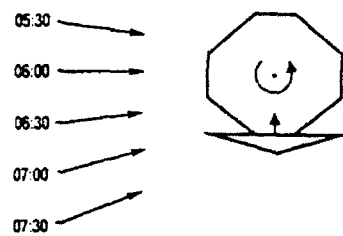
00021.2

Figure 2. Spin Stabilized Spacecraft Structure Potentials

A. SUBSTORM INTENSITY

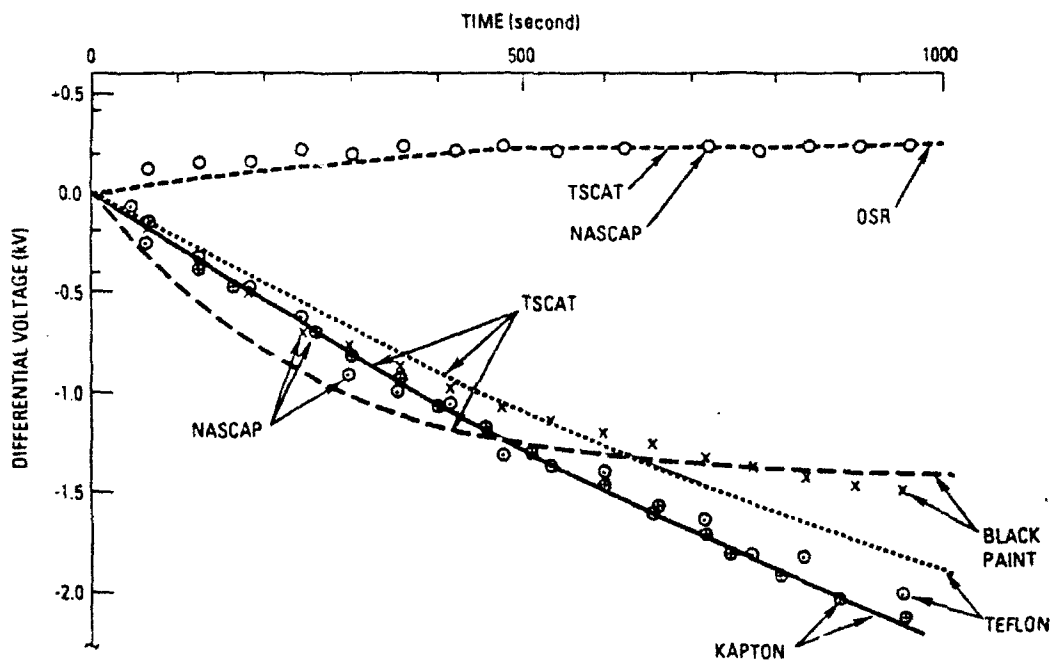


B. SOLAR INCIDENCE



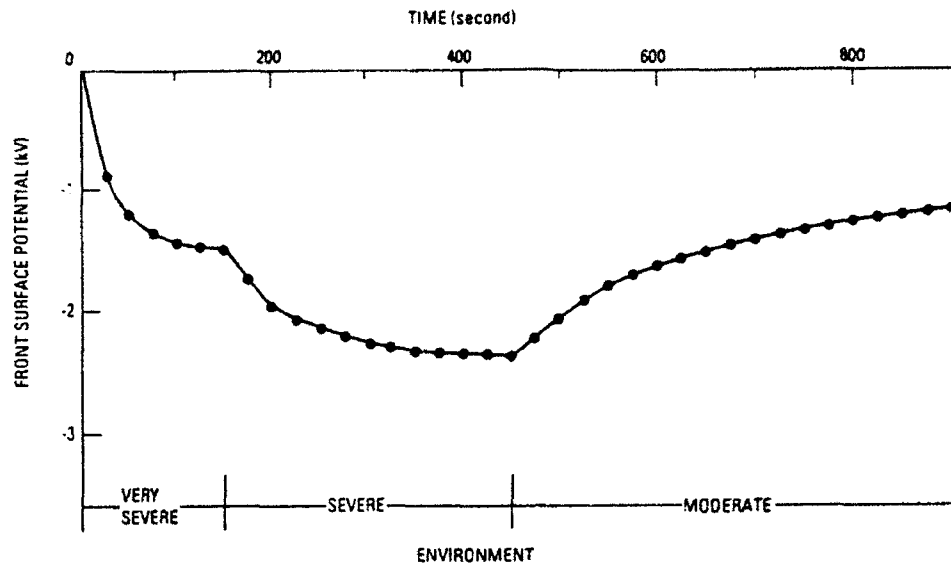
M2 Mac-00021 8

Figure 4. Environment Conditions



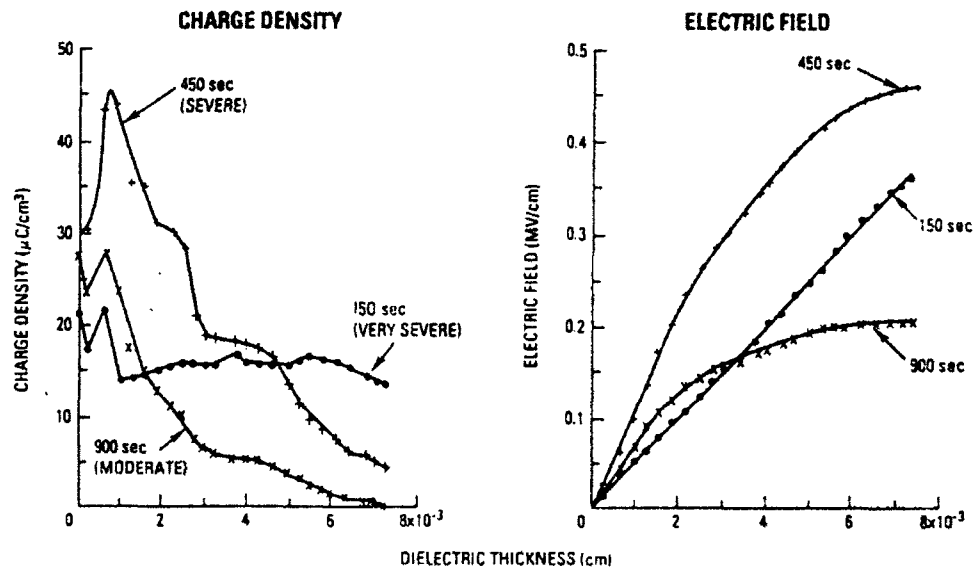
M2 Mac-00021 9

Figure 3. Spin Stabilized Spacecraft Dielectric Differential Voltages
(Severe Substorm - Midnight Simulation)



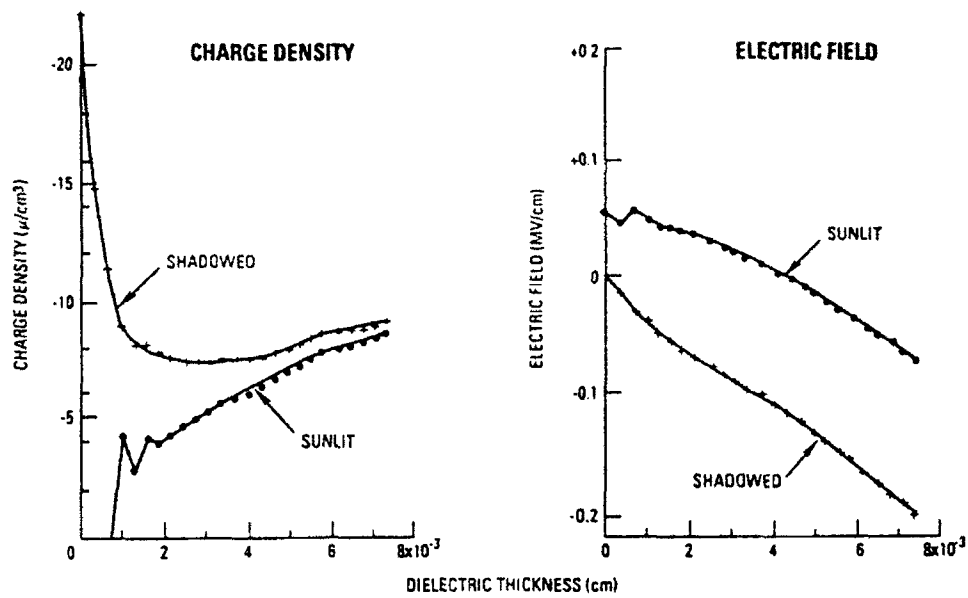
M2 Mac-00021 5

Figure 8. Predicted Front Surface Potential Due to Buried Charge (Dark 3 mil Kapton in Variable Intensity Storms)



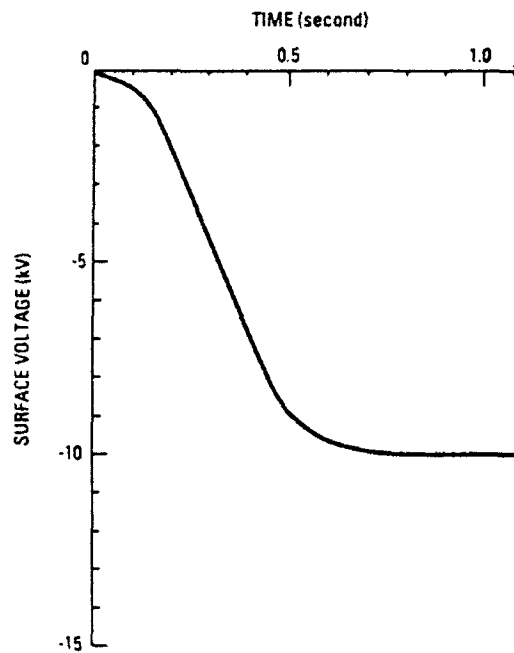
M2 Mac-00021 5

Figure 9. Predicted Internal Distributions in 3 mil Kapton (Variable Storm Intensity)



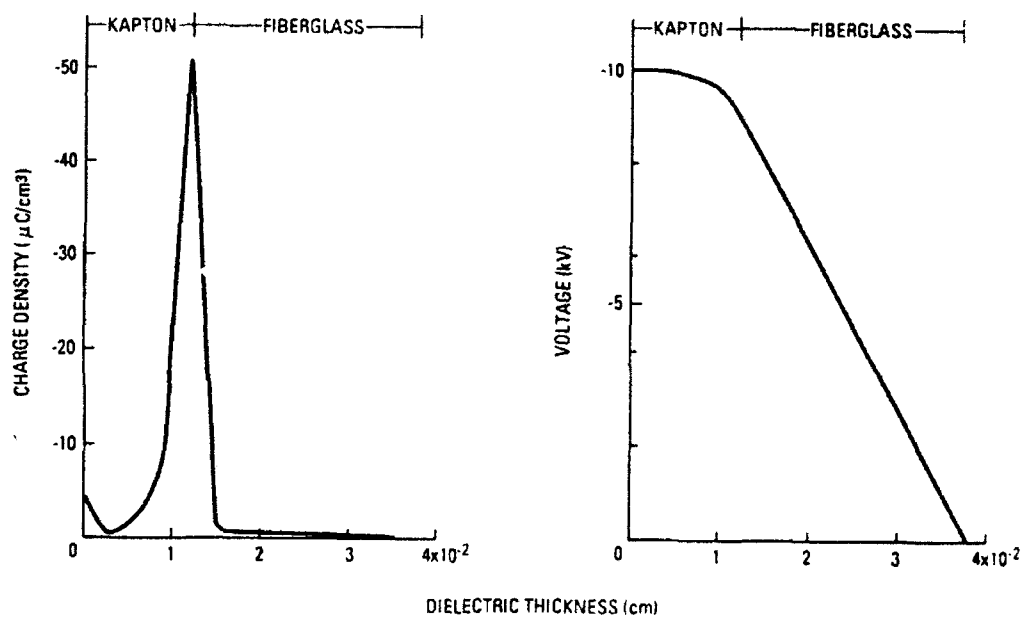
M2 Mac-00021 8

Figure 10. Predicted Change in Internal Distributions Due to Shadowing
(Very Severe Environment - 10 Seconds After Shadow)



M2 MAC-00021 3

Figure 11. Front Surface Voltage in Thermal Blanket Covered Substrate
(Very Severe Environment)



M2 Mac 00021.1

Figure 12. Charge Density & Voltage Distribution in Thermal Blanket Covered Substrate (One Second in Very Severe Environment)

SURFACE CHARGING ON ENGINEERING TEST SATELLITE V OF JAPAN

Hironobu NISHIMOTO

Tsukuba Space Center, National Space Development Agency of Japan
2-1-1, Sengen, Tsukuba, Ibaraki 305, Japan

Haruhisa FUJII

Manufacturing Development Laboratory, Mitsubishi Electric Corporation
8-1-1, Tsukaguchi-Honmachi, Amagasaki, Hyogo 661, Japan

Toshio ABE

Kamakura Works, Mitsubishi Electric Corporation
325, Kamimachiya, Kamakura, Kanagawa 247, Japan

ABSTRACT

We developed a potential monitor to measure the surface charging potentials on insulating materials for spacecraft due to charged particles in space environment. The potential monitor was installed on geostationary Engineering Test Satellite V of Japan which was launched on August 27, 1987. Three kinds of thermal control materials were used as samples. We obtained the following observational results: (1) The level of the charging potential depended on the environmental condition and the material. (2) The rapid increase of the charging potential to be due to the shadows of the paddle and/or the antenna was occasionally observed. (3) The potential periodically changed with the temperature inside the sensing part of the potential monitor. (4) For long time, the potential gradually increased under the shaded condition, but decreased in the sunlit condition.

INTRODUCTION

Spacecrafts in Earth orbits have the duties to work normally in tenuous space-plasma environments with solar light and high-energy radiation. The space plasma consists of electrons and positive ions, mainly protons. In high-altitude orbits such as a geostationary orbit, the spacecrafts are considerably affected by these charged particles. The surface potential of a satellite in the space plasma will come into an electrical equilibrium with the potential of the plasma by developing surface charges on the satellite to reduce the net current between the satellite and the plasma to zero (Garrett, 1981; Francis, 1982; Grard et al., 1983). In the situation, the satellite covered with several kinds of insulating materials gets differentially charged. The potential differences between the surfaces of the insulating materials and the electrically conductive surfaces of the satellite could be formed. This phenomenon is referred to as "differential charging" on the spacecraft (Garrett, 1981; Grard et al., 1983). In particular, when the satellite encounters a hot plasma (or geomagnetic substorm), the potential differences would be multikilovolts. If the potential difference exceeds a breakdown threshold, a discharge will occur (Nanevicz et al., 1980; Purvis et al., 1984).

The differential charging and the discharges on the spacecraft are known to cause the degradation of surface materials, malfunctions and anomalies of on-board electronics, and so on (Garrett, 1981; Francis, 1982; Grard et al., 1983; Purvis et al., 1984). These influences must be minimized to achieve high reliability and long mission of future spacecraft system. So, it is necessary to acquire the charging characteristics of the materials in the actual space environment as well as in ground simulation experiments such as electron-beam irradiation experiments (Stevens et al., 1977; Verdin, 1981; Fujii et al., 1988).

From this viewpoint, we have developed a potential monitor to measure the surface charging potentials of insulating materials for spacecraft due to the charged particles in space (Kawanishi et al., 1986; Nishimoto et al., 1989). The potential monitor which we call as POM was installed on Engineering Test Satellite V (ETS-V) of Japan as one of Technical

Data Acquisition Equipments (TEDA) (Murayama et al., 1985, Kawanishi et al., 1986). ETS-V is the first domestically developed 3-axis stabilized geostationary satellite in Japan. It was launched from Tanegashima Space Center on August 27, 1987 and settled at 150 degrees of east longitude on the geostationary orbit.

This report describes the outline of the POM briefly and the electrostatic charging characteristics of the insulating materials which have been obtained by the POM on ETS-V for about two years (Nishimoto et al., 1989).

OUTLINE OF POTENTIAL MONITOR (POM)

The POM has the function to measure the surface charging potentials on typical insulating materials for spacecraft in the geostationary orbit and has the objective to study the electrostatic charging and discharging phenomena in cooperation with Discharge Monitor (DIM) which is also one of the TEDA (Kawanishi et al., 1986). It is expected that the acquired data are served to protect future spacecrafts from the influences caused by the electrostatic charging and discharging.

The block diagram of the POM is shown in Fig.1. The POM consists of sensing part (POM-S) and electronics (POM-E). The POM-S to be exposed to space environment is connected by cables to the POM-E. Electrostatic probe (Monroe Inc., 1017S) is located in the POM-S. The probe has an electrostatic electrode, a high-impedance pre-amplifier, a microfork chopper and the driver. The POM-E consists of two amplifiers, a phase-sensitive demodulator and an oscillator.

The sample board is set on the POM-S. A sample with metallized backing is pasted on the sample board with a conductive adhesive (ECCOBOND 56C). However, a non-metallized region of diameter of 1mm is formed on the back of the sample. The electric field which the accumulated charges generate on the front surface is detected through the non-metallized region by the electrostatic probe and the signal is recorded as the output voltage of the POM-E.

The relation between the front surface potential and the output voltage of the POM-E was calibrated by applying a known potential to a metallic plate put on the front surface. And it was also calibrated by measuring the surface potential with the electrostatic voltmeter as irradiating the front surface with an electron beam with energy of 15keV. The measurement range of the surface potential is +1kV to -10kV.

The external dimension and the photograph of the POM-S (flight model) are shown in Fig.2 and Fig.3, respectively. The POM-S consists of three sensing parts. Each sensing part has one sample of insulating material whose size is 40x40mm². The test samples installed on the POM-S are as follows;

- 1)Aluminized Kapton of 127μm thickness,
- 2)Silvered fused-silicate-glass of 200μm thickness (OSR: Optical Solar Reflector),
- 3)Silvered Teflon (FEP; fluorinated ethylene propylene copolymer) of 127μm thickness.

The POM-S is set on the south mission panel of ETS-V whose external appearance is shown in Fig.4. The POM-S is connected by cables to the POM-E which is located in the body of ETS-V in order to protect the electronics from high-energy radiation.

The POM was switched on by a command on September 7, 1987.

OBSERVATIONAL RESULTS

The following charging characteristics of the insulating materials in the space environment have been obtained for about two years.

Figure 5 shows the charging potentials on October 28, 1987. Until October 28, the amplitude of the surface potentials of the three materials was

$$\text{OSR} \geq \text{Kapton} > \text{Teflon},$$

and the potential of the OSR was beyond -10kV, the upper limit of the measurable potential. At 8:00 UT (Universal Time) on October 28, the rapid decrease of the surface potential of the OSR was observed. After that, the OSR was positively charged and the amplitude of the surface potentials of the three materials was

$$\text{Kapton} > \text{Teflon} > \text{OSR}.$$

After a few months, the surface potential of the Kapton sample became beyond -10kV .

Figures 6 and 7 show the surface charging potential of the Teflon sample with the count rates of high-energy electrons and protons on October 26 and 27, 1987, respectively. We referred to the data of the count rates of electrons ($>2\text{MeV}$) and protons ($1.4 - 4\text{MeV}$) measured by Space Environment Monitor (SEM) equipped on Geometeorological Satellite 3 (GMS-3) of Japan, "Himawari-3", which is on the geostationary orbit of 140 degrees of east longitude. The surface potentials negatively increased about 14:00UT to 20:00UT. The similar increase of the surface potentials can be also seen in Fig.5. The amplitude of the potential increase on October 27 was larger than that on October 26. October 27 was the more disturbed day than October 26, which is indicated from the count rates of the electrons and protons in Fig.6 and Fig.7.

We also observed that the surface potentials of the Teflon sample slightly changed with the temperature inside the POM-S as shown in Fig.8 (Nishimoto et al., 1989). However, there is a time lag between the charging potential and the temperature.

Figure 9 (a) and (b) show the surface potential of the Teflon sample which have been measured for about two years. In these figures, the surface potentials at 0:00UT of every day were recorded. The potential gradually increased with time from February to September, 1988 (Fig.9 (a)). It decreased from October, 1988 to February, 1989. After that it also changed to tend to increase from February to September, 1989 (Fig.9 (b)).

DISCUSSION

In general, the formation of the surface potential V_s on an insulating material in a charged-particles environment is expressed as follows (Garrett, 1981; Purvis et al., 1984);

$$dV_s/dt = A/C \cdot (J_e - (J_p + J_{se} + J_{bs} + J_{pe} + J_c)), \quad \dots (1)$$

where

- J_e ; incident electron current density,
- J_p ; incident positive-ion current density,
- J_{se} ; secondary electron current density,
- J_{bs} ; back-scattered electron current density,
- J_{pe} ; photo-emitted electron current density,
- J_c ; conduction current density through the bulk of the material,
- A ; exposed area of the material,
- C ; capacitance of the material,
- t ; time.

Taking this equation (1) into account, we will discuss the observational results.

Since the POM-S was set on the south mission panel of ETS-V, the POM-S is in the sunlit condition from the autumnal equinox (September 23) to the vernal equinox (March 20). The rest of a year gives the shaded condition to the south mission panel. The incident angle of solar light to the south mission panel changes with time in the sunlit condition. As ETS-V has the structure shown in Fig.4, the shadows of the L-band antenna reflector and/or the solar array paddle are considered to be cast on the south mission panel depending on the position of the orbit. As an example, the shadows which are formed on the south mission panel at 1:40 LT (Local Time) on a certain day near the winter solstice are shown in Fig.10. The shadow is cast on the POM-S at least three times during 0:00LT and 12:00LT. (0:00 LT corresponds to 14:00 UT.)

When the shadow is cast on the insulating material, the effect of photo-electron emission from the surface disappears. In the equation (1), J_{pe} becomes zero and the surface potential V_s negatively increases. The rapid increases of the surface potentials about 14:00UT to 20:00UT as shown in Fig.5, Fig.6 and Fig.7 are considered to be due to the shadow formed on the POM-S. As the shadow is formed on the POM-S about the same time every day, the increase of the surface potentials should have been observed every day. However, the increase is not always observed every day as shown in Fig.8. The observed charging properties are not explained only by the effect of the shadow. At this stage, however, the reason is not clear.

From the comparison between the SEM data of GMS-3 in Fig.6 and that in Fig.7, the conditions of the charged particles on October 27 is considered to have been more disturbed than that on October 26. Under the disturbed condition, the fluxes and the average energies of the charged particles increase (for example, Purvis et al., 1984). In this case, the incident electron current density to the satellite surface, J_e in the equation (1), increases. Also, as seen in the SEM data in Fig.7, the count rate of the proton drastically decreased on October 27. This may cause the decrease of the incident proton current density J_p . From these, the amplitude of the surface potential change in the shadow becomes large as seen in Fig.7.

Figure 8 shows that the surface potential of the Teflon sample periodically changed with the temperature inside the POM-S. To clarify whether the periodical change of the surface potential is due to the electronic circuit used in the POM-S or due to the sample material itself, we tested the temperature dependence of the electronic circuit. The test was performed by applying a constant voltage to a metallic plate on the POM-S and changing the ambient temperature from -20°C to 40°C . Figure 11 shows the result. This indicates that the output voltage has no temperature dependence. Therefore, we concluded that the periodical change of the surface potential is affected by the temperature dependence of the sample material itself.

Generally, the volume resistivity ρ of an insulating material decreases with the temperature as follows (for example, O'Dwyer, 1973);

$$\rho = \rho_0 \cdot \exp(E_a/kT), \quad \dots (2)$$

where E_a , k and T are the activation energy of the insulating material, Boltzmann's constant and the absolute temperature, respectively. ρ_0 is a constant value for the material. ρ_0 and E_a are determined by experiments. Then J_l (leakage current density through the bulk of the material) increases with increase of the temperature. Therefore, from the equation (1), the charging potential decreases with the temperature.

In Teflon (FEP), E_a is reported as 1.95eV (for example, Gross, 1980) and the volume resistivity ρ at room temperature (300K) is $2 \times 10^{18} \Omega \text{ cm}$. We calculated the temperature dependence of the surface potential of the Teflon (FEP) sample installed on ETS-V by using these values, the equivalent electrical circuit model as shown in Fig.12 (Massaro et al., 1977) and the environmental condition measured by SCATHA satellite (Mullen and Gussenhoven, 1982; Purvis et al., 1984). The result is shown in Fig.13. This indicates that the decrease of the volume resistivity ρ of Teflon due to the temperature increase decreases the surface potential. Therefore, the periodical change of the temperature inside the POM-S whose period is one day causes that of the surface potential of the Teflon sample.

And the fact that the sample is exposed to the space environment and the temperature sensor is inside the POM-S causes the time lag between the surface potential and the temperature.

If the same charge density is deposited on the front surface of each sample, the amplitude of the potentials ought to be

$$\text{Teflon} > \text{OSR} > \text{Kapton},$$

when taking the thickness and the dielectric constant into consideration. (The dielectric constants of Teflon, OSR and Kapton are 2.1, 3.9 and 3.5 respectively.) In fact, it is reported that the amplitude of the charging potentials was

$$\text{Teflon} > \text{OSR} > \text{Kapton}$$

in shadow by Satellite Surface Potential Monitor on SCATHA satellite on April 29, 1979 (Mizera, 1981).

However, our observational result indicated that the potential of the Teflon sample is lower than that of the Kapton as shown in Fig.5. This may be due to the difference of the secondary-electron emission properties. The rapid decrease of the surface potential of the OSR was observed at 8:00UT on October 28, 1987 as shown in Fig.5. This may indicate that the surface discharge occurred on the OSR. (However, the Discharge Monitor did not detect the signal in the event.) According to our ground simulation experiment, OSR is, however, vulnerable to discharge at the edge (Fujii et al., 1988).

As shown in Fig.9, the surface potential of the Teflon sample at 0:00 UT had a gradual change for long term of two years. In the sunlit condition, the surface potential gradually decreased. On the other hand, in the shaded condition, it gradually increased. From these data, we calculated the rates of the change of the deposited charges, dQ/dt . The results are shown in Fig.9. We estimate the results as follows. High-energy electrons penetrate deeply in the bulk of the sample. These are gradually accumulated in the bulk of the sample under the shaded condition, irrespective of the leakage of electrons through the bulk. However, these electrons are gradually photo-emitted with weak intensity of the solar light due to large incident angle of solar light because the POM-S is set on the south mission panel of ETS-V as described previously.

As shown in Fig.9, dQ/dt from February to September of 1989 is smaller than that from February to September of 1988. It is considered that the Teflon sample was deteriorated by high-energy radiation for long time and the volume resistivity decreased.

CONCLUDING REMARKS

The following results of the surface charging on the insulating materials were obtained by the POM installed on ETS-V.

- (1)The level of the charging potential depended on the environmental condition and the material.
- (2)The rapid increase of the potentials was occasionally observed. It seems to be due to the shadows of the antenna and/or the solar array paddle.
- (3)The potentials periodically changed with the temperature inside the POM-S.
- (4)For long time, the potentials gradually increased under the shaded condition, but decreased in the sunlit condition.

The data on the surface potentials are normally obtained by the POM on ETS-V until now.

We are now developing an improved POM for ETS-VI (to be launched in 1993) from the experience of the development and the performance of the POM installed on ETS-V.

REFERENCES

- Francis, C.R.; "Electrostatic charging problems of spacecraft," J. Electrostatics, vol.11 (1982) p.265
- Fujii, H., Y.Shibuya, T.Abe, R.Kasai and H.Nishimoto; "Electrostatic charging and arc discharges on satellite dielectrics simulated by electron beams," J. Spacecraft & Rockets, vol.25 (1988) p.156
- Garrett, H.B.; "The charging of spacecraft surfaces," Rev. Geophys. Space Phys., vol.19 (1981) p.577
- Grard, R., K.Knott and A.Pedersen; "Spacecraft charging effects," Space Science Rev., vol.34 (1983) p.289
- Gross, B.; "Radiation-induced charge storage and polarization effect," "Electrets" edited by G.M.Sessler (Springer Verlag, Berlin) (1980) p.217
- Kawanishi, T., H.Nishimoto, T.Koizumi and T.Abe; "Satellite Environmental Monitor and Material Degradation Monitor installed on Engineering Test Satellite (ETS-V)," IFAC Workshop on Electrostatic Charges and Discharges and Cosmic Ray Interaction in Satellites (1986)
- Massaro, M.J., T.Green and D.Ling; "A charging model for three-axis stabilized spacecraft," Proc. Spacecraft Charging Technology Conf., AFGL-TR-77-0051/NASA-TMX-73537 (1977) p.237 ADA045459
- Mizera, P.F.; "Charging results from the Satellite Surface Potential Monitor," J. Spacecraft & Rockets, vol.18 (1981) p.506
- Mullen, E.G. and M.G.Gussenhoven; "SCATHA environmental atlas," AFGL-TR-83-0002 (1983) ADA131456
- Murayama, H., K.Nakamaru, S.Yamada, T.Ueda, R.Kasai and M.Ohmura; "Experiments by ETS-V," J. Space Technology and Science, vol.1 (1985) p.20
- Nanevicz, J.E. and R.C.Adamo; "Occurrence of arcing and its effects on space systems," Prog.

- Astron. Aeron., vol.71 (1980) p.252
- Nishimoto, H., H.Fujii and T.Abe;"Observation of surface charging on Engineering Test Satellite V of Japan," AIAA 27th Aerospace Science Meeting, AIAA-89-0613 (1989)
- O'Dwyer, J.J.;"The theory of electrical conduction and breakdown in solid dielectrics" (Clarendon Press, Oxford) (1973)
- Purvis, C.K., H.B.Garrett, A.G.Whittlesey and N.J.Stevens;"Design guidelines for assessing and controlling spacecraft charging effects," NASA Technical Paper 2361, (1984)
- Stevens, N.J., F.D.Berkopec, J.D.Staskus, R.A.Blech and S.J.Narciso;"Testing of typical spacecraft materials in a simulated substorm environment," Proc. Spacecraft Charging Technology Conf., AFGL-TR-77-0051/NASA-TMX-73537 (1977) p.431 **ADA045459**
- Verdin, D.;"Electrostatic charging of spacecraft materials," J. Electrostatics, vol.11 (1981) p.249

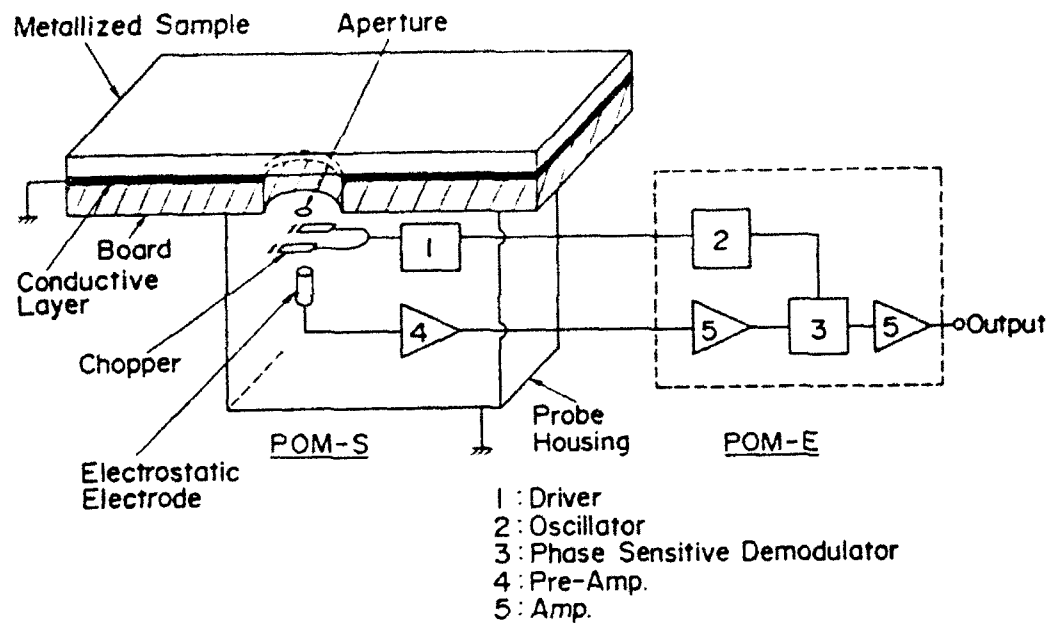


Fig.1 Block diagram of POM.

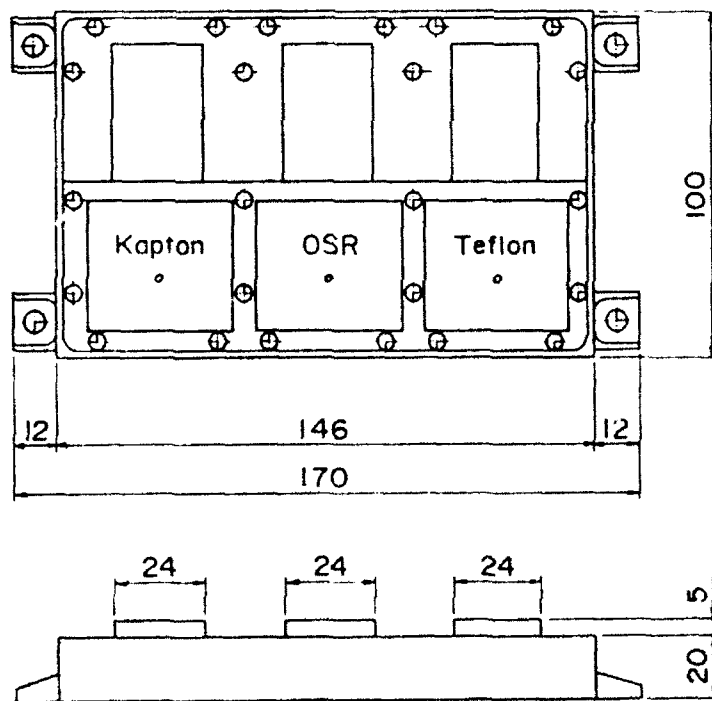


Fig.2 External dimension of POM-S installed on ETS-V.

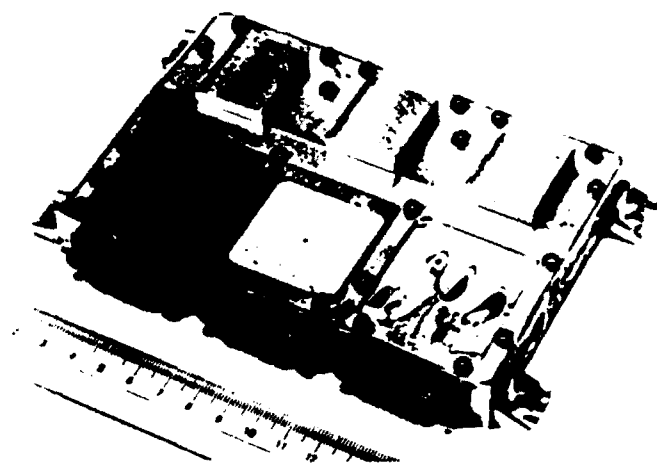


Fig.3 Photograph of POM-S installed on ETS-V.

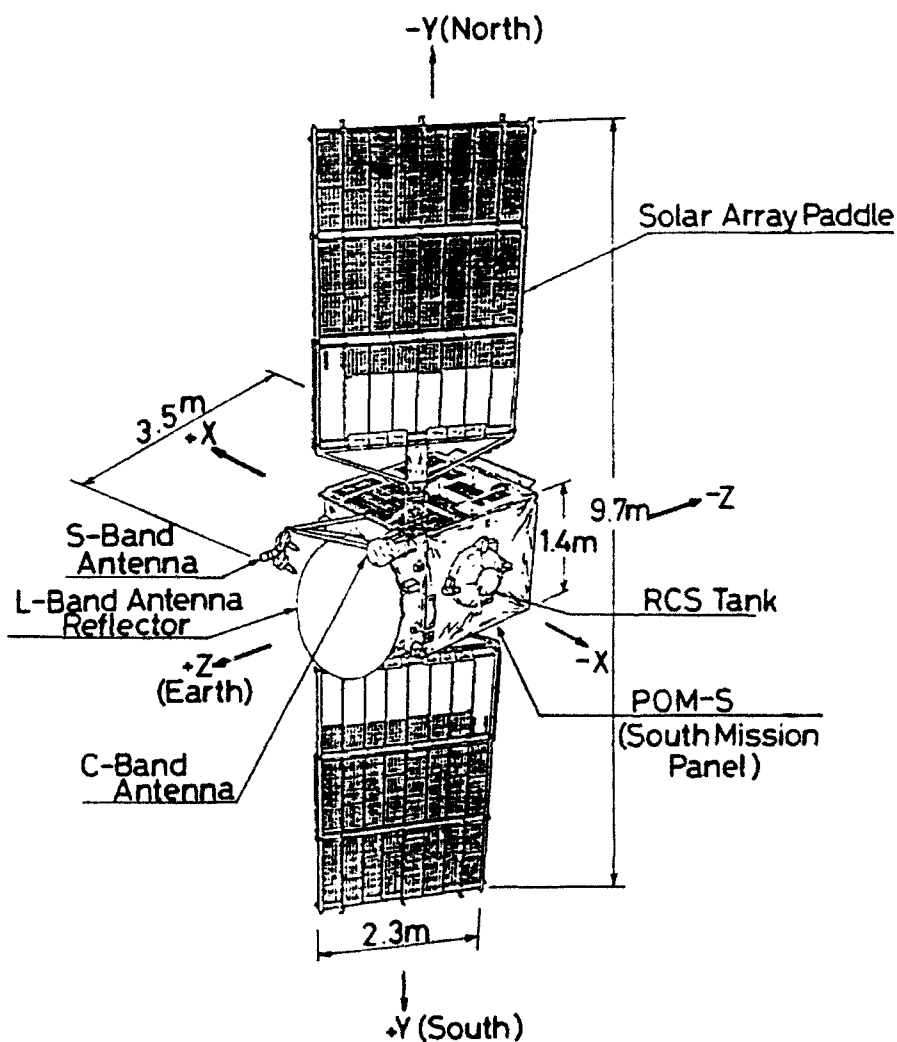


Fig.4 External appearance of ETS-V.

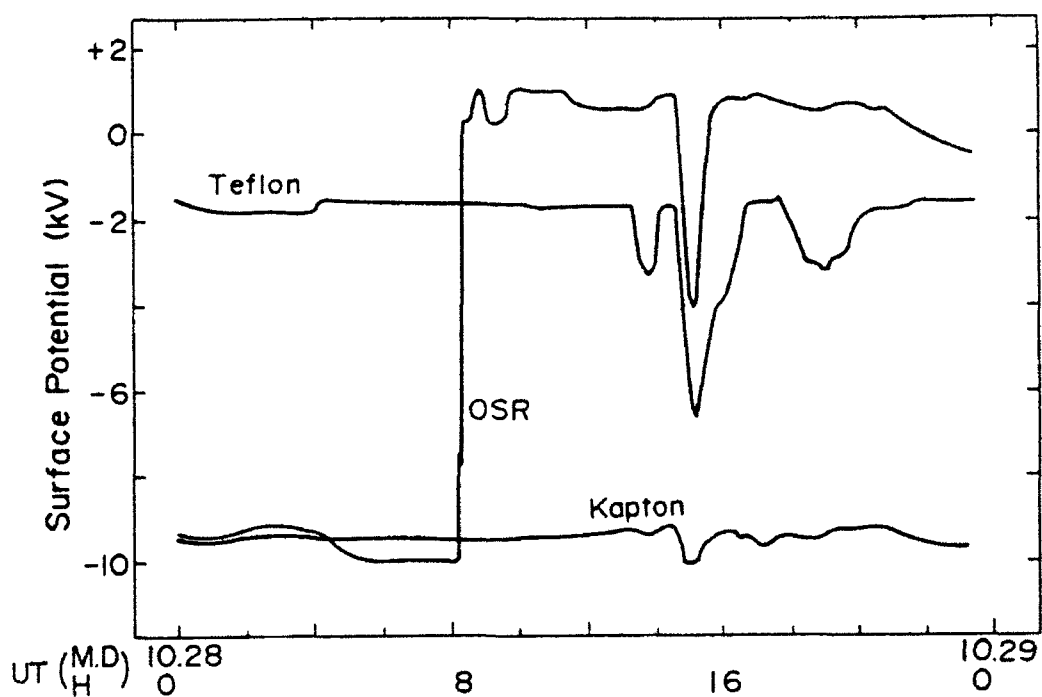


Fig.5 Surface charging potentials on October 28, 1987.

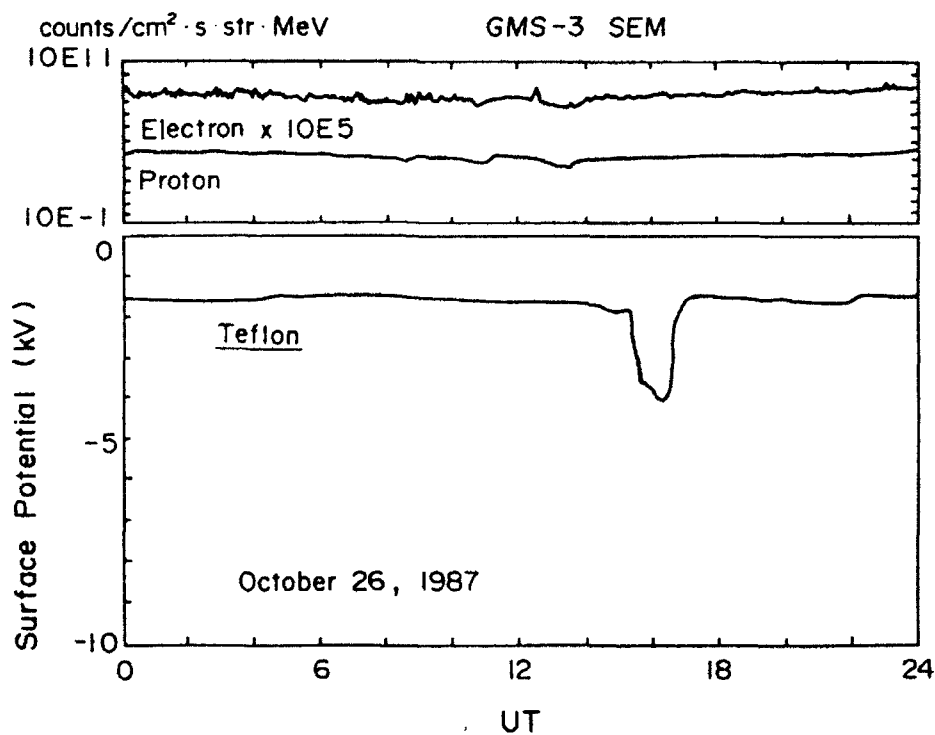


Fig.6 Surface charging potential of Teflon and count rates of electrons (>2MeV) and protons (1.4 - 4MeV) on October 26, 1987.

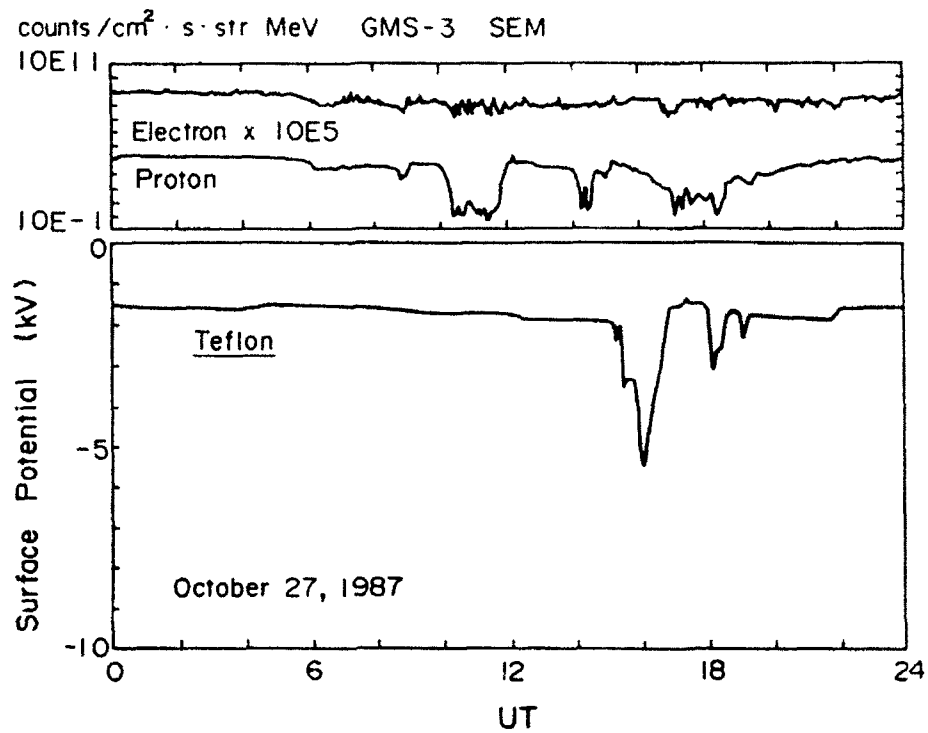


Fig.7 Surface charging potential of Teflon and count rates of electrons (>2MeV) and protons (1.4 ~ 4MeV) on October 27, 1987.

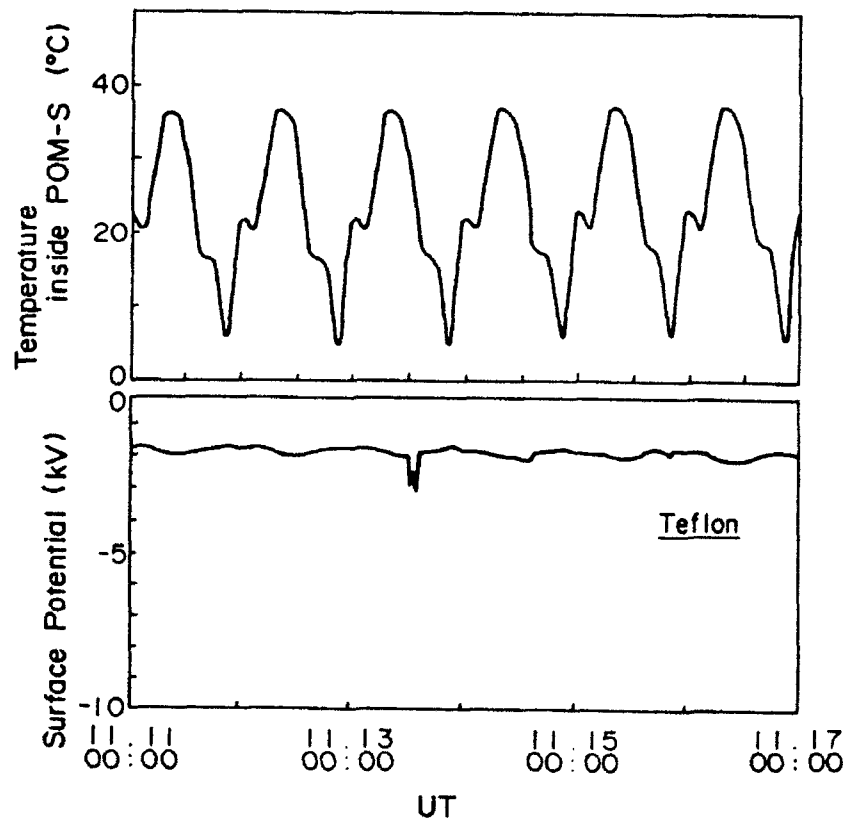
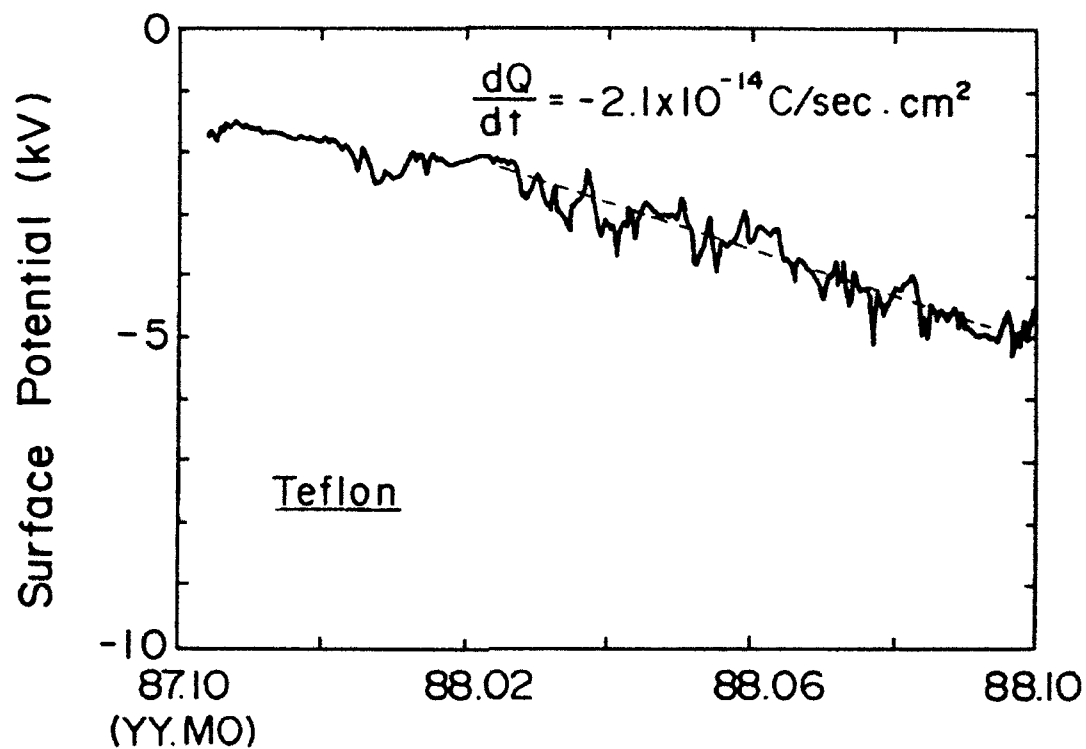
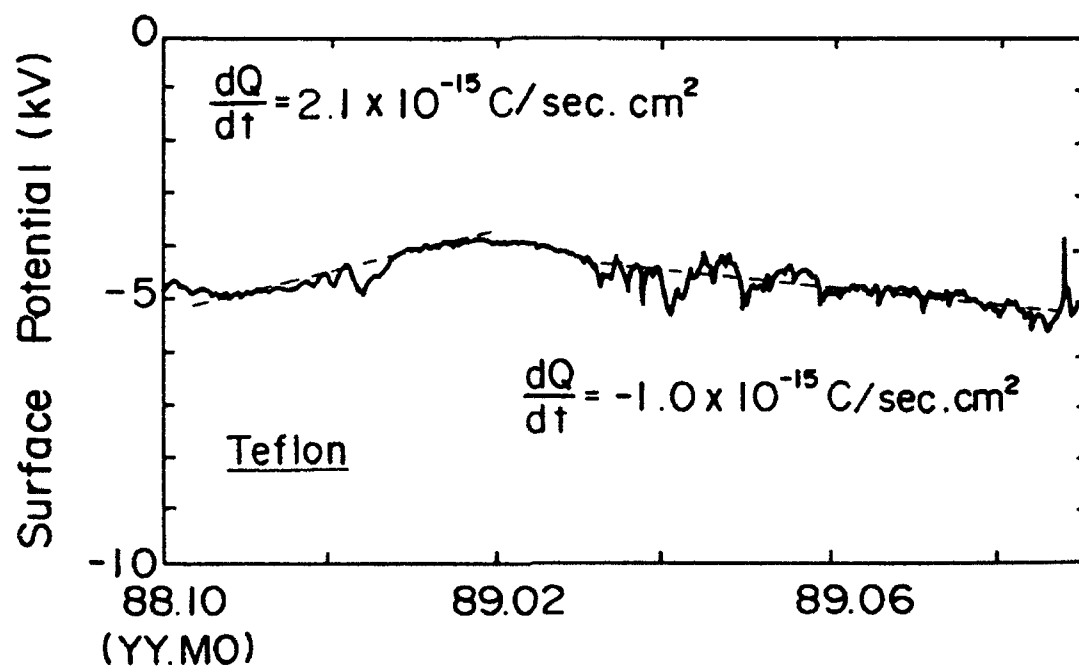


Fig.8 Surface charging potential of Teflon and temperature inside the POM-S on November 11 to 16, 1987.



(a)



(b)

Fig.9 Surface charging potential of Teflon at 0:00UT from October, 1987 to September, 1989.

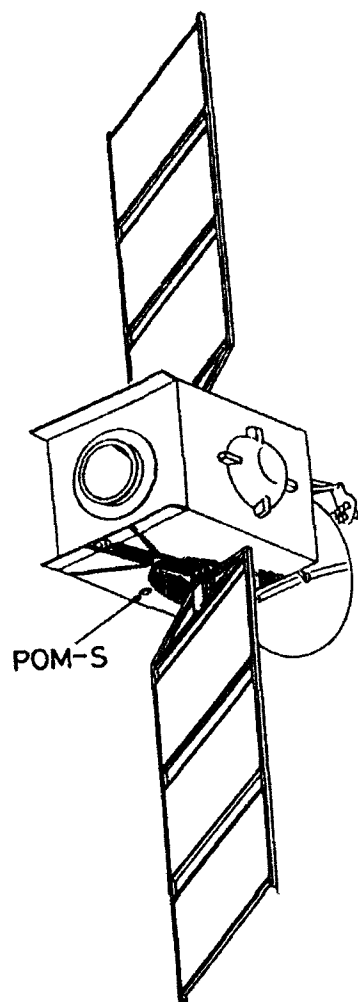


Fig.10 Shadows cast on the south mission panel of ETS-V at 1:40LT on one day near the winter solstice.

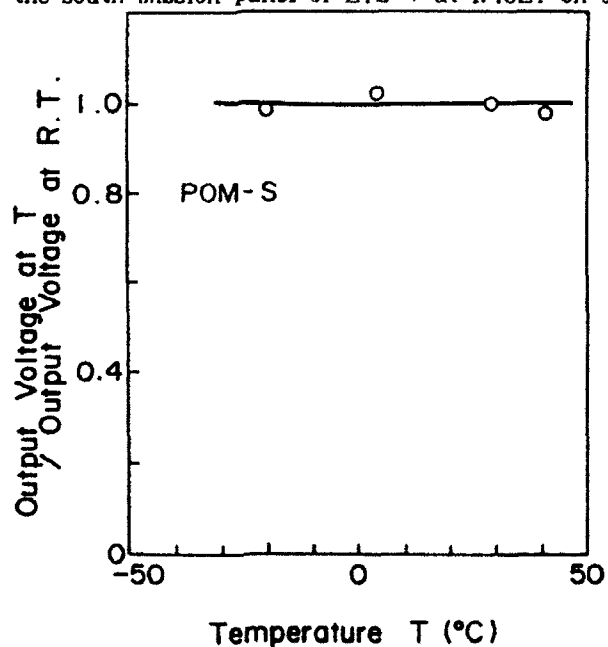


Fig.11 Temperature dependence of the output voltage of POM.

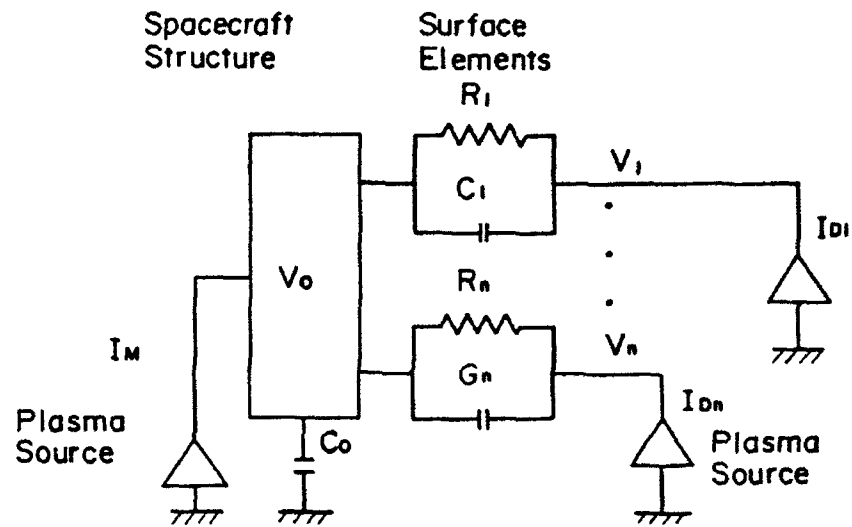


Fig.12 Spacecraft equivalent circuit model (Massaro et al., 1977).

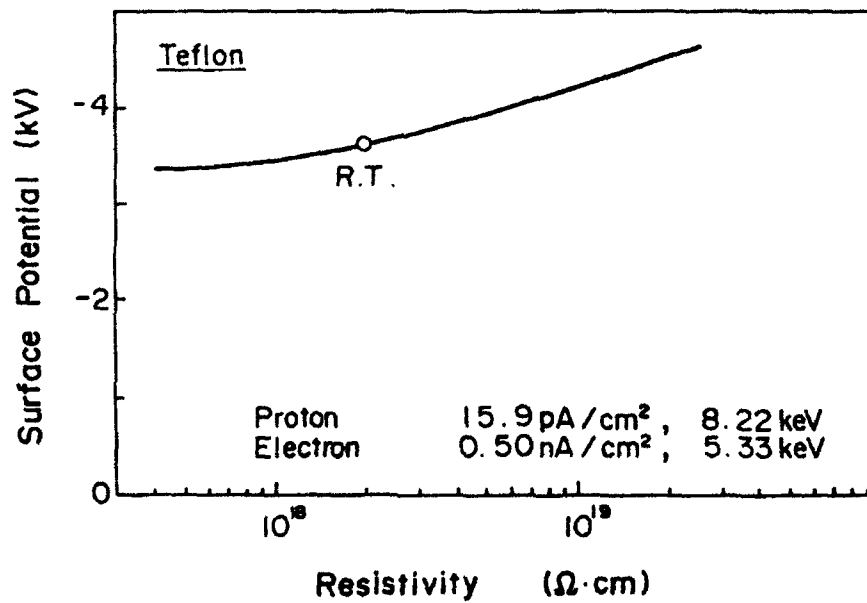


Fig.13 Surface potential of Teflon calculated by using the model shown in Fig.12.

IDENTIFICATION AND SOLUTION OF A CHARGING PROBLEM IN A HIGH-ALTITUDE DETECTOR

George J. Berzins, John E. Valencia, and Harry E. Felthausen

(Los Alamos National Laboratory, Los Alamos, NM)

and

Joseph E. Nanevich and Jeffrey S. Thayer

(SRI International, Menlo Park, CA)

I. INTRODUCTION

The unwanted response of spacecraft borne instruments to electrons and other charged particles in orbit has long been at least a nuisance. In the benign case these particles generate background signals that require processing on orbit, increasing the instrument "dead time", and sometimes interfere with the measurement of small effects. In the severe extreme, electrons can charge dielectrics in or near the instrument. Such charging can be followed by a breakdown discharge that can either generate false data, or, in rare cases, cause malfunction of the instrument.

Instruments flown on one of the Los Alamos programmatic missions have experienced all of these effects. Initially, some of these were not understood, and were regarded as simply "false data". A few years ago we began a systematic study of our database that had been accumulating for several years and included data from similar instruments on several spacecraft. We focused especially on the unusual and unexplained signatures. Observations that resulted from the sifting of that database, followed by correlations with measurements of background electron activity, suggested that, in at least some instances, charging might be the culprit. In the case of one particular set of false data signatures, we were able to postulate a model from such observations, were able to test some aspects of that model in laboratory simulations, and perhaps most important, were able to devise and effect a cure that has eliminated the particular problem.

In recounting how we identified and solved the problem, we would like to do so from the viewpoint of experimenters who were unfamiliar with the phenomenology of spacecraft charging and unaware of the considerable work that had been done already on the subject. Such a perspective is not only descriptive, but may be potentially useful to others in similar situations. A preliminary report was presented as a poster paper at the 1986 Hardened Electronics And Radiation Technology (HEART) conference.

II. DETECTOR, SPACECRAFT, AND DATA

Representations of the programmatic detector and of the satellite are diagrammed in Figs. 1 and 2, respectively. Two, nominally identical instruments, referred to as Detectors 1 and 2, are located diametrically opposite on the slowly spinning ($1 \text{ sec} < T < 1 \text{ min}$) spacecraft (Fig 2.) in high altitude orbit. Each detector has four similar input channels. Pertinent details of a typical channel are visible in Fig. 1.

The detector senses charged particles via a traditional, standard technique. The particles enter through a window and strike a scintillator whose light output is seen (through a lightpipe) by a photodiode. The charge pulse from the photodiode is amplified and can be digitized. The four input channels differ primarily in their window and scintillator material compositions and thicknesses. Count rates (number of pulses per unit time that exceed a preset threshold) are tallied and recorded for each channel. Simultaneous signals in multiple channels, such as would arise from cosmic-ray showers, for example, are defined as "events". The amplitudes of the signals that constitute an event are digitized and recorded.

Two categories of event amplitudes are shown in Fig. 3. The lower data are representative of events recorded several times per day by each detector, and have been attributed to cosmic-ray showers. The upper curve typifies a signature that had puzzled us for several years. This signature, recorded with similar frequency by all detectors of this type, is characterized by a very large signal amplitude in Channel 1 (thinnest input window), and much smaller signals in the other channels.

III. OBSERVATIONS

As we examined the database and attempted to understand some of the unusual signatures, our attention focused on events represented by the upper curve in Fig. 3. We noted specifically that

1. Events of this type had been recorded by all detectors of this type, on all spacecraft, and with about the same occurrence rate.
2. The large amplitude signal was essentially always in channel 1 (i.e. channel with the thinnest input window). The large amplitude was present in another channel less than about 0.01% of the time. In these latter cases channel 1 recorded a small amplitude.
3. A modified version of this detector did not record any events of this type. The modification involved removal of the scintillator and light pipe (see Fig. 1) from the front end. Specifically, a silicon photodiode replaced the scintillator in a geometry similar to that in Fig 1, and the light pipe was replaced by a (shorter) support stand.
4. Events tended to occur at a greater rate during periods of elevated, high-energy electron flux. An example that spans 6 consecutive days in December, 1983 is shown in Fig. 4. The curve represents the count rate in an instrument designed to specifically measure high energy (> 1.0 MeV) electrons. Rates lower than 10 and greater than about 100 are regarded as indicative of low- and high-level background electron activity, respectively. Occurrence of the strange events is indicated by the triangles on the time lines for detectors 1 and 2 (on the same spacecraft) below the count rate plots.
5. During the more intense periods, such as 12/7 through 12/9 in Fig. 4, there was a suggestion of "pairing" in events recorded by the two detectors. Namely, an event in either detector was soon followed by an event in the other detector. We pursued this observation by examining the entire database. We tabulated (a) whether, following any event in either detector, the next event occurred in the same detector or in the other detector, and (b) the time of the next event. The results for one spacecraft, displayed in Fig. 5., showed that the next event was likely to occur soon (next few hours) and was likely to be in the other instrument. In cases where the events were far apart (many hours, as during periods of low background electron activity), the next event was about as likely in either detector.

IV. THE HYPOTHESIS

The above observations indicated that electrons played a role, ruled out cosmic-ray showers (i.e. pairing), implied that the scintillator and/or lightpipe were somehow involved (i.e. modified vs. original instrument). To reconcile all of the observations we postulated that

- (a) the scintillator or light pipe becomes charged by the background electrons, and
- (b) the resulting discharge breakdown is accompanied by an intense light flash and by copious rf that couples into the electronics.

Besides accounting for the existence of the event (coupling of rf into all channels to satisfy coincidence criteria), and for the signature (very large amplitude in channel 1 only as a result of the light flash), this hypothesis provided a way to at least qualitatively reconcile all of the observations.

1. All detectors on all spacecraft were similar and on a long-term average basis sampled a similar environment. Thus they should all respond similarly.
2. Since channel 1 had the thinnest window, it was the most likely one to charge to breakdown potential. The window thickness in terms of electron penetration energy is shown for the four channels against a typical electron spectrum measured during a disturbed period in Fig. 6. That figure shows, for example, that electrons need to have at least 70 keV energy to penetrate the window in channel 1, and nearly 300 keV to penetrate that in channel 2. The data suggest that channel 1 is therefore subjected to at least 10 times as much charge. The very rare instances when the observed event had the large amplitude in channel 2 would therefore occur only when the background flux levels are extremely high, which is reasonably consistent with observations.
3. The modified detectors did not contain a scintillator or light pipe, hence the absence of these events. In those detectors almost all of the input area exposed to electrons is conductive.
4. There is an apparent lack of consistency (as opposed to inconsistency) between the data in Figs. 4 and 6, since the former shows a correlation with high-energy (> 1 MeV) electrons, and the latter suggests that lower energies (> 70 keV) should be responsible. However, a more recent, rather cursory examination has not shown the occurrence correlation to be any better with softer electrons. A speculative interpretation might be that the higher energies may somehow be more directly associated with the discharge mechanism. This could be an interesting area for subsequent study.
5. The "pairing" arises as a natural consequence of charging. Both detectors accumulate charge at about the same rate (i.e. because spacecraft spins, both sample a similar time-averaged environment). Thus a discharge in either is more likely to be followed by a discharge in the other, because the latter is "primed", while the first one must now accumulate more charge.

V. SIMULATOR TESTS

We felt that a limited set of tests in a simulator facility might be useful, realizing that the conditions on-orbit could be only poorly approximated. As a further complication, there were no more complete detectors available. The last instrument that had been fabricated had been delivered to the spacecraft contractor some time earlier and was undergoing flight qualification tests.

The available parts included several front end assemblies (without electronics), which were, of course, the critical components. We therefore experimented with these in the simulator facility at SRI International. A diagram of the experiment is shown in Fig. 7. External bias was supplied to the photodiode, and signals from the diode were recorded directly on an oscilloscope. Signals from a nearby electric-field sensor were also recorded. Because of the low electron energy (selectable 20 to 40 keV), the detector window material was removed and the electrons impinged on the scintillator directly.

Results of the simulation supported our hypothesis. Scintillator breakdown could be observed visually, and was accompanied by a large signal from the photodiode and by a substantial signal from the E-field sensor. Amplitudes recorded with the photodiode were typically 2 to 3 times smaller than those recorded in orbit. In view of the different conditions (electron spectrum, flux level, vacuum, etc.) we felt this agreement to be remarkably good.

The unavailability of a full detector, or even of relevant components, precluded any useful interpretations of the measured rf signal, other than to confirm its existence.

VI. PROOF-OF-THE PUDDING

During the course of the simulator tests we pursued a notion based on work that had been done earlier at SRI. We coated the outside surface of the scintillator with a thin (less than 100 nm) layer of aluminum, which in turn was grounded. Our assumption was that the proximity of a grounded conductor would permit the embedded charge to leak off more readily (i.e. leakage path less than 1 mm, vs. several cm in the original, uncoated version). Tests with the aluminized units confirmed this to be a fruitful approach. No discharges were observed.

We were sufficiently encouraged by the support that the simulator tests gave to our hypothesis that we obtained permission to exchange the front end assembly of channel 1 of the last, remaining instrument that was awaiting launch. Success was obvious in the first few weeks after launch. In the first six weeks of operation the detector with the aluminized scintillator did not register any of the large-amplitude, scintillator-discharge caused events, while other, similar instruments in orbit averaged 13 events per instrument. After more than a year of operation these events were still absent. Real events, such as cosmic-ray showers, on the other hand, have been recorded at the anticipated rate and with amplitudes consistent with a slight, calibrated, sensitivity change due to the aluminizing.

VII. CONCLUDING REMARKS

It was extremely gratifying to effect a cure that could be flight tested. We only wish that we had been able to do so earlier in the program. A review of the experience and knowledge gained from this entire exercise seems to single out a few, important points.

1. Correlation with the background electron environment was critical toward the suggestion that charging was the problem. However, in this case it was not necessary to possess detailed knowledge such as electron spectral data or high-resolution time information. Namely, an electron monitor was crucial, but a crude monitor would suffice.
2. The charging details and the mechanism that produced the unusual signals were identified from instrument- and project specific observations, i.e. comparison of performance histories of the "standard" and "modified" detectors, and the "pairing" that resulted from geometric symmetry.
3. A knowledge of the answer may be justification for a further and more detailed study of correlation details with the electron environment. Such a study might uncover subtle features that could lead to isolation of mechanisms in other, still unresolved, charging situations.
4. As of this writing, the evaporated aluminum coating on the scintillator appears to be functioning satisfactorily and has weathered numerous storms. Appearance of the suppressed event signatures, or other change in detector performance, will be an indication of environment-induced changes and one measure of the lifetime of such a cure.

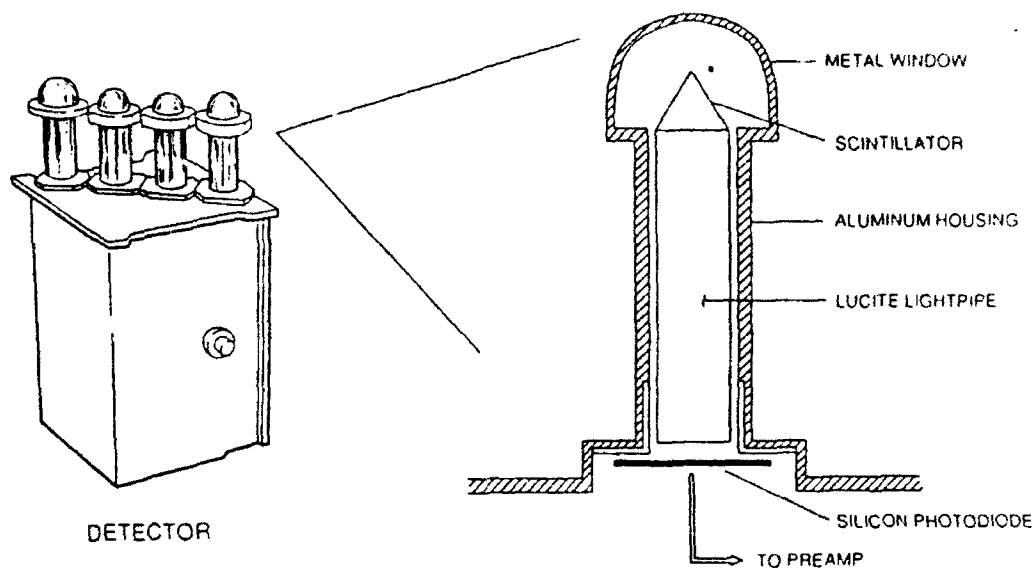


Fig. 1. Diagram of programmable detector with four input channels. Charged particles enter through metal window and strike scintillator, whose light is seen by photodiode.

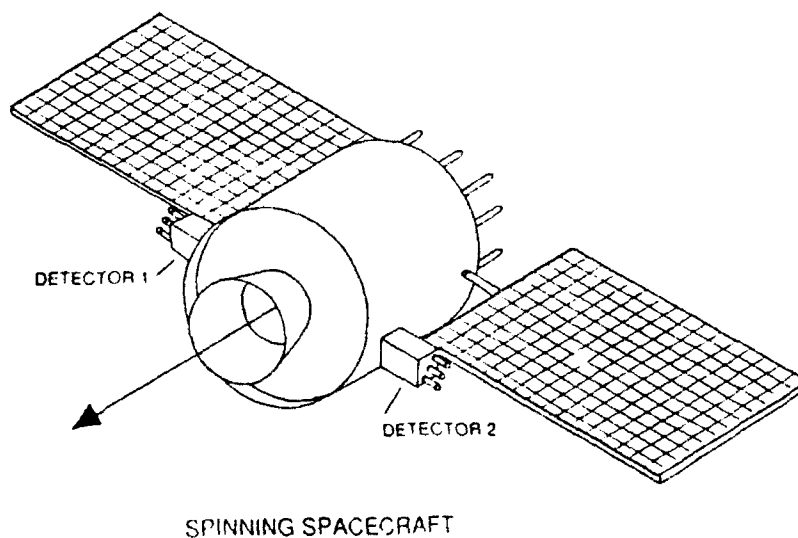


Fig. 2. Artist's sketch of spacecraft. Note relative orientation of detectors.

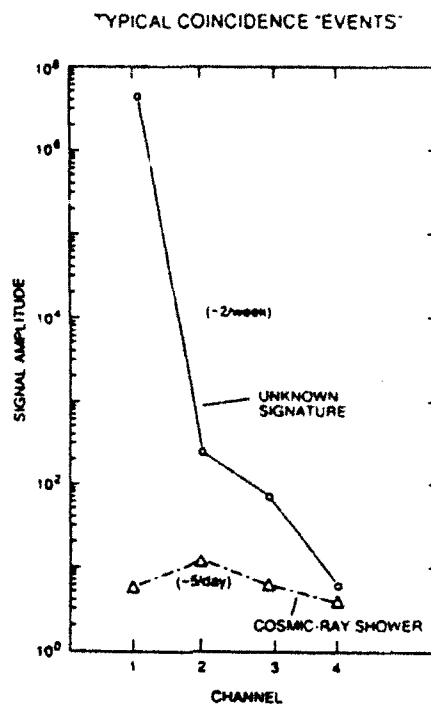


Fig. 3. Representative "event" data.

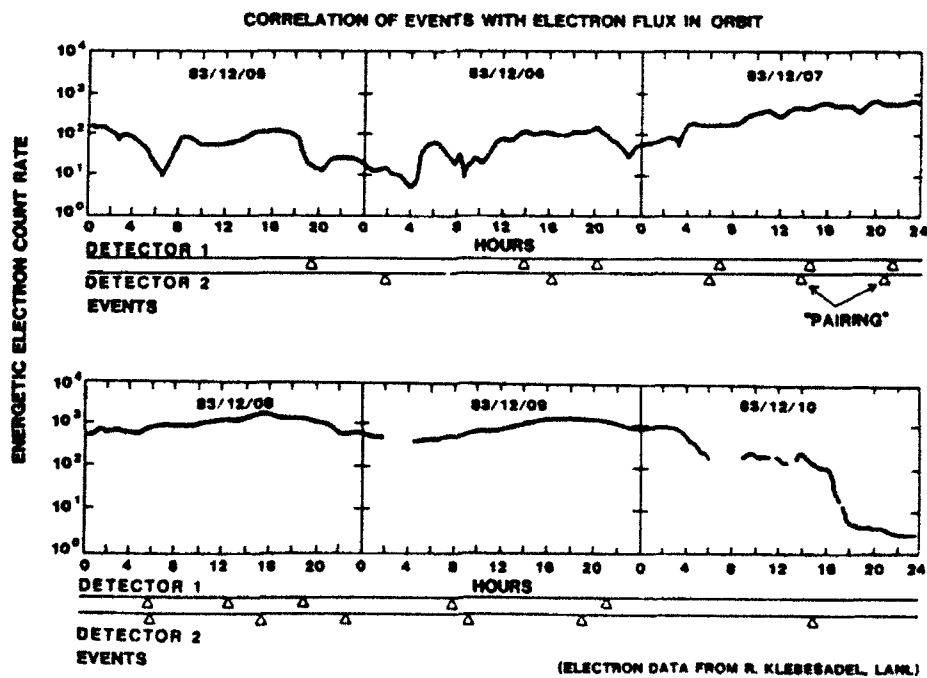


Fig. 4. Time history of charging-related events (triangles) plotted below count rate from high-energy background electron detector on same spacecraft. The six-day period shown here is representative of periods of fairly intense electron activity, and is typical of conditions encountered 8-12 times per year. Note the "pairing" visible on 12/7-12/9.

04/01/82 - 07/31/85

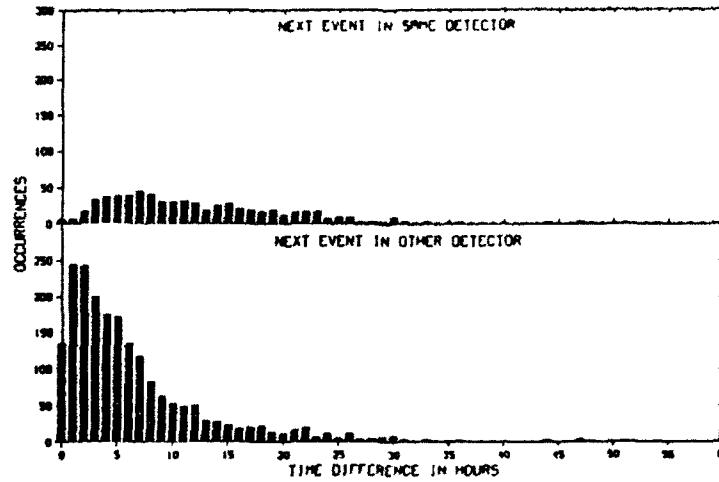


Fig. 5. Tabulation of the time-distribution of "next events" after any event if next event was observed in the same detector and if next event was observed in the other detector.

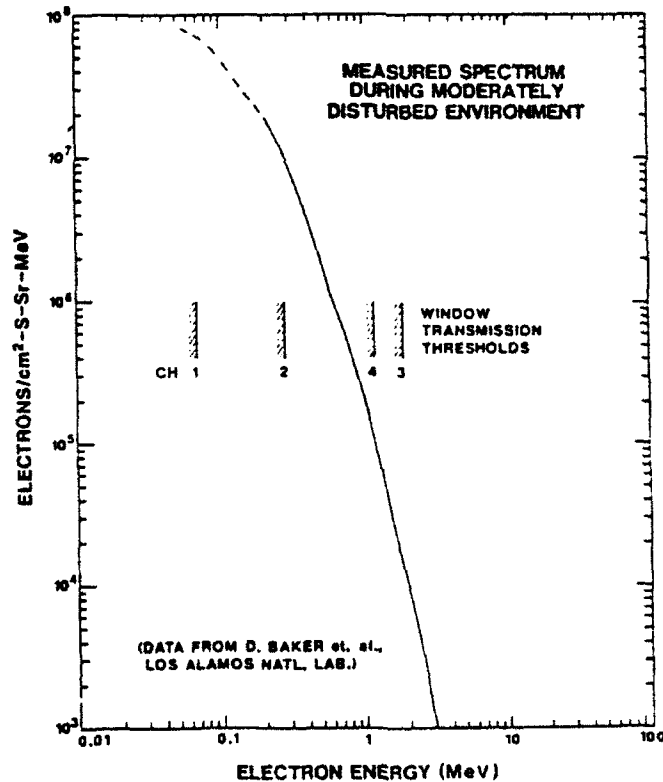


Fig. 6. Representation of window thickness in the four input channels in terms of electron minimum penetration energy, plotted against a typical electron spectrum measured during moderately disturbed conditions.

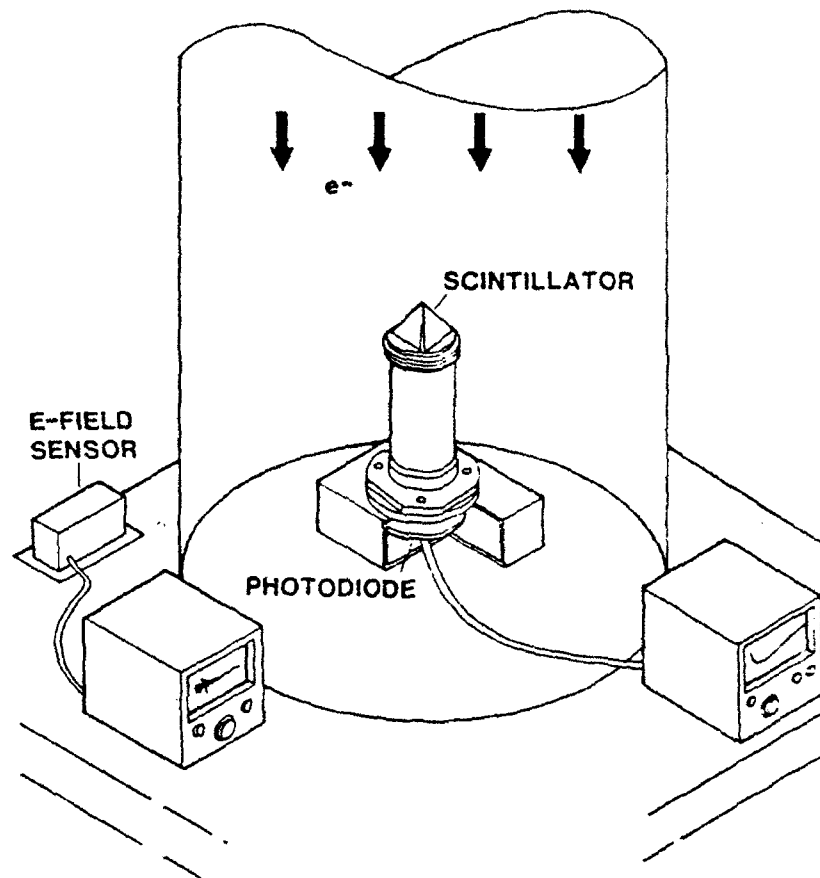


Fig. 7. Diagram of the simulation experiment showing a front end assembly in an evacuated bell-jar, equipped with an electron gun at the top. Light output from the photodiode and the signal from an rf sensor (external to the chamber) were recorded on oscilloscopes.

Quest for the source of Meteosat anomalies

A.J.Coates, A.D.Johnstone, D.J.Rodgers

Mullard Space Science Laboratory, University College London,
Holmbury St Mary, Dorking, Surrey RH5 6NT, UK

G.L.Wrenn

Space Department, Royal Aerospace Establishment,
Farnborough, Hants GU14 6TD, UK

Abstract

Three ESA Meteosat geostationary satellites have suffered from a series of anomalies which disturb routine operations; most commonly, the scan of the radiometer has stopped or jumped requiring a reset command to be sent.

Experience with Meteosat-F1 launched in 1977 (Robbins, 1979) prompted the installation of an AFGL electron spectrometer (50eV-20keV) on Meteosat-F2, in an attempt to demonstrate a direct link between the anomalies and surface charging. Data spanning August 1981 to March 1987 have provided interesting evidence for differential charging (Wrenn and Johnstone, 1987) and permit the establishment of an empirical model of charging fluxes through a solar cycle. However, the reported anomalies do not fit the pattern for surface charging effects and no real link was found. Deep dielectric charging has now become the most likely explanation and consequently Meteosat-P2, launched in June 1988, carries a LANL monitor of 43-300 keV electrons.

The Meteosat anomaly chronicle is the result of reliable recording procedures at ESOE and it represents a unique data base for an important class of ESD effects which occur at Geosynchronous orbit. This paper gives some preliminary results from Meteosat P2 and attempts to assess their relevance within the context of earlier conclusions from the Meteosat-F2 studies.

INTRODUCTION

Since Meteosat-F1 suffered many operational anomalies it was decided to include a spacecraft charging monitor on F2 to see whether the anomalies were related to spacecraft surface charging. While that experiment certainly showed strong evidence of charging on F2 there was no correlation with the occurrence of unexplained anomalies, which were also present on F2. The decision was then made to investigate the higher energy range of electrons associated with deep dielectric charging. Thus SEM-2 was commissioned to study the 30-300keV range of electrons.

The sensor unit was provided by Los Alamos National Laboratory, USA as a spare Lo-E sensor [Aiello et al, 1975] from other programmes, to the Mullard Space Science Laboratory of University College London (MSSL) which provided the power supplies, data processing unit and interface to the Meteosat spacecraft. MSSL was further responsible for integration, testing and calibration of the instrument, and delivery of the instrument to the spacecraft. MSSL also provided a memory upset monitor (MUM) in this instrument, as requested by ESA.

This paper describes briefly the history of the F1 and F2 studies, in particular the role of spacecraft charging in generating the anomalies and the possibility of deep dielectric charging as an explanation. We then go on to a description of the SEM-2 instrument, and the conversion of the observed counts to physical units. Typical natural events in the spacecraft environment as seen by SEM-2 are shown. The correlation of the energetic electron fluxes to the occurrence of anomalies, which on P2 occur at a rate which is about four times that of F2, are the major results. As data have accumulated we have been able to show a striking correlation between the energetic electron fluxes and the spacecraft anomalies. For the first time it appears that the measurements provide a good indication of anomalies.

1 Meteosat operational anomalies and spacecraft charging

1.1 Meteosat-F1

When Meteosat-F1 was launched in 1977 many operational anomalies occurred (about 150 in 3 years) for which there was no immediate explanation. However, their occurrence was related to geophysical factors outside the normal realm of spacecraft engineering, namely that they were more likely when there was strong geomagnetic activity and they exhibited a tendency to occur at certain times of day [Robbins, 1979]. It had recently been discovered then that geosynchronous spacecraft could charge up to many thousands of Volts [deForest, 1972] in the ambient plasma so it was natural to attribute the anomalies to charging, or more precisely to differential charging. Unless the complete outer surface of the spacecraft is conductive and

electrically connected, it is normal for different parts of the spacecraft to charge to different voltages. At times, adjacent surfaces can be more than a thousand volts apart. This in turn leads to arcing between the surfaces and results in large electrical transients in the spacecraft harness. After the problems were encountered by Meteosat-F1 a series of laboratory tests was carried out which demonstrated that arcing occurred if the spacecraft was illuminated by an electron beam, and that electrical transients could induce anomalous behaviour. It was not possible to simulate in-orbit conditions completely and thus it was not possible to establish the causal chain completely.

1.2 Meteosat-F2

Before the second spacecraft Meteosat-F2 was launched some changes were made to reduce the susceptibility to differential charging, namely grounding of thermal shields and hardening of some critical electrical interfaces, and to include two charging monitors to complete the link between the anomalies and spacecraft charging. One of the monitors was designed to detect arcing transients on a short antenna within the spacecraft. In flight no such events were detected, but it is not known whether the instrument was sensitive enough, or whether it was not operating correctly or whether there were no significant transients. Therefore we can say no more about it. The second monitor measured the ambient plasma electrons in the energy range 50eV to 20KeV and therefore could measure the charging current directly. Not only that but it was anticipated that in the event of spacecraft charging the energy spectrum would be modified in a manner which would allow the spacecraft potential to be measured. Briefly, the objective of the instrument was to see if the anomalies occurred when the spacecraft was charged. The results of this investigation have been published in a number of reports [Johnstone et al, 1985, Wrenn and Johnstone, 1987]. Although no direct link between differential charging and anomalies was found there were several interesting and significant (for this problem) findings which we summarize here.

1. Two types of differential charging were observed. One type occurred during eclipses and had been expected. The second type, called a "barrier event", only occurred when the radiometer mirror was completely in shadow and was therefore probably because the mirror was charging up. The two types are illustrated in Figures 1 and 2 and explained in the figure captions.
2. A charging index based on an estimate of the net electron flux to the spacecraft (incident electrons minus secondary emitted electrons) was 95 percent successful in predicting whether the spacecraft would charge up in any particular eclipse.

3. There was an indication in the electron spectrum during eclipse charging that the voltages in differential charging were limited by discharging currents of secondary electrons from one part of the spacecraft to another.
4. Only one anomaly, in more than 100, occurred at any time near an observable differential charging event. In all cases there was no evidence that the spacecraft was charged to more than a few volts.
5. The anomalies attributed for lack of a better cause to arcing did, as before on Meteosat-F1, show a dependence on geophysical parameters, ie local time, solar aspect angle and geomagnetic activity [see Figure 3].
6. When separated into four types of anomaly the solar aspect angle, and local time dependence was different for all four groups.
7. The most common type of anomaly, the radiometer stoppage or position jump was most common at the equinox and was associated with a period of sustained high geomagnetic activity.

The conclusions of the analysis were that the anomalies were not the result of differential charging but that they were caused by some external geophysical effect. The four types of anomaly were caused by four different mechanisms.

Frezet et al [1989] have made an analysis of the charging of Meteosat with the NASCAP charging analysis code. They find that the differential voltages developed are greater at equinox and suggest that this is the explanation for the occurrence of radiometer anomalies at this time. The charging levels they obtain are many thousands of volts. However the only differential charging of the radiometer is observed away from equinox, when the radiometer mirror is totally in shadow. Also when anomalies occur there is no evidence of any charging. Finally Frezet et al only developed such a charging scenario when extreme plasma conditions are used and such extreme conditions were not observed by the monitors on Meteosat-F2 itself.

We were left with the situation that we still do not know what caused the anomalies on Meteosat-F1 or F2. Spacecraft surface charging, or differential charging, appears to be ruled out. In their final report Johnstone et al [1985] suggested that it might be caused by penetrating electrons producing deep dielectric charging. This was partly based on the observation that a sustained period of high geomagnetic activity was required to develop the effect, and that the trapped energetic electrons are known to be slower to respond to geomagnetic activity than the plasma at energies of less than 20KeV. Therefore it was suggested that the third Meteosat flight should carry a detector of more energetic electrons. Accordingly it was decided to include in the payload the SEM-2 detector which measures the energy and angular distribution of electrons in the energy range 30KeV to 300KeV.

The behaviour of electrons above 30keV at Geosynchronous orbit has been studied by the Los Alamos group [Baker et al, 1981]. In Figure 4 the average fluxes for the whole of 1977 and 1978 are compared to the particles' range in aluminium as calculated by the SHIELDOSE program: this shows that higher energy particles can penetrate appreciable distances before being stopped. To penetrate 0.5mm into polythene, an electron requires an energy of 200KeV (see Figure 5 from Powers et al. [1981]). Deep dielectric charging, where penetrating electron fluxes may cause buildup of charge and eventual breakdown in insulators, has been postulated as the reason for anomalies on other spacecraft [eg Baker et al, 1986].

2 Instrumentation

The measurement of electrons above 30 keV implies a different type of sensor to the F2 instrument, which consisted of two electrostatic energy analyser/channeltron combinations, giving differential energy measurements. The standard technique for tens to hundreds of keV particles has become the surface barrier solid-state detector [eg Aiello et al, 1975]. Using electronic thresholds this technique also gives differential energy measurements.

SEM-2 contains five surface barrier detector-collimator systems, arranged to accept particles from 5 different angular ranges. The 5 ranges are of spacecraft polar angle: azimuthal angle measurements are achieved by timing. Each of the detectors has 5 different energy ranges; the energy acceptances were found by calibration at the Goddard spaceflight center and are as follows:

Energy level	E_{min} (keV)
E5	42.9
E4	59.4
E3	90.7
E2	134.9
E1	201.8

Table 1: Lower level discriminator settings for SEM-2

Full details of the operation of the instrument are given in the final report to ESA (Coates et al, 1989). Here we restrict ourselves to a description of the information transmitted.

A transmission list is accumulated in 4 formats, approx 100 seconds. A complete experiment cycle takes 500 or 600 seconds since one polar angle is sampled in each 4-format cycle. The raw parameters received on the ground are as follows, every 100 seconds.

- A 5-point energy spectrum, compressed counts E1-E5, for a particular polar angle, summed over azimuth.
- A 6-point azimuth array, compressed counts A1-A6, for a particular polar angle, summed over energy.
- Overflow information as appropriate for each of the above bins.
- Timing information to relate azimuth to spin phase.
- Synchronisation information for data checking.
- MUM parameters on SEU and latch-up.

Counts are converted to flux and plotted. The principal result of the data processing was the provision of summary plots of the data from SEM-2. It is essential that users of the SEM-2 data be able to tell from the plots alone, the general behaviour of the plasma environment at all times and be able to identify times of particular interest. To enable this, the plots contain parameters that summarise the data, parameters that interpret the data further and associated parameters for comparison. This led to the choice of eight panels of data presented on a single page with one page per day; an example is shown in Figure 6. These panels are: Total Flux; Flux; Spectral Index; Polar Flow; Azimuthal Flow; Anisotropy Index and axis of symmetry; Kp; MUM and Latch-up.

2.1 Total Flux

Total flux of electrons within the energy range of the detector (42.9-300keV) and summed over all polar and azimuthal bins.

2.2 Flux

This is the Flux (expressed as a grey scale level) in the 5 energy bands of the analyser, from 43 to 300KeV. These energy bands are: 42.9 to 59.4KeV, 59.4 to 90.7KeV, 90.7 to 134.9KeV, 134.9 to 201.8KeV, 201.8 to 300(nominal)KeV. These data are summed over all polar and azimuthal angle bins.

The analyser returns integral measurements of counts versus energy. Counts are measured as the energy cut-off or threshold of the instrument is progressively raised. To calculate the counts in one energy band, the counts measured with the cut-off at the top and bottom of that band are subtracted.

2.3 Spectral Index

This index determines the 'hardness', or shape of the energy spectrum. This is generally negative because, except in extraordinary cases, there are less particles at high energy than at low energy. The index is simply the slope of the log of the energy spectrum.

2.4 Polar Flow

This is the flux (expressed as a grey scale) in the 5 polar angle sectors of the analyser. These sectors look in the polar directions 30°, 60°, 90°, 120° and 150° to the spacecraft spin axis. The spacecraft spin axis is to a good approximation parallel to the Earth's spin axis. The angle bins cover a nominal $\pm 5^\circ$.

2.5 Azimuthal Flow

This is the flux (expressed as a grey scale) in the 6 azimuthal angle sectors of the analyser. These sectors cover the angles 0° to 60°, 60° to 120°, 120° to 180°, 180° to 240°, 240° to 300° and 300° to 360°, in spacecraft coordinates. Note that at 0° the analyser looks towards the sun.

2.6 Anisotropy Index and axis of symmetry

The anisotropy index describes the angular shape of the plasma distribution relative to its axis of symmetry, shown as theta and phi. A trapped particle distribution is a 'pancaked' i.e. enhanced perpendicular to the magnetic field compared to along it. Where plasma is newly injected it tends to lie along the field line in a 'cigar-shaped' distribution. The index is positive for pancaked distributions and negative for cigar-shaped distributions. The anisotropy index is calculated [using techniques adapted from Sanderson and Page, 1974, Sanderson and Hynds, 1977, Higbie and Moomey, 1977] by fitting the data to a set of spherical harmonics. Since we believe that the magnetic field organizes the plasma, then the axis of symmetry represents the magnetic field direction. However, it does not distinguish between positive and negative field directions.

2.7 Kp and Kp(τ)

Kp is an index of planetary magnetospheric activity for the whole of Earth, in a three hour period. In the monthly plots, Kp(τ) is plotted. This is a weighted average of successive Kp values and was devised by Wrenn [1987]. Many magnetospheric processes are more dependent on the general level of magnetospheric activity in the recent past than on the present level. Wrenn showed that anomalies on Meteosat-F2

was better correlated with an appropriately time-averaged activity index than with the real-time index.

2.8 MUM

The Memory Upset Monitor results are displayed as lines in the bottom panel. These display the number of 'single-event upsets' i.e. errors found in a known memory pattern, in the 4 memory zones of the test RAM. A test pattern is seen in the plot when the instrument is first powered on. A fifth line in this plot shows the occurrence of 'Latch-ups' where the test RAM attempts to draw excessive current. This line can take only values 1 - Latch-up and 0 - no latch-up.

3 Typical events

To illustrate the environment at Geosynchronous orbit as seen by Meteosat-P2 SEM-2 we include some data examples.

27th June 88 (Figure 6): On the dayside, eg at 1300Z, a "pancake" distribution is seen in the polar angle plot where fluxes are peaked at the equator: this is typical for a trapped electron distribution diffusing into the loss cone. At approximately 0200Z there is a typical isolated, injection event which shows some important features. First the total flux drops by two orders of magnitude, relatively slowly. Then it increases sharply to a level greater than before. Finally it decreases slowly to the initial level.

In Figure 7 we have looked at the results from 4 satellites simultaneously to the injection in Figure 6. Local time around the Earth is seen in the small inset diagram; spacecraft 1 and 2 (Meteosat) see the injection, while 3 and 4 show velocity dispersion with higher energy electrons arriving first.

The monthly summary example in Figure 8 shows the wider view of the dramatic events during March 1989. The spacecraft was outside the magnetopause for significant times on March 13 since the magnetosphere was severely compressed at that time.

4 Meteosat anomaly correlations

When comparing the occurrence of anomalies with the results from SEM-2 on a monthly basis it soon became apparent that anomalies, particularly radiometer anomalies, nearly always occurred when the flux of energetic electrons was high. The problem then becomes to verify such an association statistically and then to try and determine a causal link. While we have been able to achieve the former,

the latter is still some way from a satisfactory conclusion. In other words there is no doubt that anomalies and high energetic electron fluxes are linked but we do not yet know if the energetic electrons cause anomalies and if they do, how they do. Alternatively the high electron fluxes may themselves be the consequence of another agent which is the actual cause of the anomalies.

A plot of the anomalies we have used in this study is given in Figure 9, where we have organized the anomalies as follows:

RPJ Radiometer position jump
RDS Radiometer stoppage
RGC Radiometer gain change
BAT Battery anomaly
SIC SIC anomaly
OTH Other anomaly

RDS is by far the most frequent type of anomaly.

First we establish that the radiometer anomalies show the same systematic behaviour as on the previous Meteosat flight models. Figure 9 shows the local time and annual distribution for the 76 unexplained anomalies seen in the first year. They are essentially identical with distributions obtained for F2. In local time the peak occurrence is in the period 02 to 05 local time but there is a non-negligible rate of occurrence throughout the day. This distribution is reminiscent of the distribution of a type of charging event on Meteosat-F2 which were called barrier events [Johnstone et al, 1985]. However none of the Meteosat-F2 anomalies was concurrent with a barrier event. Anomalies are, as with F2, are most likely at the equinoxes and least likely at the solstices. This demonstrates once again essentially a dependence on solar aspect angle. The main conclusion we wish to draw from this diagram is that the radiometer anomalies are caused by the same mechanism as on Meteosat-F2. It is interesting to note that the anomaly rate is approximately 4 times that of F2, which suffered 80 anomalies in 4 years.

In the next series of plots the statistics of the average daily flux is examined. Figure 10 is a histogram of the number of days in the year a particular value of the daily average flux was recorded. For example the column labelled 7 contains number of days the average fluxes were in the range 7000 to 7999. Thus this graph if normalized would show the probability that the average flux has a particular value. It could be used for example to calculate the amount of radiation a geosynchronous satellite would encounter. Figure 11 shows the yearly total number of anomalies which occurred on days with that average daily flux. Compared with the distribution of Figure 10 it is clearly strongly biased towards the higher fluxes. By dividing the distribution of Figure 11 by that in Figure 10 we calculate the average number of anomalies in a day if the average flux has the given value. This produces the very striking distribution shown in Figure 12. Once the flux exceeds 19000 the average daily rate is greater than one. This can be interpreted as the probability of an

anomaly in given flux conditions. It is the first time we have achieved a connection between a characteristic of the plasma environment and the occurrence of anomalies. No such connection was found between the low energy plasma ($E < 20$ KeV) environment and anomalies on Meteosat-F2.

This does not yet establish a causal connection because the high fluxes could be caused by the same unknown phenomenon which causes the anomaly. What about the annual variation in the occurrence? This could arise because the energetic electron fluxes have a similar annual variation. In Figure 13 the mean monthly flux (dotted line) is plotted with the monthly number of anomalies. Both show a peak in March and April which were two of the most active months magnetically for a long time. In Sept and Oct where the anomaly rate peaks the monthly mean flux actually has its minimum value for the year. This suggests that there are at least two independent factors responsible for radiometer anomalies; one is associated with high fluxes of energetic electrons fluxes, and the other with the solar aspect angle.

It is possible that there is a third factor, which we see in the form of the local time variation of anomalies. This is likely however to be linked to a local time variation in the energetic electron fluxes. We have not been able to test this hypothesis yet because of the need to develop some specialised software to access this aspect of the data.

These results give us a positive result on the cause of anomalies for the first time. It is difficult to achieve a better level of proof without having a clearer idea of the mechanism which will allow us to develop a physical model which can be directly tested. An attempt to do this based on deep dielectric charging will form the next stage of our investigation.

The interaction between Meteosat and the environment is clearly a very complex one which we do not yet understand. Although spacecraft charging is significant, and needs to be minimized as we have now learned, there are other things going on for which we have not yet found the appropriate ameliorative methods.

Clearly the investigation should continue. Ideas of such effects as deep dielectric charging are still vague and need to be sharpened. This may require laboratory testing to try to replicate the phenomena, and the development of physical models which can be tested against the observations. There is also still a need to observe in more detail the interaction of a spacecraft with its environment and over a wide range of energies.

5 Summary of results

- Unexplained anomalies on Meteosat-P2 have continued at a rate about 4 times higher than that observed on F2. The P2 and F2 anomalies show a similar local time and seasonal dependence.

- The anomalies show a good correlation with electron fluxes in the range 43-300keV. This is the first time that a correlation of anomalies has been demonstrated with the Meteosat in-situ environment monitor data - the charging instrument on F2 saw charging events but they did not correlate with anomalies. Taken on its own the P2 correlation would confirm deep dielectric charging as a possible mechanism.
- However the seasonal dependence of anomalies, which strongly peak at equinox, show that at least one additional process is at work.
- We still maintain that spacecraft charging cannot explain the observed Meteosat anomalies, although it should still be minimised to avoid others.

6 Further study

Future study will be pursued on the following items:

- Processing of further SEM-2 data (already underway at MSSL).
- An explanation should be sought for the seasonal variation of anomalies on Meteosat.
- Further study is needed on the deep dielectric charging mechanism.
- Further effort should be put into calculating dose rates and penetration depths from the SEM-2 data.
- Further instruments should be included on future spacecraft, not only Meteosat, to look at both charging and deep dielectric effects. For the Meteosat series, higher energy electrons measurements extending up to 1MeV are encouraged to study the deep dielectric charging in more detail.

ACKNOWLEDGEMENTS

Most of this work was performed as part of ESA contract 7879/88/F/TB. The SEM-2 sensor head was provided by Los Alamos National laboratory, thanks are due to R.Belian and W.Aiello. T.A.Fritz made a new unit available when launch delays caused calibration and noise problems; he also provided the Los Alamos data shown in Figure 7. Calibration was done at NASA-Goddard Spaceflight Center: S.Brown and C.Smith are gratefully acknowledged. The interest, help and patience of the ESA Meteosat project team, principally J.Aasted, was much appreciated particularly regarding installation of the new sensor head.

7 References

- Aiello, W.P., Belian, R.D., Conner, J.P., Higbie, P.R., Martin, W.B. & Singer, S., "An energetic particle detector for a synchronous satellite", *IEEE Trans Nucl Sci*, NS-22, 575, 1975.
- Baker, D.N., Belian, R.D., Higbie, P.R., Klebsadel, R.W. and Blake, J.B., "Deep dielectric charging effects due to high energy electrons in Earth's outer magnetosphere", submitted to *J.Electrostatics*, 1986.
- Baker, D.N., Higbie, P.R., Belian, R.D., Aiello, W.P., Hones, E.W., Jr., Tech, E.R., Halbig, M.F., Payne, J.B., Robinson, R. and Kedge, S., "The Los Alamos Geostationary Orbit Synoptic Data Set: a compilation of energetic particle data", *Los Alamos report LA-8849*, 1981.
- Coates, A.J., Johnstone, A.D., Rodgers, D.J and Huckle, H.E., "SEM-2 ,data processing 22 June 1988 to 30 June 1989", report on ESA contract 7879/88/F/TB, 1989.
- DeForest, S.E., "Spacecraft charging at synchronous orbit", *J.Geophys.Res.*, 77, p651, 1972.
- Frezet, M., Daly, E.J., Granger, J.P and Hamelin, J., "Assessment of electrostatic charging of satellites in the geostationary environment", *ESA Journal*, 13, 89-117, 1989.
- Higbie P.R. and Moomey W.R. "Pitch Angle Measurements from Satellites Using Particle Telescopes with Multiple View Directions", *Nucl. Instrum Methods*, 146 p.439, 1977.
- Johnstone A.D., Wrenn G.L., Huckle H.E. and Scott R.F. "Meteosat-F2 Spacecraft Charging Monitors", Final Report ESA contracts 4715/81/F/CG, 5911/84/F/CG, 1985.
- Powers W.L., Adams B.F. and Inouye G.T. "Electron Penetration of Spacecraft Thermal Insulation", *Spacecraft Charging Technology 1980*, AFGL-TR-81-0270, p.86, 1981. ADA114426
- Robbins, A., "Meteosat spacecraft charging investigations", final report, ESA contract 3561/78F/CG/SC, 1979.

- Sanderson T.R. and Hynds R.J. "Multiple Telescope Measurements of Particle Anisotropies in Space", *Planet. Space Sci.*, **25** p.799, 1977.
- Sanderson T.R. and Page D.E. "Spherical Harmonic Analysis of Satellite Anisotropy Measurements", *Nucl. Instrum. Methods*, **119**, p.177, 1974.
- Wrenn G.L., "Time-Weighted Accumulations $ap(\tau)$ and $Kp(\tau)$ ", *J. Geophys. Res.*, **92**, no. A9, p.10125, 1987.
- Wrenn, G.L. and Johnstone, A.D., "Evidence for differential charging on Meteosat-2", *J. Electrostatics*, **20**, 59-84, 1987.

8 Figure captions

Figure 1 - An eclipse charging event seen by the F2 experiment. From the change in the energy spectrum it is inferred that the potential of the whole satellite went 5kV negative relative to space in this eclipse. The rising peak is due to differential charging of another part of the spacecraft at an even more negative potential (up to 600V more negative). [from Johnstone et al, 1985].

Figure 2 - Example of a "barrier event" on F2. This is where part of the spacecraft, electrically isolated from the rest, is shadowed and charges negatively as the whole spacecraft does in eclipse. High potential differences between adjacent parts of the spacecraft may then result in arcing. The low energy electrons observed in the event are due to reflection by the potential barrier of photo- and secondary electrons back to the spacecraft. While these events were correlated with radiometer mirror shadowing they were not correlated with observed anomalies. [from Johnstone et al, 1985].

Figure 3 - Distribution of F2 anomalies in local time and season [from Wrenn, 1989].

Figure 4 - Average electron flux spectra averaged over the 2 years 1977 and 1978. 90% of the samples are below the top curve and above the bottom curve. Mean electron ranges are also plotted. [fluxes from Baker et al, 1981, range from SHIELDOSE code developed by Seltzer (NBS 1116)]

Figure 5 - Electron range in polyethylene [from Powers et al, 1981]

Figure 6 - Daily plot for 27 June 88 showing an injection event at 0220Z.

Figure 7 - Energetic electron measurements from various positions at Geosynchronous orbit around the earth (see inset), showing the 27 June injection on spacecraft 1 and 2 (Meteosat) and velocity dispersion effects on 3 and 4. 1,3,4 are US spacecraft, those data courtesy LANL.

Figure 8 - Monthly plot for March 89

Figure 9 - All P2 anomalies as a function of local time and date

Figure 10 - Number of days with given average flux (thousands of flux units)

Figure 11 - Anomalies as a function of daily flux

Figure 12 - Average daily anomaly rate (anomaly probability) as a function of daily flux

Figure 13 - Anomalies (solid line) and monthly mean flux (dotted line for different months

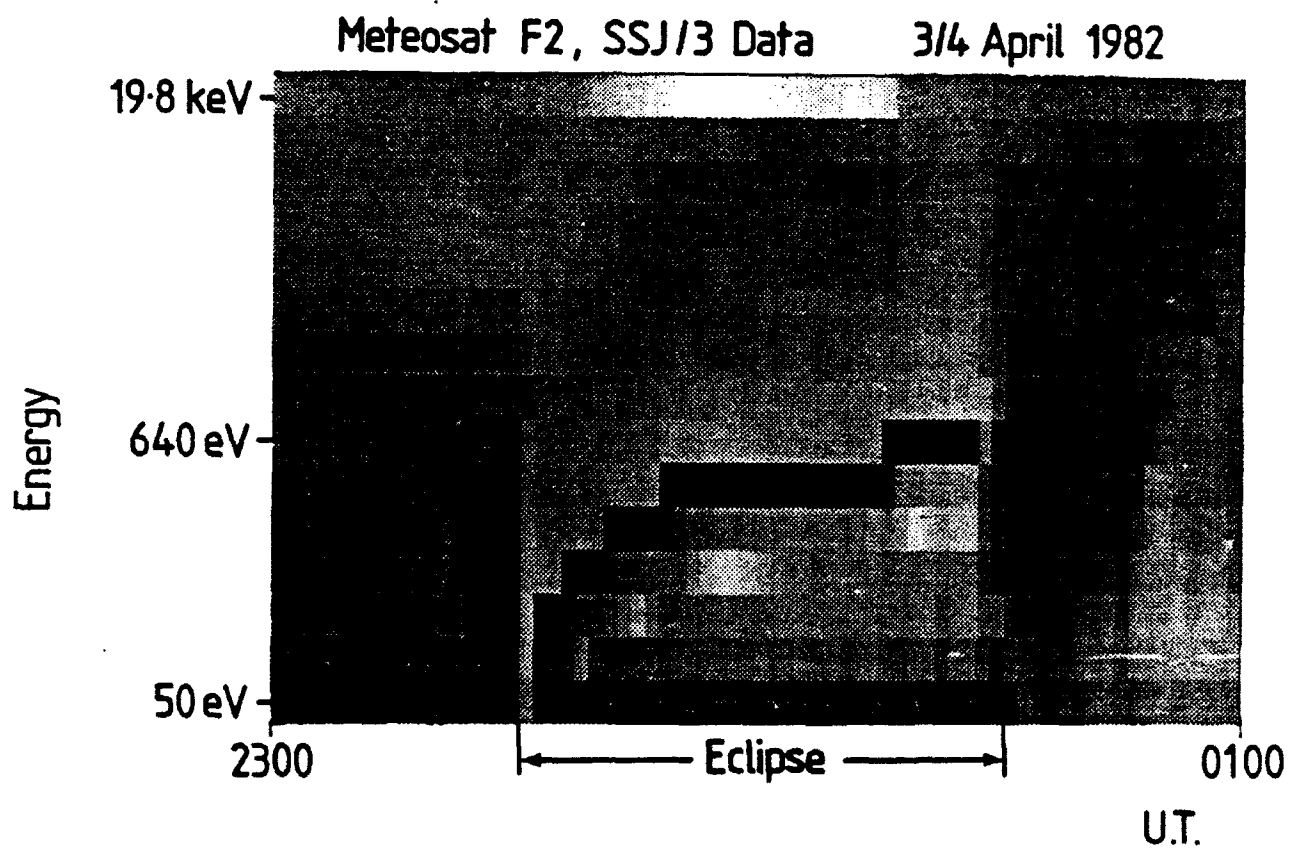


Figure 1

METEOSAT F2, SSJ/3 DATA
STARTING AT 3 1 41.8 ON 25/ 7/82

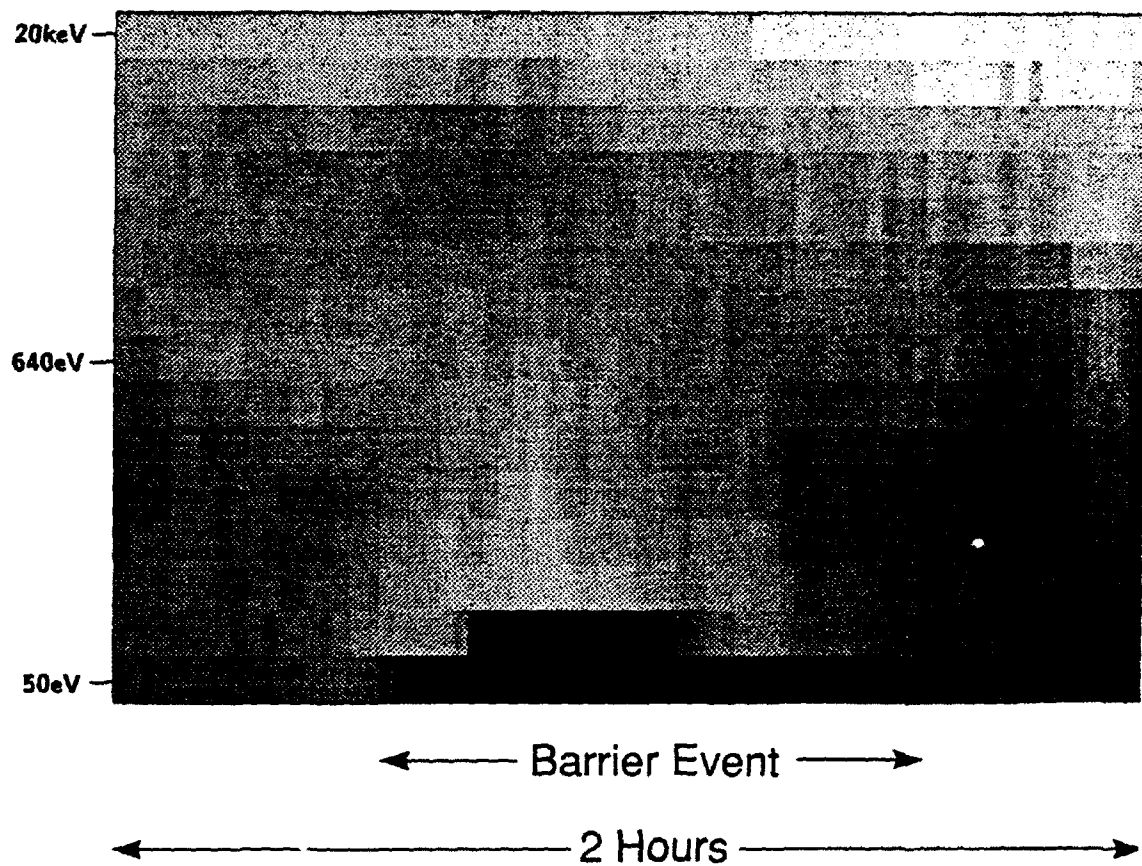


Figure 2

METEOSAT ANOMALIES (1981-85)

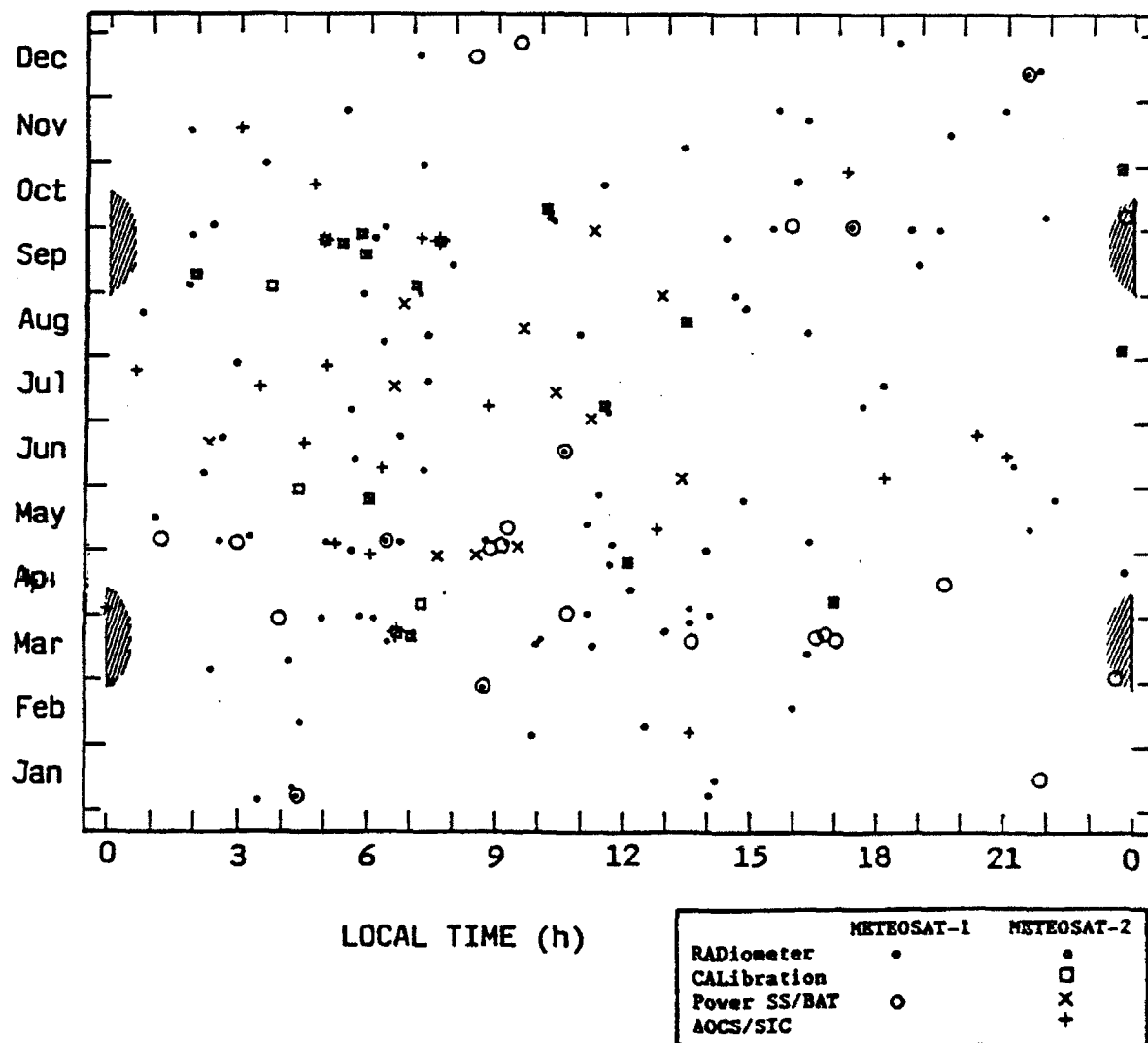


Figure 3

ENERGETIC ELECTRON FLUX and RANGE **ALL LOCAL TIMES, 1977 & 1978**

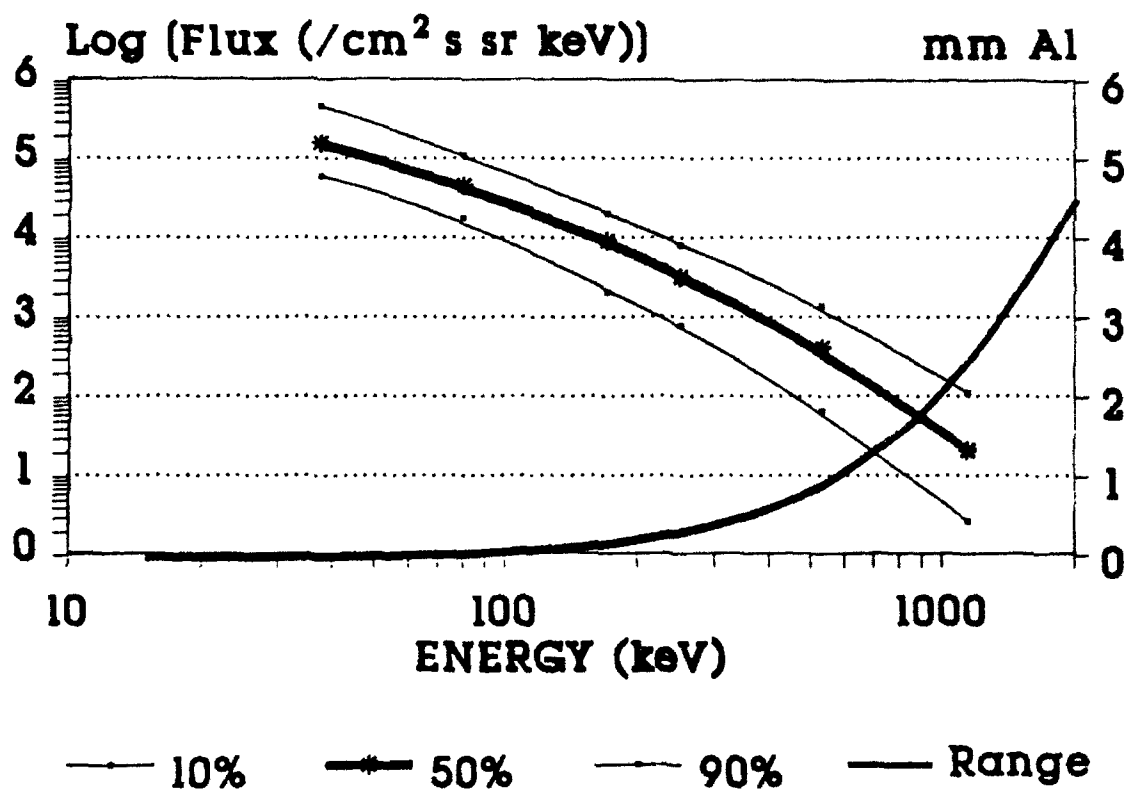


Figure 4

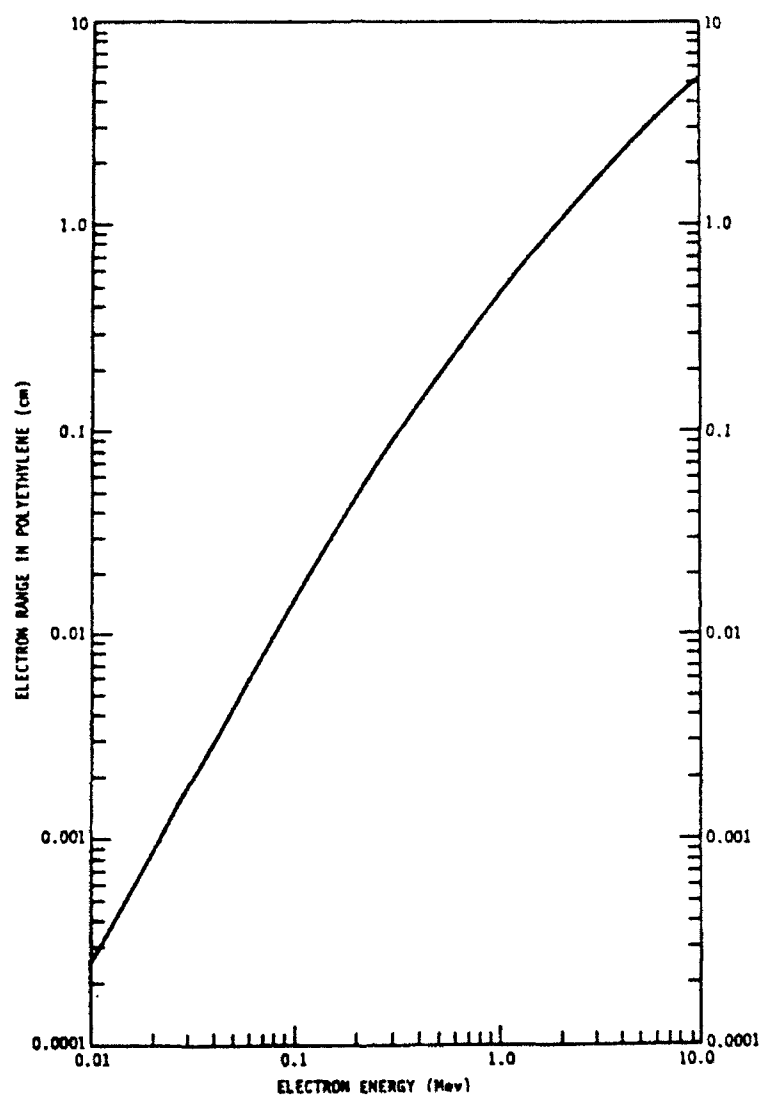


Figure 5

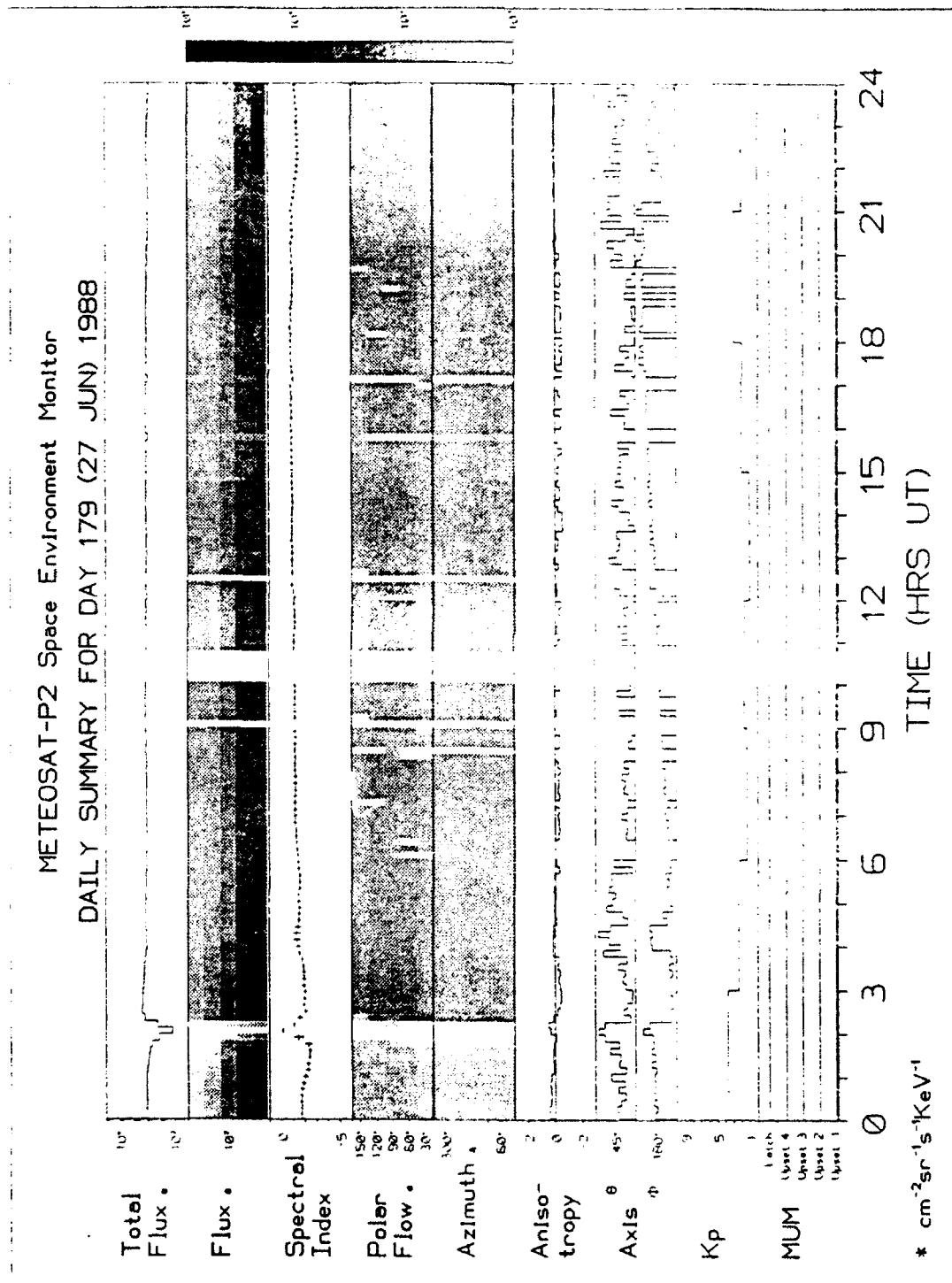


Figure 6

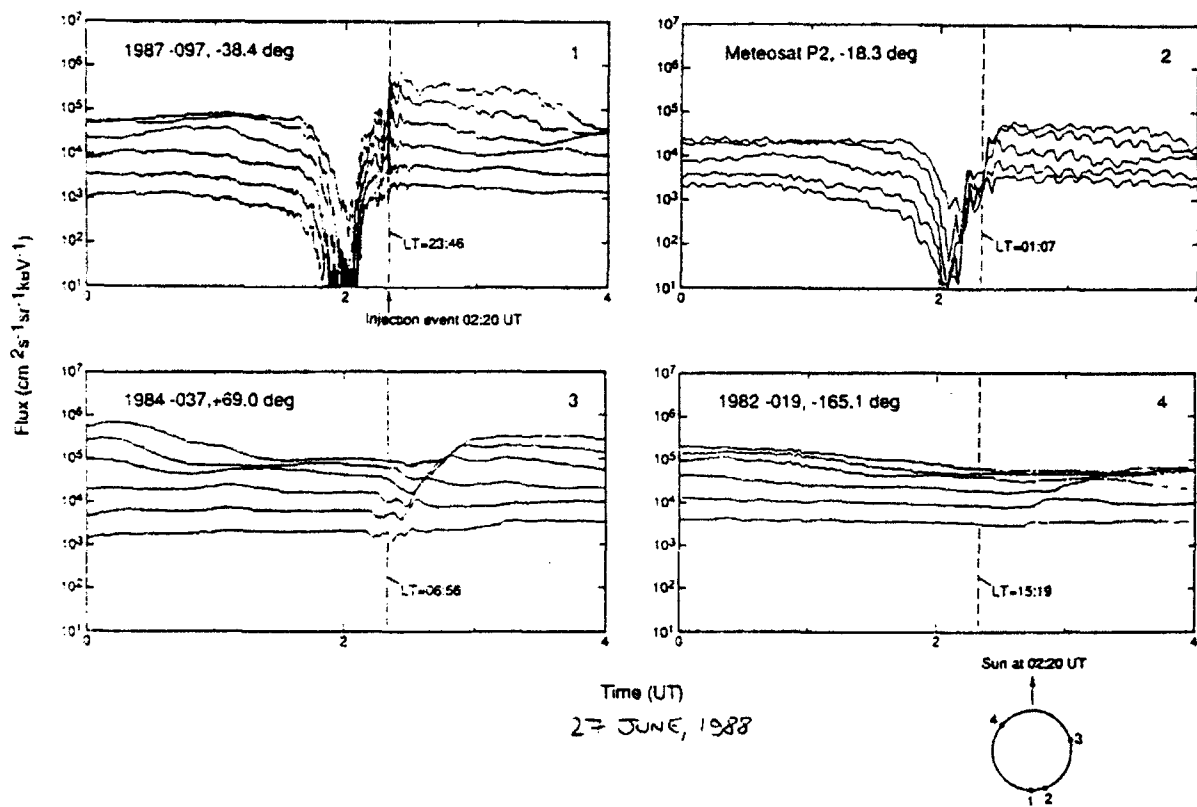


Figure 7

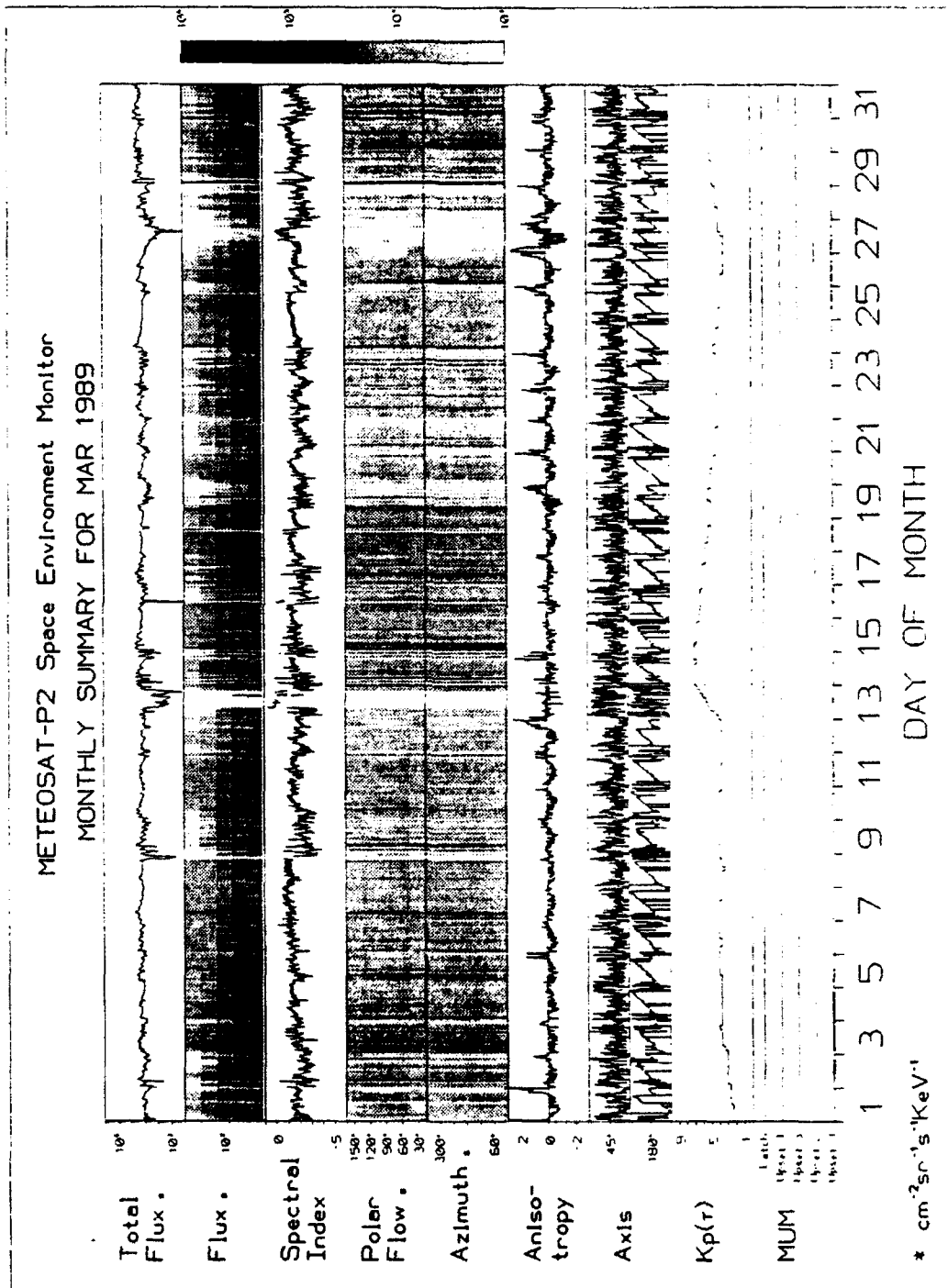


Figure 8

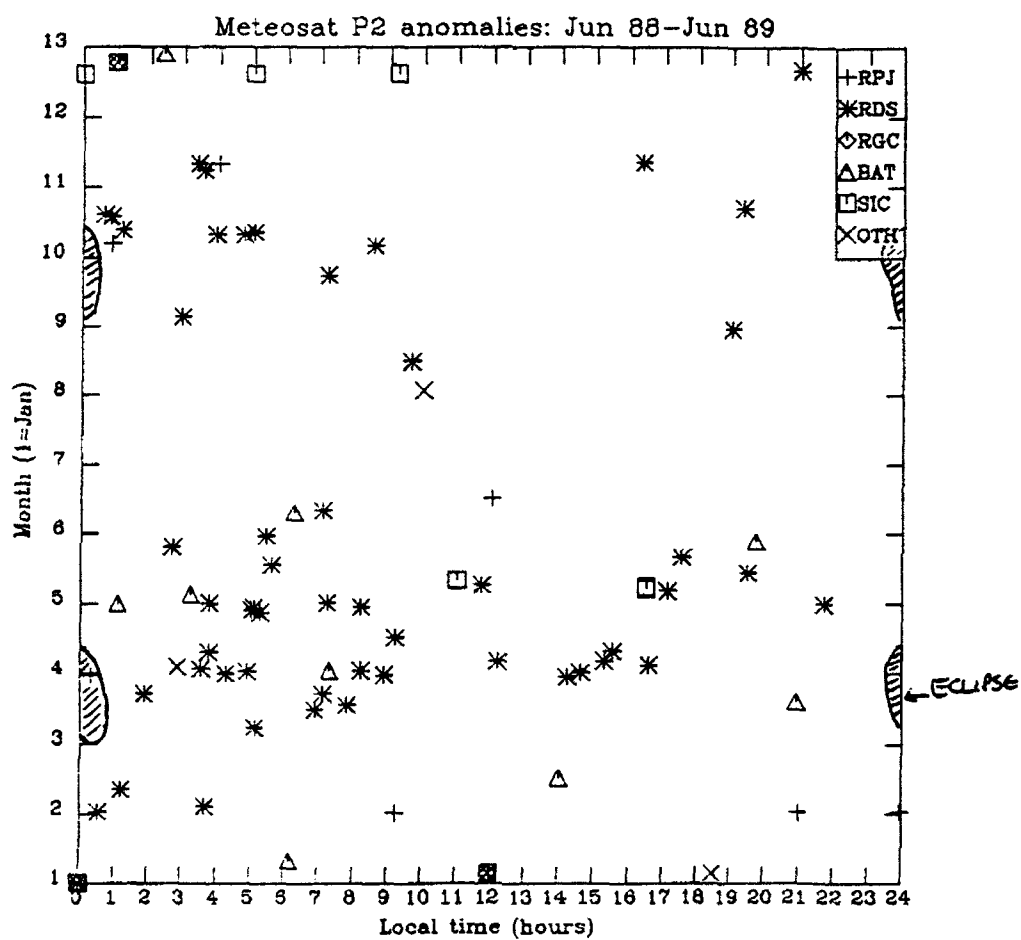


Figure 9

july 1988 to june 1989

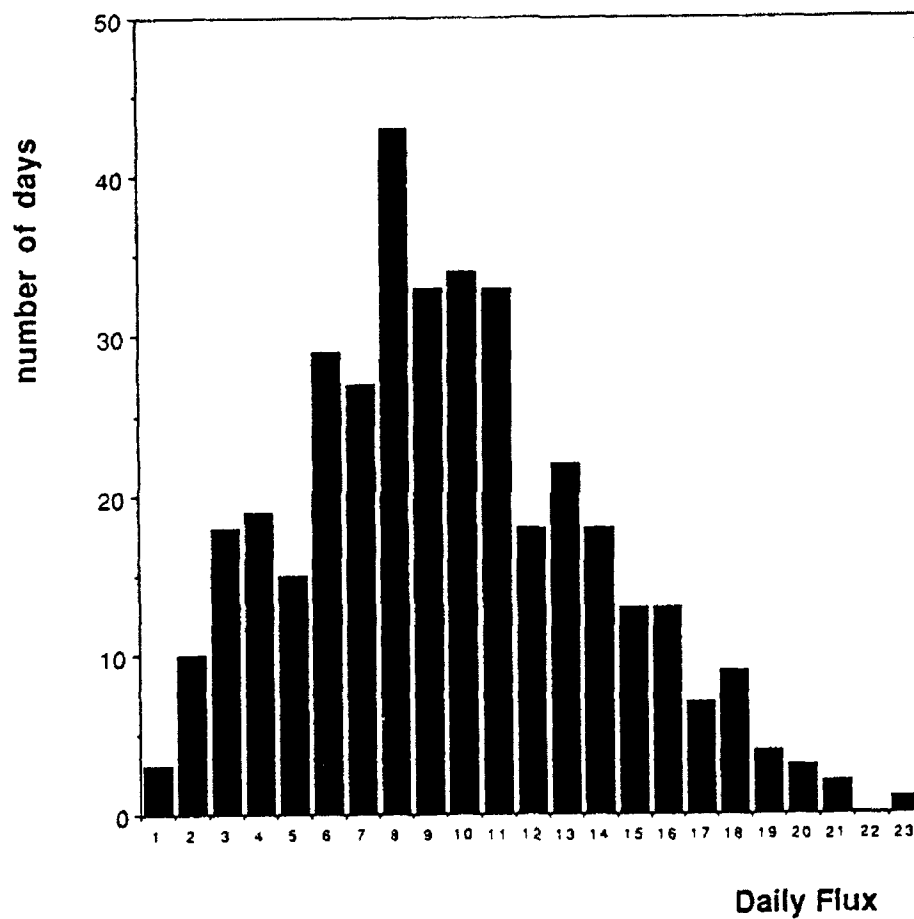


FIGURE 10

July 1988 to June 1989

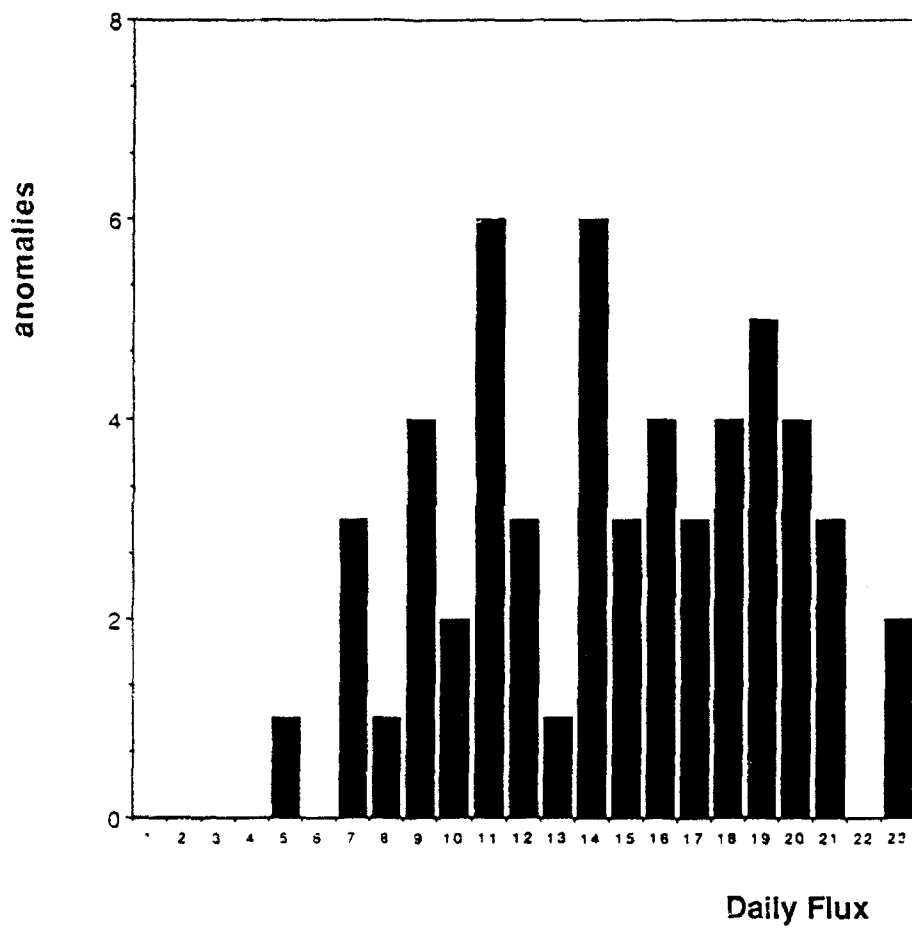


Figure 11

July 1988 to June 1989

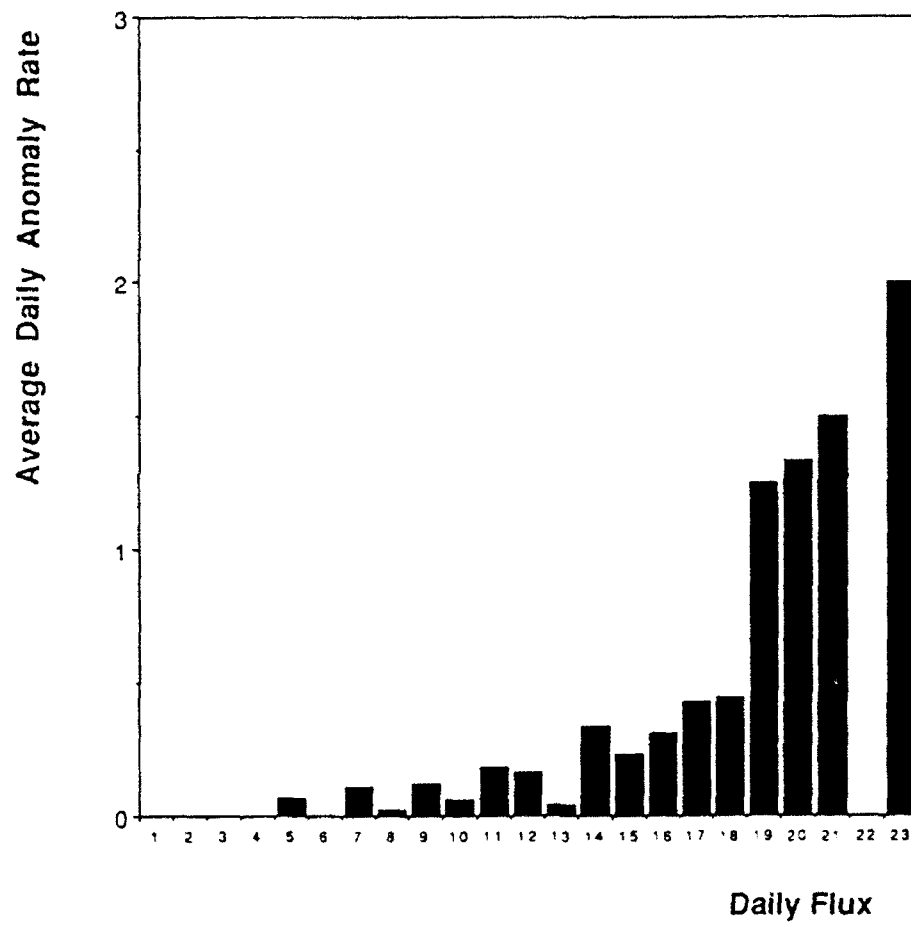


Figure 12

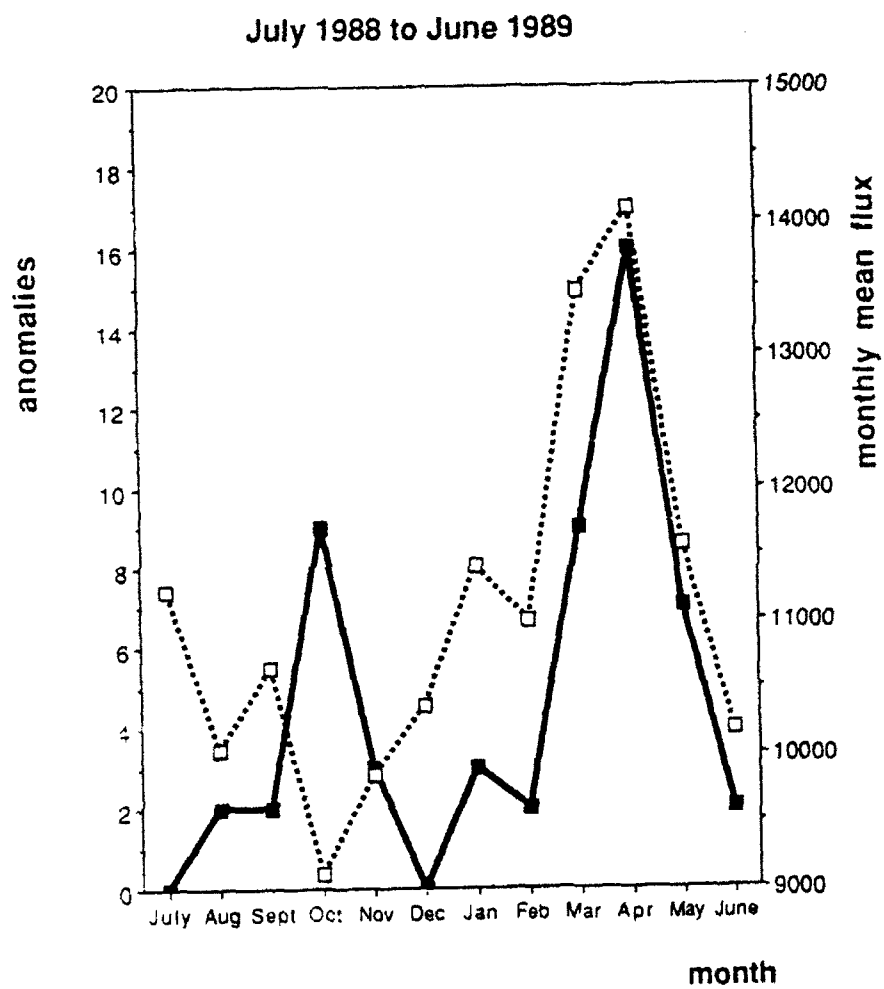


Figure 13

SENSITIVITY ANALYSIS WITH A SIMPLE CHARGING CODE

Andrew J. Sims and Gordon L. Wrenn
Space Department, Royal Aerospace Establishment,
Farnborough, Hants GU14 6TD, U.K.

Abstract

Computer simulation techniques using codes such as NASCAP have proved very successful in tackling the spacecraft charging problem. Although a full dynamic three dimensional code is required to model a spacecraft in orbit, simpler codes (eg MATCHG) can do much to clarify the interaction between the environment and a surface. It is difficult to obtain complete data on either the incident particle fluxes or the material properties which determine the various current components. The latter are dependent upon particle energy which is in turn a function of surface potential; therefore the resulting equilibrium and the charging time to attain this potential, are controlled by a long list of input parameters. In order to assess the sensitivity of a solution to each of these inputs, a simple code (EQUIPOT) is used to calculate the net current as surface potential is stepped from zero to that required for equilibrium ($J_{net} = 0$). The required accuracy for all the parameters is then established by successively introducing a delta of 10% on each. This sensitivity analysis is performed on the properties of a shaded kapton patch on a spherical, conducting, sunlit spacecraft subject to an ambient plasma environment which will produce large, negative potentials. Two main results are obtained: firstly, identification of the important role played by the high incident energy part of the secondary electron yield curve and secondly the ability of a low density, cold plasma component to limit negative charging.

1. Introduction

Much effort has been expended in the development of software used to model the charging of spacecraft by magnetospheric plasmas [eg Katz et al, 1977]. Fully dynamic, three dimensional codes are essential for determining the complex potential contours and differential potentials which develop around a spacecraft composed of many different surface materials in a complicated geometry. In order for such codes to give reliable results, it is essential that the basic interaction between the plasma environment and a given surface material is well understood.

By considering incident ion and electron currents to a surface (a function of the plasma environment and surface potential) and the secondary currents emitted from a surface (a function of the incident currents and surface material properties) it is possible to construct a simple numerical simulation to determine the equilibrium surface potential at which the net current to the surface is zero. Such a code may be used to assess the sensitivity of the solution to small changes in the input parameters which define the plasma environment and the surface material properties. The results of such a sensitivity analysis provide an estimate of the error bars on the results of more complex charging codes and also indicate where more accurate material data or plasma measurements must be made.

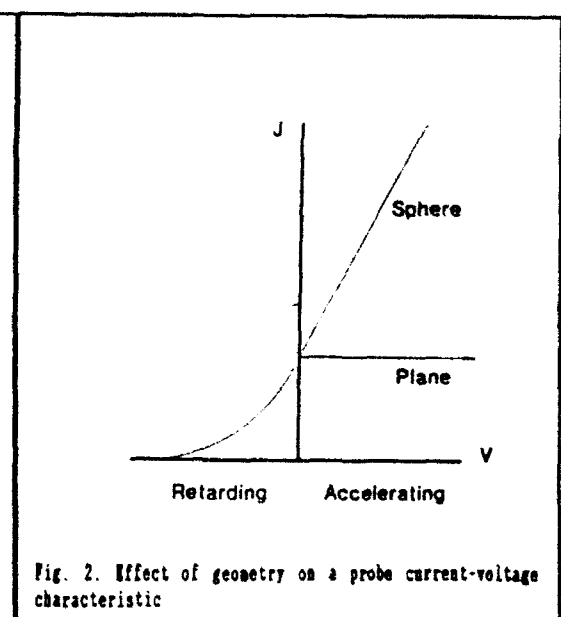
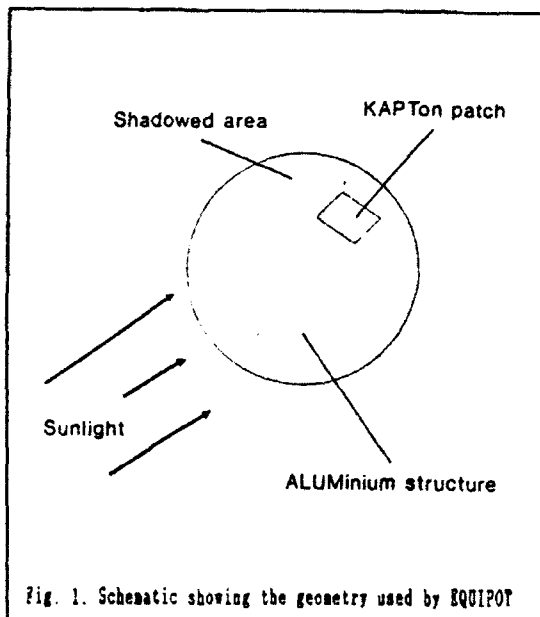
The EQUIPOT code has been developed to compute the equilibrium potential of a surface in a given plasma environment, and therefore provides an ideal framework for carrying out a detailed sensitivity analysis. This paper gives a brief overview of the

code and presents the results of a sensitivity analysis performed using the code. The scope of the analysis described here is limited to the study of a shadowed or partially illuminated kapton patch on a sunlit, conducting aluminium spacecraft structure. The environment chosen is a severe double maxwellian, with an additional component representing the cold plasma population. The results presented show the effects of small changes in the surface characteristics of kapton and the incident environment.

2. The EQUIPOT code

The development of EQUIPOT is based on a number of requirements. These are described below, together with details of the code.

- i. *The basic geometry used by the code should be as simple as possible in order to allow modelling of differential charging.* EQUIPOT computes the equilibrium potential of a patch of dielectric material (or floating conductor) on an underlying spherical, conducting spacecraft. The solar illumination of the patch and the structure may be varied independently. The Debye sheath which develops around the patch may be set as either planar or spherical. The simple geometry used by EQUIPOT is shown in fig. 1. It is intended that the planar, or thin sheath approximation resulting from sheath limited



collection is used in conjunction with LEO environments, where the Debye length is of the order of a few millimetres; the spherical or thick sheath approximation, resulting from orbit limited collection is more representative of the conditions which prevail in GEO where the Debye length is of the order of hundreds of metres, much larger than a typical spacecraft. Clearly, these two approximations represent limiting cases, realistic conditions will fall between these extremes, as shown in fig. 2. Following Katz and Mandell [1982], the currents considered are due to incident electrons,

backscattered electrons, incident ions, secondary electrons from incident electrons and ions, photo-emission and conduction. The latter involves the thickness and conductivity of an insulating material, or the thickness and conductivity of a dielectric substrate for an isolated conductor. The relative permittivity of the dielectric in each case affects the capacitance of the surface element and the resulting charging time.

ii. *The numerical methods used throughout the code should be as simple as possible and run times should be consistent with an interactive code.* EQUIPOT uses a simple voltage stepping algorithm in order to determine the equilibrium potential. Mathematically, finding the equilibrium potential is a straightforward root-finding exercise; therefore it would be possible to employ fast and efficient algorithms to determine the solution. However, simply stepping the surface potential from an arbitrary starting point (usually 0 volts), computing the net current at each point until the solution is reached ensures

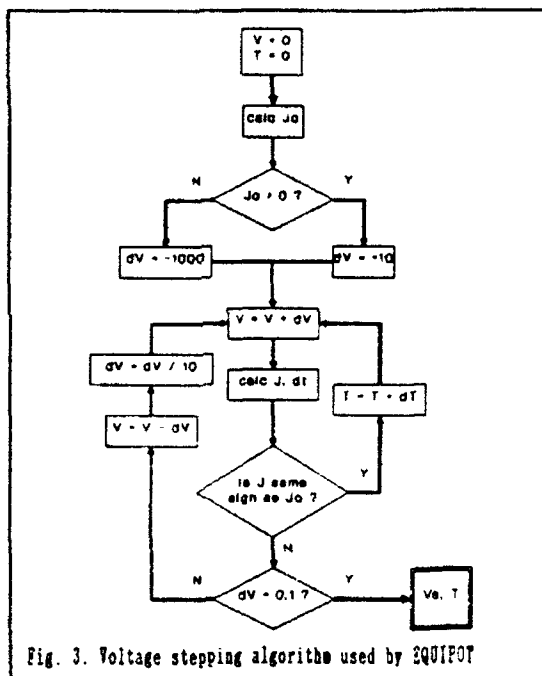


Fig. 3. Voltage stepping algorithm used by EQUIPOT

that multiple root cases are handled properly, and also shows how each component of the net current changes as a function of surface potential. EQUIPOT also includes a facility to compute the current-voltage relationship for a surface between user defined potentials. Fig. 3 shows the simple voltage stepping algorithm used by EQUIPOT.

iii. *The environment definition should be as flexible as possible.* EQUIPOT accepts plasma environments as tables of measured particle spectra, single, double or triple maxwellian components, or combinations of all these. For example, if measured spectra are available for a given energy range, it is possible to append maxwellians which give realistic fluxes outside this range. Alternatively, the environment may be defined entirely by maxwellian components. EQUIPOT splits the incident particle spectra into a series of monoenergetic "swarms" and computes the net current due to each "swarm".

Hence the speed and accuracy of the simulation are functions of the number of equal logarithmic energy steps used to define the incident particle energy range (usually from 1 eV to twenty times the temperature of the hottest maxwellian component). In general, it has been found that 100 steps per integration give sufficiently accurate and quick results.

iv. *Material properties should be defined in the standard NASCAP form.* Although EQUIPOT uses the same general format as NASCAP [Mandell et al, 1984], there are some important differences. The properties of thickness, conductivity and dielectric constant relate to the insulating patch, or to the dielectric separating the floating conductor from the spacecraft structure. Hence, these values are input to the code separately from the normal material properties. Secondly, NASCAP replaces some of the input property values relating to secondary electron emission with re-computed values. Since EQUIPOT treats secondary electron emission (SEE) differently, this method is not adopted.

v. *Emphasis should be placed on modelling the secondary electron emission yield function.* This plays a crucial role in the computation of equilibrium potential [Katz et al, 1986]. Hence EQUIPOT supports a number of different empirical and theoretical secondary electron emission yield models: these will be referred to as the "Katz" model [Katz et al, 1977], the "Whipple/Dionne" model [Whipple, 1981] and the "Sternglass" model [Sternglass, 1954]. EQUIPOT also supports normal or isotropic SEE yield functions.

vi. *The code should be an interactive, "engineering" tool.* EQUIPOT has been developed with a menu-driven user interface, pre-defined material and environment definition files and a continuously displayed panel indicating current set-up (eg floating and structure material type, integration step size etc). For a given set of input parameters, the equilibrium potential is computed in a time of typically 1-2 minutes, allowing many permutations and combinations of parameters to be assessed at a single session.

3. Sensitivity Analysis

Method

The analysis was performed assuming a kapton patch on a spherical, aluminium spacecraft. The structure is assumed to be sunlit, and therefore floats at a few volts positive. The surface properties of kapton are given below (E.J. Daly, ESA, unpublished communication, 1989):

Thickness : 25 μ m
relative permittivity : 3.0
conductivity : 1.0E-15 mho/m
atomic number : 5.0
Max. normal SEE yield : 1.9
Energy at max normal SEE yield : 0.20 KeV
yield of 1 KeV protons : 0.455
energy at max proton yield : 140.0 KeV
photoelectron yield : 2.0E-5 Am⁻²

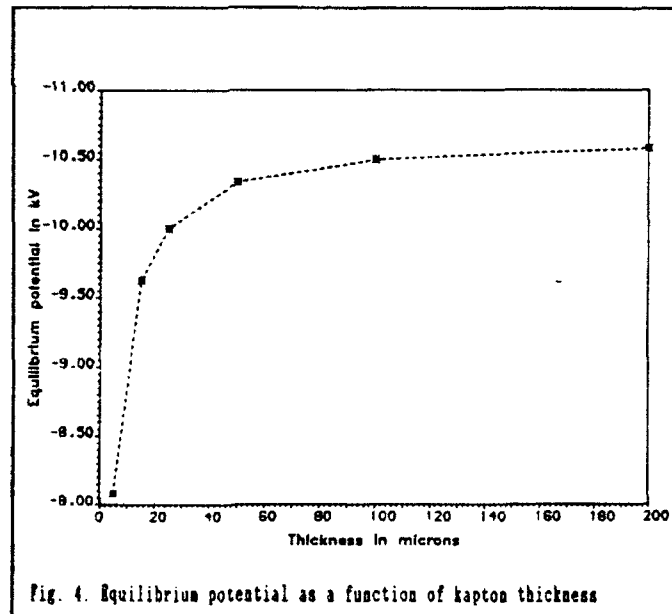
The sensitivity analysis computes the change in equilibrium potential as each parameter on this list is varied. Where appropriate, the input parameters are varied by 10% in each direction. The environment chosen for the study is a variation of the worst-case SCATHA environment [Mullen and Gussenhoven, 1982], modified to give an equilibrium

potential of -10.0 kV when applied to the definition of kapton given above. This provides a convenient datum which is used throughout the study, since the percentage change in the result is simply the amount that the equilibrium differs from -10.0 KV divided by 100. The double maxwellian environment with an additional cold plasma component is defined as follows;

$$\begin{aligned} Ne_1 &= 0.9 \text{ cm}^{-3}, Te_1 = 600.0 \text{ eV} \\ Ne_2 &= 2.1 \text{ cm}^{-3}, Te_2 = 26000.0 \text{ eV} \\ Ne_3 &= 0.1 \text{ cm}^{-3}, Te_3 = 1.0 \text{ eV} \\ Ni_1 &= 1.0 \text{ cm}^{-3}, Ti_1 = 350.0 \text{ eV} \\ Ni_2 &= 0.7 \text{ cm}^{-3}, Ti_2 = 25000.0 \text{ eV} \\ Ni_3 &= 0.1 \text{ cm}^{-3}, Ti_3 = 1.0 \text{ eV} \end{aligned}$$

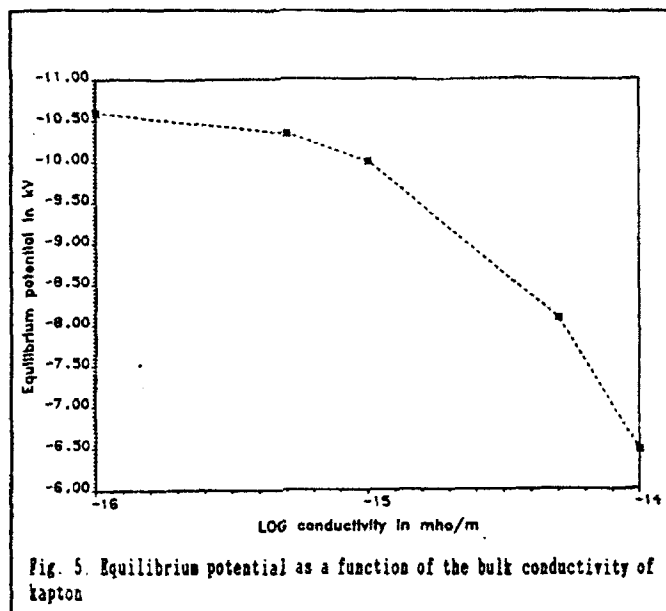
This differs from the SCATHA worst case environment in two ways; firstly a low density, cold plasma component has been added and secondly the electron and ion densities of the "hot" component have been adjusted to give the required equilibrium potential.

It should be noted that the equilibrium potential of -10.0 KV obtained with the data shown above used the Katz model of secondary electron emission and assumed isotropic particle incidence. The time taken for the kapton to reach this equilibrium potential was 4.0 hours.



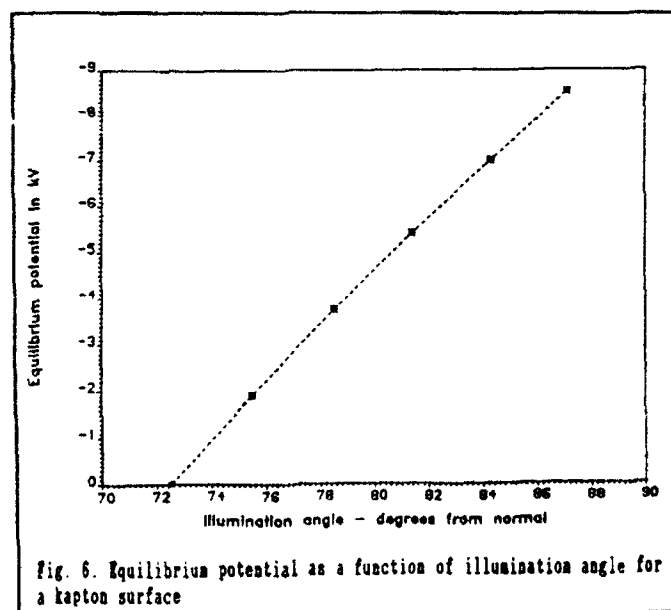
Variation of parameters affecting the conductivity current

The thickness of kapton and its conductivity affect the conduction current to the structure and hence the equilibrium potential. Fig. 4 shows how the equilibrium potential, V_e , varies as the thickness of kapton is increased from 5 μ m to 200 μ m. At thicknesses above 50 μ m, V_e is relatively insensitive to changes in thickness, whilst



below this value, changes in thickness cause major changes in V_s . Fig. 5 shows how V_s varies for 25 μ m kapton as bulk conductivity ranges from $1.0\text{E}-14$ to $1.0\text{E}-16$ mho/m. The significant change resulting from making kapton slightly more conductive is evident.

Variation in the photoelectric yield current



It is instructive to illuminate the kapton patch at oblique angles of incidence. EQUIPOT allows the cosine of the sun angle to be input, where 1.0 represents normal solar incidence. Fig. 6 shows how V_e is affected by the variation of illumination angle from complete shadow (90.0°) to near 72° when negative charging is completely prevented by the current of photoelectrons.

Variation of SEE current for isotropic particle incidence

An isotropic flux tends to increase the value of the maximum secondary electron

TABLE 1. Parameters defining the isotropic SEE yield function

SEE model	d_{max}	E_{max} (eV)
Katz et al, 1977	2.74	338.0
Whipple, 1981	2.77	338.0

TABLE 2. Results of variations in the isotropic Katz expression.

Variation	d_{max}	E_{max} (eV)	V_e (V)
default	2.740	338.0	-10000
$d_{max} + 10\%$	3.014	338.0	-9879
$d_{max} - 10\%$	2.466	338.0	-10152
$E_{max} + 10\%$	2.740	371.8	-9998
$E_{max} - 10\%$	2.740	304.2	-10004

emission yield and moves its position to a higher energy [Whipple, 1981]. Two of the secondary electron emission yield models supported by EQUIPOT (the Katz and Whipple/Dionne expressions) include an expression which corrects for isotropic incidence. The positions of the peaks in the corrected models are shown in table 1 and the full SEE curves are shown in fig. 7. Although the peak positions are in good agreement, the main difference between the curves is apparent at high incident energies where the Whipple/Dionne expression gives a much higher yield.

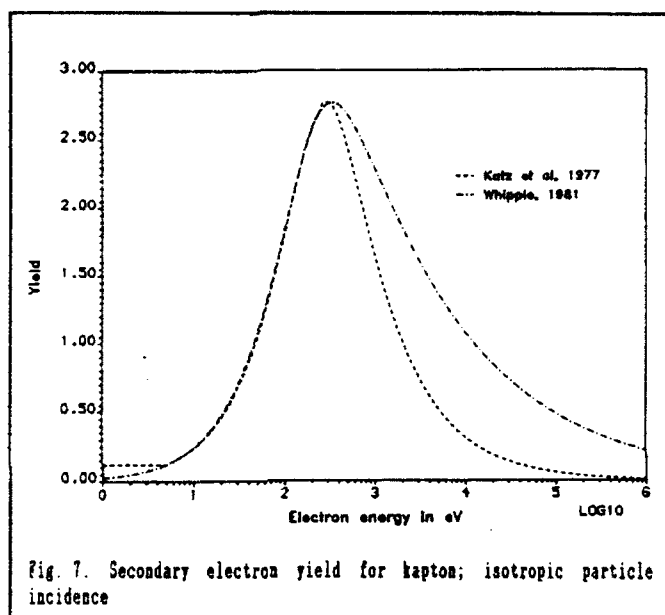
Table 2 shows the results of varying the maximum yield and its position for the (isotropic) Katz expression by 10% in both directions. Since only the position of the peak is being changed by small amounts, and the shape of the high energy tail of the distribution changes very little, the equilibrium potential is affected only slightly (less than 2%).

TABLE 3. Results of variations in the isotropic Whipple/Dionne expression

Variation	d_{max}	E_{max} (eV)	V_e (V)
default	2.770	338.0	-2905
$d_{max} + 10\%$	3.047	338.0	0
$d_{max} - 10\%$	2.493	338.0	-4130
$E_{max} + 10\%$	2.770	371.8	-2257
$E_{max} - 10\%$	2.770	304.2	-3327

Table 3 shows the results of a similar analysis performed using the Whipple/Dionne expression. Two points are evident: firstly the absolute equilibrium potential is only -2.8 kV, significantly different from the results obtained with the Katz model, and secondly, V_e is much more sensitive to small changes in the peak position. Once again, it is the high incident energy tail of the distribution which gives a much higher yield than the Katz expression, and is much more sensitive to changes in the peak position.

It is not intended that these results make any statement about the applicability



of various SEE models, but they provide a clear illustration that the choice of SEE model is critical. In particular, they demonstrate the importance of correctly modelling the high incident energy tail of the SEE yield function.

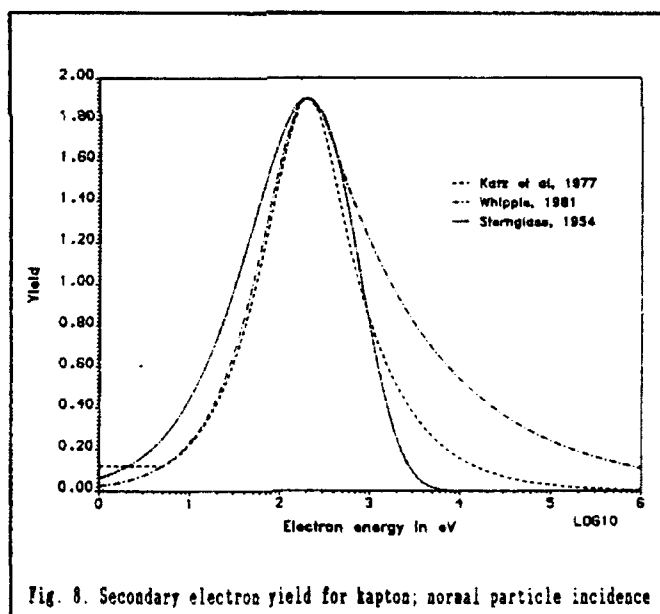
Variation in SEE current for normal particle incidence

TABLE 4. Results of varying the normal SEE function

Variation	d_{max}	E_{max} (eV)	SEE function		
			Katz V_e	Whipple V_e	Sternglass V_e
default	1.90	200.0	-15008	-11913	-15642
d_{max} + 10%	2.09	200.0	-14941	-11463	-15640
d_{max} - 10%	1.71	200.0	-15075	-12337	-15644
E_{max} + 10%	1.90	220.0	-15007	-11765	-15637
E_{max} - 10%	1.90	180.0	-15009	-12068	-15647

It is instructive to repeat the calculations of the previous section for SEE yield functions based on normal particle incidence. It should be noted that the expression for backscattered electrons is also corrected for normal incidence. For this case, EQUIPOT also supports the commonly used Sternglass expression as well as the normal versions of the Katz and Whipple/Dionne expressions. Fig. 8 is a plot of the three functions. By definition, all three curves share the same peak position although it is once again evident that the main difference occurs at high incident energies. Table 4 shows the results of small (10%) movements of the position of the peak on equilibrium potentials obtained with each of the three expressions. For the Katz yield function, changing to normal incidence has reduced the total secondary yield, such that the equilibrium potential is now near -15 kV. Both the Katz and Sternglass expressions are relatively insensitive to moving the location of the peak, in fact, small changes in the energy of the peak have almost no effect. Changing the maximum yield by 10% induces changes of less than 1% in the equilibrium potential. V_e computed with the Whipple/Dionne expression changes by almost 4% for 10% changes in the position of the peak.

As observed for isotropic incidence, the equilibrium potential is much more



sensitive to changing the secondary yield model rather than changing the peak position for any single model.

Changes in the current of backscattered electrons

The model used for the backscattered electron yield is that described by Whipple [Whipple, 1981]. The yield is a function of the atomic number of the surface material and also whether particles are incident normally or isotropically. EQUIPOT uses the

TABLE 5. Result of small changes in Z.

Variation	Z	V_e (V)
default	5.0	-10000
Z + 10%	5.5	-9933
Z - 10%	4.5	-10077

isotropic correction automatically if the SEE yield function is chosen as isotropic, hence effects of the different backscatter coefficient for normal or isotropic incidence are included in the analysis of the secondary electron yield function. Therefore the atomic number provides the only parameter which might sensibly be varied over a limited range in order to investigate changes in the energy dependent backscatter coefficient. The results are shown in table 5 and demonstrate that the effect of changing Z is small (less than 1% for 10% changes in Z).

Changes in the secondary electron current due to ion impact

The yield function used is that described by Whipple [Whipple, 1981] and is

TABLE 6. Effect of varying SEE due to ion impact

Variation	Yield (1 KeV)	E_{max} (KeV)	V_e (V)
Default	0.455	140.0	-10000
Yield at 1 KeV + 10%	0.501	140.0	-9604
Yield at 1 KeV - 10%	0.410	140.0	-10483
Max yield energy + 10%	0.455	154.0	-9965
Max yield energy - 10%	0.455	126.0	-10049
No SEE due to ions			-20797

defined by two parameters; the yield for incident 1 KeV protons, and the energy at the maximum yield. The results of varying these parameters by 10% are shown in table 6. All resulting changes in V_e are less than 5%. However, it is interesting to note the effect of neglecting this current component; the equilibrium potential approaches -21 KV.

Changes in the definition of the plasma environment

Finally, it is important to assess the effects of making small changes in the density and temperature of the maxwellian components used throughout this study. Firstly, the effect of the cold plasma added to the severe SCATHA environment must be investigated. A density of 0.1 cm^{-3} is too small to be measured, the effects of both removing it completely and also increasing it are summarised in table 7. This is a very significant result and shows how the presence or absence of cold plasma at GEO can significantly affect spacecraft charging.

TABLE 7. Effect of varying the thermal ion density

Variation	N_{i_2} (cm^{-3})	T_{i_2} (eV)	V_e (V)
Thermal ions absent	0.0	1.0	-16056
Default	0.1	1.0	-10000
Increased density	0.2	1.0	-7829

Table 8 shows the results of varying the density and temperature of the two main

TABLE 8. Effect of varying plasma density and temperature.

Variation	V_e (V)
Default	-10000
$N_{e_2} + 10\%$	-10651
$N_{e_2} - 10\%$	-9362
$N_{i_2} + 10\%$	-9925
$N_{i_2} - 10\%$	-10082
$T_{e_2} + 10\%$	-10721
$T_{e_2} - 10\%$	-9282
$T_{i_2} + 10\%$	-9975
$T_{i_2} - 10\%$	-10032
$N_{e_1} + 10\%$	-10000
$N_{e_1} - 10\%$	-10000
$N_{i_1} + 10\%$	-9818
$N_{i_1} - 10\%$	-10225
$T_{e_1} + 10\%$	-10000
$T_{e_1} - 10\%$	-10000
$T_{i_1} + 10\%$	-10085
$T_{i_1} - 10\%$	-9911

electron and ion plasma components by 10%. The colder (600 eV) electron component does not contribute to the current balance when the spacecraft potential exceeds several thousand volts negative, hence, as observed, it has no effect on a spacecraft equilibrium potential of around -10 KV. Changing the temperature and density of the "hot" electron component results in changes of less than 3% in V_e , whilst similar changes in the "hot" ion component give rise to changes in V_e of less than 1%. It is

interesting to note that an increase in the temperature of the "hot" ion component makes V_e less negative, whilst increasing the temperature of the cold component has the opposite effect, although both changes are small (less than 1%).

4. Conclusions

Although the scope of this study is limited to a single material in a single type of environment, it has yielded some valuable results. Two main features have emerged; the importance of correctly modelling the high incident energy part of the secondary electron emission yield function and the importance of the role played by a cold plasma population.

The temperature of the "hot" electron population (25 KeV) chosen for this study corresponds to a position on the SEE yield curve of between 75 and 125 times the energy of the yield peak. It is at these energies, where the yield is less than 0.2, where various models disagree. Further SEE yield measurements at high incident energies are necessary to resolve this problem. It may be more sensible for codes such as EQUIPOT to use direct SEE yield data, rather than rely on an empirical relationship.

Since thermal ions are rarely completely absent from the geostationary plasma environment, particularly during prolonged geomagnetically quiet periods, it is essential to include their effect in any charging simulation.

EQUIPOT has proved to be a very flexible tool in performing this type of analysis. Future studies are proposed which include investigation of the behaviour of materials in measured geostationary plasma environments with a view to explanations of the "eclipse" and "barrier" charging events observed on the Meteosat-2 spacecraft [Wrenn and Johnstone, 1987].

References

- Katz, I., D.E. Parks, M.J. Mandell, J.M. Harvey, D.H. Brownell, S.S. Wang, M. Rotenberg, A three dimensional study of electrostatic charging in materials, NASA CR-135256, 1977.
- Katz, I., M.J. Mandell, Differential charging of high voltage spacecraft : the equilibrium potential of insulated surfaces, *J. Geophys. Res.*, **87**, p4533, 1982.
- Katz, I., M.J. Mandell, G. Jongeward, M.S. Gussenhoven, The importance of accurate secondary electron yields in modelling spacecraft charging, *J. Geophys. Res.*, **91**, A12, pp 13703-13744, December 1986.
- Mandell, M.J., P.P. Stannard, I. Katz, NASCAP programmers reference manual, Report from NASA contract 22826, March 1984.
- Mullen, E.G., M.S. Gussenhoven, High level spacecraft charging environments near geosynchronous orbit, AFGL-TR-82-0063, Feb 1982. **ADA118791**
- Sternglass, E.J., Theory of secondary electron emission, *Phys. Rev.* **95**, 345, 1954.
- Whipple, E.C., Potentials of surfaces in space, *Rep. Prog. Phys.*, **44**, pp 1197-1250.
- Wrenn, G.L., A.D. Johnstone, Evidence for differential charging on Meteosat-2, *J. Electrostatics*, **20**, pp 59-84, 1987.

LABORATORY STUDIES OF SPACECRAFT CHARGING MITIGATION TECHNIQUES

K.L. Giori, R.C. Adamo, J.E. Nanevich, J. Kositsky
SRI International

INTRODUCTION

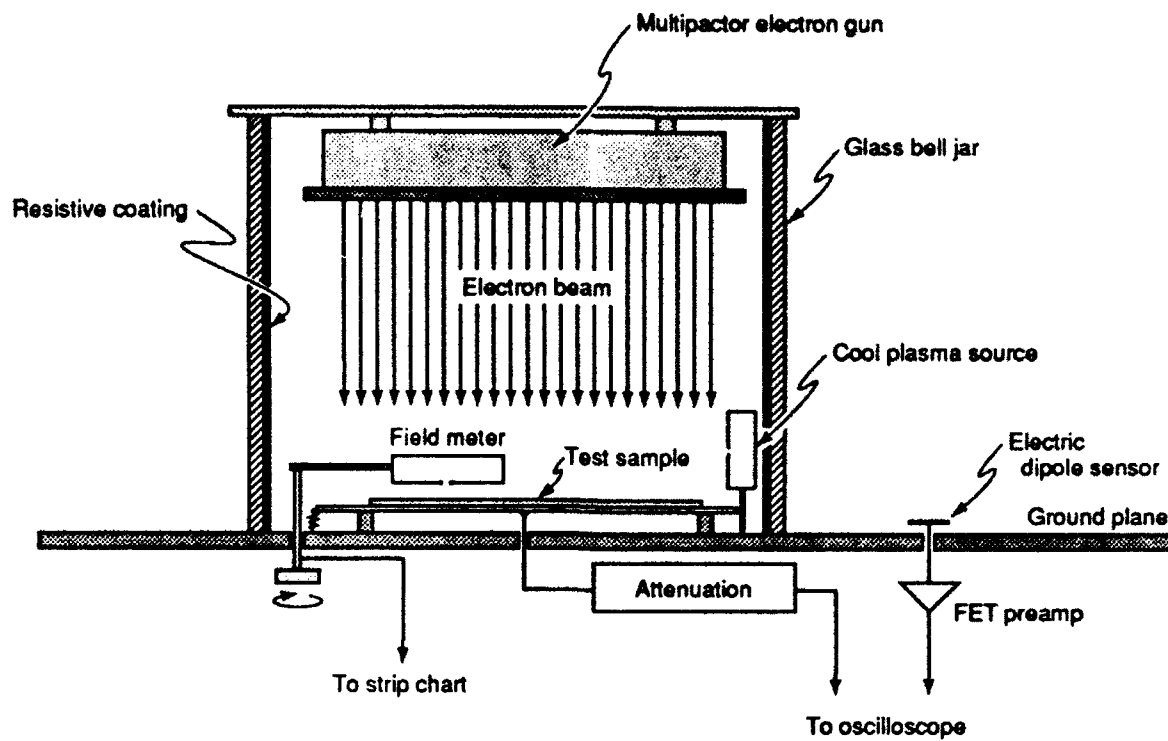
In the early 1970s, spacecraft charging was first suspected as the cause of numerous scientific and operational anomalies on synchronous orbit spacecraft. Since then, various tools and techniques have evolved in an effort to study and mitigate undesirable charging effects. These tools range from sophisticated, complex theoretical and computer model analyses and system-level tests to over-simplified paper studies and "band-aid fixes," several of which appear to have had, on occasion, some success.

Aside from single-event upsets (which are not addressed here), the most common spacecraft charging problems on nonscientific geosynchronous spacecraft result from differential static-charge buildup. When this differential charging, on the surface of (or interior to) the spacecraft, reaches a level sufficient to cause energetic electrostatic discharges (ESDs), circuit errors or damage may result.

As is true of virtually all electromagnetic transient interactions with systems, the undesirable effects of charging and subsequent discharging can best be mitigated by reducing or eliminating the electromagnetic sources themselves. If this procedure is not practical or possible, an alternative approach is to reduce the coupling of the troublesome transients to the sensitive systems by employing sound electromagnetic design techniques. Reducing the susceptibility of the systems themselves to the effects of electrical transients is still another possible approach.

This paper deals with practical internal and surface discharge mitigation techniques developed and verified as part of SRI's ongoing spacecraft-charging studies.

All of the measurements described here were performed in the SRI Spacecraft Charging Simulation Facility (schematically illustrated, in one possible configuration, in Figure 1). This facility has evolved over the past two decades to include environment-simulation components (high-energy electrons, vacuum, and optical illumination) with electromagnetic and electrostatic measurement instrumentation. It provides a flexible environment for reliably measuring key parameters in charging studies of spacecraft materials and components [Nanevich and Thayer, 1986; Thayer et al., 1987; and Nanevich et al., 1988].



p90-021/11

Figure 1 EXPERIMENTAL SETUP

Internal (Deep Dielectric) Charging and Discharging Mitigation

Internal charging is caused by high-energy charged particles (typically 0.3 to 5 MeV electrons) that penetrate the outer layers of spacecraft structures and collect in internal dielectric materials. If these materials are sufficiently good insulators, charge build-up may proceed faster than charge bleed-off, even at low incident flux densities (a few pA/cm²). The resulting electrostatic fields and subsequent discharges from internal system components (such as fiberglass circuit-boards or Teflon-insulated wires) can couple very strongly to sensitive components causing system upset or damage.

The flux of energetic particles that can penetrate the satellite skin is much smaller than the flux of particles that can charge surface dielectrics to discharge levels. Thus, far fewer internal discharges are expected to occur. Those that do occur, however, are much more likely to affect internal systems, since the source and the victim-circuit are more closely coupled by their proximity.

Possible solutions to the internal discharge problem include (1) the use of additional conductive shielding material in the satellite skin and internal electronic boxes, and (2) the use of lower resistivity materials in internal assemblies. The first solution, however, often imposes unacceptable weight penalties, while the second is difficult to implement either due to functional requirements or to a lack of qualified materials and processes.

Perhaps the most widely used electronic-system component that can produce serious internal discharge problems is the ubiquitous printed circuit board. By nature of its primary function, the circuit board typically consists of large areas of excellent insulating material in intimate contact with sensitive electronic components. The experimental work described here was based on the conjecture that appropriate circuit board coatings could control the static field structure at the board's surface, thereby reducing the occurrence and severity of internal discharges without degrading the overall circuit-board function.

In our initial experiments, we used fiberglass/epoxy circuit cards, typical of those used in fabricating spacecraft instrumentation. Copper traces were etched on these circuit boards, but no components were installed. For each set of tests, three identical cards were prepared. One was left bare, one was coated with a standard conformal protective coating, and the third was flashed with an approximately 2000 Å layer of aluminum over a conformal coating.

Both the uncoated and the conformally coated circuit boards experienced many electrostatic discharges. The frequency of these ESDs increased with the test electron-beam current density. The morphology of these ESDs is such that electrons are thought to "blow off" the surface, causing radiated electric fields that propagate and possibly couple into sensitive systems. These discharge processes can be very energetic, with

a typical blow-off current pulse peak of 4 A and a radiated electric field of 2 kV/m in the immediate vicinity of the discharge (≤ 10 cm).

The vacuum-deposited aluminum coating on the third board constrained the charge embedded in the dielectric into either bleeding off or producing only minor discharges to the conductive aluminum. No discharges above the instrumentation thresholds were observed on the aluminum-coated circuit board [Nanevycz and Thayer, 1986].

An aluminum flash coating has been used and flown as a mitigation technique for some Los Alamos National Laboratory sensors that were experiencing frequent anomalies in space. The aluminum flash technique was successful in eliminating all such anomalies on later sensors. These results are detailed elsewhere in these proceedings in a paper by Berzins et al.

A follow-on experiment was performed at SRI on functioning microprocessor circuit boards. These were exposed in the vacuum chamber facility to particle-radiation conditions simulating the synchronous space environment. The boards (containing CMOS components) ran identical looping programs to write to and read from memory, while an external computer checked for errors. Again, uncoated, conformally coated, and specially treated circuit boards were tested. The special treatment in this case was a carbon-loaded acrylic topcoat over the conformal coating.

As before, the untreated and conformally coated circuit boards experienced ESDs that caused upset and latchup. The boards with a carbon-loaded topcoat, however, showed no evidence of discharges or circuit upset, even when exposed to the harshest beam conditions. The effectiveness of the resistive topcoat is believed to be due to the same mechanisms that worked for the aluminum flash coat: (1) the addition of the resistive topcoat may significantly reduce regions of high field concentration where discharges tend to be initiated, (2) the resistive coat may act as a sink that facilitates charge migration through the dielectric conformal coating, and (3) the resistive coat may limit the size or energy of the discharges such that the signals produced are below the threshold of detection and upset [Thayer et al., 1987].

External Charging and Discharge Mitigation

External discharge phenomena are caused by charged particles (typically 1 to 100 keV) that deposit in the outer dielectric materials of the spacecraft structure. Materials with sufficient insulating properties may readily charge in the space-plasma environment.

Spacecraft materials, such as optical solar reflectors (OSRs) or various types of multilayer insulation (MLI) that typically blanket the spacecraft, are chosen primarily for their excellent thermal-optical properties. Each material tends to charge and discharge at varying threshold energy and current flux levels. The presence of exposed conductors and other materials complicates the mechanisms of differential charg-

ing and discharging, as well as the strength, frequency, and location of surface ESDs. Furthermore, the susceptibility of interior components depends on the electromagnetic interference and compatibility protection offered by the satellite's design (i.e., whether the satellite acts like a good Faraday shield against externally generated electromagnetic radiation).

Mitigating external discharges is difficult because of the limited selection of materials that can provide the necessary thermal-optical properties. In addition, the design and fabrication of a Faraday barrier that is robust enough to exclude all external discharges from coupling to internal electronics may be logistically prohibitive or require too much added weight.

An effective and feasible means of controlling large surface discharges may be the introduction of a low-density cool plasma about the spacecraft. Studies performed in SRI's Spacecraft Charging Simulation Facility show that the presence of an ambient plasma greatly modifies the way in which charge collects on a dielectric surface. In particular, the addition of a low-density cool plasma reduced the charge residing on a Kapton sample surface to zero. The same sample readily charged and discharged in the absence of cool-plasma injection. This result may have important implications in the design of automatic systems for the discharge of satellites [Nanevycz et al., 1988].

Another mitigation technique that was experimentally tested at SRI was the use of thin thermal blankets. Very thin Kapton (< 1 mil, aluminized on the inside grounded surface) did not produce a detectable discharge, but thicker Kapton readily charged and discharged. Surface potential measurements of the very thin Kapton samples were very much below the high surface potential values of the thick Kapton. The lack of charge buildup in thin Kapton may be due to (1) the ability of the more energetic electrons to pass directly through the thickness of the samples, and (2) the reduction of the charge relaxation time for thin samples, whereby charged particles embedded in the Kapton can migrate quickly through to the conducting bottom surface [Adamo et al., 1987].

SRI also tested the charging and discharging characteristics of various other spacecraft materials. Flex cable made of copper interconnects embedded between two layers of Kapton produced discharges, some of which were dramatic and extended the entire length of the copper strip.

Conclusions

SRI's laboratory measurements verify that system anomalies, upset, or damage can be caused by electrical discharges that may occur on internal or external surfaces and couple large unwanted transient signals into satellite circuitry.

Internal circuit boards that may store charge, and subsequently discharge, constitute the most direct energy coupling available to damage

components. Laboratory measurements also verify that conductive or resistive coatings applied on the surface of such boards minimize charging and eliminate discharges.

External dielectric surfaces such as Kapton and OSRs were observed to charge and discharge. Introduction of a low-density cool plasma eliminated these discharges. When using thin (< 1 mil) instead of thick Kapton, the discharges also disappeared.

Various types of materials, cables, and other exposed elements of satellite systems can be tested for charging or discharging characteristics in SRI's Spacecraft Charging Simulation Facility. Using laboratory measurements performed on a Los Alamos sensor experiencing anomalies, we proposed a "modification" that was later flown successfully in space.

An important step forward in the future of space experimentation will be the ability to verify laboratory and theoretical modeling studies with in situ experiments. A small, lightweight, low-power diagnostic package should be flown on many operational satellites to monitor the space-plasma environment, record the strength of any ESDs, and provide quasi real-time data on satellite interaction with the environment. Such data would enhance our understanding of the link between the space environment and satellite anomalies.

SRI's continued involvement in spacecraft charging and ESDs has led to the development of a prototype diagnostic package to monitor the environment and transients. The subsequent flight hardware will weigh an estimated 5 kg, consume approximately 7 W of power, and require about 4000 cm^3 of space.

REFERENCES

R.C. Adamo, R. Briet, T. Chin, and J.S. Thayer, "The Importance of Using Thin Kapton Outer Layers to Prevent Discharges on Multilayer Space Blankets," IEEE NEMP Conference, Snowmass, Colorado, 1987.

J.E. Nanevich and J.S. Thayer, "Experimental Studies of Deep Dielectric Charging and Control Techniques," International Federation of Automatic Control Workshop, Paris, France, 1986.

J.E. Nanevich, J.S. Thayer, and K.L. Hewitt (Giori), "Effects of Ambient Electron Plasma on Spacecraft Charging and Discharging," paper presented at the Fourth International Symposium on Spacecraft Materials in a Space Environment, Toulouse, France, 1988.

J.S. Thayer, P.G. Sechi, and J.E. Nanevich, "Experimental Studies of Interior Dielectric Charging in Spacecraft and Charging Control Techniques," paper presented at the 1987 IEEE Nuclear and Space Radiation Effects Conference (NSREC), Snowmass Village, Colorado, 27-31 July 1987.

THE ELECTRICAL PROPERTIES OF ZOT AFTER
A LONG TERM EXPOSURE TO THERMAL VACUUM ENVIRONMENT

by

PHILIP LEUNG

Jet Propulsion Laboratory
Pasadena, California

ABSTRACT

Experimental results show that the moisture content of ZOT paint provides a medium for ionic conductivity to occur, increasing its observed conductivity significantly. By extrapolating the test data the resistivity of ZOT, in the absence of moisture, is determined to be 10^{14} ohm-cm. Therefore, ZOT cannot be regarded as a conductive paint.

INTRODUCTION

The Galileo (GLL) spacecraft (Leung, 1985), which was launched from Shuttle in October, 1989, will orbit Jupiter in 1995. One of the scientific objectives of Galileo is to perform detailed measurements of the charged particle distributions at Jupiter; in particular, the charged particles that carry the current in the Io flux tube. The Plasma Instrument (PLS) on board Galileo was designed to accomplish this goal. It has the capability of measuring charged particles in the energy range of 0.1 eV to 5 eV.

In order for PLS to achieve its measurement objectives, the electric field gradient in the vicinity must be minimized. For this reason, a rigid equipotential requirement was imposed on Galileo. Specifically, the potential difference between any two surfaces had to be less than 10 volts, making Galileo an almost equipotential spacecraft. In order to qualify as such most of the Galileo surfaces were made from conductive materials. However, in some cases, conflicts with other engineering constraints required the use of new materials with marginal or unknown properties. The acceptability of these materials was usually evaluated by tests which included:

1. measurement of conductivities;
2. measurement of the surface potential in the simulated charging environments.

Usually at least one of the above tests was performed. A typical example is the evaluation of thermal control white paint. Unlike the black paints, which can easily be made conductive with the addition of the appropriate amount of carbon, white paints are usually nonconductive. For Galileo, an effort was made to identify/formulate paints which would satisfy the Galileo equipotential requirements. Zinc orthotitanate (ZOT) was identified as a possible candidate conductive white paint. During the development of the Galileo spacecraft, several sets of tests were performed to determine the acceptance of ZOT paint. This paper summarizes the results obtained in the latest round of tests.

TEST SETUP AND ENVIRONMENTAL CONSIDERATIONS

Since the space environment plays a very important role in determining the electrical properties of a material, the parameters which can affect the electrical properties of ZOT must be carefully considered in this test. For paints, the important parameters are:

1. space plasma environment,
2. surface temperature,
3. moisture content.

Extensive literature is available on the simulation of the charging environment in space (Adamo, 1985). For this program, the energetic electron environment of Jupiter is simulated by the use of a mono-energetic electron beam. Although this technique may over estimate the levels of differential charging, it does provide an upper bound to the predicted charging levels.

In a typical test, a test sample is irradiated by an electron beam (Fig. 1) and the resulting surface potential is measured by a non-contacting electrostatic probe. The parameters of the electron beam are selected so that the charging environments to be encountered can be adequately simulated. For the Galileo project, these environments are Jupiter's Plasma Sheet and Earth's Geosynchronous environment. Table 1 shows the test parameters corresponding to these two environments.

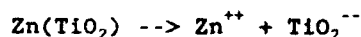
Table I. Simulation of Galileo Charging Environment

Regions	Electron Beam Parameters
Jupiter's Plasma sheet	10 KeV at 0.05 nA/cm ²
Earth's Geosynchronous	10 KeV at 0.5 nA/cm ²

Temperature is a very important factor in determining the conductivity of a non-conductive material. For a good dielectric material, the conduction of charge/current is a direct result of electron motion through the material (Sessler, 1980) and hence its conductivity is directly proportional to the mobility of electrons within the material. Depending on the particular material, the electron mobility can be very sensitive to temperature. Therefore, the charging of ZOT should be performed at its predicted temperatures. In the test setup, a baffle which allows the passage of liquid nitrogen (LN₂) or hot gaseous nitrogen is used to control the temperature of the test sample (Fig. 1).

When paints are first mixed and applied to a surface, their moisture content is usually very high. Even after curing, water molecules are still chemically bonded to the paint constituents, and these molecules are often difficult to remove. In addition, ZOT absorbs moisture from the ambient environment rapidly. In an environment of 50% relative humidity, the moisture content of ZOT could amount to as high as 0.1% of its mass.

The presence of moisture can modify the observed conductivity significantly through the process of ionic conductivity. In the presence of water content, the chemicals in the paint can be dissociated into ions. For example, in ZOT the following dissociation process may take place:



In the presence of an external electric field due to charging or from an external bias, these ions can move along the field lines and contribute to the measured current. Consequently, the observed conductivity of ZOT is usually higher in the presence of moisture. For an aqueous solution, the ionic conductivity increases with the number of ions present (Crow, 1974). For this reason, the apparent conductivity of ZOT would increase with the amount of water in the paint.

The Galileo spacecraft will transverse within 0.5 AU of the sun, and six years will elapse before its first encounter with Jupiter. It is expected that the moisture content of ZOT will be almost zero by the time of the Jupiter encounter.

Originally, it was believed that if a material evaluation test was performed under vacuum conditions, the moisture content of the sample would not be significant, and the ionic conductivity would not play a role. However, preliminary results of conductivity measurements (Robinson, 1981) obtained under vacuum conditions seemed to indicate that the conductivity of paint does tend to decrease as a function of time. A possible explanation for this phenomenon is that the water content of the paint sample has not been completely eliminated. Consequently, a method must be devised to perform the charging/ conductivity tests with the water content of the paint sample resembling what it would be after prolonged exposure to the space environment. For this recent test program, the ZOT paint sample was exposed to a sequence of thermal/vacuum conditions aimed at driving the water out of the test sample in the shortest time possible.

DESCRIPTION OF TEST TIMELINE

The timeline of this test sequence is shown in Figure 2. In designing this timeline, the cost of using the vacuum chamber (which is the main cost driver) was taken into account. Therefore, only five days of test time was allotted. The sample was placed in an oven and after being prepared, underwent a preliminary bakeout process at 140°C under atmospheric pressure. The sample was then transferred to a vacuum chamber and underwent further bakeout at a temperature of 120°C. This bakeout process occurred with the ambient pressure maintained at 10^{-5} torr or below. During this time, the sample was irradiated by an electron beam and the resulting surface potential was measured (Fig. 2). At the end of the fourth day, the bakeout process was

terminated. The surface potential of the ZOT paint sample, when irradiated by an electron beam at various temperatures, was taken and measurements were performed over a two day period. Once the ZOT sample was placed in the vacuum chamber, it was continually exposed to vacuum conditions during the five days of test. This was to prevent the absorption of moisture content from the atmosphere.

RESULTS OF THE ELECTRON BEAM IRRADIATION EXPERIMENT

Figure 3 shows the surface potential of ZOT when it was irradiated by a 10 KeV electron beam at different current densities. For each beam current density, the ZOT surface was irradiated for a period of 10 minutes. At low current densities, $<0.1 \text{ nA/cm}^2$, the 10 minute interval was probably not sufficient for the paint surface to come into equilibrium. At Jupiter, the environment is very dynamic; Galileo is not expected to stay in the same type of environment for more than 10 minutes. Therefore, these test results provide reasonably good predictions of the charging conditions that Galileo may have at Jupiter. One of the most distinct features of Figure 3 is that the surface potential increases with the duration of the bakeout period. That is, the effective conductivity of ZOT decreases as a function of the time exposure in vacuum. The potential of the paint surface after 66 hours of bakeout is several times the charging level before the bakeout process (all measurements were taken at 25°C). This indicates that moisture content plays a very important role in determining the charging level. The test results also imply that exposing ZOT to four days of vacuum bakeout does not completely deplete the test sample of water content. An increase in the charging level between day 4 and day 5 indicates that an equilibrium moisture content level was never achieved.

As expected, the charging level and hence the conductivity of ZOT decreases with its temperature (Fig. 4). For this study, the paint sample was allowed to come into equilibrium with the hot/cold plate for an hour before the initiation of electron beam irradiation. The test results show that the conductivity changes by more than two orders of magnitude, from 400K to 240K (127°C to -33°C). Between 240K to 94K (-33°C and -179°C), the change in charging potential is extremely small. In Figure 5, the resistivity of ZOT as a function of temperature is plotted. This resistivity is derived from Ohm's law and assumes uniform irradiation of the ZOT surface. The data indicates that the resistivity of ZOT can be as high as $3 \times 10^{15} \text{ Ohm-cm}$, therefore, it should not be considered as a conductive paint.

DISCUSSION

The test results clearly demonstrate the dependence of ZOT's charging level/conductivity on its moisture content. It should be noted that the time allotted for vacuum bakeout is not sufficient to completely eliminate the water content of ZOT. However, an upper bound in the surface potential can be developed from the surface potential data at temperatures below the freezing temperature of water. As the temperature of the test sample is lowered to below 273K (0°C), the water inside the sample should be frozen and the degree of ionic conductivity should be completely curtailed. Consequently, the surface potential measured at temperatures below 273K could be free of the effects of ionic conductivity. The data displayed in Figure 3 indicate that the water content of the sample was completely frozen at 240K (-33°C). The

variation in the surface potential between 240K to 94K could be due to variation in the mobility of ZOT at different temperatures. Since the surface potential varies slowly at this temperature, the resistivity of ZOT is a weak function of temperature between 240K and 94K.

Using the data at 240K, an upper bound on the surface potential of the ZOT sample can be obtained. If this approach is taken, the worst case potential of ZOT in the Jovian Plasma Sheet environment would be 150 volts, and its surface potential in the vicinity of Earth's geosynchronous environment would be 1500 volts.

Charging only occurs on shadowed surfaces. Since the photo-current dominates the electron current of the expected environment (Table 1), no charging should occur at sunlit surfaces.

CONCLUSIONS

The presence of moisture provides a medium for ionic conductivity to occur in ZOT paint, increasing its observed conductivity. When most of the moisture is eliminated the conductivity decreases by more than two orders of magnitude. Therefore, care must be taken when using ZOT (or other 'conductive paints') in space systems.

As for the ZOT surfaces of Galileo, they violate the equipotential requirement and work is being performed to evaluate the impact of this on the plasma instrument.

ACKNOWLEDGEMENT

The research described in this paper was carried out by the Jet Propulsion Laboratory, California Institute of Technology, under a contract with the National Aeronautics and Space Administration.

REFERENCES

1. Adamo, R. and J. Nanevich, "Development of a Continuous Broad-Energy-Spectrum Electron Source", *Spacecraft Environmental Interaction Technology 1983*, NASA Conference Publication 2359, pp 465-470, 1985.
2. Crow, D.R., *Principles and Applications of Electrochemistry*, Chapman and Hall, London 1974.
3. Leung, P., G. Plamp and P. Robinson, "Galileo Internal Discharge Program", *Spacecraft Environmental Interactions Technology 1983*, NASA Conference Publication 2359, pp 423-436, 1985.
4. Robinson, P., and A. Whittlesey, "Electrostatic Charging Characteristics of Thermal Control Paints as a Function of Temperature", *Space Charging Technology 1980*, NASA Conference Publication 2182, pp 309-319, 1981.
5. Sessler, G., *Topics in Applied Physics*, vol. 33, *Electrets*, Edited by G. Sessler, Springer-Verlag, pp. 13-75, 1980.

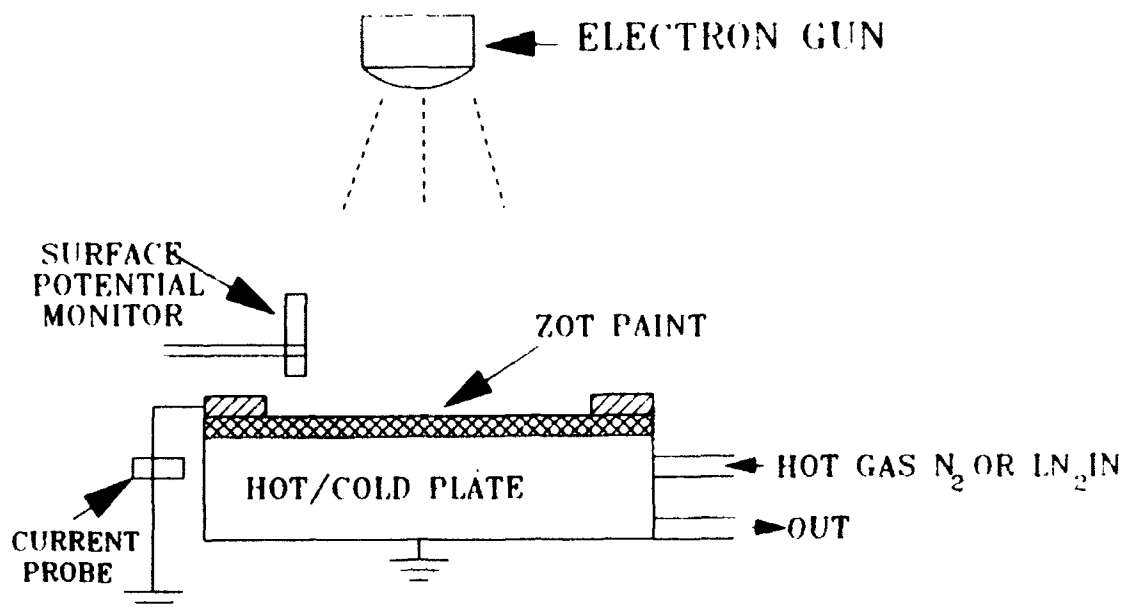


Figure 1. Schematics of the experimental setup.

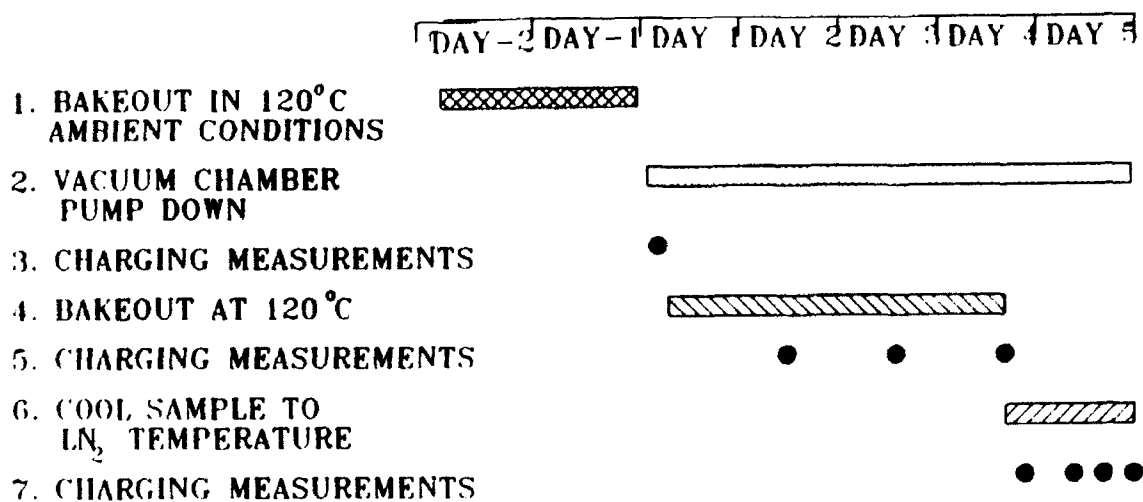


Figure 2. Timeline of test sequence.

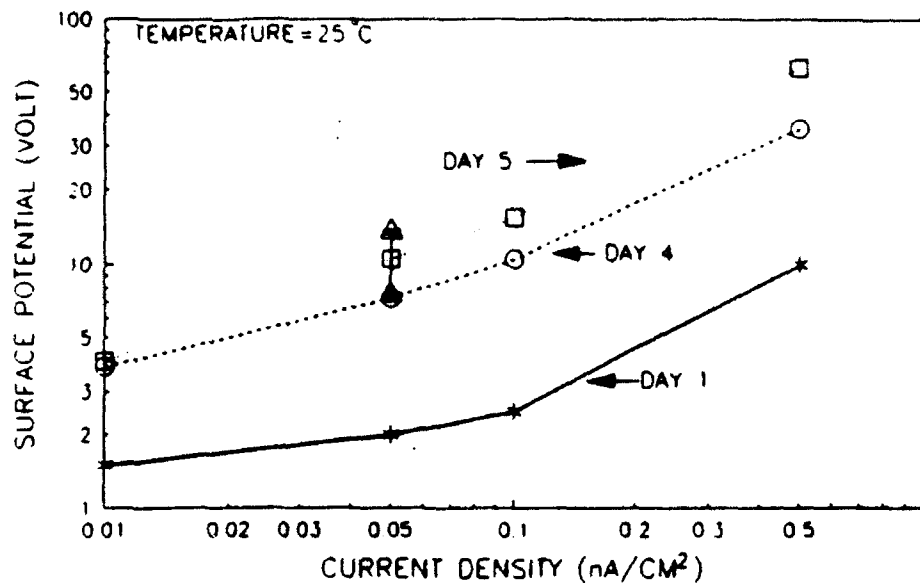


Figure 3. The surface potential of ZOT when it is irradiated by a 10 KeV electron beam at different current densities.

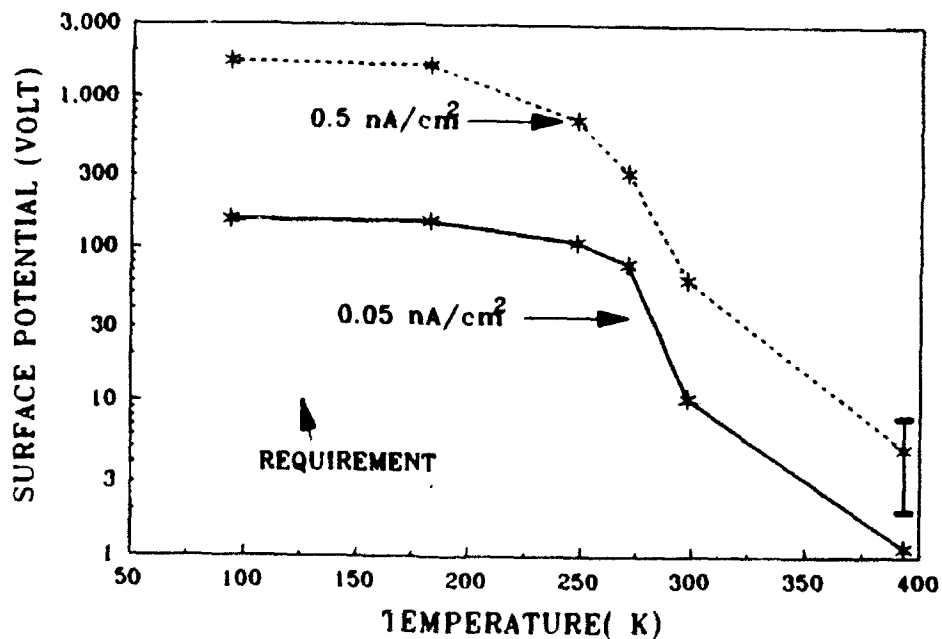


Figure 4. Surface potential of ZOT as a function of temperature at two different current densities. The dotted line indicates the Galileo surface potential requirement.

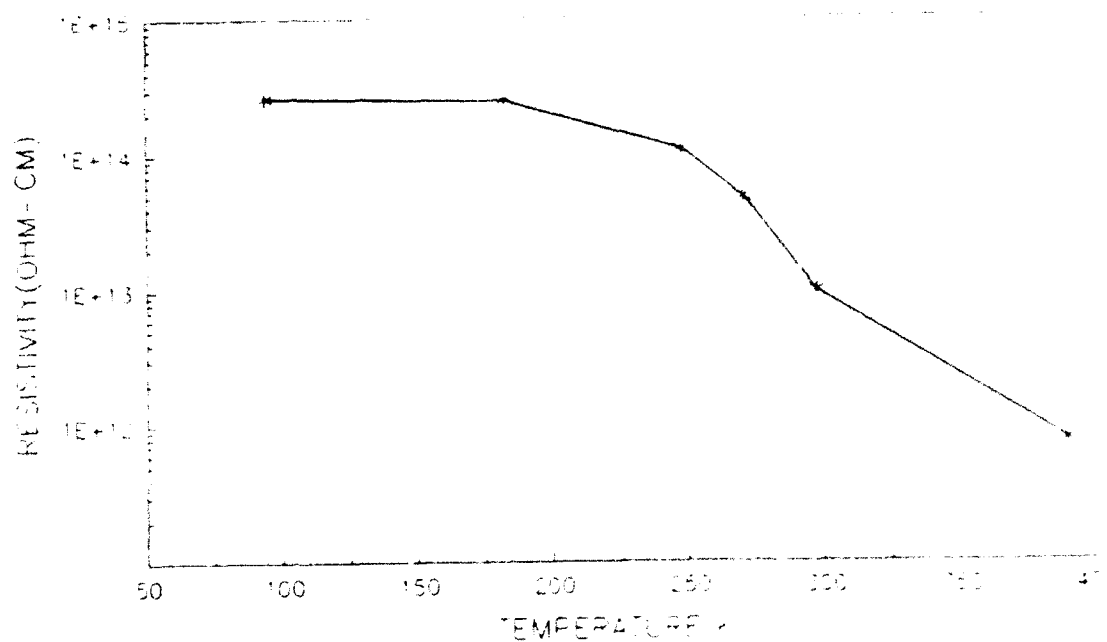


Figure 5. Resistivity of ZOT as a function of temperature.

Active Spacecraft Potential Control by Emission of Weak Ion Beams

K.M. TORKAR and W. RIEDLER

*Space Research Institute
Austrian Academy of Sciences
Inffeldgasse 12, A-8010 Graz, Austria*

R. SCHMIDT and H. ARENDS

*Space Science Department of ESA
Noordwijk, The Netherlands*

and

F. RÜDENAUER

*Austrian Research Center Seibersdorf
Seibersdorf, Austria*

State-of-the-art plasma and electric field measurements in space require that the electrostatic potential of the spacecraft body be kept close to the ambient plasma potential. In particular, the tenuous plasmas in the outer magnetosphere force the spacecraft potential to values in excess of +50 V in sunlight. For scientific spacecraft, it is advantageous or even mandatory to actively control the surface potential and maintain it close to the ambient plasma potential. This requires conductive surfaces and active control of the potential by emission of charged particles.

Two ion emitter concepts are presented that are presently under development and will be flown in the early and mid 90's on a number of scientific space missions. The saddle field ion source ionises a gaseous substance in a chamber with a particular configuration of the internal electric field. A rather complex gas flow control system is required. The liquid metal ion source is based on field emission of In^+ from a sharp tip. A cartridge containing the liquefied metal supplies indium to the tip where ion extraction due to extremely high electric field gradients takes place. This concept allows for a small and light-weight design with enough redundancy to achieve the desired lifetime.

The instruments are designed to allow control of the beam current in an on-board control loop with measurements of the spacecraft potential.

1. INTRODUCTION

Accurate low energy plasma and electric field measurements in space require that the electrostatic potential of the spacecraft body be kept close to the ambient plasma potential. In steady state a spacecraft will charge to an equilibrium potential where the sum of the currents to the spacecraft vanishes so that there is no net transfer of charge between the spacecraft and the environment (see *Grard* [1973] or *Whipple* [1981] for reviews). Outside the plasmasphere where the plasma density is low, and as long as the electron temperature is not too high (less than a few keV), current balance to a spacecraft with conductive surfaces is usually between the plasma electron current and photo-emission, and spacecraft potentials are a few volts positive. It has been shown for GEOS-2 and ISEE-1 (see e.g. *Schmidt and Pedersen* [1987] and *Lindqvist* [1983]) that the potentials for these spacecraft were determined

by the quantity $(n\sqrt{T})$, where n is the plasma electron density and T the electron temperature. In extremely low density plasmas such as in the lobes of the Earth's magnetotail, the resulting potentials can be as high as +50 V and more. Such potentials not only degrade but occasionally even render impossible cold ion and electron- as well as quasi-static electric field measurements. For scientific spacecraft it is advantageous or even mandatory to actively control the surface potential and maintain it close to the ambient plasma potential. This requires conductive surfaces and active control of the potential by emission of charged particles.

A number of methods for charge control can be envisaged (see e.g. *Pedersen et al.*, 1983). A reliable long-term behaviour, combined with realistic mass and power requirements has to be sought in the technical realisation.

This paper deals with two related experiments where high energy ion beams with emission cur-

rents of typically $10 \mu\text{A}$ are generated by two different systems: One system ionises nitrogen in a so-called saddle field ion source (SFIS) while the other one is based on a liquid metal ion source (LMIS). The instruments described in the following are presently under development and will be flown in the 90's on a number of scientific space missions with eccentric magnetospheric orbits and apogees of about $20 R_E$ and above. The basic concepts have been described by Schmidt *et al.* [1988] and Riedler *et al.* [1988]. Although the designs are widely different, they have a few common features: both instruments apply ion beams in the range 4–7 keV to reduce high positive potentials and they control the spacecraft potential by a feedback loop with on-board measurements of the potential.

2. SCIENTIFIC OBJECTIVES

A perhaps over-simplified but nevertheless basic picture of the current-voltage characteristics of a spacecraft is given in Fig. 1. It shows

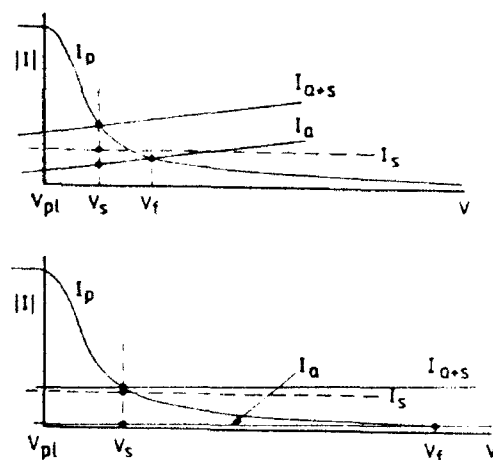


Fig. 1. Simplified current-voltage characteristics of a spacecraft, showing the effect of active ion emission in dense (top panel) and tenuous (bottom panel) plasma. V_f ... floating potential for $I_s=0$, V_s ... potential with ion emission, I_a , I_p , I_s ... ambient electron, photo-electron, and ion source currents.

the currents flowing from and to a sunlit sphere in a plasma. This figure shall, however, just illustrate the basic approach to the active control of the

spacecraft potential by an energetic ion beam, taken in the experiments described below.

The floating potential is in first approximation determined by the equilibrium between photo-electron current, the current due to incident ambient electrons and ions, and the actively emitted ion current. The photo-electron current is essentially determined by the surface properties. The mean photo-electron temperature can be assumed with about 1.5 eV [Grard, 1973]. The saturation current density is of the order of nA cm^{-2} , and the photo-current in saturation for an average size spacecraft is some $100 \mu\text{A}$. The variations of the ambient plasma current in space and time are not fully predictable. It varies with density and temperature as indicated by the top and bottom parts of the Fig. 1.

The method for active potential control in regions where the photo-electron current dominates is twofold: At first the potential must be clamped somewhere in the steep part of the photo-emission characteristics of the spacecraft. In this way the effects of irregular variations of the ambient electron current on the spacecraft potential are very much reduced. In a second step the actively emitted ion current shall be adjusted to compensate for all natural current variations and to clamp the spacecraft potential at a fixed value. The corresponding modes of operation are described in section 5.

The advantage of a controlled electrostatic environment for other experiments in the fields of low energy plasma and electric field measurements is obvious.

The feedback from on-board measurements of the spacecraft potential is a requirement for full operation of the system. It has been shown that double-probe electric field experiments such as the one flown on GEOS-2 can provide a reference at about 1 V above the local plasma potential [Schmidt and Pedersen, 1987]. Double-probe experiments will also be flown e.g. on the Interball, Geotail, and Cluster [Gustafsson *et al.*, 1988] spacecraft. Low energy electron measurements [Johnstone *et al.*, 1988] also gain from a spacecraft potential close to zero, because high positive potentials would accelerate ambient electrons too much. The distribution would become highly compressed and difficult to resolve in an analyser. Below the energy corresponding to spacecraft potential the sensor would detect photo-electrons. The spacecraft potential will appear in the energy spectrum as a minimum in the flux. This information, distributed via an on-board data link to the ion emitter experiment, can also be used for controlling the potential.

The following sections describe the technical realisation of the ion sources and the envisaged modes of operation.

3. THE SADDLE FIELD SYSTEM

3.1. The Saddle Field Ion Source. The saddle field ion source (SFIS) is a type of cold cathode source, based on the effect that electrons describe long oscillatory paths in the presence of an electrostatic saddle potential field. This configuration increases the probability for ionising the gas in the source. Pure nitrogen is used in the application described here. A discharge can be maintained at considerably lower pressure than in conventional cold cathode tubes without a magnetic field, which makes the design easier for magnetically clean scientific spacecraft. General properties of such ion sources have been described e.g. by Franks [1979]. A cross-section of the SFIS is shown in Fig. 2.

By differential pumping and by the special configuration of the SFIS a relatively high pressure of

10^{-1} to 10^{-2} mbar can be achieved that is required to maintain the discharge. At the same time scattering of the beam is avoided by a low pressure of 10^{-3} to 10^{-4} mbar in the environment. The electrostatic field has a saddle point in the centre of the source. The positive ions formed in the discharge are accelerated towards both cathodes. A beam of hot ions emerges through the cathode aperture. The ionisation efficiency of the beam is dependent on the beam current drawn. Ions accelerated to the bottom-side in Fig. 2 hit the deflecting plate and are diffused to the cylindric cathode wall. This electrode may be isolated from the housing of the emitter and serve for monitoring the beam current. The ratio between the current flowing through this electrode and the emission current is constant over a wide range of currents.

The diameter of the cathode opening is determined by a trade-off between electrical efficiency, discharge voltage, and stability of the beam in the low-current region. For a given inlet pressure a larger opening would increase the fraction of the beam current relative to the total discharge current, but also increase the discharge voltage because of the lower pressure in the discharge region. The diameter used in the present design is 1.5 mm and takes into account the gradual widening of the hole by erosion.

Fig. 3 shows the beam current which can be extracted from the source as a function of the total discharge current for some values of the gas pressure. For a fixed geometry the current efficiency increases with decreasing gas pressure, together with obvious benefits for the gas consumption. On the other hand with decreasing pressure the discharge voltage soon reaches an upper limit determined by the electrical design of the source.

The selection of suitable materials for the source was lead by the design goal of a lifetime of 5,000 hours. The major limitations encountered were erosion of the cathode disc by sputtering and subsequent deposition of sputtered material on the walls. Both processes change the electrical properties of the source. Sputtered material is likely to form thin layers at the walls which lose contact and short-circuit the source when it is subject to thermal variations. The erosion of a usual cathode after some 1,000 hours operation may also be severe. Apart from its influence on the gas flow the resulting roughness of the surface is unwanted from the stand-point of high voltage safety. In previous tests it was found that cathodes made of stainless steel were subject to unacceptably strong degradation after a few hundreds of hours operation time. A harder material (a car-

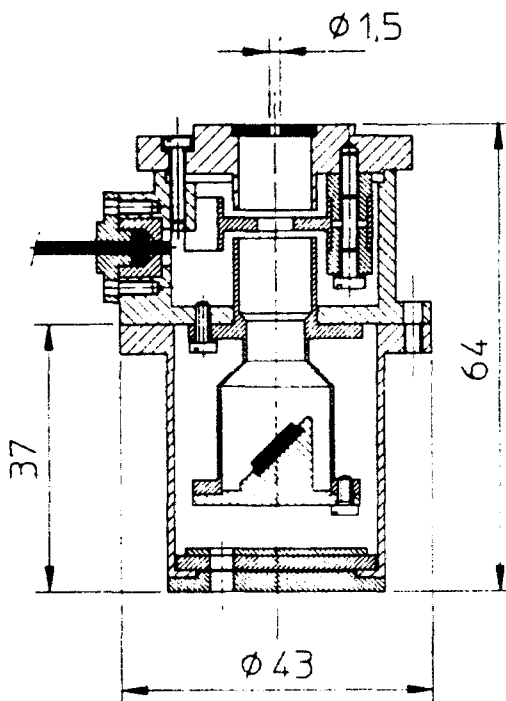


Fig. 2. Cross-section of the saddle field ion source.

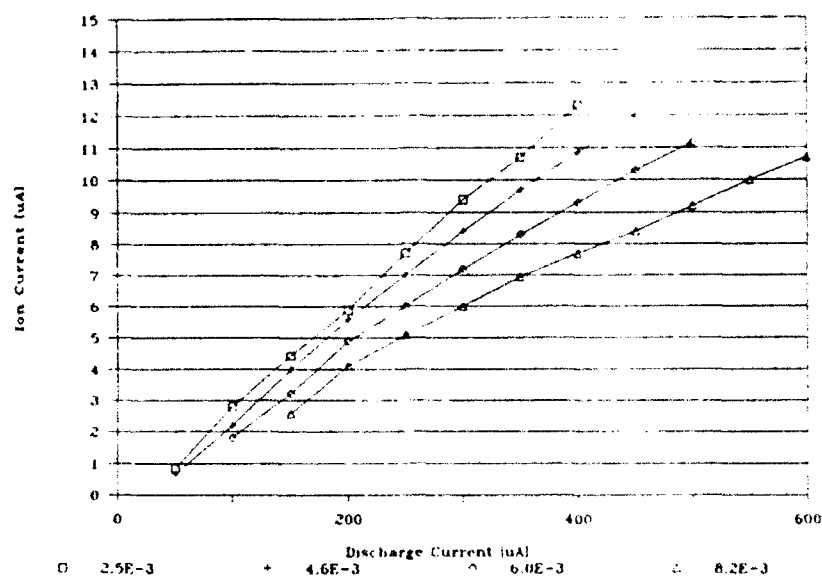


Fig. 3. Beam current extracted from the SFIS as a function of total discharge current for some values of the gas pressure (in bar).

bide) with low sputter yield was chosen for the final design of the cathode disc and the rear deflection plate. Titanium is the material used for the cathode walls to save some mass. As a side-effect the layers of sputtered material formed in a

titanium-nitrogen environment consist of a considerable fraction of titanium nitride, which in contrast to most other nitrides is conductive. This avoids the accumulation of charges on the walls and subsequent secondary effects.

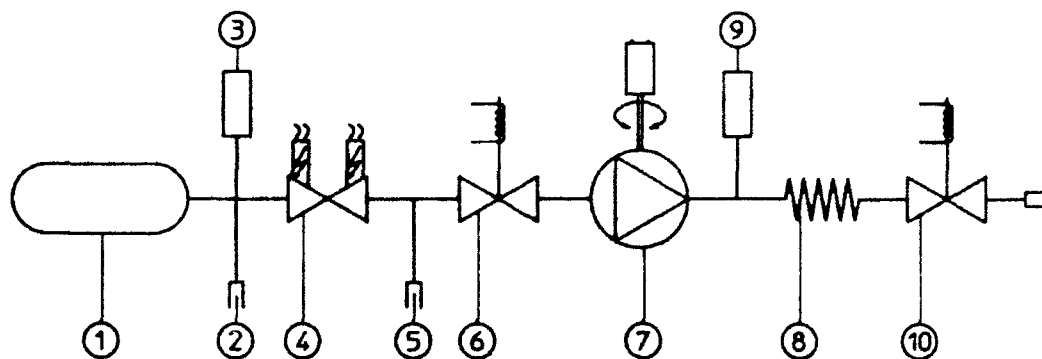


Fig. 4. Scheme of the gas flow control system for the SFIS. (1) gas bottle, (2) filling nipple, (3,9) pressure transducers, (4) pyro-valve, (5) test port, (6,10) latching valves, (7) pressure regulator, (8) constant impedance.

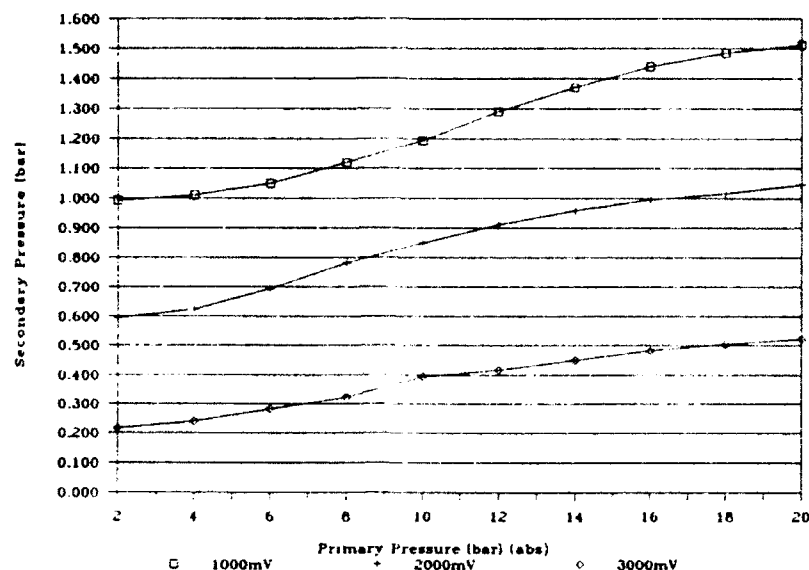


Fig. 5. Variation of secondary pressure with changing primary pressure at different settings of the pressure regulator.

3.2. The Gas Flow Control System. A gas flow control system (GFCS) had to be constructed that reduces the high gas pressure inside a bottle to a constant low value by means of a pressure regulator for very small flows. The system has been described in full detail by *Arends and Scheper* [1989]. A scheme is shown in Fig. 4.

The starting point for the design of the GFCS was the optimum gas pressure at the source, which was found to be 2.5×10^{-3} mbar, and the corresponding gas flow of $1.6 \text{ N cm}^3 \text{ hour}^{-1}$. A gas bottle (1) with 0.5 l volume, initially filled with pure nitrogen at 18 bar was found sufficient for 3,000 hours of operation.

The gas pressure is measured by two pressure transducers (3,9). Their output is used by the on-board microprocessor to adjust the pressure regulator (7). The pressure regulator will keep the secondary pressure constant almost independent of the primary pressure. Only small corrections are needed when the bottle is emptied. The valve (4) secures a hermetically sealed volume of gas and can be opened by a redundant pyrotechnic piston actuator. The latching valves (6,10) take over the function of the pyro valve after this has been activated. The drift of the secondary pressure with changing primary pressure, i.e. the supply effect of the source is depicted in Fig. 5. It amounts to 25 mbar bar^{-1} , and a few turns of the motor valve are sufficient to compensate for large variations from 18 down to 2 bar of the pressure in the gas

bottle. The effect of ambient temperature is as small as -1 mbar/K .

The most delicate element in this system is the constant impedance (8), a glass capillary with a leak-rate of $6 \times 10^{-4} \text{ mbar ltr s}^{-1}$ for air at 1 bar. The scheme in Fig. 5 gives an idea of the complexity of the system which is its major drawback. Both the SFIS and the GFCS of the engineering model have undergone the usual environmental tests (sine vibration, shock test, etc.).

4. THE LIQUID METAL ION SOURCE

4.1. Operating Principle. The alternative approach to achieve a high energy ion beam is based on the liquid metal ion source. This ion emitter is a solid needle - type liquid metal ion source, previously described in the literature using indium as charge material [*Evans and Hendricks*, 1972; *Wagner and Hall*, 1979; *Dixon and Engel*, 1980]. A solid needle, made of tungsten, with a tip radius between 2 and $15 \mu\text{m}$ is mounted in a heated reservoir containing the charge material (Fig. 6). A potential of 5–7 kV is applied between the needle and an extraction electrode. If the needle is well wetted by the metal, the electrostatic stress at the needle tip pulls the liquid metal towards the extractor electrode. This stress is counteracted by the surface tension forces of the liquid. One of the equilibrium configurations the liquid surface can assume is that of a so-called Taylor-cone [Taylor,

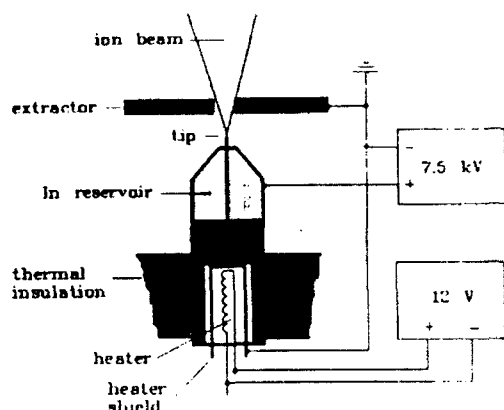


Fig. 6. Individual liquid metal ion emitter.

1964] with a total tip angle of 98.6° . The apex of the Taylor-cone in practice reaches a diameter of 1 to 5 nm [Kingham and Swanson, 1984]. The field evaporation of positively charged metal atoms in the strong apex field leads to emission of a high brightness external ion beam from this cone apex with a beam brightness of the order of $10^6 \text{ A cm}^{-2} \text{ sr}^{-1}$ at 10 keV beam energy.

Since the emission zone is in the liquid state, ions leaving the surface can be continuously replenished by hydrodynamic flow of liquid metal from the reservoir to the needle apex so that a stable emission can be maintained.

Due to the extremely high source brightness, the LMIS is particularly suited for formation of microfocused ion beams and has found wide application in microelectronic technology: ion beam lithography, writing ion implantation, ion microfabrication, and microanalysis [Rüdenauer, 1984]. The advantages of the LMIS principle are:

- low power consumption; mostly determined by the heater power to keep the indium reservoir above 429 K;
- high mass efficiency;
- compactness and low mass; one individual emitter has a volume of 170 mm^3 and a mass $< 5.2 \text{ g}$.

Indium has been chosen as ion source charge material because of its low vapour pressure. This prevents contamination of the source insulators and ambient spacecraft surfaces. On the other hand, the melting point is high enough that melting of an unheated source charge cannot occur even at the maximum expected elevated environmental temperature.

The individual emitters (Fig. 6) are of cylindrical geometry. The indium and the needle are kept at high tension. The sources are individually and indirectly heated by a thick film resistor embedded into a ceramic insulator tube. Al_2O_3 was chosen for superior high voltage insulation characteristics. This scheme enables the source to be heated from a grounded power supply and the tip itself still being kept at high voltage.

4.2. Design of the LMIS Module. Figure 7 shows the schematic design of an ion emitter module. One such module consists of an array of 5 individual ion emitters which are operated one at a time. They are mounted in a slab of porous ceramic with extremely low heat conduction ($< 5 \times 10^{-4} \text{ W K}^{-1} \text{ cm}^{-1}$). All emitters have a common extraction and focusing lens arrangement consisting of a grounded extractor electrode, a focusing electrode at beam potential and a second ground electrode. These electrodes constitute a unipotential lens with the tip apex located in one focal point. The divergent ion beam (opening angle $< 30^\circ$) emitted from the tip is focused by this lens into a nominally parallel beam after passage through the ground electrode.

Due to the wide-angle nonparaxial rays entering the electrode system, the lens aberrations actually will produce a divergence of 15° (half maximum)

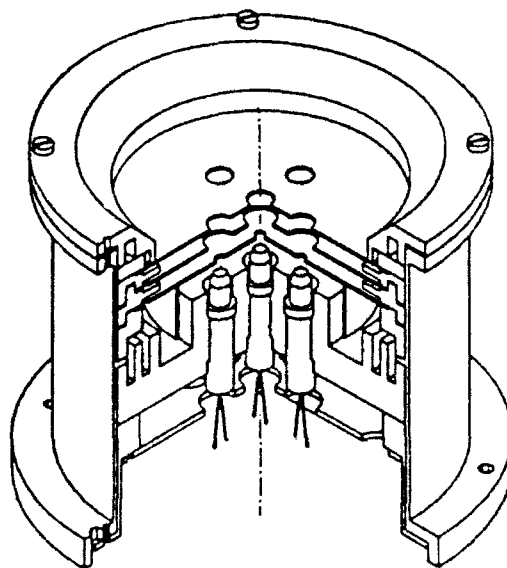


Fig. 7. Schematic of the LMIS module.

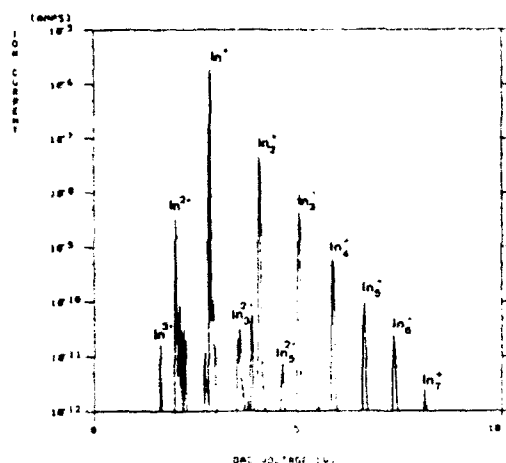


Fig. 8. Mass spectrum of the LMIS at $10\ \mu\text{A}$ extraction current.

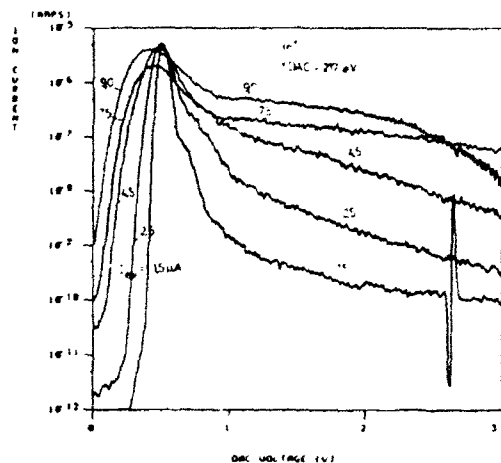


Fig. 9. Energy spectrum of the In^+ -peak with the currents at the extraction electrode as parameter ($1.5, 2.5, 4.5, 7.5$, and $9\ \mu\text{A}$).

in the outgoing beam (11). Tip and focusing electrode are on the same potential so that no additional power supply or voltage divider is required for beam focusing. Since the beam shaping and focusing optics is purely electrostatic, the lens properties and the beam shape remain unchanged if the tip voltage (which is identical to the focusing voltage) changes.

All outer surfaces are electrically connected to spacecraft ground. The cold secondary side of the high voltage supply, which is connected to the inner shield and focusing system inside the emitter housing, is floating at $<0.5\ \text{V}$ because of a beam current monitor circuit.

4.3. Performance of the LMIS module. The energy spread and the composition are important properties of the ion beam. Fig. 8 shows a mass spectrum of the extracted ion beam for typical operating conditions. Various peaks of different indium molecules and clusters with single, double and triple charges are visible, but singly charged In^+ with 115 amu dominates all other species by a factor of 40. The average charge number per emitted charged indium atom is 0.976. The emitted In^+ ion current shows some broadening of the energy spectrum with increasing currents at the extraction electrode from 1.5 to $9\ \mu\text{A}$, as shown in Fig. 9. At an emission current of $10\ \mu\text{A}$ the energy width is 150 eV, but a low intensity, low energy tail down to more than 500 eV below nominal beam energy can be expected.

Major efforts were put in the design of the thermal isolation of the source because of its immedi-

ate effect on the total power consumption. Whereas the 50-90 per cent of the energy provided by the high voltage supply that go into the emitted ion beam require $<1\ \text{W}$ primary power going into the supply, the additional power for the heating of the indium is about 0.8 W.

5. FLIGHT OPERATIONS

The operation modes in flight have to be optimized with respect to the requirements of the low energy plasma and electric field experiments and have to avoid interference with other experiments on plasma waves, high energy particles, and optical experiments. The effects on the environment must be well-defined and preferably synchronised with scans, sampling intervals etc. of other experiments. The electrical parameters of the ion beam must be known to all experimenters to facilitate their data reduction. For the same reason rapid variations of the beam current are undesirable except for very short periods of so-called active experiments as described below.

Two operation modes are foreseen on a regular basis:

In the feedback mode mentioned before a measurement of the spacecraft potential is supplied by either the electric field experiment or the low energy electron analyser and this information is then used to adjust the emission current sufficient to reduce the spacecraft potential to within some predetermined value, as described in the discus-

sion of Fig. 1. The required ion current would be the order of a few tens of μA . In the case of plasma current domination, the required emission current would be smaller.

It may be a difficult problem to use the on-board software to select either the electric field or the electron analyser data if the signals differ from each other. It is planned to analyse the first orbits and to uplink some decision rules for the on-board processor. Robustness against spurious commands and on-board memory errors is another important software requirement.

In case no on-board data on spacecraft potential from any experiment is available, the stand-alone mode involves setting the emission current to some predetermined value based on the spacecraft current-voltage characteristics, and perhaps a measure of the ambient plasma density and temperature. In this mode, the emission current must be set to a level to insure that the spacecraft potential is not driven negative. The control of the potential would not be as good in this case as in the feedback mode, but could still be used to reduce the spacecraft potential to a few volts positive relative to the ambient plasma potential.

In a so-called active mode scientific investigations of the photoelectric characteristics, dependence of the spacecraft potential on plasma parameters, and of spacecraft charging in different plasma environments can be carried out. In accordance with the scientific operation plan for the spacecraft and in agreement with other experimenters the optimum ion current will be varied in a defined way for a short time to enable the co-operating plasma experiments to calibrate their response to spacecraft potential variations between the unregulated and the clamped, near-

zero values. The current-voltage characteristics of the spacecraft will be determined as well. Such experiments will be carried out at large, but regular intervals.

If the uncontrolled spacecraft potential is negative with respect to the ambient plasma, any ion beam emission would lead to an even greater negative potential and should be avoided. In feedback mode the on-board software of the instrument will switch off the ion beam in such a case. In stand-alone mode the beam current should be set to a predetermined value derived from theoretical considerations and preceding in-flight tests. This value can be preprogrammed to vary according to the expected plasma environment along the trajectory including a safety margin to avoid beam-induced negative charging under abnormal conditions.

6. DISCUSSION

6.1. Comparison of the SFIS and LMIS systems. The main instrument data are listed in Table 1. The first column contains the numbers for a combined SFIS-LMIS instrument to be flown on an Interball spacecraft. Its mass and power are governed by the requirements of the gas system. The second column is for the experiment flown on Cluster (ASPOC, Fig. 10), which contains two independent LMIS modules for redundancy or for an extended operation time.

The SFIS has a low efficiency (3-5 per cent) and a requirement for short-time power to operate the valves. The LMIS has a higher efficiency in the high voltage circuit itself: about 50-90 per cent of the total current go into the beam, the remaining fraction is diverted to the focusing system.

Experiment Name Spacecraft Ion Sources	RON Interball SFIS + LMIS	ASPOC Cluster 2 LMIS
Mass [kg]	7.5	1.5
Size [mm]	300x250x250	180x125x140
Power (max.) [W]	10.5	3
Telemetry Rate [bit s ⁻¹]	20-200	100
Beam Opening Angle [deg]	± 10	± 15
Design Lifetime [h]	10,000	10,000
Ion Species	N ₂ ⁺ , In ⁺	In ⁺

Table 1. Instrument data summary.

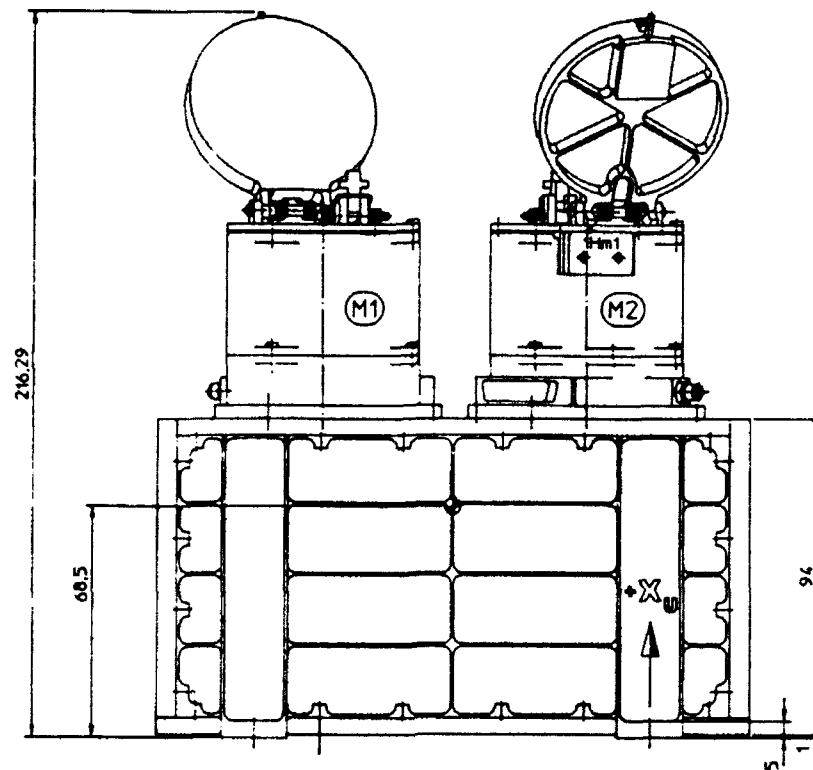


Fig. 10. Drawing of the experiment ASPOC (Cluster spacecraft) with two LMIS modules on top of an electronics box.

However, additional heating power for the charge material is required (typically 600 mW).

The other major differences between SFIS and LMIS beyond mass and power resources relate to the ion species, chemical cleanliness, and ground operations.

6.2 Electromagnetic Compatibility. Any harmful effect on any other experiment by actively controlling the spacecraft potential is unlikely if the emission current is kept within reasonable limits. However, the necessity of operating the emitter in close consultation with all the other experimenters is acknowledged.

The emission of a charged particle beam into a plasma is a potential source of electromagnetic noise. The extent of this possibility for the present applications is not yet well understood, especially since a dedicated active potential control experiment using an ion beam has not yet been operated on a spacecraft. Theoretical work on the triggering of activity by beams with current densities as low as in the present experiments and at 4–7 keV is practically non-existent in the literature. Ion beams with two orders of magnitude higher cur-

rent densities were injected into the ionosphere and generated waves around the lower hybrid resonance frequency. Other experiments found increased emission in the magnetic field around the local electron cyclotron frequency. In this case the electric field antenna did not measure any effect. It is known that a small opening angle of a beam tends to increase the probability of wave generation. For this reason the beam focusing system is designed for a large opening angle of 15° half width.

6.3. Chemical Contamination by the Ion Beam. Chemical interaction that could be considered as potential concerns to the spacecraft or instruments covers:

- condensation of neutral indium in the vicinity of the LMIS emitter,
- return of ions to the spacecraft after one or more gyrations,
- interaction of the ion beam with spacecraft surfaces.

The condensation of neutral indium on cold surfaces is extremely unlikely. The vapour pressure of indium is only 1.1×10^{-19} Torr at the melt-

ing point and the total surface from which indium evaporates is in the order of 1 mm^2 for the active, hot emitter and about 9 mm^2 for the surfaces at the environmental temperature. Neutrals that penetrate through the orifice are expected to drift freely into the ambient plasma. Their return to the spacecraft skin can only occur through two processes which have been found very unlikely [Riedler *et al.*, 1988]: collision with other neutrals and photo-ionisation.

6.4. **Constraints.** The advantage of low mass and high efficiency of the LMIS is balanced by some constraints for active ion beam emission and handling on ground. It is not possible to operate the LMIS at total pressures $> 3 \times 10^{-6}$ Torr for extended time periods (> 1 hour), and the LMIS must be stored in dry nitrogen to avoid oxidation. This makes the instrument subject to similar purging requirements as for a number of other experiments. A third constraint, namely the restriction to control only positive spacecraft potentials, applies to both positive ion sources and has been mentioned in section 5.

7. SUMMARY

Two widely different designs for ion sources to control the spacecraft potential have been presented along with a short description of their application in two instruments and the anticipated modes of operation. Each system has its advantages. The first test in orbit with both systems combined into one instrument is to be carried out in the early nineties. Experience collected in this mission will help to improve the design and operation of the LMIS system that has been selected for the Cluster spacecraft.

REFERENCES

- Arends, H. and R. Scheper, Gasflow Control System for Very Low Gasflows to Maintain a Constant Pressure in a Saddle-Field Ion-Source, *Internal Report, SSD of ESA/ESTEC*, Noordwijk, The Netherlands, 1989.
- Dixon, A.J. and A. von Engel, Studies of Field Emission Gallium Ion Sources, *Inst. Phys. Conf. Ser.* 54, 292, 1980.
- Evans, C.A.Jr. and C.D. Hendricks, An Electrohydrodynamic Ion Source for the Mass Spectrometry of Liquids, *Rev. Sci. Instrum.* 43, 1527, 1972.
- Franks, J., Properties and Applications of Saddle-Field Ion Sources, *J. Vac. Sci. Technol.*, 16 (2), 181, 1979.
- Grard, R.J.L., Properties of the Satellite Photoelectron Sheath Derived From Photoemission Laboratory Results, *J. Geophys. Res.* 78, 2885, 1973.
- Gustafsson, G., C. Cattell, J.-P. Lebreton, C.-G. Fälthammar, H. Singer, P. Tanskanen, A. Egeland, T. Aggson, L.J.C. Woolliscroft, A. Roux, D. Gurnett, P. Décréau, P. Kintner, C. Harvey, P. Kellogg, S. Klimov *et al.*, The Spherical Probe Electric Field and Wave Experiment, *ESA SP-1103*, 31, 1988.
- Johnstone, A., A.J. Coates, D.S. Hall, B.N. Mæhlum, S.J. Schwartz, M. Thomsen and J.D. Winningham, 'PEACE' - A Plasma Electron and Current Experiment, *ESA SP-1103*, 77, 1988.
- Kingham, D.R. and L.W. Swanson, Mechanics of Ion Formation in Liquid Metal Ion Sources, *Appl. Phys.* A34, 123, 1984.
- Lindqvist, P.-A., The Potential of ISEE in Different Plasma Environments, in: "Spacecraft Plasma Interactions", Proc. 17th ESLAB Symposium, Noordwijk, The Netherlands, *ESA SP-198*, 25, 1983.
- Pedersen, A., C.R. Chapell, K. Knott and R.C. Olsen, Methods for Keeping a Conductive Spacecraft Near the Plasma Potential, in: "Spacecraft Plasma Interactions", Proc. 17th ESLAB Symposium, Noordwijk, The Netherlands, *ESA SP-198*, 185, 1983.
- Riedler, W., R. Goldstein, M. Hamelin, B.N. Mæhlum, J. Troim, R.C. Olsen, A. Pedersen, R.J.L. Grard, R. Schmidt, F. Rüdener, W. Steiger, R. Torbert, K.M. Torkar, N. Valavanoglou and E. Whipple, Active Spacecraft Potential Control - An Ion Emitter Experiment, *ESA SP-1103*, 95, 1988.
- Rüdener, F.G., Liquid Metal Ion Sources For Scanning SIMS, *Secondary Ion Mass Spectrometry; SIMS IV*, Eds.: A. Benninghoven *et al.*, Springer Verlag, Berlin, 133, 1984.
- Schmidt, R., H. Arends, N. Nikolaizig and W. Riedler, Ion Emission to Actively Control the Floating Potential of a Spacecraft, *Adv. Space Res.* 8 (1), 187, 1988.
- Schmidt, R. and A. Pedersen, Long-Term Behaviour of Photo-Electron Emission From the Electric Field Double Probe Sensors on GEOS-2, *Planet. Space Sci.* 35, 61, 1987.
- Taylor, G.I., Disintegration of Water Drops in an Electric Field, *Proc. Royal Soc. (London)* A280, 383, 1964.
- Wagner, A. and T.M. Hall, Liquid Gold Ion Source, *J. Vac. Sci. Tech.* 16, 1871, 1979.
- Whipple, E.C., Potentials of Surfaces in Space, *Rept. Prog. Phys.* 44, 1197, 1981.

Plasma Sources for Active Charge Control

V. A. Davis and I. Katz

S-CUBED Division of Maxwell Laboratories, Inc., La Jolla, California

Spacecraft surfaces develop high potentials when the spacecraft is in the presence of a hot plasma or when the spacecraft is actively biased. Potential differences between the spacecraft and the surrounding plasma and between spacecraft surfaces can interfere with the mission by disturbing instrument measurements, causing surface breakdown, or enhancing surface erosion. A plasma source is an active device that reduces the potentials. The high-density, low-temperature plasma emitted by a plasma source provides the particles needed to discharge insulating surfaces. Additionally, applied potentials of tens of volts can generate ampere-level currents through the quasi-neutral plasma plume. The direction and amplitude of current flow is determined by the balance of the barometric and electric field forces on the electrons. When a plasma source operates as an electron emitter, the barometric force is stronger and the net electron current flow is opposite the electric field force. When the source is collecting electrons and the applied potential is too high for the plasma to remain quasi-neutral throughout space, a nonneutral region known as a double layer forms to separate the quasi-neutral plasma plume from the ambient plasma.

INTRODUCTION

Charge can accumulate on the surfaces of a spacecraft embedded in the plasma environment of earth orbit when the spacecraft is in the presence of a hot plasma, or when the spacecraft is actively biased. Potential differences due to charge accumulation can interfere with the spacecraft mission by disturbing instrument measurements, enhancing surface erosion, or causing surface breakdown. Active control of spacecraft surface potentials can reduce or, in some cases eliminate, these problems. Plasma sources act as plasma contactors by providing a path for low-impedance current flow between spacecraft surfaces and the ambient plasma environment.

The potential on a spacecraft surface is determined by the net current flow to the surface. The major components of the net current are summarized in Figure 1. The floating potential of a surface in a given environment is the potential at which no net current flows to the surface. Electrons and ions impinge on any surface in a plasma. As electrons are faster than ions of equal energy, in the absence of significant photoelectron or secondary electron currents, surfaces accumulate excess negative charge. When a surface reaches a negative potential a few times the electron temperature, nearly all of the electrons are repelled so that the electron and ion currents balance. In sunlight, photoelectrons usually dominate the current. Sunlit surfaces float a few volts positive in order to retain the photoelectrons. The secondary and backscattered electron currents reduce the net current to the surface. For plasma with effective plasma temperatures below 30 keV, the secondary yield of most spacecraft materials is high enough that the surface floating potential remains near the plasma potential (Mullen, *et al.* 1986; Katz *et al.*, 1987; Katz *et al.*, 1986). Different materials have different secondary, backscatter, and photo electron yields. Some surfaces are sunlit while others are in eclipse. The thickness and conductivity of surfaces

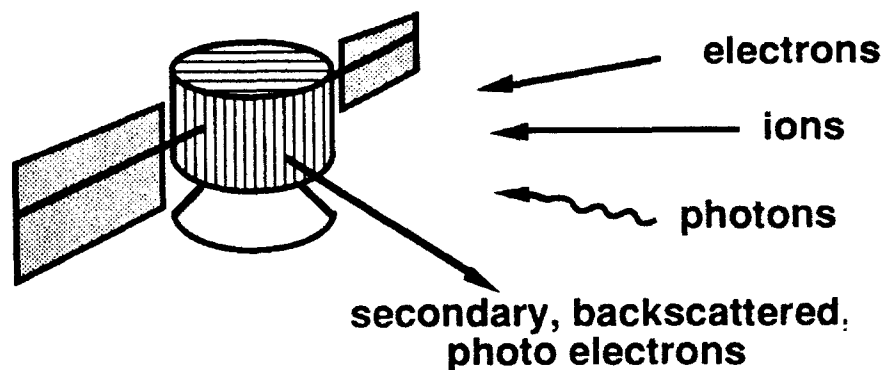


Fig. 1. The major components of current to spacecraft surfaces. The floating potential of a surface is the potential at which there is no net current to the surfaces.

vary. As each surface has different properties, each surface has a different floating potential. Differences in surface potentials and differences from plasma ground can interfere with the spacecraft mission.

Various active processes such as the emission of particle beams and the biasing of spacecraft surfaces can lead to the development of large potentials on spacecraft. Other processes such as the operation of an electrodynamic tether require the exchange of charged particles with the environment in order to complete a circuit and allow current to flow. Some of these processes are shown in Figure 2.

An electrodynamic tether system is composed of a spacecraft connected to a subsatellite by a conducting tether. The motion of the tether through the earth's magnetic field generates a potential difference between the spacecraft and the subsatellite with the upper body at a higher potential. If electrons are collected at the upper body and emitted at the lower body, a current will flow through the tether. This current can provide electrical power to the spacecraft at the expense of orbital energy. Current can also be forced to flow in reverse in order to convert electrical energy generated on board the spacecraft, such as from solar arrays, to orbital energy. In order for a current to flow, electrons must be collected

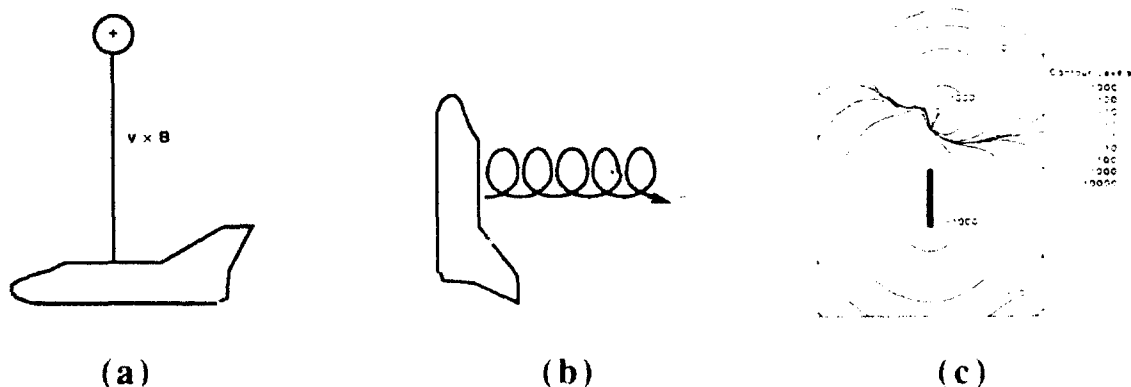


Fig. 2. (a) The operation of an electrodynamic tether. (b) the emission of particle beams, and (c) the biasing of exposed spacecraft surfaces are processes that actively charge spacecraft.

from, and emitted to, the ambient plasma. A plasma source is a versatile plasma contactor as current can flow either way through the plasma cloud.

A spacecraft emitting an electron or ion beam can achieve substantial potentials. As with natural charging, the spacecraft will accumulate charge and the potential will rise until the net current is zero. The three primary contributions to the current are the emitted beam current, the collected sheath current, and the beam current that is attracted back to the spacecraft. For beam currents high compared with the sheath current at the beam potential, the potential rises to or above (Mandell and Katz, this proceedings) the beam potential and nearly all the beam current returns to the spacecraft. A plasma source provides another current to balance the beam current and can be used to maintain a beam-emitting spacecraft near plasma ground.

The ground potential on spacecraft adjusts to the potential at which no net current flows from the plasma. When a spacecraft has exposed biased surfaces, some surfaces float positive and some float negative. Complicated sheath geometries develop (Katz *et al.*, 1989), which may interfere with the desired operation of the spacecraft. A plasma source can maintain a given part of the spacecraft near plasma ground and therefore sets the spacecraft potential with respect to the plasma.

OTHER ACTIVE POTENTIAL CONTROL TECHNIQUES

The immediately obvious way to increase the flow of electrons (or ions) from a spacecraft to the environment is to use an electron (ion) source such as a hot wire or an electron (ion) gun. As shown in Figure 3a, for spacecraft entirely covered with conducting surfaces connected to a common ground, a nonneutralized charged particle source can maintain the spacecraft at plasma ground. Typically, spacecraft do not only have conducting surfaces but also have large areas of insulating surfaces, such as thermal blankets and glass coverslips over solar cells. In the presence of a hot plasma, both the conducting and insulating surfaces can accumulate a net negative charge. As an electron beam cannot discharge a negatively charged insulating surface, the conducting surfaces are near plasma ground and the insulating surfaces are at elevated potentials as illustrated in Figure 3b. When a nonneutralized charged particle source is used on an initially grounded spacecraft, such as during an electron or ion beam experiment, the insulating surfaces remain at plasma ground and the conducting surfaces are at elevated potentials. In both cases, the differential potentials can interfere with spacecraft operations.

When large areas of the spacecraft surface are insulating and an unneutralized charged particle source is used to maintain the spacecraft at plasma ground, potential barriers that prevent the escape of the emitted particles can form. This effect is illustrated in Figure 4. The figure shows potential contours around a "quasi-spherical" object. The calculation is a 3-dimensional NASCAP/LEO (Mandell *et al.*, 1982; Katz *et al.*, this proceedings) computation of the potentials about the 26-sided object. Most of the surfaces are at -5 kV. A conducting surface that is emitting electrons is represented by a single side of the object at -1 kV. The figure shows a slice through the grid. The gray area is the object. On the -1 kV surface, the electric field points away from the object. Electrons will be attracted back to this surface even though the entire object is negative with respect to plasma ground. Potential barriers have been observed to prevent the escape of electrons under space conditions on ATS-6 (Olsen, 1985).

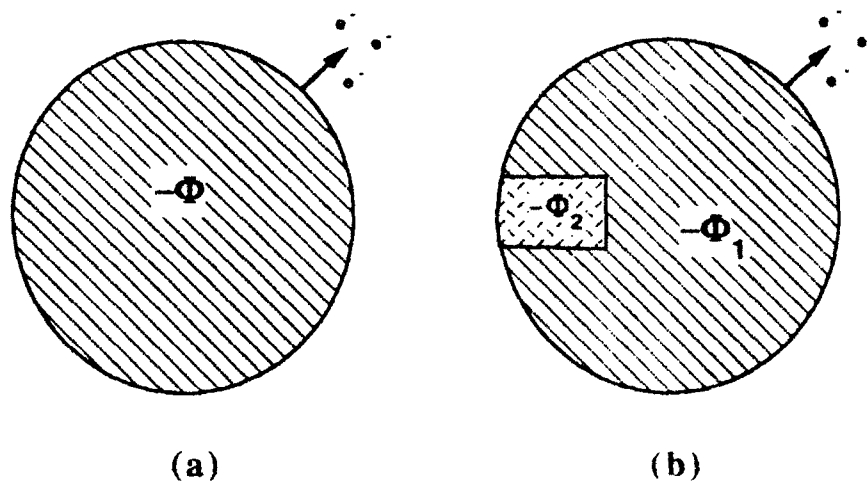


Fig. 3. An active electron source can discharge a negatively charged completely conducting spacecraft, but insulating surfaces are not discharged. Differential potentials are enhanced.

For some active experiments, large current flows are desired. When electrons are emitted from a positively charged spacecraft (resulting in an increase in potential), the electrons are emitted into an electron-rich sheath as illustrated in Figure 5a. For ampere-level currents, kilovolt electron guns are needed. Figure 5b shows emission of an electron beam from a negatively charged spacecraft (reducing the overall potential) into an ion-rich sheath. The positive charge within the sheath helps neutralize the beam and reduces the beam energy required. Even under these conditions, large currents require substantial voltages.

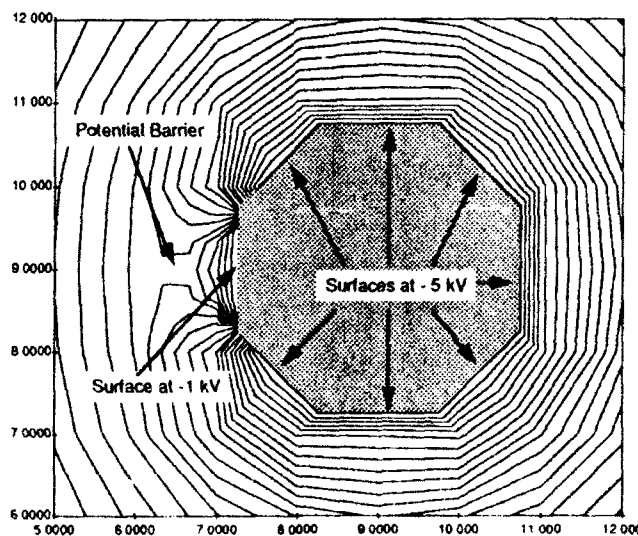


Fig. 4. Potentials around a 26-sided object. The gray area is the object. The figure shows a slice through a 3-dimensional grid. One surface is at -1 kV and the rest are at -5 kV. A 1 kV potential barrier prevents the escape of lower energy electrons from the -1 kV surface. The contour levels are drawn at 200 V intervals. A mesh unit is 0.2 m and the debye length is 1 m.

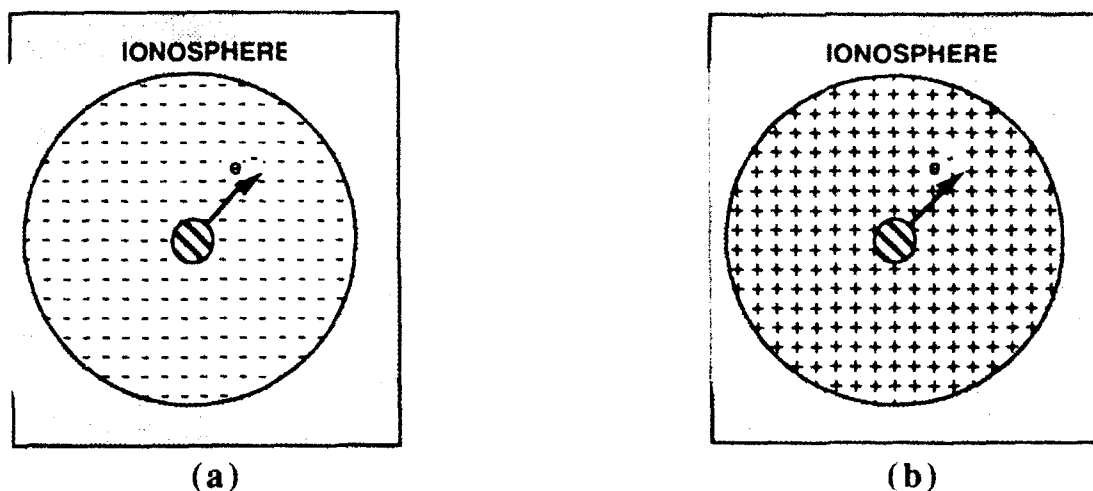


Figure 5. (a) Electrons emitted from a positively charged spacecraft are emitted into a negatively charged sheath. (b) Electrons emitted from a negatively charged spacecraft are emitted into a positively charged sheath. The sheath ions help neutralize the beam. In either case, thousands of volts are required for ampere currents.

PLASMA SOURCES - PHYSICAL MECHANISMS

Plasma sources have been observed to effectively discharge spacecraft surfaces in space. Olsen (1985) describes clear evidence for the discharging of ATS-6 by ion engines and ion engine neutralizers. ATS-6 was discharged from -3 kV to near zero in eclipse and from -45 V to less than -3 V in sunlight. Collaborating evidence has been obtained from other spacecraft.

The primary characteristic of plasma sources that makes them excellent at discharging spacecraft surfaces is the generation of a high-density ($10^{17}/\text{m}^3$), low-temperature (1 eV) plasma. As illustrated in Figure 6, the plasma provides particles of both signs to discharge the surfaces of insulators on the spacecraft. The discharging of insulating surfaces eliminates potential barriers and reduces the differential charging of surfaces. The low temperature of the high-density plasma reduces the floating potential of the surfaces.

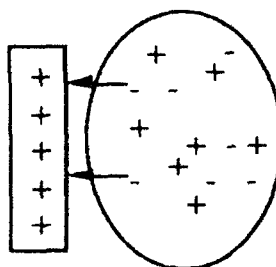


Fig. 6. The high-density, low-temperature plasma generated by a plasma source discharges surfaces.

A plasma source emits both electrons and ions. Electrons carry the current between the spacecraft and the ambient plasma. The slow-moving ions neutralize the space charge so that the electrons can flow freely. As long as the potentials are not too high, the plasma cloud is quasi-neutral throughout. In a quasi-neutral argon plasma at equilibrium, the thermal electron current is 270 times the thermal ion current. If the electrons are hotter than the ions, as is the case for plasmas created by hollow cathodes, the thermal electron current is even larger. If an expanding plasma has a density of $10^{11}/\text{m}^3$ and a temperature of 1 eV at 28 cm from the source, the plasma can carry an electron current of up to 270 mA and an ion current of 1 mA or a net current of up to 269 mA toward the source through the 28 cm radius spherical surface surrounding the source (or up to 271 mA away from the source if electrons are available from the ambient plasma).

The amount of argon gas needed to sustain this plasma plume is minimal. If the process of ionization of the argon gas to create the ions is only 1 percent efficient, 30 kg/year of argon is needed to emit 270 mA of electrons. Both sources with ionization efficiencies of 50 percent and devices that allow the plasma source to be turned on only when needed have been constructed (Williamson *et al.*, this proceedings). When a high efficiency source is used, the gas needed to maintain current flow is not an important design constraint.

The mechanism for current flow through the plasma plume can be illustrated with an examination of the no current flow case. As Figure 7 shows, particles flow from regions of higher density to regions of lower density. The electrons move faster and therefore reach the regions of lower density faster. This current flow leaves an excess of positive charge, which retards the electrons. When there is no net electron current flow, the net force on the electrons is zero. Treating the electrons as a fluid, and balancing the pressure force with the electrostatic force, this criteria gives

$$\theta \nabla n - en \nabla \phi = 0 \quad (1)$$

which gives

$$n_e = n_0 e^{\phi/\theta} \quad (2)$$

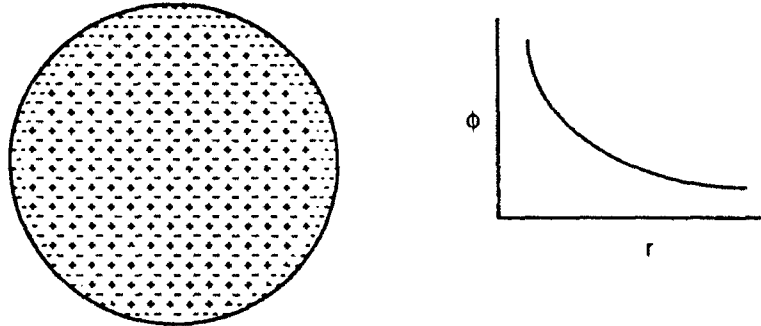


Fig. 7. Electrons flow from regions of high density to regions of low density. The resulting charge separation gives rise to the retarding barometric potential.

The variation in plasma density results in a barometric potential that is positive in regions of higher particle density. If the potential at the source is higher than the barometric potential, electron current will flow toward the source. If the potential at the source is lower than the barometric potential, electron current will flow away from the source.

Figure 8 illustrates how small perturbations from the barometric potential generate large current flows. The source emits 800 mA of electrons into a $10^{11}/\text{m}^3$, 0.1 eV plasma. The thermal current in the ambient is 10^{-3} A/m^2 . The sheath size through which the 800 mA of current will flow is 8 m in radius. The plasma density 3 cm from the source is $10^{17}/\text{m}^3$, the ion temperature is 0.1 eV, and the potential is 20 V. Ions expanding from this point have a density of $10^{11}/\text{m}^3$ 8 m away. The electron current at 3 cm for 5 eV electrons (typical near hollow cathode plasma sources) is 6000 A/m^2 . For the current flow at 8 m to be 800 mA, a net current of 70 A/m^2 , or 1 percent of the total thermal current, flows through the 3 cm surface.

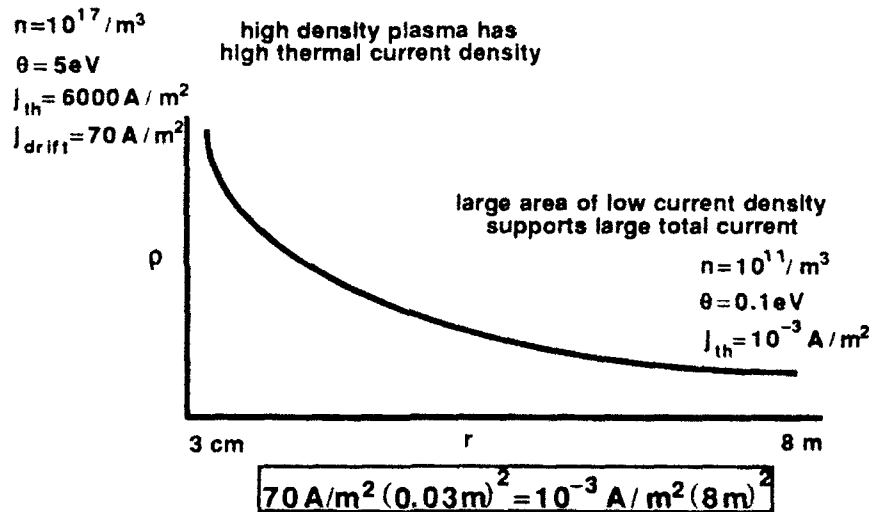


Fig. 8. A high-density plasma can support a high-thermal current density. After expansion, the large area of low-current density supports a high total current.

When the barometric pressure dominates electron flow, the net electron flow is from regions of higher potential to regions of lower potential. The potential variation near a hollow cathode plasma source is shown in Figure 9a. The potential is negative near the orifice. In the vicinity of the keeper, where ionization is taking place, the plasma density is high and therefore the potential is elevated. As the plasma expands, the barometric potential drops to zero as the source plasma blends into the ambient. Early measurements of the plasma in the vicinity of electron-emitting plasma sources appeared to show a resistive force as seen in Figure 9b. Recent potential measurements show the shape shown in Figure 9a (Williams and Wilbur, 1989). The reason for the discrepancy is that potential measurements near the potential peak are difficult because emissive probe measurements can be misleading in regions of high-plasma densities (Wilbur, private communication).

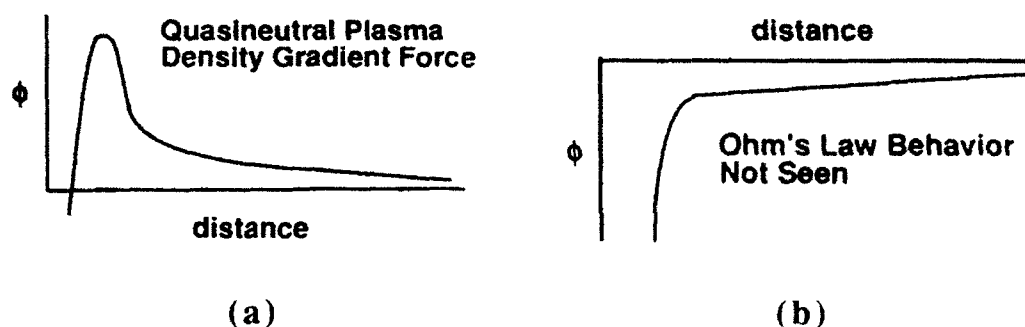


Fig. 9. (a) Potential variation in the vicinity of an electron-emitting plasma source. Electron motion is determined by the balance of the density gradient force and the electrostatic force. (b) The plasma does not act as a resistor.

When the potential is above the barometric potential, the net electron flow is toward the source. The ions still flow outward. When the ambient plasma is not a significant source of electrons, the maximum current available is the ion current. However, when the ambient plasma is dense enough, the ambient thermal current is attracted to the plasma source. For small potentials, quasi-neutrality can be maintained between the ions from the source and the electrons attracted from the ambient. At higher potentials, quasi-neutrality cannot be maintained everywhere and a double layer forms between the source plasma and the ambient plasma as illustrated in Figure 10 (Wei and Wilbur, 1986). A double layer is composed of two charge layers across which there is a sharp potential drop. On both sides of the double layer, the plasma is quasi-neutral and the potential varies slowly.

When the potential across the double layer exceeds the ionization potential of the gas emitted by the source, electrons attracted from the ambient plasma ionize neutral gas from the source. When enough gas is present and the potential is high enough, the sheath ionization provides the bulk of the plasma. The operation of a hollow cathode plasma source in this manner is known as the "ignited mode" (Patterson, 1987).

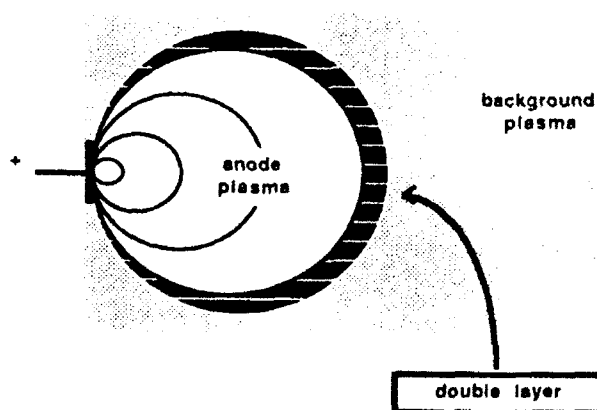


Fig. 10. When the applied potential is too high for quasi-neutrality to be maintained throughout the plasma, a localized nonneutral region known as a double layer forms. The anode plasma can be created by the plasma source or by sheath ionization.

The CHARGE-2, ECHO-7, and SPEAR I rockets all observed abrupt potential drops when thruster firings occurred during high potential operations (Neubert *et al.*, this proceedings; Raitt *et al.*, this proceedings; Malcolm *et al.*, this proceedings). It is believed that ambient electrons attracted by the high potentials (or in the case of SPEAR I, secondary electrons accelerated by the high potentials) ionized the neutral gas from the thrusters. Under these conditions, the thrusters were plasma sources that grounded the spacecraft to the ambient plasma. The amount of gas typically emitted by thrusters is orders of magnitude more than the minimum needed to sustain ampere current flows (Davis *et al.*, 1990).

CONCLUSION

The reliable operation of spacecraft sometimes requires the active control of surface potentials. Plasma sources provide a flexible means to minimize the potentials on spacecraft surfaces. The high-density, low-temperature plasma emitted provides particles that discharge the insulating surfaces of the spacecraft, eliminating potential barriers. The net current flow is toward or away from the spacecraft as needed. When the plasma source is used as an electron collector with low potentials or as an electron or ion emitter, quasi-neutrality is maintained throughout the plasma plume. The net current flow is determined by the balance of the density gradient forces and the electrostatic force. When the current flow is primarily due to electron flow away from the source, the electrons flow from a region of high potential to a region of low potential. This flow is dominated by the barometric pressure. When the potential at the source is too high to maintain quasi-neutrality throughout space, a double layer forms between the source plasma and the ambient plasma.

Acknowledgements. The authors thank Dr. Myron J. Mandell for his invaluable help during the preparation of this manuscript. This work was supported by NASA Lewis Research Center, Cleveland, Ohio, under contract NAS3-23881.

REFERENCES

- Davis, V. A., I. Katz, and M. J. Mandell, Plasma contactor modeling with NASCAP/LEO: extending laboratory results to space systems, AIAA paper 90-0726, January, 1990.
- Katz, I., M. Mandell, G. Jongeward, M. S. Gussenhoven, The importance of accurate secondary electron yields in modeling spacecraft charging, *J. Geophys. Res.*, *91*, 13,739, 1986.
- Katz, I., M. Mandell, J. C. Roche, and C. Purvis, Secondary electron generation, emission and transport: effects on spacecraft charging and NASCAP models, *J. Electrostatics*, *20*, 109, 1987.
- Katz, I., G. A. Jongeward, V. A. Davis, M. J. Mandell, R. A. Kuharski, J. R. Lilley, Jr., W. J. Raitt, D. L. Cooke, R. B. Torbert, G. Larson, and D. Rau, Structure of the bipolar plasma sheath generated by SPEAR I, *J. Geophys. Res.*, *94*, 1450, 1989.
- Mandell, M. J., I. Katz, and D. Cooke, Potentials on large spacecraft in LEO, *IEEE Trans. Nucl. Sci.*, *NS-29*, 1584, 1982.
- Mullen, E. G., M. S. Gussenhoven, D. A. Hardy, T. A. Aggson, B. G. Ledley, and E. Whipple, SCATHA survey of high-level spacecraft charging in sunlight, *J. Geophys. Res.*, *91*, 1474, 1986.
- Olsen, R. C., Experiments in charge control at geosynchronous orbit--ATS-5 and ATS-6, *J. Spacecraft*, *22*, 254, 1985.
- Patterson, M. J., Hollow cathode-based plasma contactor experiments for electrodynamic tether, AIAA paper 87-0571, January, 1987.

Wei, R., and P. J. Wilbur, Space-charge-limited current flow in a spherical double sheath, *J. Appl. Phys.*, 60, 2280, 1986.

Williams, J. D., and P. J. Wilbur, Ground-based tests of hollow cathode plasma contactors, Proceedings of Third International Conference on Tethers in Space Toward Flight: 17-19 May, 1989, San Francisco, Calif., pp. 77-87.

POLAR CODE SIMULATION OF DMSP SATELLITE AURORAL CHARGING

David L. Cooke,
M. S. Gussenhoven, David A. Hardy,
Air Force Geophysics Laboratory, Hanscom AFB, MA, 01731

Maurice Tautz, Radex Inc, Bedford MA, 01731

Ira Katz, Gary Jongeward, John R. Lilley Jr.,
Scubed, LaJolla CA, 92038

A study of the charging of the DMSP satellites by auroral electrons is conducted by comparison of numerical simulation, POLAR code, with observations of charging on the DMSP-F6 and F7 spacecraft. These observations have shown that the combined condition of low plasma density and high electron flux will allow charging, with a maximum reported spacecraft ground potential about -1.5 kV. POLAR is a three dimensional Fortran code that solves the Poisson-Vlasov system for self-consistent steady state plasma density and currents around a charged spacecraft. Comparisons have been made between POLAR results and three observations representing distinct parameter regimes. For the one observation where environmental parameters were within POLAR's nominal capabilities, the modeled frame potential of -220 Volts, agreed very well with the observed -215 Volts. Two other observations were chosen to test POLAR on its limits for low plasma density, and low potential charging; producing bad and reasonable agreement respectively. Code results also show significant differential charging due to ram-wake effects, and an effect of spacecraft size and design on charging.]f1

1. Introduction

The charging of satellites in polar orbit by auroral electrons has been a topic of interest and debate for some time. The relative high density of the Low Earth Orbit (LEO) plasma originally led some to believe that LEO charging would be negligible compared to that observed in Geostationary Orbit (GEO). This early anticipation has been confronted by direct observation of hundreds of volts of negative charging on both the DMSP-F6 and -F7 spacecraft [Besse, 85; Gussenhoven et.al., 85] with a maximum of -1.5 kV observed so far (unreported observation). Although this is

less than the charging levels observed at GEO, it is significant, and the possibility for higher levels of charging on other systems cannot be precluded without reference to some model or theory.

The Air Force Geophysics Laboratory has sponsored the development of a charging analysis code, POLAR (POtential of Large Spacecraft in the Auroral Region), to specifically study auroral charging. It is essential that any model or theory be tested against observation, and the DMSP data is an obvious choice for comparison with POLAR. This comparison is important for the validation of POLAR, but also for advancing

our understanding the mechanisms of spacecraft charging. The DMSP observations have shown that combinations of high flux and low background density will lead to charging, but do not tell us much about such factors as composition, shape or size.

II. Observations

The DMSP F6 satellite was launched on December 20, 1982 into a sun synchronous, dawn-dusk, circular orbit at an altitude of 840 km, orbital period of 101.5 min, and an inclination of 99°. The DMSP F7 satellite was launched in November, 1983, into a similar orbit in the 1030-2230 magnetic local time (MLT) meridian. The two satellites each carry the SSJ/4 instrument which measures precipitating ions and electrons, and the SSIE instrument, which measures thermal plasma.

The SSJ/4 sensor consists of four cylindrical curved plate electrostatic analyzers arranged in two pairs. One pair measures electron fluxes in 20 logarithmically spaced energy channels between 30 eV and 30 keV, executing a complete sweep each second. The other measures ions over the same range. The analyzer apertures always face local vertical, and thus measure only the precipitating particle populations with an angular acceptance of $10^\circ \times 10^\circ$.

The thermal plasma detector, SSIE consists of a spherical Langmuir probe to measure thermal electrons and a planar retarding potential analyzer, RPA, to measure thermal ions. The Langmuir probe consists of a 1.75 inch diameter collector surrounded by a concentric wire mesh grid of 2.25 inch diameter. It is mounted at the end of a 2.5 foot rigid boom. Complete descriptions of the SSIE instruments, modes of operations, and data analysis methods are

given in Smiddy *et al.*, [1978]. From the SSIE data, the thermal plasma density can be determined.

The observations are summarized in Table 1, taken from Gussenhoven *et al.*, [1985], where it was demonstrated that the occurrence and level of charging are well correlated with the ratio of electron flux with energy greater than 14 keV divided by the ambient plasma density ($IF(\geq 14 \text{ keV})/n_{th}$). They also present other evidence to established that these events do indeed correspond to the passage of the satellites through visibly bright auroral arcs.

III. The POLAR Code

POLAR [Lilley *et al.*, 1985] is a self-consistent three dimensional Poisson-Vlasov code, that provides steady state solutions by iterating between potential (Poisson) and density (Vlasov) solutions on a cubical mesh. A versatile set of building elements can be combined to form complex objects with a variety of surface materials and electrical connections. A surface charging module can be added to the iteration to provide the spacecraft charging response to both natural and active charge drivers. The Poisson solver uses a finite element conjugate gradient method, with a unique technique of filtering charge densities to suppress grid noise, and produce stable solutions. POLAR calculates particle densities by a method that divides space into (one or more) sheath and non-sheath regions separated by a sheath edge(s), located as an equi-potential, near kT . External to this surface the plasma distribution is presumed to be Maxwellian with possible flow. External densities are determined by geometric ray tracing with first order electric field corrections. This approach has been shown to correctly predict wake formation about the Space Shuttle Orbiter [Murphy *et al.*, 1987]. At the sheath

TABLE 1. Summary of 11 Charging Events in 1983. [Gussenhoven et al., 1985]

Satellite	Day	Year	UT _{max} s	Δr s	-Δφ ₀ ^a V	n ₀ (ions/cm ³)	IF ₀ (Electrons/cm ² s sr ⁻¹)	IF ₀ (≥ 14 keV) (Electrons/cm ² s sr ⁻¹)	IF (Ion Peak) (ions/cm ² s sr ⁻¹)
F6	Jan 5	1983	49,480	24	213	2.57 × 10 ³	1.43 × 10 ⁴	1.20 × 10 ⁴	3.12 × 10 ⁴
F6	Jan 10	1983	74,722	12	68	1.34 × 10 ³	3.79 × 10 ⁴	2.11 × 10 ⁴	3.93 × 10 ⁴
F6	Jan 12	1983	35,377	17	462	5.37 × 10 ²	1.02 × 10 ¹⁰	9.40 × 10 ⁴	4.53 × 10 ⁷
F6	Jan 20	1983	50,047	3	679	1.49 × 10 ²	5.86 × 10 ¹⁰	6.24 × 10 ⁴	3.84 × 10 ⁵
F6	Jan 21	1983	54,937	12	100		1.82 × 10 ⁴	1.49 × 10 ⁴	5.26 × 10 ⁴
F6	Nov 26	1983	47,712	18	517		1.32 × 10 ¹⁰	4.58 × 10 ⁴	1.79 × 10 ⁴
F6	Nov 26	1983	66,068	16	462		1.67 × 10 ⁴	4.79 × 10 ⁴	2.20 × 10 ⁴
F7	Nov 26	1983	43,841	4	47	1.25 × 10 ³	7.86 × 10 ⁴	5.37 × 10 ⁴	1.78 × 10 ⁷
F7	Nov 26	1983	49,843	60	314	1.25 × 10 ²	1.59 × 10 ⁴	1.14 × 10 ⁴	2.07 × 10 ⁴
F7	Dec 01	1983	1,458	2	215	3.55 × 10 ³	2.37 × 10 ⁴	1.95 × 10 ⁴	3.01 × 10 ⁷
F7	Dec 31	1983	14,007	62	462	1.22 × 10 ¹	2.39 × 10 ⁴	2.23 × 10 ⁴	1.48 × 10 ⁴

^aThe parameter Δφ₀ is inferred from the central energy E_c of the ion energy channel in which the charging peak is identified. ΔE/E_c is 9.3% for both DMSP F6 and F7.

edge reasonable assumptions about the external potential structure and the usual constants of motion are used to determine the flux and velocity of ions entering the sheath which are assigned to a super-particle and tracked inward. Internal sheath densities are determined from the time spent in each volume element, and surface currents from their final deposition. When particles are repelled, their density is assumed to be Boltzmann.

Auroral electrons are introduced with three distinct energetic populations [Fontheim, 1982]: Power Law, specified by intensity, exponent, lower and higher cutoffs; Maxwellian, specified by density and temperature; Gaussian, specified by intensity, energy peak, and peak width. Auroral electrons are assumed to not contribute significant space charge so they are decoupled from the P-V portion of the iteration. They and other sources of current are accounted for during a charging step which updates conductor and surface potentials. The Auroral electron flux is assumed to be isotropic, with no surface - surface shadowing, and secondary and backscatter currents are determined from surface potential and material properties [Katz, 1986]. The isotropy assumption is a

limitation on accuracy, and could be straight forwardly removed, but remains since 4π observations are not usually available, and since a charging code is often used for 'worst case' analysis. Photo electron currents are also included, with shadows calculated from sun direction information.

In modeling DMSP, POLAR is hampered by its single sized grid structure. In designing POLAR to model the Shuttle Orbiter in the 200 - 400 km altitude range, with an ambient plasma density range of $10^3 < N_e < 10^7 \text{ cc}^{-1}$, $10 > \lambda_D > 0.1 \text{ cm}$, it was decided that a single grid would be adequate for shuttle, sheaths, and scope of project. A plasma sheath thickness will always be bounded by the planar Child-Langmuir length, $D_{CL} = \lambda_D (eV/kT)^{3/4}$, which will always be comparable to the shuttle scale. DMSP orbits at 840 km, where the plasma density varies from $10 < N_e < 10^5 \text{ cc}^{-1}$, $100 > \lambda_D > 1 \text{ cm}$. With a satellite size of approximately 2 meters, hundred volt sheaths in the low density extreme will become much larger than the satellite. If we choose a fine resolution of the satellite, the total number of nodes will increase run times to prohibitive levels (the high resolution DMSP model at UT1458 employed 2.5×10^5 nodes and required about

200 hours at 10^6 flops). POLAR manages memory better than it does time by maintaining a data base on disk and paging fragments of the problem into core so the largest problems can be run on small high performance workstations. POLAR does not require that the Debye length be resolved as is common in explicit particle simulations. Because of a technique called Charge Stabilization [Cooke et al., 1985], the grid interval can be very large with respect to λ_D without Poisson instability, but sheaths do tend to expand since in reality the sheath edge has λ_D scale structure which expands to the grid interval. With an inflated sheath comes higher sheath currents.

The large DMSP sheaths are also a problem for POLAR's sheath current and density algorithm. In the space charge limited regime where sheath thickness is less than or comparable to object size, angular momentum effects on the trajectories of incoming ions can be reasonably modeled with a single super-particle at each sheath element. For large sheaths, this friendly feature is lost. In a stationary plasma, one can appeal to the analytic orbit-limited limit [Laframboise and Parker, 1973], but in LEO, the orbital momentum of the incoming ions is not only high, its not even spherically symmetric. In the course of the DMSP study, the POLAR sheath model was extended to optionally replace a single sheath particle with a distribution of 5 particles that better samples the momentum of the incoming particles.

In the low density extreme, it would appear desirable to abandon particle tracking. Inspection of large sheath particle tracks in POLAR models reveals very chaotic orbital motion, and surface deposition patterns, that can be quite sensitive to initial conditions. Since it is not practical to approach problems with an ensemble of variant calculations, one

is inclined to give up the pursuit of surface level accuracy for a more efficient approach to the bulk charging. On a trial basis, we have introduced an ad hoc 'Orbit Limited' type model, where we seek a formula for the net surface current as an analytic function of potential, similar to the successful approach employed by NASCAP [Katz, 1978]. This formula gives for surface current density,

$$J = J_{th} \left\{ 1 + \sqrt{\frac{\pi}{8}} M \right\} \left\{ 1 - eV/kT \left[1 + M^2 \right] \right\}$$

, $J_{th} = \sqrt{kT/2\pi m}$, $M = \text{velocity} \sqrt{m_i/kT}$. The second term in the first braces is the ram current to a disk assuming a thermal current to a sphere. The second term in the second braces converts the orbit limited temperature to the flow energy.

POLAR is also challenged by small potentials. The Poisson solver is not bothered, but when surfaces have potential near kT , zero, or $M^2 kT/2e$, currents can be difficult to calculate, particularly near higher surface and space potentials.

IV. Satellite Models

The observations presented in table 1 represent a very wide range of parameters. Some of these cannot be reasonably modeled with POLAR, due to constraints posed by the combination of density and potential. For example, the F6 observations on Jan. 12 & 20, indicate high level charging with low ambient density. These conditions will produce a very extended sheath, which is difficult to model for the reasons presented in the previous section. Reducing the object and grid resolution can help, and in this study, two different resolution DMSP satellite models have been used. These models and the distribution of materials were derived from satellite documentation [DMSP, 1983], and from a cardboard, CAE model of DMSP

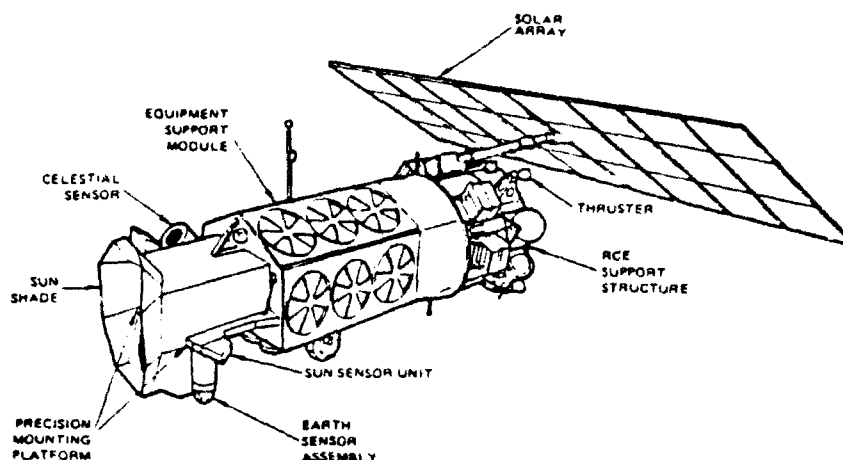


Figure 1. Illustration of DMSP [DMSP, 1983]

provided by RCA Astro Div. (now GE Astro Space Div.). A sketch of DMSP from the documentation with a few features is shown in figure 1. The high resolution POLAR model is shown viewed from ram and wake in figures 2 and 3 along with material designations.

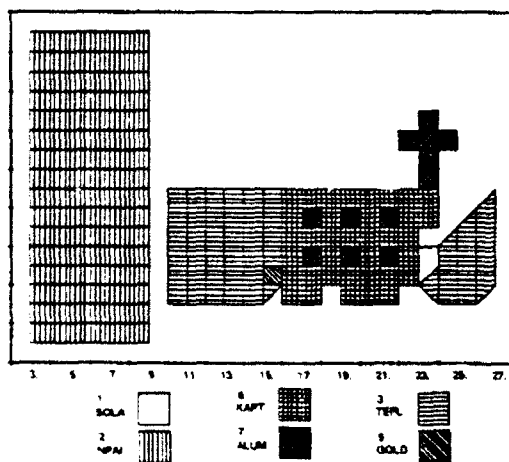


Figure 2. Surface cell material composition as viewed from the + X direction.

The gold patch on the ram side represents the location of the SSIES RPA on later versions of DMSP. The SSIE RPA for F6 and F7 is the round disk located on the boom just above the satellite in figure 1. It is too small to be separately modeled with POLAR. The cross structure above the satellite in figure 2

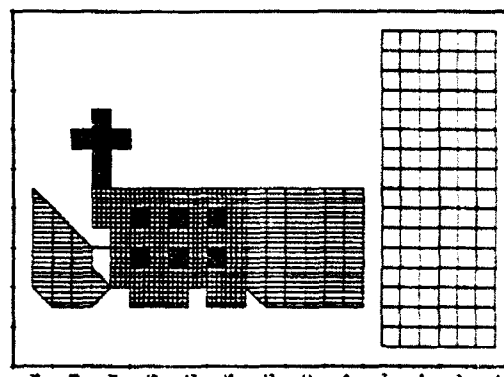


Figure 3. Surface cell material composition as viewed from the - X direction.

represents a microwave imaging sensor (actually round), found on some versions of DMSP. All material were chosen from the default list of POLAR (NASCAP) materials, which in some cases are guesses. The worst guesses are probably the non-conducting paint used on the back side of the solar cells, and the assumption that the aluminized backing of the teflon and kapton thermal blankets is always uniformly grounded. The solar cells have been modeled as uniform solar cell cover glass. The real mix of glass and conducting interconnects has a complex current collection characteristic that cannot be treated as a simple material. NASCAP/LEO [Mandell, 1986] employs a promising hybrid potential and electric field

dependent material treatment that could be adopted if this appears to be a limiting factor.

V. Comparisons

Three observations were chosen from Table 1 for comparison with POLAR. Charging on F6, Jan. 10, 1983, UT74,722, is chosen because the plasma density and sheath size are reasonable for POLAR, and because the low potential will test POLAR's ability to model threshold charging. Charging on F7, Dec. 01, 1983, UT1,458, is chosen because the charging is significant with a plasma density sufficient to produce a tractable sheath size. Charging on F7, Dec. 31, 1983, UT14,007 produces an impossibly large sheath, but was included as a test of the analytic Orbit limited ion model. These events are hence tagged by their Universal Times.

The first step in developing the POLAR models was fitting the observed electron spectra. For this purpose, representative spectra were chosen from the observations, fitted by the POLAR spectral parameters, and assumed to be constant over the event duration. It would have been preferable to compute the average observed spectra before fitting, but this was not done. Better still would be to introduce new fits to spectra as they varied, but since the fitting is now done by hand and eye, this would have been prohibitively time consuming. Possibly the best approach would have been for POLAR to accept numerical spectra, but presently, that option does not exist.

Figure 4 shows the fit at UT1,458, where the resultant POLAR line and the observation are almost identical. Figure 5 shows the poorest fit which is for UT74,722. The spectra at UT14,007 is similar to UT1,458. Significant uncertainty enters the models with respect to the environments. From the observations, we do not know the electron

population above 30 keV, or the extent outside of the observation solid angle, and the reported ion density can be influenced by space potential focusing effects. In all calculations, the ion density was set to that reported in Table 1, and 0.02 eV was used for the ion temperature.

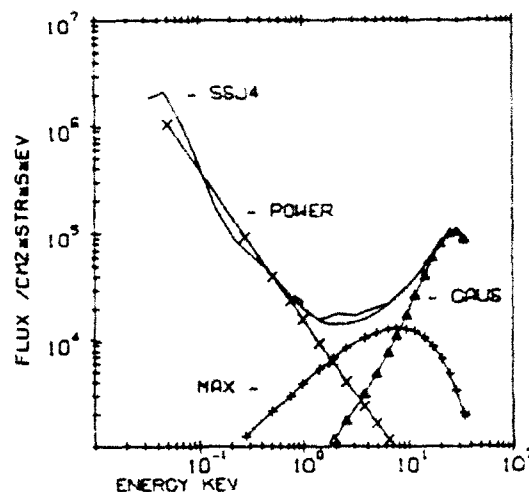


Figure 4. POLAR fit to the F7 SSJ4 spectrum. Observations on Dec 01, 1983, UT 1,458, fitted with Power law, Maxwellian, and Gaussian components.

Charging at UT1,458 and UT74,722 was modeled with both the high resolution DMSP model and DMSPWE. Because of the the compute time required for the high resolution model, large time steps were taken. POLAR's charging algorithm has implicit stability, but the nature of that algorithm in it's implicit limit leaves the temporal fidelity suspect. Therefore, in figure 6, we present the charging history at UT1,458 for the DMSPWE only.

The charging history suggests that the frame potential reaches equilibrium very early with respect to the dielectric surfaces which is as expected since the dielectric to conductor capacitance will be much higher than from the frame to infinity. Given the uncertainties, the close agreement between

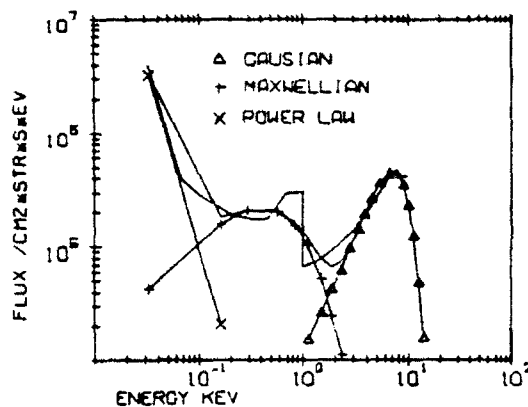


Figure 5. UT 74,722 observation and POLAR fit.

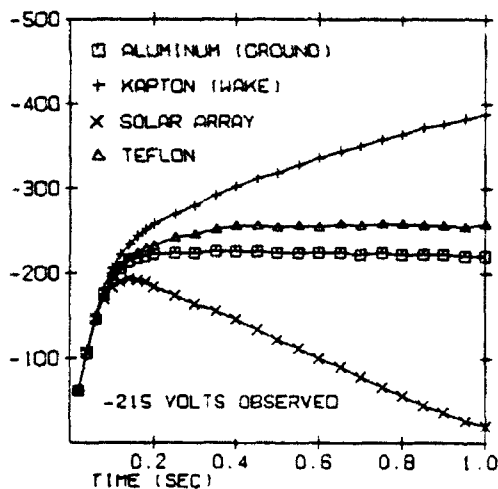


Figure 6. DMSPWE Charging history for selected surfaces at UT 1,458.

this model and observation reflects some degree of luck. Wake side surface potentials for DMSPWE are shown in figure 7, where not surprisingly, the highest potentials are found on the wake side teflon surfaces. For comparison, the high resolution model wake side potentials are shown in figure 8. Here the same teflon surfaces are highly charged, but a few kapton surfaces partially hidden in a cleft have taken the lead. The high res. ram side is presented in figure 9, which exhibits lower potentials because of the ram ion flux. The exception is the edge of the solar array

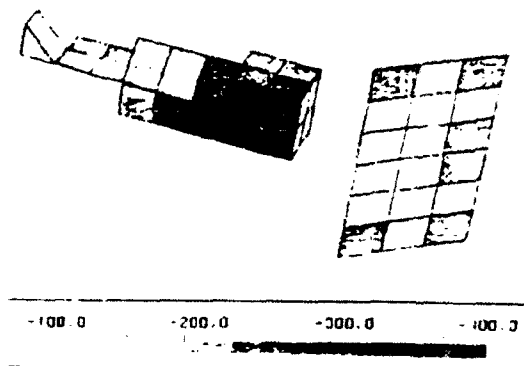


Figure 7. DMSPWE wake side surface potentials

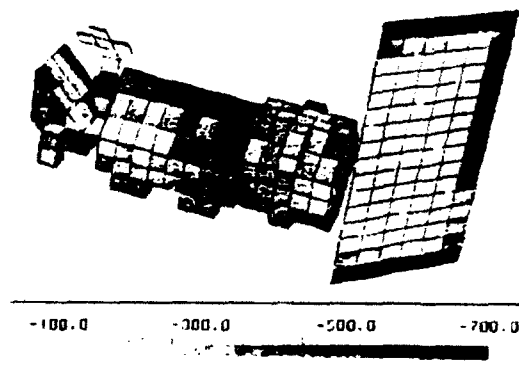


Figure 8. DMSP wake side surface potentials

which charges on both the ram and wake sides. The charging of the ram side of the solar array appears to be an artifact of a surface current smoothing algorithm that has moved some of the ram side current to the back, leaving the ram edge with insufficient ion flux to prevent charging.

Figure 10 is a 2D cut through the 3D POLAR grid showing a shadow outline of the satellite, and space potential contours. The sheath edge used to compute ion fluxes and launch the tracked particles lies at a slightly more negative potential than the kT contour labeled in the figure.

Spacecraft frame potentials calculated by POLAR and observed on DMSP at all three times are summarized in Table 2. In all three cases POLAR and observations are in rough

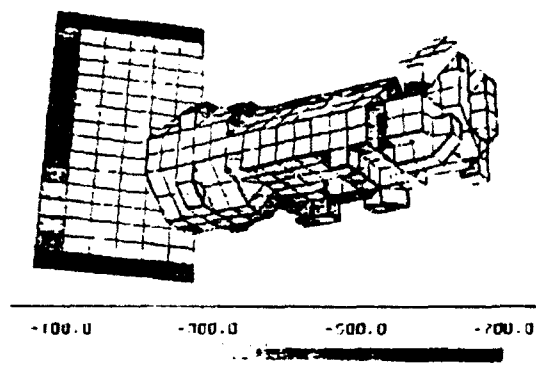


Figure 9. DMSP ram side surface potentials

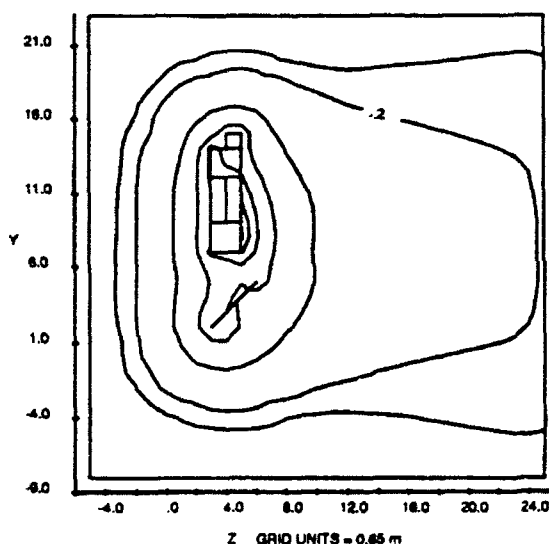


Figure 10. Contour plot of DMSPWE at UT 1,458.

agreement. The trends are correct, and the values are as close as one can expect given the uncertainty in code physics, environmental uncertainty, and model fidelity.

We may also use POLAR to assess whether additional uncertainty can be attributed to the measurement of ion density. Figure 11 is a plot of ram side ion currents for UT1,458. The ion flux to a square surface of an uncharged satellite would be 2.6×10^{-7} Amp, which would be mostly

TABLE 2. Computed and Observed Frame Charging Potentials (Volts)			
Tag	UT1,458	UT14,007	UT74,722
F7 / F6	215	500	68
Polar			
DMSP	390	—	12
DMSPWE	230	1200	11
Big PWE	802	—	—

white in figure 11. As we can see most surfaces collect more.

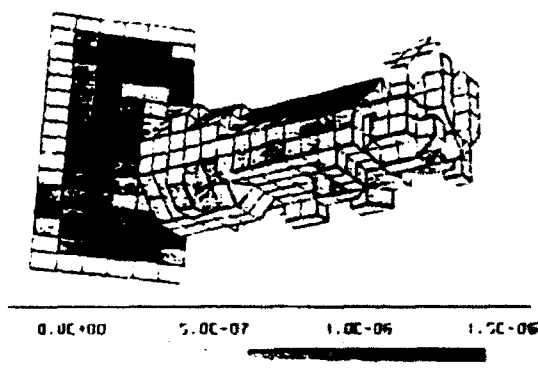


Figure 11. Ram side ion surface currents at UT 1,458.

Without knowledge of the actual focusing factors, which vary with the interaction, it is reasonable to assume no focusing in determining an observed density. ($N = \text{Flux}_{\text{observed}} / V_{\text{orbis}}$) We must however assume that the measured ion density has an interaction induced uncertainty when charging occurs. In fact, if we reduce the ion density in the POLAR UT 74,722 model by a factor of two, the satellite charges to -57 Volts with the ram side focusing factors exceeding 2 for some surfaces.

The differences between the high and low resolution models tell us about the effect of some of the assumptions discussed in section 3. Note that for UT 1,458, the high resolution model charged to the higher potential. The increased variegation on the high res. model without surface shadowing increases the net electron flux. The lower resolution model has slightly higher net ion

fluxes due to sheath thickening effect of the charge stabilization, so in comparison, the high res. has lower fluxes. Both of these effects are of about the same magnitude and contribute to the higher high res. charging.

We can also take this opportunity to take a look at the size effect. In the model listed as "BIG PWE" in table 2, the DMSPWE calculation was rerun with the mesh size parameter increased by a factor of four, which produced an almost four fold increase in charging.

VI. Conclusions

The results and comparisons in this study have shown that POLAR is capable of modeling at least some of the DMSP charging events. This was not a blind study, and for that reason, the conclusions are not as strong as otherwise. Had table 1 been presented to those of us who set up the POLAR runs without the charging levels, most would have been run. Those models with low density and presumably high charging levels would have been abandoned when sheaths grew too large. Although incomplete, runs abandoned due to charging would have strengthened an affirmative assessment of POLAR capability. In the course of pursuing these results a few bugs were fixed, and some extensions were made. The most significant extensions were the 'orbit limited' extension which is mostly a conceptual start, and the thermal sheath particle spreading, which has been of continuing usefulness.

We may also recommend (to ourselves) changes that would improve the code. The surface current spreading should be either eliminated, or made smarter. Wake side charging bleeding onto the ram could be mistaken for a real phenomenon. Although the net ion fluxes are conserved, barrier effects and the secondary currents that might

or might not be suppressed, could depend upon the actual location of surface potential. Incorporating available improvements in solar cell treatment would also be desirable. We also saw how two small effects, artificial sheath current enhancement in low resolution models, and the lack of self-shadowing in auroral electron current deposition, combined to produce a weak scale dependence for charging. While individually small effects, their ability to combine suggests that they are best corrected.

A nested grid capability would definitely enhance POLAR. The large sheath problems would run quicker, but the idea of mapping currents from a sheath edge to surfaces probably breaks at some point which may lie within present capabilities. If one anticipates such a breakdown, it should be addressed before extending POLAR. Another reason for wishing a nested or multi-grid capability, would be the ability to enhance surface resolution. The value here is again subject to the mapping accuracy question, and to limits of the building block approach, which should be updated along with any improvements in gridding.

In conclusion, POLAR, does appear capable of predicting the presence and levels of auroral charging.

References

- Besse, A.L., A.G. Rubin, and D.A. Hardy, "Charging of DMSP/F6 in Aurora on 10 January 1983", in *proc. Spacecraft Environmental Interactions Tech. Conf.* ed. by C.K. Purvis and C.P. Pike, NASA Conf. Pub. 2359, AFGL-TR-85-0018, 1985. ADA202020
- Cooke, D.L., I. Katz, M. Mandell, J.R. Lilley Jr., and A.J. Rubin, "A Three-Dimensional Calculation of Shuttle Charging in Polar Orbit", in *proc. Spacecraft Environmental Interactions Tech. Conf.* ed. by C.K. Purvis and C.P. Pike, NASA Conf. Pub. 2359, AFGL-TR-85-0018, 1985. ADA202020
- DMSP, "Defense Meteorological Satellite Program (DMSP) Block 5D-2 System Analysis Report". Prep.

- by DMSP Prog. Off. RCA Gov. Sys. Div.,
Astro-Electronics, Princeton, N.J., for Space Division
(YD), USAF, Los Angeles, CA, CDRL Item C108,
Contract F04701-75-C-0182, Nov. 1984.
- Fontheim, E.G., K. Stasiewicz, M.O. Chandler,
R.S.B. Ong, E. Gombosi, and R.A. Hoffman,
"Statistical Study of Precipitating Electrons", J.
Geophys. Res., V87, A5, 1982.
- Gussenhoven, M.S., D.A. Hardy, F. Rich, and W.J.
Burke, "High-Level Spacecraft Charging in the
Low-Altitude Polar Auroral Environment", J.
Geophys. Res., Vol.90, No.A11, pp. 11,009-11,023,
Nov. 1985.
- Katz, I., M.J. Mandell, G. Jongeward, M.S.
Gussenhoven, "The Importance of Accurate
Secondary Electron Yields in Modeling Spacecraft
Charging, J. Geophys. Res., V91, No.A12, pp 13,744;
1986
- Katz, I., M.J. Mandell, G.W. Schnuelle, J.J. Cassidy,
P.G. Steen, and J.C. Roche, "The Capabilities of the
NASA Charging Analyzer Program", in proc.
Spacecraft Charging Technology Conference,
AFGL-TR-79-0082, NASA Conference Pub 2071,
1978. ADA084626
- Lilley J.R., Jr., D.L. Cooke, G.A. Jongeward, I. Katz,
"POLAR Users Manual", AFGL-TR-85-0246, 1985. ADA173758
- Laframboise, J.G., and L.W. Parker, "Probe design for
orbit-limited current collection", Physics of Fluids,
V16, #5, May 1973.
- Mandell, M.J., I. Katz, G.A. Jongeward, J.C. Roche,
"Computer simulation of plasma electron collection by
PIXII, J. Spacecraft and Rockets, V23, #5, Sept 1986.
- Murphy, G., and I. Katz, "The POLAR Code Wake
Model: Comparison with in Situ Observations",
J. Geophys. Res., V94, pp. 1,450, 1989.
- Smiddy M., R.C. Sagalyn, W.P. Sullivan, P.J.L.
Wildman, P. Anderson, and F. Rich, "The Topside
Ionosphere Plasma Monitor (SSIE) for the Block
5D/flight 2 DMSP Satellite", Rep.,
AFGL-TR-78-0071, Hanscom AFB, Mass. 1978.
ADA058503

Numerical Simulation of the Wake of Non Equipotential Spacecrafts in the Ionosphere

A. Soubeyran, L. Lévy

Département d'Etudes et de Recherches en Technologie Spatiale, Centre d'Etudes et de Recherches de Toulouse, 2 av. E. Belin, 31055 Toulouse Cedex, France

E. Coggiola

245, Petrie Science Building/ Physics Department/ North York, Ontario/M3J 1P3/ Canada

ABSTRACT

We studied the spacecraft/plasma interaction in the particular case of differential charging of satellites in Low Earth Orbit. The environment of such a satellite is very anisotropic, especially because of the mesosonic character of his velocity. We have tried to investigate numerically this "worst case" situation for infinite cylinders and spheres.

The code which we have developed, solves selfconsistently the coupled Hamilton and Poisson equations, in polar coordinates. It takes into account a differential polarisation on the rearward side of the spacecraft, where it is most likely to appear. Electrons are supposed in thermal equilibrium.

It follows from our simulations performed with this code, that the wake of a satellite in L.E.O. is generally shorter than expected from simple thermal considerations. For middle class satellites, severe disturbances could occur, which remain confined in the ionic shadow of the spacecraft. The wake density is decreasing when the differential potential is increasing. For a small mock-up, the potential disturbances could extend well out of the wake. The wake density increases with the backward side polarisation.

The near wake is always empty of drifting ions, so it seems likely that the back side charge cannot be neutralized by such ions.

1. INTRODUCTION

Owing a large number of failures on geostationaries spacecrafts, the interactions between them and the plasma at these altitudes were largely studied and today mainly understood as result of energetic electrons precipitations (see for example Fennel et al. 1983, and Levy et al. 1986). A first analysis of such interactions at ionospheric altitudes leads to the conclusion that, except perhaps in very special conditions (as for DMSP, Gussenhoven et al. 1985, and Yeh et al. 1987), the absolute potential of an equipotential satellite must remain around a few negative volts. This is due to the smallness of the Debye length with respect to the spacecraft dimensions, in this colder and denser plasma (Al'Pert et al. 1965) (table 1). Despite these reassuring conclusion, and the fact that no failures due to anomalous charging was actually reported on low earth orbit (L.E.O.), we decided to investigate the case of non equipotential spacecrafts (already tackled by L.W. Parker 1978, 1983). Contrary to the geostationary case, the plasma environment of a spacecraft in the ionosphere, is very anisotropic : due to the mesosonic character of the spacecraft speed, a wake appears behind it, where the conditions could approach those of the geostationary plasma (Samir et al. 1986). In such a rarefacted medium, high charging levels are likely to occur, especially during auroral precipitation of energetic electrons, on insulated parts (floating metalizations or dielectrics) (Coggiola 1988) (figure 1). On futur spacecrafts, active polarisation may also induce high voltages on parts of the external surface.

To better understand the interaction between the wake and such polarisations, and therefrom deduce whether ambient ions could be dragged to such charged area on the wake side or not, we developed a suitable numerical simulation.

2. NUMERICAL MODEL

In low orbit conditions, the space-charge coupling, the magnetic field effects, and the ion flow effects could all be important. As a result, modelling of spacecraft-environment interactions appears likely to be a difficult task (Laframboise 1983). Therefore, we must use some approximations to develop our numerical simulation.

2.1. Simplifications

- 1- The spacecraft is only bipotential, with a main surface at the rear of the spacecraft, at various fixed negative potentials, up to -1kV.
- 2- We assume no magnetic field and
- 3- no secondary emission or photo-emission of electrons.
- 4- In such conditions, we choose spherical or infinite cylindrical structures to obtain a purely bidimensional geometry, which reduces greatly the computation work.
- 5- Moreover, we decided to limit the computation area to the back side of the spacecraft, around the wake. So, all effects arising in front of the spacecraft are neglected. This seems to be realistic because of the thinness of the sheath on this side.
- 6- We assume only one sort of ions (O^+ or Ar^+) with a drift velocity and eventually a small thermal component.
- 7- The electrons are supposed in thermal equilibrium, and so modeled using the Boltzmann factor.
- 8- The plasma is collisionless on the scale of the interaction area.

The modeled situation could be considered as a "worst case" for the differential charging of a non equipotential satellite. The charge is located in the ion depleted wake, where it is likely to appear under auroral precipitation (Katz et al. 1985), and it could only be limited by collection of drifting ions of the ambient plasma.

Under these assumptions, we developed the following numerical algorithm.

2.2. Algorithm Description

This code solves selfconsistently the coupled Hamilton and Poisson equations, in polar coordinates.

As seen above, the simplified geometry of the interaction is bidimensional (2d2v) and, as we have already a physical discontinuity of the voltage on the spacecraft surface, we choose to solve the equations in polar coordinates, to avoid a second, geometrical, discontinuity. These coordinates result either from cylindrical coordinates invariant along Z, or from spherical coordinates invariant around the system axis as shown on figure 2.

In the collisionless medium which is being treated, the particles density and velocity distributions are well described by the kinetic theory, expressed through the Vlasov equation (Delcroix 1963). But this form is difficult to solve directly for a complex system, and we replace it by the integration of Hamilton's motion equations over a large number of simulation particles. These particles (equivalent to real ions packets) are all introduced during one first time step. They form a charging front which is moved over the computational mesh by integrating the Hamilton's equations, taking into account the fixed electric fields deduced from a potential distribution.

At each time step, each particle leaves a charge on the four nearest grid points by means of a bilinear deposition scheme (PIC method described by Birdsall and Langdon

1985, see fig). When all particules of the front have reached the boundaries (satellite surface or external boundary), we sum at each grid point the charges accumulated during the process on all trajectories. After some weighing by the cell surfaces and normalisation, the ionic density is deduced at all nodes.

This is used as input for the Poisson equation which is expressed in a finite-difference form over the same grid as above. Owing to the Boltzmann factor (electronic density), the resulting system of equations is not linear. Nevertheless, it can be solved by a Gauss-Seidel algorithm. We thus obtain a discrete potential distribution which gives us the electric field at any place in the computation area, through a finite differentiation, and eventually a bilinear interpolation if the point is not at a node. This is used in its turn, as input for the integration of Hamilton equations.

For the first iteration of this algorithm (figure 3), we choose everywhere a zero potential, and so a zero electric field. Then we perform the above scheme until self-consistence is achieved : the density distribution must give, using the Poisson equation, a potential distribution which gives back, after the integration of Hamilton equations, the same density distribution.

In relation with the assumptions made before, with computational capacities, and with observations of preliminary results, we are able to set rough estimations of limits to the input parameters.

2.3. Limits of the Simulation

As seen from the boundary conditions, there is no treatment of the forward region of the spacecraft, and we assume a cylindrical (resp. plane) symmetry around the drift direction, behind a sphere (resp. an infinite cylinder). These remarks lead to the quarter shaped working area of figure 2.

All the boundary conditions are independent of time and so we obtain only stationary results. These could eventually be approximations in particular cases.

All the calculations are made with dimensionless normalized variables and parameters, in order to simplify the formulation, and make comparisons easier. The interaction parameters are limited as it follows :

$$100 \geq \zeta = R_{\text{sat}} / L_{\text{Debye}} \geq 10$$

The upper bound is due to limits in computational capacities, because the spatial grid step must be taken of the order of the Debye length : L_D (Birdsall and Langdon 1985). The lower bound comes from physical considerations about the thickness of the sheath (a few L_D), and his effects in front of the spacecraft which we neglect (Al'Pert et al. 1965).

$$40 \geq M_i = V_{\text{sat}} / V_{\text{th},i} \geq 5$$

As above, the upper bound comes from computational limitation, because the interesting area may reach about $(M_i R_{\text{sat}})$ behind the spacecraft (Gurevich et al. 1969, and Samir et al. 1981). The lower bound was deduced from tests which showed that for low values of M_i , particules seem to be trapped near the axis of the wake, and prevent the algorithm from converging. This can result from turbulences and/or inadequate space sampling and to few particules.

$$5 \geq \eta_c = -e\phi_{\text{conduct}} / kT \geq 0$$

The upper bound is necessary for the thickness of the plasma sheath to remain of the order of the Debye length. The lower bound is dictated by the assumption of a thermal equilibrium for the electrons.

$$1000 \geq \eta_d = -e\phi_{\text{diel.}} / kT \geq 0$$

The upper bound was deduced again from observations of trapped particules at "focal point-like features" on the axis of the wake, which we suspect to give rise to

some turbulence phenomena. The lower bound comes as above from the approximation of the electronic density by the Boltzmann factor.

All these constraints are broad approximations, subject to evolutions in relation with improvements of the code.

We will now examine a few interesting results of our code. These are only early calculations, and they will need further investigations.

3. RESULTS AND DISCUSSION

We present here two configurations, corresponding to two very different situations, showing the versatility of our code. The first one is corresponding to a middle-class satellite in the ionosphere, the second one could be interpreted as a mock-up in the plasma stream of an experimental chamber.

3.1. Middle-Class Satellite in the Ionosphere (see table 2 and figures 4 a-f)

The three backside potentials have been chosen to represent :

- equipotential structure at floating potential
- active polarisation coming from experiments or power supply
- charging under energetic electrons precipitation

The main surface is fixed at the floating potential, and this seems to influence the wake shape as already pointed out by Stone (1981). Indeed, we observe a wake void shorter than would be expected from simple thermal calculations (i.e. $Mi.R_{sat}$), even for an equipotential satellite (fig. 4 b). This length is better obtained by taking into account the floating potential and the negative space charge of the wake :

$$L_{wake} = \frac{V_{||}}{V_{\perp}} = \sqrt{\frac{E_{drift}}{E_{float} + E_{wake}}} \approx \sqrt{\frac{5.3}{.36 + .6}} \approx 2.3$$

and we observe : $L_w \approx 2.5$ in good agreement with the calculated length.

Between L_w and $Mi.R_{sat}$ (limits of our system), we observe a very inhomogeneous wake, with a strong focussation on the axis, behind the sphere. In the case of a cylinder, the geometry leads to a lower axial concentration, but the potential disturbance is more extended and it results in lower densities around the axis, but the wake is wider.

When the differential polarisation grows up, the potential disturbance extends but remains mainly confined in the ionic "shadow" of the spacecraft (fig. 4 c,e). So, the flux of particules which enters the wake doesn't increase very much, but these particules are more and more accelerated. Thus, their local density decreases around the central axis, where they tend to accumulate in localized areas (fig. 4 d,f). Perhaps is it an indication of axial turbulence ? Indeed, for very high potentials (-1kV) the density distribution given by the code is not really stable. Nevertheless, it seems that the polarised surface remains always in a near wake almost empty of ions and is not expected to be discharged through a current coming from the drifting ions.

3.2. Mock-up in a Stream of Drifting Ions in a Plasma Chamber (see table 3 and figures 5 a-f and 6 a-d)

In this case, the main surface remains at zero potential, and we fixed for the rearward surface the same potentials as before. We find this time that for a structure wholly at zero potential, the shape of the near wake is controlled both by the backward negative space charge and by the thermal motions :

$$L_w \approx \sqrt{\frac{E_{\text{drift.}}}{E_{\text{th.i.}} + E_w}} = \sqrt{\frac{42}{.1 + .3}} \approx 10.$$

and we observe : $L_w \approx 9$ (fig. 5 b, 6 b)

When the differential potential is growing up, the particles are driven toward the wake axis with increasing velocities, as above for a satellite. But now, the mock-up is too small ($\zeta_{\text{mock-up}} < \zeta_{\text{spacecraft}}$) to shield the potential disturbance for high potentials, and this extends well out of the wake (fig. 5 e) and even around the mock-up itself for a cylindrical geometry (fig. 6 c). So, the flux of ions entering the properly so called wake, increase simultaneously with their speed, and the ionic density is not decreasing as above, but on the contrary, generally increasing too (fig. 5 f), except for very high polarised cylinders (fig. 6 d).

For both studies, a differential polarisation limited to a few tens of volts does not affect the wake; some modifications begin to appear around hundred volts (fig. 4 c,d and 5 c,d).

We never observed any collection of ions on the polarised rearward surface, which is always remaining in a near-wake empty of particles, limited by our sensitivity : i.e. $(.03 \cdot N_0)$ around the spacecraft and $(.003 \cdot N_0)$ around the mock-up. This seems to be due to the fact that ions which experience the potential disturbance are accelerated at first almost along the drift direction and slightly repelled from the spacecraft surface, because of the shape of the isopotentials around the satellite. After this acceleration, the potential crossed by the particles is decreasing and not strong enough to attract them back. Moreover, the potential decreases very rapidly near the polarised surface and the ions do only cross regions of potential lower than their own drifting energy. For higher potentials, or different geometries, this result could become invalide.

4. CONCLUSIONS

In the limits expressed before (§2.3.), the code which we developed gives interesting new results about the wake structure of a non equipotential probe in a drifting plasma. We conclude that :

- 1- For a differential potential lower than 100 Volts, the wake disturbance remains weak.
- 2- For higher potentials, the disturbance depends mainly on the $\zeta = R_{\text{sat}}/L_{\text{Debye}}$ parameter :
 - For low ζ (≤ 10) the potential disturbance extends in the plasma around the wake, and the density in the wake increases with the differential potential.
 - For high ζ (> 10) the probe shields the potential disturbance which remains confined in the near-wake, and the density in the mid-wake decreases when the potential increases.

However, the density is always increasing with the potential on the axis behind a sphere, because of focusing effects. Furthermore, these conclusions concern mainly the spherical probe. It seems probable that the transition value of ζ is higher for a cylinder, due to the fact that, at equal applied potential, the disturbance is far more extended around a cylinder than around a sphere. In this case, there is a competition between lower geometrical condensation, but higher electric field focusing effect.

3- Last but not least, even for differential potentials as high as -1kV, we do not observe any discharging current coming from the drifting ions. This confirms the possibility of high differential potentials on spacecrafts, in particularly hard conditions, such as shadow and energetic electrons precipitations without enough secondary emission. It is although obvious that any ionic population without drift

movement with respect to the probe (plasma emitted from it or resulting from ionisation or charge exchange on non drifting neutrals...) will probably be very sensitive to the potential hole in the wake and could strongly modify the above results as suggested by the results of experiments of Coggiola (1988).

REFERENCES

- Al'Pert, Y.A., Gurevich, A.V., and Pitaevskii, L.P., "Space Physics with Artificial Satellite", Consultant Bureau, New York, 1965.
- Birdsall, C.K., and Langdon, A.B., "PLasma Physics via Computer Simulation", McGraw-Hill, New York, 1985.
- Coggiola, E., "Etude Théorique et Expérimentale de l'Ecoulement de Plasma autour d'un Cylindre Non Equipotentiel", Thèse doctorat ENSAE, CERToulouse/DERTS, 16 Juin 1988.
- Delcroix, J.L., "Physique des plasmas I", Monographie Dunod, Paris, 1963.
- Fennel, J.F., Koons, H.C., Leung, M.S., and Mizera, P.F., "The Aerospace Corporation - A Review of SCATHA Satellite results : Charging and Discharging", ESA-SP-198, Noordwijk, The Netherlands, Sept. 1983.
- Gurevich, A.V., Pitaevskii, L.P., and Smirnova, V.V., "Ionospheric Aerodynamics", Space Sci. Rev., Vol. 9, P. 805, 1969.
- Gussenhoven, M.S., Hardy, D.A., Rich, F., Burke, W.J., and Yeh, H.-C., "High-Level Spacecraft Charging in the Low-Altitude Polar Auroral Environment", J. Geophys. Res., Vol. 90, N° A11, P. 11009, 1985.
- Katz, I., Mandell, M.J., Jongeward, G.A., and Lilley, Jr., J.R., "Astronaut Charging in the Wake of a Polar Orbiting Shuttle", AIAA-85-7035-CP, S-CUBED, AIAA Shuttle Environment And Operations II Meeting, Nov. 13-15, 1985.
- Laframboise, J.G., "Is There a Good Way to Model Spacecraft Charging in the Presence of Space-Charge Coupling, Flow, and Magnetic Fields", Proc. Air Force Geophys. Lab., Report N° AFGL-TR-83-0046, P. 57, 1983. ADA134894
- Levy, L., Sarraill, D., Philippon, J.P., Catani, J.P., and Fourquet, J.M., "Sur la Possibilité de Charge Différentielle de Plusieurs Kilovolts dans le Secteur Jour de l'Orbite Géosynchrone", AGARD Conference on "The Aerospace Environment at High Altitudes and its Implications for Spacecraft Charging and Communication", The Hague, The Netherlands, P. 17-1/12, 2-6 June 1986.
- Parker, L.W., "Differential Charging and Sheath Asymetry of Non-Conducting Spacecraft Due to Plasma Flows", J. Geophys. Res., Vol. 83, N° A10, P. 4873, 1978.
- Parker, L.W., "Contributions to sheath and Wake Modelling", Eur. Space Agency Spec. Publ., ESA SP-198, P. 81, 1983.
- Samir, U., Wildman, P.J., Rich, F., Brinton, H.C., and Sagalyn, R.C., "About the Parametric Interplay Between Ionic Mach Number, Body Size, and Satellite

Potential in Determining the Ion Depletion in the Wake of the S3-2 Satellite", J. Geophys. Res., Vol. 86, N° A13, P. 11161, 1981.

Samir,U., Stone,N.H., and Wright,Jr.,K.H., "On Plasma Disturbances Caused by the Motion of the Space Shuttle and Small Satellites : A Comparison of In Situ Observations", J. Geophys. Res.,Vol. 91, N° A1, P. 277, Jan. 1, 1986.

Stone,N. H., "The Plasma Wake of Mesosonic Conducting Bodies, Part 1, An Experimental Parametric Study of Ion Focusing by the Plasma Sheath", J. Plasma Phys., Vol. 25, P. 351, 1981.

Yeh,H.C., and Gussenhoven,S.M., "The Statistical Environment for Defense Meteorological Satellite Program Eclipse Charging", J. Geophys. Res., Vol. 92, N° A7, P. 7705, 1987.

FIGURE 1 :

Ion flow effects in low earth polar orbit

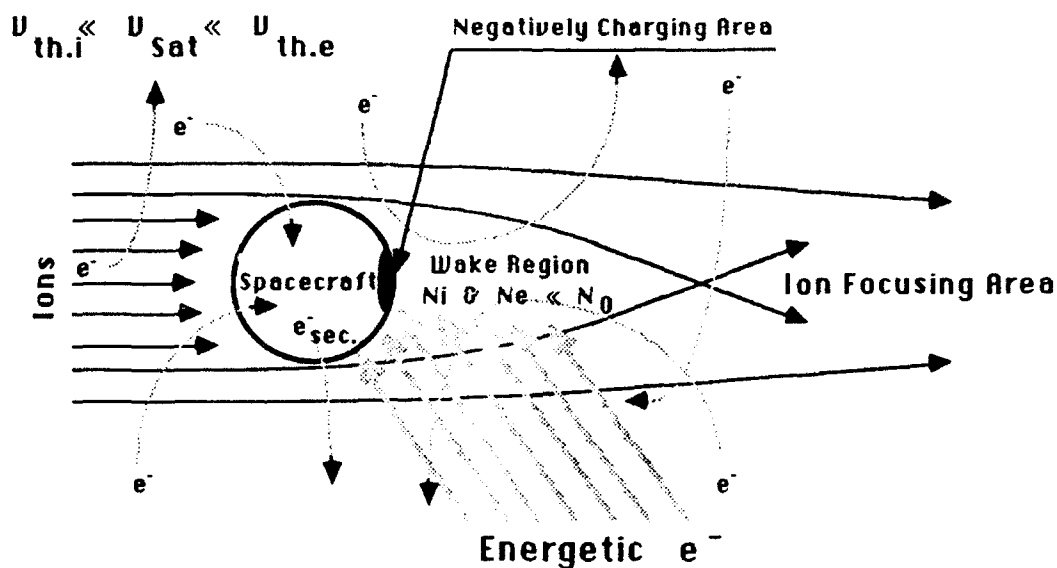


FIGURE 2 :

Diagram of the calculation area. It shows the polar computational mesh and the boundary conditions. The entrance frontier for particles (ions) is tint.

R_{sat} : spacecraft radius

$V_d = -V_{sat}$: ion drift velocity

$V_{th.i}$: ion thermal velocity

$M_i = V_{sat} / V_{th.i}$: ionic MACH number

ϕ_c & ϕ_d : potentials of the main structure and of the isolated part

(r, θ) : polar coordinates

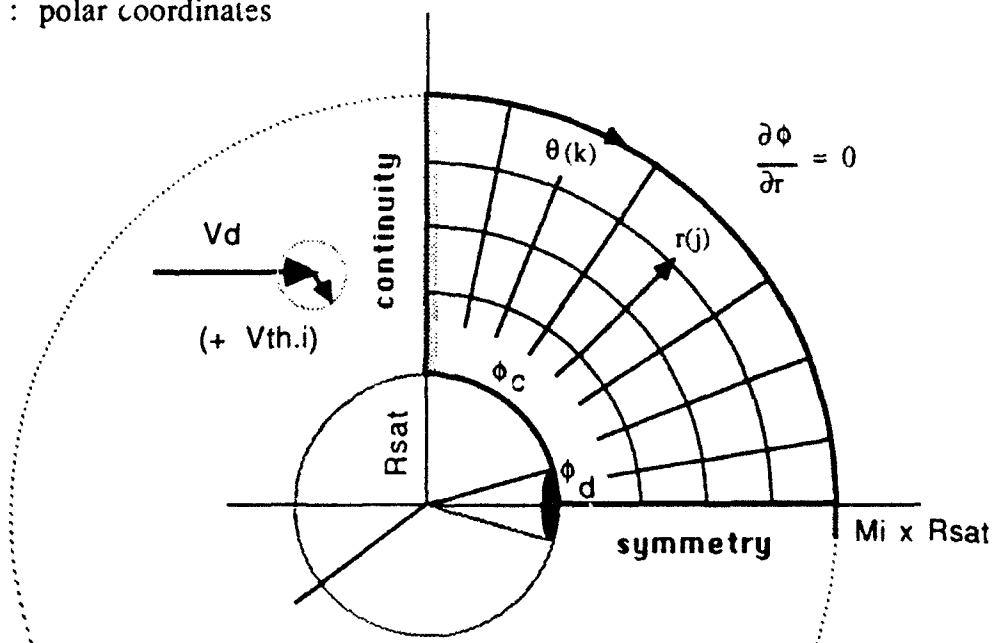
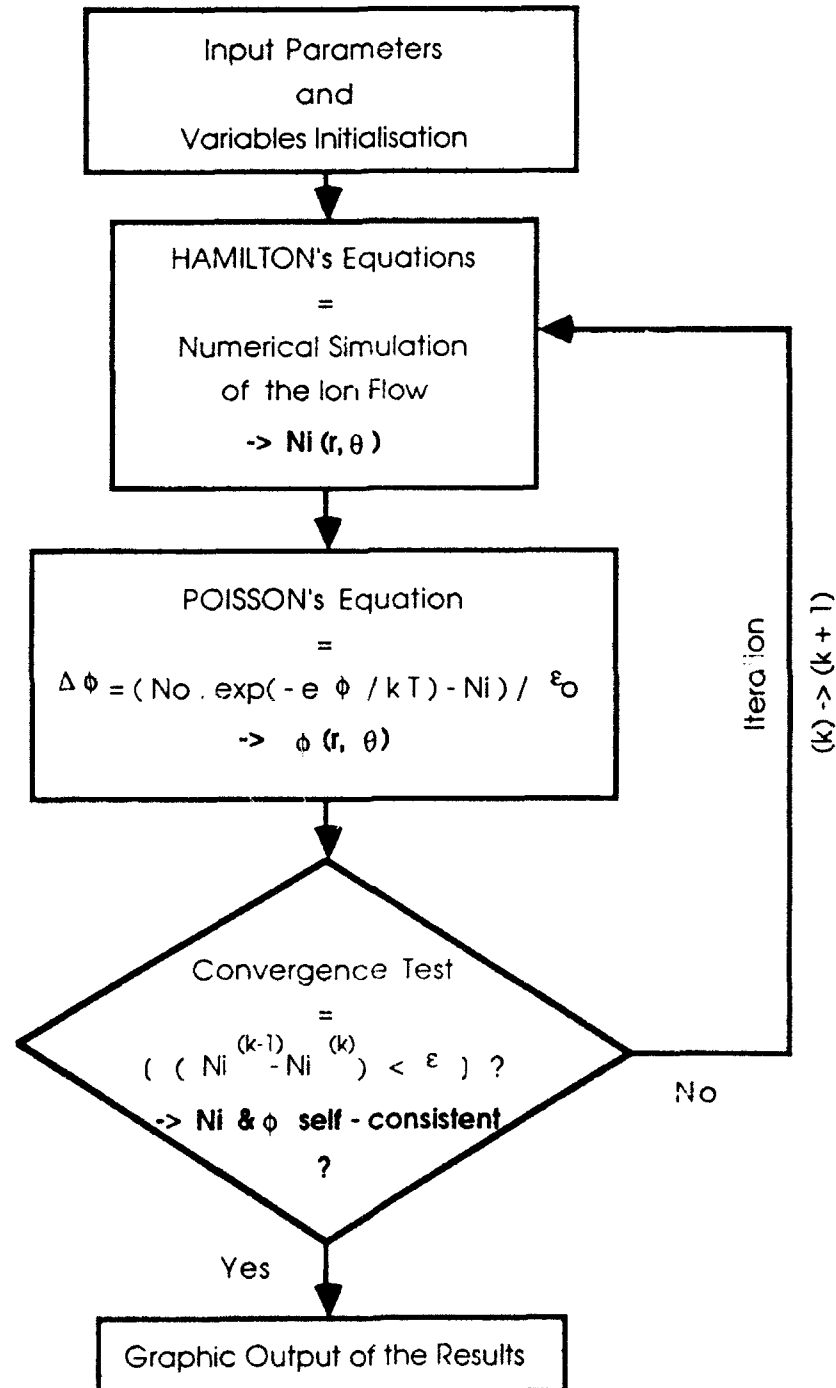
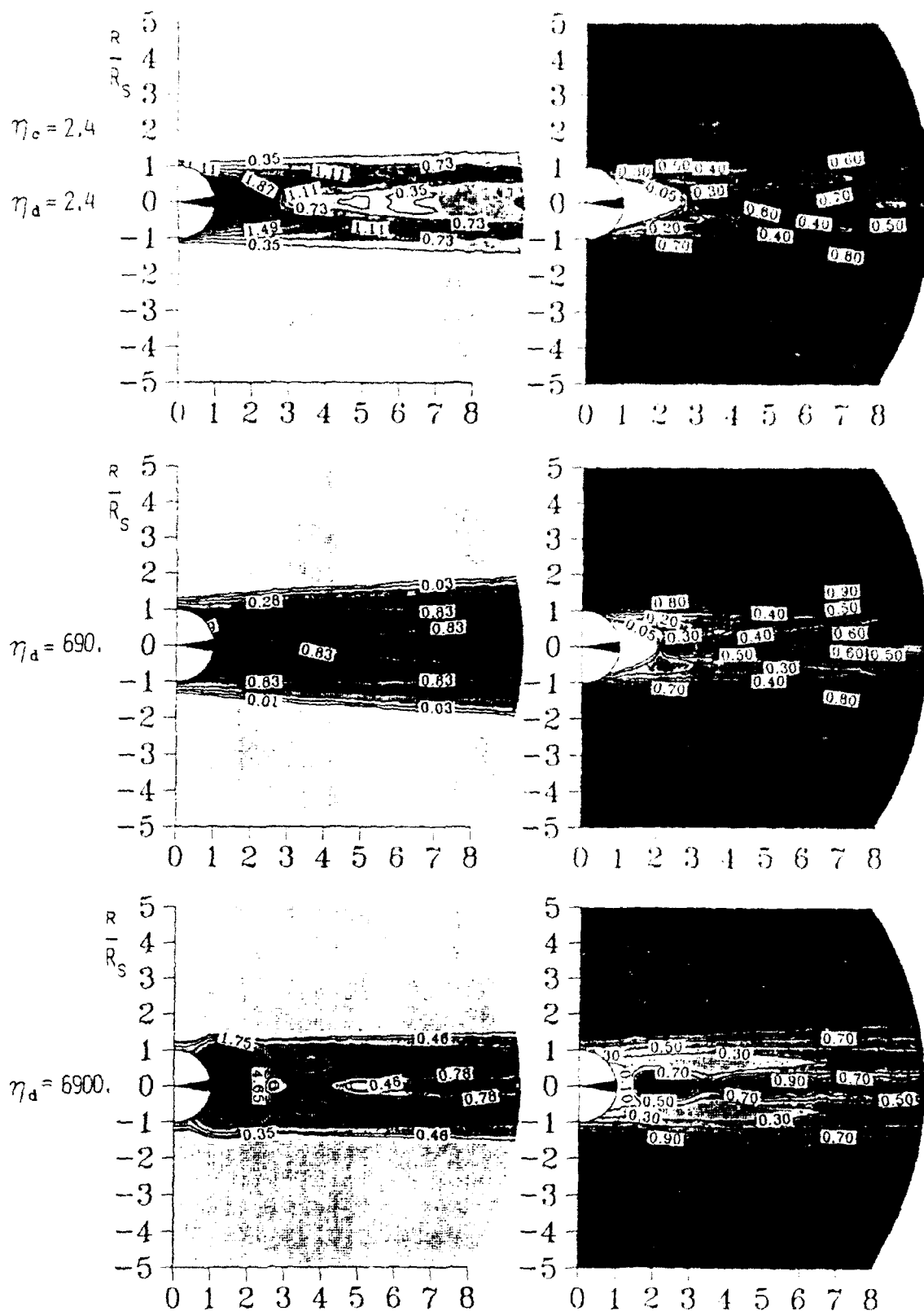


FIGURE 3.:

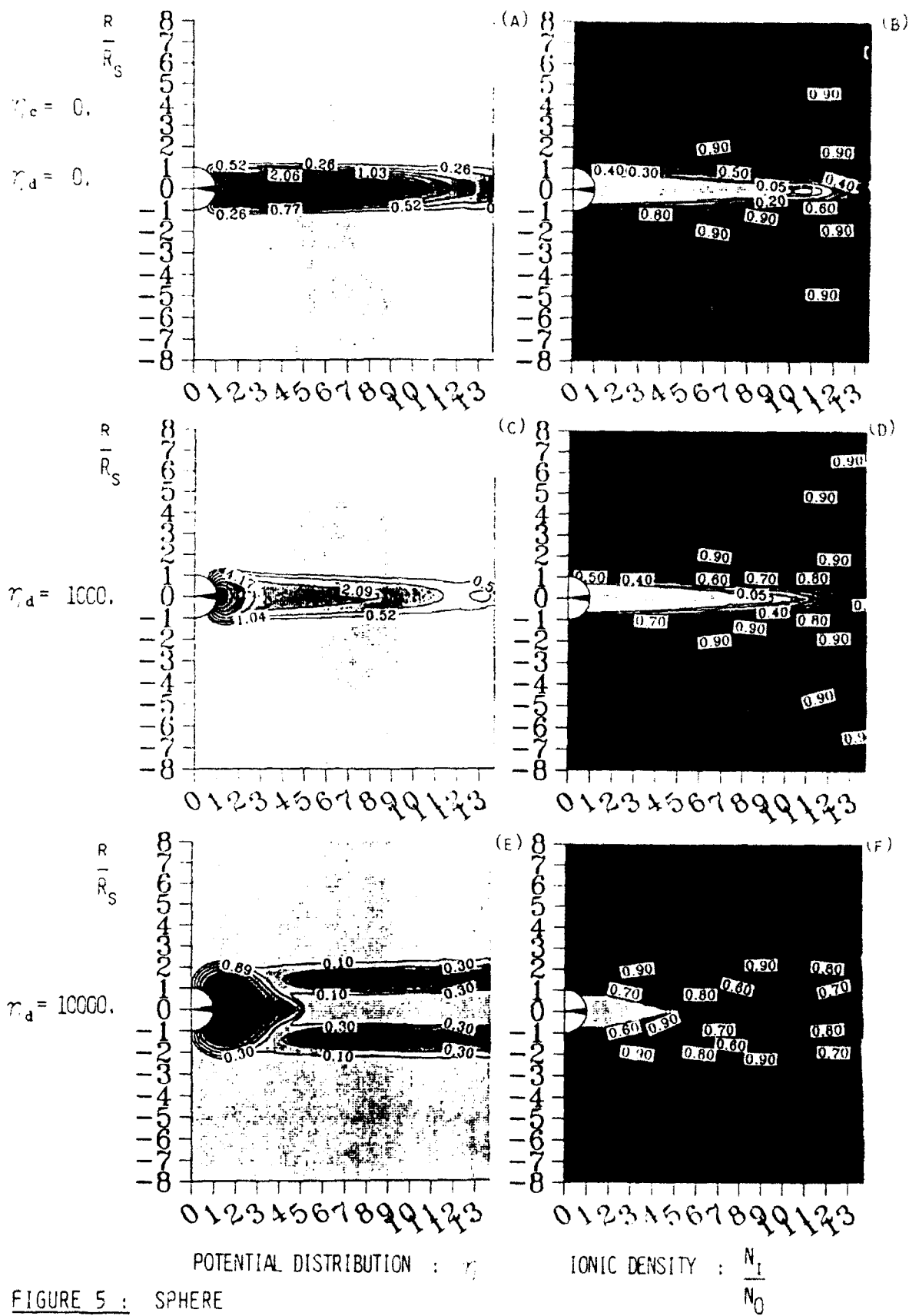
Numerical algorithm for the resolution of the coupled Hamilton's and Poisson's equations.





POTENTIAL DISTRIBUTION : η
 FIGURE 4 : SPHERE

IONIC DENSITY : $\frac{N_1}{N_c}$



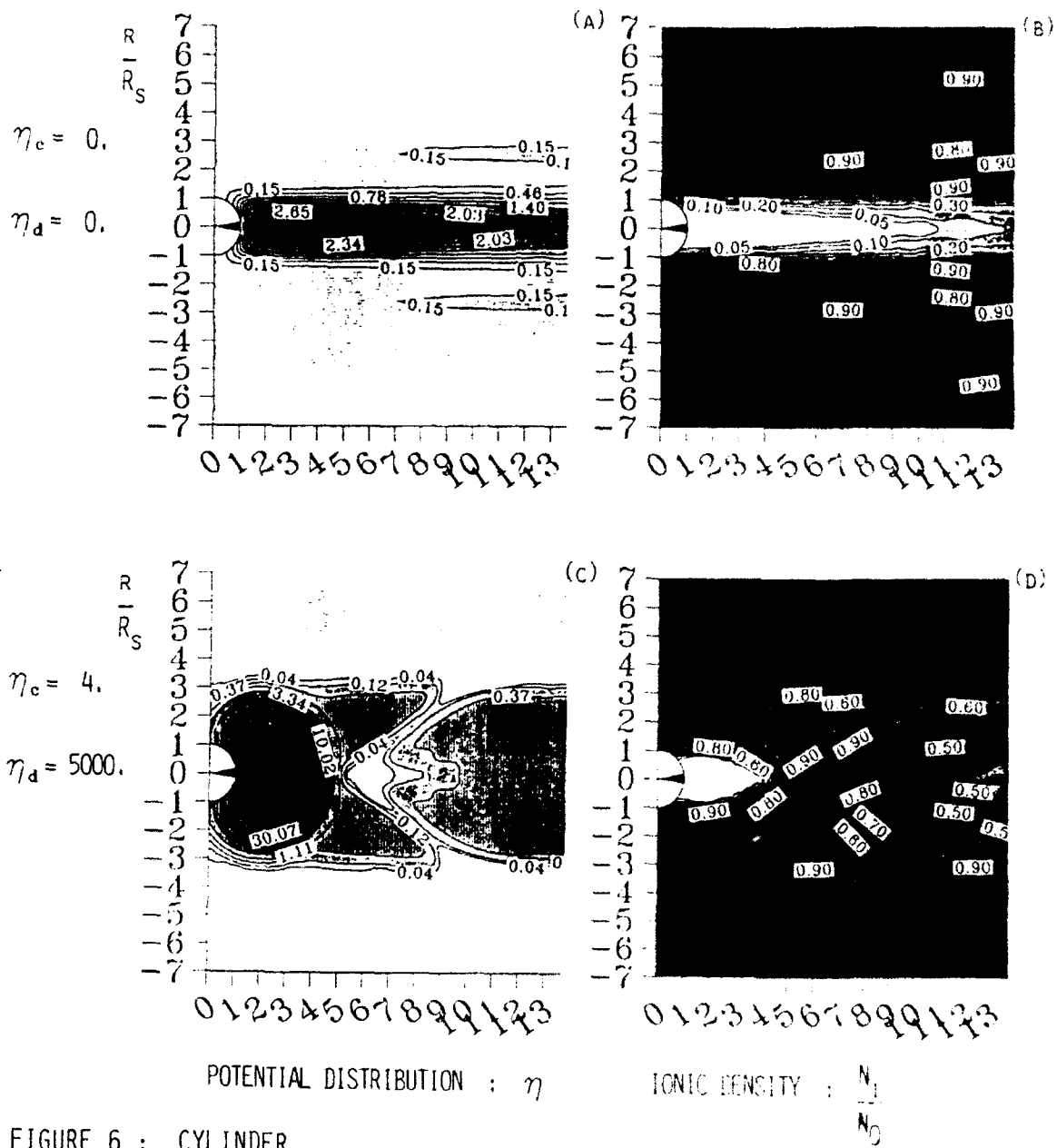


TABLE 1:

Ionospheric Parameters around 500 km high. This plasma is colder and denser than the one at geostationary orbit.

VELOCITIES

electron or ion thermal energy :	1000 °K \approx 0.1 eV
Electron thermal speed :	$2 \cdot 10^5 \text{ m.s}^{-1}$
Ion (O^+) thermal speed :	10^3 m.s^{-1}
Spacecraft velocity :	$8 \cdot 10^3 \text{ m.s}^{-1}$

DENSITY

Plasma density :	10^{10} m^{-3}
-------------------------	--

LENGTHS

Electron-ion mean free path :	10^4 m
Ambient Debye length :	$2 \cdot 10^{-2} \text{ m}$
Ambient Electron gyroradius :	$3 \cdot 10^{-2} \text{ m}$
Ambient Ion (O^+) gyroradius:	5 m

TABLE 2 :

Characteristics of a middle-class spacecraft and its environment in low earth orbit. The satellite radius is much greater than the Debye length, contrary to geostationary orbit conditions.

$R_{sat.}$	= 1 m
$T_e = T_i$	= .15 eV
$m_i (O^+)$	= 2.66×10^{-26} kg
V_{sat}	= 8×10^3 m.s ⁻¹
N_0	= 1×10^{10} m ⁻³
$\phi_c = \phi_{float.}$	= -.36 V
ϕ_d	= -.36, -100., -1000. V

Normalised Parameters used by the code :

$\eta_c = -\phi_c / T(\text{eV})$	= 2.4
$\eta_d = -\phi_d / T(\text{eV})$	= 2.4, 690., 6900.
$\zeta = R_{sat} / \lambda_{Debye}$	= 35.
$M_i = V_{sat} / V_{th.i}$	= 8.4

TABLE 3 :

Characteristics of a mock-up and its environment in a plasma chamber. This plasma is denser and drifts faster than the ionospheric one, around a structure much smaller than a real satellite.

R_{sat}	= 0.1 m
$T_e = T_i$	= 0.1 eV
$m_i (Ar^+)$	= 5.98×10^{-26} kg
V_{sat}	= 15×10^3 m.s ⁻¹
N_0	= 1×10^{11} m ⁻³
ϕ_c	= 0. V
ϕ_d	= 0., -100., -1000. V

Normalised Parameters used by the code :

$\eta_c = -\phi_c / T(\text{eV})$	= 0.
$\eta_d = -\phi_d / T(\text{eV})$	= 0., 1000., 10000.
$\zeta = R_{sat} / \lambda_{Debye}$	= 13.
$M_i = V_{sat} / V_{th.i}$	= 29.

High-Voltage Auroral-Zone Charging of
Large Dielectric Spacecraft: A Wake-Induced-
Barrier-Effect Mechanism

J.G. Laframboise and J. Luo*

Physics Department
York University
Downsview, Ontario, Canada M3J 1P3

ABSTRACT

The Shuttle Orbiter is likely to enter the auroral plasma during high-inclination missions such as the proposed WISP/OMV mission. The usual mechanism for high-voltage spacecraft charging involves the overcoming of secondary electron emission from spacecraft surfaces by an ambient electron distribution which contains mostly energies well above the secondary yield maximum. We discuss a different mechanism, which involves suppression of emitted-electron escape by a potential barrier downstream of the spacecraft, produced by unbalanced electron space charge in its wake. We obtain a tentative prediction that this mechanism can produce potentials roughly 100 V negative with respect to space, on downstream-facing Orbiter surfaces. Predicted potentials become more negative as spacecraft size increases. Shuttle tiles and spacesuit outer fabric have low enough photoelectron yields that daylight auroral-zone high-voltage charging appears possible for these materials. Essentially the entire content of this paper is contained in: J.G. Laframboise and J. Luo, *High-Voltage Polar-Orbit and Beam-Induced Charging of a Dielectric Spacecraft: A Wake-induced Barrier Effect Mechanism*, *J. Geophys. Res.* **94**, 9033 (1989).

Work supported by Air Force Geophysics Laboratory contract no. F19628-83-K-0028.

*Present address: Physics Department, Rice University, Houston, Texas 77251.

SOME EUROPEAN ACTIVITIES ON SPACECRAFT/PLASMA
INTERACTIONS IN LOW EARTH ORBIT

A.R. Martin, P.M. Latham and R.A. Bond
Culham Laboratory, Abingdon, Oxon OX14 3DB, England

ABSTRACT

This paper describes some current European activities on the topic of spacecraft/plasma interactions in low Earth orbit.

One programme is concerned with a study of the mechanisms governing the formation of plasma wakes by large bodies. The work involves both simulation in the laboratory and computational studies using existing computer codes. Although aimed at attaining a better understanding of these mechanisms, the study will provide input to large platform design studies, and into the requirement for the second activity, described below.

The second programme is concerned with spacecraft/plasma interactions and electromagnetic effects in low Earth and polar orbits. It involves the study of plasma wake formation and spacecraft charging phenomena. Again, both experimental and computational work is involved. A suite of computer codes to model various aspects of the interactions is being developed. The intention is to produce an engineering tool for use in spacecraft design studies, and for the assessment of the impact of the space environment on the spacecraft. Cross-validation of the experimental and computational results is seen as an important aspect of this work.

1. INTRODUCTION

In the first decades of the space age, European organisations were active in studying the topic of spacecraft/plasma interactions (SPI) in low Earth orbit (LEO). The work was in support of both space science studies and spacecraft design efforts. Activity ranged from measurements in space (Samir and Willmore, 1965; Samir and Wrenn, 1972), through laboratory simulation (Cox, 1965; Clayden and Hurdle, 1967; Agnello, 1969; Pigache, 1971), to computational studies (Martin, 1974).

After this initial period where interest was concentrated on LEO, the emphasis then moved to the study of phenomena occurring in geostationary orbit, and in particular of spacecraft charging and discharging in the space environment. Several European spacecraft suffered from flight anomalies, causing computer upsets and spurious commands, and a significant amount of effort was expended in this area. A recent, comprehensive summary paper is available (Frezet et al, 1989).

More recently still, with the advent of large-scale programmes such as Columbus, MTFF, and Polar Platform, the focus of interest has moved once again, returning to LEO and the questions of the SPI of large, active, long-lived structures in LEO in general, and the polar orbit environment in particular (Thiemann and Bogus, 1986; Martin, 1986; Coggiola et al, 1988; Coggiola, 1988). These studies represent a significant area of activity in Europe at present, and indeed several contributions arising from the work appear in these Proceedings (Wrenn and Sims, 1989; Soubeyran and Levy, 1989).

This paper describes two programmes of work on SPI under way at present in Europe, among other on-going activities just mentioned. The first programme is being carried out by Culham Laboratory (A.R. Martin, R.A. Bond, P.M. Latham) on behalf of the Royal Aerospace Establishment (RAE) at Farnborough in the United Kingdom (Project Monitor, G.L. Wrenn). This is concerned with a study of the mechanisms governing the formation of plasma wakes by large bodies. The work involves both simulation in the laboratory and computational studies using existing computer codes.

The second programme is being carried out on behalf of the European Space Agency (ESA; Project Monitors, E.J. Daly and J. Hamelin). Culham Laboratory is heading a consortium including the Mullard Space Science Laboratory (MSSL) of University College London (A.D. Johnstone, D.J. Rodgers, R.L. Kessel), the Norwegian Defence Research Establishment (B.M. Maehlum, J. Troim) the Technical University of Graz in Austria (W. Riedler, M. Friedrich, K. Torkar), and RAE Farnborough (G.L. Wrenn, A.J. Sims).

The ESA programme is concerned with SPI and electromagnetic effects in LEO and polar orbit, involving the study of plasma wake formation and spacecraft charging phenomena. Following a review and identification of the important interactions, experimental and computational simulations are being carried out, and a suite of computer codes is being developed with the

intention of providing an engineering tool for use in spacecraft design studies, and for the assessment of the impact of the space environment upon spacecraft.

The two programmes are harmonised and co-ordinated to produce a cohesive and comprehensive study. The programme contents are described in more detail in the remainder of this paper.

2. LARGE BODY PLASMA WAKE FORMATION

2.1 Introduction

A spacecraft moving through the LEO plasma does so at a velocity which is hypersonic with respect to the ambient ions, but subsonic with respect to the electrons. This flow condition is referred to as mesothermal, and the motion of the spacecraft will give rise to "plasma aerodynamics" effects. The wake structure caused by the spacecraft, and the associated potential distribution perturbations about the body, will play a critical role in such areas as spacecraft charging, the excitation of turbulence and electromagnetic noise, diagnostic equipment positioning, communications links, etc.

A thorough understanding of the fundamentals of the interaction of large bodies in the LEO ionosphere is a necessary first step towards the study of spacecraft charging and other problems of current interest. Likewise, the conditions in the ionosphere (and in particular in polar orbit) must be quantified and rationalised in order for any computational or experimental work to result in accurate simulation and prediction of the spacecraft - ionosphere interactions.

A large amount of work, both theoretical and experimental, has gone into the study of plasma wakes around vehicles moving in the ionosphere. However, the vast majority has been for the case where the body dimensions are of the order of, or less than, the Debye length λ_D , in the ambient plasma. For the case of large spacecraft, where the R/λ_D ratios are of the order of 100 or more, then there is little previous work to rely on, with the exception of some very recent STS data.

Experimentally, the largest bodies that have been investigated generally had a dimension to Debye length ratio of 40-50, and were simple cylinders or spheres. The wake behaviour was probed axially downstream of the body. While not as complex as the wake produced by small obstacles, there was still structure to be seen and the general characteristics were sufficiently different to those of smaller bodies to discourage extrapolation from one to the other. The potentials applied to the bodies were also modest and not representative of those anticipated in a polar orbit. In addition, the parameter variations (Debye length, ion speed ratio, etc.) were limited.

Computationally and theoretically the situation is somewhat more optimistic. Until relatively recently the largest body modelled has been of the order of 25 Debye lengths. However, in the past few years larger body dimensions have been investigated. At present this has only been carried out using one method of computation and comparison with results from a different mathematical approach is needed. Again, the parametric variation has been limited.

Work carried out for ESA/ESTEC (Coggiola et al, 1988) has shown that the case where the rear of a large spacecraft is shielded from ion fluxes, as a result of the wake set up by its motion through the plasma, and where a large, energetic electron stream is being collected can result in differential charging levels of many kilovolts. This in turn, has the effect of modifying further the potential and density contours about the body and leads to a very complicated flow-field structure. It is this structure that must be better investigated and understood before extensive programmes of work into the detailed mechanisms of the charging problem are embarked upon.

2.2 Computational Simulation

The computational simulation work uses an existing computer code SATIN3, which is a much enhanced version of a code used in previous work (Martin, 1974).

This program represents the distribution of ions by a cold beam and the distribution of electrons by the Boltzmann factor i.e. "cold ion" approximation. The method of solution of the coupled Vlasov-Poisson equations for particle density and electric potential is via the use of flux-tubes. In this method the flux of particles in the tube is constant, and the tube is defined by two neighbouring trajectories. Since the cross-sectional area of the tube is known from trajectory calculations, and the particle velocity is also known, the particle density at any point in the tube can be computed. The flow field being investigated is represented by a mesh array of points and the calculated density is assigned to the nearest grid point along the path of the tube. The flux tube evolution is followed from far away towards the body, and the solution method is therefore one of the family of "outside-in" techniques.

The program can solve for the cases of a disc, with axisymmetric rotation about the centre axis, or for a long plate (both bodies are transverse to the plasma flow). Input variables such as ion mass, satellite velocity, body potential etc. are provided for control of the modelling. Large bodies (of the order of 100 Debye lengths) have been modelled in work to date. The limit will probably be set by computer time (and cost) considerations, but this is offset to some extent by the relatively fast computational speed of the program.

The major disadvantage of the code is that the method of solution fails if trajectories attempt to cross over or to reverse direction; a condition which is velocity dependent but in practice occurs at dimensionless body

potentials of - 35 to - 40, where this is defined as the body potential divided by the electron temperature (in electron volts). However, the code will also tackle the case of a second body (or surface) immediately in the shadow of the main body i.e. representative of a high level of differential charging at the rear of the body. In this case, second body potentials as low as - 5,000 have been modelled.

The code has a wide range of graphical output options, including colour contour plotting using customised subroutines. Figure 1 shows an example of the ion density contours and an isometric representation of this and Figure 2 shows the potential and density contours for a disc, with a dimensionless body potential of - 4 and an area immediately behind this with a potential of - 5,000.

As well as this numerical work, the output from the computer runs are being used as data for input into the development of semi-empirical models (Martin, 1974; Stone, 1981) which predict the wake dimensions and shape as a function of parameters such as body size, spacecraft Mach number and spacecraft potential. As an example, Figure 3 shows a comparison of numerical data (points) with semi-empirical model fits (solid lines), for the variation of the length of the wake behind a body as a function of Mach number, for three different sized bodies.

2.3 Experimental Simulation

The experimental work is being carried out in a large LEO plasma simulation facility at Culham. Some relevant details of the facility are given in Table 1, together with the corresponding characteristics of the test facility at the Norwegian Defence Research Establishment (NDRE) (Troim, 1989), used in work to be discussed in the next section.

Facility calibration has been carried out with a range of diagnostics mounted in the facility to determine the range of plasma temperatures and densities which can be produced. This allows the corresponding range of orbital altitudes which can be simulated in the facility to be evaluated. In terms of LEO plasma environment simulation, altitudes between 200 km and around 1,000 km can be simulated. Ion Mach numbers of $M = 10$ can be simulated, which is somewhat higher than conditions found in LEO. The hypersonic characteristic of the flow should be well modelled, nevertheless.

The experimental programme will map the interaction of large bodies with the above simulated environment. A range of spacecraft size, spacecraft velocity (Mach number) and body potential will be used. The plasma flow fields will be mapped, both axially and radially. The validity of the simulation (scaling laws, facility background pressure effects, etc.) will be investigated. A comparison will then take place of numerical and experimental wake interaction results, together with a critical assessment of the validity or otherwise of each approach.

Critical issues raised by the numerical and experimental work will then be identified, and their impact upon large bodies in LEO, and the proposed Polar Platform in particular, will be investigated. Areas of incomplete assessment will be indicated, together with proposals to rectify this.

3. SPI AND ELECTROMAGNETIC EFFECTS

3.1 Introduction

The second programme of work to be described is wider ranging than that discussed in Section 2 above, and involves the coverage of a wide range of SPI topics.

As background to the study, the concern and activity in Europe over high levels of spacecraft charging in geostationary orbits was referred to above. Interest in the behaviour in LEO was started by the realisation that auroral precipitation zones could cause the same types of effects, with impact on spacecraft, and particularly on large structures (Parks and Katz, 1980). These early numerical studies were followed by evidence from sensors on-board the DMSP spacecraft that suggested that charging up to kilovolt levels did indeed occur (Gussenhoven et al, 1985). Preliminary laboratory experiments (Coggiola et al, 1988; Coggiola, 1988) suggested that high levels of charge could be sustained on a model spacecraft, even in conditions where a relatively high plasma background level was present.

A wide-ranging review of the available literature was carried out, to identify and focus on the effects that may be of great concern for future missions. Topics covered included the effects caused by the hypersonic spacecraft motion through the plasma, the effects caused by exposure to high energy auroral electron fluxes, effects on solar arrays operating in the relatively dense plasmas in LEO, the effects of contamination (both of the spacecraft itself, and by the spacecraft on the ambient neutral and plasma environment), and effects leading to the generation and emission of plasma waves and electromagnetic radiation.

This review, which was written as a detailed and self-contained document, formed the basis for the choice of content of the current programme of work, described in more detail below.

3.2 Computational Simulation

The interaction of a space vehicle with its surroundings in low Earth orbit is a complex phenomena and no simple description will allow all the features to be adequately quantified. The use of computer codes, does, however, provide the spacecraft designer with a powerful tool to analyse some of the effects since many of the physical processes occurring may be included in such codes. Nevertheless, despite the potential of computational methods, it is not realistic, at present, to design a code which includes all the physical processes that may be present in a rigorous and self-consistent manner. Instead it is proposed that a suite of codes be provided each of which will perform an analysis of the spacecraft/plasma

interaction on the basis of a specific but restricted set of assumptions. While each code individually will allow only part of the problem to be addressed the entire suite will allow a much more complete picture to be obtained.

The software being developed will consist of a suite of programs, written in a modular manner, allowing further program additions to take place without disrupting the overall software package. Each program within this suite is assigned to a particular level, generally reflecting the complexity of the program, and of the problem being studied, and also reflecting the level of familiarity required to run and interpret a particular program. Three levels are proposed and these are described in more detail below.

Level 1 is the simplest level of software. It is intended to allow someone unfamiliar with the subject of spacecraft/plasma interactions to define a particular spacecraft and mission requirement, in outline terms, and the software should then determine the characteristics of the space environment which may then be used in more specialised programs in order to study the problem further. Input to the software will consist of, information on the orbital characteristics (altitude, inclination), mission characteristics (time of launch, duration) and spacecraft characteristics (size, materials, solar array dimensions).

The software will interpret this input in terms of plasma interaction parameters relevant to the problem assessment (densities, temperatures, Debye length, high energy particles) as a function of the input parameters (altitude, inclination, time of launch, mission duration).

Level 2 represents a more complicated set of software than Level 1, but still consists of programs which a non-specialist should be capable of running and interpreting. It will consist of several independent programs, each simulating a particular aspect of spacecraft/plasma interactions. At the initial stage, each program will be stand alone, requiring separate dedicated input. The programs will, however, be written in such a way that future enhancements to the software should allow a common data input set to be used with the programs, and commonality of data input will be implemented from the outset.

The types of software intended to be provided at Level 2 are as follows:

- a) A program which gives an estimate of the charge that a body would acquire in a plasma. Analytical relationships will be used, and the code should have a rapid turn-around. Different materials and plasma conditions should be able to be input by the user.
- b) A program which gives an estimate of the current collection, and associated power loss, that a solar array would experience in a

plasma. Empirical relationships, from laboratory simulations and in-orbit testing will be used. Different voltages and plasma conditions should be able to be input by the user.

Additional programs may be added to this level at a future date. An example would be:

- c) A program which gives an estimate of the wake extent and structure that a body would create in moving through a plasma. Semi-analytical relationships from laboratory simulations and in-orbit experiences would be used. Different body characteristics and plasma conditions should be able to be input by the user.

Level 3 represents the most complex set of software, requiring specialist knowledge to run and interpret. It will consist of several independent programs, each simulating a particular aspect of the spacecraft/plasma interactions in detail. The programs may be large and may require substantial amounts of CPU time to run, but anticipated continuing improvements in computer power may alleviate this problem in the medium term. Each program will stand alone, and will require a dedicated data input set.

The types of software intended to be provided at Level 3 are as follows:

- a) A program which gives a self-consistent solution, using particle-mesh numerical methods, to the charge that a body would acquire in a plasma. Different materials and plasma conditions should be able to be input by the user. The output will be written to dedicated files, and a wide range of post-processing options will be available, particularly graphical representation.
- b) A program which gives a self-consistent solution, using particle-mesh numerical methods, to the particle and potential distribution about a body moving through a plasma. Different body characteristics and plasma conditions will be able to be input by the user. The output will be written to dedicated files, and a wide range of post-processing options will be available, particularly graphical representation of the output to enhance interpretation.

As in Level 2 other programs could be integrated into this level.

The proposed structure of the Spacecraft/Plasma Interactions and Electromagnetic Effects program suite is illustrated in Figure 4. Five codes will be developed encompassing all three levels. These codes are as follows:

- LEOPOLD Determination of the characteristics of the low Earth and polar orbit environments. This software is being written at Culham.
- EQUIPOT Analysis of material charging in the low Earth and polar orbit environments. A O-d code. This package is being written at RAE (Wrenn and Sims, 1989).
- SOLARC Analysis of the current collection and associated power loss of solar arrays in the LEO and polar orbit environments. Again a O-d code. This software is being written at Culham.
- PICCHARGE Detailed analysis of spacecraft charging and local plasma modification in the LEO and polar environments. A 2-d or 2.5-d code. This package is being written at MSSL.
- SAPPHIRE Detailed analysis of ram and wake flows due to a charged spacecraft in the LEO and polar orbit environments. A 2-d code. This package is being written at Culham.

(It should be noted that the code names are at this stage only tentative.)

As an example of the way the codes in the suite interrelate, it is envisioned that the user will use the Level 1 software code LEOPOLD to generate the basic space environment data such as particle densities, temperatures and average ion masses that may then be used as part of the input data to the codes at higher levels. Whilst initially and within the current study this will be performed manually, further development will allow this operation to be performed automatically.

As a further example, the use of the Level 2 code EQUIPOT will allow the user to obtain rapid information as to the extent of charging likely for a given material. If a more detailed analysis is required the user will then use PICCHARGE to obtain a detailed and accurate picture of the charging level to be expected.

3.3 Experimental Simulation

The content and scope of the proposed experimental programme will be such that model geometries, plasma conditions, and diagnostic measurements will provide a direct comparison with the output of the computational codes being developed in parallel with this work. The comparison of experimental data and computational output is an essential part in the evolution of accurate, reliable, and validated computational tools. The experimental programme will also aim to provide a complete and self-consistent set of measurements, and to characterise the plasma phenomena over as wide a range of relevant parameters as is feasible within the constraints of the study.

Two main areas of prime concern are being investigated. The first of these is a study of the interaction of a streaming plasma with various bodies of relatively simple geometry, in conditions relevant to the ionosphere. The second area is the charging of bodies with conducting and dielectric materials subjected to the high energy electron bombardment characteristic of the auroral regions, both with and without the presence of a streaming plasma.

The experimental work will be carried out in the LEO plasma simulation facilities at Culham and NDRE, some details of which were given in Table 1. At Culham, the facility has the advantage of greater size, much greater pumping speed, and lower base pressure (several orders lower than the typical working pressure quoted in Table 1). In general more detailed measurements will be taken than at NDRE. The effect of pressure variation on the slow ion fraction in the facility will be investigated, to validate the wake measurements. The wake measurements themselves will be performed for a variety of relevant operating parameters.

The complete list of parameters to be varied, measurements to be made, and the diagnostic requirements which these imply, is necessarily limited by the scope of the overall study, and a trade-off between the experimental and other major aspects of the study must be made. In particular, the balance between the software development requirements, and the need for experimental understanding and validation of codes has been considered carefully.

At NDRE the facility has the ability to vary the ambient magnetic field in the plasma, via the use of an array of Helmholtz coils. The main objective will be to establish the effects of the magnetic field on the properties of the wake region behind a body. The field will be varied to give less than 0.02 gauss throughout the controllable region, 1 gauss in the y-direction, 1 gauss in the z-direction, and a field duplicating the fixed field measured in the Culham facility.

For the charging studies, two models are proposed to provide direct comparison with the computer codes. The first of these consists of a metal plate, illustrated in Figure 5, which can be biased by an external supply. Along the centreline are positioned a number of isolated plugs, designed so that the insulator is not directly irradiated by the electron gun. The charging of these under different conditions will be measured externally using a high impedance probe.

The second model is also a metal plate, illustrated in Figure 6, which can be biased by an external supply, or left electrically floating. Provision will be made for attaching one or more smaller segments of a variety of dielectric materials. The aim is to determine how the presence and irradiation of a significant area of dielectric alters the charging of the model under various conditions.

The measurements to be made in each of the above cases consist simply of the potentials either of the metal plugs or the model as a whole. As

with the wake simulation studies, the range of parameters to be varied must necessarily be restricted.

While the experimentation will be carried out at Culham and NDRE, the data will also be made available to MSSL and Graz. All four organisations will participate in data analysis and interpretation. The latter two organisations are also providing diagnostic equipment to be used in addition to the standard diagnostics already available.

MSSL are developing a miniature microchannel plate analyser with good angular resolution and excellent charge/mass and energy resolution, of such a size that perturbation of the ambient plasma should be kept to a minimum. Such an analyser should give far greater sensitivity than a conventional retarding potential analyser and this should be very valuable when measuring ion directional information by rotating the analyser.

The Technical University of Graz has produced a compact probe consisting of a small sphere surrounded by a grid. This is a scaled down version of a diagnostic which has been successfully flight tested. When biased negative in the ion saturation region, the sphere acts as an ion probe, providing data on ion current and density. It can also be used as a Langmuir probe, by applying a sweeping voltage and measuring the current response. This should provide the electron temperature and an estimate of the electron density and plasma potential. To minimise stray fields, the correct grid potential and open area are clearly important.

In addition to the main programme described above, it is proposed to perform two other simulations at Culham, with interpretation taking place at all locations. The charging of a second body, such as a small sphere in the wake of a larger body, subject to electron irradiation will be investigated. This relatively simple experiment may elucidate the two body problem, and provide information and a starting point for future investigations.

It is also proposed to investigate the effects on the wake of ejecting a stream of gas from the downstream side of one of the existing models. The aim is to simulate crudely the effects of outgassing or thruster firing. As with the two body charging experiments, the extent of any measurements will be limited. Previous investigations (Martin and Barton, 1974) suggest that the effects on the wake of introducing the gas locally are quite different to those obtained by raising the ambient gas pressure. Again, this work would aim to determine whether further or more detailed investigations are warranted.

4. CONCLUSIONS

As input to the two studies described above a wide range of spacecraft/plasma interactions and their effects have been discussed. Many hold potentially serious implications for future large, long lived, active structures in space, and in some cases could adversely affect the operation and safety of such systems.

Laboratory experiments can adequately simulate the space environment and its interaction with spacecraft, but attention must be paid to the validity of the simulation. Plasma wake studies have generally only covered small to medium vehicles. A reasonable data base on solar array interactions exists. Spacecraft charging studies in polar orbit conditions are in their infancy.

Numerical and computational studies can aid in interpretation of the interaction phenomena and, to a lesser extent, in spacecraft design. The assumptions inherent in several codes limit their application to design activities, until a more fundamental understanding of the basics behind the interactions has been achieved.

There is a large literature concerned with space-based experiences, but interpretation is, at times, difficult and contradictory. Vehicle charging in polar orbits has been indicated, and the adverse effects that active beam emissions can have on vehicles are well established. Again, a reasonable data base on solar array interactions exists, but it should be noted that this is in conflict with ground data.

It is hoped that the work described in this paper will make a significant contribution to the study of spacecraft/plasma interactions, and to the methods used in designing future spacecraft.

ACKNOWLEDGEMENTS

The authors have presented this paper on behalf of our co-investigators at MSSL, NDRE, Graz and RAE, and ourselves. We would like to acknowledge the many helpful discussions and meetings with those listed by name in Section 1. We would also like to acknowledge the interest and encouragement of E.J. Daly, J. Hamelin and J.P. Lebreton of ESA/ESTEC.

This work is carried out under MoD(PE) Contract SLS32A/1937 and ESA/ESTEC Contract Number 7989/88/NL/PB(SC).

REFERENCES

Agnello, V., A plasma-beam system for simulating the interaction of a spacecraft with the ionosphere, ESRO SN-104 (ESTEC), 1969.

Clayden, W.A., and C.V. Hurdle, An experimental study of plasma-vehicle interaction, p. 1717 in *Rarefied Gas Dynamics* (5th Symp.), C.L. Brundin (Ed.), Vol. 2, Academic Press, 1967.

Coggiola, E., Etude theorique et experimentale de l'ecoulement de plasma autour d'un cylindre non equipotential, Doctoral Thesis, ENSAE Toulouse, June 1988.

Coggiola, E., L. Levy, D. Sarraill and H. Thiemann, Spacecraft charging study in polar orbit, Final Report on ESA Contract 7141.87, January 1988.

Cox, R.N., Laboratory simulation of the perturbations of the ionosphere by space vehicles, *Astron. Acta*, 11, 183 (1965).

Frezet, M., E.J. Daly, J.P. Granger, and J. Hamelin, Assessment of electrostatic charging of satellites in the geostationary environment, *ESA Journal*, 13, 89 (1989).

Gussenhoven, M.S., D.A. Hardy, F. Rich, W.J. Burke, and H-C. Yeh, High-level spacecraft charging in the low-altitude polar auroral environment, *J. Geophys. Res.*, 90, 11009 (1985).

Martin, A.R. Numerical solutions to the problem of charged particle flow around an ionospheric spacecraft, *Planet. Space Science*, 22, 121 (1974).

Martin, A.R., Polar Platform plasma wake and charging studies, p. 88 in A. Balogh et al (compilers), *Proc. ESA/BNSC/CNES Workshop on Solar-Terrestrial Physics on Space Station/Columbus*, October 1986.

Martin, A.R., and R.F. Barton, Interaction of a neutral gas jet with a plasma stream, The City University, London, Dept. of Aeronautics Research Memorandum, October 1974.

Parks, D.E., and I. Katz, Charging of a large object in low polar Earth orbit, p. 979 in *USAF/NASA Spacecraft Charging Technology Conference III*, NASA CP-2182, Nov. 1980.

Pigache, D., A laboratory simulation of the ionospheric plasma, *AIAA Paper No. 71-608* (1971).

Samir, U., and A.P. Willmore, The distribution of charged particles near a moving spacecraft, *Planet. Space Science*, 13, 285 (1965).

Samir, U., and G.L. Wrenn, Experimental evidence of an electron temperature enhancement in the wake of an ionospheric satellite, Planet. Space Science, 20, 899 (1972).

Soubeyran, A., and L. Levy, Numerical simulation of the wake of the equipotential spacecraft in the ionosphere, these proceedings, 1989.

Stone, N.H., The aerodynamics of bodies in a rarefied ionised gas with applications to spacecraft environmental dynamics, NASA Tech. Paper TP-1933, 1981.

Thiemann, H., and K. Bogus, Anomalous current collection and arcing of solar cell modules in a simulated high density LEO plasma, ESA Journal, 10, 43 (1986).

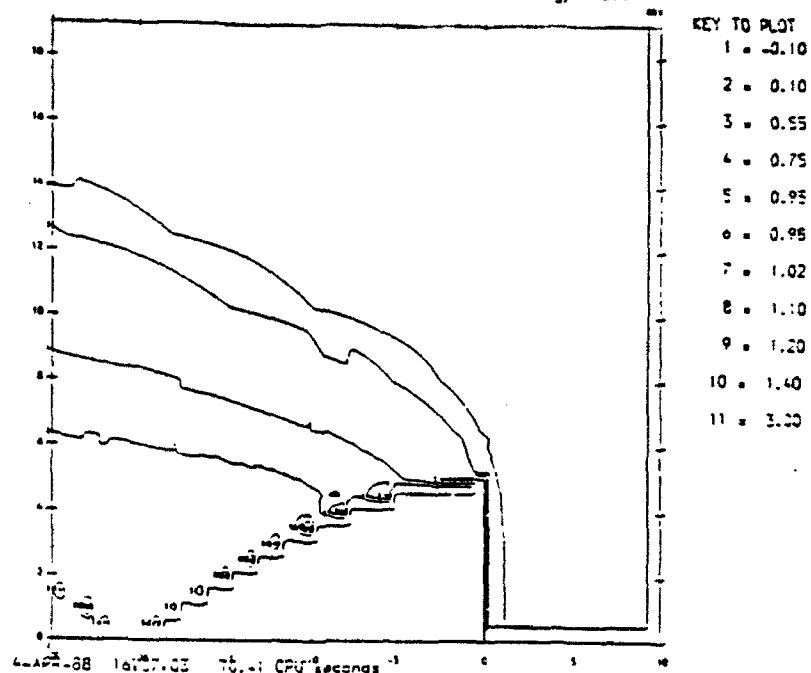
Troim, J., NDRE, Private Communication October 1989.

Wrenn, G.L., and A.J. Sims, Sensitivity analysis with a simple charging code, these proceedings, 1989.

Table 1 LEO Plasma Simulation Facility Characteristics

Parameter	Culham Facility	NDRE Facility
Maximum diameter (m)	1.3	0.96
Total length (m)	5.9	2.0
Total volume (m ³)	7.8	1.45
Type of pumping	Liquid helium and turbopump	Liquid helium and turbopump
Pumping speed (N ₂) (l/sec)	75,000	1,500
Working pressure (mbar)	5 x 10 ⁻⁶	6 x 10 ⁻⁶
Magnetic field	Earth	Variable

Contour plot of ion density for a plate of 5.0 Debye length
 Satellite body potential -1.50 Volts Velocity 0.0345
 Ion Mach number 4.90 Mass ratio 20190.0 Kinetic energy 12.019



Contour plot of ion density for a plate of 5.0 Debye length
 Satellite body potential -1.50 Volts Velocity 0.0345
 Ion Mach number 4.90 Mass ratio 20190.0 Kinetic energy 12.019

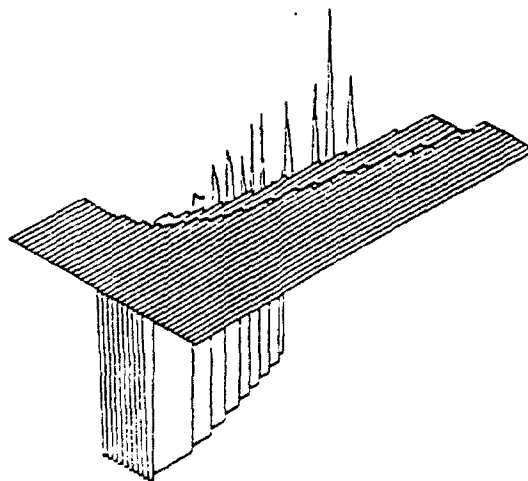


Figure 1 An example of density data generated by SATIN3.

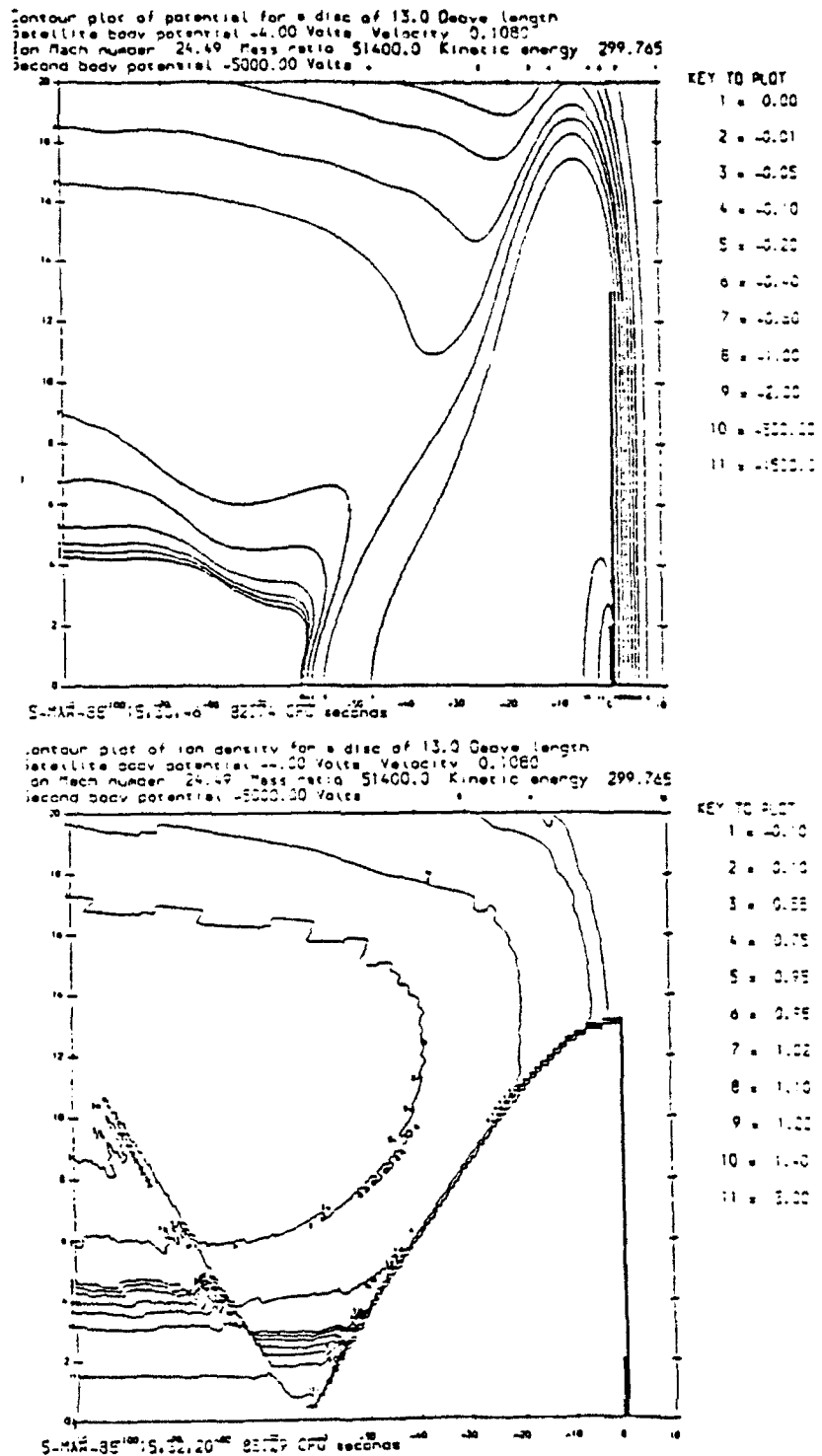


Figure 2 SATIN3 simulation of a body with differential charging.

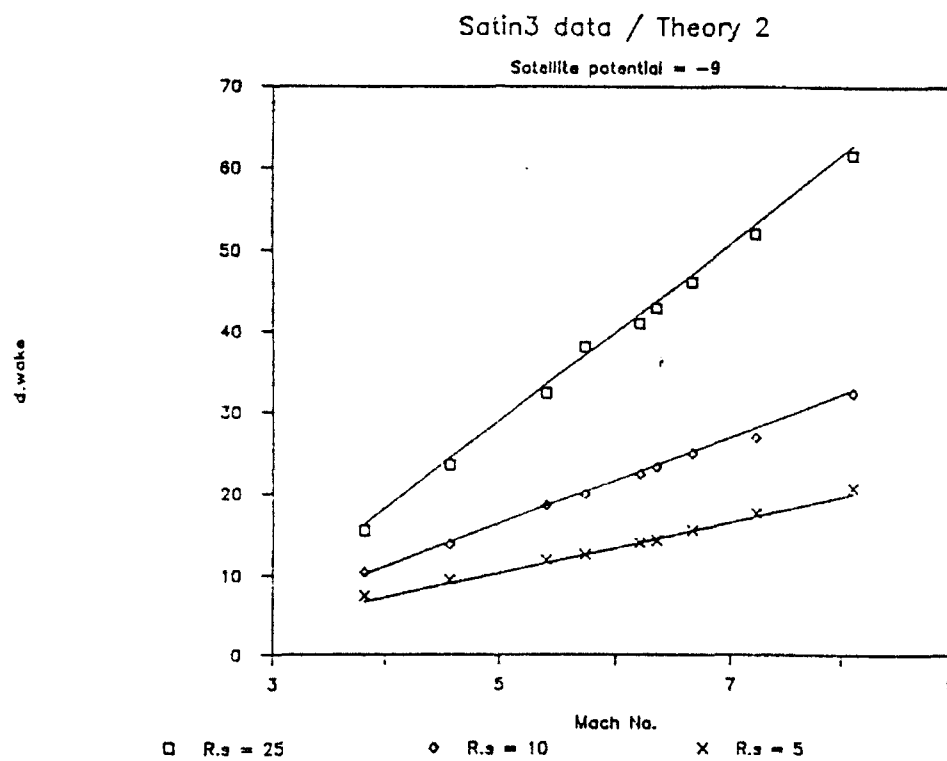


Figure 3 Comparison of SATIN3 data with a semi-empirical model for the wake dimension.

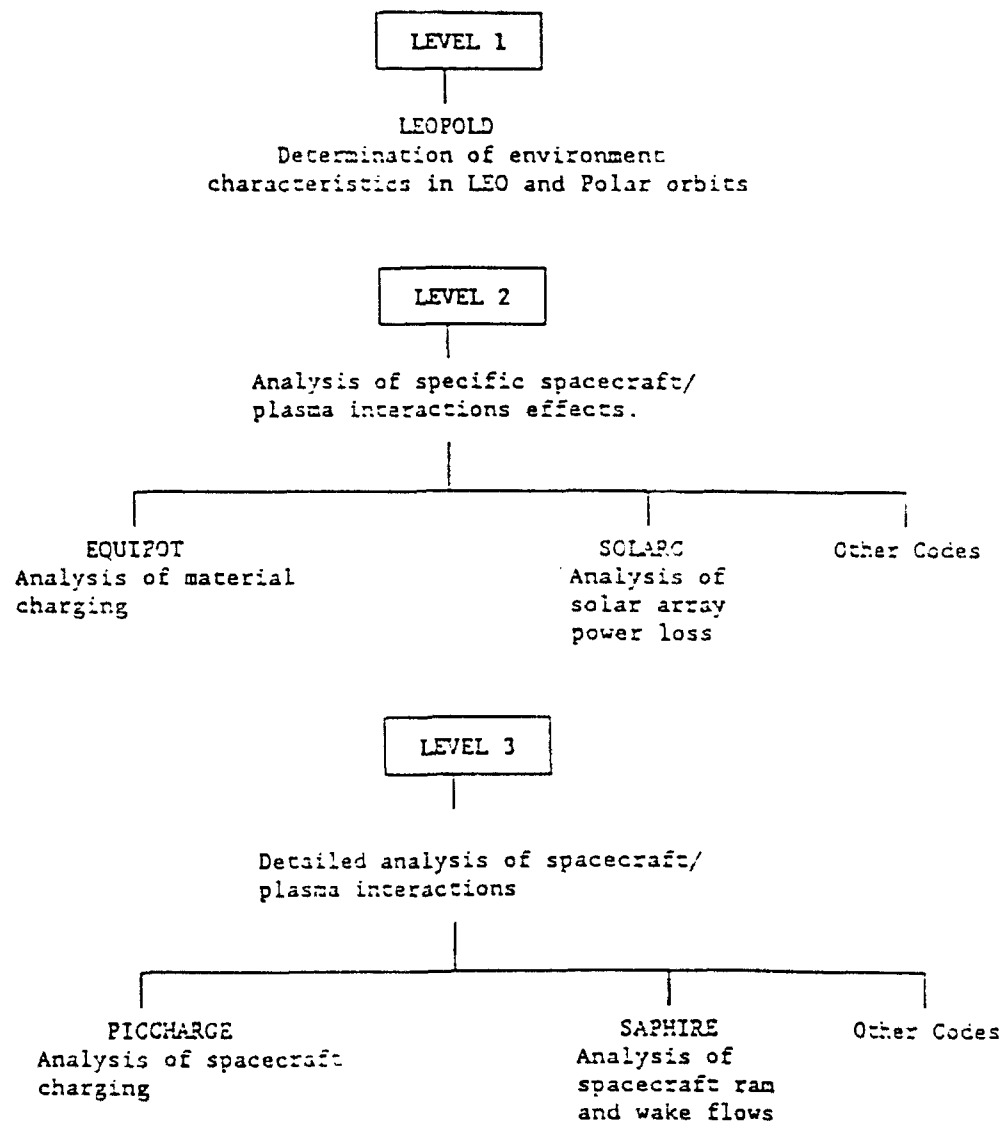


Figure 4 Spacecraft plasma interactions and electromagnetic effects program suite.

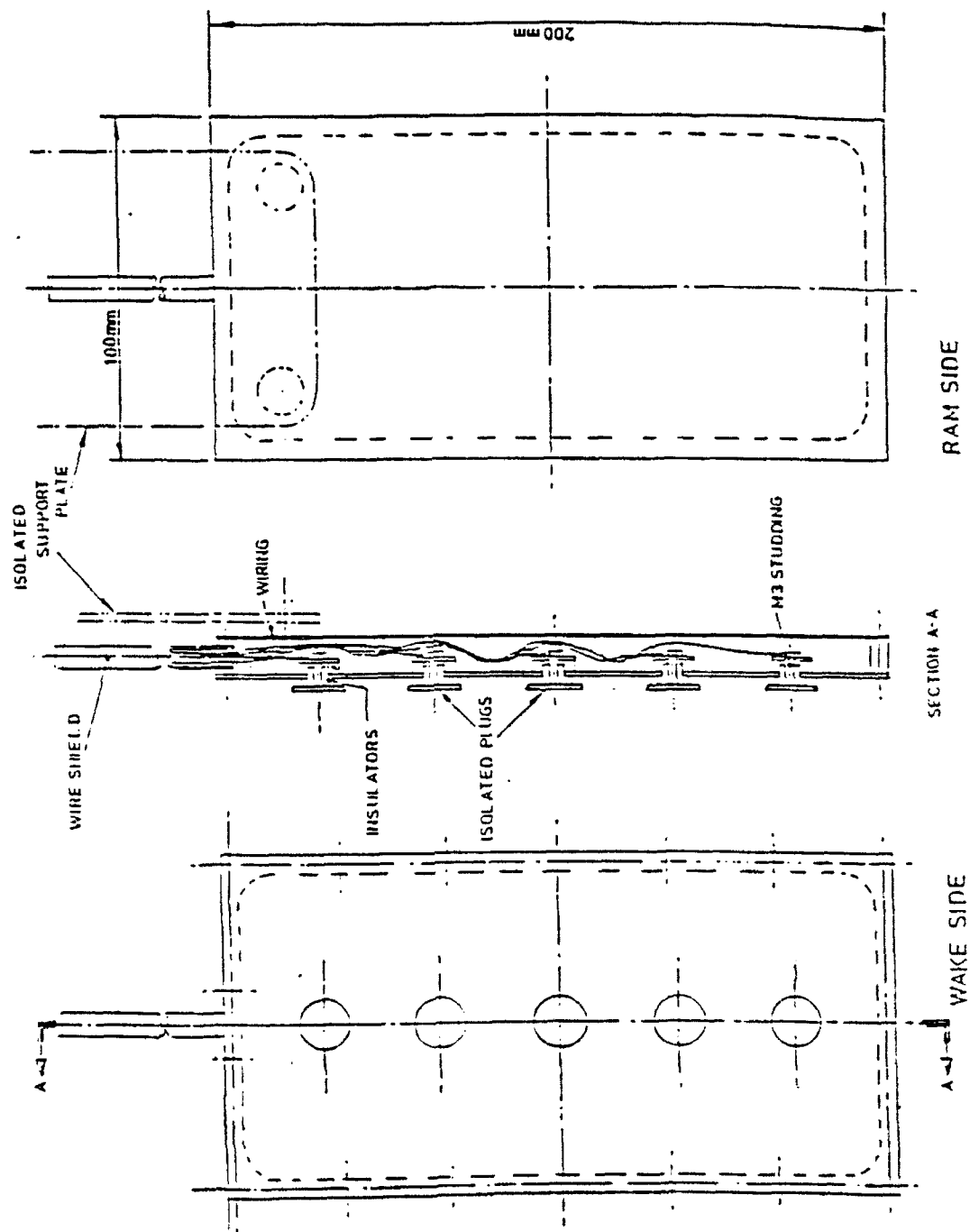


Figure 5 Schematic diagram of the model with isolated plugs, to be used in charging experiments.

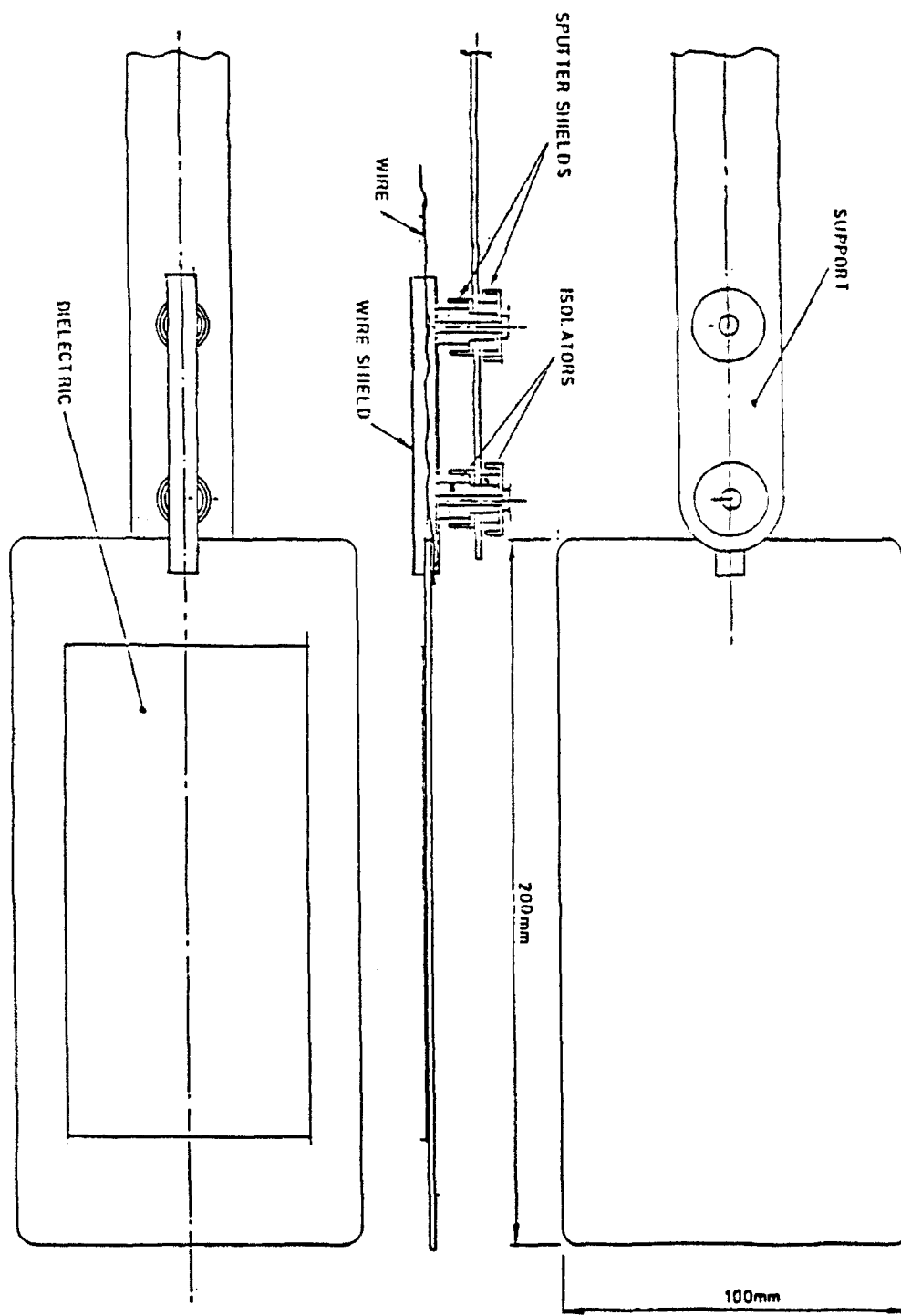


Figure 6 Schematic diagram of the model with dielectric segments, to be use in charging experiments.

A New $2\frac{1}{2}$ -D PIC Charging code for Low Earth Orbit

D.J.Rodgers, R.L.Kessel, A.Etemadi
*Mullard Space Science Laboratory, University College London
Dorking, Surrey, RH5 6NT, UK*

S.T.Brandon
Lawrence Livermore, Livermore, CA, USA

Presented at the Spacecraft Charging Technology Conference - 1989
Monterey, California, USA 31st Oct to 3rd Nov 1989

This work supported by ESA contract no. 7989/88/NL/PB(SC)

Abstract

We describe the construction of a new charging code. This is based on a $2\frac{1}{2}$ -D particle-in-cell code that moves ions and electrons in a self-consistent electric field until an equilibrium is reached. The original code was designed to simulate laboratory experiments at NASA Lewis consisting of a conducting disk plus dielectric or a conducting disk alone, in an isotropic plasma.

The new code includes the effects of a non-self-consistent magnetic field and bulk plasma flow. It can also simulate more general object shapes. It is designed to simulate charging in the Low Earth Orbit environment and more general Laboratory simulations.

1 Introduction

This code, presently named PICCHARGE, is being developed as part of a study [1] being performed for the European Space Agency, involving the Mullard Space Science Laboratory, Culham Laboratory, the Norwegian Defense Research Establishment and the Technical University, Graz. In this study, a suite of computer programs is being developed to enable the scientific investigation of spacecraft/plasma interactions as well as to provide predictions of surface charging for engineering purposes. The engineering aims are met mainly by other elements of the suite, however we expect that PICCHARGE will also be used by engineers to examine small parts of a spacecraft surface where the charging behaviour is unknown. One of the principal features of the whole study is the comparison of results from computer codes with a detailed laboratory simulation program.

2 Origins of the code

We started with a code that had been developed at the University of Kansas to compare with experimental tests being performed at NASA Lewis [2]. This is a particle-in-cell code which tracks positive and negative ions explicitly in a self-consistent electric field. It is 2-dimensional in position but 3-dimensional in velocity, hence it has been described as a $2\frac{1}{2}$ -D code. Figure 1 shows the 2-dimensional spatial grid. Macroparticles having the charge of hundreds or thousands of ions or electrons and of finite size are moved rather than individual ions and electrons, thus speeding up the simulation. The two dimensions of the grid are termed z and r because the space is defined to be cylindrically symmetric about an axis (the z axis). The electric potential is defined at the centre points of the grid cells and is found by 'Successive Over-Relaxation', a finite difference method which uses numerical techniques to come to a rapid convergence. The electric field is found by differentiating the potential. The particles are moved under the influence of this electric field only. When a particle reaches the edge of the simulation area, it is lost to the simulation. However, new particles are continually introduced at these edges. In this code, the new particles have an isotropic Maxwellian distribution and this forms one of the boundary conditions of the simulation. The original code was severely limited in the target objects it could include in the simulations. It would only handle metal disks, with or without a coating of a single dielectric. This disk always lay along the $z=0$ boundary of the simulation space.

We wanted to convert this code from one that simulated a particular laboratory configuration, to one that was more generally applicable to charging in the Low Earth Orbit (LEO) environment and to more general laboratory simulations. To

do this, the following changes were chosen:

a) The mover should be replaced by one that moves particles according to a steady magnetic field as well as an electric field. The magnetic field need not be self-consistent since any induced fields are likely to be far smaller than the strong ambient field present in the Low Earth Orbit region.

b) The plasma introduced at the boundaries should be allowed to have strong drift velocities. This is because satellites in Low earth Orbit typically have velocities through the plasma of about eight times the thermal velocity of the plasma.

c) More general object shapes and positions should be allowed. This allows more complex objects to be simulated and the difference between ram and wake directions to be explored. The objects should, in addition, have multiple surface materials.

d) Dielectric properties should be made more realistic, in particular with the introduction of finite conductivity.

e) Streaming high-energy electrons should be introduced to simulate the effects of precipitating auroral electrons in polar regions.

f) Backscatter electrons should be included. These are electrons reflected from the object surface with almost their input energy. The probability for this process is material-dependent.

g) For better comparison with laboratory experiments it is desirable to be able to introduce a population of cold ions, created from the residual gases by the charge-exchange process and with essentially zero kinetic energy.

h) The original code was written in Rationalized FORTRAN, an uncommon FORTAN dialect. The new code is targeted for VAX/VMS computers but is written in essentially standard FORTRAN-77 so that it can be run almost anywhere.

Items a) b) and h) of this code have been completed, integrated into the existing code and tested. Item c), which is the largest change to the code has been completed, and integrated with the existing code but has not yet been fully tested. Items d), e), f) and g) are expected to be complete soon. The following sections describe work on items a), b) and c).

3 The Mover

The movement of particles may be expressed by equations of motion. In this code these ordinary differential equations (below left) are replaced by 'finite difference' equations (below right) in which the dt term is replaced by a finite time difference Δt .

$$\begin{array}{ll} m \frac{dv}{dt} = F & m \frac{v_{new} - v_{old}}{\Delta t} = F \\ \frac{dx}{dt} = v & \frac{x_{new} - x_{old}}{\Delta t} = v \end{array}$$

The mover calculates the velocity and position one half time-step out of phase. This 'Leap-Frog' method gives the code greater stability which means that larger values of Δt can be used without the code becoming inaccurate. In the new code, the equations of motion take into account the electric and magnetic fields, i.e.

$$m \frac{dv}{dt} = q(E + v \times B)$$

This equation is actually solved by a three-step process devised by Boris [3] that separates the electrostatic and magnetic effects.

Starting at time $t - \Delta t/2$, the particle is accelerated by half of the electric field:

$$v^- = v_{t-\Delta t/2} + \frac{qE\Delta t}{2m}$$

Then, the velocity vector is rotated according to the magnetic field as if there were no electric field.

$$\tan(\theta/2) = -\tan(qB\Delta t/2m)$$

$$v_x^+ = \cos(\theta)v_x^- - \sin(\theta)v_y^-$$

$$v_y^+ = \sin(\theta)v_x^- + \cos(\theta)v_y^-$$

Finally, the particle is accelerated by the second half of the electric field to yield the velocity at time $t + \Delta t/2$.

$$v_{t+\Delta t/2} = v^+ + \frac{qE\Delta t}{2m}$$

Although this mover is performing more complex calculations than the simple electrostatic mover, most of the complicated terms can be precalculated at the start of the simulation and so the new mover is only about 10% slower than the original.

Figure 2 shows a test that was performed on the mover to see if the time step that was chosen by the code was appropriate. The figure shows three trajectories, one with time step Δt as chosen by the code, another with $10 \times \Delta t$ and another with timestep $0.1 \times \Delta t$. The trajectory produced with timestep $10 \times \Delta t$ shows significant deviation from the other two trajectories which are practically overlaid. This means that the chosen timestep is appropriate because the trajectory is accurate to far less than the grid cell dimension and yet the timestep is not unnecessarily small.

When the magnetic field was set to zero, the new mover produced trajectories that were identical to the old electrostatic mover. Figure 3 shows an example when the electric field was set to zero. Here the particle simply gyrates around the magnetic field. The gyroradius or 'Larmor radius' of such motion is easily calculated analytically. The diameter of this gyration produced by the code agrees with the theoretical value to 6 significant places, which is easily accurate enough for our simulations.

4 Introducing Drifting Plasma at the Boundaries

The code considers this process in two parts: assigning the correct velocity to a particle entering at a boundary; and calculating how many new particles will enter.

It is necessary to give the new particle a random velocity so that when many particles have been added, they will have the desired velocity distribution. Figure 4 [4] shows the technique used. The desired normalized distribution, $p(y)$ is integrated to form $F(y)$. A random number from the computer random number generator is a 'uniform deviate' i.e. it has uniform probability between 0 and 1. When such a random number value has been obtained, y is chosen such that $F(y)$ has this value. The code only evaluates $F(y)$ at the start when it creates a table of $F(y)$ values.

We consider the three velocity components of the particle separately. When a particle enters a boundary, the probability distribution for the velocity vectors parallel to that boundary will simply be the velocity distribution of the plasma, i.e. $p(y) = f(y)$ where y is the velocity in appropriate units. However, for the velocity perpendicular to the boundary the probability is altered by the fact that particles with high velocities perpendicular to the boundary are more likely to cross the boundary, i.e. $p(y) \propto y f(y)$.

The non-drifting 1-d Maxwellian distribution is:

$$f(y) = \left(\frac{m}{2\pi KT} \right)^{1/2} \exp(-y^2)$$

where $y = v/v_{th}$, v is the velocity and v_{th} is the thermal velocity. Integrating this for the case of velocity parallel to the boundary, to obtain $F(y)$ produces:

$$F(|y|) = \frac{2}{\pi} \int_0^y \exp(-y^2) dy \equiv \text{erf}(y)$$

In the case of the drifting plasma, the same $F(y)$ can be used as long as the drift velocity v_D is added to the resulting velocity.

For velocities perpendicular to the boundary, $vf(y)$ is normalized and integrated to find $F(y)$. For the non-drifting case:

$$F(y) = 1 - \exp(-y^2)$$

In the drifting case, the drifting Maxwellian must be used:

$$f(v) = \left(\frac{m}{2\pi KT} \right)^{1/2} \exp\left(-\frac{(v - v_D)^2}{v_{th}^2}\right)$$

and so

$$p(y) = (yv_{th} + v_D) \left(\frac{m}{2\pi KT} \right)^{1/2} \exp(-y^2)$$

where we now define that $y = (v - v_D)/v_{th}$. The resulting $F(y)$ is more complicated than before:

$$F(y) = \frac{1}{c} \left[-\frac{1}{2} \left(\exp(-y^2) - \exp\left(-\frac{v_D^2}{v_{th}^2}\right) \right) + \frac{v_D}{v_{th}} \frac{\sqrt{\pi}}{v_{th}} \left(\operatorname{erf}\left(\frac{v_D}{v_{th}}\right) + \operatorname{erf}(y) \right) \right]$$

$$\text{where } c = \frac{1}{2} \exp\left(-\frac{v^2}{v_{th}^2} + \frac{v_D}{v_{th}} \frac{\sqrt{\pi}}{2} \left(1 + \operatorname{erf}\left(\frac{v_D}{v_{th}}\right)\right)\right)$$

When $v_D = 0$, this equation becomes identical to the non-drifting case.

The expected flux Γ of new particles is found by integrating the differential number flux $\gamma(v)$ over all velocities.

$$\gamma(v) = nvf(v)$$

For a non-drifting Maxwellian:

$$\gamma(v) = \frac{nv}{\sqrt{\pi}v_{th}} \exp\left(-\frac{v^2}{v_{th}^2}\right)$$

$$\Gamma = \int_0^\infty \frac{nv}{\sqrt{\pi}v_{th}} \exp\left(-\frac{v^2}{v_{th}^2}\right) dv = \frac{nv_{th}}{2\sqrt{\pi}}$$

For a drifting Maxwellian:

$$\gamma(v) = \frac{nv}{\sqrt{\pi}v_{th}} \exp\left(-\frac{(v - v_D)^2}{v_{th}^2}\right)$$

$$\Gamma = \frac{nv_{th}}{2\sqrt{\pi}} \exp\left(-\frac{v_D^2}{v_{th}^2}\right) + \frac{nv_D}{2} \left(\operatorname{erf}\left(\frac{v_D}{v_{th}}\right) + 1 \right)$$

Again, when $v_D = 0$ this drifting case becomes identical to the non-drifting case.

There were numerous tests performed to see that these complicated algorithms produced sensible results in the code. Perhaps the most useful are tests of the stability of the number of particles in the population. In one test where the drift velocity was set to zero, a calibration mode was used in which there was no object in the simulation and particles were reflected from the lower boundary. In this case, the number of particles in the simulation remained stable over a large number of timesteps.

A similar test was performed with a drift velocity 8 times the thermal velocity in the $-z$ direction. The same calibration mode was no longer appropriate and so particles were absorbed along the $z=0$ boundary by a conducting disk held at

zero potential. The fact that no particles could enter at this boundary was not important because the drift velocity was sufficiently high compared to the thermal velocity that essentially no particles would enter from this boundary anyway. In this case too, the population remained stable over a large number of time steps.

5 A More General Shape Definition

The existing grid characteristics were left unchanged when we introduced a more general way of defining objects. This was to minimize the effects of the new changes on the existing code.

Previously, the target object was always a disk lying on the $z=0$ axis. A new method of defining objects has been defined. In this, an object may be built up from blocks the size of the grid cells. The object may be placed anywhere within the simulation grid as long as each of its corners lies at the centre of a grid cell and its edges are parallel to the r and z axes. Different surface materials may be defined beginning at one grid cell centre and extending to another. An example of a simple object is shown in figure 5. This illustrates the one exception to the rule that the corners must lie at the centre of grid cells. If the left hand edge of an object is defined at the centre of the first cell in the r direction, then the code automatically assumes that the user intends the object to extend all the way to the $r=0$ axis. This is necessary to ensure that objects without central holes may be defined.

An individual particle knows whether it is inside the obstacle or not by means of a 'logical grid'. In this system, each grid cell is divided up into 4 quarters that may be individually set to be 'metal' or 'vacuum', i.e. part of the object or not. Figure 6 illustrates the different combinations of metal and vacuum that can be found in one cell. Figure 7 shows what a simple cylinder looks like under this system. The main purpose of this system is for identifying particle impacts on the object. If a particle lies in a grid cell which is not all vacuum, then its trajectory is analysed to see if it has struck the object, and if so where. The charge of the macroparticle is then added to the surface and secondaries emitted as appropriate.

The potential solution is still performed using successive over-relaxation, but the solver has been rewritten. The basic problem is to solve the Poisson equation:

$$\nabla^2 \Phi = -4\pi\rho$$

$$\text{or in cylindrical coordinates: } \frac{\partial^2 \Phi}{\partial r^2} + \frac{1}{r} \frac{\partial \Phi}{\partial r} + \frac{\partial^2 \Phi}{\partial z^2} = -4\pi\rho$$

The finite element representation of this equation is:

$$4\Phi(r, z) - \Phi(r, z+h) - \Phi(r, z-h) - \left(1 + \frac{h}{2r}\right) \Phi(r+h, z) - \left(1 - \frac{h}{2r}\right) \Phi(r-h, z)$$

$$= 4\pi h^2 \rho(r, z)$$

where h is the grid cell length. The code takes account of the presence of an object inside the simulation space, by solving this equation first in a box enclosing the object and then in the space above, below and to either side of the object. The entire calculation is iterated many times until the required accuracy is achieved. Figure 8 shows an example of a potential solution around a simple cylinder. Although this shows the qualitative behaviour we expect, a more rigorous validation of this potential solver is being sought.

6 Summary

We started with a $2\frac{1}{2}$ -D particle-in-cell code of known value in simulating a particular NASA Lewis laboratory charging experiment. In creating PICCHARGE, we have extended this code to treat the effects of magnetic fields and drifting plasmas, which are prominent features of the LEO environment. We have introduced a flexible and more general method of defining objects, so that a greater range of objects may be studied, with more surface materials. In addition, we can now examine differences in wake and ram characteristics. More, extensions to the code are planned to improve the simulation in terms of auroral electrons and material properties and to make comparisons with laboratory experiments easier.

7 References

- [1] Martin A.R and Latham P.M 'Current European activities in Spacecraft/Plasma Interactions in Low Earth Orbit', This Conference.
- [2] S.T.Brandon 'Numerical Simulations of Positively-Biased and Dielectric-Conductor Disks in a Plasma', Thesis, University of Kansas, 1984
- [3] J.P.Boris, 'Relativistic Plasma Simulation - Optimization of a Hybrid Code', Proc. 4th Conference on Numerical Simulation of Plasmas, NRL, Washington D.C., 1970
- [4] W.H.Press, B.P.Flannery, S.A.Teukolsky and W.T.Vetterling 'Numerical Recipes', Cambridge University Press, 1986

CAPTIONS

Figure 1. The 2-D spatial grid of the original code, showing one macroparticle and the conductor and dielectric at the lower edge of the simulation space. From Brandon [1].

Figure 2. Three trajectory plots with timesteps $10 \times \Delta t$, Δt and $0.1 \times \Delta t$. $\Delta t = 3.7 \times 10^{-9}$ s. The trajectory with points most widely spaced had the longest timestep.

Figure 3. Calculated trajectory of a particle gyrating in a magnetic field. Input parameters: R-velocity = -6×10^7 cm/s, Z-velocity = 3×10^7 cm/s, $B_z = 6 \times 10^{-5}$ T. The diameter of this gyration is 11.3713cm, compared with a theoretical value of 11.37136cm.

Figure 4. Transformation method for generating a random deviate y from a known probability distribution $p(y)$. The indefinite integral of $p(y)$ must be known and invertible. A uniform deviate x is chosen between 0 and 1. Its corresponding y on the definite-integral curve is the desired deviate. (Adapted from [4].)

Figure 5. A simple object in the simulation grid. The coordinates describing the corners are shown.

Figure 6. Examples of the combinations of 'metal' and 'vacuum' that can occur in a single cell in the logical grid.

Figure 7. A simple cylinder as it appears to the logical grid system. Each surface cell has an associated number.

Figure 8. An example of a potential solution around a simple object.

V	M
V	V

Lower left corner

V	M
V	M

Left edge

M	M
V	M

Interior upper right corner

M	M
M	M

Interior of object

V	V
V	V

Exterior to object

Figure 6

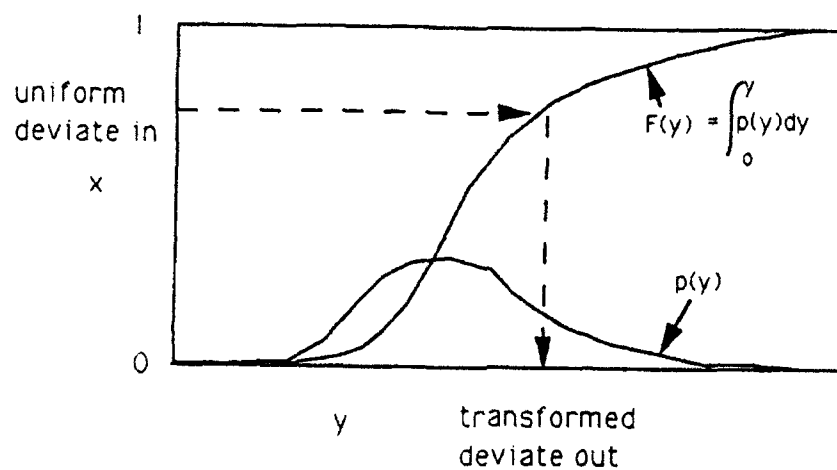


Figure 4

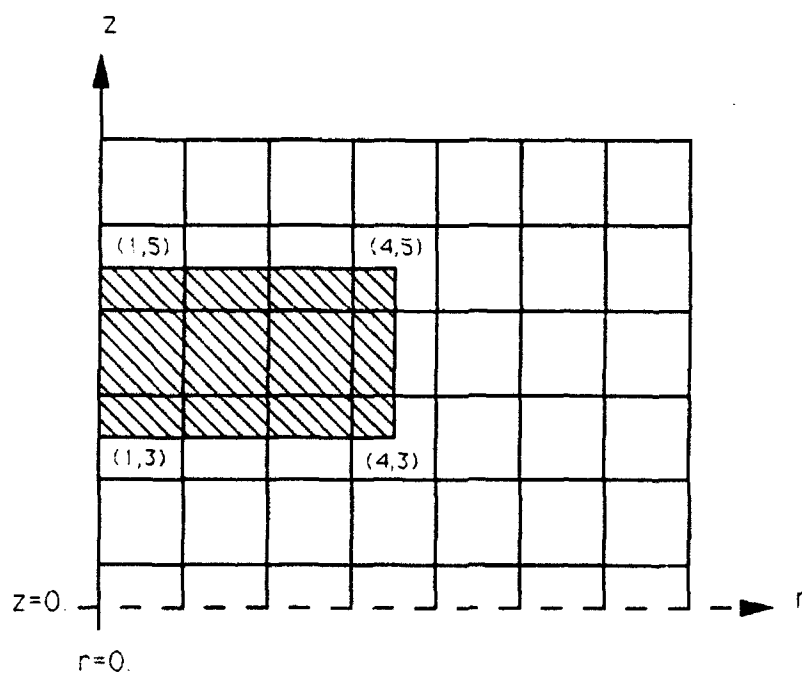
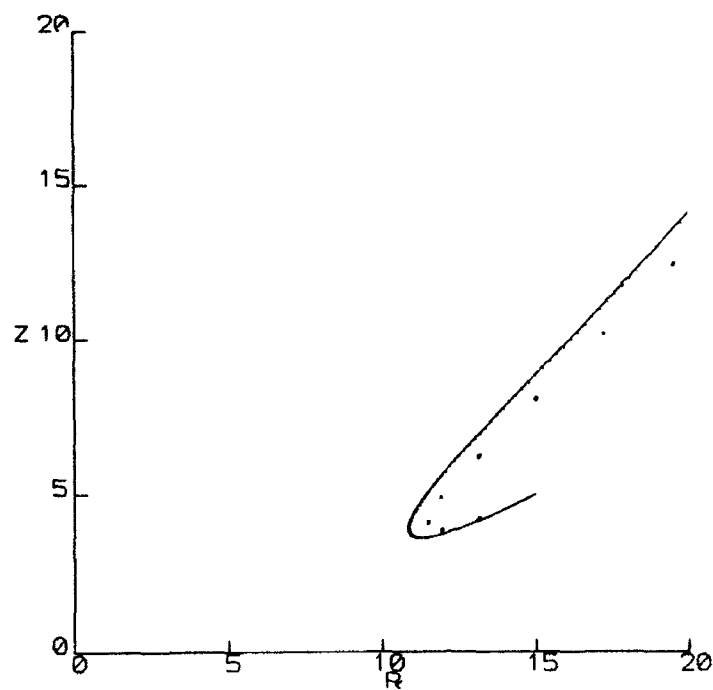
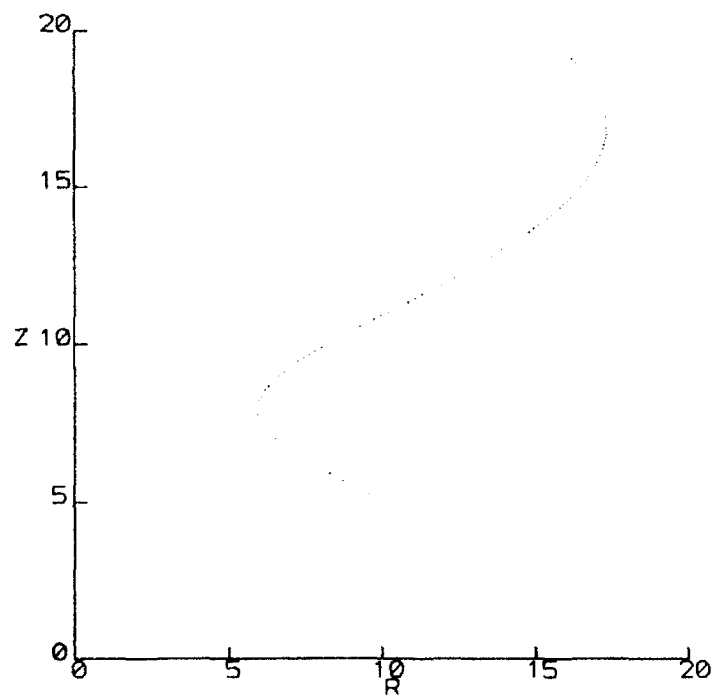


Figure 5



Plot Date: 21-JUN-98 15:44:12
Frame: 5 / 1 User: DJR

Figure 2



Plot Date: 21-JUN-98 15:43:17
Frame: 6 / 1 User: DJR

Figure 3

THE SIMULATION GRID

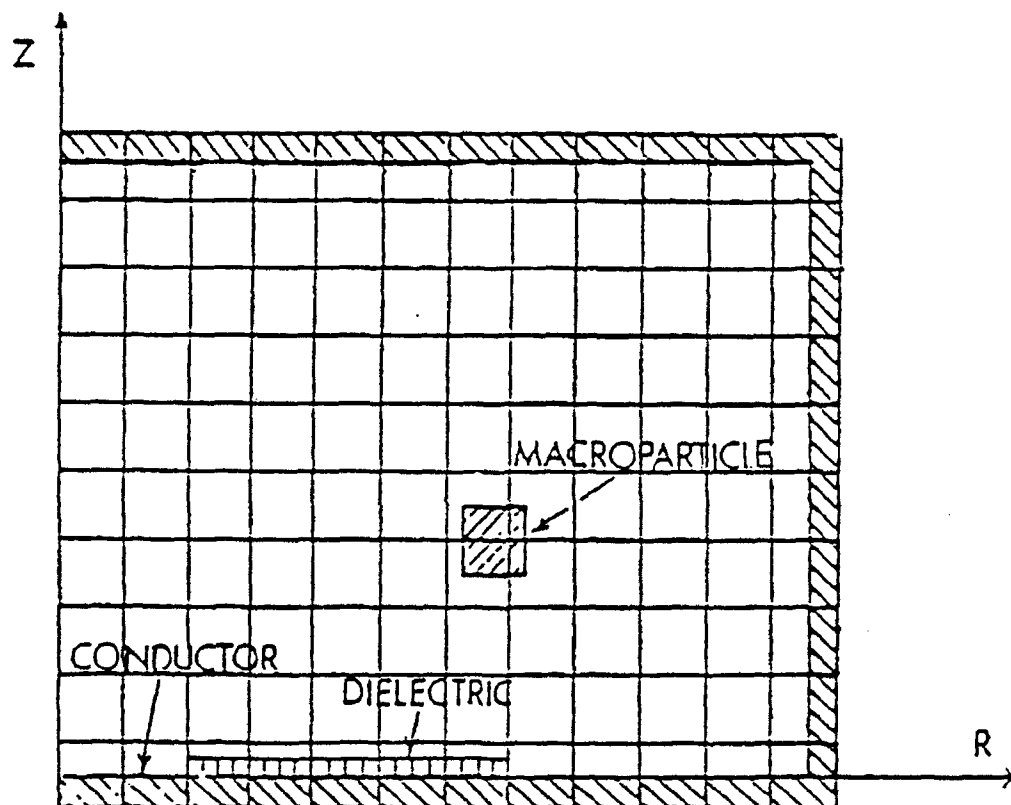


Figure 1

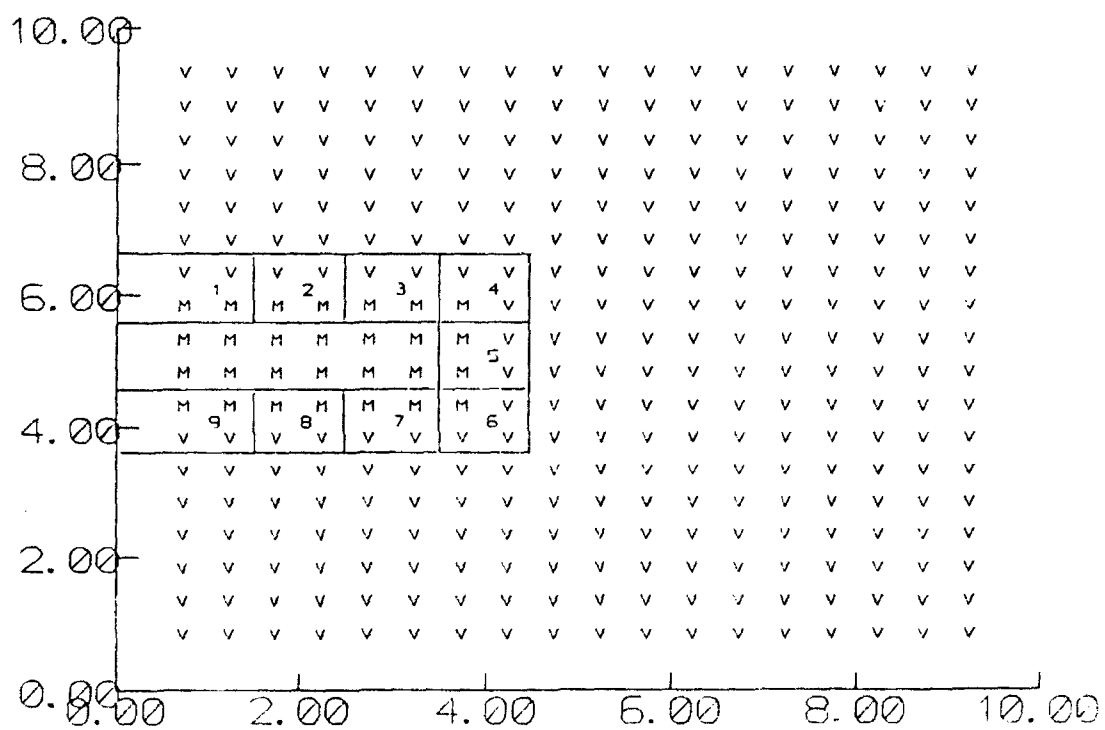


Figure 7

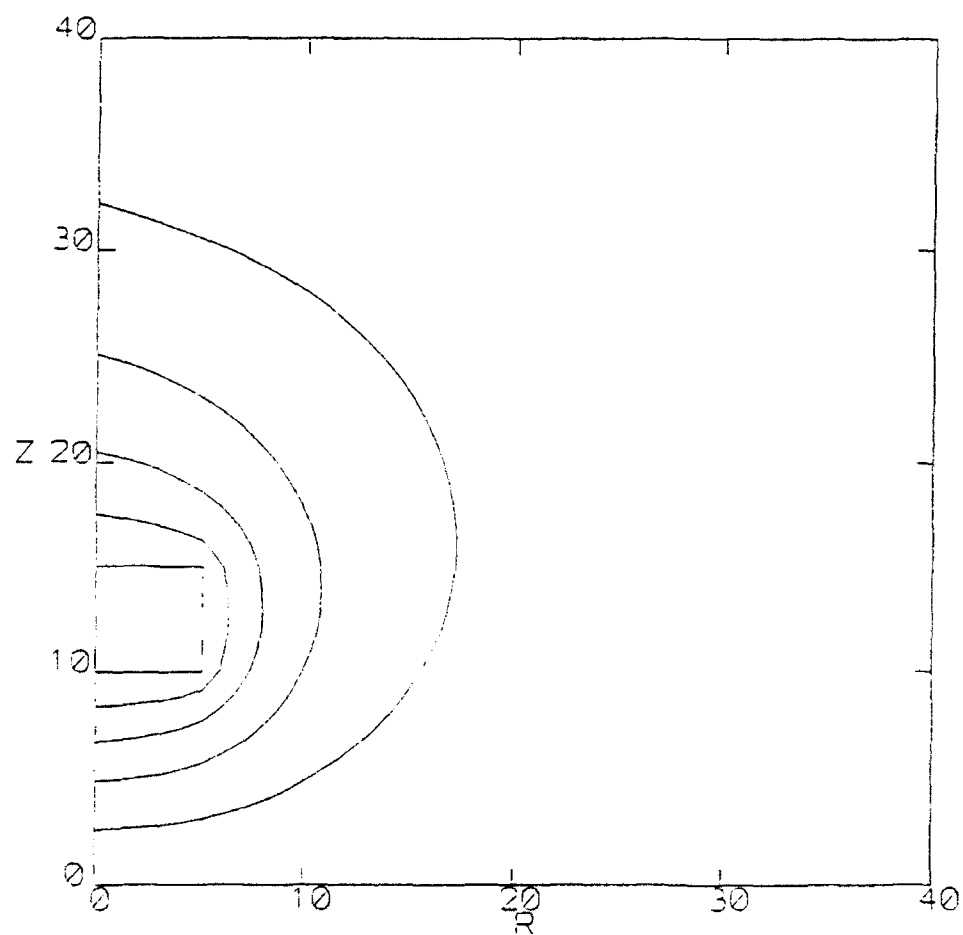


Figure 8

CHARGE ACCUMULATION AND ION FOCUSING FOR DIELECTRICS EXPOSED TO ELECTRON AND ION BEAMS

Gordon McKeil and Keith G. Balmain
Department of Electrical Engineering
University of Toronto
Toronto, Ontario, Canada, M5S 1A4

Abstract

Numerical simulations are reported which successfully reproduce the experimentally observed properties of surface charge accumulation on spacecraft dielectrics exposed to a moderate energy electron beam (20 keV) and low energy positive ions. The ions focus to produce strong differential charging with a sharply defined region of ion neutralization of the dominant negative electron charge. The properties of this "ion spot" vary with ion beam energy, current density, and beam size. The strong peaking of the surface charge at the edge of the ion spot is investigated. The electron and ion currents at the surface are obtained by calculating the particle trajectories in the electrostatic fields of the charged surface and the metal sample mounting components. Two approaches for solving these fields are attempted and discussed, a boundary-charge method and a finite-element method.

Introduction

Spacecraft dielectrics, such as thermal blankets and solar panels, accumulate charge when exposed to the ambient charged particle environment. The exposed dielectrics become negatively charged because typically the electron flux is higher and more energetic than the ion flux. As a first approximation to space conditions, materials and components are often tested in the laboratory by exposing them to electron beams alone. The positive ions could be important, however, because they would be strongly attracted by

This work was supported by U.S. Air Force Weapons Laboratory and the Computer Sciences Corporation (both in Albuquerque, NM), by the Natural Sciences and Engineering Research Council of Canada, and by the Ontario Institute for Space and Terrestrial Science.

Paper presented at the Spacecraft Charging Technology Conference, held at the Naval Postgraduate School, Monterey, Calif., 31 October - 3 November 1989.

surfaces that are at high negative potential either as the result of buildup of electron charge or due to biasing (as with large solar panels).

To investigate the effects of positive ions during charging, laboratory experiments were conducted [Gossland and Balmain, 1983; Balmain *et al.*, 1985] in which samples of polymer sheet were exposed simultaneously to a moderate energy electron beam (typically 20 keV) and low energy ions (< 1 keV). Subsequently, numerical simulations of this electron-ion charging process were undertaken, the results of which are presented in this paper.

The experimental arrangement is depicted in Figure 1. A sample of dielectric sheet with a typical thickness of 100 μm was laid over a grounded metal substrate and covered with a grounded metal mask, thickness 1 or 2 mm, having a circular aperture with diameters from 5 mm to 50 mm. When the electron beam was initially turned on, the entire sample luminesced due to energetic electron impact with the surface. With continued exposure, the luminescence diminished as the surface acquired a negative potential which retarded the incoming electrons. When the ion source was included, a central luminescent spot which did not fade was seen. This spot is interpreted as a region of ion neutralization of the accumulated electron charge, which allowed the incoming electrons to strike the surface with most of their beam energy, causing the strong luminescence. The luminescent spot had sharp boundaries and expanded with increased ion current. Subsequent arc discharges tended to avoid the region of the spot.

Thus the positive ion charge did not distribute uniformly, resulting in some general reduction of the negative charge buildup, but concentrated in an isolated region producing strong differential charging. Other investigators [McCoy and Konradi, 1978] have reported similar luminescence patterns during charging of solar arrays with high negative bias in a plasma.

Surface Current Calculations through Trajectory Mapping

To study the focussing of ions theoretically, it is useful to examine the trajectories of ions approaching a negative charge distribution. Such a charge model with the resultant ion trajectories is shown in Figure 2. The ions can be seen to concentrate strongly at the center of the sample. From such trajectories, the ion current at the sample surface may be calculated [McKeil and Balmain, 1986] for a particular surface charge distribution.

To follow the time development of the surface charge accumulation, a simple "quasi-static" approach is taken. A set of trajectories is calculated for the electrons and the ions in the electrostatic fields due to the accumulated charge on the dielectric surface up to that point in time. The charged-particle currents incident on the dielectric surface are calculated from these trajectories. From the impact velocities and angles, the secondary emission coefficients are calculated and used to obtain the net currents and associated charges deposited. These currents are held constant for a time step, accumulating more charge on the surface. A new set of trajectories is then calculated for the updated charge configuration, and the process is repeated. In this way, the charge on the sample surface is stepped through time and its evolution followed.

To describe the secondary emission and backscattering for electron bombardment, the following expression was used [Wall *et al.*, 1977]

$$SE + BS = K \times E^{-0.725} \times e^{(2(1-\cos\theta))} + (0.1 \times E^{-0.2}) \cos\theta$$

where:

E = impact energy in keV

θ = impact angle of incidence

K = a constant (0.847 for Mylar)

For polymers, the secondary electron emission coefficients due to ion bombardment are not well reported in the literature. For other materials, the values range from SE=1 for metals and semiconductors, to SE=10 for inorganic dielectrics [Krebs, 1983]. In these simulations, the following simple estimate was used.

$$SE = 0.4 \times E^{1/2}$$

Most of the computer time is consumed evaluating the electrostatic fields for the trajectory calculations. To increase efficiency, a solution for these fields allowing quick evaluation is required. Simulations are done here for cylindrically symmetric geometries. Two solution techniques were attempted and are discussed. They are designated as the filamentary-ring-boundary-charge model and the finite-element field solution.

Filamentary-Ring Boundary-Charge Model

In this model, the charge distribution on the sample surface and the surrounding grounded mask is represented by filamentary rings of charge, as shown in Figure 3. Typically fifty to one hundred rings are used to represent the sample and about twenty rings are used for the mask edge.

This approach seems to work well for early charging. However, as the surface charge increases, anomalous ion trajectories with unstable and erratic behavior are seen. Figure 4 shows an example of this, where two of the ion trajectories "skip" across the sample surface. The close-up view shows that the positive ions approach negatively charged regions of the surface and are repelled away instead of being attracted as is physically expected. The reason for this is that the field solution provided by the filamentary charge model is inadequate. Figure 5 shows the solution for the electric field normal to a negatively charged surface over a ground plane. We see that, close to the charged surface, the normal field is not uniformly attractive but oscillates between attractive and repulsive. To attempt to overcome this by increasing the number of charge filaments or by replacing the filaments with a smoother boundary-charge representation, such as with piecewise continuous sections or polynomials, would result in prohibitive computational requirements. To evaluate the field for each charge ring, a second-order elliptic integral must be evaluated. Any smoother charge representation would require third-order elliptic integrals. The boundary-charge technique is judged to be not suitable for use in this simulation of charge accumulation as field evaluations very close to the boundary-charge layer (the sample surface) are required.

Finite-Element Field Solution and Simulation Results

A solution to the electrostatic field problem was obtained using triangular finite elements of cubic order [Silvester and Konrad, 1973]. Over two hundred elements with over eight hundred nodes are used, with smaller elements near the charged surface and mask, and larger elements farther away. Figure 6 shows equipotential lines for a uniformly charged sample. The outline of the grounded mask can be discerned. This finite-element approach eliminates the anomalous trajectories and, since the field is described by bipolynomials within each element, evaluation times are fast. The drawbacks include discontinuous electric fields at the element boundaries and difficulty in obtaining good accuracy estimates [Zienkiewicz, 1971].

The first results of the simulation are given in Figure 7. The accumulated surface charge density is shown in a three dimensional perspective plot as a function of time and radial position. Figure 7 shows the surface charge development for a sample of Mylar sheet 100 μm thick with a circular region 75 mm in radius exposed to a 20 keV electron beam at a current density of 1 nC/mm²/sec and a 1 keV proton beam at 0.005 nC/mm²/sec (5% of the electron current). Initially, the ion beam is undeflected by accumulated surface charge and covers a region with a radius of 100 mm, 4/3 as large as the exposed sample radius. The central region of the sample (at the left side of the plot) with markedly less negative charge accumulation corresponds to the ion spot. The spot edge is very sharp, as was the experimentally observed luminescence pattern.

In the simulation, the energy, current density, and size of the ion beam are varied to see the effect on the surface charge accumulation. Holding the other parameters constant and increasing the ion beam energy produces a larger, less intense ion spot, as shown in Figures 8 and 9. The region of partial ion neutralization of the negative electron charge is larger, but the intensity, the degree of charge neutralization inside the ion spot, is reduced. Varying the ion beam current, but holding the ion beam energy at 1 keV, reproduces the effect seen experimentally that the larger the ion beam current, the larger the ion spot, as shown in Figures 10 and 11. The ion spot also is more intense for larger ion currents.

Finally, Figures 12 and 13 show the effect of varying the size of the ion beam. Shown is the surface charge development for ion beams which initially, without any deflection by surface charge, cover regions of radii 50 mm, 75 mm, 100 mm, and 300 mm, or 2/3, 1, 4/3, and 4 times the radius of the exposed dielectric sample. The ion spot shrinks with reduced ion beam size, but the intensity remains roughly the same. Figure 14 shows how the ion trajectories for the widest ion beam completely envelope the sample area. Therefore, if the size of the ion beam were further increased, the additional ions would hit the grounded mask and not the dielectric sample and the surface charge accumulation or ion spot size would be unchanged.

The surface charge densities show a curious peak just at the edge of the ion spot where the charge density actually reaches positive values for some cases. Examination of the charge accumulation due to the electrons and ions separately indicates that two different mechanisms are involved in the formation of these peaks, depending on the size of the ion beam. Figure 15 shows the separate electron and ion charge distributions for the case with the ion beam having a radius equal to the sample radius. Here the spot-edge peak is not due to any extreme concentration of ions, as the ions-only charge profile

contains no such feature. Rather, the electron and ion surface charge profiles each have abrupt changes at the spot edge which tend to cancel each other, and the spot-edge peak arises because of the relative alignment of these abrupt changes. It is not clear yet whether this is a physical or numerical effect. For the widest ion beam of four times the sample radius the peak is much broader, as Figures 12 and 13 show. Separating the surface charge due to the electrons and ions for this wide ion beam case, as shown in Figure 16, reveals that the peak is now reflected in a concentrated build-up of ion charge. This ion concentration at the spot edge can be seen as well in the trajectories of Figure 14. Because of the similarity between the ions-only charge profile and the electrons-plus-ions charge profile, the edge-peak for the wide beam case is thought to be a physical, rather than purely numeric effect. Other authors have also seen strong peaking of incident ion current at the edge of a region of ion focussing [Parker *et al.*, 1983].

Conclusion

The simulation study confirms the experimental observations of strong differential charging and the formation of the ion spot when lower-energy positive ions are included during electron beam charging of spacecraft dielectrics. The spot characteristics have been shown to depend on the parameters of the ion beam, that is the beam energy, current and size. The boundary-charge model used to describe the accumulated surface charge is inaccurate when calculating trajectories of lower energy particles which closely approach the charged surface. The finite-element approach is a more accurate alternative. In general, it is observed that ion focussing strongly affects the currents incident at the surface of exposed materials and therefore should be considered in the design of systems where charge accumulation or particle bombardment are of concern.

References

- Balmain, K. G., A. Battagin, and G. R. Dubois, Thickness scaling for arc discharges on electron-beam-charged dielectrics, *IEEE Trans. Nucl. Sci.*, NS-32(6), 4073-4078, 1985.
- Gossland, M., and K. G. Balmain, Incident ion effects on polymer surface discharges, *IEEE Trans. Nucl. Sci.*, NS-30(6), 4302-4306, 1983.
- Krebs, K. M., Recent advances in the field of ion-induced kinetic electron emission from solids, *Vacuum*, 33(9), 555-563, 1983.
- McCoy, J. E., and A. Konradi, Sheath effects on a 10 meter high voltage panel in simulated low earth orbit plasma, in *Proceeding of the Spacecraft Charging Technology Conference - 1978*, NASA CP-2071, AFGL-TR-79-0082, pp. 315-340, National Aeronautics and Space Administration, Washington, D.C., 1978. **ADA084626**
- McKeil, G., and K. G. Balmain, Analysis of the ion spot phenomenon on beam-charged dielectrics, *IEEE Trans. Nucl. Sci.*, NS-33(6), 1396-1401, 1986.
- Parker, L.W., E. G. Holeman, and J. E. McCoy, Sheath shapes: a 3-D generalization of the Child-Langmuir sheath model for large high-voltage space structures in dense plasmas, in *Proceedings of the Air Force Geophysics Laboratory Workshop on Natural Charging of Large Space Structures in Near Earth Polar Orbit*, AFGL-TR-83-0046, edited by R. C. Sagalyn, D. E. Donatelli, and I. Michael, pp. 337-389, Air Force Geophysics Laboratory, Massachusetts 1983. **ADA134894**
- Silvester P., and A. Konrad, Axisymmetric triangular finite elements for the scalar Helmholtz equation, *Int. Jour. Numer. Meth. Eng.*, 5, 481-497, 1973.
- Wall, J. A., E. A. Burke, and A. R. Frederickson, Results of a literature search on dielectric properties and electron interaction phenomena related to spacecraft charging, in *Proceedings of the Spacecraft Charging Technology Conference - 1977*, NASA TMS-73537, pp. 569-592, National Aeronautics and Space Administration, Washington, D.C., 1977.
- Zienkiewicz, O. C., *The Finite Element Method in Engineering Science*, McGraw-Hill, New York, N.Y., 1971.

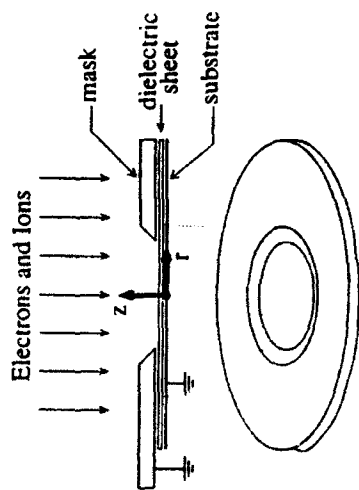


Figure 1

Schematic of experimental arrangement used to expose samples to electron and ion beams. Dielectric sheets were sandwiched between a metal substrate and a metal mask with a circular aperture. The r - and z -axes of the cylindrical coordinate system used throughout the paper are also shown.

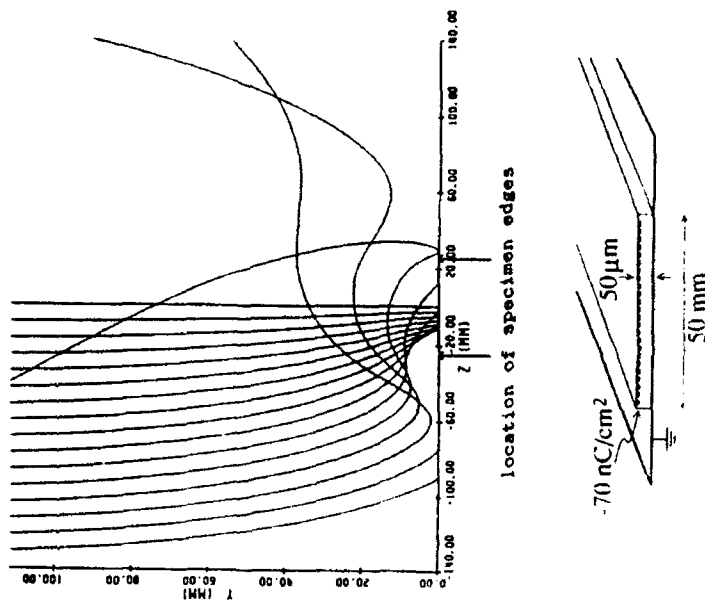


Figure 2

An example of a negative charge distribution and the ion charge trajectories in the resultant electrostatic field showing ion focussing towards the center.

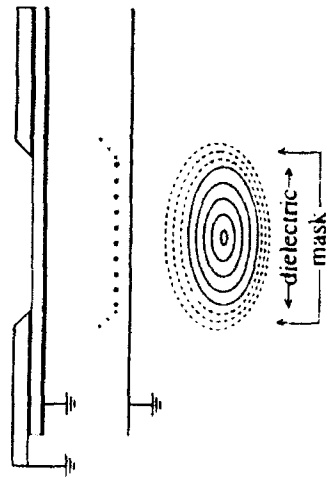


Figure 3

In the filamentary ring boundary charge model the charged dielectric sheet and the surrounding metal mask are represented by filamentary rings of charge over a ground plane, as shown.

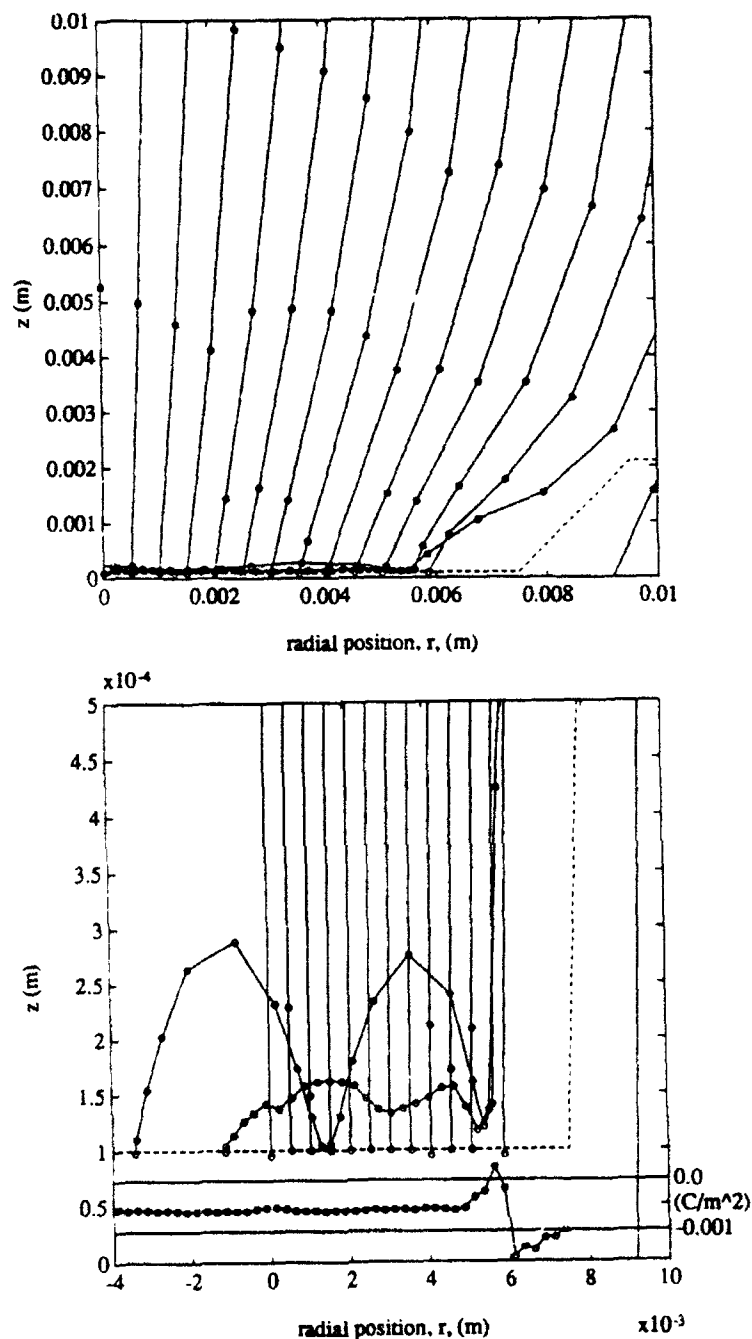


Figure 4

Anomalous trajectories for positive ions approaching a highly charged dielectric and grounded mask. The outline of the dielectric surface and mask are shown with the dashed line. The lower chart shows a close-up view with an expanded vertical distance scale given at the left. A sketch of the surface charge density is included at the bottom with its scale indicated to the right. Two of the right-most trajectories approach negatively charged regions of the surface but are repelled instead of being attracted.

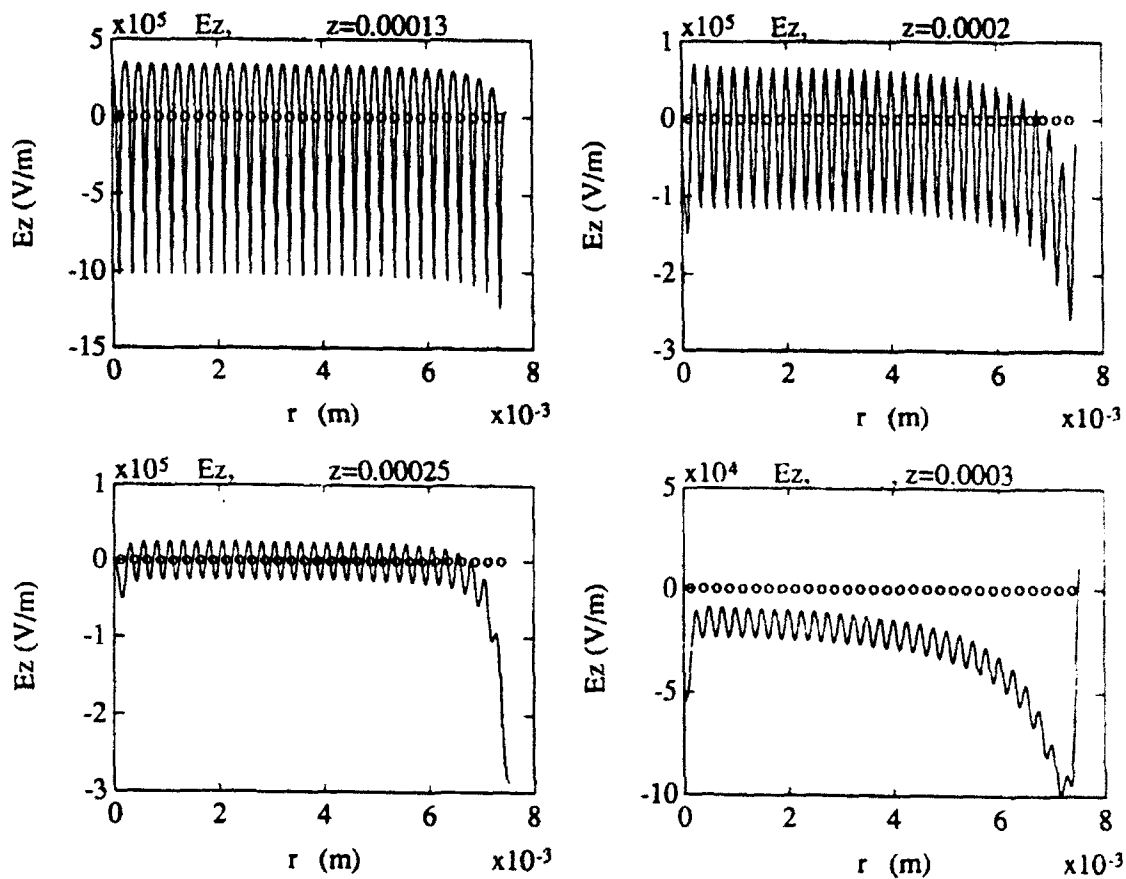


Figure 5 Solution for the normal electric field obtained using the filamentary ring boundary charge model for a dielectric sample with uniform negative surface charge density. The sample thickness is 0.0001 m and the normal field is given for positions of $z = 0.00013$ m, 0.0002 m, 0.00025 m, and 0.0003 m. Physically, the fields are expected to be negative, except perhaps near the mask edge, however, due to inadequacies of the model, the field oscillates wildly near the surface. The charge model and the coordinate system used are depicted in Figure 3.

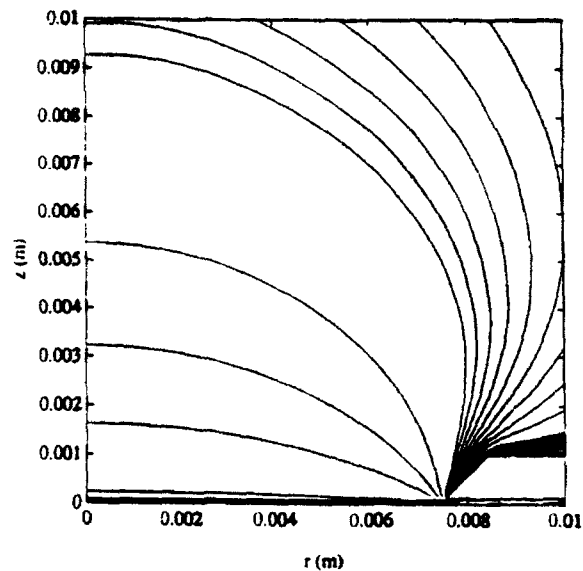


Figure 6 Equipotential lines of the finite element solution for a uniformly charged sample. The outline of the grounded mask can be discerned at the lower right.

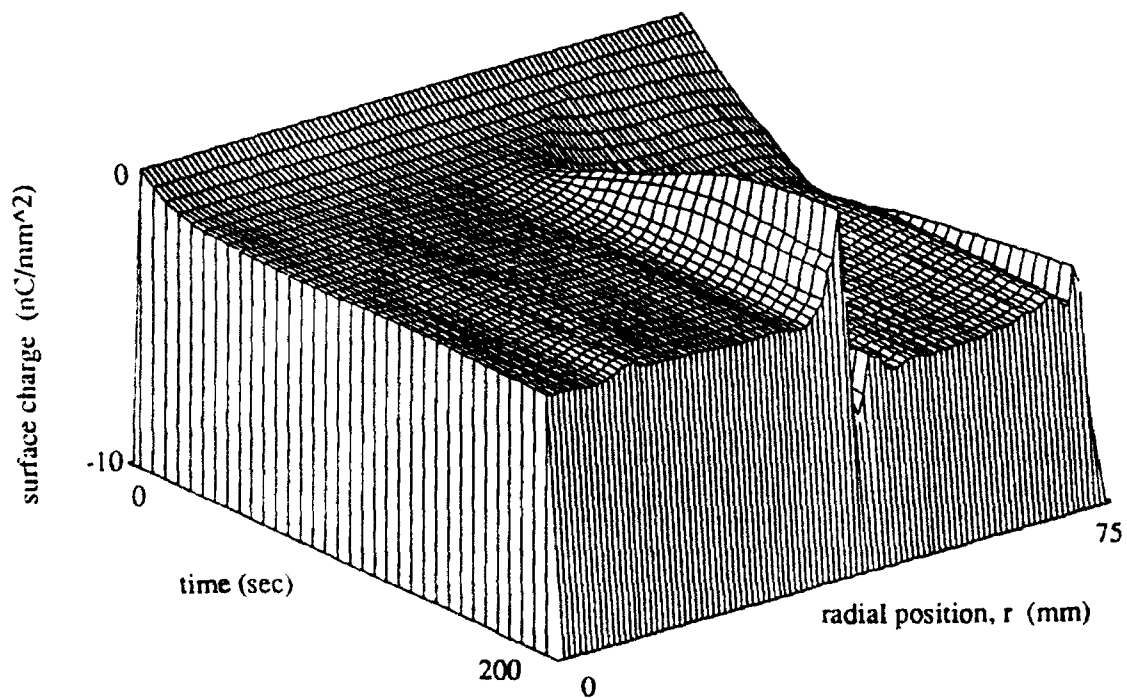


Figure 7 Developing surface charge density shown in a 3-D perspective plot as a function of time and radial position for a $100\text{ }\mu\text{m}$ thick Mylar sample with a circular region of radius 75 mm exposed to a 20 keV , $1\text{ nC/mm}^2/\text{sec}$ electron beam and a 1 keV , $0.005\text{ nC/mm}^2/\text{sec}$ proton beam which initially, before deflection by surface charge, extends to a radius of 100 mm , or $4/3$ as large as the dielectric sample.

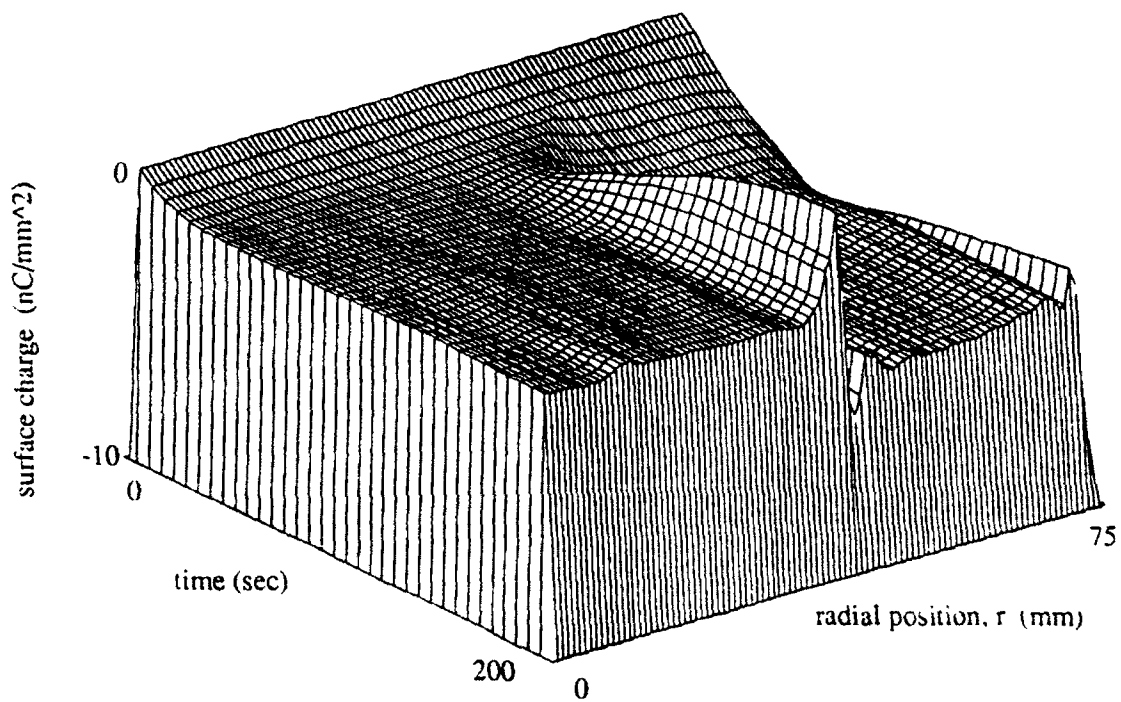


Figure 8a) Surface charge accumulation with an ion beam energy of 1 keV.

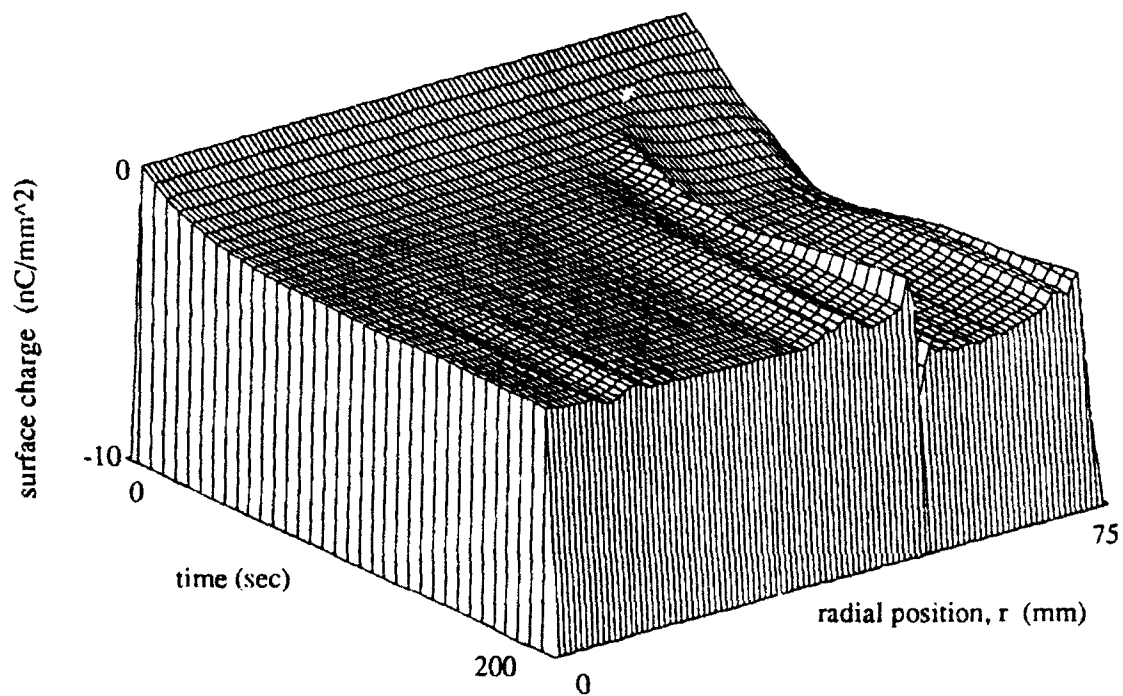


Figure 8b) Surface charge accumulation with an ion beam energy of 2 keV.

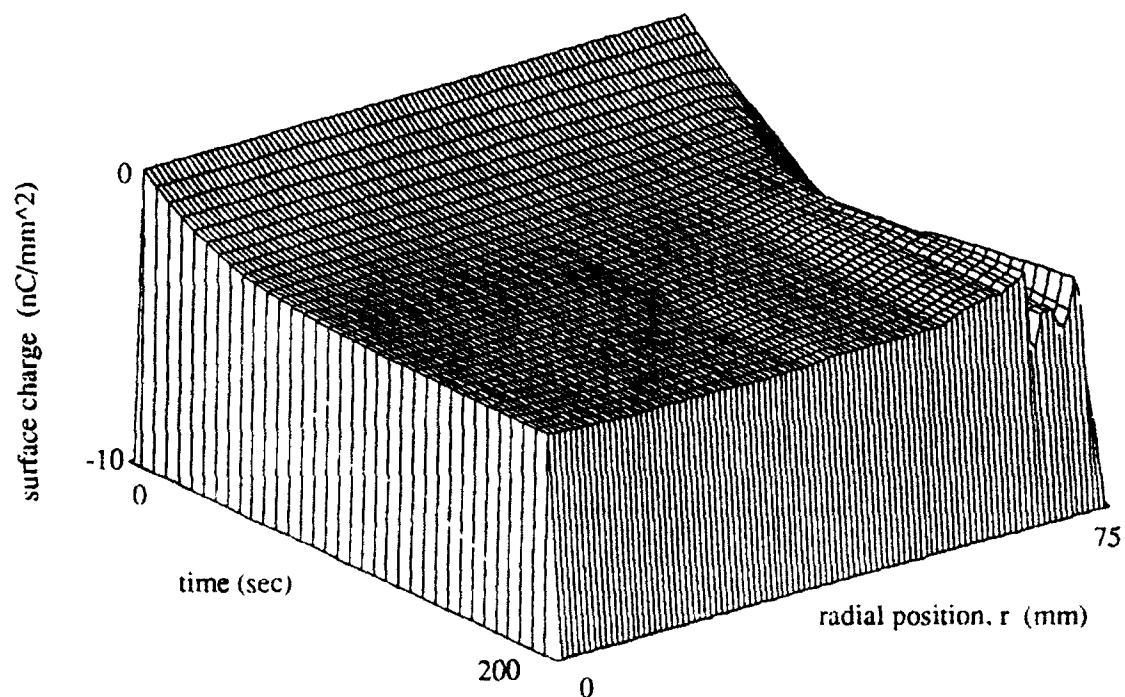


Figure 8c) Surface charge accumulation with an ion beam energy of 5 keV.

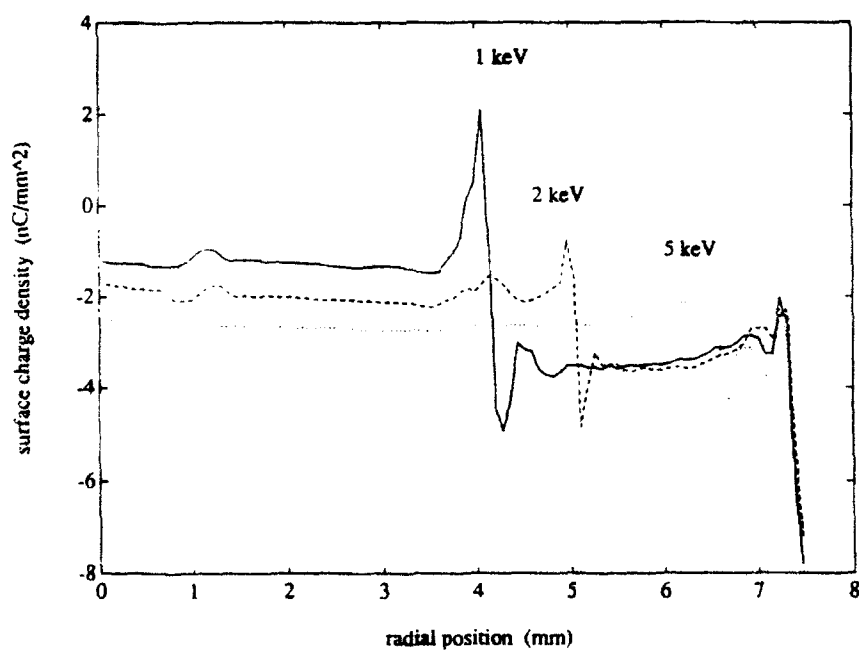


Figure 9 Ultimate surface charge accumulation on a dielectric sample exposed to ion beams of three different energies.

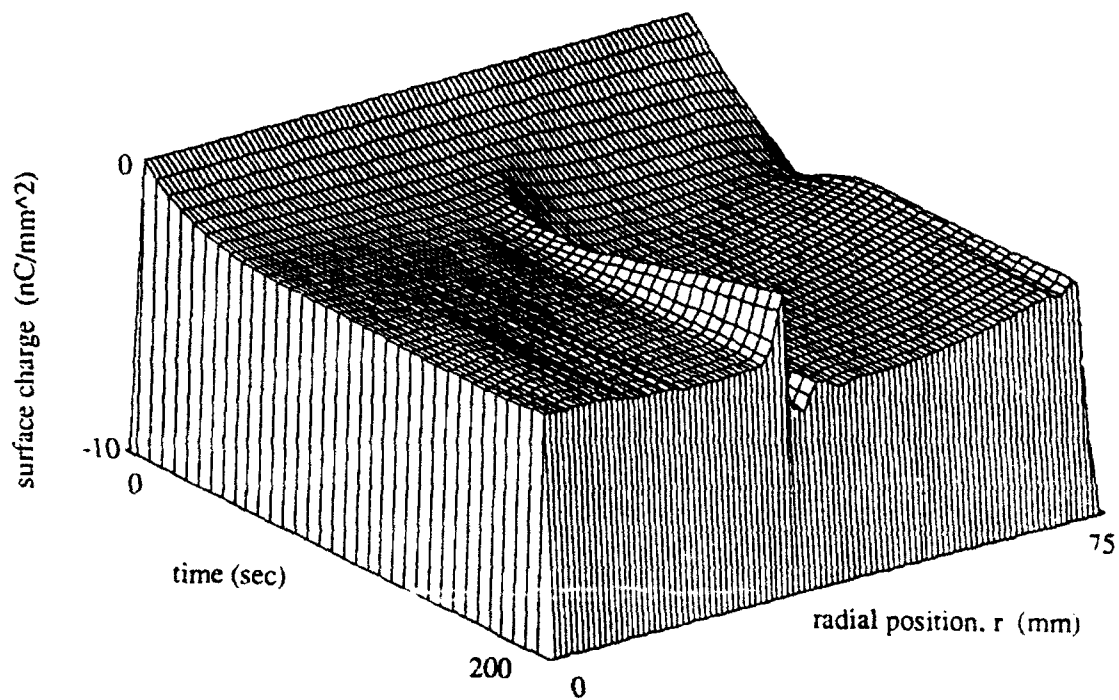


Figure 10a) Surface charge accumulation with ion beam current density of $0.002 \text{ nC/mm}^2/\text{sec}$, 2% the electron current density

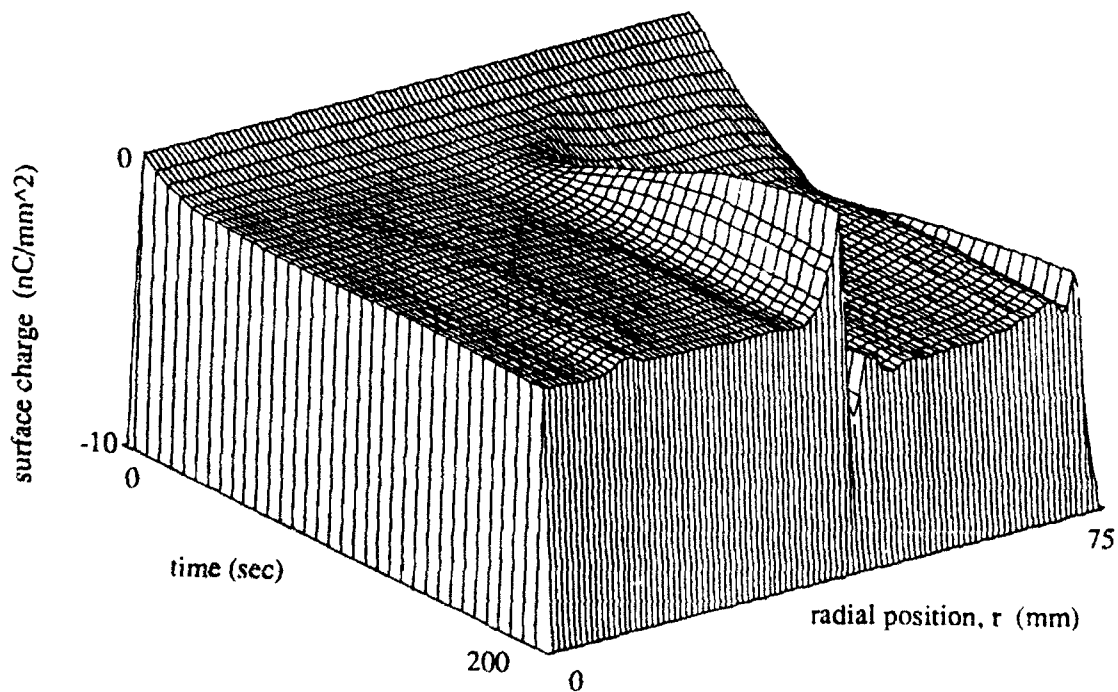


Figure 10b) Surface charge accumulation with ion beam current density of $0.005 \text{ nC/mm}^2/\text{sec}$, 5% the electron current density.

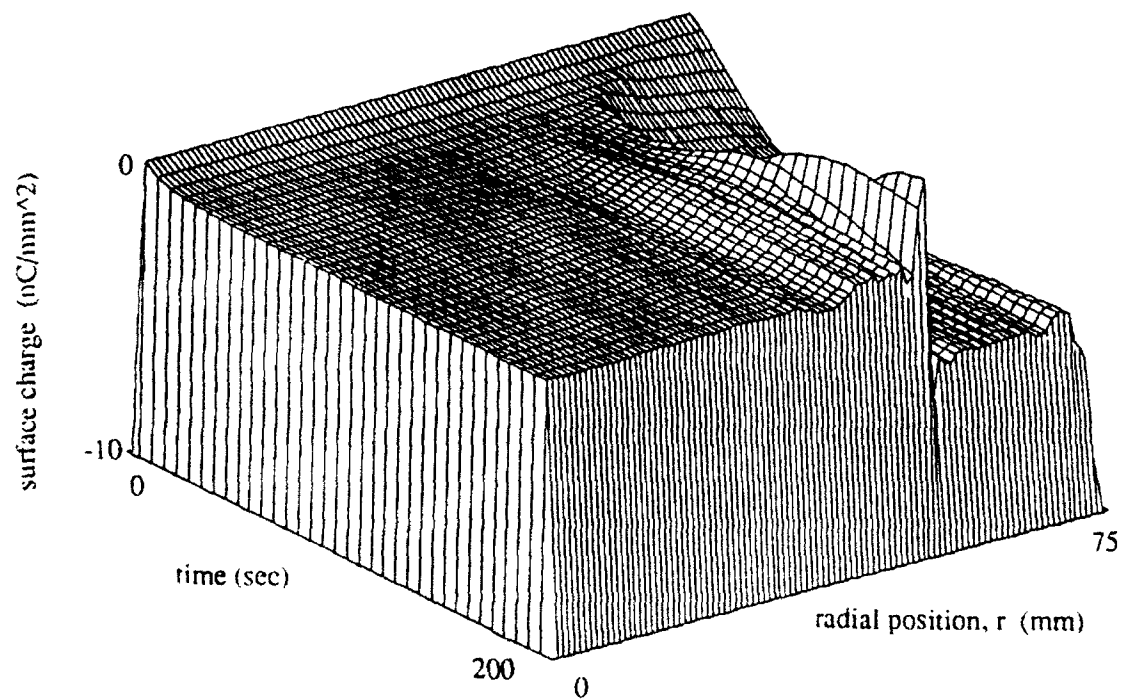


Figure 10c) Surface charge accumulation with ion beam current density of $0.010 \text{ nC/mm}^2/\text{sec}$, 10% the electron current density

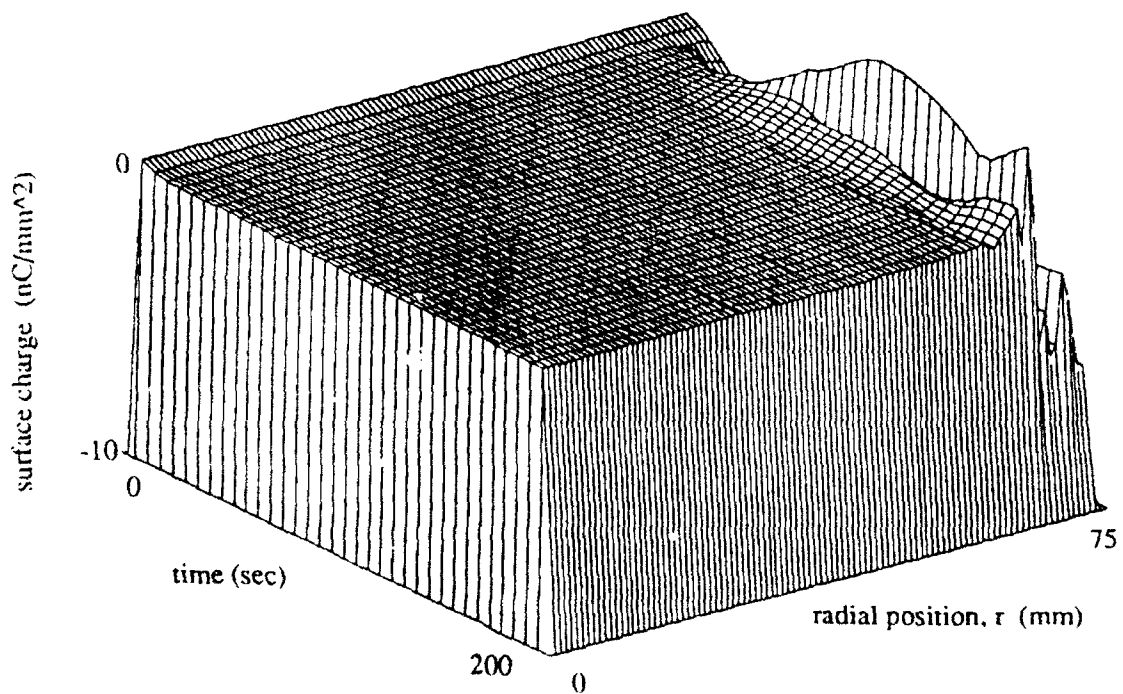


Figure 10d) Surface charge accumulation with ion beam current density of $0.020 \text{ nC/mm}^2/\text{sec}$, 20% the electron current density

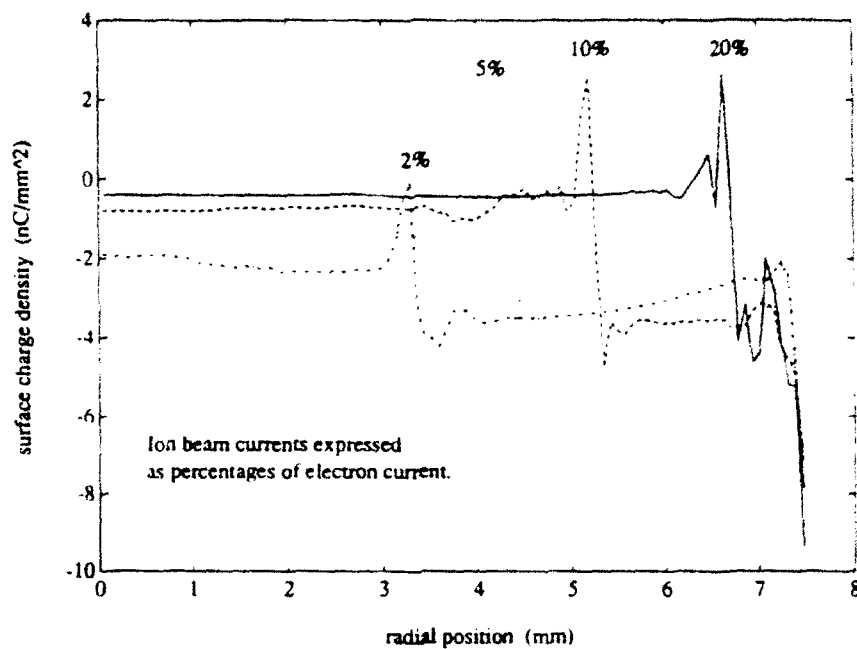


Figure 11 Ultimate surface charge accumulation on a dielectric sample exposed to ion beams of four different current densities.

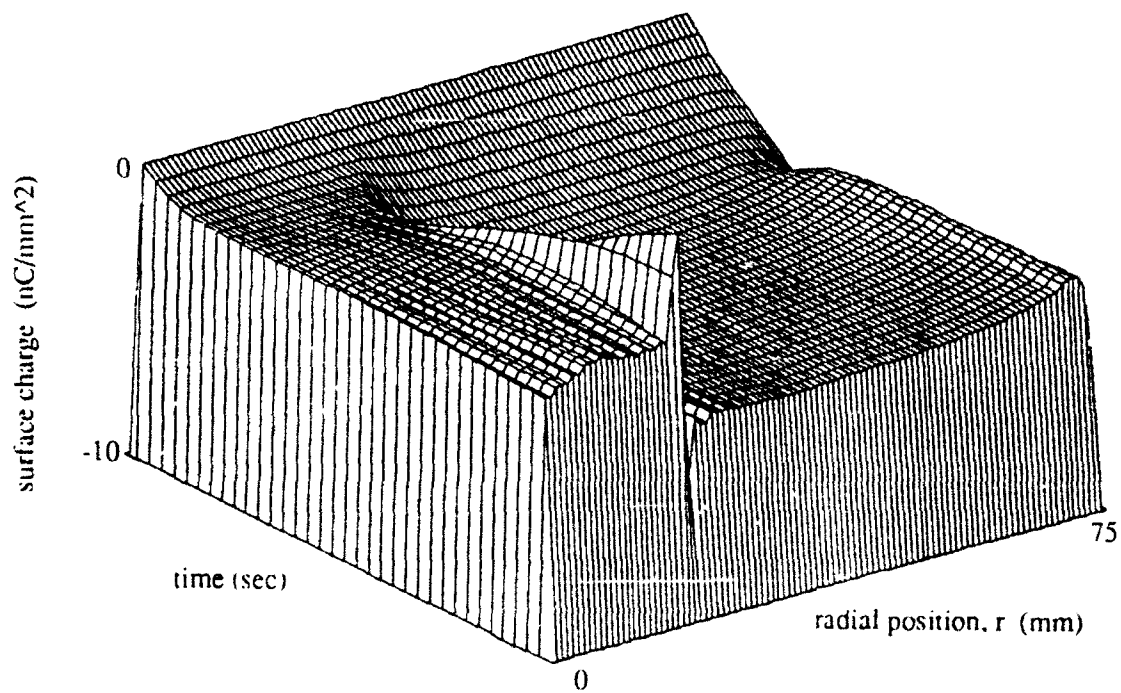


Figure 12a) Surface charge accumulation with ion beam of radius of 50 mm, $\frac{2}{3}$ the sample radius.

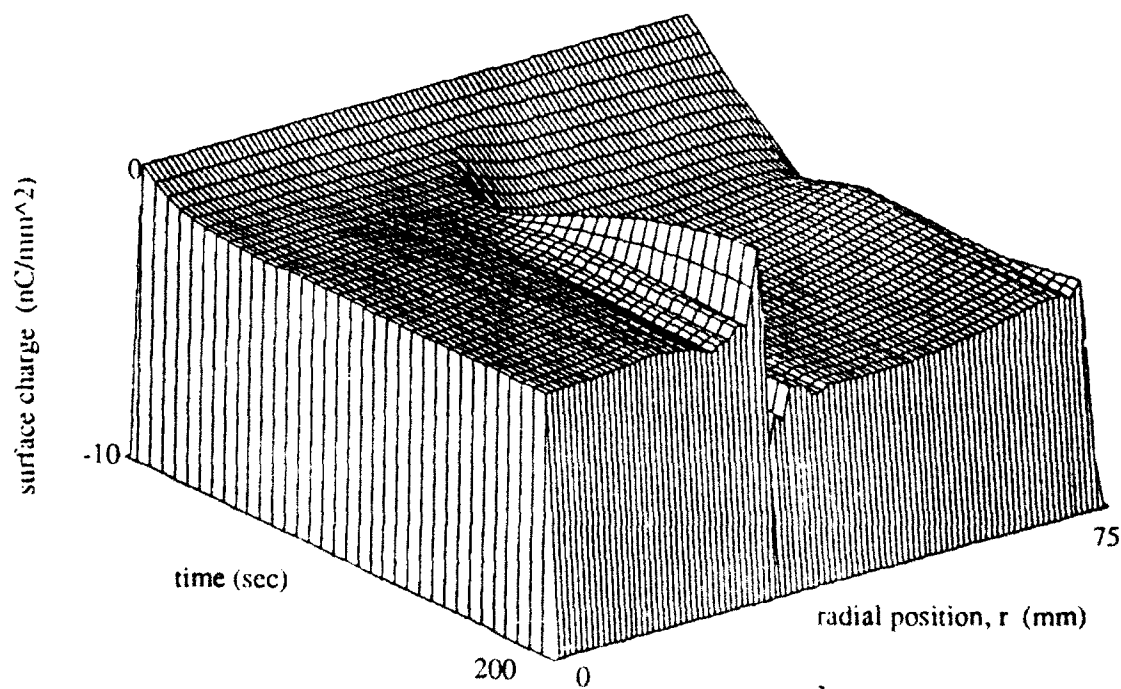


Figure 12b) Surface charge accumulation with ion beam of radius equal to sample radius.

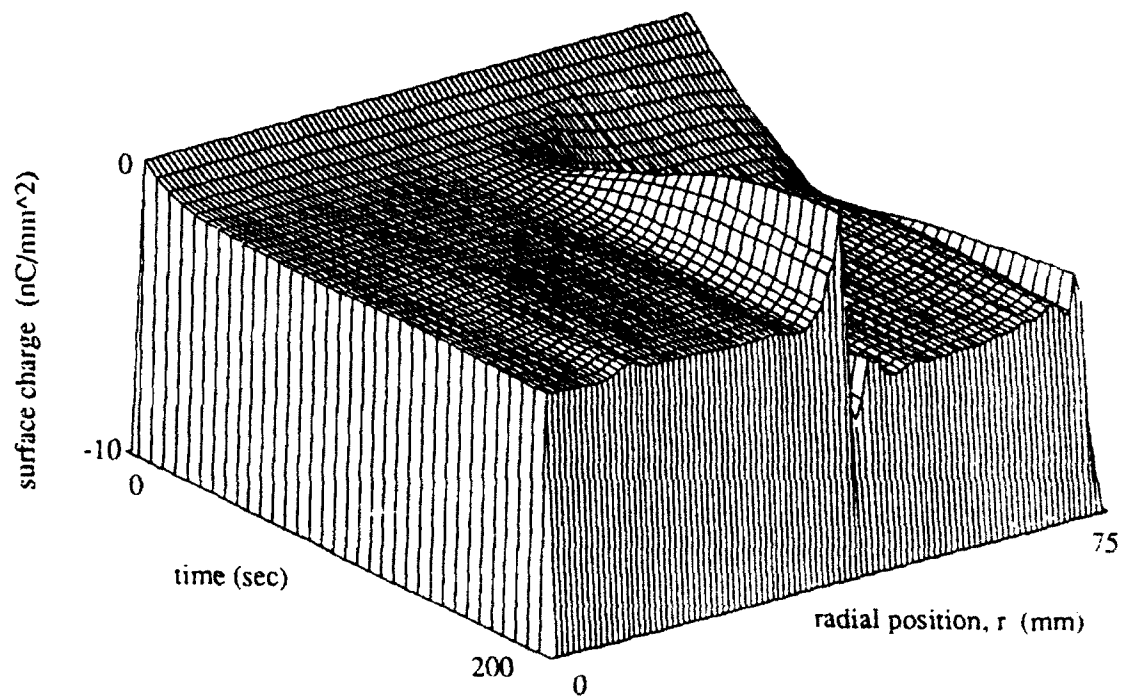


Figure 12c) Surface charge accumulation with ion beam radius of 100 mm, $\frac{4}{3}$ the sample radius.

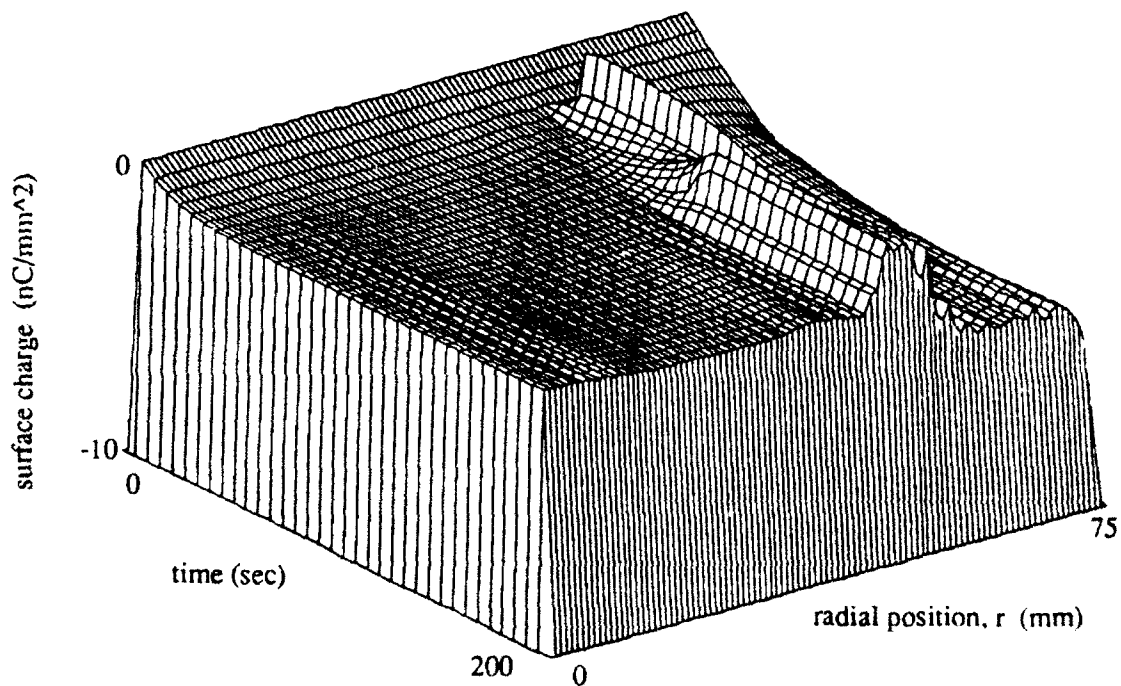


Figure 12d) Surface charge accumulation with ion beam radius of 300 mm, 4 times the sample radius.

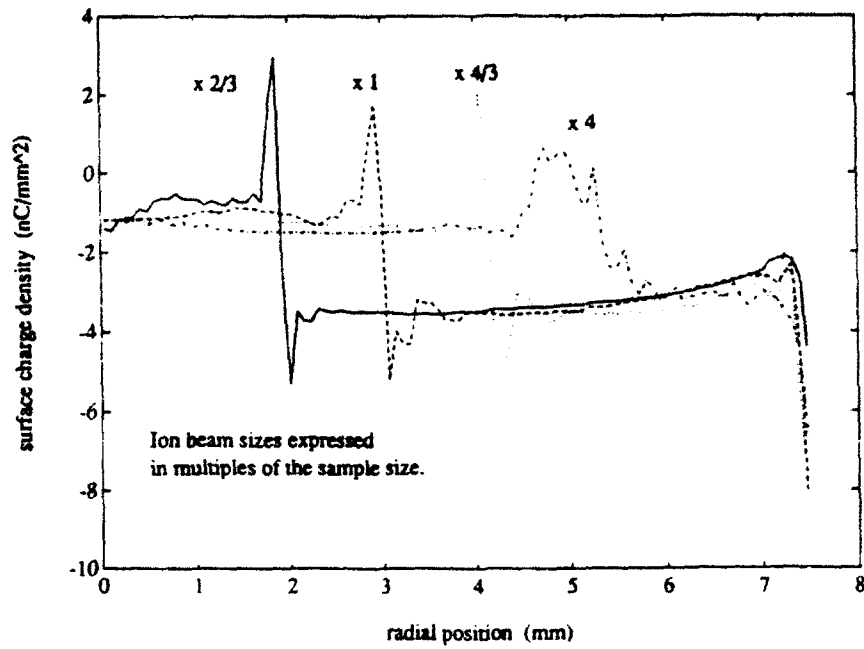


Figure 13 Ultimate surface charge accumulation on a dielectric sample exposed to ion beams of four different sizes.

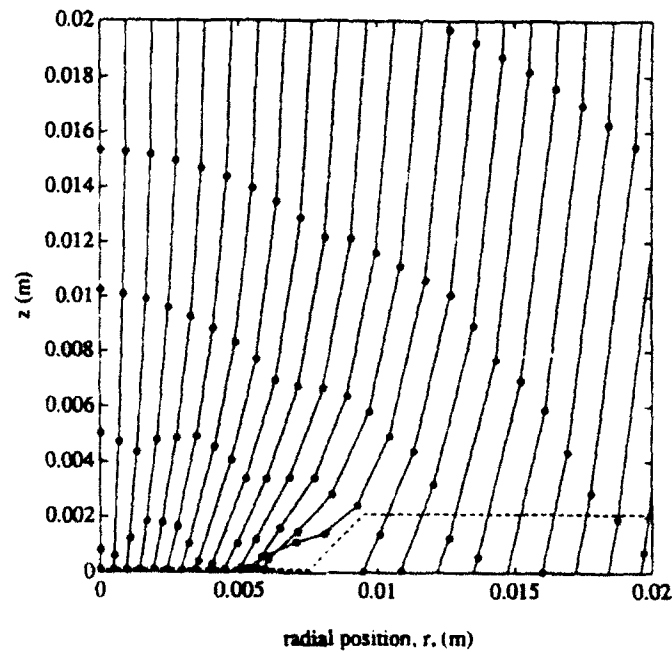


Figure 14 Ion trajectories for the ion beam with radius 4 times as large as the sample. The outline of the charge surface and the grounded mask is shown by the dashed line.

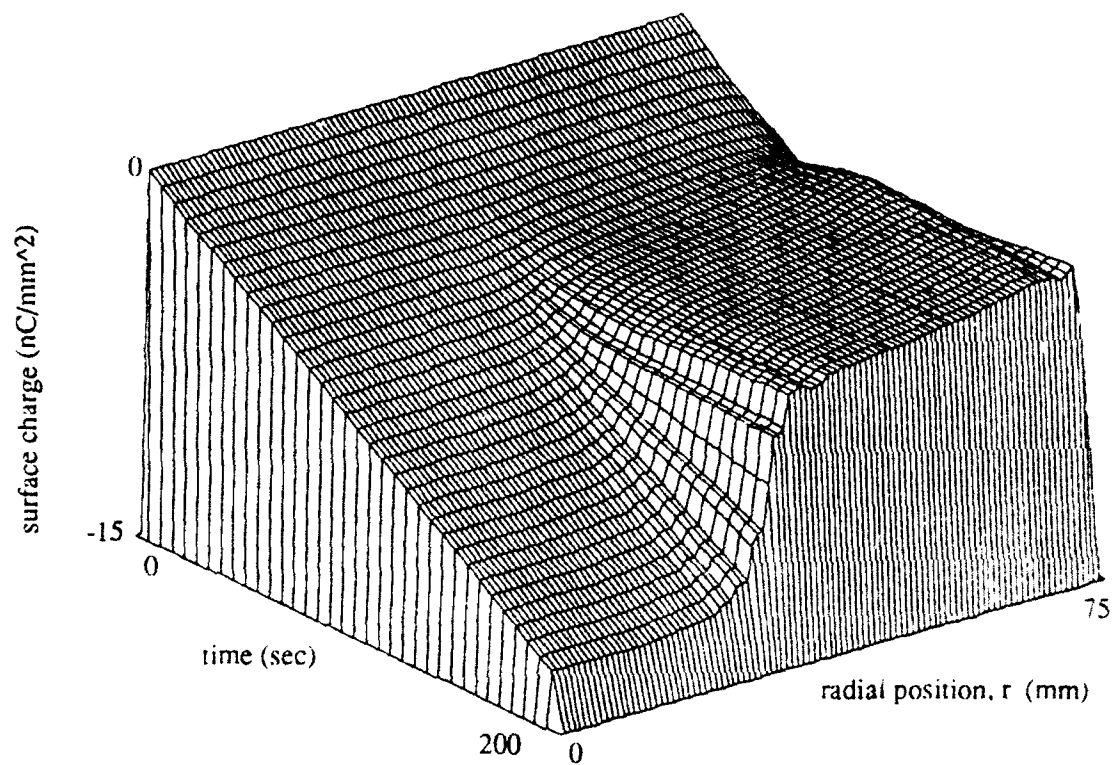


Figure 15a) Surface charge due to electrons only
with ion beam of radius equal to sample radius.

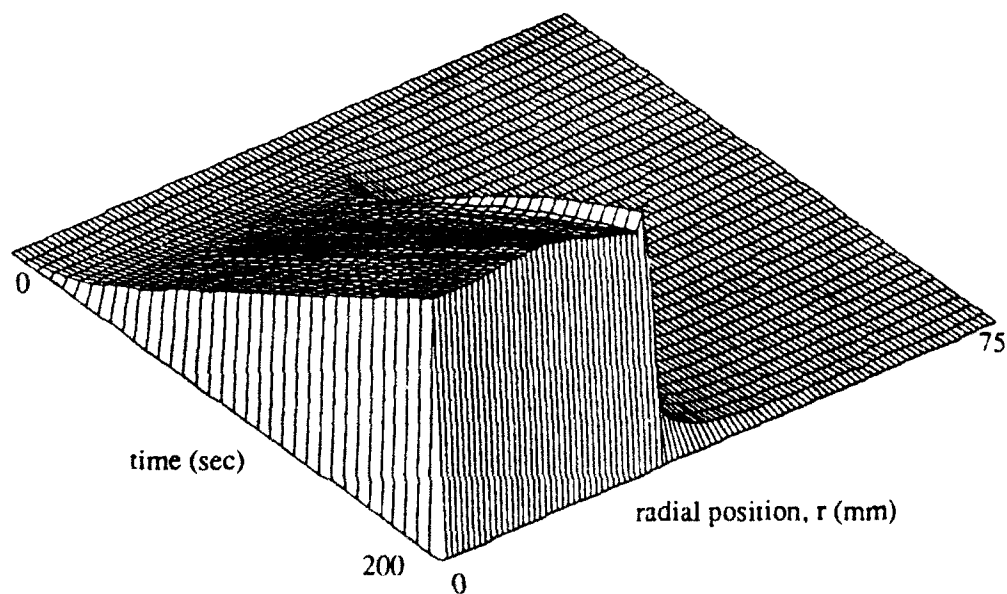


Figure 15b) Surface charge due to ions only
with ion beam of radius equal to sample size.

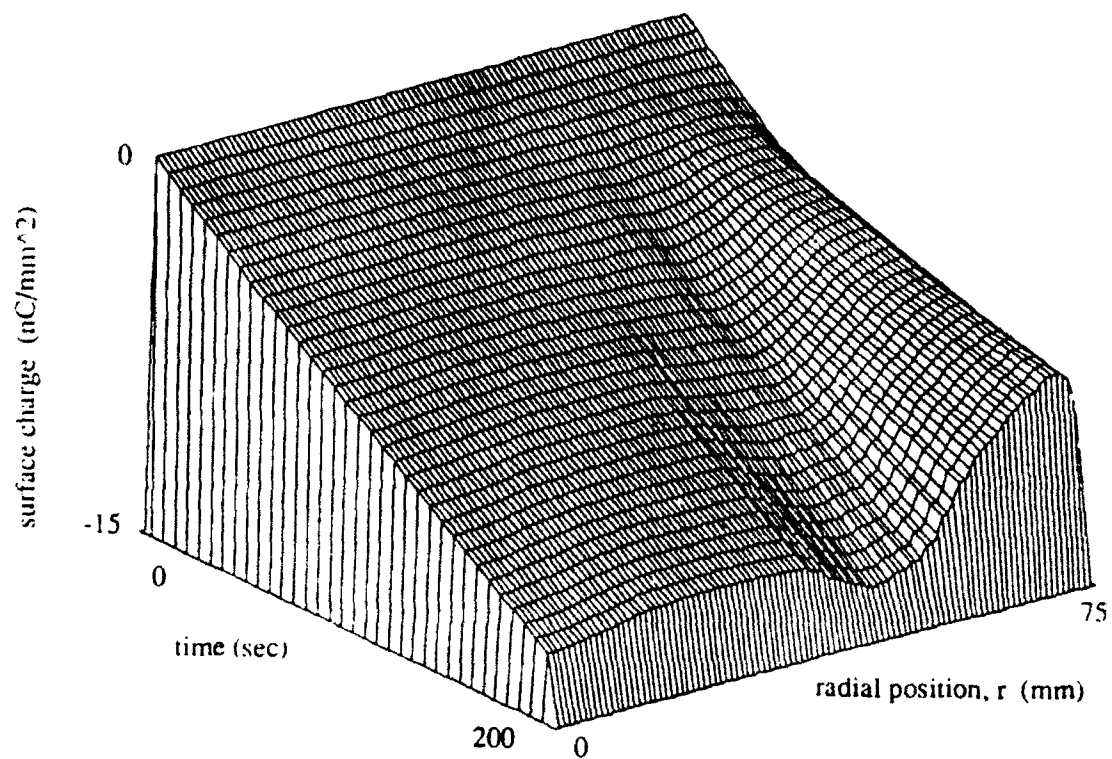


Figure 16a) Surface charge due to electrons only
for an ion beam radius of four times the sample radius.

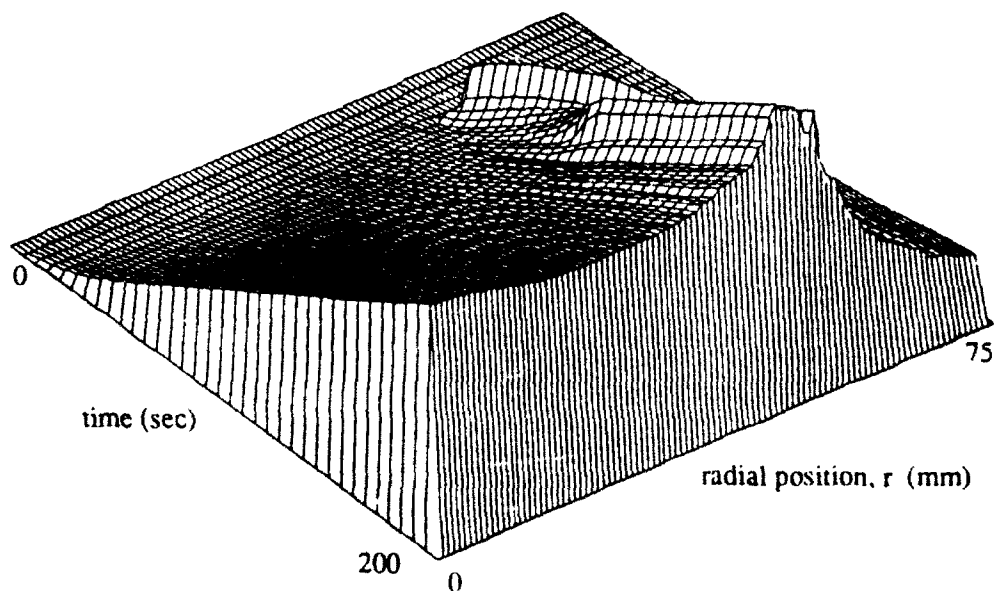


Figure 16b) Surface charge due to ions only
for an ion beam radius of four times the sample radius.

A Threshold Voltage for Arcing on Negatively Biased Solar Arrays

Daniel E. Hastings,* Guy Weyl† and Donald Kaufman‡
Physical Sciences Inc.
Andover MA 01810

Abstract

Negatively biased high voltage solar arrays in low earth orbit are known to undergo arcing below a critical voltage with respect to the plasma environment. It is proposed that the arcing is due to the breakdown of gas which is emitted under electron bombardment from the coverglass on the solar cells. A voltage threshold is predicted along with the scaling of the threshold on the key parameters

1 Introduction

As the space program matures there is a growing demand for large power generating systems to be available in low earth orbit (LEO). For example on the planned international space station, there is a current need for 75 kW of power to be made available for housekeeping and scientific experiments. It is desirable to supply this power at high voltage and low current in order to minimize resistive losses and the mass of cabling and harnesses. If this power is supplied by photovoltaic means then the solar arrays will be operating at high voltages. The term high voltage here typically implies voltage drops across the array on the order of one hundred to five hundred volts. Typical solar arrays currently in use have voltage drops ranging from 28 volts to 75 volts.

High voltage solar arrays have been found to undergo two distinct sets of interactions with the space environment above a given threshold[1,2,3,4,5,6]. For reasons of mass savings and also due to insulator degradation on orbit, in some designs the interconnects between the solar cells are exposed directly to the space environment. It is found for the positively biased interconnects with respect to the space potential that the current collection from the space environment can be anomalously large. For the negatively biased interconnects it is observed that below a critical voltage arc discharges occur on the solar array. These arc discharges give rise to electromagnetic noise and may also damage the solar cells[6].

*Permanent Address: Dept. of Aeronautics and Astronautics, MIT, Cambridge MA; Class of 1956 Career Development Associate Professor of Aeronautics and Astronautics, Member AIAA

†Principal Research Scientist

‡Principal Scientist; Current Address: USS Tech Center, 4000 Tex Center Dr, Monroeville, PA 15146

©Copyright ©Daniel Hastings, 1989. All rights reserved.

There have been many observations of the arcing phenomenon on high voltage solar arrays in ground based tests[7,8,9] and in flight tests[10,11]. The only theoretical hypothesis so far has been in Ref. [12]. In this work it was proposed that there is a thin layer of insulating contaminant over each of the interconnects. Such contaminant could arise by exposure to air or be created in the manufacturing process. Ions from the space plasma are attracted by the negative potential on the interconnects. These ions accumulate in the surface layer resulting in a buildup of electric field in the layer. As the layer continues to charge the internal field becomes large enough to cause electron emission into the space plasma. This electron current leads to subsequent heating and ionization in the layer. This is what is seen as the discharge.

In this paper we have concentrated on the behaviour of negatively biased solar arrays in LEO and we propose a new explanation for the arcing observed. It is proposed that the prebreakdown current observed experimentally causes neutral gas molecules to be desorbed from the sides of the coverglass over the solar cells. These molecules build up over the interconnects and arcing occurs inside this surface gas layer. An expression for the voltage threshold is derived and the scalings with the gas and geometric properties are examined. The voltage threshold is independent of the plasma density and depends strongly on the geometric structure of the solar cell-interconnect connection.

In section 2 the experimental work is reviewed and the plasma and neutral environment characterized for LEO. In section 3 the breakdown model is developed and the breakdown threshold obtained. In section 4 we discuss the scaling with gas and geometric parameters and the application of experimental data to this theory. Finally in the last section a number of experimental tests are proposed to elucidate the theoretical model.

2 Review of Experimental Work

Experimental work has been undertaken in ground based plasma chambers[2,7,8,9] as well as in two flight experiments, the plasma interactions experiments I and II (PIX I and II)[10,11]. The plasma and neutral gas environments in the plasma chambers are typically Argon or Nitrogen with a pressure range of 10^{-7} to 10^{-5} torr. The plasma density range is from 10^3 cm^{-3} to 10^6 cm^{-3} . The ion energy ranges between 1 and 100 eV while the electron thermal energy is approximately 0.1 to 0.3 eV. By contrast the ambient space environment at the altitude (300-500 km) where high voltage solar arrays will operate is mainly atomic and ionic oxygen. The pressure range is from 10^{-8} to 10^{-7} torr with a plasma density of the order of 10^4 cm^{-3} to 10^6 cm^{-3} . The ram energy of the ions is 5 eV while the electron thermal energy (T_e) is in the range 0.05 to 0.1 eV. However the environment around the solar array may differ substantially from the ambient space environment if the solar array is mounted on a large vehicle which is actively emitting effluents. This is very likely since it is precisely such vehicles which will demand large amounts of power and hence will need the high voltage solar arrays. The evidence from the Shuttle[15] suggests that the solar arrays could have an environment which has enhanced neutral and plasma densities relative to the ambient. The enhanced densities will be about an order of magnitude above the ambient. The enhancement arises from passive emissions from the vehicle such as outgassing of water as well as active emissions such as the products of thruster firings or liquid dumps. A neutral build-up may occur on surfaces exposed to the ram direction if the incoming streaming neutral

particles substantially accommodate on the surfaces. The enhancement depends strongly on the surface accommodation coefficients which are not well known for the impact of 5 eV atomic and ionic oxygen. If the ambient oxygen neutrals are reflected after thermal accommodation on the surface then for numbers typical of LEO a density enhancement of fifty might be expected as can be obtained from simple flux balance. Hence for orbits in LEO it is not unreasonable to assume that the neutral density around a solar array may be one to two orders of magnitude above the ambient densities.

The experimental work suggests the following observations: firstly, the key elements involved in the discharge process are the solar cell coverglass, the metallic interconnect and the plasma environment. This can be deduced from a set of experiments by Fujii et al[9]. In their experiments a metallic plate biased to highly negative voltages was exposed to the plasma in a plasma tank. No arcing was observed except for very large negative voltages where the arc took place to the substrate. The plate was then partially covered with silica coverglass slides. Arcing was now observed at the interfaces of the metal and the coverglasses. When actual solar cells were used with coverglasses the arcing results were qualitatively similar. Secondly, there is a prebreakdown electron current that flows away from the interconnect prior to a discharge. This electron current was observed in the experiments of Fujii et al [9] as well as the experiments of Snyder[7]. Calculation of the electron trajectories in the electric field of the interconnects indicate that the electrons must be coming from the interconnect and not from the plasma[12]. The source of this current is hard to understand. Fujii et al. speculate that this is due to field enhanced emission from the interconnect. The evidence for this is that as the number of coverglasses is increased, presumably increasing the local electric fields over the neighbouring interconnects, the electron current is observed to increase. On the other hand in the experiments of Snyder at low plasma densities and very negative voltages no electron current flowing away from the interconnect was seen. This does not prove that no current existed since it could have been below the threshold for detection in the experiments. However as the plasma density was increased and all other factors kept constant the ion current to the interconnect increased and the electron current appeared. Therefore the electron current seems to depend on the presence of a certain level of incoming ion current as well as the local electric field.

It is easy to see that the electron current flow is unlikely to be due to field emission from a calculation of the field emission current. The field emission current density[14] is

$$j_{IF} = \frac{1.55 \times 10^{-6}}{\phi} E^2 \exp\left(-\frac{6.85 \times 10^9}{E} \phi^{3/2}\right)$$

where ϕ is the work function of the surface, E the electric field right over the surface and all quantities are in MKS units. Even if E is said to be enhanced by whiskers on the surface of the conductor so that E is estimated by $E \simeq \beta V/d$ where β is the aspect ratio of the whisker then for reasonable values of $\beta = 100$, $V = 500$ Volts, $d = 150 \mu m$ and taking the work function for silver as $\phi = 4.3$ eV, the current density is of the order of 10^{-68} A/m². This is far too low to account for the electron current observed in the experiments.

The sequence of events associated with the arcing is the following: if a conductor with an insulating coverglass attached is put into the plasma and the conductor is initially not biased then both the conductor and coverglass accumulate a negative charge. This occurs since the electrons

are more easily collected than the ions. The final negative potential achieved ($V_{surface} \simeq -4T_e$) is such as to make the net electron flux equal to the net ion flux. If the conductor is now biased to a large negative potential then the cover glass initially takes the same potential as the conductor and then slowly returns to a slightly negative potential with respect to the plasma. This is because ions are initially attracted to the system and accumulate on the surface of the coverglass. The conductor below the coverglass acquires a negative (image) charge as shown in Fig. 1. The potential drop between the conductor and the surface of the coverglass is almost equal to the bias voltage ($|V|$). The surface charge density is $\sigma = C|V|$ where C is the capacitance per unit area of the coverglass. Below a certain voltage an electron current is observed to flow from the conductor. Some of the electrons leaving the interconnect strike the coverglass. There are two pieces of evidence which support this observation. First there is observed to be a potential barrier over the interconnect[6] which tends to keep the electrons from escaping to space. Secondly the surface potential of the coverglass is observed to undergo frequent fluctuations towards negative potentials[13]. As the bias on the conductor becomes more negative the magnitude of the voltage fluctuations on the coverglass increases and below a critical voltage a discharge occurs from the interconnect. The discharge time is typically a few microseconds[7] and once the discharge occurs the surface charge on the coverglass is neutralized and the cover glass potential becomes the same as the conductor potential[7]. The sequence now repeats itself with the cover glass slowly reaccumulating positive charge from the plasma.

The flight data from the PIX I and II experiments were taken at 900 km and show similar results to the ground based data. The current collection to the interconnects was measured to scale linearly with the voltage. There was substantial difference in the arc rate as compared to the ground based data. The arc rate \dot{R} was measured[16] to scale as

$$\dot{R} \sim n_i(T_i^{1/2}/m_i^{1/2})V^a \quad (1)$$

where $a \simeq 3$ for flight data and $a \simeq 5$ for ground data. In Eq. 1 all quantities with subscript i refer to ions. The ambient plasma density is n , the ambient temperature is T and the mass of the ambient plasma particles is m . The dependence of the arc rate on these quantities can be explained as due to the recharging of the coverglass surface by the thermal flux of ions. The thermal ion current scales as $n_i(T_i^{1/2}/m_i^{1/2})r_s^2$ with a sheath radius r_s .

The voltage threshold appears to be of the order of -200 to -250 Volts in some ground based tests[13] and -400 to -500 Volts on other tests[6,9]. It has been suggested that the voltage threshold depends on the plasma density[9,12] although the data range is not large and the evidence for a density dependence is ambiguous. If it exists it is very weak.

From these experimental observations two questions arise:

What causes the initial electron current flow from conductor to either space or the insulator?

What causes the electron current flow to avalanche and leads to a discharge?

The two questions can be addressed independently. The answer to the first question probably lies in the details of the interconnect surface and the fine structure of the electric field over the surface. In this paper we shall leave this question alone and assume that an electron current exists and is flowing from the interconnect. With this assumption we shall show that with reasonable bounds on the current it is possible to construct a consistent model of electron induced desorption of neutral

gas from the coverglass which then undergoes breakdown. From this model we can derive a voltage threshold and deduce how it scales with key parameters.

3 Breakdown Model

We shall work with a model for the coverglass/conductor interface as shown in Fig. 2. As assumed from the experimental results we take there to be a precursor electron current flow from the conductor to the coverglass. The coverglass is taken to have material properties typical of fused silica, namely that above a threshold energy and under electron bombardment the material emits secondary electrons. For all insulating materials the secondary electron yield as a function of incident electron energy increases monotonically from zero for small incident energy until a maximum yield is reached and then asymptotically approaches zero as the incident energy becomes very large. If the maximum yield of the material exceeds one then there are two distinct incident energies at which the yield is unity. We shall call these two energies \mathcal{E}_1 and \mathcal{E}_2 where $\mathcal{E}_1 < \mathcal{E}_2$. Typical values for $\mathcal{E}_1 \simeq 30 - 100$ eV and $\mathcal{E}_2 \geq 1$ keV[17,18,19].

Our basic model is that neutral gas is desorbed from the coverglasses due to bombardment by ions and electrons. Some of this neutral gas accumulates in the gap between coverglasses where it forms a (possibly) high pressure layer which can break down when the experimentally observed electron current from the interconnect flows through it. We shall take the ordering $d \ll l_i \ll l_c$. The smallest dimension of the gas slab over the interconnect is d so that a *sufficient* condition can be placed on the electron mean free path for ionization by requiring that it be less than d . If this is the case then there is a high probability that the gas slab will ionize so leading to a discharge. A *necessary* condition is that the electron mean free path for ionization be less than the largest dimension of the gas slab i. e. l_i . If this condition is violated then it is highly unlikely that as the electrons flow from the interconnect through the gas slab that they will have enough ionizing collisions to initiate a discharge. Hence we can obtain a *lower* bound on the discharge voltage by taking

$$\lambda_{mfp} \leq l_i \quad (2)$$

where $\lambda_{mfp} = 1/(n_n \sigma_{ion})$ is the electron mean free path for ionization for the electrons flowing through the neutral gas with n_n being the average neutral density and σ_{ion} being the ionization cross section. The distance l_i can be interpreted as the maximum distance an electron can travel between the coverglasses before it escapes.

The sides of the coverglasses are being bombarded by electrons. These electrons arise from two sources. Firstly the current flow from the interconnect and secondly by secondary electrons which are emitted from the cover glass under the primary electron bombardment and which then return to the surface. It is well known that insulators like silica will desorb neutral gas under electron bombardment[22,23]. This phenomena of electron bombardment causing desorption of gas molecules from surfaces is well known, and is called electron stimulated desorption (ESD). ESD has been the subject of several recent reviews[20,21]. The electron bombardment induces desorption by causing an electronic excitation in the adsorbed molecule. This causes the molecule to go from a energetically stable condition to an antibonding condition that leads to desorption. It is this electronic mechanism that occurs as opposed to other possible mechanisms such as energetic

impact or thermal heating. Yields have been found to be as high as 10^{-2} atoms per impacting electron[22,23]. Desorption yields mostly neutrals although emission of ions is also possible. The impacting electron must have an energy of greater than 5 eV for desorption to occur.

If we call the desorption efficiency Γ , the primary electron current $I_e(V)$ and N_t the multiplication factor due to the emission and reabsorption of secondary electrons then the neutral density over the surface of the interconnect is given by a flux balance

$$An_n v_n = \Gamma N_t \frac{I_e(V)}{e} \quad (3)$$

where A is the area of the edge of the cover glass participating in the process, v_n is the average velocity of the neutral gas leaving the surface and e is the charge on an electron. If we combine Eqs. (2) and (3) and define the primary electron current density as $J_e(V) = I_e(V)/A$ then we obtain an equation for the threshold voltage V_t above which a discharge is possible

$$\frac{ev_n}{\Gamma I_t \sigma_{ion}} = N_t J_e(V_t). \quad (4)$$

The multiplication factor N_t can be estimated in the following manner. If an electron is released from a surface with mean energy ξ_0 under the influence of a normal and tangential electric field as shown in Fig. 3 then the mean distance that the electron will go antiparallel to the direction of the tangential electric field[24] is given by

$$l_{mean} = - \left(\frac{E_t}{E_n} \right) \frac{\xi_0/e}{E_n}. \quad (5)$$

A normal field must exist if the coverglass edge has accumulated any charge. If we consider the electric field tangential to the side of the coverglass (see Fig. 2) then from Maxwell's equations the field just outside the coverglass is the same as the tangential field just inside the coverglass which we can estimate as

$$|E_t| = \frac{V}{d} \quad (6)$$

where we have taken the voltage on the upper surface of the coverglass as being approximately at plasma ground. If the secondary electron yield per primary electron is greater than one then the coverglass will charge positively under the electron bombardment. The experimental data suggests that the charge on the coverglass is not increasing[7] so that we can bound the secondary yield at one. This means that electrons are striking the surface with at most energy ξ_1 so that one electron is emitted for each electron that impacts. We can solve for the ratio E_t/E_n necessary to achieve this impact energy[24]. We find that

$$\left(\frac{E_t}{E_n} \right)^2 = \frac{\xi_1 - \xi_0}{2\xi_0}. \quad (7)$$

We use Eqs. (6) and (7) in (5) to obtain

$$\frac{l_{mean}}{d} = \frac{(\xi_1 - \xi_0)/e}{2V}. \quad (8)$$

The number of secondary electrons generated per incoming primary electron is d/l_{mean} . This assumes that we are only considering electrons to contribute as long as they are striking the side of the coverglass. Electrons may continue to hop along the top surface of the coverglass but in this case the neutral gas released will easily escape and will not contribute to the dense gas layer over the interconnect. Therefore the total number of electrons generated per primary electron is

$$N_t = 1 + \frac{2V}{(\xi_1 - \xi_0)/e}. \quad (9)$$

From the assumptions used to obtain this we can see that Eq. (9) represents an *upper bound* on the number of electrons generated per primary electron.

With Eq. (9) used in Eq. (4) we can obtain an equation for the threshold voltage if we know the explicit functional dependence of J_e on V . In the absence of knowing this explicit form we can place an *upper bound* on the current density by the space charge limited current density that can be pulled from the interconnect out to the edge of the coverglass. This upper bound is

$$J_e(V_t) = 0.83\epsilon_0 \left(\frac{2e}{m_e} \right)^{1/2} \frac{|V_t|^{3/2}}{d^2}. \quad (10)$$

where ϵ_0 is the permittivity of free space and m_e is the mass of an electron. This expression is correct for space charge limited one dimensional flow of outgoing electrons and incoming ions over a distance d . For this space charge limited flow the ratio of the electron to ion current density ratio must scale as the square root of the ion to electron mass ratio. A more complete space charge limited expression will still scale as $V^{3/2}$ on dimensional grounds but will differ in the premultiplying numerical factors. The experimental evidence suggests that when the electron current is not space charge limited then it is proportional to the incoming ion current. This ion current will depend on the plasma density.

We take the neutral flow out of the region between the coverglasses to be choked. Hence if γ is the ratio of specific heats for the neutral gas and if the gas is in thermal equilibrium with the coverglass surface then $v_n = \sqrt{\gamma T_s/m_n}$ where T_s is the surface temperature. This assumption is based on the presence of the high density gas slab over the interconnect surface so that as fresh gas is desorbed from the coverglass it quickly equilibrates with the gas there which is taken to be in thermal equilibrium with the surface. This is a strong and important assumption which sets the magnitude of the neutral velocity. It is possible that the neutrals may leave with much larger velocities since the energy with which a gas molecule leaves a surface on which it has been absorbed can vary from 1 eV to 10 eV if it is expanding into a vacuum. With the use of Eq. (10) in Eq. (4) and since N_t and J_e are upper bounds we obtain a lower bound for the threshold voltage for an arc as

$$V_t = \left[0.605 \frac{e}{\epsilon_0} \left(\frac{d}{l_i} \right) \left(\frac{\gamma T_s/e}{2m_n/m_e} \right)^{1/2} \frac{[(\xi_1 - \xi_0)/e]d}{\Gamma \sigma_{ion}} \right]^{2/5}. \quad (11)$$

In obtaining Eq. (11) we have taken $N_t \simeq [2V/(\xi_1 - \xi_0)/e]$.

In Fig. 5 we show the threshold voltage as a function of coverglass thickness over a range of values for ϵ_1 . The range for ϵ_1 was chosen to reflect the range of secondary emission properties that might result from different coatings on the coverglasses. The dependence on energy at which the yield is unity arises from the assumption used to obtain the bound on the ratio of the tangential to normal electric field at the coverglass surface. By contrast with the weak dependence associated with the coverglass material, the dependence on the geometric lengths is much stronger. The threshold voltage increases with the thickness of the coverglass since the space charge limited current density available for ionization decreases with thickness. The voltage decreases with length of the interconnect since the electrons can stay within the neutral gas cloud longer as the length increases. These results suggest a set of experiments to systematically vary the lengths associated with the coverglass and conductor so as to determine the scaling of the threshold voltage with these lengths.

The threshold voltage found in Eq. (11) does not contain any dependence on the plasma density. As we have seen the ionization takes place in the gas layer coming from the surface of the coverglass. The electron current flow from the interconnect that we have taken is a space charge limited bound and hence density independent. For smaller electron currents there will be a dependence on the plasma density arising from the proportionality to the ion current. The plasma does play a crucial role in supplying the initial positive charge on the coverglass and in resupplying the positive charge once the arc discharge has occurred. Hence we expect a dependence of the arc rate on plasma density but within the context of our model do not find any dependence of the threshold voltage on the plasma density. The data for LEO conditions indicates very weak, if any, dependence on plasma density in the plasma density range 10^3 cm^{-3} to 10^5 cm^{-3} covered by both laboratory and PIX data[25].

Finally we note that differential charging of the interconnector and the coverglass can be realized in several ways. One way is under the influence of a photon flux due to the photoelectric effect while another way is due to an electron beam striking the insulator when the secondary electron emission yield is larger than one. In both cases the threshold differential voltage for arcing is the same as when the charging is due to the ambient plasma[26]. Based on our model, this arcing will occur for the same reasons as on a solar array, namely that breakdown occurs in a gas surface layer desorbed by the electrons.

Recently, another hypothesis has been advanced, namely that the breakdown is the result of the electrons desorbing ions rather than neutrals[27]. The ion return current from the side of the coverglass in the model of Ref. [27] is given by

$$J_{ir} = (\gamma_{ie} J_i) P_e \gamma_{ee}^N \Gamma_{ie}. \quad (12)$$

In this expression, J_i is the incoming ion current to the interconnector, γ_{ie} is the yield of secondary electrons emitted from the interconnector under ion bombardment, P_e is the probability of the electron emitted from the interconnector reaching the side of the coverglass, γ_{ee} is the secondary electron yield of the coverglass and Γ_{ie} is the ion yield of the coverglass surface under electron bombardment. Breakdown will occur when $J_{ir} \geq J_i$.

A typical number for $\gamma_{ie} \approx 0.1$ while a typical number for $\Gamma_{ie} \approx 0.0001$ since it usually two orders of magnitude less probable than neutral desorption[28]. The probability that an electron

strikes the coverglass is a complex function of many parameters but a good estimate is 0.01. Hence $\gamma_{ee}^{N_i} > 10^7$ in order that $J_{ir} \geq J_i$. Clearly if $\gamma_{ee} = 1$ then this condition cannot be met and breakdown cannot occur by this means. The condition $\gamma_{ee} = 1$ comes from the requirement of steady state charge balance on the surface. Under this condition each incoming electron causes the emission of an electron so that the net charge on the surface does not change. If $\gamma_{ee} > 1$ then breakdown is possible, however the surface will not be in an equilibrium state. We might anticipate that if the timescale for the surface to reach equilibrium is much smaller than the discharge time then the condition $\gamma_{ee} = 1$ must be true and no breakdown is possible. On the other hand if the timescale to reach equilibrium is much larger than the discharge time then a discharge can develop. This will depend on the capacitance of the coverglass and the magnitude of the current flowing to it during the discharge. If we assume that the capacitance of the coverglass is very large then we can obtain the lower bound on the voltage by taking the maximum value for γ_{ee} . For SiO_2 the maximum value of $\gamma_{ee} = 2.4$. If we use Eq. (9) then for $\mathcal{E}_1 = 250$ eV; $\mathcal{E}_0 = 2$ eV we obtain the threshold voltage as approximately -1800 Volts. This indicates that this ion desorption mechanism may be possible and may give reasonable breakdown voltages. From an experimental point of view, it would be possible to distinguish between the gas desorption process and the ion desorption process by changing the capacitance of the coverglass. This may be done by changing the area of the coverglass while keeping all other parameters constant.

5 Conclusions

We have developed a simple model to describe arcing on a high voltage solar array. The basic elements of the model are an electron current flow from the interconnect to a neighbouring coverglass which desorbs neutral molecules under the electron bombardment. These neutral molecules form a gas layer over the interconnect which breaks down when the voltage on the interconnect is sufficiently high. The model makes specific scaling predictions with the geometric structure and with the gas properties.

In Ref. [6] the authors speculated that the ionization might take place in the background neutral gas. The work in this paper suggests that this is unlikely since the gas cannot be concentrated enough (at least four orders of magnitude) to give breakdown thresholds in the range observed. In Ref. [12] the authors suggested that ionization took place in the solid phase at the surface of the interconnect. In this work we suggest in contrast to earlier work that the ionization takes place in a gas layer generated from the coverglass surface. We note that while in this paper we have suggested that the ionization takes place in a gas layer which is desorbed from the coverglass surface, a gas layer may be created by some other means. One such means is the outgassing of the adhesives used to bind the solar cell to the substrate[29]. While in this case the source of the gas differs from our hypothesis, the gas pressure required for breakdown will be similar to the numbers in this work since this is determined only by the condition that the mean free path be smaller than the geometric size of the interconnect. These differing ideas suggest that a spectroscopic analysis of the radiation emitted during the arcing may shed light on the molecules participating in the discharge.

In order to elucidate the fundamental physics of the arcing on high voltage solar arrays it is proposed that experiments be undertaken to understand the role of the interconnect and coverglass

materials by detailed electron micrographs. It is also proposed that the density dependence, if any, of the threshold voltage be clarified. This can be done by careful and systematic tests over a wide range of plasma densities. It is very important to understand this since operation of planned systems may be affected by the results. Finally the nature of the electron current flow from the interconnect must be clarified.

6 Acknowledgements

This work was supported by NASA Lewis Research Center under NASA contract NAS3-25402. The authors are very grateful for useful insights and the experimental understanding of Dr. David Snyder. The authors would also like to thank Dr. Haruhisa Fujii for making his experimental results available to us. In addition we would like to thank one of the referees for bringing many useful references to our attention.

References

- [1] B. G. Herron, J. R. Bayless and J. D. Worden, *High Voltage Solar Array Technology*, Journal of Spacecraft and Rockets, **10**, 457, 1973.
- [2] K. L. Kennerud, *High Voltage Solar Array Experiments*, NASA CR-121280, 1974.
- [3] N. J. Stevens, J. C. Roche and N. T. Grier, *Large Space System-Charged Particle Environment Interaction Technology*, NASA TM-79156, 1979.
- [4] N. J. Stevens, H. E. Mills and L. Orange, *Voltage Gradients in Solar Array Cavities as Possible Breakdown Sites in Spacecraft-Charging-Induced Discharges*, IEEE Transactions in Nuclear Science, **NS-28**, No. 6, 1981.
- [5] N. J. Stevens, *Review of Interactions of Large Space Structures with the Environment, Space Systems and their Interactions with Earth's Space Environment*, Progress in Aeronautics and Astronautics, **71**, AIAA, Washington D. C., p 437-454, 1980.
- [6] H. Thiemann and K. Bogus, *Anomalous Current Collection and Arcing of Solar-Cell Modules in a Simulated High-Density Low-Earth-Orbit Plasma*, ESA Journal, **10**, 43-57, 1986.
- [7] D. B. Snyder, *Discharges on a Negatively Biased Solar Cell Array in a Charged Particle Environment*, Spacecraft Environment Interactions Technology Conference, Colorado Springs, CO, Oct 4-6, 1983, NASA CP-2359, p 379-388.
- [8] D. B. Snyder and E. Tyree, *The Effect of Plasma on Solar Cell Array Arc Characteristics*, NASA TM-86887, 1985.
- [9] H. Fujii, Y. Shibuya, T. Abe, K. Ijichi, R. Kasai and K. Kuriki, *Laboratory Simulation of Plasma Interactions with High Voltage Solar Arrays*, Proceedings of the 15th International Symposium on Space Technology and Science, Tokyo, 1986.

- [10] N. T. Grier and N. J. Stevens, *Plasma Interaction Experiment (PIX) Flight Results*, Spacecraft Charging Technology-1978, NASA CR-2071, p 295-314.
- [11] N. T. Grier, *Plasma Interaction Experiment II: Laboratory and Flight Results*, Spacecraft Environment Interactions Technology Conference, Colorado Springs, CO, Oct 4-6, 1983, NASA CP-2359, p 333-348.
- [12] D. E. Parks, G. Jongeward, I. Katz and V. A. Davis, *Threshold-Determining Mechanisms for Discharges in High-Voltage Solar Arrays*, Journal of Spacecraft and Rockets, **24**, 367-371, 1987.
- [13] D. B. Snyder, *Discharges on a Negatively Biased Solar Array*, NASA TM-83644, 1984.
- [14] J. D. Cobine, *Gaseous Conductors: Theory and Engineering Applications*, Dover Publications, New York, 1958.
- [15] G. E. Caledonia, J. C. Person and D. E. Hastings, *The Interpretation of Space Shuttle Measurements of Ionic Species*, Journal of Geophysical Research, **92**, 273-281, 1987.
- [16] D. C. Ferguson, *The Voltage Threshold for Arcing for Solar Cells in LEO-Flight and Ground Test Results*, NASA TM-87259, 1986.
- [17] N. R. Whetten, *Methods of Experimental Chemistry*, Academic Press, Inc., New York, 1963
- [18] P. Dawson, *Secondary Emission Yields of some Ceramics*, Journal of Applied Physics, **37**, 3644, 1964.
- [19] J. G. Laframboise and M. Kamituma, *The Threshold Temperature Effect in High-Voltage Spacecraft Charging*, Proceedings of the Air Force Geophysics Laboratory Workshop on Natural Charging of Large Space Structures in Near Earth Polar Orbit, AFGL-TR-83-0046, p294-306, 1983. ADA134894
- [20] T. E. Mandy, D. E. Ramaker and R. Stockbauer, *Characterization of Surfaces through Electron and Photon Stimulated Desorption*, Ann. Rev. Phys. Chem, **35**, 215, 1984.
- [21] D.P. Woodruff and T.A. Delchar, *Modern Techniques of Surface Science*, Cambridge University Press, Cambridge, 1988.
- [22] H. C. Miller and R. J. Ney, *Gases released by Surface Flashover of Insulators*, Journal of Applied Physics, **63**, 668-673, 1988.
- [23] R. A. Anderson and J. P. Brainard, *Mechanism of Pulsed Surface Flashover involving Electron-Stimulated Desorption*, Journal of Applied Physics, **51**, 1414-1421, 1980.
- [24] K. D. Bergeron, *Theory of the Secondary Electron Avalanche at Electrically Stressed Insulator-Vacuum Interfaces* Journal of Applied Physics, **48**, 3073-3080, 1977.
- [25] N. J. Stevens, *Interactions between Large Space Power Systems and Low-Earth-Orbit Plasmas*, Spacecraft Environment Interactions Technology Conference, Colorado Springs, CO, Oct 4-6, 1983, NASA CP-2359, p263.

- [26] R. C. Chaky and G. T. Inouye, *Characteristics of EMI Generated by Negative Metal/Positive Dielectric Voltage Stresses due to Spacecraft Charging*, Spacecraft Environment Interactions Technology Conference, Colorado Springs , CO, Oct 4-6, 1983, NASA CP-2359., p437-452.
- [27] H. Kuninaka, Y. Nozaki and K. Kuriki, *High Voltage Solar Arrays Interacting with Ionospheric Plasma*, Space Power, 8,51-68, 1989
- [28] T. E. Madey and T. Yates, Jr, *Electron-stimulated desorption as a tool for studies of chemisorption: a review*, J. Vacuum Science and Technology,8,525,1971
- [29] W. Knauer, J. R. Bayless, G. T. Todd and J. W. Ward, *High Voltage Solar Array Study*, NASA CR-72675, 1970.

Figure Captions

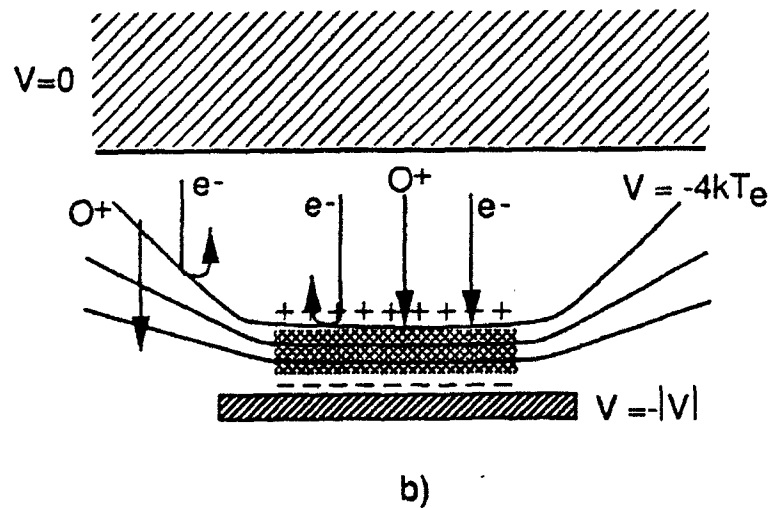
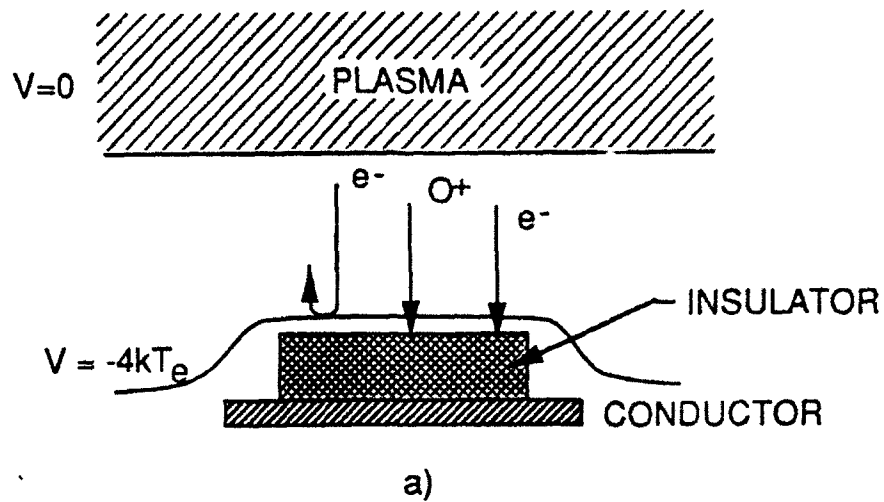
Figure 1 Schematic showing charge and equipotential contours for an insulator on (a) an unbiased and (b) a biased conductor

Figure 2 Geometric Structure of Coverglass/Conductor Interface

Figure 3 Electron Motion under the Normal and Tangential Electric Fields

Figure 4 Bound on Threshold Voltage versus surface temperature showing range of variation with gas desorption efficiency. Other parameters are: $m_n = 44$ amu; $\mathcal{E}_1 = 40$ eV; $\mathcal{E}_0 = 2$ eV; $d = 0.15$ mm; $d/l_i = 0.1$; $\sigma_{ion} = 10^{-20}$ m² and $\gamma \approx 1.2$

Figure 5 Bound on Threshold Voltage versus coverglass thickness showing range of variation with secondary emission properties. Other parameters are: $m_n = 44$ amu; $T_s = 300$ K, $\Gamma = 0.03$; $\mathcal{E}_0 = 2$ eV; $d/l_i = 0.1$; $\sigma_{ion} = 10^{-20}$ m² and $\gamma = 1.2$.



B-2400

Figure 1: Schematic showing charge and equipotential contours for an insulator on (a) an unbiased and (b) a biased conductor

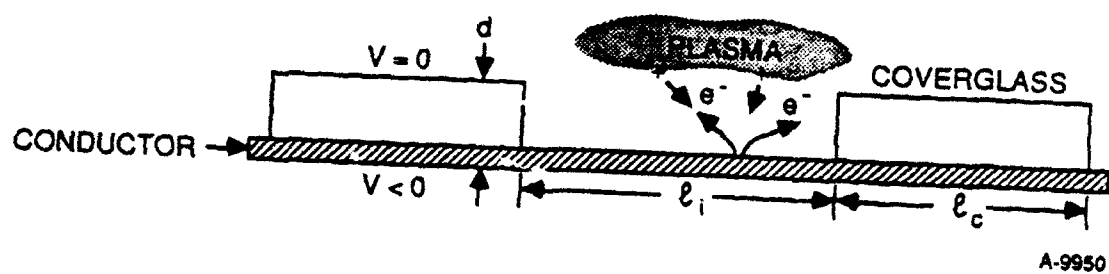


Figure 2: Geometric Structure of Coverglass/Conductor Interface

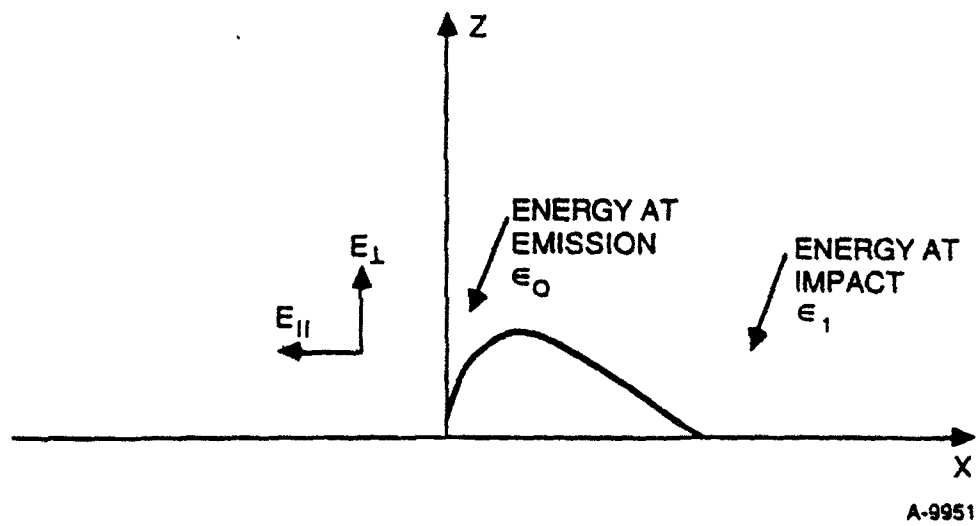


Figure 3: Electron Motion under the Normal and Tangential Electric Fields

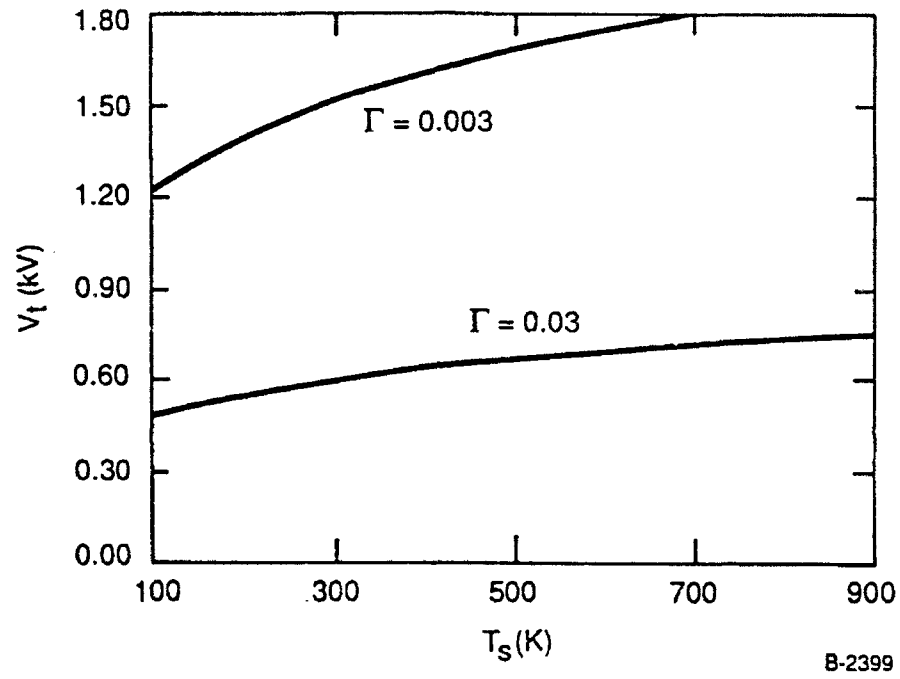


Figure 4: Bound on Threshold Voltage versus surface temperature showing range of variation with gas desorption efficiency. Other parameters are: $m_n = 44$ amu; $\mathcal{E}_1 = 40$ eV; $\mathcal{E}_0 = 2$ eV; $d = 0.15$ mm; $d/l_i = 0.1$; $\sigma_{ion} = 10^{-20}$ m² and $\gamma = 1.2$

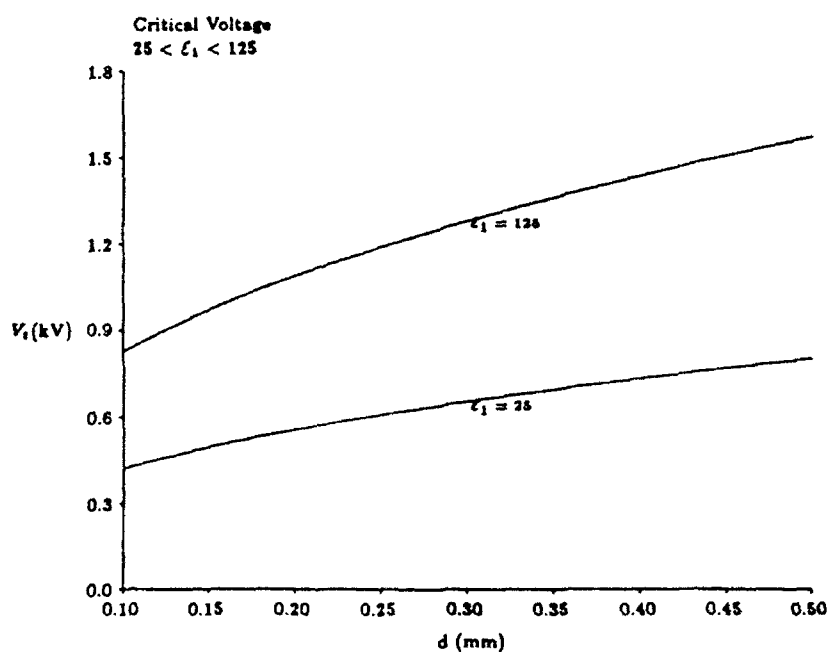


Figure 5: Bound on Threshold Voltage versus coverglass thickness showing range of variation with secondary emission properties. Other parameters are: $m_n = 44$ amu; $T_s = 300$ K, $\Gamma = 0.03$; $\epsilon_0 = 2$ eV; $d/l_i = 0.1$; $\sigma_{ion} = 10^{-20} \text{ m}^2$ and $\gamma = 1.2$.

The Nature of Negative Potential Arcing: Current and Planned Research at LeRC

G. Barry Hillard
Sverdrup Technology, Inc.
Lewis Research Center Group
Cleveland, Ohio 44135

ABSTRACT

Research in progress at LeRC to study the breakdown of negatively biased conductors in an ambient plasma will be described. Possible breakdown mechanisms will be reviewed with an emphasis on applicability to the observed arcing of negatively biased solar arrays. Experiments underway to study the nature of the breakdown process will be described.

INTRODUCTION

For many years the problem of negative potential arcing from surfaces exposed to space plasma has engaged the attention of researchers and spacecraft designers. Despite considerable progress, the fundamental nature of the arcing process remains both controversial and poorly understood. The arcing problem has two separate aspects which must be addressed. The first concerns the breakdown mechanism while the second deals with the nature of the arc discharge itself.

Previous discussions of arcing have usually been in terms of a Paschen discharge process occurring either in background gas or in gases desorbed from the surface. Research now in progress at LeRC is directed at exploring the possibility that negative potential arcing is fundamentally a special case of the classical vacuum arc. As will be discussed below, most breakdown mechanisms previously proposed for arcing can be accommodated within a vacuum arc picture. Furthermore, we will argue that the presence of either background gas or adsorbed gases will only modify the arcing process once it has been initiated. Finally, experiments now underway to support this hypothesis will be described.

THE PHYSICS OF NEGATIVE POTENTIAL ARCING

Despite many years of work by investigators all over the world, the fundamental nature of negative potential arcing in a space plasma environment remains unclear. Experimental work has so far concentrated on characterizing such parameters as breakdown thresholds, arc rates, and voltage or current waveforms ($V(t)$ or $I(t)$). Notably lacking from existing experimental work are measurements of optical spectra and a determination of the volt-ampere characteristic. As a result, several hypotheses are consistent with experimental data and the basic question of "what exactly is

discharging" remains controversial.

Most previous treatments of arcs are based on Paschen breakdown processes either in background gas [Thiemann and Bogus] or in desorbed gas [Hastings et. al.]. Research now underway at LeRC is investigating the possibility that the phenomena of interest is really a special case of the vacuum arc.

The term "vacuum arc" is an unfortunate historical misnomer. More correctly called "metal vapor arc in vacuum" the term refers to arcs from cold metal surfaces under conditions of high vacuum. The name derives from the fact that in the early part of this century, when such phenomena first came to be studied, the hardest vacuum that could be achieved under laboratory conditions was of the order 10^{-8} torr. Such arcs have been studied extensively over the past few decades and a number of comprehensive reviews are available [see the books by Lafferty [1980], Latham [1981], and Mesyats [1989] as well as the excellent review article by Farrall [1973]].

A simple picture of the vacuum arc will begin with electric field enhancement at the surface of a negatively biased conductor. Given that this occurs, by possible mechanisms that will be discussed later, the arc erupts explosively with the ejection of a small amount of cathode material. This material forms a plasma jet, sometimes called a cathode flare, with bulk velocities exceeding 10^6 cm/sec. The arc then develops as a breakdown in the ejected metal vapor. Since the vacuum arc is a cold cathode phenomena, it typically undergoes self extinction within a few microseconds [Farrall 1980, pp 184-195] generally terminating quite abruptly. Such an arc has a number of distinguishing signatures which may make identification possible in the laboratory.

First, the optical spectrum of the vacuum arc is characteristic of the metal from which the cathode is made. In the case of solar cell arcing, alternate theories of the nature of the arc would predict a spectrum typical of either background gas or desorbed gases. Experimental measurement of an arc spectrum should therefore unambiguously determine the nature of the arc.

Second, we recall that a well known property of arcs in gases is that the volt-ampere characteristic has a negative slope. A fundamental difference between conventional arcs and the vacuum arc is that the latter is known to have a positive volt-ampere characteristic [see Farrell, 1973 p 1118]. Measurements of the VI curve in the lab will be difficult but are clearly desirable.

Finally, we note that the vacuum arc forms by an eruption from a very small area on the cathode surface. The emission sites are usually on the order of 1 to 5 microns in diameter resulting in power densities greater than 10^5 amps/cm². As a result, there is considerable damage to the surface in the immediate vicinity of the arc site. There have been numerous published photographs of such damage [see Harris pp. 137-145 and Mesyats pp. 104-117] and all of them show a strikingly similar pattern. When the

arc occurs, it leaves behind a small pit having a bell shaped appearance in the cathode surface. These so called "cathode spots" are always present and may be considered to be a fundamental part of the vacuum arc process. If arcing is heavy, they overlap and cover the entire surface leaving a landscape which often appears to have completely melted and resolidified.

Over the many years that the vacuum arc has been studied numerous models of the initial breakdown have been proposed [see Mesyats et. al. chapter 2, and Farrell, 1980]. The basic problem is that breakdown cannot arise from standard Fowler-Nordheim tunneling because the electric field strength at the surface of the cathode is typically two or three orders of magnitude too small. This is certainly the case for solar cell arcing where fields are on the order of 10^7 V/M rather than the 10^9 V/M [Jongeward et. al. 1985] required for tunneling.

The most commonly invoked mechanism for field enhancement involves the presence of micropoints, sometimes called whiskers, on the cathode surface [Farrall 1980, pp 24-35]. Because of their small size, high ratio of length to width, and generally pointed terminus, these can easily result in the hundred fold increase in field strength needed to initiate breakdown. If present on the surface of the cathode, such structures will almost always be the preferential emission sites.

Perhaps more important for our problem, it has long been recognized that dielectric impurities on the surface of a conductor can provide the necessary emission sites [Mesyats et. al. pp 9-11]. The role of such non-metallic inclusions, as they are commonly referred to in the vacuum arc literature, is to support charge buildup which results in increasing fields in the dielectric and eventually in rupture and breakdown. While not identical, the process is remarkably similar to what is arguably the current leading model of solar cell arcing [Jongeward et. al.] in which the key process is specifically identified as Malter emission [Malter 1936].

Finally, we should point out that the vacuum arc is quite often preceded by a series of "microdischarges". This prebreakdown phenomena is attributed variously to such things as the vaporization of submicropoints or to the explosion of local clusters of adsorbed gas atoms [Mesyats, pp 12-14]. It is interesting to note that similar predischage phenomena have long been observed in studies of solar cell arcing [I. Katz, private communication].

Before proceeding, we should point out that the vacuum arc is normally associated with a low pressure neutral gas while the arcing of interest to the space community involves a process in plasma. This is not as great a difference as it may first seem. In fact, there is a considerable body of work on vacuum arc processes in plasmas for two reasons.

First, much of the work done has been under conditions of alternating current. In this case, the arc extinguishes and reignites every half cycle [Farrall 1980 pp 184-227]. Because of the times scales for the various atomic processes involved, there is

usually a plasma present when reignition occurs. Second, a particular variant of the device, known as the triggered vacuum arc [Farrall 1980 pp 107-119], uses an auxiliary electrode arrangement to create a cloud of plasma in the vicinity of the electrodes resulting in immediate breakdown and arc formation.

The general experience has been that the presence of plasma changes breakdown conditions but not the nature of the arc. By this we mean that such commonly measured parameters as breakdown threshold and arc rate will be strongly affected by the presence of plasma. Once breakdown occurs, however, the arc is still characterized by the properties discussed above, e.g. is a metal vapor arc, has a positive VI curve, and operates in spot mode.

EXPERIMENTAL PROGRAM AT LeRC

The experimental program in negative potential arcing at LeRC is closely tied to the upcoming SAMPIE space experiment [D. Ferguson, this volume]. In addition to activities necessary for direct support, it is desirable that as much as possible be done to understand the fundamental nature of the arcing process.

The first step will be to establish unambiguously that the arcing of interest is in fact a case of the vacuum arc. As mentioned above, a key signature can be found in the optical emission spectrum. To record this, we will use an optical multichannel analyzer. Selected solar cells will be placed in one of the vacuum chambers available at LeRC and biased to sufficient negative potential to cause arcing. A fiber optic cable will be used to collect the emitted light and transfer it to a spectrometer. The dispersed light will finally be sent to a linear array of 512 photodetectors. With appropriate triggering and gating we expect to obtain a complete spectrum from a single arcing event. Our earlier prediction that plasma alters only the breakdown threshold will be tested by taking spectra over the full range of plasma densities that we can generate, typically $10^3/\text{cm}^3$ - $3 \times 10^5/\text{cm}^3$, as well as with the plasma generators turned off.

The second signature that we will look for is evidence of spot mode operation. The procedure here is very straightforward and amounts to doing SEM scans of solar cells subjected to various degrees of arcing. The presence of cathode spots will be a positive indicator that vacuum arcs at least play a role in the overall process.

We will try to do the early measurements with cells that have been carefully cleaned and baked to removed adsorbed gas. Our basic working assumption then predicts that the arcing phenomena can be explained entirely as a vacuum arc. If the cells are allowed to have gases adsorbed onto their surfaces, the arcing process may become much more complicated. We will study this by allowing different gases to be adsorbed on the surface, (e.g. xenon, krypton) while the background gas in the vacuum tank will be kept the same (argon).

When an arc occurs, it may have the effect of blowing off desorbed gas. The

metal vapor arc that occurs in the first few microseconds may then undergo a transition to an arc in gas. The first observable consequence of such an event may be a considerable increase in the duration of an arc from a few microseconds to perhaps as long as milliseconds. In addition, the optical spectrum would reflect the changed nature of the arc. It is not clear at this time that we will be able to time resolve various stages of an arc. Even if not, the appearance of strong emission lines characteristic of the desorbed gas in what is otherwise a metal vapor spectrum will allow us to determine at least qualitatively what is going on.

The final breakdown mechanism that we wish to investigate in detail concerns the role of charged particle bombardment. It has long been thought that incoming ions impacting with the surface of a biased cathode play a major role in the initiation of the vacuum arc [Mesyats et. al. pp 31-32]. At the same time, work in the space sciences community has indicated that breakdown on negatively biased conductors in space is caused, or at least strongly influenced, by ion bombardment. The impressive work done in connection with the SPEAR program [Katz, 1989] has shown that a key role is played by ion bombardment of triple points, where conductor, insulator, and plasma meet.

We will study this by two means. First, we will construct solar cell interconnects, or mechanical simulations of them, which have been designed so that electric field lines lead incoming charged particles away from these junctures. The design of such devices will depend heavily on computer modeling and we will use the NASCAP/LEO computer code [Mandell et. al.] to seek optimum geometries. Our effort here will be very similar to what was done by the SPEAR team.

Second, we will investigate various ways of simply insulating the interconnects so that incoming ions cannot strike the critical junctures. Such things as simply extending the cover slides so that the interconnects are shielded or actually providing a separate coating will be looked at.

This part of our program is directly related to the SAMPIE flight experiment. It is our hope to demonstrate in the laboratory that the breakdown threshold for arcing from solar cells can be significantly modified by relatively simple changes to the standard design. If we are successful, variants of these experiments will be flown on SAMPIE.

CONCLUSIONS

The subject of negative potential arcing has been of considerable interest for many years. Two different groups of researchers, the traditional gas discharge community and those whose interests have been in space science, have pursued various aspects of the problem. We believe that we can demonstrate that most negative potential arcing is at least closely related to the classical vacuum arc. In addition to researching the nature of the phenomena, we hope to demonstrate that arc suppression techniques are feasible and to fly such technology on SAMPIE.

REFERENCES

- Farrall, G.A., "Vacuum Arcs and Switching", Proceedings of the IEEE, vol. 61, no. 8, 1973, pp. 1113-1137
- Farrall, G.A., "Electrical Breakdown in Vacuum", Vacuum Arcs Theory and Application, edited by J.M. Lafferty, John Wiley and Sons, New York, 1980, pp. 20-80
- Farrall, G.A., "Current Zero Phenomena", Vacuum Arcs Theory and Application, edited by J.M. Lafferty, John Wiley and Sons, New York, 1980, pp. 184-227
- Ferguson, D., "SAMPIE - A Shuttle Based Solar Array Arcing Experiment", this volume
- Harris, L.P., "Arc Cathode Phenomena", Vacuum Arcs Theory and Application, edited by J.M. Lafferty, John Wiley and Sons, New York, 1980, pp. 120-168
- Hastings, D., Weyl, G., and Kaufman, D., "A Simple Model for the Threshold Voltage for Arcing on Negatively Biased High Voltage Solar Arrays," submitted to Journal of Spacecraft and Rockets.
- Hastings, D. and Cho, M., "A Simple Model for the Arcing Development on Negatively Biased Voltage Solar Array", this volume.
- Jongeward, G.A., Katz, I., Mandell, M.J., and Parks, D.E., "The Role of Unneutralized Surface Ions in Negative Potential Arcing", IEEE Transactions on Nuclear Science, Vol. NS-32, No. 6, Dec. 1985, pp 4087-4091
- Katz, I. et. al., "Preventing Ion Bombardment caused breakdown in High Voltage Space Power Systems and Applications to Space Power Experiments Aboard Rockets (SPEAR)". presentation to 24th Intersociety Energy Conversion Engineering Conference, Arlington VA, August 10, 1989
- Lafferty, J.M. editor, Vacuum Arcs Theory and Application, John Wiley and Sons, New York, 1980
- Latham, R.V., High Voltage Vacuum Insulation, Academic Press, London, 1981
- Malter, L., "Thin Film Field Emission", Physical Review, vol 50, July 1, 1936, pp 48-58
- Mandell, M.J., Jongeward, G.A., and Katz, I., "NASCAP/LEO Reference Manual", SSS-R-85-7300, NASA Contract Report, June 1985

Mesyats, G.A. and Proskurovsky, D.I., Pulsed Electrical Discharge in Vacuum, Springer-Verlag, New York, 1989

Thiemann, H. and Bogus, K., "Anomalous Current Collection and Arcing of Solar-Cell Modules in a Simulated High-Density Low-Earth-Orbit Plasma," ESA Journal, Vol. 10, 43, 1986.

COMPARISON OF CURRENTS PREDICTED BY NASCAP/LEO MODEL SIMULATIONS
AND ELEMENTARY LANGMUIR-TYPE BARE PROBE MODELS
FOR AN INSULATED CABLE CONTAINING A SINGLE PINHOLE

Joel T. Galofaro
NASA Lewis Research Center

ABSTRACT

The behavior of a defect in the insulation of a short biased section of cable in a Low Earth Orbital (LEO) space environment is examined. Such studies are of the utmost importance for large space power systems where great quantities of cabling will be deployed. An insulated probe containing a pinhole is placed into a hypothetical high-density LEO plasma. The NASA Charging Analyzer Program (NASCAP/LEO) is used to explore sheath growth about the probe as a function of applied voltage and to predict I-V behavior. A set of independent current calculations using Langmuir's formulations for concentric spheres and coaxial cylinders are also performed. The case of concentric spheres is here extended to include the case of concentric hemispheres. Several simple Langmuir-type models are then constructed to bracket the current collected by the cable. The space charge sheath radius and impact parameters are used to determine the proper current regime. I-V curves are plotted for the models and comparisons are made with NASCAP/LEO results. Finally NASCAP/LEO potential contours and surface cell potential plots are examined to explain interesting features in the NASCAP/LEO I-V curve.

INTRODUCTION

Current collection by a partially insulated probe has been a long standing area of study in many spacecraft/plasma interaction processes. All spacecraft incorporate a large number of dielectric surfaces for thermal control, e.g. shuttle heat tiles, and for electrical power generation, e.g. solar cell arrays. Large dielectric surfaces can be differentially charged along their length because of locally variable incident charged particle fluxes. Staskus [1983], for example, has observed arc discharging between the 15 cm and 20 cm square tiles from the Space Shuttle Thermal Protection System exposed to monoenergetic multi-KeV electron beams.

Exposed conducting surfaces present quite a different problem in spacecraft charging, especially at the interfaces between adjacent insulator/conductor surfaces. Here, for example, Snyder [1983] observed arcing between fused silica cover slides and silver interconnects that were biased between -500 VOLTS and -1400 volts.

Conductors can either be biased or floated with respect to the spacecraft floating potential. Floating conductors are uninteresting because they tend to charge only to a negative potential of a few kT,

with respect to the plasma potential. This is due to the difference in the mobility of each charge species present; electrons possess a much greater mobility than ions by virtue of their lower atomic mass. Conductors biased with respect to spacecraft ground, by contrast, act as current sinks, creating field intensive regions which promote the collection of large currents.

All space plasmas have a tendency to remain electrically neutral. A slight imbalance in the space charge density gives rise to strong electrostatic forces which act to restore electrical neutrality in the plasma. In regions where the space plasma is subjected to strong electric fields, the plasma will attempt to readjust its charge distribution to shield itself from the field by forming a charge sheath. It should be evident that all spacecraft are intimately coupled to their plasma environment.

BACKGROUND

A striking phenomenon, that has been a subject of great interest, is the high currents collected through a pinhole in the dielectric covering a charged metal. Sullen, et al. [1969], evidently was the first to report of such an instance. This appears to have triggered a number of other papers looking into the same phenomenon, among which are those by Grier and McKinzie [1971], Kennerud [1974], Stevens [1978] and, Meulenbergh and Robinson [1980].

Floating potential is measured with respect to a fixed potential in space called the plasma potential. The net current to a probe at its floating potential is zero [Reitz, 1969]. Therefore, a necessary condition for currents to be collected through a pinhole in a dielectric material is that the bias voltage of the substrate must not be equal to the floating potential. Hereafter, I will call the substrate bias exposed by the pinhole the pinhole bias. If the bias voltage is allowed to go slightly negative of the floating potential, electrons will start to be repelled, and the net current collected through the pinhole will be due to ions. If the pinhole bias is made negative enough, the number of collected ions will become saturated, and only the ion current density J_i will be collected, resulting in a positive charge sheath. Alternatively, if the pinhole bias is allowed to go slightly positive to that of the floating potential, ions will start being repelled and more electrons than ions will be collected by the pinhole. If the pinhole bias is increased just past that of the plasma potential, the ions will redistribute themselves away from the immediate vicinity of the pinhole. A negative charge sheath will form, and the electron current density J_e will be collected by the pinhole. Finally, if the pinhole bias is made even more positive, the pinhole will exhibit a rather complicated current-voltage relationship, depending on the constituency and the bulk properties of the plasma.

Sudden sheath growth about a pinhole that is biased significantly above or below the plasma potential is often attributed to the onset of secondary electron emission [Katz, et al., 1977; Stevens, 1978]. Because charged particles entering the sheath region are subject to motion constraints imposed on them by their own angular momentum electric field, a certain percentage of them will miss the pinhole completely and strike the dielectric at a nearby point. If the

energy of the particle upon collision is above a certain energy threshold (determined by the bulk properties of the dielectric) and below a certain energy maximum, there is a high probability that more than one secondary electron will be liberated from the surface of the dielectric, causing the dielectric to charge positive. As the pinhole bias is increased, so too does the effective collecting area of this sheath, causing a yet greater number of high energy charged particles to enter the pinhole sheath region. As a result, more and more secondary electrons will be liberated causing a positive surface charge sheath to form on the dielectric. This phenomenon will henceforth be called "snapover."

With the new era of space exploration before us, the advent of Space Station Freedom, and TSS-1 Electrodynamic Tether applications, large amounts of insulated electrical cabling will be deployed in the construction and operation of these missions. Of increasing importance is the question of how such cables will perform in space, and, specifically here, how defects in the insulation might influence the behavior of a long insulated wire.

The present work will attempt to look into these issues by making use of a theoretical charging analyzer computer program (for low earth orbit) developed for NASA, called NASCAP/LEO. An insulated probe of appropriate geometry, containing a single pinhole, is defined and hypothetically placed into a known space environment. The code will then be used to explore sheath growth around the probe as a function of potential. Next, a bare cylindrical probe model will be presented and the I-V curves obtained by it plotted for comparison against those obtained by the NASCAP/LEO. Finally, a means of calculating the current collected by a spherical and a hemispherical probe, each having the same effective area as that of the pinhole, will be presented. These results will then be compared to the current collected by the pinhole as obtained from the NASCAP/LEO.

PROCEDURE

NASCAP/LEO is a finite element computer code designed expressly for the study of the electrostatic interaction between a spacecraft having charged surfaces and a cold dense plasma. Environmental parameters under NASCAP/LEO are user-specified parameters that need to be input prior to the calculation. Surface cell currents and potentials are particularly sensitive to the environment, and so some thought must be given to accurately describe the plasma environment for the model in question. The plasma environmental parameters used here and for all subsequent runs were based on typical high-density (worst case) LEO plasmas. (Plasma density was set at 10^{12} m^{-3} , electron temperature at 0.1 eV, ion mass was set to $2.656 \times 10^{-26} \text{ kg}$ for oxygen ions, and the sheath boundary potential was set at 0.0873 eV.) NASCAP/LEO allows the user to specify the object geometry, material composition of conductors and insulators, conductor biases, scale size, and the placement of the object to be modeled in the NASCAP/LEO primary grid space.

The object modeled consisted of a short section of a copper conductor covered by a thin Kapton insulating jacket. A single puncture through the insulated jacket exposed a small area of the

underlying conductor. (NOTE: The surface area of the pinhole is much smaller than the surface area of the object.) The conductor was then biased in the code positively with respect to the plasma potential, while all the Kapton insulating surfaces were allowed to float. Initially, the insulating surfaces (for low conductor biases) were predicted to sit at a small negative potential relative to the plasma, and then to become more and more positive as the conductor bias increases. It was possible to keep track of how the charge sheath should propagate over the insulator surfaces, by looking at all insulator surface potentials over a range of varying conductor biases between 1 and 1000 volts.

Typical outputs from NASCAP/LEO consisted of 2-D potential contour plots (YZ and XY views) in the space around the object at a given conductor bias, as defined in the primary grid computational space. Other types of numerical outputs for individual surface cells were also obtained. These consisted of surface cell number and surface cell potential and current at each given conductor bias. By adding up the individual currents going to each surface cell, the incident total current collected by the object can be obtained. The total incident current to the object was then plotted versus the conductor bias to obtain the object's I-V curve characteristics.

In order to verify NASCAP/LEO results, several comparisons were made. The first of these comparisons involved the application of Langmuir's space charge limited current (SCLC) equation for parallel plates [Langmuir and Blodgett, 1924] (appendix C, eqs. 1.a and 1.b) and his SCLC equation for bare coaxial cylinders [Langmuir and Blodgett, 1923; (appendix D, eq. 3.a2)]. Assuming both planar-[Mandell and Jongeward, 1985] and cylindrical-type charge sheaths, these equations were solved for the space charge sheath radius (SCSR); the thickness between: (1) the bare cylindrical probe and a planar charge sheath boundary (appendix D, eq. 1.c) and (2) for the space charge sheath thickness between the bare cylindrical probe and a coaxial cylindrical charge sheath boundary (appendix D, eq. 3.c). Such SCSR determinations are a necessary step in finding the proper type of current collection regime that applies.

The relevancy of performing the above calculations should be clarified. What is being attempted here is a direct and independent current calculation of the object previously defined under the NASCAP/LEO. These calculations are to be performed from "first principals," starting with Langmuir's formulations for the Space Charge Limited Current to a bare parallel plate, sphere, and cylinder. In order to understand how an insulated object with a pinhole collects current, we first need to understand how this current compares to a similar object of the same geometry and dimensions, but containing no insulating surfaces. Hence, we need to deal with bare probe equations. Secondly, because the NASCAP/LEO object defined is an idealized object (constructed from a finite number of cubes of the same size) due to code limitations, it lacks the true geometry we are trying to model. Consequently, rather than finding the current to a bare object of length L of square cross section, we choose to approximate it, instead, by calculating the current to a bare cylinder of length L , having a surface area approximately equal to the NASCAP/LEO defined object.

Whenever planar conditions are assumed, that is, the charge sheath is assumed to be locally parallel to each point on the

surface, then the problem reduces to finding the SCSR, R_0 (i.e., that distance between a biased planar anode on the surface of the object and a parallel charge sheath boundary). Fortunately, this problem is amenable to the type of solution Langmuir used for finding the maximum current between two biased parallel plates. [Mandell, M. J.; Jongeward, G. A., et al.] As a result, appendix D, eq. 1.c may be used to estimate the SCSR for a probe of any geometry.

The next set of comparisons involves calculating the Space Charge Limited Current collected by an insulated cylindrical probe containing a single pinhole. Because the pinhole contains the only exposed conductor on the surface of the object, it is the region where the largest currents will be collected, and so it is the logical choice of places to model. For simplicity, the model only considers conducting surfaces, leaving all insulator surfaces untreated. The assumption here is that the insulated portions of the probe will be at some small negative potential both far from and near to the pinhole if "snapover" type effects are not considered. As a result, only the exposed conducting area due to the pinhole was considered in the formulation of this model.

For the case of a pinhole, whose surface area is very small compared to the rest of the object, one would suppose current collection to be defined by a spherical or hemispherical geometry. As the scale size of the pinhole increases so that surface area of the pinhole becomes a more significant portion of the entire surface area, one would suppose current collection to be dependent upon the geometry of the exposed region.

The present paper will, therefore, attempt to calculate the the Space Charge Limited Current to an insulated conductor with a pinhole by employing both a bare conducting sphere and hemisphere, each having a surface area equal to the area of the pinhole. A close examination of the NASCAP/LEO object (appendix A, figure A-2) reveals the appropriate scale dimensions in the pinhole region. Appendices B and C show the calculations used to find the radius of a sphere and hemisphere of equal surface area to the pinhole. In the hemispherical case where we use a slightly larger probe radius, we use Langmuir's spherical form of the equation for the current (appendix D, eq. 4.a2), and cut the collected current in half (eq. 4.a1). This is equivalent to doubling the surface area of the hemisphere so that we are effectively collecting current from a larger spherical geometry probe from which we only accept half of the current. The comparisons here involve the application of Langmuir's SCLC equations for parallel plates (appendix D, eqs. 1.a and 1.b), Langmuir's SCLC equation for concentric spheres (appendix D, eq. 2.a2), and the subsequent derived expression for the SCLC equation for concentric hemispheres (appendix D, eq. 4.a2). Assuming both planar- and spherical-type charge sheaths for the bare spherical pinhole model, Langmuir's bare concentric sphere SCLC expression for the SCSR is solved for the thickness between: (1) a bare sphere and a locally parallel planar charge sheath boundary (appendix D, eq. 1.c) and (2) for the thickness between a bare sphere and a concentric spherical charge sheath boundary (appendix D, eq. 2.c). The last comparison assumes a hemispherical-type charge sheath for the bare hemispherical pinhole model. A solution is found for eq. 4.a2 in appendix D for the SCSR, the thickness between a bare hemispherical collector and a concentric hemispherical sheath

boundary (appendix D, eq. 4.c). After finding the SCSR for each case above, the applicable current collection regime was determined. Then I-V curves were plotted for each of the above pinhole models.

Appendix D, Table D-1 lists all the relevant equations cited previously. Although many of the equations compiled under this table can be readily obtained from a number of sources, to the best of this author's knowledge this appears to be the first time all pertinent equations have been presented in a single location. Because Langmuir's original work [Langmuir and Blodgett, 1923; Langmuir and Blodgett, 1923;] only extended over the cases of the parallel plates, coaxial cylinders, and concentric spheres, the concentric hemispherical equations presented in the table are newly derived. Fortunately, this was easily accomplished because the sphere and the hemisphere share the same geometry and only minor changes had to be incorporated into the case of Langmuir's concentric spheres to make them applicable to the hemispherical case. It should be noted that a minor error was found in Langmuir's expression for the current between concentric spheres [Langmuir & Blodgett, 1924]. His quoted parameters for D (for ions and electrons) could not be found, as stated, because of an inconsistency in the dimensions of his current equation. The error appears to have been propagated from the differences between the Gaussian and rationalized MKS units. Inclusion of a term for the permittivity of free space in the product of his current term rectifies the situation. All units for the equations in appendix D have been given in rationalized MKS so as to avoid any confusion as to which system is being used.

As stated previously, before any I-V curves can be calculated for the current collected by any of the geometries listed above, we first need to know which type of current collection regime applies at a given potential bias. I have already presented the calculations for one type of current collection regime, the space charge limited current regime. There is only one other type of current collection, the so-called orbit limited current regime, that can apply.

Whereas the space charge limited current is determined by the modification of the electric field near the sheath boundary (as a result of the space charge of electrons in that region), the orbit limited current collection is dominated by the orbital motion of electrons captured by the sheath. For the orbit limited case, the sheath radius is determined by the applied potential, the electron temperature, their angle of incidence upon entering the sheath and additionally the radius of the probe. Therefore electrons entering the sheath will either have: (1) too little energy to escape the sheath region and will end up striking the probe; or (2) they will have too great an energy to be captured, but due to their trajectory will still strike the probe; or (3) they will have too great an energy to be captured and will miss the probe completely leaving the sheath region altogether. The impact parameter is used to determine the sheath thickness for the orbit limited case.

Appendix E, eq. 5.0 defines the impact parameter. Table 2 gives us a means of calculating the type of current collection regime that applies at a given potential bias. Here, one first chooses the type of geometry he is interested in. Next, he calculates the space charge sheath radius for that geometry and the impact parameter and compares the two values obtained. When the space charge sheath radius is less than the impact parameter, a space charge limited

calculation holds. Equations 5.1a through 5.4a in table E-1 of appendix E are then used to calculate the current. When the impact parameter is less than the space charge sheath radius, an orbit limited calculation holds, and eqs. 5.1b through 5.4b may be used to estimate the collected current. Finally, when the space charge sheath radius is equal to the impact parameter and either set of formulations may be used for the current. This procedure outlined above is carried out for the range of potentials to be used in the NASCAP/LEO simulation. I-V curves are then obtained for direct comparisons with the NASCAP/LEO curve.

RESULTS

Figures f-1, f-2, f-3, f-4, and f-5 of appendix F show a comparison of the space charge sheath radius R_0 and the impact parameter P versus the applied voltage V for five different sheath thickness approximations. The first of these approximations (figure f-1) plots R_0, P versus V , using a planar type sheath approximation (appendix D, eq. 1.c) for R_0 . The second type of approximation (figure f-2) uses a cylindrical sheath approximation (appendix D, eq. 3.c) for R_0 . Figures f-3, f-4, and f-5 also plot R_0, P versus V but use planar (appendix D, eq. 1.c), spherical (appendix D, eq. 2.c), and hemispherical (appendix d, eq. 4.c) approximations respectively for the space charge sheath radius R_0 .

It should be noted that the plots of R_0, P in figures f-1 through f-5 are dependent upon the particular probe geometry and the probe radius, a . The bare cylindrical probe models, which use a planar (figure f-1) and a cylindrical charge sheath thickness approximation (figure f-2) for R_0 , have the same probe geometry and probe radius. Here the radius has been set equal to 1/2 the grid spacing (xmesh) used in the NASCAP/LEO object or $a = 1.5875 \times 10^{-3}$ meters. The spherical pinhole models, using planar (figure f-3) and spherical (figure f-4) space charge sheath thickness approximations for R_0 , also use the same value for the probe radius $a = 2.2391 \times 10^{-4}$ meters determined from appendix B. The final hemispherical pinhole model uses a hemispherical charge sheath thickness approximation (figure f-5) for R_0 and uses the value of the probe radius $a = 3.1666 \times 10^{-4}$ meters, which is derived in appendix C.

Inspection of figures f-1 through f-5 show that R_0 is greater than P at any specified voltage along each of the curves. Therefore an orbit limited calculation is correct for all Langmuir-type probe models considered.

Figure f-6 (appendix f) shows a comparison of the currents collected by two different bare cylindrical probe models (curves e and f). Both of these models yield the same I-V curve. The same equation (appendix E, eq. 5.3b) is used to compute the current collected by both bare cylindrical probe models here. Referring back to figures f-1 and f-2 of appendix F, one can see that the range of values for R_0 varies considerably between the planar and cylindrical sheath thickness cases. One would, therefore, expect very different currents from each of these models were it not for the fact that neither of these sheath distances for R_0 is used in the current calculations for these models (since the orbit limited regime applies in both cases). Because each of these models uses the impact

parameter P (appendix E, eq. 5.0) in its current calculations, this leads to the same value of P at a given voltage and to the same I-V curve in both of these models. It should also be noted that the plots of V versus P in figures f-1 and f-2 are actually the same curve by virtue of eq. 5.0 in appendix E. (Because of the rescaling of the Y-axis dimension to the maximum value of R_0 in each case, P is plotted accordingly.) Similarly, figures f-3 and f-4 of appendix F, also yield the same value for P for the reasons indicated above.

In figure f-6 of appendix F, curves a, b, and c show a comparison of the collected current between three different pinhole models. The resultant I-V curves are the same regardless of which of the probe models (spherical or hemispherical) is applied. What is also evident here is that the pinhole current collected by a bare spherical probe of equal surface area to that of the pinhole is about two orders of magnitude less than what would be collected by a non-insulated cylindrical probe of the same overall dimensions as the entire NASCAP/LEO object.

Consequently, the current collected by an insulated cylindrical probe containing a single pinhole has been bracketed. The actual current collected should fall somewhere between curves a, b, and c and curves e and f of figure 6 in appendix F. (Actually, one would suppose the collected current to be closer to curves a, b, and c, where the collecting surfaces are equal in area to that of the pinhole.)

Curve D in figure f-6 of appendix F shows the resultant I-V curves obtained from NASCAP/LEO runs for an insulated cylindrical probe containing a single pinhole. This curve contains many noteworthy features. Up to about 600-volts potential, the NASCAP/LEO curve appears to predict somewhat less current than either the spherical or hemispherical pinhole curves, although the current continues to converge to the 600-volt NASCAP/LEO current throughout this range. (It should also be noted that in the potential range, 25 volts through 115 volts, the current collected by the spherical and hemispherical pinhole models is approximately a factor of 4 greater than that predicted by the NASCAP/LEO model at any specified voltage within this range. The reason for this discrepancy will be explained in the conclusions.) In the range 130 volts to 600 volts, the current from the spherical, hemispherical pinhole models, and NASCAP/LEO curves appear to converge with one another. In the voltage range 620 volts to 680 volts, the spherical and hemispherical pinhole models collect nearly the same amount of current as predicted by the NASCAP/LEO simulation. In the potential range 685 volts to 1000 volts, the NASCAP/LEO curve appears to collect about a factor of 4 greater current than the spherical or hemispherical pinhole curves.

There are also several knee regions on the NASCAP/LEO curve where the current collection changes rather sharply. These regions occur between 100- and 130-volts, 600- to 640-volts, and 680- to 700-volts potential and can be attributed to the "snapover phenomenon."

The analysis begins by looking at NASCAP/LEO-generated contour plots of equipotentials and plots of surface cell potentials in each of the specified voltage regions above. The position of the zero-potential contour line, with respect to the pinhole, as well as changes in the insulator surface cell potentials will be used as an

indicator of the extent of the sheath edge or boundary. Thus drastic changes in the position of the sheath boundary should signal that "snapover" is occurring or has occurred.

Figures G-1(a) through G-8(a) of appendix G show a face on view of an x-z cutplane slicing through the pinhole. Figures G-1(b) through G-9(b) show a cross-sectional end on view of an x-y cutplane slicing through the pinhole. Figures G-1(c) through G-9(c) show a close-in view of the subdivided region, with all surface cells labeled and surface potentials plotted. Figures G-1(d) through G-9(d) show a full object view of the cable with all corresponding surface cell potentials and cell numbers plotted. For convenience, the plots are organized such that the contours and surface cell potential maps at a given bias voltage appear horizontally across two consecutive pages.

The two contour plots [figures G-1(a) and G-1(b), appendix G] show that the sheath, which propagates from the pinhole, looks like a narrow ring of charge at 75-volt potential. The corresponding surface potential maps [figures G-1(c) and G-1(d)] show nothing out of the ordinary. At 100-volt potential the contour plots [figures G-2(a) and G-2(b)] show only a slight expansion in sheath size. However, the corresponding surface cell potential maps [figure G-2(c)] for the first time show that the potential on the pinhole's nearest neighboring surface cells has undergone a sign change. The voltage on these cells has changed from something under -1 volt to something in the range of +1 volt. This appears to be the first evidence that "snapover" has begun. Next, at 130-volts potential figures G-3(a) and G-3(b) of appendix G show that the sheath edge has grown considerably. The x-y cross-sectional view [figure G-3(b)] shows that the sheath boundary has begun to wrap around the object past the front surfaces. Figure G-3(c) demonstrates that snapover is indeed occurring. The surface cell potentials of adjacent, nearest neighboring cells have increased greatly. This coincides with the sharp change in current predicted by the NASCAP/LEO curve (figure f-6, curve d of appendix F) between 100-volts and 130-volts potential. By 600-volts potential, it is evident that the sheath edge (zero-potential contour line) completely surrounds the object [x-y view, figure G-4(b)] and that the 0.1-volts potential contour line (same view) wraps around three sides of the object. The surface cell potentials [figure G-4(c)] at this point are nearly all positive, except for the concentric ring of cells about the center and each of the surface cells on the right- and left-hand sides of the pinhole which are still between -1-volts and 0-volts potential. Evidently, secondary electron focusing, due to the applied field, seem to be the cause here. All other surface cells outside of the subdivided region [figure G-4(d)] still appear to be at a small negative potential. At 620-volts potential, the +0.1-volts potential contour line has completely snapped around the object [figure G-5(b)]. The zero-volt potential contour line [figure G-5(a)] appears to start growing along the length of the cylinder outward from the pinhole center. In figure G-5(c) the surface cell potential map at 620-volts potential clearly demonstrates that most surface cells within the subdivided region have dramatically increased in potential. This coincides with the sharp jump in current collection between 600 and 620 volts on the NASCAP/LEO predicted I-V curve. All surface cells outside of the subdivided

region, however, still remain at a small negative potential. At 680-volts potential there appears to be no significant change in either the contour plots or surface cell potential maps [figures G-6(a), G-6(b), G-6(c), and G-6(d), appendix G]. Finally, figures G-7(a) and G-7(b) show significant changes in sheath structure. It seems that the pinhole at this point begins to collect current like a larger bare sphere, as borne out by figures G-7(a) and G-7(b) and the NASCAP/LEO I-V curve at this voltage. It is also evident from figures G-7(c) and G-7(d) that considerable changes have taken place here also. For the first time we see that the surfaces of two cells on the top and bottom faces of the cable (outside the subdivided region) are beginning to grow to a substantial positive potential. This appears to account for the observed current shift between 680-volts and 685-volts potential.

Although there are no sharp changes in the current collected by the NASCAP/LEO I-V curve for the voltage range 690 through 1000 volts, for the sake of completeness, plots are presented in the 800- and 1000-volt potential region. At 800-volts potential, figure G-8(d) shows that the cell potentials of two adjacent cells (one cell flanking each side of the subdivided region on the front face of the cable) have charged to a slightly positive potential. This indicates that a positive charge sheath is beginning to grow over these surfaces along the length of the cable. The 1000-V surface cell potential map [figure G-9(d)] shows the same features with the only difference being that the voltage of the two adjacent cells has greatly increased.

CONCLUSIONS

The NASCAP/LEO I-V curve (appendix F, figure f-6) demonstrates that there are a number of different types of "snapover effects" occurring throughout the applied voltage range (as opposed to just one type that occurs throughout the entire pinhole bias voltage region as previously thought). Indeed, three such snapover effects were found in the present cable simulation and there could conceivably be more at higher bias voltages. (At 1000-volts potential, the majority of surface cells outside the subdivided region remain at approximately -1-volt potential. Therefore, at some higher potential it is conceivable that when all insulated surface cells become charged positive, there could be yet another large shift in current collection.) It is also conceivable that probe geometry, sharp edges, and pinhole size could have an effect on the exact number of snapover effects observed.

The first observed type of snapover effect occurs between 100 and 130 volts where the charge sheath first jumps to the insulator surfaces in the adjacent vicinity of the pinhole. This is probably due to the onset of significant secondary electron emissions in this voltage region.

The second type of snapover effect occurs between 600 and 620 volts, where the positive charge sheath in space completely surrounds the radius of the cable (as evidenced by the x-y view of the +0.1 contour line in figure G-5(b) of appendix G). The second type of snapover effect appears to be a necessary precursor to the third type of snapover effect observed.

The third and final type of snapover effect seems to be an edge effect occurring between 680- and 685-volts potential. It is here where the positive charge sheath has propagated from the front face to the sides of the cable and so is termed the "snap-around effect." In a perfect cylindrical cable, which has no sharp edges, this effect would probably not be seen until the positive surface charge sheath has completely wrapped around the cylinder. One must also conclude from the surface potential maps and the resultant NASCAP/LEO I-V curve that the positive surface charge sheath must snap around the cable before it can grow along its length.

Particularly disturbing is the lower voltage region (0- to 100-volts potential) where NASCAP/LEO predicts about a factor of 4 lower current than any of the Langmuir-type pinhole models (LTPM). Because NASCAP/LEO and the LTPMs solve Poisson's equation, and since "snapover-type effects" are not applicable at lower voltages, it was assumed that the NASCAP/LEO predicted values would yield the same result as the LTPMs. The reason that they do not agree is that the NASCAP/LEO simulation assumes space charge limited currents where, in fact, the LTPMs have shown the current collection to be orbit limited. For the case where the Debye length is greater than the pinhole dimensions, many of the particles traced through the sheath boundary will miss the pinhole completely. As a result, less current is predicted by the current NASCAP/LEO simulations than by the LTPM approximations.

Langmuir-type probe models that attempt to bracket NASCAP/LEO current solutions, for an insulated cable with a pinhole, appear to suggest that current collection should favor an orbit limited current calculation. Furthermore, for small object dimensions (on the order of a centimeter), it is evident that at lower voltages LTPMs more accurately predict collected current, because NASCAP/LEO only makes its calculations in the space charge limited current regime.

Overall, (all low-voltage behavior aside), the Langmuir-type models (LTM) do quite well in bracketing the current collected by an insulated cable with a pinhole. Specifically, here the bare spherical and hemispherical LTM approximations, while they are not able to predict the sharp changes in current observed in the NASCAP/LEO-generated I-V curve, are within a factor of 4 of those values. The reason for this is clear. No bare probe model, however sophisticated, can hope to include secondary electron emission from the dielectric. Consequently, it is impossible for a bare probe model to predict snapover effects. Even so, the bare LTM approximations of the aforementioned geometries offer a reasonably good estimate of the current for a biased insulated probe with a pinhole without the need to resort to a number of lengthy NASCAP/LEO computer runs. For this reason they are quite useful. Such models have also been useful in understanding NASCAP/LEO results.

REFERENCES

- Chen, F. F., "Electric Probes," Plasma Diagnostic Techniques, edited by R. H. Huddleston and S. L. Leonard--Pure Applied Physics, Vol. 21, Academic Press, New York, 1965, chapter 4, pp. 113-200.
- Cole, R. K., Ogawa, H. S., and Sellen, J. M., Jr., "Operation of Solar Cell Arrays in Dilute Streaming Plasmas," TRW Systems, Redondo Beach, Calif., TRW-09357-6006-R000, March 1968. (NASA CR-72376.)
- Grier, N. T. and McKinzie, D. J., Jr., "Current Drainage to a High Voltage Probe in a Dilute Plasma," NASA TMS 67890, 1971.
- International Dictionary of Physics and Electronics, 2nd Ed., D. Van Nostrand Company, Inc., Princeton, New Jersey, p. 1060, 1961.
- Katz, I., et al., "A Three Dimensional Dynamic Study of Electrostatic Charging in Materials," (SSS-R-3367), Systems, Science and Software (NASA Contract NAS 20119) NASA CR-13526, August 1977.
- Kennerud, K. L. "High Voltage Solar Array Experiments," NASA CR-121280, 1974.
- Langmuir and Blodgett, "Currents Limited by Space Charge Between Concentric Spheres," Physical Review, Vol. XXII, 49, July 1924.
- Langmuir and Blodgett, "Currents Limited by Space Charge Between Coaxial Cylinders," Physical Review, Vol. XXII, 347, October 1923.
- Mandell, M. J., Jongeward, G. A., and Katz, I., "NASCAP/LEO Reference Manual," SSS-R-85-7300, NASA Contract Report pp. 4-9, June 1985.
- Meulenber, A., Robinson, Jr., "Conduction Through Punctures in Metal Backed Dielectrics," 3rd Spacecraft Charging Technology Conference, Colorado Springs, Colorado, November 1980, pp. 342-352.
- Parker, L. W., "Plasma-Photosheath Theory for Large High-Voltage Space Structures," Progress in Aeronautics and Astronautics, Vol. 71, New York, New York, American Institute of Aeronautics and Astronautics (edited by Garrett and Pike), 1980.
- Reitz, J. R. and Milford, F. J., Foundations of Electromagnetic Theory, Reading, Maine, Addison-Wesley Publishing Company, 2nd Ed., 1969, pp. 269-292.
- Snyder, D. B., "Discharges on a Negatively Biased Solar Cell Array in a Charge-Partial Environment," 4th Spacecraft Environmental Interactions Conference, Colorado Springs, Colorado, October 1983, pp. 379-388.
- Staskus, J. A., "Electron Beam Charging of Space Shuttle Thermal Protection System Tiles." 4th Spacecraft Environmental Interactions Technology Conference, Colorado Springs, Colorado, October 1983, pp. 91-102.
- Stevens, N. J., "Interactions Between Spacecraft and the Charged Particle Environment," 2nd Spacecraft Charging Technology Conference, Colorado Springs, Colorado, October 31 - November 2, 1978, pp. 276-277.
- Stevens, N. J., et al., "Investigation of High Voltage Spacecraft System Interactions with Plasma Environments," NASA TM-78831, 13th Electronic Propulsion Conference, San Diego, California, 1978.

LIST OF APPENDICES

APPENDIX A	Fig. A-1 Fig. A-2	NASCAP/LEO Object (full view) NASCAP/LEO Object (subdivided region with pinhole)
APPENDIX B	Calculations for the radius of a sphere of equal surface area to the pinhole in NASCAP/LEO defined object.	
APPENDIX C	Calculations for radius of a hemisphere of equal surface area to the pinhole in NASCAP/LEO defined object.	
APPENDIX D	Table D-1	Space charge limited equations for a parallel plate, concentric spheres and hemispheres, coaxial cylinders.
APPENDIX E	Table E-1	Determination of space charge limited or orbit limited currents for planes, spheres, cylinders, and hemispheres.
APPENDIX F	Fig. F-1 Fig. F-2	Plot of V versus R_0, P for bare cylindrical probes using a planar sheath geometry for R_0 . Plot of V versus R_0, P for bare cylindrical probes using a cylindrical sheath geometry for R_0 .
APPENDIX G	Fig. F-3 Fig. F-4 Fig. F-5 Fig. F-6	Plot of V versus R_0, P for bare spherical probes using a planar sheath geometry for R_0 . Plot of V versus R_0, P for bare spherical probes using a spheri- cal sheath geometry for R_0 . Plot of V versus R_0, P for bare hemispherical probes using a hemispherical sheath geometry for R_0 . Comparison of collected currents between various Langmuir-type probe models and NASCAP/LEO values.
APPENDIX G	Figs G-1(a), G-1(b) G-1(c), & G-1(d) Figs. G-2(a), G-2(b) G-2(c), & G-2(d) Figs. G-3(a), G-3(b) G-3(c), & G-3(d) Figs. G-4(a), G-4(b) G-4(c), & G-4(d)	75-volt contour plots and surface cell potential maps. 100-volt contour plots and surface cell potential maps. 130-volt contour plots and surface cell potential maps. 600-volt contour plots and surface cell potential maps.

APPENDIX G (continued)	Figs. G-5(a), G-5(b) G-5(c), & G-5(d)	620-volt contour plots and surface cell potential maps.
	Figs. G-6(a), G-6(b) G-6(c), & G-6(d)	680-volt contour plots and surface cell potential maps.
	Figs. G-7(a), G-7(b) G-7(c), & G-7(d)	685-volt contour plots and surface cell potential maps.
	Figs. G-8(a), G-8(b) G-8(c), & G-8(d)	800-volt contour plots and surface cell potential maps.
	Figs. G-9(a), G-9(b) G-9(c), & G-9(d)	1,000-volt contour plots and surface cell potential maps.

APPENDIX A

CYLINDRICAL OBJECT WITH A PINHOLE

MESH = 1/8 IN. = .09375 METERS

DIMENSIONS:

X	Y	Z
1	1	30

KAPTON 120 SURFACE CELLS (12 CELLS IN SUBDIVIDED REGION)

SUBDIVIDE REGION:

X	Y	Z
0	8	16
2	2	2

(12 SURFACE CELLS)

KAPTON 120 SURFACE CELLS

(PINHOLE)

GOLD 4 SURFACE CELLS

OBJECT FULL VIEWS:

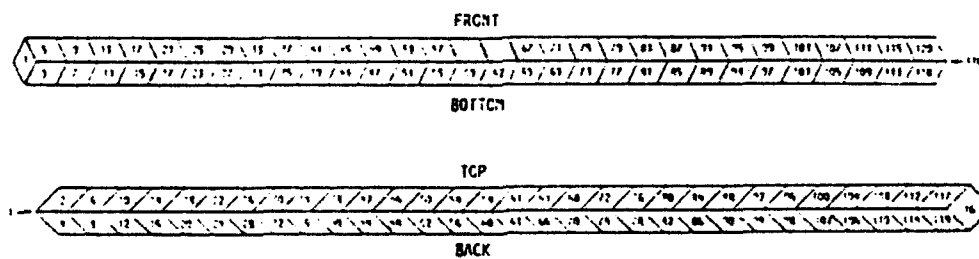


FIGURE A-1.

SUBDIVIDED REGION (EXPANDED VIEW):

MATERIAL
CODE



KAPTON



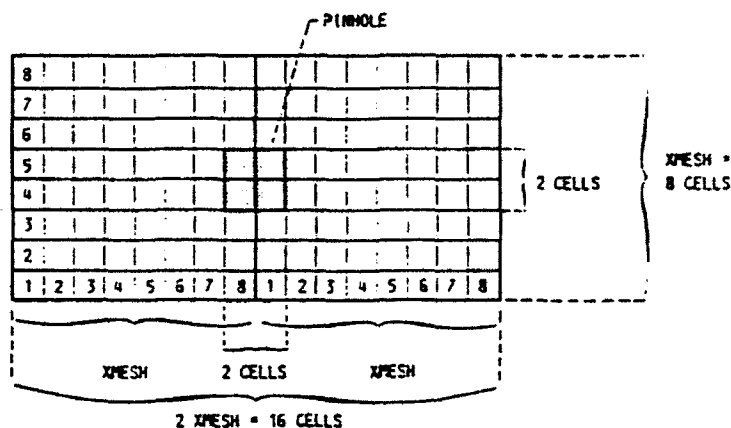
COPPER

229	230	231	232	233	234	235	236	237	238	239	240	241	242	243	244
213	214	215	216	217	218	219	220	221	222	223	224	225	226	227	228
197	198	199	200	201	202	203	204	205	206	207	208	209	210	211	212
183	184	185	186	187	188	189	247	248	190	191	192	193	194	195	196
169	170	171	172	173	174	175	245	246	176	177	178	179	180	181	182
153	154	155	156	157	158	159	160	161	162	163	164	165	166	167	168
137	138	139	140	141	142	143	144	145	146	147	148	149	150	151	152
121	122	123	124	125	126	127	128	129	130	131	132	133	134	135	136

FIGURE A-2.

APPENDIX B

$$X_{MESH} = 1/8 \text{ IN.} = 3.175 \times 10^{-3} \text{ METERS}$$



$$\text{TOTAL NUMBER OF CELLS IN SUBDIVIDED REGION} = 8 \times 16 = 128 \text{ CELLS}$$

$$\text{TOTAL NUMBER OF CELLS IN PINHOLE} = 4 \text{ CELLS}$$

$$\text{TOTAL SURFACE AREA OF SUBDIVIDED REGION} = S.A._{SUBD} = (2) (X_{MESH}) (X_{MESH})$$

$$\text{SURFACE AREA OF PINHOLE} = S.A._{PIN} = \frac{4}{128} (2) (X_{MESH})^2$$

$$\text{SURFACE AREA OF SPHERE} = S.A._{SPH} = 4\pi r^2 \quad ; \quad r_{SPH} = \text{SPHERE RADIUS}$$

$$S.A._{SPH} = S.A._{PIN}$$

FINDING RADIUS (r) OF A SPHERE OF EQUAL SURFACE AREA TO THAT OF THE PINHOLE IN NASCAP/LEO OBJECT:

$$S.A._{PIN} = 4\pi r^2$$

$$r_{SPH} = \sqrt{\frac{S.A._{PIN}}{4\pi}} = \frac{X_{MESH}}{8\sqrt{\pi}} = 2.23912 \times 10^{-4} \text{ METERS}$$

FIGURE B-1.

APPENDIX C

FINDING THE RADIUS OF A HEMISPHERE (a_{HEM}) OF EQUAL SURFACE AREA TO A SPHERE OF RADIUS (a_{SPH})

SURFACE AREA OF SPHERE = S.A.SPH

SURFACE AREA OF HEMISPHERE = S.A.HEM

LET:

$$S.A.SPH = S.A.HEM = S.A.PIN$$

THEN:

$$S.A.SPH = 4\pi a_{SPH}^2$$

$$S.A.HEM = 2\pi a_{HEM}^2$$

$$\left. \begin{array}{l} S.A.SPH = 4\pi a_{SPH}^2 \\ S.A.HEM = 2\pi a_{HEM}^2 \end{array} \right\} \text{ WHERE: } S.A.PIN = \frac{X_{MESH}^2}{16}$$

THEREFORE:

$$a_{SPH} = \frac{X_{MESH}}{8\sqrt{\pi}} \text{ AND } a_{HEM} = \frac{X_{MESH}}{4\sqrt{2\pi}}$$

$$\frac{a_{HEM}}{a_{SPH}} = \sqrt{2} \text{ OR } a_{HEM} = \sqrt{2} a_{SPH} = 3.16659 \times 10^{-11} \text{ METERS}$$

FIGURE C-1.

APPENDIX D

BARE PROBE GEOMETRY	I CURRENT (AMPS)	j_r RANDOM THERMAL CURRENT DENSITY (A/m ²) $= \frac{He \sqrt{kTe}}{\sqrt{2\pi m}}$	THICK SHEATH r_0 APPROXIMATION
			SPACE CHARGE SHEATH RADIUS (METERS)
			$r_0 = r_0 + a$
11 FLAT PLATES:	CHEN: (1.a) ✓ $I = j_r$	CHILD (1.b) ✓ $j_r = \frac{4\epsilon_0}{9} \sqrt{\frac{2e}{m}} \frac{V^{3/2}}{r_0^2}$	S-CUBED (1.c) * $r_0 = \left[\frac{(8\epsilon_0)^2}{9e} \pi \right]^{1/4} \frac{V^{3/4}}{\sqrt{N} (kT)^{1/4}}$ 9330
CONCENTRIC SPHERES:	CHEN: (2.a1) ✓ $I = 4\pi r_0^2 j_r$ LANGMUIR: (2.a2) ✓ $I = \frac{4\sqrt{2}\epsilon_0}{9} \sqrt{\frac{e}{m}} \frac{V^{3/2}}{a^2}$ SMALLER SPHERE KENNERUDE: (2.a3) ✓ $a^2 = 1.16 (r_0/a)^{3/2}$	(2.b) ✓ $j_r = \frac{\epsilon_0}{9\pi} \sqrt{\frac{2e}{m}} \frac{V^{3/2}}{r_0^2 a^2}$	(2.c) * $r_0 = \left[\frac{2\epsilon_0}{\sqrt{109} \pi e} \right]^{2/7} \frac{(aV)^{3/7}}{N^{2/7} (kT)^{1/7}}$ 86.31
COAXIAL CYLINDERS:	LANGMUIR: (3.a1) ✓ $I = 2\pi r_0 L j_r$ (3.a2) ✓ $I = \frac{8\pi\epsilon_0}{9} \sqrt{\frac{e}{m}} \frac{V^{3/2}}{r_0 (\ln r_0/a)^2}$	(3.b) ✓ $j_r = \frac{4\epsilon_0}{9} \sqrt{\frac{2e}{m}} \frac{V^{3/2}}{r_0^2 (\ln r_0/a)^2}$	(3.c) * $r_0 \ln (r_0/a) = \left[\frac{(8\epsilon_0)^2}{9e} \pi \right]^{1/4} \frac{V^{3/4}}{\sqrt{N} (kT)^{1/4}}$ 9330
CONCENTRIC HEMISPHERES: NOTE: a IS THE SAME VALUE FOR SPHERES AND HEMISPHERES.	(4.a1) ✓ $I = 2\pi r_0^2 j_r$ (4.2) ✓ $I = \frac{4\sqrt{2}\epsilon_0}{9} \sqrt{\frac{e}{m}} \frac{V^{3/2}}{a^2}$ LARGER SPHERE (4.3) ✓ $a^2 = 1.16 (r_0/\sqrt{2}a)^{3/2}$	(4.b) ✓ $j_r = \frac{2\epsilon_0}{9\pi} \sqrt{\frac{2e}{m}} \frac{(\sqrt{2}aV)^{3/2}}{r_0^2 a^2}$	(4.c) * $r_0 = \left[\frac{4\epsilon_0}{\sqrt{109} \pi e} \right]^{2/7} \frac{(\sqrt{2}aV)^{3/7}}{(N)^{2/7} (kT)^{1/7}}$ 105.21

APPENDIX D. TABLE 1 - (ALL SPECIFIED RELATIONS ARE IN MKS UNITS. ✓ THESE RELATIONS ARE FOR ELECTRONS OF MASS m . FOR IONS MULTIPLY R.H.S. OF CURRENT BY $\sqrt{\frac{m}{M}}$; M BEING THE MASS OF THE IONS. * ALL VALUES OF kT ARE IN UNITS OF eV).

APPENDIX E

- (5.0) p = IMPACT PARAMETER, $cm = a \sqrt{1 + \frac{qV}{E}}$
 V = APPLIED VOLTAGE
 r = SPACE CHARGE SHEATH RADIUS, m
 E = ENERGY IN, $eV = kT$
 j_r = RANDOM THERMAL CURRENT DENSITY, $amps/m^2$
 a = PROBE RADIUS, m
 L = PROBE LENGTH, m
 q = ELECTRONIC OR IONIC CHARGE

TABLE 2

ORBIT LIMITED CURRENT	$P < R_0 < P$	SPACE CHARGE LIMITED CURRENT
(5.1b) —————	PLANAR GEOMETRY	$I = j_r$ (5.1a)
(5.2b) $i = 4\pi p^2 j_r$	SPHERICAL GEOMETRY	$i = 4\pi R_0^2 j_r$ (5.2a)
(5.4B) $i = 2\pi p L j_r$	CYLINDRICAL GEOMETRY	$i = 2\pi R_0 L j_r$ (5.3a)
(5.4B) $i = 2\pi p^2 j_r$	HEMISPHERICAL GEOMETRY	$i = 2\pi R_0^2 j_r$ (5.4a)

FIGURE E-1.

APPENDIX F

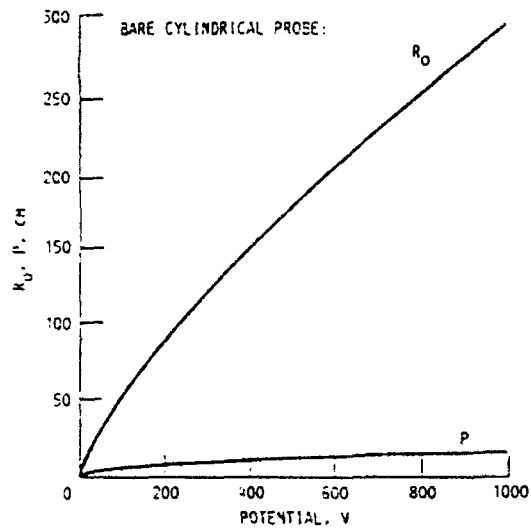


FIGURE F-1. - PLANAR CHARGE SHEATH APPLIED TO A CYLINDRICAL PROBE GEOMETRY.

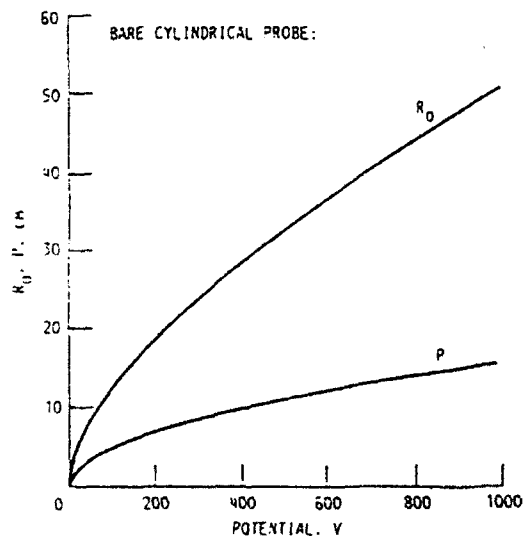


FIGURE F-2. - CYLINDRICAL CHARGE SHEATH APPLIED TO A CYLINDRICAL PROBE GEOMETRY.

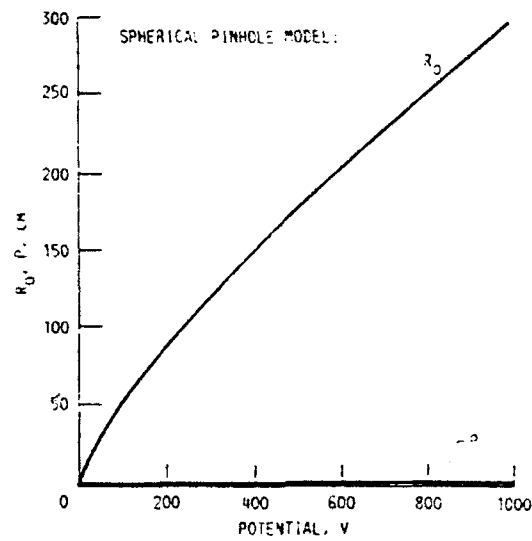


FIGURE F-3. - PLANAR CHARGE SHEATH APPLIED TO A SPHERICAL PINHOLE GEOMETRY.

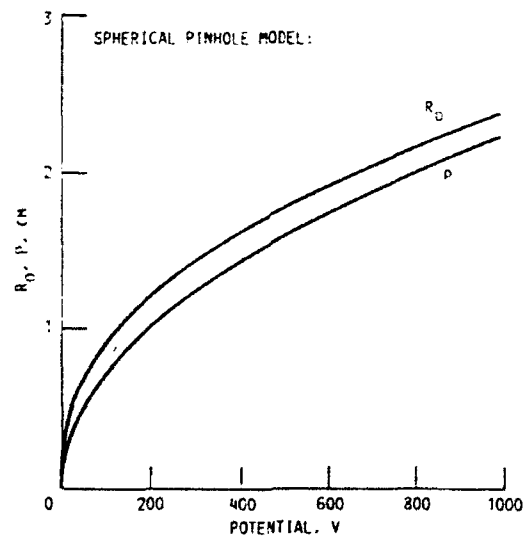


FIGURE F-4. - SPHERICAL CHARGE SHEATH APPLIED TO A SPHERICAL PINHOLE GEOMETRY.

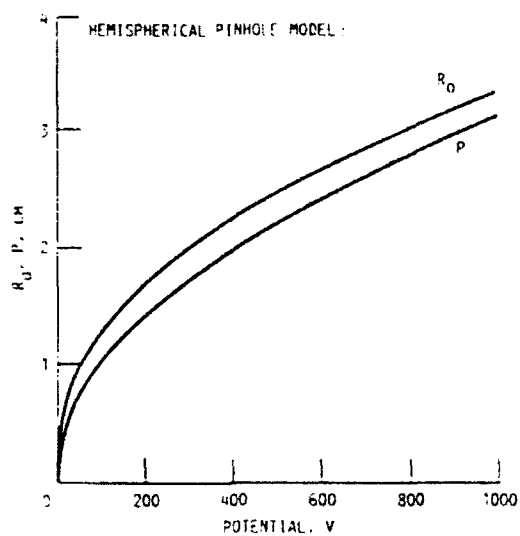
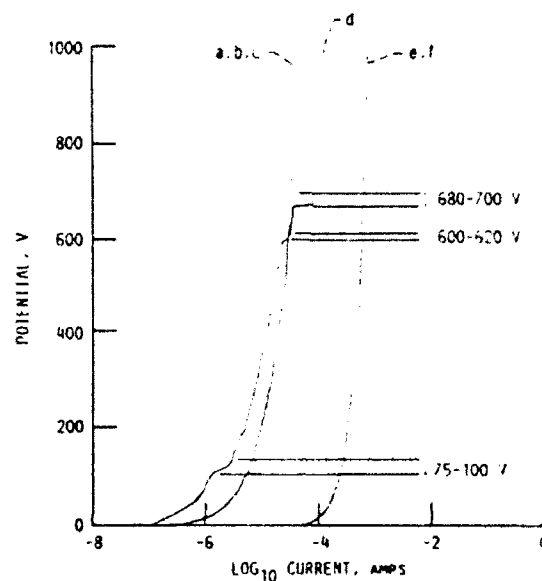


FIGURE F-5. - HEMISPHERICAL CHARGE SHEATH APPLIED TO A HEMISPHERICAL PINHOLE GEOMETRY.



- (a) ORBIT LIMITED CURRENT RESULTING FROM A PLANAR SPACE CHARGE SHEATH THICKNESS BEING APPLIED TO A SPHERICAL PINHOLE CURRENT.
- (b) ORBIT LIMITED CURRENT RESULTING FROM A SPHERICAL SPACE CHARGE SHEATH THICKNESS BEING APPLIED TO A SPHERICAL PINHOLE CURRENT.
- (c) ORBIT LIMITED CURRENT RESULTING FROM A HEMISPHERICAL SPACE CHARGE SHEATH THICKNESS BEING APPLIED TO A HEMISPHERICAL PINHOLE CURRENT.
- (d) NASCAP/LED PREDICTED CURRENT FOR AN INSULATED CABLE WITH A SINGLE PINHOLE.
- (e) ORBIT LIMITED CURRENT RESULTING FROM A PLANAR SPACE CHARGE SHEATH THICKNESS BEING APPLIED TO A CYLINDRICAL PROBE CURRENT (SAME OVERALL DIMENSIONS AS NASCAP/LED OBJECT).
- (f) ORBIT LIMITED CURRENT RESULTING FROM A CYLINDRICAL SPACE CHARGE SHEATH THICKNESS BEING APPLIED TO A CYLINDRICAL PROBE CURRENT (SAME OVERALL DIMENSIONS AS NASCAP/LED OBJECT).

FIGURE F-6.

APPENDIX G

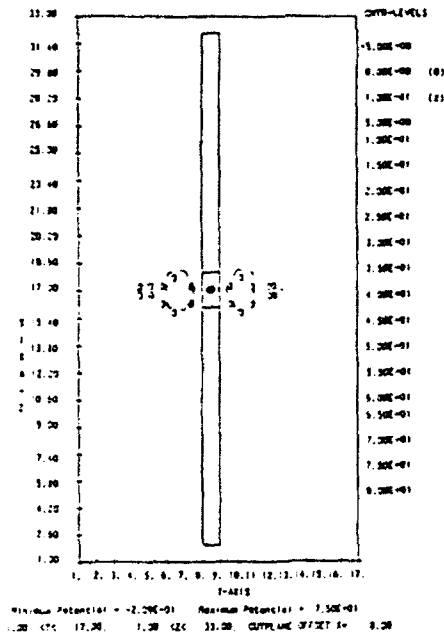


FIGURE G-1(a).

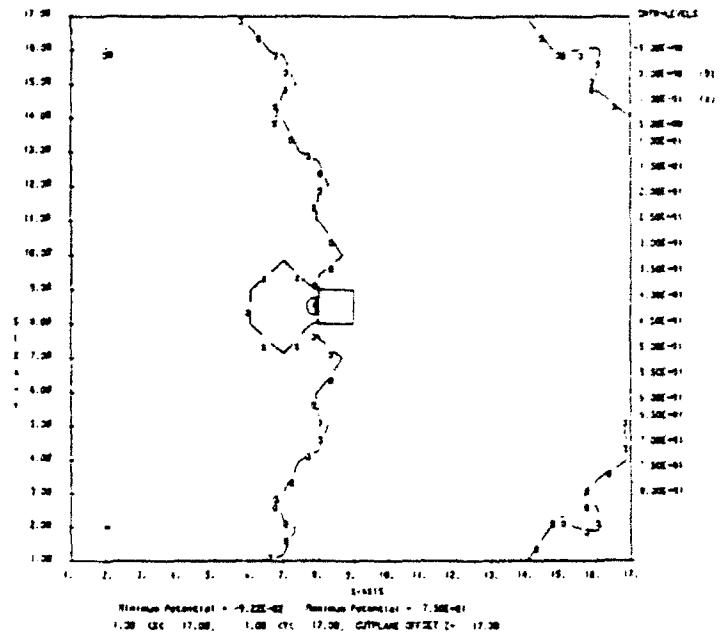


FIGURE G-1(b).

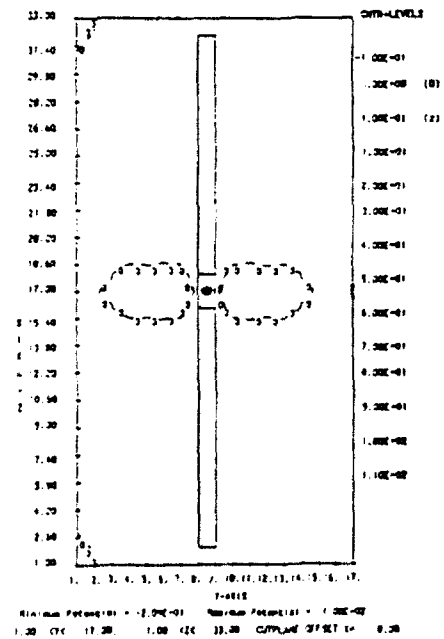


FIGURE G-2(a).

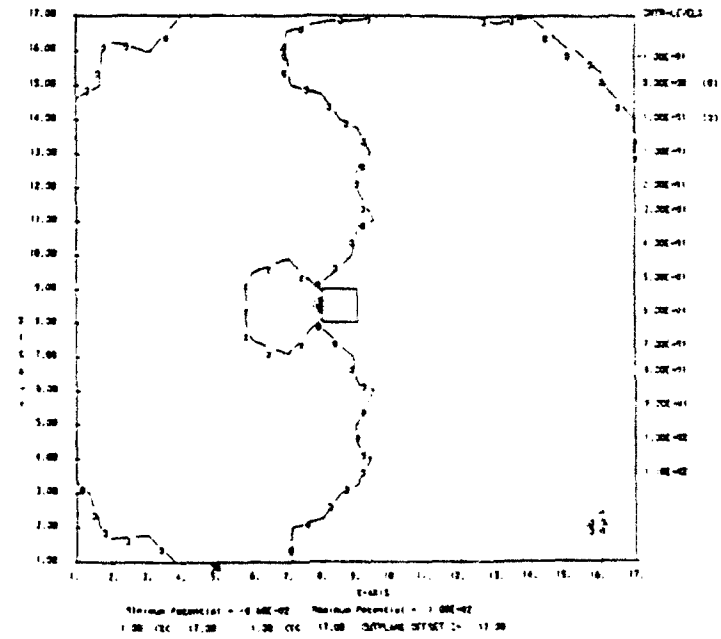


FIGURE G-2(b).

229	230	231	232	233	234	235	236	237	238	239	240	241	242	243	244
213	214	215	216	217	218	219	220	221	222	223	224	225	226	227	228
197	198	199	200	201	202	203	204	205	206	207	208	209	210	211	212
183	184	185	186	187	188	189	247	248	190	191	192	193	194	195	196
169	170	171	172	173	174	175	245	246	176	177	178	179	180	181	182
163	164	165	166	167	168	169	160	161	162	163	164	165	166	167	168
137	138	139	140	141	142	143	144	145	146	147	148	149	150	151	152
121	122	123	124	125	126	127	128	129	130	131	132	133	134	135	136

FIGURE G-1(c).

004	008	012	016	020	024	028	032	036	040	044	048	052	056	060	064
-----	-----	-----	-----	-----	-----	-----	-----	-----	-----	-----	-----	-----	-----	-----	-----

BACK

003	007	011	015	019	023	027	031	035	039	043	047	051	055	059	063
-----	-----	-----	-----	-----	-----	-----	-----	-----	-----	-----	-----	-----	-----	-----	-----

BO-CW

002	006	010	014	018	022	026	030	034	038	042	046	050	054	058	062
-----	-----	-----	-----	-----	-----	-----	-----	-----	-----	-----	-----	-----	-----	-----	-----

TOP

005	009	013	017	021	025	029	033	037	041	045	049	053	057	061	065
-----	-----	-----	-----	-----	-----	-----	-----	-----	-----	-----	-----	-----	-----	-----	-----

FRONT

☐ $-1 < V \leq 0$
☐ $0 < V \leq +1$
☐ $+1 < V \leq +10$
☐ $+10 < V \leq +100$
☐ $+100 < V \leq +1000$

229	230	231	232	233	234	235	236	237	238	239	240	241	242	243	244
213	214	215	216	217	218	219	220	221	222	223	224	225	226	227	228
197	198	199	200	201	202	203	204	205	206	207	208	209	210	211	212
183	184	185	186	187	188	189	247	248	190	191	192	193	194	195	196
169	170	171	172	173	174	175	245	246	176	177	178	179	180	181	182
163	164	165	166	167	168	169	160	161	162	163	164	165	166	167	168
137	138	139	140	141	142	143	144	145	146	147	148	149	150	151	152
121	122	123	124	125	126	127	128	129	130	131	132	133	134	135	136

FIGURE G-2(c).

004	008	012	016	020	024	028	032	036	040	044	048	052	056	060	064
-----	-----	-----	-----	-----	-----	-----	-----	-----	-----	-----	-----	-----	-----	-----	-----

BACK

003	007	011	015	019	023	027	031	035	039	043	047	051	055	059	063
-----	-----	-----	-----	-----	-----	-----	-----	-----	-----	-----	-----	-----	-----	-----	-----

BO-CW

002	006	010	014	018	022	026	030	034	038	042	046	050	054	058	062
-----	-----	-----	-----	-----	-----	-----	-----	-----	-----	-----	-----	-----	-----	-----	-----

TOP

005	009	013	017	021	025	029	033	037	041	045	049	053	057	061	065
-----	-----	-----	-----	-----	-----	-----	-----	-----	-----	-----	-----	-----	-----	-----	-----

FRONT

FIGURE G-2(d)

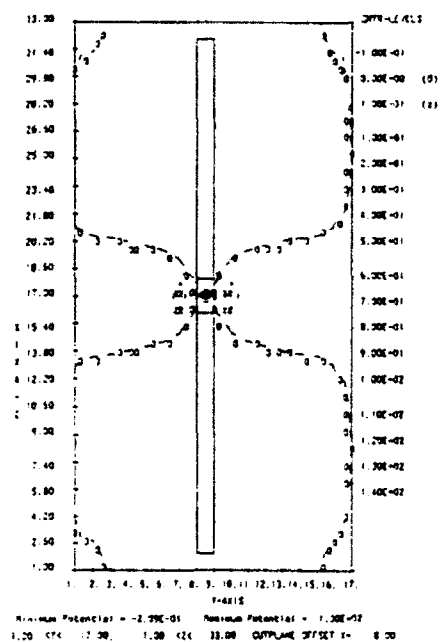


FIGURE G-3(a).

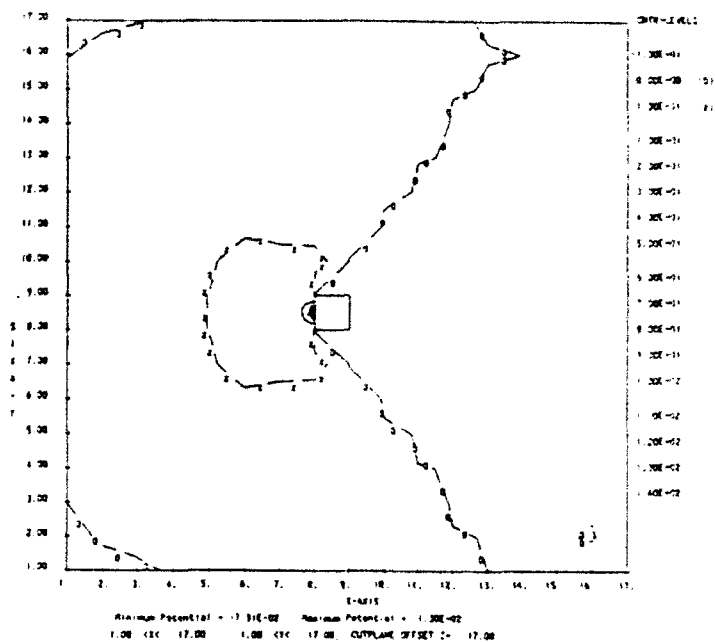


FIGURE G-3(b).

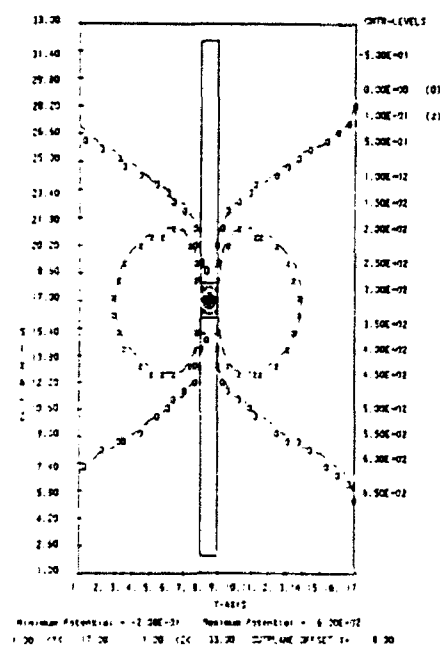


FIGURE G-4(a).

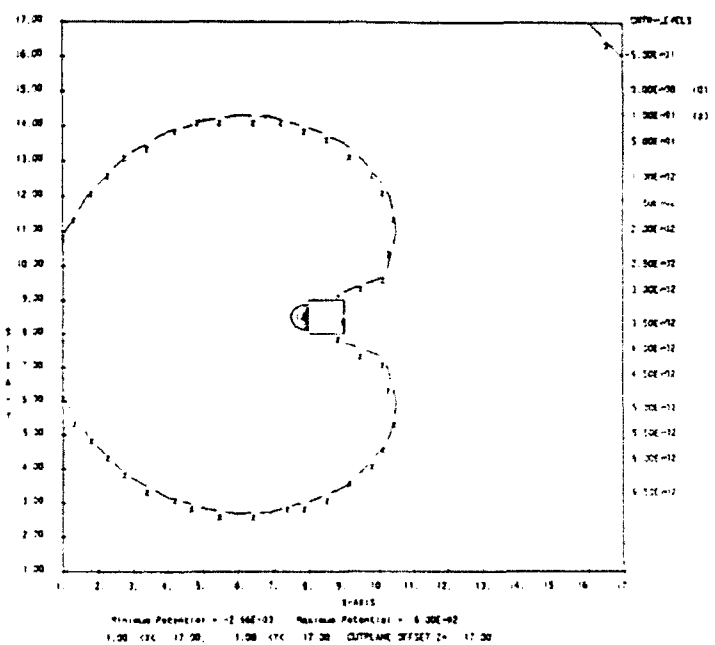
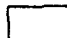



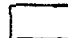
FIGURE G-4(b).


229	230	231	232	233	234	235	236	237	238	239	240	241	242	243	244
213	214	215	216	217	218	219	220	221	222	223	224	225	226	227	228
197	198	199	200	201	202	203	204	205	206	207	208	209	210	211	212
183	184	185	186	187	188	189	247	248	190	191	192	193	194	195	196
169	170	171	172	173	174	175	245	246	176	177	178	179	180	181	182
163	164	165	166	167	168	169	180	181	182	183	184	185	186	187	188
137	138	139	140	141	142	143	144	145	146	147	148	149	150	151	152
121	122	123	124	125	126	127	128	129	130	131	132	133	134	135	136


FIGURE G-3(c).

 $-1 < V \leq 0$

 $0 < V \leq +1$

 $+1 < V \leq +10$

 $+10 < V \leq -100$

 $+100 < V \leq -1000$

229	230	231	232	233	234	235	236	237	238	239	240	241	242	243	244
213	214	215	216	217	218	219	220	221	222	223	224	225	226	227	228
197	198	199	200		202	203	204	205	206	207	208	209	210	211	212
183	184	185	186	187	188	189	247	248	190	191	192	193	194	195	196
169	170	171	172	173	174	175	245	246	176	177	178	179	180	181	182
163	164	165	166	167	168	169	180	181	182	183	184	185	186	187	188
137	138	139	140	141	142	143	144	145	146	147	148	149	150	151	152
121	122	123	124	125	126	127	128	129	130	131	132	133	134	135	136

FIGURE G-4(c).

004	008	012	016	020	024	028	032	036	040	044	048	052	056	060	064	068	072	076	080	084	088	092	096	100	104	108	112	116	120
-----	-----	-----	-----	-----	-----	-----	-----	-----	-----	-----	-----	-----	-----	-----	-----	-----	-----	-----	-----	-----	-----	-----	-----	-----	-----	-----	-----	-----	-----

BACK

003	007	011	015	019	023	027	031	035	039	043	047	051	055	059	063	067	071	075	079	083	087	091	095	099	103	107	111	115	119
-----	-----	-----	-----	-----	-----	-----	-----	-----	-----	-----	-----	-----	-----	-----	-----	-----	-----	-----	-----	-----	-----	-----	-----	-----	-----	-----	-----	-----	-----

BOTTOM

002	006	010	014	018	022	026	030	034	038	042	046	050	054	058	062	066	070	074	078	082	086	090	094	098	102	106	110	114	118
-----	-----	-----	-----	-----	-----	-----	-----	-----	-----	-----	-----	-----	-----	-----	-----	-----	-----	-----	-----	-----	-----	-----	-----	-----	-----	-----	-----	-----	-----

TOP

005	009	013	017	021	025	029	033	037	041	045	049	053	057	061	065	069	073	077	081	085	089	093	097	101	105	109	113	117	121
-----	-----	-----	-----	-----	-----	-----	-----	-----	-----	-----	-----	-----	-----	-----	-----	-----	-----	-----	-----	-----	-----	-----	-----	-----	-----	-----	-----	-----	-----

FRONT

FIGURE G-3(d).

004	008	012	016	020	024	028	032	036	040	044	048	052	056	060	064	068	072	076	080	084	088	092	096	100	104	108	112	116	120
-----	-----	-----	-----	-----	-----	-----	-----	-----	-----	-----	-----	-----	-----	-----	-----	-----	-----	-----	-----	-----	-----	-----	-----	-----	-----	-----	-----	-----	-----

BACK

003	007	011	015	019	023	027	031	035	039	043	047	051	055	059	063	067	071	075	079	083	087	091	095	099	103	107	111	115	119
-----	-----	-----	-----	-----	-----	-----	-----	-----	-----	-----	-----	-----	-----	-----	-----	-----	-----	-----	-----	-----	-----	-----	-----	-----	-----	-----	-----	-----	-----

BOTTOM

002	006	010	014	018	022	026	030	034	038	042	046	050	054	058	062	066	070	074	078	082	086	090	094	098	102	106	110	114	118
-----	-----	-----	-----	-----	-----	-----	-----	-----	-----	-----	-----	-----	-----	-----	-----	-----	-----	-----	-----	-----	-----	-----	-----	-----	-----	-----	-----	-----	-----

TOP

005	009	013	017	021	025	029	033	037	041	045	049	053	057	061	065	069	073	077	081	085	089	093	097	101	105	109	113	117	121
-----	-----	-----	-----	-----	-----	-----	-----	-----	-----	-----	-----	-----	-----	-----	-----	-----	-----	-----	-----	-----	-----	-----	-----	-----	-----	-----	-----	-----	-----

FRONT

FIGURE G-4(d).

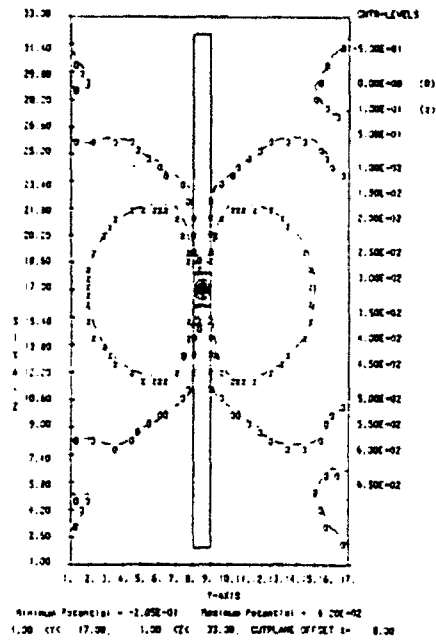


FIGURE G-5(a).

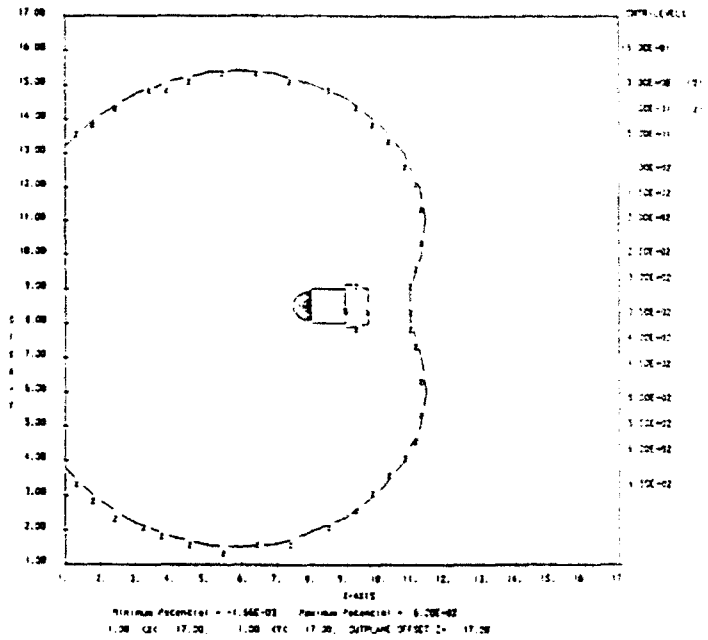


FIGURE G-5(b).

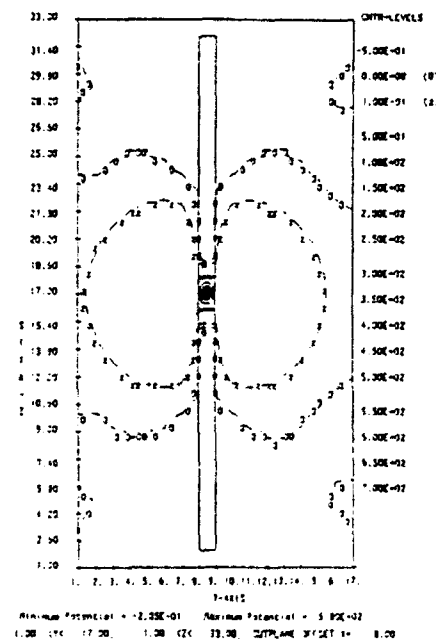


FIGURE G-5(c).

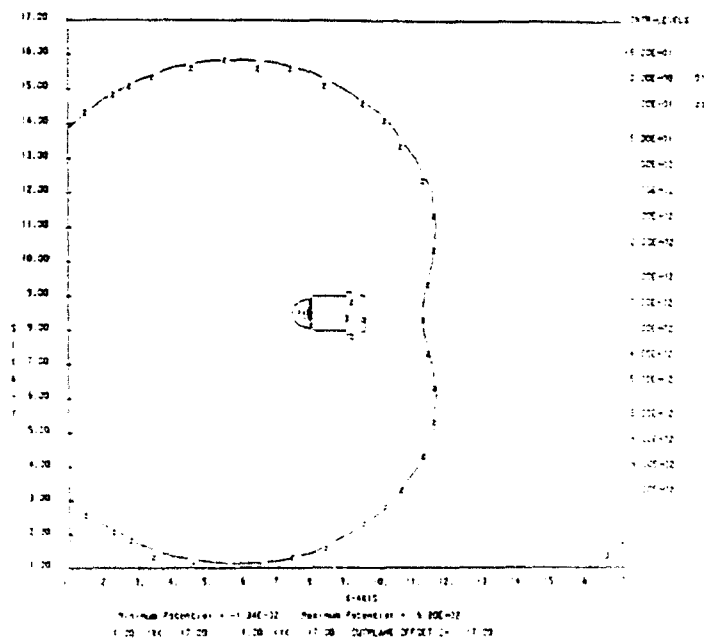


FIGURE G-5(d).

229	230	231	232	233	234	235	236	237	238	239	240	241	242	243	244
213	214	215	216	217	218	219	220	221	222	223	224	225	226	227	228
197	198	199	200	201	202	203	204	205	206	207	208	209	210	211	212
183	184	185	186	187	188	189	247	248	190	191	192	193	194	195	196
169	170	171	172	173	174	175	245	246	176	177	178	179	180	181	182
163	164	165	166	167	168	169	180	181	182	183	184	185	186	187	188
137	138	139	140	141	142	143	144	145	146	147	148	149	150	151	152
121	122	123	124	125	126	127	128	129	130	131	132	133	134	135	136

FIGURE G-5(c).

004	008	012	016	020	024	028	032	036	040	044	048	052	056	060	064	068	072	076	080	084	088	092	096	100	104	108	112	116	120
-----	-----	-----	-----	-----	-----	-----	-----	-----	-----	-----	-----	-----	-----	-----	-----	-----	-----	-----	-----	-----	-----	-----	-----	-----	-----	-----	-----	-----	-----

BACK

003	007	011	015	019	023	027	031	035	039	043	047	051	055	059	063	067	071	075	079	083	087	091	095	099	103	107	111	115	119
-----	-----	-----	-----	-----	-----	-----	-----	-----	-----	-----	-----	-----	-----	-----	-----	-----	-----	-----	-----	-----	-----	-----	-----	-----	-----	-----	-----	-----	-----

BOTTOM

002	006	010	014	018	022	026	030	034	038	042	046	050	054	058	062	066	070	074	078	082	086	090	094	098	102	106	110	114	118
-----	-----	-----	-----	-----	-----	-----	-----	-----	-----	-----	-----	-----	-----	-----	-----	-----	-----	-----	-----	-----	-----	-----	-----	-----	-----	-----	-----	-----	-----

TOP

005	009	013	017	021	025	029	033	037	041	045	049	053	057	061	065	069	073	077	081	085	089	093	097	101	105	109	113	117	121
-----	-----	-----	-----	-----	-----	-----	-----	-----	-----	-----	-----	-----	-----	-----	-----	-----	-----	-----	-----	-----	-----	-----	-----	-----	-----	-----	-----	-----	-----

FRONT

229	230	231	232	233	234	235	236	237	238	239	240	241	242	243	244
213	214	215	216	217	218	219	220	221	222	223	224	225	226	227	228
197	198	199	200	201	202	203	204	205	206	207	208	209	210	211	212
183	184	185	186	187	188	189	247	248	190	191	192	193	194	195	196
169	170	171	172	173	174	175	245	246	176	177	178	179	180	181	182
163	164	165	166	167	168	169	180	181	182	183	184	185	186	187	188
137	138	139	140	141	142	143	144	145	146	147	148	149	150	151	152
121	122	123	124	125	126	127	128	129	130	131	132	133	134	135	136

FIGURE G-6(c).

004	008	012	016	020	024	028	032	036	040	044	048	052	056	060	064	068	072	076	080	084	088	092	096	100	104	108	112	116	120
-----	-----	-----	-----	-----	-----	-----	-----	-----	-----	-----	-----	-----	-----	-----	-----	-----	-----	-----	-----	-----	-----	-----	-----	-----	-----	-----	-----	-----	-----

BACK

003	007	011	015	019	023	027	031	035	039	043	047	051	055	059	063	067	071	075	079	083	087	091	095	099	103	107	111	115	119
-----	-----	-----	-----	-----	-----	-----	-----	-----	-----	-----	-----	-----	-----	-----	-----	-----	-----	-----	-----	-----	-----	-----	-----	-----	-----	-----	-----	-----	-----

BOTTOM

002	006	010	014	018	022	026	030	034	038	042	046	050	054	058	062	066	070	074	078	082	086	090	094	098	102	106	110	114	118
-----	-----	-----	-----	-----	-----	-----	-----	-----	-----	-----	-----	-----	-----	-----	-----	-----	-----	-----	-----	-----	-----	-----	-----	-----	-----	-----	-----	-----	-----

TOP

005	009	013	017	021	025	029	033	037	041	045	049	053	057	061	065	069	073	077	081	085	089	093	097	101	105	109	113	117	121
-----	-----	-----	-----	-----	-----	-----	-----	-----	-----	-----	-----	-----	-----	-----	-----	-----	-----	-----	-----	-----	-----	-----	-----	-----	-----	-----	-----	-----	-----

FRONT

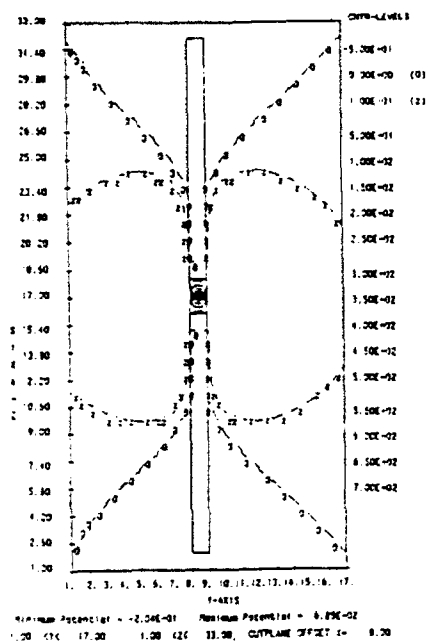


FIGURE G-7(a).

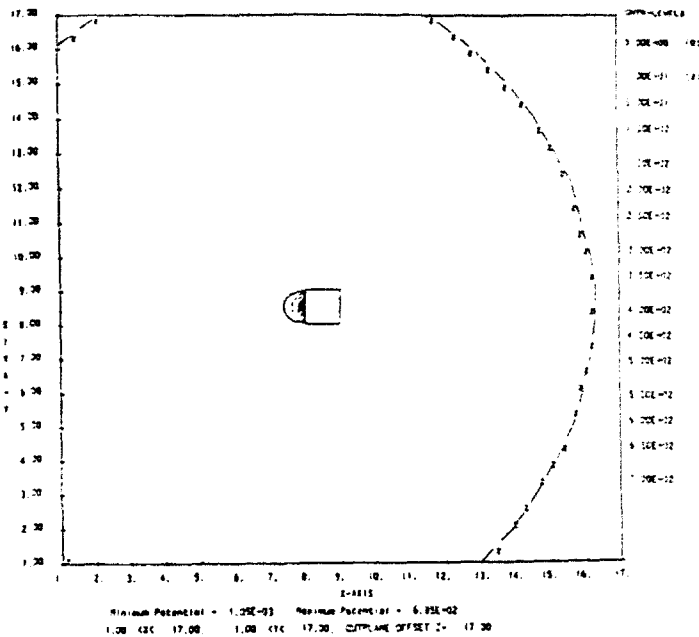


FIGURE G-7(b).

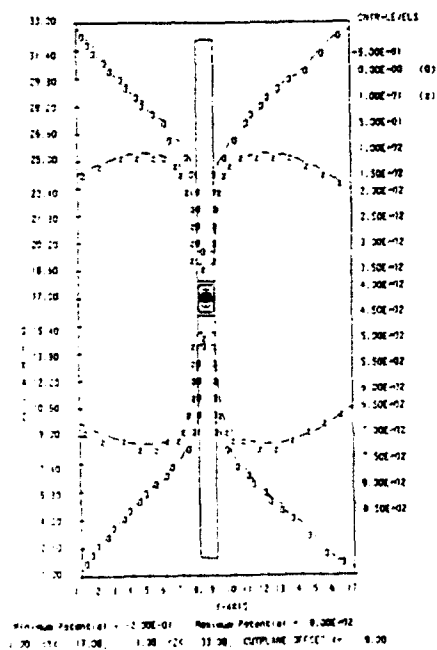


FIGURE G-8(a).

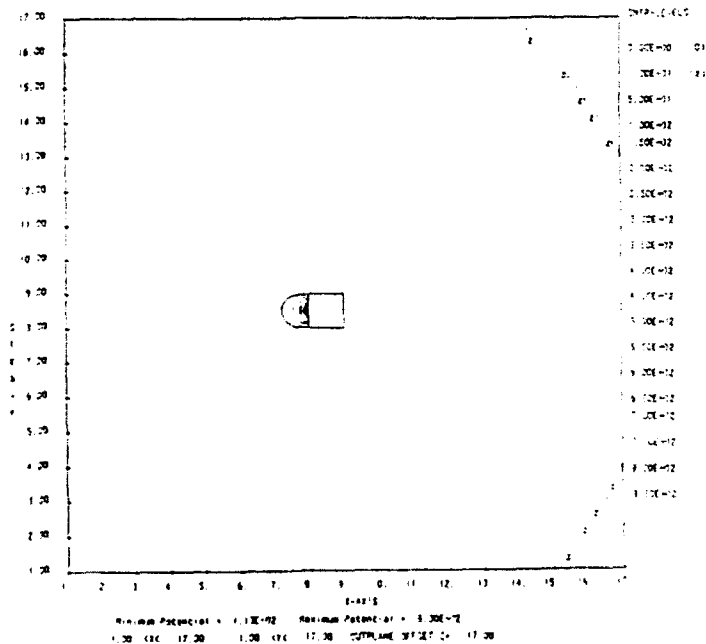


FIGURE G-8(b).

229	230	231	232	233	234	235	236	237	238	239	240	241	242	243	244
213	214	215	216	217	218	219	220	221	222	223	224	225	226	227	228
197	198	199	200	201	202	203	204	205	206	207	208	209	210	211	212
183	184	185	186	187	188	189	247	248	190	191	182	193	194	195	196
169	170	171	172	173	174	175	245	246	176	177	178	179	180	181	182
163	164	165	166	167	168	169	188	189	180	181	182	183	184	185	186
137	138	139	140	141	142	143	144	145	146	147	148	149	150	151	152
121	122	123	124	125	126	127	128	129	130	131	132	133	134	135	136

FIGURE G-7(c).

004	008	012	016	020	024	028	032	036	040	044	048	052	056	060	064
-----	-----	-----	-----	-----	-----	-----	-----	-----	-----	-----	-----	-----	-----	-----	-----

BACK

003	007	011	015	019	023	027	031	035	039	043	047	051	055	059	063
-----	-----	-----	-----	-----	-----	-----	-----	-----	-----	-----	-----	-----	-----	-----	-----

3C-CW

002	006	010	014	018	022	026	030	034	038	042	046	050	054	058	062
-----	-----	-----	-----	-----	-----	-----	-----	-----	-----	-----	-----	-----	-----	-----	-----

OP

005	009	013	017	021	025	029	033	037	041	045	049	053	057	061	065
-----	-----	-----	-----	-----	-----	-----	-----	-----	-----	-----	-----	-----	-----	-----	-----

FRONT

FIGURE G-7(d).

☐ $-1 < V \leq 0$
☐ $0 < V \leq 1$
☐ $+1 < V \leq +10$
☐ $+10 < V \leq +100$
☐ $+100 < V \leq +1000$

229	230	231	232	233	234	235	236	237	238	239	240	241	242	243	244
213	214	215	216	217	218	219	220	221	222	223	224	225	226	227	228
197	198	199	200	201	202	203	204	205	206	207	208	209	210	211	212
183	184	185	186	187	188	189	247	248	190	191	182	193	194	195	196
169	170	171	172	173	174	175	245	246	176	177	178	179	180	181	182
163	164	165	166	167	168	169	188	189	180	181	182	183	184	185	186
137	138	139	140	141	142	143	144	145	146	147	148	149	150	151	152
121	122	123	124	125	126	127	128	129	130	131	132	133	134	135	136

FIGURE G-8(c).

004	008	012	016	020	024	028	032	036	040	044	048	052	056	060	064
-----	-----	-----	-----	-----	-----	-----	-----	-----	-----	-----	-----	-----	-----	-----	-----

BACK

003	007	011	015	019	023	027	031	035	039	043	047	051	055	059	063
-----	-----	-----	-----	-----	-----	-----	-----	-----	-----	-----	-----	-----	-----	-----	-----

3C-CW

002	006	010	014	018	022	026	030	034	038	042	046	050	054	058	062
-----	-----	-----	-----	-----	-----	-----	-----	-----	-----	-----	-----	-----	-----	-----	-----

OP

005	009	013	017	021	025	029	033	037	041	045	049	053	057	061	065
-----	-----	-----	-----	-----	-----	-----	-----	-----	-----	-----	-----	-----	-----	-----	-----

FRONT

FIGURE G-8(d).

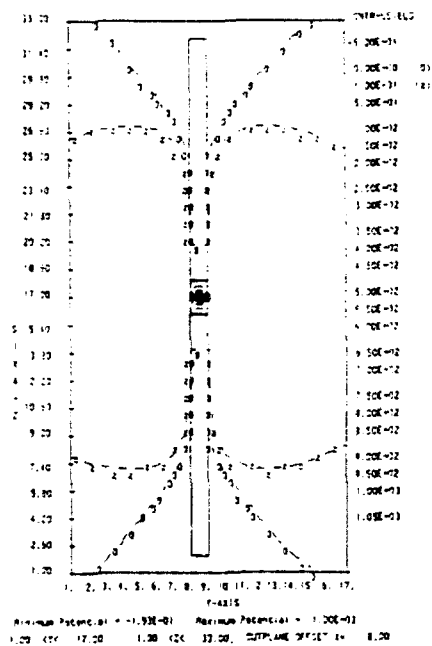


FIGURE G-3(A).

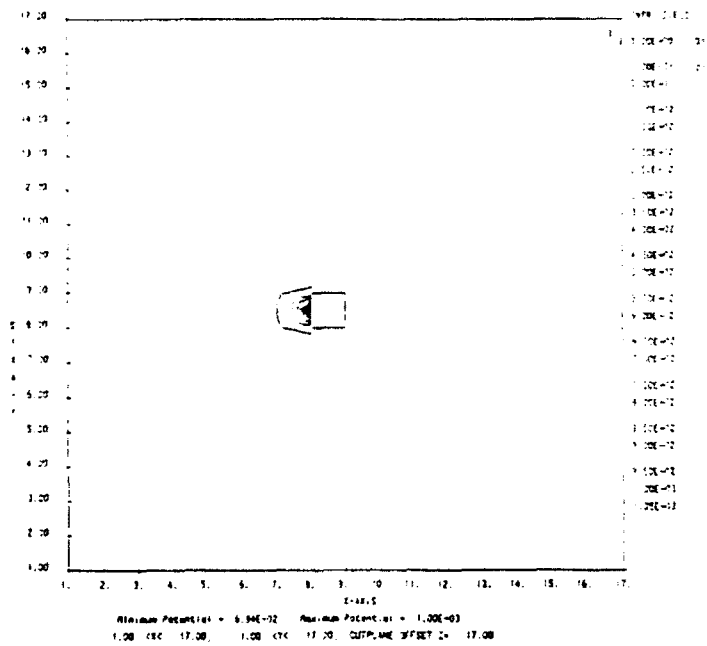


FIGURE G-3(B).

229	230	231	232	233	234	235	236	237	238	239	240	241	242	243	244
213	214	215	216	217	218	219	220	221	222	223	224	225	226	227	228
197	198	199	200	201	202	203	204	205	206	207	208	209	210	211	212
183	184	185	186	187	188	189	247	248	190	191	192	193	194	195	196
169	170	171	172	173	174	175	245	246	176	177	178	179	180	181	182
163	164	165	166	167	168	169	180	181	182	183	184	185	186	187	188
137	138	139	140	141	142	143	144	145	146	147	148	149	150	151	152
121	122	123	124	125	126	127	128	129	130	131	132	133	134	135	136

FIGURE G-9(c).

004	008	012	016	020	024	028	032	036	040	044	048	052	056	060	063	066	070	074	078	082	086	090	094	098	102	106	110	114	119
BACK																													
003	007	011	015	019	023	027	031	035	039	043	047	051	055	059	062	065	069	073	077	081	085	089	093	097	101	105	109	113	118
BOTTOM																													
002	006	010	014	018	022	026	030	034	038	042	046	050	054	058	061	064	068	072	076	080	084	088	092	096	100	104	108	112	117
TOP																													
005	009	013	017	021	025	029	033	037	041	045	049	053	057																
FRONT																													
067	071	075	079	083	087	091	095	099	103	107	111	116	120																

FIGURE G-9(d).

<input type="checkbox"/> $-1 < V \leq 0$	<input type="checkbox"/> $0 < V \leq +1$	<input type="checkbox"/> $+1 < V \leq +10$	<input type="checkbox"/> $+10 < V \leq +100$	<input type="checkbox"/> $+100 < V \leq +1000$
--	--	--	--	--